SISSA

Scuola
Internazionale
Superiore di
Studi Avanzati

Physics Area – Ph.D. course in
Theory and Numerical Simulation of Condensed Matter

Collective Modes and Strong Correlations from a Quantum Gutzwiller Ansatz

Candidate:
Fabio Caleffi

Supervisor:
Prof. Massimo Capone (SISSA)

Referees:
Prof. Alessandro Toschi
(TU Wien)

Prof. Michiel Wouters
(University of Antwerp)

Co-supervisors:
Dr. Alessio Recati
(INO-CNR BEC Center)

Dr. Iacopo Carusotto
(INO-CNR BEC Center)

Academic Year 2021-2022

"We have a habit in writing articles published in scientific journals to make the work as finished as possible, to cover all the tracks, to not worry about the blind alleys or to describe how you had the wrong idea first, and so on. So there is not any place to publish, in a dignified manner, what you actually did in order to get to do the work."

– Richard P. Feynman
The Development of the Space-Time View of Quantum Electrodynamics,
Nobel Lecture (December 11, 1965)

Dedicated to those that were behind
and ahead of me.

Contents

THE QUANTUM GUTZWILLER APPROACH: THEORY AND APPLICATIONS

TOWARDS A THEORY OF QUANTUM FLUCTUATIONS IN A DRIVEN-DISSIPATIVE FLUID OF LIGHT

APPENDIX

Acknowledgements

Here I am: the time has finally come to write the very first, but last page of this intellectual effort. Right now, it seems to me that this will be the hardest blank space to fill, despite the arduous writing path that led me up to this point. This is because I am a wandering type of storyteller: I feel that condensing too much in a tiny place is not always the best option to stick to. Therefore, I have taken my time to express my feelings, before that this part of my life comes to an end. Neither subtle truths nor witty jokes will decorate what follows. Only my flow of consciousness, unfolded as it is.

First of all, I want to express my sincere gratitude to my supervisor, Prof. Massimo Capone, for his constant support and for having always fostered my personal growth and creativity, encouraging my self-determination as a scientist, and listening to my thoughts along the way. A significant role in my scientific formation has been played also by Dr. Alessio Recati, who has been the counterpart of countless physics discussions, and has really helped me build my scientific groove. In third but not the least place, much is due to Dr. Iacopo Carusotto, who accompanied me along my scientific projects with his unique insights and enthusiasm. Furthermore, I want to acknowledge the outstanding contribution of all my collaborators, wonderful people whom I had the honour to meet and work together with: Dr. Inés de Vega, Dr. Victor E. Colussi, Dr. Chiara Menotti and Dr. Florencia M. Ludovico. I want also to express my gratitude to those people who enriched my adventure with their valuable suggestions and expertise: Dr. Lorenzo del Re, Dr. Marco Schiró, Dr. Alberto Biella, Dr. Ivan Amelio and Dr. Marco Di Liberto. I am also very grateful to Prof. Alessandro Toschi and Prof. Michiel Wouters for having read this Thesis meticulously and providing me with their extremely valuable feedback.

The hustle and bustle of everyday hard-work activities is not enough to describe what a life of a Ph.D. student is all about. This is why a major *thank you* is dedicated to my colleagues: Alberto S., who has had the patience to bear many morning-time conversations with me; Vittorio, who has been the inspiration for many keywords and considerations; Martino, the near-desk companion of a number of physical puzzles; moreover, it has been a pleasure to be the colleague of Mandana, Paolo, Riccardo and Philip, who have greatly contributed to make this itinerary a wonderful experience to live.

As it happens in a puzzle, where even small pieces turn out to unveil eye-catching details when put together, other people, ranging from veterans to younger minds, have been important in shaping my days in SISSA: Matteo S., Cristiano, Davide, Claudio, Alberto M., Santo, Matteo F., Andrea R., Zeno, Gabriele. I am particularly indebted to Matteo S., who has introduced me to exciting research directions and, more generally, I consider to be my informal *senpai* (先輩).

Special thanks to three precious people are in order, whose friendship dates back to a long time. Andrea, who has always found time to reach me and listen to my stories, as well as to share belly laughs. Nicola, who has always appreciated my strange facets and encouraged me to look at them through the powerful lens of irony. Thank you guys for gifting me with so much even in the last four years. Last but not least, a heartfelt thank is due to Riccardo, a sincere person to whom I owe the value of a hundred of conversations.

I am extremely proud of writing that who I am is not only due to what I have built for myself, but also what stands behind me, starting from a long time ago. A chest of wisdom and centenary affections, slowly passed to a guy who is understanding them only after years of gangly, inexperienced youth. My parents, Davide and Cristina, deserve much more gratitude than the one that my mind is able to realise. They have been always there for me, making me reflect on my failures (and flaws) and, above all, praising my successes. I love you so much. Giant actors of my travel up to now have been also my grandparents: Ennio, Ave and Danilo. My grandfather Ennio, especially, is probably the person from

whom I inherited the most part of my personality: in retrospect, in spite of the age gap, he has given me the wisest suggestions I could think of. Moreover, I cannot forget to thank those who are not here anymore, and whose lives have a peculiar meaning to me: Rosa, Massimo and Giovanni, thank you from the bottom of my heart. For a couple of reasons that I do not have enough space to write about, I want also to heartfully thank my second uncle Luigi, the smartest old guy that I have ever met.

Finally, I want to speak to the person who has been always on my side and without whom these years would not have had the same colours and tastes. Luana, you mean every second of happiness to me. Even in the darkest moments, you have been akin to the grain of hope at the bottom of Pandora's box. The many evenings warmed by your words, the solid presence of your constant support, the unconditional love which you never missed to show are the most invaluable treasures that I can imagine of in this right moment. All the words that could be written down here are too prosaic to really express what my heart is overflowing with and how much important you have been to my itinerary. Everything that needs to be said has been entrusted to my verses, and to sounds that you only could hear.

"La meta è partire. (The destination is to leave.)" – G. U. (1919)

<div align="right">

Fabio Caleffi
Trieste, November 15, 2022

</div>

Statement of originality

I, Fabio Caleffi, declare under my own responsibility that the content of the present Thesis is a genuine product of my own intellectual work, and that all the scientific collaborators which have supported and took part in my research activity have been properly acknowledged where appropriate.

Moreover, I declare that the unpublished contents of this Thesis are integral part of my sole intellectual property and have not been released elsewhere but in this document.

Finally, I certify that the work hereby reported has not been submitted and will not be submitted, either fully or partially, for the award of any other degree or diploma in either SISSA or any other academic institute.

Trieste, November 15, 2022

Fabio Caleffi

Abstract

The present Thesis aims to deepen the understanding of the physics of strongly-correlated systems along diverse directions with a common denominator, namely a focus on the physical role played by the *collective modes* shaping quantum many-body correlations. This investigation has been mostly led through the heuristic application of the *Quantum Gutzwiller Approach*, a recently developed theory of the quantised excitations above the Gutzwiller approximation for strongly-interacting systems on a lattice.

In the first place, the intertwining between quantum correlations and collective effects is explored in the context of Bose-Hubbard models, intended both as simple yet highly non-trivial realisations of complex many-body scenarios, and as controllable environments for the quantum simulation of impurity problems. In particular, we are able to provide a comprehensive and semi-analytical description of quantum fluctuations across the critical regimes induced by the proximity of a Mott transition (*Mottness*), ranging from accurate predictions for the superfluid density and pair correlations across quantum critical regimes to the Andreev-Bashkin effect in a two-component bosonic mixture.

As case studies for the effectiveness and flexibility of our approach, we give a detailed account of the rich behaviours of a quantum impurity, either fixed or itinerant, immersed in a Bose-Hubbard environment, showing that both the decoherence dynamics of spinful particle and the resulting Bose polaron in the second case are extremely sensitive probes of the type of critical fluctuations experienced by the surrounding system. Additionally, we extend our analysis of quantum fluctuations to the Fermi-Hubbard model, where we uncover the interplay between low-energy quasiparticles and bosonic elementary excitations in determining two-particle correlations.

A more complex physical scenario addressed in this Thesis is represented by *driven-dissipative interacting systems*, which find a state-of-the-art technological implementation in circuit QED platforms, among others. Inspired by the experimental interest in these systems as a potential toolbox for the generation of exotic quantum states of light, we consider a strongly-correlated fluid of photons on a lattice stabilised via incoherent drive and dissipation, and examine its collective fluctuations across the out-of-equilibrium insulator-to-superfluid transition of the system. Specifically, establishing a conceptual parallelism with our approach to fluctuations at equilibrium, we develop a linear-response theory of the excitations on top of the Gutzwiller stationary state of the Lindblad dynamics, and characterise their physical role in quantum observables and response functions. Taking advantage of our formalism, we describe also dynamical instabilities and novel physical regimes arising in the ultrastrong coupling limit of the superfluid phase. Among the most remarkable results, we bring to light the paradoxical nature of the Mott-like insulating phase of the system, whose peculiar one-body dynamical fluctuations are shown to echo the behaviour of a lasing state.

Encompassing diverse modern domains of many-body physics, our investigation goes in the direction of solidifying the interpretation of collective modes as fundamental actors in correlation-induced phenomena under a unified physical picture.

Publications and contributors

The relevant publications included in this Thesis are listed below, together with a brief description of the contribution of the undersigned author when appropriate.

▶ Fabio Caleffi, M. Capone, C. Menotti, I. Carusotto, and A. Recati, *Quantum fluctuations beyond the Gutzwiller approximation in the Bose-Hubbard model*, Physical Review Research **2**, 033276 (20 August 2020)

  Work motivated by the results of the Master's Thesis of the author [1], under the supervision of IC, AR and MC. FC performed the numerical calculations, all the authors substantially contributed to the manuscript.

▶ Fabio Caleffi, M. Capone, I. de Vega, and A. Recati, *Impurity dephasing in a Bose–Hubbard model*, New Journal of Physics **23**, 033018 (15 March 2021)

  Publication resulting from a collaboration with IdV as an expert in the field of open quantum systems. FC performed the numerical calculations, all the authors contributed to the writing process of the manuscript.

▶ V. E. Colussi, Fabio Caleffi, C. Menotti, and A. Recati, *Quantum Gutzwiller approach for the two-component Bose–Hubbard model*, SciPost Physics **12**, 111 (29 March 2022)

  Joint research effort done in collaboration with members of the BEC Center group of the University of Trento. VEC performed the numerical calculations, FC significantly contributed to part of the analytical calculations and understanding the physical content of the results. All the authors were involved in the development of the manuscript.

▶ V. E. Colussi, Fabio Caleffi, C. Menotti, and A. Recati, *Lattice polarons across the superfluid to Mott insulator transition*, arXiv:2205.09857 (20 May 2022), Under consideration for publication in Physical Review Letters

  Work born out of a collaboration with members of the BEC Center group of the University of Trento. VEC performed the numerical calculations, FC has developed the analytical description of the system, benchmarked the analytical calculations and provided theory support. All the authors contributed to editing the manuscript.

▶ Fabio Caleffi, and M. Capone, *Slave boson fluctuations and collective modes from a quantum Gutzwiller ansatz*, In preparation (2022)

▶ Fabio Caleffi, M. Capone, and I. Carusotto, *Collective excitations of a strongly-correlated non-equilibrium photon fluid across the Mott/superfluid phase transition*, In preparation (2022)

  Work done in collaboration with IC as an expert in the field of driven-dissipative photonic systems. FC has performed the numerical calculations and proposed physical interpretations for the results under the supervision of the other authors.

► V. E. Colussi, <u>Fabio Caleffi</u>, C. Menotti, and A. Recati, *Properties of the polaron cloud in a Bose-Hubbard lattice*, In preparation (2022)

      Work done in synergy with members of the BEC Center group of the University of Trento. VEC has performed the numerical calculations, both VEC and <u>FC</u> have contributed to designing the analytical description of the polaron properties of interest. G. M. Bruun and I. Bloch are acknowledged for having inspired the research targets of the work.

► <u>Fabio Caleffi</u>, M. Capone, I. Carusotto, *Phase diagram of a non-equilibrium Bose-Einstein condensate of exciton-polaritons*, Project under definition (2022)

      Project under construction in collaboration with IC as a leading expert in the field of exciton-polariton condensates. The analytical material derived by <u>FC</u> has been obtained as an unexpected branch of the work done on driven-dissipative photonic lattices.

The following work is not included in the present Thesis and will be the subject of a future publication.

► <u>Fabio Caleffi</u>, M. Stefanini, M. F. Ludovico, and M. Capone, *Quantum fluctuations behind the Coulomb drag in coupled quantum dots*, In preparation (2022)

      Work done in collaboration with MFL as an expert in the field of transport phenomena involving interacting quantum dots. <u>FC</u> and MS have developed the theoretical framework and performed the numerical calculations, MFL has provided the theory support.

Motivation and plan of the thesis

Ubiquitously present in the numerous fields of condensed matter physics, collective excitations are abstract physical entities which do not incorporate individual particles, but involve a cooperative and wave-like motion of many particles simultaneously. Ergo, the very concept of collective mode represents the nucleus of the many-body problem, building on the general idea that describing the physics of many interacting objects cannot overlook their mutual correlations, even when the latter are weak. In the realm of quantum systems, typical examples of collective effects include modes of atomic vibrations (phonons), magnetic oscillations (magnons), and composite electronic objects (excitons and Cooper pairs). From an experimental perspective, understanding the dynamics of these modes has far-reaching implications, since collective excitations give direct access to the intrinsic strength and space-time character of quantum correlations. At the same time, collective behaviours lie at the origin of an uncountable number of phenomena, being the mediators of dynamical instabilities, phase transitions, and more elusive crossovers. Besides their fundamental relevance, harnessing collective excitations appear to be also promising and flexible tools for future technological applications, especially in relation to energy warehousing strategies and health sciences, as well as in the rapidly growing field of quantum information and computing as regards data storage and signal processing protocols. In the latter case, trailblazing goals include the engineering of novel devices where collective modes can be efficiently generated, manipulated, and detected [2–4], similarly to what occurs in electronics and photonics with more physically intuitive objects as electrons and photons, respectively.

In this Thesis, we take into consideration the collective modes problem in the rich landscape of quantum many-body lattice systems and, in order to deal with the challenging complexity of such scenarios, we propose novel methodologies to access quantum fluctuations with a minimal computational effort based on a simple yet effective theory of collective excitations themselves. In doing so, we will start from the seminal lesson of Bogoliubov on low-energy excitations of *weakly-interacting* degenerate systems [5, 6] to propose a more general scheme designed for *strong correlations*. Primary tool of this theoretical operation will be the so-called Gutzwiller approximation [7–11], which has been proven to interpolate between diverse interaction regimes in a broad range of physical situations, ranging from e.g. the description of quantum critical systems [12, 13] to time-dependent problems [14, 15] and dissipative processes [16, 17]. More specifically, in the same way as Bogoliubov's theory takes into account small fluctuations on top of a macroscopic coherent field describing the whole system, our scheme aims at capturing (small) quantum fluctuations living above the Gutzwiller wave function, which is assumed to be a sort of fictitious condensate of the effective bosonic degrees of freedom of the system.

In addition to probing the footprint of different manifestations of strong correlations in the collective behaviour of a many-body system, the common denominator of all the applications illustrated in this Thesis is the special attention paid to the essential features of Mottness in the exemplary case of Hubbard models, intended as a paradigm of the impact of strong interactions on the quantum-coherent character of a lattice system. Indeed, aside from analysing in detail the spectral properties of Mott insulating regimes, the present Thesis has the goal of addressing more fundamental questions concerning the influence of Mott localisation on the elementary excitations of the surrounding quantum-degenerate (superfluid) or metallic phases and, most importantly, on how collective effects mould actual quantum observables of common interest. In this respect, we will illustrate that specific types of quantum correlations, comprising i.e. the superfluid density in bosonic systems and dynamical correlations to mention a few, can represent accurate probes of the structural changes of collective modes due to strong

correlations. Confirming long-standing physical intuitions [18], this will be shown to particularly apply to the state of quantum impurities interacting with the excitations of correlated environments realised in ultracold atomic gases, a scenario that naturally generalises the archetypal electron-phonon coupling occurring in real materials. From a more fundamental point of view, we will also spot several curious analogies between the collective modes of the bosonic and fermionic formulations of the Hubbard model, implicitly suggesting the existence of a close relationship between the two manifestations of Mottness. A consistent part of the Thesis will be also devoted to show how the introduction of engineered dissipation mechanisms strongly modifies the Hubbard scenario at equilibrium in the presence of strong correlations. The out-of-equilibrium competition between coherence and interactions will be examined in the thriving context of driven-dissipative arrays of optical cavities, where the problem of stabilising insulating phases of the Mott class is an experimental challenge that has attracted an enormous attention in recent years [19–25]. Here, both the Mott state and its opponent (superfluid) phase will be shown to have surprising collective properties, which in the former case translate into a striking discrepancy with respect to the dynamical correlations of a standard Mott insulator.

The Thesis is organised in two distinct Parts, revolving around different but closely related research directions inspired by the above motivations. Part I deals with the development of the Quantum Gutzwiller Approach in the context of Hubbard models at equilibrium and, in the bosonic case, its heuristic application to the study of modern impurity problems in a strongly-correlated environment. Part II is dedicated to the physics of out-of-equilibrium quantum fluids of light and, in particular, the collective dynamics of a driven-dissipative lattice of strongly-interacting photons. For the sake of readability, each Part is divided into self-contained Chapters focusing on different yet linked topics and whose comprehension does not require any specific reading order – with the exclusion of Chapter 1 of Part I, introducing the reader to the Quantum Gutzwiller Approach framework. We also anticipate that each Chapter opens with a prefacing Section and ends with a set of conclusive observations. Finally, each Part is closed by a proper Conclusion, as we detail below. Given their volume, this organisation of the Thesis contents has the purpose of giving particular emphasis to the original results discussed herein.

Part I is organised as follows. We preface our discussion with an introduction to the Quantum Gutzwiller Approach for lattice bosons in Chapter 1, illustrating its application to the single-band Bose-Hubbard model. The method is shown to give accurate predictions for non-trivial quantum correlations, ranging from the coherence function to the superfluid density and density fluctuations, across the Mott-to-superfluid transition of the model. Also, the possibility of investigating non-linear effects involving the collective modes of the system is explored. In Chapter 2, the Quantum Gutzwiller Approach is generalised to the binary Bose-Hubbard model. In this case, particular importance is given to the characterisation of different superfluid states and the estimation of density/spin correlations. In Chapters 3 and 4, the predictive power of the method is employed to investigate the physics of both static and mobile impurities immersed in the Bose-Hubbard model. In the former case, the dephasing dynamics of the impurity is qualified from an open quantum system perspective, while the spectral properties of the resulting polaronic quasiparticle are analysed in the latter. In both cases, a detailed account of impurity physics across diverse strongly-interacting and quantum critical regimes is provided. In Chapter 5 the Quantum Gutzwiller Approach is discussed in the framework of the Fermi-Hubbard model in the paramagnetic sector. Besides uncovering the physical role of the collective modes in different observables, the method is also shown to provide a physical understanding of the interaction between such modes and the fermionic quasiparticles of the model. Concluding remarks and future perspectives are finally considered in Chapter 6.

Part II has the following structure. In Chapter 1, we give a brief introduction to out-of-equilibrium superfluids, with particular reference to their realisation in excitation-polariton condensates. A

thorough description of the physical properties of these systems is provided, highlighting in particular those dynamical features which link with the driven-dissipative scenario discussed in Chapter 2. Here, we analyse the collective excitations and Gaussian fluctuations of a strongly-interacting quantum fluid of light realised via non-Markovian pumping and dissipation in a circuit QED configuration. Starting from a Gutzwiller approximation for the non-equilibrium stationary state and the excitation spectrum, we derive a unified picture of the insulating and superfluid phases made possible by our driven-dissipative protocol, suggesting its potential in realising novel forms of quantum correlations inaccessible at equilibrium. We conclude in Chapter 3 with a summary of the main results and intriguing open questions, as well as an outlook to future investigations.

Part I

THE QUANTUM GUTZWILLER APPROACH:
THEORY AND APPLICATIONS

Quantum fluctuations beyond the Gutzwiller approximation in the Bose-Hubbard model

1

This Chapter is a review of selected results of the following works and publications, integrated by unpublished results.

▶ Fabio Caleffi, M. Capone, C. Menotti, I. Carusotto, and A. Recati, *Quantum fluctuations beyond the Gutzwiller approximation in the Bose-Hubbard model*, Master's Degree Thesis (24 October 2018)

▶ Fabio Caleffi, M. Capone, C. Menotti, I. Carusotto, and A. Recati, *Quantum fluctuations beyond the Gutzwiller approximation in the Bose-Hubbard model*, Physical Review Research **2**, 033276 (20 August 2020)

1.1 Introduction

The Hubbard model is one of the most celebrated models of quantum condensed matter theory. In all probability, the main reason lies in widespread belief that its two-dimensional fermionic version holds the key to understand how high-temperature superconductivity emerges upon doping a Mott insulator [26, 27]. Its central feature is the competition between the kinetic energy term, which favours delocalized states, and the local Coulomb repulsion, which on the contrary favours localization [28, 29]. In the two-dimensional fermionic model, this physics is however somewhat hidden by the presence of other phases bridging between the Mott insulator, the superconducting and the metallic states, including the celebrated pseudogap [30] and charge-ordered [31] phases.

The archetypal competition between the kinetic and interaction energies finds a particularly neat realisation in the bosonic version of the model, the so-called Bose-Hubbard (BH) model [32], where it manifests itself as a direct quantum phase transition between a superfluid and a Mott insulator. As a consequence of its paradigmatic nature, this transition has attracted an enormous experimental interest in the last years, fostering implementations with cold atoms trapped in optical lattices [33–40] and, more recently, implementations with photons in the novel context of non-equilibrium phase transitions [25, 41, 42], around which Part II of the Thesis will revolve.

On the theoretical side, a very popular approach to the BH model is based on the Gutzwiller ansatz [11, 43]. While many important features of both the superfluid and the insulating phases are accurately captured by the Gutzwiller wave function, its local, site-factorized form typically makes physical quantities involving off-site quantum correlations to be missed. In the weakly-interacting regime, a Bogoliubov approach for the fluctuations around the mean-field Gross-Pitaevskii ground state of a dilute Bose-Einstein Condensate (BEC) provides an accurate description of the equilibrium state and of the excitations of the gas [40, 44], including quantum correlations between particles [45]. In the strongly-interacting regime, however, mean-field theory and the Bogoliubov approach based on it become clearly inadequate. The rich physics of the strongly interacting BH model across the Mott-superfluid transition and specifically in the insulating phase has been attacked through a number of different approaches, rang-

ing from semi-analytical methods as RPA [46–48], Slave Boson (SB) representations [49, 50] and the time-dependent Gutzwiller approximation [51, 52] to numerical techniques including Quantum Monte Carlo (QMC) methods [53–56], bosonic Dynamical Mean-Field Theory (DMFT) [57–59] and Numerical Renormalization Group (NRG) [60, 61]. All these methods provide qualitatively concordant results on the phase diagram as well as on the spectral properties of the model. The collective phonon excitations of the Bogoliubov theory of dilute condensates are replaced by a multi-branch spectrum of excitations [48, 51, 52, 62], containing in particular the gapless Goldstone mode and a gapped (improperly refereed to as Higgs) mode on the superfluid side and the particle/hole excitations in the insulating phase (see e.g. [52, 63, 64]).

In spite of these remarkable advances, a complete, easily tractable and physically intuitive description of the collective excitations and their fingerprint on quantum observables across the whole phase diagram of the model is still lacking. In particular, the development of non-local correlations across the Mott-superfluid transition and the proper characterization of the strongly-interacting superfluid state and of its excitation modes remain challenging problems.

In this introductory Chapter, we combine the successful features of the Gutzwiller and Bogoliubov approaches to develop a new strategy to systematically quantize fluctuations on top of the time-dependent Gutzwiller ansatz, which will be termed as the Quantum Gutzwiller Approach (QGA) in the rest of the Thesis. In spite of the local nature of the Gutzwiller state – see Eq. (5.1) below –, its accurate description of the excitations and, in particular, of their zero-point fluctuations allows to correctly reproduce the non-local many-body correlations in the different phases, as well as the different critical behaviours of the commensurate and incommensurate phase transitions [32, 63]. Time-dependent Gutzwiller approaches addressing the linear-response dynamics in the BH model [51] and in lattice Fermi systems [65] have been recently developed. The advantage of our formalism is that it directly includes quantum fluctuations of the collective modes and could naturally incorporate those effects beyond linearised fluctuations that stem from interactions between the normal modes of the system. This is essential to successfully tackle problems such as the finite lifetime of quasiparticles via Beliaev-like non-linear interaction processes and the quantum correlations between the products of their decay, a subject which will be touched in the last Section of this Chapter.

The Chapter is organized as follows. Section 1.2 is devoted to the derivation of the bosonic formulation of the QGA for the BH model. The original features of the method are highlighted and its advantages and disadvantages are discussed in comparison to other approaches. In Section 1.3, we present the predictions of the quantum Gutzwiller method for observables in which local and non-local quantum correlations strongly modify the standard mean-field picture, such as two-point correlation functions, superfluid density and pair correlations. We conclude in Section 1.5 with an outlook on possible extensions of the QGA formalism, laying the premises for the theoretical applications discussed in the next Chapters.

1.2 Quantum Gutzwiller theory of the Bose-Hubbard model

1.2.1 Lagrangian formulation within the Gutzwiller ansatz

Let us consider the BH model on a d-dimensional square lattice with lattice spacing a, governed by the Hamiltonian

$$\hat{H}_{\mathrm{BH}} \equiv -J \sum_{\langle \mathbf{r}, \mathbf{s} \rangle} \left(\hat{a}_{\mathbf{r}}^{\dagger} \hat{a}_{\mathbf{s}} + \mathrm{H.c.} \right) + \frac{U}{2} \sum_{\mathbf{r}} \hat{n}_{\mathbf{r}} \left(\hat{n}_{\mathbf{r}} - 1 \right) - \mu \sum_{\mathbf{r}} \hat{n}_{\mathbf{r}} \,, \qquad (1.1)$$

where J is the hopping energy, U the on-site interaction and μ the chemical potential, while $\langle \mathbf{r}, \mathbf{s} \rangle$ labels all the pairs of nearest-neighboring sites. The annihilation and creation operators of a bosonic particle at site $\mathbf{r}$ are $\hat{a}_{\mathbf{r}}$ and $\hat{a}_{\mathbf{r}}^{\dagger}$ respectively, with $\hat{n}_{\mathbf{r}} \equiv \hat{a}_{\mathbf{r}}^{\dagger} \hat{a}_{\mathbf{r}}$ being the local density operator. In the remainder of the Thesis, we will resort to the notation $z = 2\,d$ to conveniently indicate the coordination number of the square lattice; additionally, we will impose natural physical units as $\hbar = a = 1$.

We introduce the bosonic Gutzwiller ansatz [11, 43, 51]

$$|\Psi_{\mathrm{G}}\rangle \equiv \bigotimes_{\mathbf{r}} \sum_{n} c_n(\mathbf{r}) \, |n, \mathbf{r}\rangle \,, \qquad (1.2)$$

having the form of the most general site-factorised wave function, where the complex amplitudes $c_n(\mathbf{r})$ are variational parameters with normalisation condition $\sum_n |c_n(\mathbf{r})|^2 = 1$. By the ansatz (1.2), we can reformulate the BH model in terms of the following Lagrangian functional,

Gutzwiller ansatz

$$\mathfrak{L}[c, c^*] \equiv \langle \Psi_{\mathrm{G}} | \, i \, \partial_t - \hat{H}_{\mathrm{BH}} \, | \Psi_{\mathrm{G}} \rangle \qquad (1.3)$$
$$= \frac{i}{2} \sum_{\mathbf{r}, n} [c_n^*(\mathbf{r}) \, \dot{c}_n(\mathbf{r}) - \mathrm{c.c.}] + J \sum_{\langle \mathbf{r}, \mathbf{s} \rangle} [\psi^*(\mathbf{r}) \, \psi(\mathbf{s}) + \mathrm{c.c.}] - \sum_{\mathbf{r}, n} H_n \, |c_n(\mathbf{r})|^2 \,.$$

In the previous equation, the dot indicates the temporal derivative,

$$H_n \equiv \frac{U}{2} \, n \, (n-1) - \mu \, n \qquad (1.4)$$

gathers the on-site terms of the Gutzwiller energy functional, and

$$\psi(\mathbf{r}) \equiv \langle \hat{a}_{\mathbf{r}} \rangle = \sum_{n} \sqrt{n} \, c_{n-1}^*(\mathbf{r}) \, c_n(\mathbf{r}) \qquad (1.5)$$

is the mean-field order parameter. Within such formulation, the conjugate momenta of the parameters $c_n(\mathbf{r})$ are given by their complex conjugates $c_n^*(\mathbf{r}) = \partial \mathfrak{L} / \partial \dot{c}_n(\mathbf{r})$. The classical Euler-Lagrange equations associated to the Lagrangian (1.3) are a simple instance of the so-called Time-Dependent Gutzwiller Equations (TDGE) for a bosonic system, as derived e.g. in [46], and from which the excitation spectrum can be determined via linear response theory [51]. In a uniform system, the stationary solutions are homogeneous: in particular, the system is in a Mott Insulator (MI) state if $\psi(\mathbf{r}) = 0$ and in a Superfluid (SF) state otherwise. Moreover, we recall here that the TDGE are identical to the Gross-Pitaevskii Equation (GPE) of a weakly-interacting condensate when $U/J \ll 1$ and, at the same time, describe the dynamics of a perfect Mott state ($J = 0$) exactly [51].
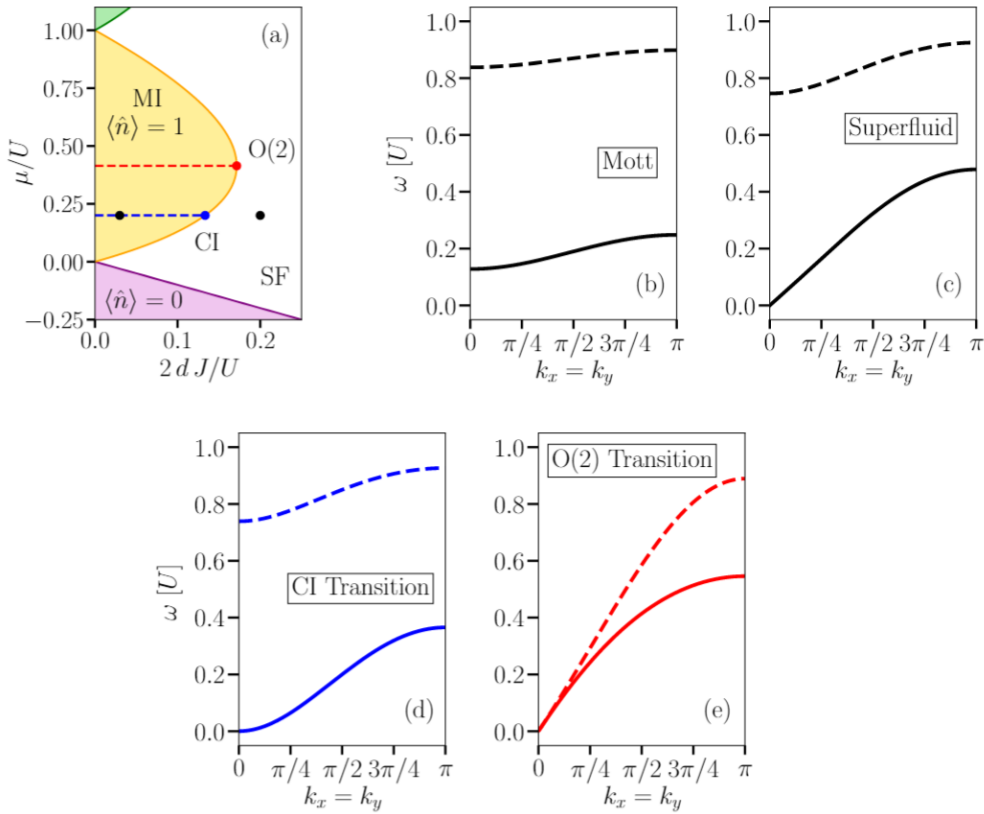
Figure 1.1: (a) Mean-field Gutzwiller phase diagram around the $\langle \hat{n} \rangle = 1$ MI lobe. The black points refer to the MI and SF spectra shown in panels (b)-(c), while the blue and red points indicate the CI and O(2) critical points respectively. (b) Energy spectra of hole (solid line) and particle (dashed line) excitations in the MI phase for $\mu/U = 0.2$ and $2\,d\,J/U = 0.03$. (c) Goldstone mode (solid line) and Higgs mode (dashed line) energy dispersion in the strongly-correlated SF phase for $\mu/U = 0.2$ and $2\,d\,J/U = 0.2$. (d) Excitation spectrum at the CI critical point corresponding to $\mu/U = 0.2$ and $2\,d\,J/U = 0.1\overline{3}$, see the blue dot in panel (a). (e) Excitation spectrum at the O(2)-invariant critical point, see the red dot in panel (a). Both modes become gapless and display a linear dispersion at low momenta.

The spectrum of the collective modes of the system $\omega_{\alpha,\mathbf{k}}$ for $d = 2$ is plotted in Figure 1.1 in different regions of the phase diagram shown in panel (a). In the MI phase [panel (b)], the two lowest excitation branches are the gapped particle and hole excitations. In the SF phase [panel (c)], the lowest of them becomes the gapless Goldstone mode of the broken U(1) symmetry. The other gapped excitation is often referred to as the Higgs mode [52, 64, 66–68] and is related to pure fluctuations of the amplitude of the order parameter in peculiar regions of the phase diagram [52].

The quantum phase transition from the MI to the SF phase can belong to two different universality classes [32, 63] depending on whether the transition is crossed while changing the density – the so-called Commensurate-Incommensurate (CI) transition [blue point in panel (a)] – or it is crossed at a fixed and commensurate filling (at the tip) – formally known as the O(2) transition [red point in panel (a)]. At the CI transition points on the edge of the Mott lobes, only one mode becomes gapless (the Goldstone branch in the SF), whereas the other mode is gapped and continuously connected to the particle or hole branch of the MI depending on the chemical potential [panel (d)]. On the other hand, at the tip critical point both the modes become gapless [panel (e)].

1.2.2 The quantum Gutzwiller theory

In order to go beyond the Gutzwiller ansatz reviewed in the previous Subsection, it is natural to consider how quantum (and thermal) effects populate the excitation modes of the system and to address how they affect the observable quantities. The key idea of the QGA is to include quantum fluctuations by building a theory of the many-body excitations starting from the Lagrangian (1.3) via canonical quantisation [69, 70], namely promoting the coordinates of the Gutzwiller problem and their conjugate momenta to operators and imposing equal-time canonical commutation relations,

$$\left[\hat{c}_n(\mathbf{r}), \hat{c}_m^\dagger(\mathbf{s})\right] = \delta_{n,m}\,\delta_{\mathbf{r},\mathbf{s}}\,. \tag{1.6}$$

In analogy with the number-conserving Bogoliubov approximation for dilute BEC's [44, 71, 72], we expand the operators $\hat{c}_n(\mathbf{r})$ around their ground state values c_n^0, obtained by minimising the energy $\langle\Psi_G|\,\hat{H}_{BH}\,|\Psi_G\rangle$, as

$$\hat{c}_n(\mathbf{r}) = \hat{A}(\mathbf{r})\,c_n^0 + \delta\hat{c}_n(\mathbf{r})\,. \tag{1.7}$$

The *normalisation operator* $\hat{A}(\mathbf{r})$ is a functional of $\delta\hat{c}_n(\mathbf{r})$ and $\delta\hat{c}_n^\dagger(\mathbf{r})$ whose purpose is to restrict the action of the Gutzwiller operators to the physical subspace, in relation with the original normalisation constraint $\sum_n \hat{c}_n^\dagger(\mathbf{r})\,\hat{c}_n(\mathbf{r}) = \hat{\mathbb{1}}$. By restricting to local fluctuations orthogonal to the ground state $\sum_n \delta\hat{c}_n^\dagger(\mathbf{r})\,c_n^0 = 0$, one has

$$\hat{A}(\mathbf{r}) = \left[1 - \sum_n \delta\hat{c}_n^\dagger(\mathbf{r})\,\delta\hat{c}_n(\mathbf{r})\right]^{1/2}\,. \tag{1.8}$$

In a homogeneous system, it is convenient to work in momentum space by writing

$$\delta\hat{c}_n(\mathbf{r}) \equiv \frac{1}{\sqrt{V}}\sum_{\mathbf{k}\in BZ} e^{i\mathbf{k}\cdot\mathbf{r}}\,\delta\hat{C}_n(\mathbf{k})\,, \tag{1.9}$$

where V is the lattice volume and the momentum sum runs over the first Brillouin Zone (BZ). Inserting Eqs. (1.7) and (1.9) in $\langle\Psi_G|\,\hat{H}_{BH}\,|\Psi_G\rangle$ and keeping only terms up to the quadratic order in the fluctuations, we obtain

$$\hat{H}_{QGA} = E_0 + \frac{1}{2}\sum_{\mathbf{k}}\left[\delta\hat{\underline{C}}^\dagger(\mathbf{k}), -\delta\hat{\underline{C}}(-\mathbf{k})\right]\hat{\mathcal{L}}_{\mathbf{k}}\begin{bmatrix}\delta\hat{\underline{C}}(\mathbf{k})\\ \delta\hat{\underline{C}}^\dagger(-\mathbf{k})\end{bmatrix}\,, \tag{1.10}$$

where E_0 is the mean-field ground state energy (apart from a constant shift), the vector $\delta\hat{\underline{C}}(\mathbf{k})$ contains the components $\delta\hat{C}_n(\mathbf{k})$, and $\hat{\mathcal{L}}_{\mathbf{k}}$ is a pseudo-Hermitian matrix [1] of the form

$$\hat{\mathcal{L}}_{\mathbf{k}} = \begin{pmatrix} \mathbf{H}_{\mathbf{k}} & \mathbf{K}_{\mathbf{k}} \\ -\mathbf{K}_{\mathbf{k}}^* & -\mathbf{H}_{\mathbf{k}}^* \end{pmatrix} \tag{1.11}$$

where $\mathbf{H}_{\mathbf{k}}$ and $\mathbf{K}_{\mathbf{k}}$ are matrix blocks of size $n_{max} \times n_{max}$, with n_{max} being the chosen truncated size of the local Fock space. We observe that the minus sign in the second row is a crucial consequence of Bose statistics. The matrix elements of the blocks of $\hat{\mathcal{L}}_{\mathbf{k}}$

---

[1] The spectral properties of matrix operators of the same class of $\hat{\mathcal{L}}_{\mathbf{k}}$ are discussed in depth in Appendix A.1.

are given by

$$H_{\mathbf{k}}^{nm} \equiv \varepsilon_{\mathbf{0}} \left(\psi_0^* \sqrt{m} \, \delta_{n+1,m} + \psi_0 \sqrt{n} \, \delta_{n,m+1} \right) + \left[\frac{U}{2} \, n \, (n-1) - \mu \, n - \omega_0 \right] \delta_{n,m}$$
$$+ \, \varepsilon_{\mathbf{k}} \left[\sqrt{n+1} \sqrt{m+1} \, c_{n+1}^0 \left(c_{m+1}^0 \right)^* + \sqrt{n} \sqrt{m} \, c_{n-1}^0 \left(c_{m-1}^0 \right)^* \right], \qquad (1.12a)$$

$$K_{\mathbf{k}}^{nm} \equiv \varepsilon_{\mathbf{k}} \left(\sqrt{n+1} \sqrt{m} \, c_{n+1}^0 \, c_{m-1}^0 + \sqrt{n} \sqrt{m+1} \, c_{n-1}^0 \, c_{m+1}^0 \right), \qquad (1.12b)$$

where $\varepsilon_{\mathbf{k}} \equiv -z \, J + f_{\mathbf{k}}$ with

$$f_{\mathbf{k}} \equiv 4 \, J \sum_{i=1}^{d} \, \sin \left(\frac{k_i}{2} \right)^2 \qquad (1.13)$$

is defined as the energy of a free particle on a d-dimensional lattice. The ground state energy

$$\omega_0 \equiv -2 \, z \, J \, |\psi_0|^2 + \sum_n \, H_n \left| c_n^0 \right|^2 \qquad (1.14)$$

is set by the classical stationary evolution of the c_n^0's at the mean-field level and, shifting the diagonal elements of $\hat{\mathcal{L}}_{\mathbf{k}}$ as a consequence of the normalisation operator $\hat{A}(\mathbf{r})$, is important to assure a gapless spectrum in the SF phase. A suitable Bogoliubov rotation of the Gutzwiller operators,

$$\delta \hat{C}_n(\mathbf{k}) = \sum_\alpha u_{\alpha,\mathbf{k},n} \, \hat{b}_{\alpha,\mathbf{k}} + \sum_\alpha v_{\alpha,-\mathbf{k},n}^* \, \hat{b}_{\alpha,-\mathbf{k}}^\dagger, \qquad (1.15)$$

recasts the quadratic form (1.10) into a diagonal form,

$$\hat{H}_{\mathrm{QGA}} = \sum_\alpha \sum_{\mathbf{k}} \omega_{\alpha,\mathbf{k}} \, \hat{b}_{\alpha,\mathbf{k}}^\dagger \hat{b}_{\alpha,\mathbf{k}}, \qquad (1.16)$$

where each $\hat{b}_{\alpha,\mathbf{k}}$ ($\hat{b}_{\alpha,\mathbf{k}}^\dagger$) corresponds to a different many-body excitation mode with frequency $\omega_{\alpha,\mathbf{k}}$, labelled by its own momentum $\mathbf{k}$ and branch index α. Bosonic commutation relations between the annihilation and creation operators $\hat{b}_{\alpha,\mathbf{k}}$ and $\hat{b}_{\alpha,\mathbf{k}'}^\dagger$,

QGA Hamiltonian

$$\left[\hat{b}_{\alpha,\mathbf{k}}, \hat{b}_{\alpha',\mathbf{k}'}^\dagger \right] = \delta_{\mathbf{k},\mathbf{k}'} \, \delta_{\alpha,\alpha'}, \qquad (1.17)$$

are enforced by choosing the usual Bogoliubov normalisation condition

$$\underline{u}_{\alpha,\mathbf{k}}^* \cdot \underline{u}_{\beta,\mathbf{k}} - \underline{v}_{\alpha,-\mathbf{k}}^* \cdot \underline{v}_{\beta,-\mathbf{k}} = \delta_{\alpha\beta}, \qquad (1.18)$$

where the vectors $\underline{u}_{\alpha,\mathbf{k}}$ ($\underline{v}_{\alpha,\mathbf{k}}$) gather the components $u_{\alpha,\mathbf{k},n}$ ($v_{\alpha,\mathbf{k},n}$). As a direct consequence of the spectral properties of $\hat{\mathcal{L}}_{\mathbf{k}}$ [2], the fluctuation operators $\delta\hat{c}_n(\mathbf{r})$ and $\delta\hat{c}_n^\dagger(\mathbf{r})$ satisfy quasi-bosonic commutation relations,

$$\left[\delta\hat{c}_n(\mathbf{r}), \delta\hat{c}_m^\dagger(\mathbf{s}) \right] = \left[\delta_{n,m} - c_n^0 \left(c_m^0 \right)^* \right] \delta_{\mathbf{r},\mathbf{s}}. \qquad (1.19)$$

---

[2] We refer the interested reader to Appendix A.2 for a detailed discussion of commutations relations between the quantised modes within the QGA.
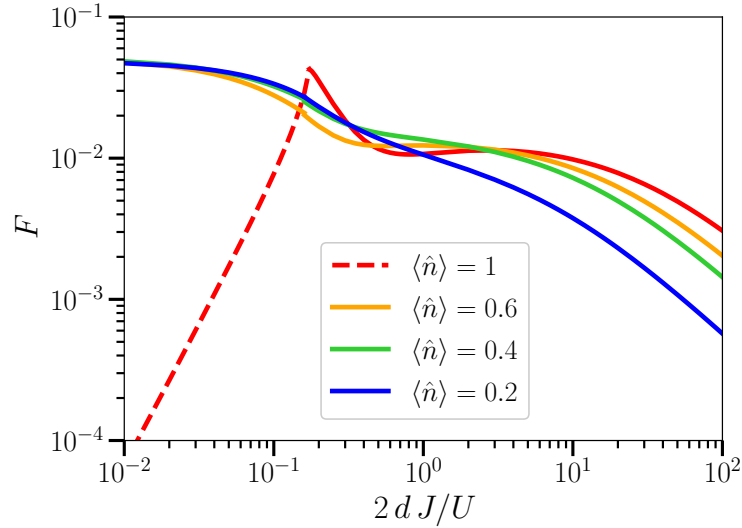
Figure 1.2: Control parameter of the theory F as defined in Eq. (1.20) plotted as a function of $2\,d\,J/U$ for different values of the lattice filling and $d = 3$. Dashed and solid lines indicate whether the system is in a MI state (only for $\langle \hat{n} \rangle = 1$) or in the SF phase, respectively.

The correction term on the right-hand side of Eq. (1.19) serves to remove those unphysical Degrees of Freedom (DoF) that are introduced by the global gauge invariance of the Gutzwiller ansatz (1.2), namely the arbitrariness of the phase of the local wave functions $c_n(\mathbf{r})$ at each site $\mathbf{r}$. Result (1.19) generalises to a strongly-interacting Bose system the formalisation of quantum fluctuations within the celebrated Bogoliubov approach on top of a condensate in a homogeneous weakly-interacting gas [71, 72].

Even though in the next Sections we will focus only on Gaussian fluctuations, the inclusion of terms beyond second order in the $\delta\hat{c}_n$'s arising from the quartic hopping term in Eq. (1.3) does not pose any fundamental difficulty in principle. As in standard Bogoliubov's theory, higher-order terms are expected to describe interactions between collective modes and the resulting decay processes (see e.g. Section III in [73] as a reference). We will touch upon this problem in Section 1.4, where we will investigate the lifetime of the amplitude (Higgs) mode in the strongly-correlated regime.

1.2.3 General remarks on the accuracy of the method

The accuracy of the QGA can be quantitatively estimated by looking at the magnitude of quantum fluctuations around the Gutzwiller mean-field state, quantified by

$$F \equiv 1 - \left\langle \hat{A}(\mathbf{r})^2 \right\rangle = \sum_n \left\langle \delta c_n^\dagger(\mathbf{r})\, \delta c_n(\mathbf{r}) \right\rangle, \qquad (1.20)$$

which represents the small control parameter of our theory [3]. As it is illustrated in Figure 1.2, this quantity remains always very small throughout the phase diagram, suggesting the overall reliability of the QGA: a small value of the magnitude of quantum fluctuations is in fact a good indication that the non-linear terms that are not included

---

[3] Within the standard Bogoliubov approach, the small parameter controlling the accuracy of the theory has the physical meaning of the non-condensed fraction of the gas. Here, it is a mathematical object indicating how much the local wave functions $c_n(\mathbf{r})$ appearing in the Gutzwiller ansatz vary under the effect of quantum fluctuations.

in Eq. (1.10) are indeed "small" and can be neglected.

In particular, for commensurate density, the quantity F approaches zero both in the deep MI (dashed line) and in the deep SF regime, that is in both the limits where the Gutzwiller ansatz recovers exactly the ground state of the BH model. As expected, its maximum is located at the transition point. For non-commensurate densities, F tends to zero in the deep SF regime (where again the Gutzwiller ansatz recovers exactly the ground state) and eventually increases in the strongly-interacting SF regime for decreasing $J/U \to 0$, where the hard-core points of the system are located. Note that this limit does not correspond to a MI and mean-field theory is not able to fully capture the ground state.

1.2.4 Calculation of the observables

In this Subsection, we summarise the protocol that we will use to compute physical observables within the QGA. The evaluation of the expectation value for any observable $\left\langle \hat{O}\left[\hat{a}_{\mathbf{r}}^{\dagger}, \hat{a}_{\mathbf{r}}\right]\right\rangle$ consists in applying the following four-step procedure.

QGA evaluation protocol

1. Determine the expression $\mathsf{O}[c_n, c_n^*] = \langle \Psi_{\mathrm{G}}| \hat{O} |\Psi_{\mathrm{G}}\rangle$ in terms of the Gutzwiller parameters $c_n(\mathbf{r})$ and $c_n^*(\mathbf{r})$.

2. Create the operator $\hat{\mathsf{O}}\left[\hat{c}_n, \hat{c}_n^{\dagger}\right]$ by replacing the Gutzwiller parameters in $\mathsf{O}[c_n, c_n^*]$ by the corresponding operators $\hat{c}_n(\mathbf{r})$ and $\hat{c}_n^{\dagger}(\mathbf{r})$ *without* modifying their ordering.

3. Expand the operator $\hat{\mathsf{O}}\left[\hat{c}_n, \hat{c}_n^{\dagger}\right]$ order by order in the fluctuations $\delta\hat{c}_n(\mathbf{r})$ and $\delta\hat{c}_n^{\dagger}(\mathbf{r})$, taking into account the dependence of the operator $\hat{A}(\mathbf{r})$ on fluctuations; the contribution of $\hat{A}(\mathbf{r})$ may be of fundamental importance when higher-order correlations become relevant.

4. For the specific case of negligible interactions between the excitation modes, invoke Wick's theorem to compute the expectation value of products of operators on Gaussian states – such as ground or thermal states obtained from $\hat{H}_{\mathrm{QGA}}$.

It must be noted that, invoking the last step of the calculation protocol, the QGA is able to estimate the impact of *non-Gaussian* vertices of the collective modes on quantum observables within a *Gaussian* description of the BH system and therefore goes beyond a standard theory of quadratic fluctuations around the mean-field predictions. Aside from the study of static correlations that we examine in the present Chapter, we anticipate that this feature of the QGA will be of crucial importance for enriching the physical models of static and mobile impurities immersed in a BH environment, which will be the subjects of Chapters 3-4 of Part I respectively.

In the following, we will systematically apply this protocol to compute predictions for both local and non-local observables; for our purposes, expectation values are intended to be evaluated on the Bogoliubov vacuum of the collective modes, defined by $\hat{b}_{\alpha, \mathbf{k}} |\Omega\rangle = 0$. Furthermore, the QGA results of this Chapter are always calculated on a $d = 3$ lattice of $V = 25^3$ sites as a reasonable approximation of the thermodynamic limit, unless otherwise specified.

1.2.5 Putting the method into perspective

Before proceeding with the presentation of the results of our theory for the single-band BH model, it is worth shortly commenting on the relation of our theory with other

competing methods.

Our approach owes much to the time-dependent Gutzwiller method outlined in [51], where the $c_n(\mathbf{r})$ parameters are regarded as $\mathbb{C}$-numbers and not as operators. In the same way as the GPE can be used together with linear response theory to obtain information on quantum fluctuations [74], the time-dependent Gutzwiller approach would give the same results as our method for a number of properties for which only quadratic fluctuations are important.

When only quadratic fluctuations above the saddle-point averages are considered, our approach to the BH model has strong similarities also to including quantum fluctuations by Slave Boson (SB) techniques, as done comprehensively e.g. in [49, 50, 75]. One important difference from this work is however the way in which the observables are calculated: in particular, we never rely on the microscopic reconstruction of the original Bose operators $\hat{a}_{\mathbf{r}}$ through the Gutzwiller fields $\hat{c}_n(\mathbf{r})$ and, from the very beginning, the dynamical variables of our approach are the unconstrained operators $\delta\hat{c}_n(\mathbf{r})$ and $\delta\hat{c}_n^\dagger(\mathbf{r})$. It is also worth mentioning that to our knowledge there are no SB calculations of the role of quantum fluctuations in the superfluid density and general many-body correlation functions. Even though for such quantities we expect the SB representation and our approach to give the same results, our method appears technically easier and more transparent. Finally, the SB approach has been shown to properly interpolate between strong coupling and Bogoliubov approaches in calculating the entanglement entropy [50], a property accessible to our approach, but not to the time-dependent Gutzwiller method.

In the next Section, we will show how the QGA can reproduce both local and non-local correlations with very high accuracy and successfully compares to QMC calculations. Moreover, the study of time-dependent problems appears to be a straightforward generalisation of our formalism. This is a crucial feature compared to QMC, which can hardly describe dynamical properties. The latter processes can be instead attacked by means of the bosonic implementation of DMFT [57–59]: while this theory is very accurate for the study of local quantities, it is however poorly reliable for the analysis of non-local correlations: in this respect, our quantum approach provides an intuitive and flexible way for integrating the physical picture of more computationally demanding precision methods.

We conclude the discussion by clarifying that the present QGA framework, being based on the quantisation of fluctuations on top of a variational ansatz, is not expected to provide a reliable qualitative description of low-dimensional phenomena, comprising e.g. the universal jump of the superfluid density at the MI-to-SF transition and Luttinger's physics for $d = 1$ at zero temperature. As a matter of fact, we find that the control parameter F increases significantly in this limit, especially around the critical points of the system. Therefore, our calculations in the present and following Chapters (including the fermionic extension of the theory in Chapter 5 of Part I) will be restricted to higher dimensions $d \geq 2$, where the QGA is expected to provide a robust approximation of the ground state. Nevertheless, on the basis of the promising results of Section 1.4 below and the significant improvement of similar methods by clustering solutions [76–78], we believe that our point-zero formulation of the QGA can be potentially improved to comprise a much broader range of physical problems, encompassing special instances of quantum correlations in low dimensions.

1.3 Quantum correlations across the MI-to-SF transition

After having introduced the QGA and its basics, in the present Section we apply it to the calculation of some relevant correlation functions of the BH model: (i) the coherence function; (ii) the current-current correlation function, from which we extract the superfluid density; (iii) the density correlation function. In order to validate the accuracy of the method, we compare our results with the predictions of QMC calculations, when available, finding a striking quantitative agreement.

1.3.1 Coherence function

The single-particle correlation function, also referred to as coherence function, is defined as

$$g^{(1)}(\mathbf{r}) \equiv \frac{\left\langle \hat{a}_{\mathbf{r}}^{\dagger} \hat{a}_{\mathbf{0}} \right\rangle}{\left\langle \hat{a}_{\mathbf{0}}^{\dagger} \hat{a}_{\mathbf{0}} \right\rangle} \rightarrow \frac{\left\langle \hat{\psi}^{\dagger}(\mathbf{r}) \hat{\psi}(\mathbf{0}) \right\rangle}{\left\langle \hat{\psi}^{\dagger}(\mathbf{0}) \hat{\psi}(\mathbf{0}) \right\rangle} \,, \tag{1.21}$$

where the last expression is the result of the quantisation protocol outlined in the previous Section. The effective single-particle field reads

$$\hat{\psi}(\mathbf{r}) \equiv \sum_n \sqrt{n} \, \hat{c}_{n-1}^{\dagger}(\mathbf{r}) \, \hat{c}_n(\mathbf{r}) \,. \tag{1.22}$$

Expanding $\hat{c}_n(\mathbf{r})$ and $\hat{c}_n^{\dagger}(\mathbf{r})$ to the lowest order in the fluctuations, one obtains

$$\begin{aligned}
\hat{\psi}(\mathbf{r}) &\approx \sum_n \sqrt{n} \left(c_{n-1}^0 \right)^* c_n^0 + \sum_n \sqrt{n} \left[\left(c_{n-1}^0 \right)^* \delta\hat{c}_n(\mathbf{r}) + c_n^0 \, \delta\hat{c}_{n-1}^{\dagger}(\mathbf{r}) \right] \\
&= \psi_0 + \frac{1}{\sqrt{V}} \sum_{\alpha>0} \sum_{\mathbf{k}} \left(U_{\alpha,\mathbf{k}} \, \hat{b}_{\alpha,\mathbf{k}} \, e^{i\,\mathbf{k}\cdot\mathbf{r}} + V_{\alpha,\mathbf{k}}^* \, \hat{b}_{\alpha,\mathbf{k}}^{\dagger} \, e^{-i\,\mathbf{k}\cdot\mathbf{r}} \right) \,,
\end{aligned} \tag{1.23}$$

where $\psi_0 = \sum_n \sqrt{n} \left(c_{n-1}^0 \right)^* c_n^0$ is the order parameter in the ground state and the one-body particle (hole) amplitudes

$$U_{\alpha,\mathbf{k}} \equiv \sum_n \sqrt{n+1} \left[\left(c_n^0 \right)^* u_{\alpha,\mathbf{k},n+1} + c_{n+1}^0 \, v_{\alpha,\mathbf{k},n} \right] \,, \tag{1.24a}$$

$$V_{\alpha,\mathbf{k}} \equiv \sum_n \sqrt{n+1} \left[\left(c_{n+1}^0 \right)^* u_{\alpha,\mathbf{k},n} + c_n^0 \, v_{\alpha,\mathbf{k},n+1} \right] \tag{1.24b}$$

satisfy the Bogoliubov normalisation [52]

$$\sum_{\alpha} \left(|U_{\alpha,\mathbf{k}}|^2 - |V_{\alpha,\mathbf{k}}|^2 \right) = 1 \,. \tag{1.25}$$

In this way, the Bose field (1.24) satisfies the usual canonical commutation relations

$$\left[\hat{\psi}(\mathbf{r}), \hat{\psi}^{\dagger}(\mathbf{s}) \right] = \delta_{\mathbf{r},\mathbf{s}} \tag{1.26}$$
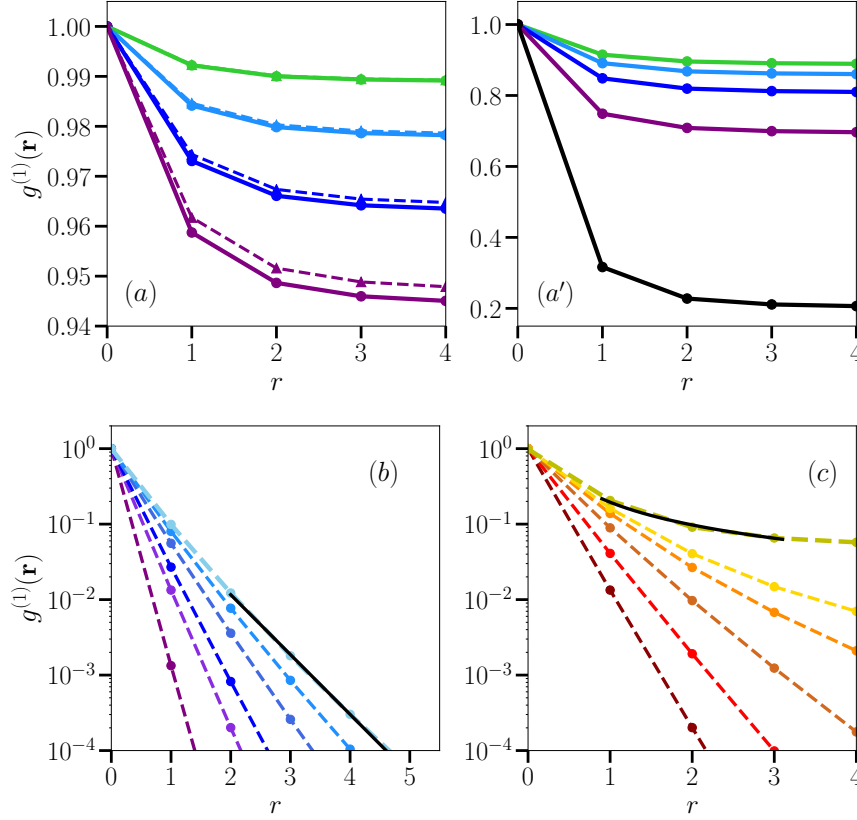
Figure 1.3: (a) Coherence function $g^{(1)}(\mathbf{r})$ for $\mu/U = \sqrt{2} - 1$ and $2\,d\,J/U = 2, 3, 5, 10$ going deeper into the SF phase (from bottom to top). Solid and dashed lines refer to the QGA and Bogoliubov predictions respectively. (a′) QGA predictions of $g^{(1)}(\mathbf{r})$ for $\mu/U = \sqrt{2} - 1$ and $2\,d\,J/U = 0.2, 0.4, 0.6, 0.8, 1.0$ upon approaching the O(2) critical point (from top to bottom). (b) Change of $g^{(1)}(\mathbf{r})$ in the MI phase for $\mu/U = 0.2$ and increasing $2\,d\,J/U = 0.002, 0.02, 0.04, 0.08, 0.11, 0.13, (2\,d\,J/U)_c$ while reaching the transition point $(2\,d\,J/U)_c$ from inside the MI lobe (purple to blue lines). (c) $g^{(1)}(\mathbf{r})$ in the MI phase for $\mu/U = (\mu/U)_{tip} = \sqrt{2} - 1$ and increasing $2\,d\,J/U = 0.02, 0.06, 0.12, 0.16, 0.17, (2\,d\,J/U)_{tip}$ moving towards the tip of the MI lobe (dark brown to red to gold lines). Dashed lines in panels (b)-(c) are the QGA predictions, and the (exponential and power-law) fits are displayed as solid black lines.

up to second order in the fluctuations. At the same level of approximation, the normalised zero-temperature one-body coherence function has the expression

$$g^{(1)}(\mathbf{r}) \approx \frac{|\psi_0|^2 + V^{-1} \sum_{\alpha,\mathbf{k}} |V_{\alpha,\mathbf{k}}|^2 \cos(\mathbf{k} \cdot \mathbf{r})}{|\psi_0|^2 + V^{-1} \sum_{\alpha,\mathbf{k}} |V_{\alpha,\mathbf{k}}|^2} \,. \tag{1.27}$$

In Figure 1.3(a-c) we plot the results for $g^{(1)}(\mathbf{r})$ along the different lines at constant chemical potential traced on the phase diagram shown in Figure 1.1(a).

In the deep SF phase [panel (a)], the spectral weight is saturated by the Goldstone mode and our prediction for $g^{(1)}(\mathbf{r})$ reduces to the result for the weakly-interacting gas (dashed lines). In the region $2\,d\,J/U \leq 1$ [panel (a′)] of a strongly-interacting superfluid, the contribution of other excitation modes [48] starts to become relevant and the Bogoliubov approach (not shown) would give much higher asymptotic values. In the MI phase [panels (b)-(c)], the QGA is able to capture an exponentially decreasing coherence $g^{(1)}(\mathbf{r}) \sim \exp(-r/\xi)/r^\nu$ with a finite correlation length ξ. A non-vanishing value of ξ provides a first drastic improvement with respect to the mean-field Gutzwiller ansatz, whose factorised form cannot predict any off-site coherence, giving $g^{(1)}_{\text{MF}}(\mathbf{r}) =$

$\left(|\langle \hat{a} \rangle|^2 / \langle \hat{n} \rangle \right) (1 - \delta_{\mathbf{r},\mathbf{0}}) + \delta_{\mathbf{r},\mathbf{0}}.$

Furthermore, the present quantum theory is also able to capture the different critical behaviours of the MI-to-SF transition depending on whether this is approached at integer or non-integer filling. Crossing the SF transition from the MI phase away from the tip of the MI lobe, the correlation length ξ of the MI grows but remains bounded [panel (b)]. As soon as one enters the SF phase, long-range order suddenly appears as a non-vanishing long-distance coherence, $\left\langle \hat{a}^\dagger_{\mathbf{r} \to \infty} \, \hat{a}_{\mathbf{0}} \right\rangle \neq 0$: such a quantity physically corresponds to the condensate density $|\psi_0|^2$ and continuously grows from zero as one enters the SF phase. On the other hand, when approaching the SF phase at the tip of the MI lobe, the correlation length ξ diverges and a power-law decay for $g^{(1)}(\mathbf{r})$ is found exactly at the critical point [panel (c)].

Resolving the universality classes of the BH model   This remarkable difference is related to the distinct universality class of the MI-to-SF transition at incommensurate or commensurate filling [63]. In all the critical points of the CI transition, either the particle or the hole excitation becomes gapless, depending on the chemical potential; since however the non-trivial short-distance coherence of the MI is due to virtual pairs of particle-hole excitations, the exponential decay of $g^{(1)}(\mathbf{r})$ is dominated by the gap of the particle (or hole) excitation which remains finite. Instead, at the critical point of the O(2) transition, both the particle and hole modes become gapless (before turning into the Goldstone and Higgs modes on the SF side), which explains the divergent coherence length.

We can gain further insights into this physics by a semi-analytical estimation of $g^{(1)}(\mathbf{r})$ on the MI side of the critical transition. In fact, in this regime we have access to a closed expression for the one-body hole amplitude $V_{\mathrm{H},\mathbf{k}}$, whose modulus reads [4]

$$\left| V_{\mathrm{H},\mathbf{k}} \right|^2 = \frac{1}{2} \left[\frac{(2 \, n_0 + 1) \, U + \varepsilon_{\mathbf{k}}}{\omega_{\mathrm{P},\mathbf{k}} + \omega_{\mathrm{H},\mathbf{k}}} - 1 \right] \tag{1.28}$$

and makes the only non-vanishing contribution to $g^{(1)}(\mathbf{r})$ in the MI phase. Notably, this expression is in excellent agreement with exact numerical calculations of the quasiparticle residue of hole excitations based on NRG techniques [60, 61]. Without loss of generality, let us consider again the $d = 3$ case and move to the continuum limit of the momentum sum yielding the numerator of Eq. (1.27),

$$g^{(1)}_{\mathrm{MI}}(\mathbf{r}) \propto \frac{1}{(2 \, \pi)^3} \int d^3\mathbf{k} \, \left| V_{\mathrm{H},\mathbf{k}} \right|^2 e^{i \, \mathbf{k} \cdot \mathbf{r}} \, . \tag{1.29}$$

At large distances $r = |\mathbf{r}| \gg 1$, we can restrict the above integral below a low-momentum cut-off $\lambda \sim a^{-1}$ set by the lattice spacing, hence

$$\begin{aligned} g^{(1)}_{\mathrm{MI}}(r \gg 1) &\propto \frac{1}{(2 \, \pi)^2} \int_0^\lambda dk \, k^2 \int_{-1}^1 d\cos(\theta) \, [f_1(k) + f_2(k)] \, e^{i \, k \, r \, \cos(\theta)} \\ &= \frac{1}{(2 \, \pi)^2 \, i \, r} \int_{-\lambda}^\lambda dk \, k \, v(k) \, e^{i \, k \, r} \, , \end{aligned} \tag{1.30}$$

where $k = |\mathbf{k}|$. The function $v(k)$ derives from the low-momentum expansion of $\left| V_{\mathrm{H},\mathbf{k}} \right|^2$

---

[4] For additional details on exact results for quantum fluctuations in the MI phase, see Appendix B.3.

and reads

$$v(k) = \frac{(2\,n_0 + 1)\,U - z\,J - \Delta}{k^2/m_r + 2\,\Delta}\,, \tag{1.31}$$

where $m_r^{-1} = m_{\mathrm{P}}^{-1} + m_{\mathrm{H}}^{-1}$ and $\Delta = \Delta_{\mathrm{P}} + \Delta_{\mathrm{H}}$ are the reduced effective mass and combined energy gap of particle and hole excitations, respectively. Allowing $\lambda \to \infty$ compatibly with the continuum limit $a \to 0$, we obtain the simple result

$$g_{\mathrm{MI}}^{(1)}(r \gg 1) \propto \frac{[(2\,n_0 + 1)\,U - z\,J - \Delta]\,m_r}{4\,\pi}\frac{e^{-r/\xi_{\mathrm{MI}}}}{r}\,, \tag{1.32}$$

where $\xi_{\mathrm{MI}} = (2\,\Delta\,m_r)^{-1/2}$ is defined as the coherence length in the MI regime. More explicitly, one can show that

$$\xi_{\mathrm{MI}}^{-2} \equiv \frac{4\,m\,\Delta^2}{(2\,n_0 + 1)\,U - z\,J}\,, \tag{1.33}$$

where $m^{-1} = 2\,J$ is the bare mass on the lattice. At the O(2) critical point located at J_c, the softening of both particle and hole modes leads to $\Delta \sim \sqrt{J_c - J} \to 0$ and $\xi_{\mathrm{MI}} \sim \Delta^{-1} \to \infty$, explaining the natural emergence of long-range order. By contrast, at the CI transition Δ is a non-vanishing quantity set by the lowest-lying gapped excitation, giving a finite coherence length as expected. We remark here that the previous calculation is conceptually robust in the case of the CI transition, whose upper critical dimension is $D_{uc} = 2$ and is therefore well described by our Gutzwiller-based theory.

As a last comment, it is worth noticing that our result for the coherence function (1.27) can be obtained within the time-dependent Gutzwiller formalism [51] as the response function of the order parameter to an external particle-hole drive. This amounts to determine the time-dependent Gutzwiller wave function resulting from applying as a perturbation the single-particle operator $\hat{a}_{\mathbf{r}}^{\dagger}$, and extracting $g^{(1)}(\mathbf{r})$ from the linear response function related to the variation of $\langle \hat{a}_{\mathbf{r}} \rangle$ (see the detailed discussion in the GPE framework of [74]). However, the QGA provides a simpler and more intuitive calculation procedure, not only for the estimation of $g^{(1)}(\mathbf{r})$, but also for an arbitrary class of correlations. First and foremost, the Bogoliubov amplitudes in (5.36) are calculated once for all and can be used to calculate the expectation value for any combination of one-body operators. This makes the calculation of quantities like the superfluid density, that we will discuss in the following Subsection 1.3.2, a straightforward task, which would otherwise require quite involved calculations using the time-dependent Gutzwiller approach. Secondly, as we will show in the next Subsection 1.3.3, there are quantities, like the density correlation function $g^{(2)}(\mathbf{r})$, for which the contribution of the normalisation operator $\hat{A}(\mathbf{r})$ is dominant, in particular close and in the MI phase: while in the time-dependent Gutzwiller approach the inclusion of the effect of $\hat{A}(\mathbf{r})$ would be at least a technically cumbersome task, our theory is able to account for the order-by-order expansion of the normalisation operator in a natural way.

1.3.2 Superfluid density

The superfluid density n_s is defined through the static limit of the transverse current response function [79, 80] of the system, namely

$$2 J n_s = \lim_{\mathbf{q}_{i\neq x}\to\mathbf{0}} \lim_{\omega\to 0} \Lambda_J^{xx}(q_x = 0, \mathbf{q}_{i\neq x}, \omega) - \left\langle \hat{K}_x(\mathbf{r}) \right\rangle, \tag{1.34}$$

where

$$\hat{K}_x(\mathbf{r}) \equiv -J \left[\hat{\psi}^\dagger(\mathbf{r} + \mathbf{e}_x)\, \hat{\psi}(\mathbf{r}) + \text{H.c.} \right] \tag{1.35}$$

is the local kinetic energy operator along a given direction x of the lattice, and

$$\Lambda_J^{xx}(\mathbf{q}, \omega) \equiv -i \int_0^\infty dt\, e^{i\omega t} \left\langle \left[\hat{J}_x(\mathbf{q}, t), \hat{J}_x(-\mathbf{q}, 0) \right] \right\rangle \tag{1.36}$$

is the response function [5] related to the current operator

$$\hat{J}_x(\mathbf{r}) \equiv i\, J \left[\hat{\psi}^\dagger(\mathbf{r} + \mathbf{e}_x)\, \hat{\psi}(\mathbf{r}) - \text{H.c.} \right]. \tag{1.37}$$

As a side note, it is interesting to observe that, in the absence of the lattice, the kinetic energy term in Eq. (1.34) is replaced by the total density due to Galilean invariance [81, 82]. The kinetic energy (1.35), as well as the response function (1.36), can be calculated by a systematic application of the protocol outlined in Subsection 1.2.4: the average kinetic energy reads

$$\left\langle \hat{K}_x(\mathbf{r}) \right\rangle = -2\, J \left[\psi_0^2 + \frac{1}{N} \sum_\alpha \sum_\mathbf{k} |V_{\alpha,\mathbf{k}}|^2 \cos(k_x) \right], \tag{1.38}$$

while the first non-vanishing contribution to the static-uniform limit of the transverse response function $\Lambda_J^{xx}(\mathbf{q}, \omega)$ turns out to be the 4th-order correlation

$$\lim_{\mathbf{q}_{i\neq x}\to\mathbf{0}} \lim_{\omega\to 0} \Lambda_J^{xx}(q_x = 0, \mathbf{q}_{i\neq x}, \omega) = -4\, J^2 \sum_{\alpha,\beta} \sum_\mathbf{k} \frac{|U_{\alpha,\mathbf{k}}\, V_{\beta,\mathbf{k}} - U_{\beta,\mathbf{k}}\, V_{\alpha,\mathbf{k}}|^2}{\omega_{\alpha,\mathbf{k}} + \omega_{\beta,\mathbf{k}}} \sin(k_x)^2, \tag{1.39}$$

where we have adopted the notation $\Lambda_J^{xx}(\mathbf{0}, 0)$ for brevity. Eq. (1.39) reveals the crucial role played by the coupling between different collective modes in suppressing the superfluid stiffness and creating a sort of normal component. The very same expression indeed gives the collisionless drag between two Bose gases at zero temperature, where the elementary excitations are the in-phase and out-of-phase modes of the condensate, see in particular [82] and the detailed study of the superfluid properties of the two-component BH model in Chapter 2 of Part I. For the sake of comparison, it is worth reminding that the ground state mean-field Gutzwiller theory would give $\left\langle \hat{K}_x \right\rangle = -2\, J |\psi_0|^2$ and a vanishing current response $\Lambda_J^{xx}(\mathbf{q} = \mathbf{0}, \omega = 0) = 0$. This incorrectly leads to equal superfluid and condensate densities, $n_s = |\psi_0|^2$.

The results of the QGA for the superfluid density are illustrated in Figure 1.4, where the black thick line indicates the superfluid fraction $f_s = n_s / \langle \hat{n} \rangle$. This quantity tends to unity in the deep SF and approaches zero at the critical point. Throughout the whole

---

[5] We refer the interested reader to Appendix C.3 for additional details on the calculation of response functions within the QGA.
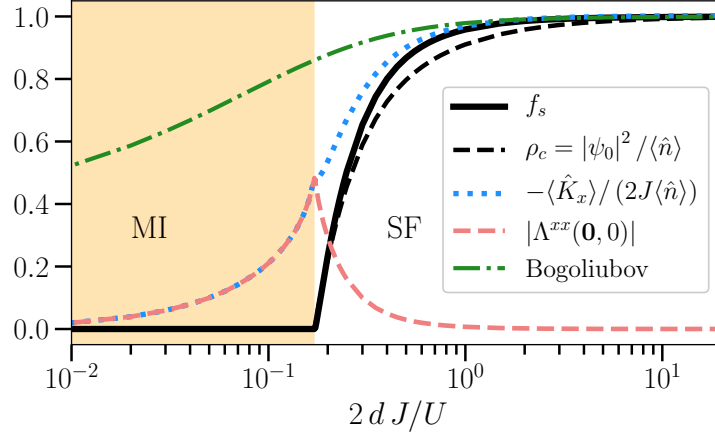
Figure 1.4: Superfluid fraction f_s along the $\mu/U = \sqrt{2} - 1$ line crossing the tip of the $\langle \hat{n} \rangle = 1$ MI lobe. The orange-shaded area indicates the MI region. Solid black line: QGA prediction. Blue dotted and light-pink dashed lines are the contributions to f_s from the kinetic energy $\hat{K}_x$ and the current response $\Lambda_J^{xx}(\mathbf{q} = \mathbf{0}, \omega = 0)$, respectively. Green dot-dashed line: result of the standard Bogoliubov theory. Black dashed line: condensate fraction $|\psi_0|^2 / \langle \hat{n} \rangle$.

SF region, it is always larger than the condensed fraction ρ_c (black dashed line), defined as usual as the $r \to \infty$ limit of the coherence function $g^{(1)}(\mathbf{r})$. In the MI region, the superfluid fraction f_s is exactly zero, as expected for a phase that does not exhibit superfluidity.

Further information is obtained by isolating the two contributions appearing on the right-hand side of Eq. (1.34). The current response $\Lambda_J^{xx}(\mathbf{q} = \mathbf{0}, \omega = 0)$ defined in Eq. (1.39) (light-pink dashed line) displays a non-monotonic behaviour as a function of J/U: it tends to zero in the deep MI and SF phases, while it reaches its maximum at the transition point. In the strongly-interacting SF regime, the Goldstone-Higgs vertex almost saturates the sum in the current response and leads to a complete suppression of n_s. As expected, the kinetic energy Eq. (1.38) (see dotted blue line) has as expected a monotonic behaviour, from zero at $J = 0$ to the weakly-interacting mean-field value $-2 J \langle \hat{n} \rangle$. In the MI phase, the vanishing n_s results from the perfect cancellation of the short-range virtual particle-hole correlations and the kinetic energy.

For completeness, in Figure 1.4 we also report the weakly-interacting Bogoliubov prediction [83] (green dashed-dotted line), to which our result converges in the limit $2 d J/U \gg 1$. Since it takes into account only the gapless Goldstone mode, such approach leads in particular to a zero current response $\Lambda_J^{xx}(\mathbf{q} = \mathbf{0}, \omega = 0) = 0$ and thus an overestimated superfluid density.

1.3.3 Density fluctuations

We consider the normally-ordered equal-time density correlation function

$$g^{(2)}(\mathbf{r}) \equiv \frac{\left\langle \hat{a}_{\mathbf{r}}^\dagger \hat{a}_{\mathbf{0}}^\dagger \hat{a}_{\mathbf{0}} \hat{a}_{\mathbf{r}} \right\rangle}{\langle \hat{n}_{\mathbf{r}} \rangle \langle \hat{n}_{\mathbf{0}} \rangle} . \tag{1.40}$$
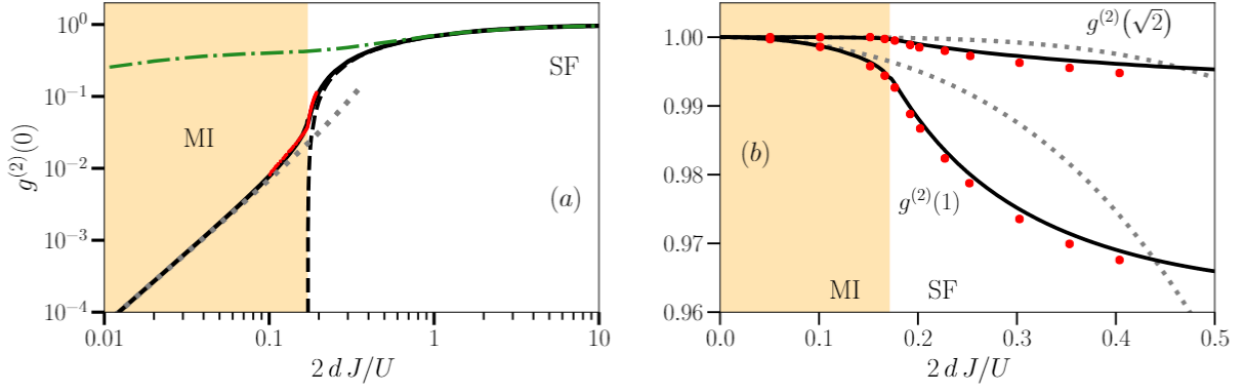
Figure 1.5: Density-density correlation $g^{(2)}(\mathbf{r})$ as a function of $2\,d\,J/U$ across the $\langle\hat{n}\rangle = 1$ commensurate MI-to-SF transition. The orange (white) background identifies the MI (SF) region. (a) On-site correlation function $g^{(2)}(\mathbf{0})$; black solid line: QGA result; black dashed line: mean-field Gutzwiller approach; green dot-dashed line: weakly-interacting Bogoliubov theory; red dotted line: QMC simulation for a lattice size of 16^3 sites [84]; grey dashed line: strong-coupling perturbation theory [43]. (b) Nearest and next-to-nearest density correlations, $g^{(2)}(|\mathbf{r}| = 1)$ and $g^{(2)}(|\mathbf{r}| = \sqrt{2})$. Black solid line: QGA prediction; grey dotted line: strong-coupling approximation; red dots: QMC calculation for a 5^3 lattice [43]. The QGA data have been obtained for the same lattice sizes of the corresponding QMC simulations.

Applying the procedure outlined in Subsection 1.2.4, and since the ground state is translational invariant, $g^{(2)}(\mathbf{r})$ reads

$$g^{(2)}(\mathbf{r}) = \begin{cases} \left[\left\langle\hat{\mathcal{D}}(\mathbf{0})\right\rangle - \left\langle\hat{\mathcal{N}}(\mathbf{0})\right\rangle\right] \big/ \left\langle\hat{\mathcal{N}}(\mathbf{0})\right\rangle^2, & \mathbf{r} = \mathbf{0}, \\ \left\langle\hat{\mathcal{N}}(\mathbf{r})\,\hat{\mathcal{N}}(\mathbf{0})\right\rangle \big/ \left\langle\hat{\mathcal{N}}(\mathbf{0})\right\rangle^2, & \mathbf{r} \neq \mathbf{0}, \end{cases} \tag{1.41}$$

where the QGA density $\hat{\mathcal{N}}(\mathbf{r})$ and the square density $\hat{\mathcal{D}}(\mathbf{r})$ operators are defined as

$$\hat{\mathcal{N}}(\mathbf{r}) \equiv \sum_n n\,\hat{c}_n^\dagger(\mathbf{r})\,\hat{c}_n(\mathbf{r}), \tag{1.42}$$

$$\hat{\mathcal{D}}(\mathbf{r}) \equiv \sum_n n^2\,\hat{c}_n^\dagger(\mathbf{r})\,\hat{c}_n(\mathbf{r}). \tag{1.43}$$

The expectation values in Eq. (1.41) are evaluated by expanding the above operators up to second-order in the $\delta\hat{c}_n$'s, hence

$$\left\langle\hat{\mathcal{D}}(\mathbf{0})\right\rangle = D_0 + \sum_n \left(n^2 - D_0\right)\left\langle\delta\hat{c}_n^\dagger(\mathbf{0})\,\delta\hat{c}_n(\mathbf{0})\right\rangle, \tag{1.44a}$$

$$\left\langle\hat{\mathcal{N}}(\mathbf{0})\right\rangle = n_0 + \sum_n (n - n_0)\left\langle\delta\hat{c}_n^\dagger(\mathbf{0})\,\delta\hat{c}_n(\mathbf{0})\right\rangle, \tag{1.44b}$$

$$\left\langle\hat{\mathcal{N}}(\mathbf{r} \neq \mathbf{0})\,\hat{\mathcal{N}}(\mathbf{0})\right\rangle = n_0^2 + \frac{1}{N}\sum_\alpha\sum_{\mathbf{k}} |N_{\alpha,\mathbf{k}}|^2 \cos(\mathbf{k}\cdot\mathbf{r})$$
$$+ \sum_{n,m} (n - n_0)(m - n_0)\left\langle\delta\hat{c}_n^\dagger(\mathbf{r})\,\delta\hat{c}_n(\mathbf{r})\,\delta\hat{c}_m^\dagger(\mathbf{0})\,\delta\hat{c}_m(\mathbf{0})\right\rangle, \tag{1.44c}$$

where

$$N_{\alpha,\mathbf{k}} = \sum_n n\left[\left(c_n^0\right)^* u_{\alpha,\mathbf{k},n} + c_n^0\,v_{\alpha,\mathbf{k},n}\right] \tag{1.45}$$

The QGA result (1.41) for the local density correlation $g^{(2)}(\mathbf{r} = \mathbf{0})$ is shown as a solid black line in panel (a) of Figure 1.5. On the SF side, the antibunching $g^{(2)}(\mathbf{0}) < 1$ due to the repulsive on-site interactions well matches the weakly-interacting Bogoliubov prediction [83] in the deep SF (green dashed-dotted line) and increases, faster than the Bogoliubov trend, when moving towards the MI-to-SF transition. On the MI side, while the mean-field Gutzwiller theory (black dashed line) predicts a perfect antibunching $g^{(2)}_{\mathrm{MF}}(\mathbf{0}) \propto D_0 - n_0 = 0$, the QGA result (1.41) is able to account for the virtual excitation of doublon-holon pairs. This leads to $g^{(2)}(\mathbf{0}) \propto (J/U)^2$ at low $2\,d\,J/U$, in excellent agreement with strong-coupling perturbative calculations (gray dotted line) [43]. Remarkably, close to and across the critical point, the QGA theory is in very good agreement with low-temperature QMC predictions [84] (red dots). In order to compare the results of the two different approaches, the hopping parameter for the QMC data has been rescaled by a factor J_c/J_c^{QMC} in order to make the position of the critical point in the two theories coincide. We highlight that no other semi-analytical theory is currently available to describe the region close to and across the critical point.

The role of quantum fluctuations and the accuracy of the method can be further explored by looking at the off-site density correlations function for $|\mathbf{r}| = 1$ and $\sqrt{2}$. In panel (b) of Figure 1.5 we report the QGA predictions for $g^{(2)}(|\mathbf{r}| = 1)$ and $g^{(2)}\left(|\mathbf{r}| = \sqrt{2}\right)$ along the $\langle \hat{n} \rangle = 1$ filling line across the tip of the MI lobe. These curves are successfully compared to available QMC data (see [43] and references therein) and to strong-coupling perturbation theory, which shows that our theory is accurate across the whole phase transition and correctly interpolates between a strongly-interacting MI phase and the weakly-interacting Bose gas.

1.4 Beyond Gaussian fluctuations: decay processes

Having demonstrated the predictive power of the QGA with respect to the physical role of Gaussian quantum fluctuations, we dedicate this Section to explore the capability of the method to describe non-linear many-body effects involving the collective excitations of the system [1]. As a simple yet non-trivial application, we specialise our investigation to the case of decay processes associated with three-body vertices of the excitations found by diagonalising the QGA theory at the quadratic level. In particular, the Hamiltonian terms responsible for these processes are given by combinations of two creation operators $\hat{b}^\dagger_{\alpha,\mathbf{k}}$ and one annihilation operator $\hat{b}_{\beta,\mathbf{p}}$.

Expanding the fluctuations operators $\delta \hat{c}_n(\mathbf{r})$ with the respect to the elementary excitations, we can gather the three-body terms of interest into

$$\hat{H}^{(3)}_{\mathrm{QGA}} = \frac{1}{\sqrt{V}} \sum_{\alpha,\beta,\gamma} \sum_{\mathbf{k},\mathbf{p}} H_{\alpha,\beta,\gamma}(\mathbf{k},\mathbf{p}) \, \hat{b}^\dagger_{\beta,\mathbf{p}} \, \hat{b}^\dagger_{\gamma,\mathbf{k}-\mathbf{p}} \, \hat{b}_{\alpha,\mathbf{k}} \,, \qquad (1.46)$$

where the vertex $H_{\alpha,\beta,\gamma}(\mathbf{k},\mathbf{p})$ can be shown to couple single-mode spectral amplitudes to two-body vertices of the collective modes [6]. To lowest order in perturbation theory, the decay rate of a given excitation $(\alpha, \mathbf{k})$ with respect to the momentum-conserving

---

[6] For a complete expression of $H_{\alpha,\beta,\gamma}(\mathbf{k},\mathbf{p})$, we refer the reader to Appendix B.4

decay process $\alpha_{\mathbf{k}} \to \beta_{\mathbf{p}} + \gamma_{\mathbf{k-p}}$ is provided by the Fermi Golden Rule (FGR)

$$\Gamma_{\alpha,\beta,\gamma}(\mathbf{k}) = \frac{2\pi}{V} \sum_{\mathbf{p}} |H_{\alpha,\beta,\gamma}(\mathbf{k},\mathbf{p})|^2 \, \delta(\omega_{\beta,\mathbf{p}} + \omega_{\gamma,\mathbf{k-p}} - \omega_{\alpha,\mathbf{k}}), \qquad (1.47)$$

where the δ-function imposes energy conservation. For instance, choosing $\alpha = \beta = \gamma$ on the Goldstone branch only, we obtain the damping rate of the so-called Beliaev decay process [85, 86].

In what follows, we examine the long-debated fate of the Higgs excitation and its coupling with the Goldstone mode around the O(2) critical point of the MI-to-SF transition. In particular, we consider the vertex relating a delocalised amplitude mode (H) at $\mathbf{k} = \mathbf{0}$ with two Goldstone modes (G), yielding

$$\Gamma = \Gamma_{\mathrm{H,G,G}}(\mathbf{0}) = \frac{1}{(2\pi)^{d-1}} \int d^d\mathbf{p} \, |H_{\mathrm{H,G,G}}(\mathbf{0},\mathbf{p})|^2 \, \delta(2\,\omega_{\mathrm{G,p}} - \omega_{\mathrm{H,0}}), \qquad (1.48)$$

where we have considered the continuum limit for simplicity and used $\omega_{\mathrm{G,p}} = \omega_{\mathrm{G,-p}}$ by inversion symmetry. Since in our formalism all quantities depend on momentum via the free-particle dispersion $\varepsilon_{\mathbf{k}}$ [7], we can transform the momentum integral of Eq. (1.48) into

$$\Gamma = \frac{1}{(2\pi)^{d-1}} \int_0^{4J} d\varepsilon \, \rho_d(\varepsilon) \, |H_{\mathrm{H,G,G}}(0,\varepsilon)|^2 \, \delta(2\,\omega_{\mathrm{G},\varepsilon} - \omega_{\mathrm{H,0}}) \qquad (1.49)$$

where the function $\rho_d(x)$ mirrors the Density of States (DoS) of the free Bose gas in d dimensions and is given by the integral

$$\rho_d(\varepsilon) \equiv 2^d \int d^d\mathbf{x} \, \delta(\varepsilon - 4J\,|\mathbf{x}|) \left[\prod_{i=1}^d \left(1 - x_i^2\right)^{-1/2} \right] \qquad (1.50)$$

over the space $[0,1]^d$. Since around the O(2) transition both the Goldstone and Higgs excitations are soft modes, the decay process is bound to take place at low energy; therefore, for arbitrary dimensions we can perform a low-momentum approximation ($|\mathbf{x}| \ll 1$) of $\rho_d(\varepsilon)$, hence

$$\rho_d(\varepsilon) \simeq 2^d \, S_d \left(\frac{\varepsilon}{4J}\right)^{d-1} \left[1 + \left(\frac{\varepsilon}{4J}\right)^2\right] \qquad (1.51)$$

where S_d is the hypersurface of the d-dimensional sphere. Finally, observing that the Higgs gap reads $\Delta_{\mathrm{H}} = \omega_{\mathrm{H,0}} = 2\,\omega_{\mathrm{G},\varepsilon} = 2\,c_s\,\varepsilon/(4J)$ by energy conservation, we obtain an approximate prediction for the Higgs decay rate given by

$$\Gamma \simeq \frac{4\,S_d\,J}{(2\pi)^{d-1}\,c_s} \left(\frac{\Delta_{\mathrm{H}}}{c_s}\right)^{d-1} \left[1 + \left(\frac{\Delta_{\mathrm{H}}}{2\,c_s}\right)^2\right] \left|H_{\mathrm{H,G,G}}\left(0, \frac{4J\,\Delta_{\mathrm{H}}}{2\,c_s}\right)\right|^2 \qquad (1.52)$$

where c_s indicates the sound velocity of the Goldstone mode.

Let us now suppose to reach the MI-to-SF criticality from the SF side of the transition at constant chemical potential μ. In this case, the Higgs gap Δ_{H} is found to scale as

$$\Delta_{\mathrm{H}}(J) \simeq A_\Delta \, (J - J_c)^{\beta_\Delta} \qquad (1.53)$$

---

[7] See Eqs. (1.12)-(1.13).
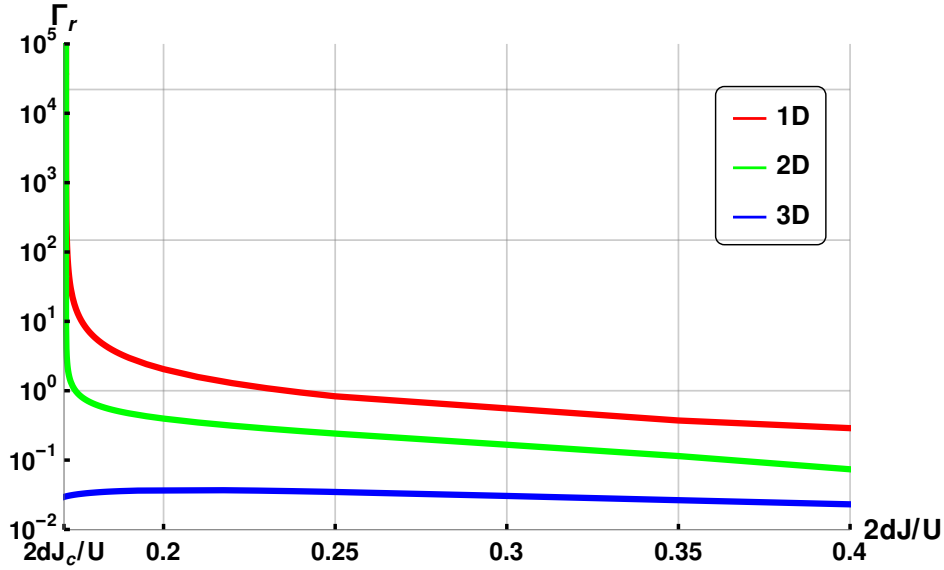
Figure 1.6: Relative decay rate Γ_r of the Higgs mode upon approaching the O(2) critical point $2\,d\,J_c/U \approx 0.172$ of the $\langle \hat{n} \rangle = 1$ MI lobe. The red, green and blue lines refer to $d = 1, 2$ and 3 dimensions respectively.

with respect to the critical hopping J_c, with the critical exponent having the mean-field value $\beta_\Delta = 1/2$ within the QGA. On the other hand, the sound velocity approaches the finite value $c_s^{\text{tip}} = \left[(J_c\,U)^2\,n_0\,(n_0 + 1) \right]^{1/4}$, where n_0 is the filling of the nearby MI lobe [8]. Then, it is straightforward to see that the *relative* Higgs damping rate $\Gamma_r = \Gamma/\Delta_{\text{H}}$ behaves as

$$\Gamma_r(J) \sim \left| H_{\text{H,G,G}}\left(0, \frac{4\,J\,\Delta_{\text{H}}}{2\,c_s} \right) \right|^2 \Delta_{\text{H}}^{d-2} \sim \left| H_{\text{H,G,G}}\left(0, \frac{4\,J\,\Delta_{\text{H}}}{2\,c_s} \right) \right|^2 (J - J_c)^{(d-2)\beta_\Delta} \ . \tag{1.54}$$

In particular, if we make the hypothesis that $|H_{\text{H,G,G}}(0, \varepsilon)|^2 \sim \varepsilon^\eta$ at low energy,

$$\Gamma_r(J) \sim (J - J_c)^{[(d-2)+\eta]\beta_\Delta} \ , \tag{1.55}$$

Non-linear effects: Higgs mode lifetime within the QGA

from which we deduce that the analytical behaviour of Γ_r has a clear algebraic dependence on the dimensionality of the system, whereas the gap exponent β_Δ works as a multiplicative factor only. Even more importantly, the only unknown (and crucial) parameter is the vertex exponent η, which is a genuine prediction of the QGA description.

A straightforward numerical calculation of $|H_{\text{H,G,G}}(0, \varepsilon)|^2$ close to the O(2) critical point provides $\eta = -1$ exactly. Therefore, we utilise this information to determine the Higgs mode damping and lifetime in proximity of the $\langle \hat{n} \rangle = 1$ MI lobe, for which we report our numerical results in Figure 1.6. In accordance with Eq. (1.55), the relative decay rate Γ_r diverges at the critical point for $d = 1, 2$, while it reaches a small finite value for $d \geq 3$. It follows that the Higgs mode ceases to be a long-lived excitation in the low-dimensional regime as a consequence of its strong coupling with the Goldstone branch, which hinders its experimental observability. Quite remarkably, these findings are in excellent agreement with the analysis of [87] based on critical field theory

---

[8] See Appendix B.2 for a thorough discussion on the behaviour of Goldstone sound velocity in proximity of the BH critical points.

arguments, albeit limited to large densities. Thus, we speculate that the QGA, although based on a mean-field ansatz, could represent a powerful tool to study non-linear effects beyond Gaussian correlations in synergy with more refined methods.

1.5 Summary and perspectives

In this opening Chapter, we have introduced a simple and powerful semi-analytical tool to study the quantum many-body physics of interacting bosons on a lattice based on the canonical quantisation of the fluctuations around the Gutzwiller ansatz. The effectiveness of the method has been validated on the archetypal case of the BH model. In spite of the locality of the underlying mean-field Gutzwiller state, the proposed quantisation procedure is able to accurately capture very non-local physical features, such as the superfluid stiffness of the SF phase, the different behaviours of the correlation functions at the different critical points, and the spatial structure of the virtual particle-hole pair excitations on top of the MI state. In particular, these last predictions are in quantitative agreement with the few QMC results available in the literature. In addition to its quantitative accuracy and computational simplicity, we have seen that the QGA has the crucial advantage over other approaches of providing a deep physical insight on the equilibrium state and the quantum dynamics of the system in terms of collective effects. Last but not least, going beyond the quadratic expansion around the mean-field level, we have also tested the potential of our formalism to incorporate non-linear effects encoding the interactions between the collective modes of the theory, so as to describe e.g. their temporal decay into entangled pairs via multi-branch Beliaev decay processes [88].

Due to its flexibility, our formalism could be straightforwardly extended to treat inhomogeneous configurations, more exotic hopping and interaction terms, and to deal with more complex forms of the initial ansatz, such as a cluster Gutzwiller wave function [89], which include short-range quantum correlations already in the zero-point ground state. In the next Chapter, we will take a first step along this research direction and generalise our analysis of quantum correlations to the richer scenario of the two-component BH mixture. Furthermore, the application of our effective theory of collective modes appears particularly promising in modelling those physical situations where the precise structure of the many-body excitations strongly influence the properties of the system. This is the case of physical phenomena involving a quantum impurity in a correlated bosonic bath, which will be taken into consideration in Chapters 3 and Chapters 4 of Part I.

Other important applications of our quantum model of many-body excitations could include the investigation of finite temperature and/or time-dependent problems, including non-equilibrium dynamics. Exciting long term perspectives comprise the application of our theoretical framework to those driven-dissipative models that can be currently realised in photonic systems [25, 41, 42]. In particular, Chapter 2 of Part II has the scope of providing a theoretical primer in view of such future developments.

This Chapter is based on a reworked version of the following publication, integrated by original findings collected in Appendix D.

▶ V. E. Colussi, <u>Fabio Caleffi</u>, C. Menotti, and A. Recati, *Quantum Gutzwiller approach for the two-component Bose–Hubbard model*, SciPost Physics **12**, 111 (29 March 2022)

2.1 The more, the better

In order to benchmark the predictive power of the QGA in more complex bosonic systems featuring strong correlations, we devote the present Chapter to generalise our analysis of the single-band BH model to its multi-component implementation, considering in particular two interacting atomic species. In the two-component BH model, a much richer phase diagram emerges, including the additional possibility of pair and counterflow superfluidity, supersolidity, charge-density quasiorder, and peculiar magnetic states [90–95]. Such coupled superfluids can also undergo mutual dissipationless transport with an induced entrainment or counterflow of one component due to a non-zero superfluid velocity of the other. This phenomenon, better known as superfluid drag, was first discussed by Andreev and Bashkin in the context of three-fluid hydrodynamics [96], but is of universal relevance to systems ranging from neutron-star matter [97–101] to multicomponent superconductors [102–104] and ultracold atomic mixtures [81, 82, 94, 105–111]. Direct measurement of this effect has however remained elusive, due in part to the low miscibility of superfluid ^{3}He and ^{4}He, and recombination heating in strongly-interacting ultracold atomic mixtures. Recently, the PSF and CFSF phase transitions of the two-component BH model have emerged as promising candidates where the drag can saturate at its maximum value [109, 110]. Still, a deeper understanding of the fundamental role played by quantum fluctuations is needed to gain insight into the physics of such strongly-correlated quantum critical regimes of Hubbard models at zero temperature.

In the following, we will study a homogeneous configuration of the binary BH model on a square lattice in the presence of short-range intra and interspecies interactions, which can be realised in optical lattices loaded with atoms of two different species or internal states [112–114]. Although the derivations presented in this work are completely general, our numerical findings are specific to two dimensions where existing QMC results [109] make quantitative comparisons with our predictions for the drag possible, and where there exists a strong motivating analogy between the fermionic version of the problem and high-temperature superconductivity [115]. We first study the rich phase diagram of the model for both repulsive and attractive interspecies interactions, finding counterflow and paired superfluid phases in addition to the MI and SF phases which carry over from single-component bosonic systems. We show how, also in the case of mixtures, the QGA provides a straightforward way to calculate linear response and correlation functions to a desired order in the quantum fluctuations. This permits a systematic study of the role of quantum corrections, which we first investigate by considering the linear response dynamics of the system to density and

spin perturbations. In this respect, we highlight the experimentally relevant signatures of the onset of the PSF and CFSF phases in the dynamical structure factor. We then focus on superfluid transport in quantum critical regimes, finding in particular a large interspecies drag comparable in magnitude with the superfluid density in the vicinity of the CFSF and PSF phases. Furthermore, we address the one and two-body correlation functions, focusing on the strongly-interacting regime, where quantum fluctuations play a crucial role. Specifically, we find that the PSF and CFSF transitions behave as channel-selective MI transitions with respect to the spin and density degrees of freedom, respectively.

2.2 Model and theoretical setting

In Subsection 2.2.1, we will analyse the binary BH model by using a suitable extension of the $\mathbb{C}$-number Gutzwiller ansatz. Subsequently, in Subsection 2.2.2, we will discuss in depth the ground state and elementary excitations for both repulsive and attractive interactions between the two components of the system. This exploration lays the theoretical background of Subsection 2.3, where we will go beyond the mean-field Gutzwiller ansatz by generalising the QGA introduced in Chapter 1 to Bose mixtures in order to calculate genuine quantum correlations. Additionally, a general understanding of the spectral structure of the binary BH mixture will serve as an insightful term of comparison for the spectrum of bosonic excitations in the Fermi Hubbard model, which will be among the subjects of Chapter 5.

2.2.1 Gutzwiller theory for bosonic mixtures

We start from the two-component BH model [33]

$$\hat{H}_{2\text{BH}} \equiv \sum_{i=1}^{2} \hat{H}_{\text{BH},i} + U_{12} \sum_{\mathbf{r}} \hat{n}_{1,\mathbf{r}} \, \hat{n}_{2,\mathbf{r}} \, , \tag{2.1}$$

where

$$\hat{H}_{\text{BH},i} \equiv -J_i \sum_{\langle \mathbf{r},\mathbf{s} \rangle} \left(\hat{a}_{i,\mathbf{r}}^{\dagger} \, \hat{a}_{i,\mathbf{s}} + \text{H.c.} \right) + \frac{U}{2} \sum_{\mathbf{r}} \hat{n}_{i,\mathbf{r}} \, (\hat{n}_{i,\mathbf{r}} - 1) - \mu \sum_{i,\mathbf{r}} \hat{n}_{\mathbf{r}} \, , \tag{2.2}$$

is the BH Hamiltonian governing each component, while U_{12} is the interspecies interaction strength. For the purpose of our discussion, we examine only the $\mathbb{Z}_2$-symmetric case where $J_1 = J_2 = J$, $\mu_i = \mu_2 = \mu$ and $U_1 = U_2 = U$, keeping always $|U_{12}/U| < 1$ to avoid phase separation for repulsive species, as well as to prevent the system from collapsing for attractive interactions [116]. The bosonic creation and annihilation operators $\hat{a}_{i,\mathbf{r}}^{\dagger}$ and $\hat{a}_{i,\mathbf{r}}$ create and destroy, respectively, a particle of species i at the lattice site $\mathbf{r}$, and are related to the corresponding local density operators via $\hat{n}_{i,\mathbf{r}} = \hat{a}_{i,\mathbf{r}}^{\dagger} \, \hat{a}_{i,\mathbf{r}}$. We also define the total density and *spin* operators as given by $\hat{n}_{d,\mathbf{r}} = \sum_i \hat{n}_{i,\mathbf{r}}$ and $\hat{n}_{s,\mathbf{r}} = \hat{n}_{1,\mathbf{r}} - \hat{n}_{2,\mathbf{r}}$, respectively. In the following, we will consider as always a uniform square lattice of volume V [1].

---

[1] In the present Chapter, the QGA results are obtained on a $d = 2$ lattice of $V = 128^2$ sites in order to minimise finite-size effects, unless otherwise specified.

The two-component Gutzwiller mean-field ansatz for the binary BH model (2.1) is a straightforward generalisation of the ansatz introduced in Eq. (1.2). Specifically, local Fock states are weighted by *composite* complex amplitudes $c_{n_1,n_2}(\mathbf{r})$ such that $\sum_{n_1,n_2} |c_{n_1,n_2}(\mathbf{r})|^2 = 1$. Consequently, the mean-field expectation value of the species-resolved density is given by

$$n_i(\mathbf{r}) \equiv \langle \hat{n}_{i,\mathbf{r}} \rangle = \sum_{n_1,n_2}^{\infty} (n_1\,\delta_{i,1} + n_2\,\delta_{i,2})\,|c_{n_1,n_2}(\mathbf{r})|^2\,. \tag{2.3}$$

In addition to the MI and SF phases in common with the one-component case, the two-component Bose mixture exhibits also the possibility of Counterflow Superfluid (CFSF) and Pair Superfluid (PSF) phases, see [91, 92, 95, 117]. To distinguish between these phases, besides the one-body order parameters

$$\psi_1(\mathbf{r}) \equiv \langle \hat{a}_{1,\mathbf{r}} \rangle = \sum_{n_1,n_2}^{\infty} \sqrt{n_1}\, c_{n_1-1,n_2}^*(\mathbf{r})\, c_{n_1,n_2}(\mathbf{r})\,, \tag{2.4a}$$

$$\psi_2(\mathbf{r}) \equiv \langle \hat{a}_{2,\mathbf{r}} \rangle = \sum_{n_1,n_2}^{\infty} \sqrt{n_2}\, c_{n_1,n_2-1}^*(\mathbf{r})\, c_{n_1,n_2}(\mathbf{r})\,, \tag{2.4b}$$

which are non-zero only in the SF phase, we introduce the *pair* and *antipair* order parameters

$$\begin{aligned}
\psi_{\mathrm{P}}(\mathbf{r}) &\equiv \langle \hat{a}_{1,\mathbf{r}}\, \hat{a}_{2,\mathbf{r}} \rangle - \langle \hat{a}_{1,\mathbf{r}} \rangle \langle \hat{a}_{2,\mathbf{r}} \rangle \\
&= \sum_{n_1,n_2} \sqrt{n_1\, n_2}\, c_{n_1-1,n_2-1}^*(\mathbf{r})\, c_{n_1,n_2}(\mathbf{r}) - \psi_1(\mathbf{r})\, \psi_2(\mathbf{r})\,,
\end{aligned} \tag{2.5a}$$

$$\begin{aligned}
\psi_{\mathrm{C}}(\mathbf{r}) &\equiv \left\langle \hat{a}_{1,\mathbf{r}}\, \hat{a}_{2,\mathbf{r}}^{\dagger} \right\rangle - \langle \hat{a}_{1,\mathbf{r}} \rangle \left\langle \hat{a}_{2,\mathbf{r}}^{\dagger} \right\rangle \\
&= \sum_{n_1,n_2} \sqrt{n_1(n_2+1)}\, c_{n_1-1,n_2+1}^*(\mathbf{r})\, c_{n_1,n_2}(\mathbf{r}) - \psi_1(\mathbf{r})\, \psi_2^*(\mathbf{r})\,,
\end{aligned} \tag{2.5b}$$

which identify univocally the PSF and CFSF phases, respectively. Notice that, in constructing the pair/antipair order parameters, disconnected contributions due to the one-body order parameters have been explicitly removed to ensure that $\psi_{\mathrm{P/C}}(\mathbf{r}) \neq 0$ reflects *intrinsically* off-diagonal (CFSF) or anomalous (PSF) local correlations between the two species.

Counterflow and pair superfluids

Generalising the procedure outlined in Chapter 1, we can readily build a Lagrangian for the multi-component Gutzwiller ansatz,

$$\begin{aligned}
\mathfrak{L}[c,c^*] &= \sum_{\mathbf{r}} \sum_{n_1,n_2} \left\{ \frac{i}{2} \left[c_{n_1,n_2}^*(\mathbf{r})\, \dot{c}_{n_1,n_2}(\mathbf{r}) - \mathrm{c.c.} \right] - H_{n_1,n_2} |c_{n_1,n_2}(\mathbf{r})|^2 \right\} \\
&\quad + J \sum_{i=1}^{2} \sum_{\langle \mathbf{r},\mathbf{s} \rangle} \left[\psi_i^*(\mathbf{r})\, \psi_i(\mathbf{s}) + \mathrm{c.c.} \right]\,,
\end{aligned} \tag{2.6}$$

where

$$H_{n_1,n_2} = \sum_{i=1}^{2} \left[\frac{U}{2}\, n_i(n_i - 1) - \mu\, n_i \right] + U_{12}\, n_1\, n_2\,. \tag{2.7}$$

The classical Euler-Lagrange equations of motion for the Gutzwiller amplitudes, with the complex conjugate parameters $c_{n_1,n_2}^*(\mathbf{r}) = \partial \mathcal{L}/\partial \dot{c}_{n_1,n_2}(\mathbf{r})$ playing again the role of canonical momenta, are given by the two-component TDGE

$$
\begin{aligned}
i\,\dot{c}_{n_1,n_2}(\mathbf{r}) = H_{n_1,n_2}\,c_{n_1,n_2} &- J \sum_{i=1}^{d} \left[\sqrt{n_1+1}\,c_{n_1+1,n_2} \sum_{s=\pm 1} \psi_1^*(\mathbf{r}+s\,\mathbf{e}_i) \right.\\
&+ \sqrt{n_1}\,c_{n_1-1,n_2}(\mathbf{r}) \sum_{s=\pm 1} \psi_1(\mathbf{r}+s\,\mathbf{e}_i) + \sqrt{n_2+1}\,c_{n_1,n_2+1}(\mathbf{r}) \sum_{s=\pm 1} \psi_2^*(\mathbf{r}+s\,\mathbf{e}_i) \\
&\left. + \sqrt{n_2}\,c_{n_1,n_2-1}(\mathbf{r}) \sum_{s=\pm 1} \psi_2(\mathbf{r}+s\,\mathbf{e}_i) \right] = \hat{H}_0 \cdot \underline{c}_{n_1,n_2}\,,
\end{aligned} \tag{2.8}
$$

where $\mathbf{e}_i$ is the versor of the ith lattice direction and which were previously derived in [118]. The above TDGE are straightforward extensions of their one-component counterparts (cfr. [51]) with the additional contribution of the diagonal interspecies coupling U_{12}. In order to explore the possible ground states of the system, we search first for the stationary solutions $c_{n_1,n_2}(\mathbf{r}) = c_{n_1,n_2}^0\,e^{-i\,\omega_0\,t}$ independent of the site index $\mathbf{r}$. The ground state energy is then given by

$$
\omega_0 \equiv -2\,z\,J \sum_{i=1}^{2} |\psi_{0,i}|^2 + \sum_{n_1,n_2} H_{n_1,n_2} \left| c_{n_1,n_2}^0 \right|^2\,, \tag{2.9}
$$

where the "0" sub/superscript indicates quantities evaluated with respect to the ground state Gutzwiller amplitudes c_{n_1,n_2}^0 obtained by diagonalising the matrix $\hat{H}_0$ on the right-hand side of Eq. (2.8). For instance, the expression of the mean-field total density is simply given by

$$
n_{0,d} \equiv \sum_{n_1,n_2}^{\infty} (n_1+n_2) \left| c_{n_1,n_2}^0 \right|^2\,. \tag{2.10}
$$

In order to study the linear response dynamics of the system around the ground state, we consider small perturbations around the stationary solution of the form

$$
c_{n_1,n_2}(\mathbf{r}) = \left[c_{n_1,n_2}^0 + \delta c_{n_1,n_2}(\mathbf{r},t) \right] e^{-i\,\omega_0\,t}, \tag{2.11}
$$

which can be expanded in terms of plane waves as

$$
\delta c_{n_1,n_2}(\mathbf{r},t) \equiv \sum_{\mathbf{k}} \left[u_{\mathbf{k},n_1,n_2}\,e^{i(\mathbf{k}\cdot\mathbf{r}-\omega_{\mathbf{k}}\,t)} + v_{\mathbf{k},n_1,n_2}^*\,e^{-i(\mathbf{k}\cdot\mathbf{r}-\omega_{\mathbf{k}}\,t)} \right]\,. \tag{2.12}
$$

Linearising the TDGE with respect to the amplitudes $u_{\mathbf{k},n_1,n_2}$ and $v_{\mathbf{k},n_1,n_2}$, one obtains the well-known Bogoliubov-de Gennes (BdG) eigenvalue equations

$$
\hat{\mathcal{L}}_{\mathbf{k}} \begin{pmatrix} \underline{u}_{\mathbf{k}} \\ \underline{v}_{\mathbf{k}} \end{pmatrix} = \omega_{\mathbf{k}} \begin{pmatrix} \underline{u}_{\mathbf{k}} \\ \underline{v}_{\mathbf{k}} \end{pmatrix}\quad,\quad \hat{\mathcal{L}}_{\mathbf{k}} \equiv \begin{pmatrix} \mathbf{H}_{\mathbf{k}} & \mathbf{K}_{\mathbf{k}} \\ -\mathbf{K}_{\mathbf{k}} & -\mathbf{H}_{\mathbf{k}} \end{pmatrix}, \tag{2.13}
$$

The positive eigenvalues $\omega_{\mathbf{k}}$ of the pseudo-Hermitian matrix $\hat{\mathcal{L}}_{\mathbf{k}}$ are identified with the multi-branch excitation spectrum of the system. The matrix blocks $\mathbf{H}_{\mathbf{k}}$ and $\mathbf{K}_{\mathbf{k}}$ are akin to those describing quantum fluctuations above the one-component Gutzwiller

state in Chapter 1,

$$
\begin{aligned}
H_{\mathbf{k}}^{n_i,n_i'} \equiv {}& (H_{n_1,n_2} - \omega_0)\, \delta_{n_1,n_1'} \delta_{n_2,n_2'} \\
& + \varepsilon_0\, \psi_{0,1} \left(\sqrt{n_1'}\, \delta_{n_1',n_1+1} + \sqrt{n_1}\, \delta_{n_1,n_1'+1} \right) \delta_{n_2,n_2'} \\
& + \varepsilon_0\, \psi_{0,2} \left(\sqrt{n_2'}\, \delta_{n_2',n_2+1} + \sqrt{n_2}\, \delta_{n_2,n_2'+1} \right) \delta_{n_1,n_1'} \\
& + \varepsilon_{\mathbf{k}} \left(\sqrt{n_1+1}\, \sqrt{n_1'+1}\, c_{n_1+1,n_2}^0\, c_{n_1'+1,n_2'}^0 + \sqrt{n_1}\, \sqrt{n_1'}\, c_{n_1-1,n_2}^0\, c_{n_1'-1,n_2'}^0 \right) \\
& + \varepsilon_{\mathbf{k}} \left(\sqrt{n_2+1}\, \sqrt{n_2'+1}\, c_{n_1,n_2+1}^0\, c_{n_1',n_2'+1}^0 + \sqrt{n_2}\, \sqrt{n_2'}\, c_{n_1,n_2-1}^0\, c_{n_1',n_2'-1}^0 \right) ,
\end{aligned}
\tag{2.14a}
$$

$$
\begin{aligned}
K_{\mathbf{k}}^{n_i,n_i'} \equiv {}& \varepsilon_{\mathbf{k}} \left(\sqrt{n_1+1}\, \sqrt{n_1'}\, c_{n_1+1,n_2}^0\, c_{n_1'-1,n_2'}^0 + \sqrt{n_1}\, \sqrt{n_1'+1}\, c_{n_1-1,n_2}^0\, c_{n_1'+1,n_2'}^0 \right) \\
& + \varepsilon_{\mathbf{k}} \left(\sqrt{n_2+1}\, \sqrt{n_2'}\, c_{n_1,n_2+1}^0\, c_{n_1',n_2'-1}^0 + \sqrt{n_2}\, \sqrt{n_2'+1}\, c_{n_1,n_2-1}^0\, c_{n_1',n_2'+1}^0 \right) .
\end{aligned}
\tag{2.14b}
$$

For later convenience, we notice that the dependence on $\mathbf{k}$ of the excitations is solely determined by the variable

$$
x \equiv \left[\frac{1}{d} \sum_{j=1}^{d} \sin\left(\frac{k_j}{2} \right)^2 \right]^{1/2} ,
\tag{2.15}
$$

which varies from 0 to 1 and scales as $x \approx |\mathbf{k}| / \left(2\sqrt{d} \right)$ at small momenta.

We conclude this Subsection by introducing some useful definitions. Making use of Eq. (2.12), the linear response dynamics of the one-body order parameter $\psi_i(\mathbf{r}, t) = \psi_{0,i} + \delta\psi_i(\mathbf{r}, t)$ can be expanded in plane waves as

$$
\delta\psi_i(\mathbf{r}, t) \equiv \sum_{\mathbf{k}} \left[U_{i,\mathbf{k}}\, e^{i(\mathbf{k}\cdot\mathbf{r} - \omega_{\mathbf{k}} t)} + V_{i,\mathbf{k}}^{*}\, e^{-i(\mathbf{k}\cdot\mathbf{r} - \omega_{\mathbf{k}} t)} \right] ,
\tag{2.16}
$$

where the particle-hole amplitudes

$$
U_{1,\mathbf{k}} \equiv \sum_{n_1,n_2} \sqrt{n_1} \left(c_{n_1-1,n_2}^0\, u_{\mathbf{k},n_1,n_2} + c_{n_1,n_2}^0\, v_{\mathbf{k},n_1-1,n_2} \right) ,
\tag{2.17a}
$$

$$
V_{1,\mathbf{k}} \equiv \sum_{n_1,n_2} \sqrt{n_1} \left(c_{n_1,n_2}^0\, u_{\mathbf{k},n_1-1,n_2} + c_{n_1-1,n_2}^0\, v_{\mathbf{k},n_1,n_2} \right) ,
\tag{2.17b}
$$

$$
U_{2,\mathbf{k}} \equiv \sum_{n_1,n_2} \sqrt{n_2} \left(c_{n_1,n_2-1}^0\, u_{\mathbf{k},n_1,n_2} + c_{n_1,n_2}^0\, v_{\mathbf{k},n_1,n_2-1} \right) ,
\tag{2.17c}
$$

$$
V_{2,\mathbf{k}} \equiv \sum_{n_1,n_2} \sqrt{n_2} \left(c_{n_1,n_2}^0\, u_{\mathbf{k},n_1,n_2-1} + c_{n_1,n_2-1}^0\, v_{\mathbf{k},n_1,n_2} \right) ,
\tag{2.17d}
$$

naturally emerge as generalisations of Eqs. (1.24) with reference to the one-component Bose field. Along similar lines, linear fluctuations of the local density for each species have the form

$$
n_i(\mathbf{r}, t) = n_{0,i} + \sum_{\mathbf{k}} \left[N_{i,\mathbf{k}}\, e^{i(\mathbf{k}\cdot\mathbf{r} - \omega_{\mathbf{k}} t)} + \text{c.c.} \right] ,
\tag{2.18}
$$

where

$$N_{i,\mathbf{k}} \equiv \sum_{n_1,n_2} (n_1\,\delta_{i,1} + n_2\,\delta_{i,2}) \left[\left(c^0_{n_1,n_2} \right)^* u_{\mathbf{k},n_1,n_2} + c^0_{n_1,n_2}\, v_{\mathbf{k},n_1,n_2} \right] \qquad (2.19)$$

is the one-boson density fluctuation amplitude.

Taking inspiration from [52], in order to enrich our analysis of the elementary excitations of the system, we introduce the function

$$\mathcal{C}_{i,\alpha,\mathbf{k}} \equiv \frac{|U_{i,\alpha,\mathbf{k}}| - |V_{i,\alpha,\mathbf{k}}|}{|U_{i,\alpha,\mathbf{k}}| + |V_{i,\alpha,\mathbf{k}}|}\,, \qquad (2.20)$$

whose zeros indicate excitation modes $(\alpha, \mathbf{k})$ matching the Particle-Hole Symmetry (PHS) condition $|U_{i,\alpha,\mathbf{k}}| = |V_{i,\alpha,\mathbf{k}}|$. We note that $\mathcal{C}_{i,\alpha,\mathbf{k}}$ is independent of species i due to the fact that, as a consequence of $\mathbb{Z}_2$ symmetry, $U_{i,\alpha,\mathbf{k}}$ and $V_{i,\alpha,\mathbf{k}}$ can differ at most by an overall phase between the two components. To quantify such phase differences, we additionally define the function

$$\mathcal{B}_{\alpha,\mathbf{k}} \equiv \frac{U_{1,\alpha,\mathbf{k}} + V_{1,\alpha,\mathbf{k}}}{U_{2,\alpha,\mathbf{k}} + V_{2,\alpha,\mathbf{k}}}\,, \qquad (2.21)$$

which can assume either the value 1 or -1 only depending on whether the excitation mode $(\alpha, \mathbf{k})$ has density or spin character, respectively.

In the following, we will use the above formal premises to analyse in the detail the peculiar properties of the ground state and its excitations inside the MI and superfluid (SF, CFSF and PSF) phases of the model, with particular attention to the structure of the collective modes across the different quantum critical regimes.

2.2.2 Ground state and excitations

In this Subsection, we explore the phase diagram of the system for repulsive ($U_{12} > 0$) and attractive ($U_{12} < 0$) interspecies interactions. Moreover, we perform a detailed characterisation of the excitations of the system across the various quantum phase transitions of the BH model. Looking ahead, the analysis of this Subsection will facilitate an in-depth understanding of the response functions and quantum correlations in terms of the spectral structure of the collective modes by means of the QGA, which is the subject of the remainder of this Chapter.

We preface our discussion by anticipating that, in addition to the physics of the single-species BH model and depending on the sign of the interspecies interaction U_{12}, CFSF and PSF phases are found to intrude between the MI regions, signalled respectively by non-zero values of the pairing order parameters $\psi_{0,\mathrm{C}}$ and $\psi_{0,\mathrm{P}}$. Moreover, these quantities may be non-zero in the vicinity of the various phase transitions alongside a finite one-body condensate $\psi_{0,i}$, which marks the entrance into the SF region. Ultimately, the pair/antipair order parameters vanish in the limit $2\,d\,J/U \gg 1$, where one-body condensation is favoured as expected.

Repulsive interaction $U_{12} > 0$

(*Mott Insulator*) – In Figure 2.1(a)-(b), we show the ground state phase diagram for two values of $U_{12} > 0$. In general, for strong enough U we find MI regions [light blue
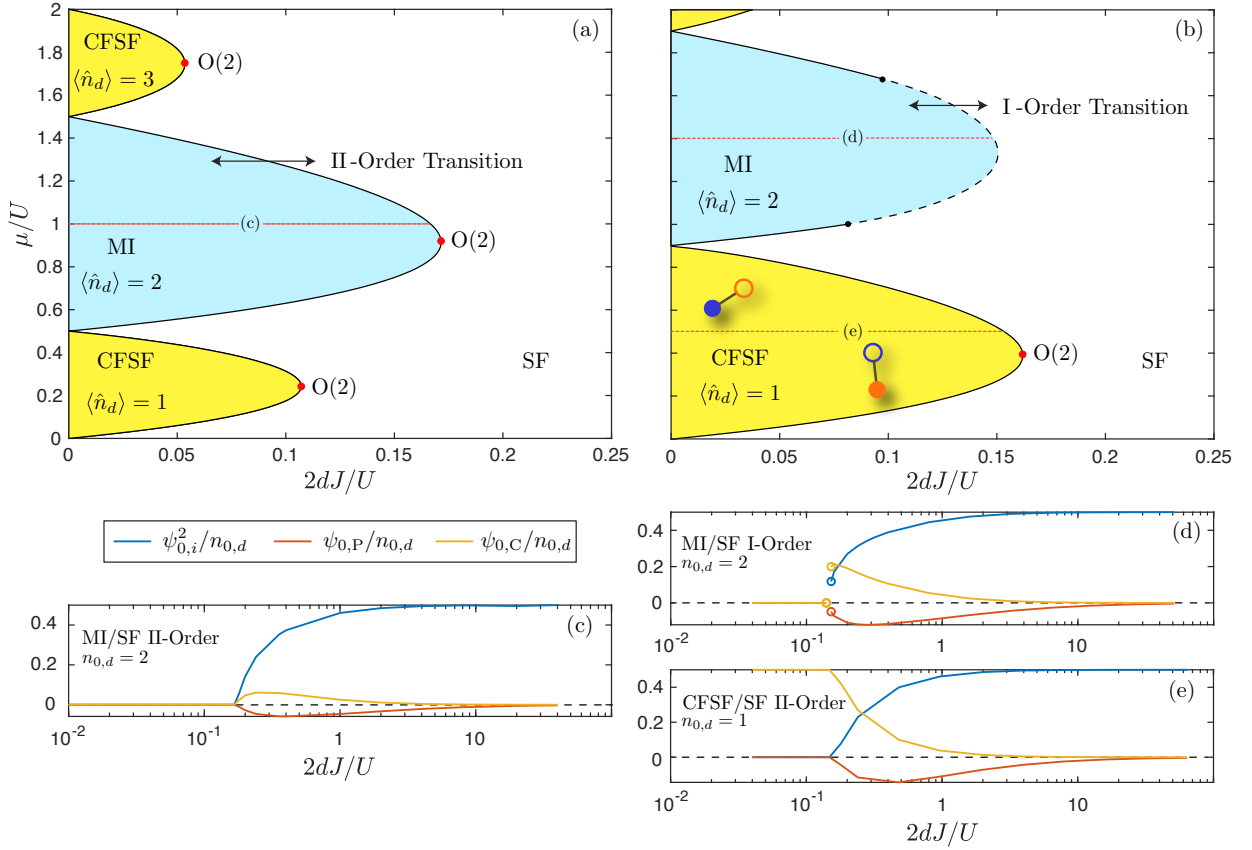
Figure 2.1: Ground state phase diagram for repulsive interspecies interactions (a) $U_{12}/U = 0.5$ and (b) $U_{12}/U = 0.9$. First and second-order transition lines are indicated by dashed and solid lines respectively, separating the MI (CFSF) lobes, identified by light blue (yellow) areas, from the SF region. The O(2) tip transitions are indicated by red dots, while the dot-shaped illustrations depict the particle-hole antipairs coupling the two components in the CFSF phase. (c) behaviour of the order parameters at the crossing of the second-order MI-to-SF transition for fixed $n_{0,d} = 2$ and $U_{12}/U = 0.5$. (d) behaviour of the order parameters at the crossing of the first-order MI-to-SF transition for fixed $n_{0,d} = 2$ and $U_{12}/U = 0.9$. (e) behaviour of the order parameters at the crossing of the second-order CFSF-to-SF transition for fixed $n_{0,d} = 1$ and $U_{12}/U = 0.9$. The solid red lines in (a) and (b) correspond to the $\mu(U)$ lines along which the data in (c), (d), and (e) are evaluated prior to the superfluid transition.

areas] at even total filling whose ground state is $|n_{0,d}/2, n_{0,d}/2\rangle$ with energy

$$\omega_0 = \frac{U}{4} n_{0,d} (n_{0,d} - 2) - \mu \, n_{0,d} + \frac{U_{12}}{4} n_{0,d}^2 . \qquad (2.22)$$

Within the MI lobes, the excitation spectrum can be calculated analytically from Eq. (2.13), with the result

$$\omega_{\pm,\mathbf{k}} \equiv \frac{1}{2} \sqrt{U^2 - 2 \, J(\mathbf{k}) \, U(n_{0,d} + 1) + J^2(\mathbf{k})} \pm \left[\frac{J(\mathbf{k}) - U(n_{0,d} - 1)}{2} - U_{12} + \mu \right] , \qquad (2.23)$$

which is a modification of the one-component result to include the mean-field interaction energy between different species. This spectrum describes four dispersive branches in total, a pair of degenerate particle ("+") branches and a pair of degenerate hole ("−") branches [2].

The second-order phase transition boundary between the MI and SF phases is

---

[2] On top of the doublon-holon excitations, Eq. (2.13) exhibits an infinity of non-zero, uncoupled diagonal

determined by the onset of a finite one-body order parameter $\psi_{0,i}$ and the disappearance of the gap in the excitation spectrum ($\omega_{\mathbf{k}=\mathbf{0}} = 0$). From Eq. (2.23), we find that this occurs for

$$2\,d\left(\frac{J}{U}\right)^{\mathrm{MI}}_{c} = \frac{(n_{0,d}/2 - \mu/U + U_{12}/U)(\mu/U - U_{12}/U - n_{0,d}/2 + 1)}{1 + \mu/U - U_{12}/U}\,, \qquad (2.25)$$

which can be linked to the MI boundary of the one-component case via the mean-field shift $\mu \to \mu - U_{12}$. The maximal value of $2\,d\,(J/U)^{\mathrm{MI}}_{c}$ determines the locations of the O(2) transitions at

$$2\,d\left(\frac{J}{U}\right)^{\mathrm{MI,tip}}_{c} = \left(\sqrt{\frac{n_{0,d}}{2}+1} - \sqrt{\frac{n_{0,d}}{2}}\right)^{2}\,, \qquad (2.26)$$

in correspondence of the *tip* of the MI lobes. We note that the chemical potential of the tip critical points is again shifted with respect to the one-component value and is given by

$$\left(\frac{\mu}{U}\right)^{\mathrm{MI,tip}}_{c} = \sqrt{\frac{n_{0,d}}{2}\left(\frac{n_{0,d}}{2}+1\right)} + \frac{U_{12}}{U} - 1\,. \qquad (2.27)$$

In Figure 2.2(a), we show how the band structure changes as the second-order MI-to-SF transition is traversed through the *edge* of the lobe (namely, away from the tip), specifically for $n_{0,d} = 2$ at $2\,d\,(J/U)^{\mathrm{MI}}_{c} \approx 0.167$ for $U_{12}/U = 0.5$ and $\mu/U = 1$. In general, in the MI phase, if the chemical potential is set above (below) its value at the tip, the first two bands are a pair of degenerate gapped particle (hole) bands of mixed spin or density character, whereas the next two bands correspond to degenerate gapped hole (particle) excitations. The doubly degenerate non-dispersive band $\omega_{0,2}$ is also visible as a dotted horizontal line. At the transition point, the gap of the lowest pair of degenerate particle (hole) bands vanish, while the hole (particle) bands remain gapped. Additionally, the gapless modes are purely quadratic at low momenta, signalling the characteristic vanishing of the speed of sound on the SF side of the transition, a feature in common with the one-component case [51].

In Figure 2.2(b), we perform a similar analysis of the spectral features of the second-order MI-to-SF transition when traversed through the tip critical point at $2\,d\,(J/U)^{\mathrm{MI,tip}}_{c} \approx 0.172$ for $U_{12}/U = 0.5$ and $(\mu/U)^{\mathrm{MI,tip}}_{c} \approx 0.914$. Most importantly, we observe that at the tip transition the gaps of the doubly degenerate particle and hole bands vanish simultaneously. Also, their dispersion becomes degenerate and perfectly linear at low momenta, giving the typical sound excitations characterising a O(2) criticality [51].

Once the SF phase takes over, both at the edge and at the tip transition, the excitation bands which become gapless hybridise into spin and density modes [see Figure 2.2(c)].

---

elements which describe non-dispersive bands with energy

$$\omega^{\mathrm{MI}}_{n_1,n_2} \equiv \sum_{i=1}^{2}\left[\frac{U}{2}n_i(n_i-1) - \mu\,n_i\right] + U_{12}\,n_1\,n_2 - \omega_0\,, \qquad (2.24)$$

where the occupation indices n_1 and n_2 must be chosen not to fall into the 4×4 block that yields the dispersive bands (2.23). Therefore, Eq. (2.24) applies to non-negative integers n_1 and n_2 such that *neither* $(n_1, n_2) = (j, j \pm 1)$ *nor* $(j \pm 1, j)$ with $j \in \mathbb{N}$ are satisfied. We note also that, as a consequence of $\mathbb{Z}_2$ symmetry, these bands are doubly degenerate under the exchange of indices $\omega^{\mathrm{MI}}_{n_1,n_2} = \omega^{\mathrm{MI}}_{n_2,n_1}$ for $n_1 \neq n_2$.
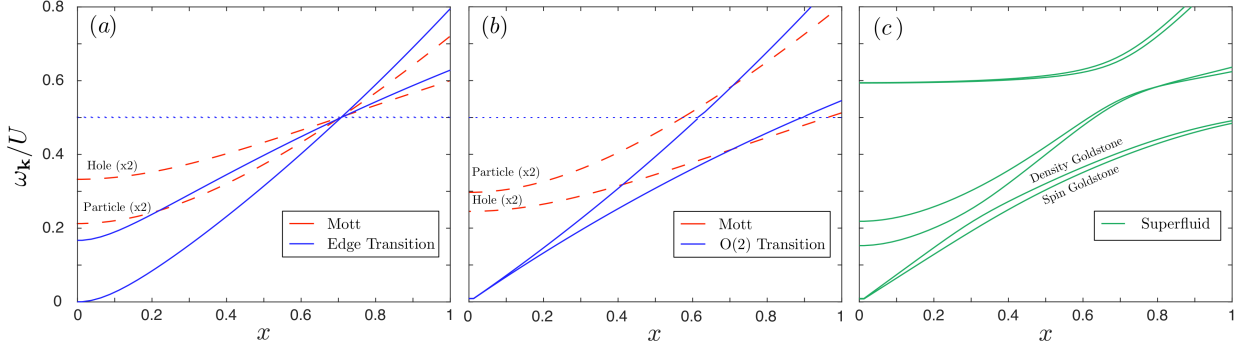
Figure 2.2: Excitation spectra across the MI-to-SF second-order (a) edge transition at $\mu/U = 1$ and (b) O(2) transition at $(\mu/U)_c^{\mathrm{MI,tip}} \approx 0.914$, as well as (c) in the SF phase for $\mu/U = (\mu/U)_c^{\mathrm{MI,tip}}$, choosing $U_{12}/U = 0.5$ at fixed $n_{0,d} = 2$ in $d = 2$. For the edge transition in panel (a), the chosen hopping energies are $2\,d\,J/U = 0.12$ (red lines) and $2\,d\,(J/U)_c^{\mathrm{MI}} \approx 0.167$ (blue lines); for the O(2) transition in panel (b), the hopping energies $2\,d\,J/U = 0.12$ (red lines) and $2\,d\,(J/U)_c^{\mathrm{MI,tip}} \approx 0.172$ (blue lines) are considered. The hopping energy in the SF phase in panel (c) is $2\,d\,J/U = 0.18$. The parentheses in panels (a)-(b) refer to the degeneracy of the hybridised particle and hole bands, while the spin and density Goldstone modes are indicated explicitly. The blue dotted horizontal lines correspond to the doubly degenerate non-dispersive band $\omega_{0,2}$.

These excitations correspond to the Goldstone modes that result from the breaking of the two U(1) symmetries of the model: one for the density (oscillations of the global phase of the binary condensate) and the other for the spin channel (oscillations of the relative phase between the order parameters of different components). Their dispersion relation approaches the Bogoliubov bands [51]

$$\omega_{\mathrm{Bog},d/s,\mathbf{k}} \equiv \sqrt{\epsilon(\mathbf{k})\left[\epsilon(\mathbf{k}) + n_{0,d}\left(U \pm U_{12}\right)\right]} \qquad (2.28)$$

Density and spin Goldstone modes

in the weakly-interacting limit $2\,d\,J/U \gg 1$. Close to the transition, the first two gapped branches, which also display individual density and spin character, are referred to as the Higgs modes of the system, in analogy to the single-component BH model [32, 66, 67, 119]. The $\omega_{0,2}$ band becomes dispersive and hybridises into spin and density excitations as well.

The transition between MI and SF phase can also be of the first order, as discussed in [91, 117, 118, 120]. In this case, the one-body order parameters $\psi_{0,i}$ display a discontinuity across the critical boundary, as shown in Figure 2.1(d). The behaviour of the discontinuity at the first-order transition was studied in the mean-field Gutzwiller analysis of [118], where it was found that: (i) the jump of the order parameter increases with U_{12} and then rapidly goes to zero as the phase separation point $U_{12}/U \sim 1$ is approached; (ii) the hopping window corresponding to the first-order transition widens with increasing U_{12} starting from the tip and reaching $J = 0$ when approaching the phase separation condition. Across the first-order critical point, the structure of the excitation spectrum changes discontinuously between the different spectral features discussed before, such that the modes in the MI and SF phases cannot be smoothly connected.

(*Counterflow Superfluid*) – In Figure 2.1(a)-(b), the phase diagram displays also CFSF phases [yellow areas] at odd total filling, characterised by a finite antipair order parameter $\psi_{0,C}$ and whose size increases with larger U_{12}. Within the CFSF lobes, one finds that the Fock states $|(n_{0,d} + 1)/2, (n_{0,d} - 1)/2\rangle$ and $|(n_{0,d} - 1)/2, (n_{0,d} + 1)/2\rangle$

are doubly degenerate with ground state energy

$$\omega_0 = U\,(n_{0,d}-1)^2 + U_{12}\,n_{0,d}\,(n_{0,d}-1) - \mu\,(2\,n_{0,d}-1)\,. \tag{2.29}$$

Comparing this energy with Eq. (2.22), we can identify the boundary between neighbouring MI and CFSF lobes at $J = 0$, which is located at $\mu = U_{12}$ in the case of the $n_{0,d} = 1$ CFSF lobe and the $n_{0,d} = 2$ MI lobe. In order to obtain the correct ground state, we symmetrise the antipair state as $[\,|\,(n_{0,d}+1)/2, (n_{0,d}-1)/2\,\rangle + |\,(n_{0,d}-1)/2, (n_{0,d}+1)/2\,\rangle\,]/\sqrt{2}$, as predicted in [54, 91, 92, 94, 95, 119].

In the CFSF phase, particle and hole excitations involve the subset of states $\{\,|\,(n_{0,d}+1)/2 \pm 1, (n_{0,d}-1)/2\,\rangle\,;\,|\,(n_{0,d}+1)/2, (n_{0,d}-1)/2 \pm 1\,\rangle\,\}$, which amount to three particle-like excitations and one (three) hole-excitations for the CFSF phase for $n_{0,d} = 1$ ($n_{0,d} \geq 3$). From these excitations, one can construct three (four) modes belonging to the density channel, plus one (two) belonging to the spin channel. The general behaviour of the excitation spectrum is such that a pair of particle and hole branches in the density channel lower their energy while moving towards the boundary of the CFSF lobe, with the particle (hole) excitation closing the gap if the transition in crossed above (below) the tip chemical potential. Exactly at the tip, the lowest particle and hole excitations in the density channel close the gap simultaneously. Remarkably, the distinction between the edge and tip critical points in the density channel closely resembles the properties of the MI-to-SF transition.

For the CFSF region with $n_{0,d} = 1$, the excitation spectrum can be calculated analytically from Eq. (2.13). In this case, the spin channel hosts only one particle branch, decoupled from the rest of the spectrum and given by

$$\omega_{\mathrm{CFSF},s,\mathbf{k}} = U - \mu - J(\mathbf{k})\,. \tag{2.30}$$

Spectrum of the CFSF phase

This corresponds to a free-particle dispersion, shifted by the mean-field local energy $U - \mu$. In the density sector, we extract two particle branches and one hole branch, whose excitation energies are the solutions of the equation

$$J(\mathbf{k})\left[U\,U_{12} - (\omega_{\mathbf{k}} \pm \mu)^2\right] \mp (\omega_{\mathbf{k}} \pm \mu)(U \mp \omega_{\mathbf{k}} - \mu)(U_{12} \mp \omega_{\mathbf{k}} - \mu) = 0\,. \tag{2.31}$$

Similarly to the spectrum of the MI phase, all the other excitations consist in an infinite sequence of non-dispersive bands, the first two of which have energies $\omega_{0,1} = \omega_{1,0} = -\mu - \omega_0 = 0$. In particular, these branches correspond to (unphysical) cost-free excitations reflecting the degeneracy of the antipair states forming the mean-field ground state of the CFSF phase [3]. In [118], these bands were found to acquire a sound-like profile when higher-order hopping processes are included perturbatively in CFSF phase. These contributions are however neglected in the TDGE (2.8), from which instead we extract higher gapped excitation modes, absent in that work, whose low-energy behaviour is strongly tied to the appearance of the SF phase and determines the one-body correlations in the CFSF phase. We will address this last point more explicitly in Section 2.3.

---

[3] We note that the flat bands $\omega_{0,1} = \omega_{1,0}$ describe (trivial) excitations within the antipair sector $\{u_{0,1}, u_{1,0}, v_{0,1}, v_{1,0}\}$ and therefore cannot describe the tunnelling of antipairs out of the ground state. Indeed, the blind inclusion of such *ghost* collective modes into our description of quantum fluctuations leads to violated completeness relations (see Appendix C.1).
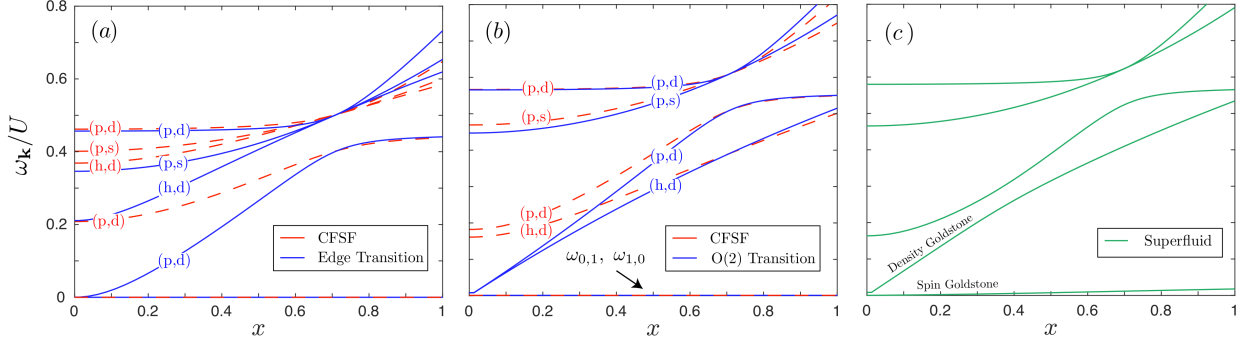
Figure 2.3: Excitation spectra across the CFSF-to-SF second-order for $U_{12}/U = 0.9$ at fixed $n_{0,d} = 1$ in $d = 2$ for: (a) the edge transition at $\mu/U = 0.5$; (b) the O(2) transition at $(\mu/U)_c^{\text{CFSF,tip}} \approx 0.391$; (c) the SF phase for $\mu/U = (\mu/U)_c^{\text{CFSF,tip}}$. For the edge transition in panel (a), the chosen hopping energies are $2\,d\,J/U = 0.1$ (red lines) and $2\,d\,(J/U)_c^{\text{CFSF}} \approx 0.154$ (blue lines); for the O(2) transition in panel (b), the hopping energies are $2\,d\,J/U = 0.14$ (red lines) and $2\,d\,(J/U)_c^{\text{CFSF,tip}} \approx 0.162$ (blue lines). The hopping energy in the SF phase in panel (c) is $2\,d\,J/U = 0.172$. The particle (hole) and spin (density) characters of gapped excitations, as well as the physical nature of the Goldstone modes, are indicated explicitly by the labels "p" ("h") and "s" ("d"), respectively.

The second-order transition boundary between the CFSF and SF phases is determined from the closure of the smallest gap in the CFSF excitation spectrum. From Eq. (2.31), we find that for $n_{0,d} = 1$ the gap closing occurs at

$$2\,d\left(\frac{J}{U}\right)_c^{\text{CFSF}} = \frac{\mu}{U}\frac{(1 - \mu/U)\,(\mu/U - U_{12}/U)}{(\mu/U)^2 - U_{12}/U}\,, \qquad (2.32)$$

whose maximal value gives the location of the tip of the CFSF lobe. As a reference, we mention that for $U_{12}/U = 0.9$ the location of the tip of the $n_{0,d} = 1$ CFSF lobe shown in Figure 2.1(b) is located at $\{(\mu/U)_c^{\text{CFSF,tip}} \approx 0.391,\ 2\,d\,(J/U)_c^{\text{CFSF,tip}} \approx 0.164\}$.

In Figure 2.3(a), we show how the excitation spectrum appears as the second-order CFSF-to-SF transition for $n_{0,d} = 1$ and $U_{12}/U = 0.9$ is crossed through the edge point at $2\,d\,(J/U)_c^{\text{CFSF}} \approx 0.154$ at $\mu/U = 0.5$. Above (below) the tip chemical potential, the gap is closed by the lowest particle (hole) band in the density channel, while the other bands remain gapped. More specifically, the particle band in the spin channel corresponding to Eq. (2.30), which is the third in ascending order at $x = 0$, never participates in the gap closure. In Figure 2.3(b), we consider the evolution of the band structure across the tip transition at $2\,d\,(J/U)_c^{\text{CFSF,tip}} \approx 0.162$ for $U_{12}/U = 0.9$ and $(\mu/U)_c^{\text{CFSF,tip}} \approx 0.391$, while holding $n_{0,d} = 1$ fixed. Indeed, we observe that at the transition point the gaps of the two lowest-energy bands in the density channel vanish, while the remaining modes retain a finite gap. In the SF region, illustrated in Figure 2.3(c), the two lowest bands in the density channel participate in the creation of the density Goldstone and the density Higgs excitation, respectively. The spin Goldstone mode emerges from the non-dispersive antipair bands $\omega_{0,1} = \omega_{1,0}$ as discussed before.

Attractive interaction $U_{12} < 0$

(*Mott Insulator*) – In Figure 2.4(a)-(b), we show the ground state phase diagram for two different values of $U_{12} < 0$. For attractive interactions, the MI lobes present the same ground state and spectral properties as their repulsive counterparts, with the spin/density character of the excitation modes being reversed. Furthermore, the MI-to-SF criticality is found again to be of either the first or second order. However, at
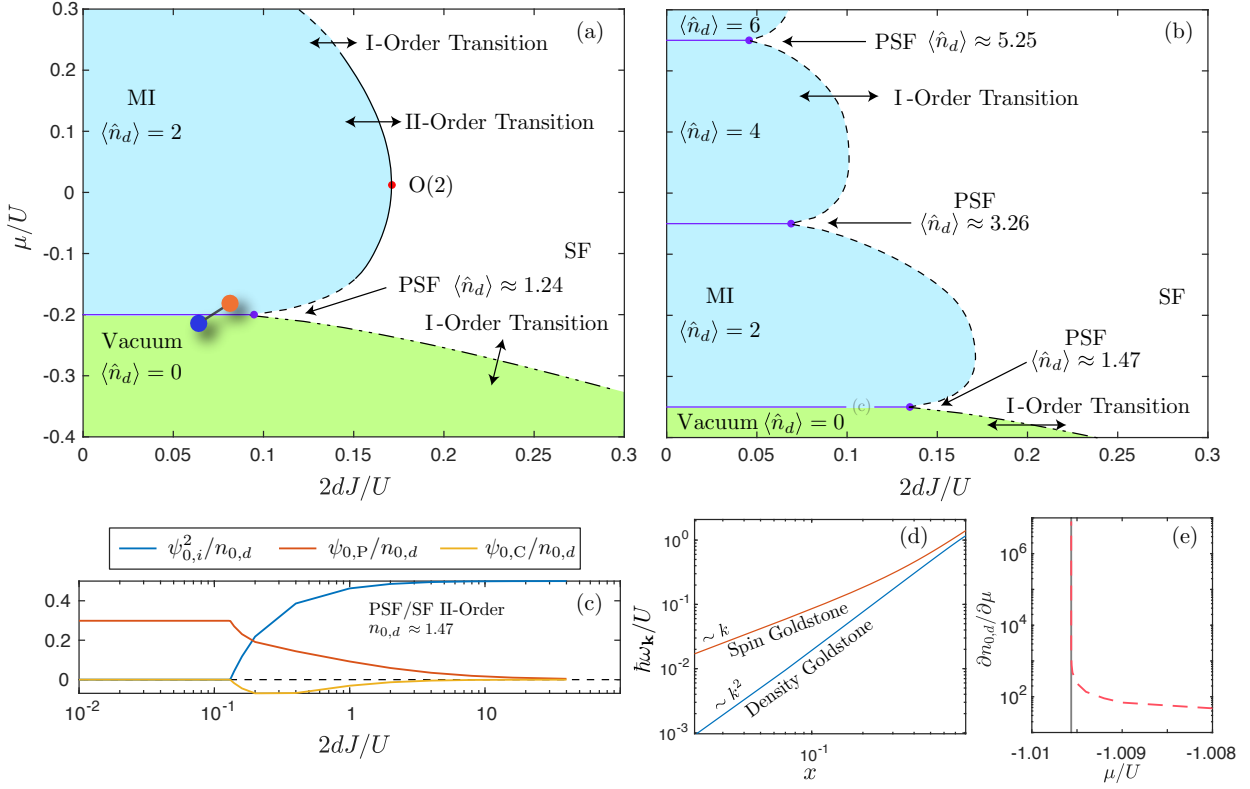
Figure 2.4: Ground state phase diagram for attractive interspecies interactions (a) $U_{12}/U = -0.4$ and (b) $U_{12}/U = -0.7$, with the order of the transition lines and O(2) critical points within the MI lobes indicated as in Figure 2.1. The PSF phase is identified by the purple horizontal lines, with total filling $n_{0,d}$ evaluated in the $\eta \to 0^+$ limit. The dot-shaped illustrations depict the particle-particle pairs that develop between the two components of the gas in the PSF phase. (c) behaviour of the order parameters along the PSF-to-SF transition line at the border between the vacuum (green-shaded area) and the $n_{0,d} = 2$ MI lobes for $U_{12}/U = -0.7$ and fixed $n_{0,d} \approx 1.47$. (d)-(e) Excitation spectrum and compressibility near the first-order vacuum-to-SF transition for $\mu/U \approx -1.01$, $2\,d\,J/U = 1$, and $U_{12}/U = -0.6$ with critical filling $n_{0,d} \approx 0.239$. The log-log scale of the vertical axis of panel (e) reveals the quadratic power law of the density Goldstone mode at all momenta.

odds with the repulsive case, the first-order boundaries appear initially at small J/U rather than close to the tip, as shown in Figure 2.4(b) for $U_{12}/U = -0.4$, eventually spanning the entire lobe boundary, as shown in Figure 2.4(b) already for $U_{12}/U = -0.7$. In addition, the boundary between the vacuum lobe [green area] and the SF phase becomes also a first-order transition line. Along this boundary, the density Goldstone mode acquires a purely quadratic dispersion $\omega_{d,\mathbf{k}} \propto \mathbf{k}^2$ at small momenta, as shown in Figure 2.4(d), which indicates the vanishing of the sound velocity of density excitations ($c_d \to 0$), while the spin sound velocity remains finite ($c_s > 0$). Accordingly, the compressibility $\partial n_{0,d}/\partial\mu$ diverges due to the discontinuity in the filling, as shown in Figure 2.4(e). These behaviours indicate that the system *collapses* along the first-order vacuum-to-SF transition boundary, presumably towards a droplet phase [121–123]. Along this line, the critical filling decreases for increasing $2\,d\,J/U$, vanishing eventually in the deep SF regime (not shown), where the transition becomes again of second order. As U_{12}/U becomes more attractive, the first-order criticality extends towards larger values of $2\,d\,J/U$.

(*Pair Superfluid*) – The MI lobes shown in Figure 2.4(a)-(b) are separated by sharp transition lines [purple horizontal lines], extending towards increasingly large values of $2\,d\,J/U$ as U_{12} becomes more and more attractive. On these lines at the boundary
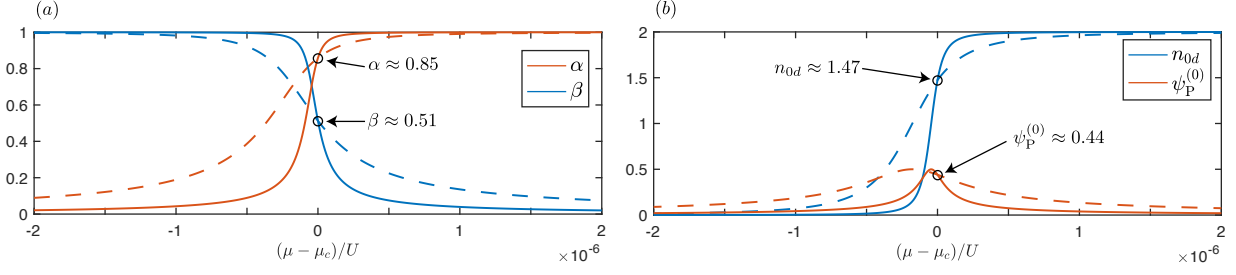
Figure 2.5: Variation of (a) $n_{0,d}$ and $\psi_{0,\mathrm{P}}$ and (b) α and β as functions of μ/U in the vicinity of the PSF line at $(\mu/U)_c^{\mathrm{PSF}} = -0.35$ for fixed $2\,d\,J/U = 0.12$ and $U_{12}/U = -0.7$. Solid (dashed) lines correspond to the symmetry-breaking offset $\eta = 10^{-3}(2 \times 10^{-3})$.

between the $n_{0,d} = 2\,j$ and $n_{0,d} = 2\,(j+1)$ MI lobes, one finds that the states with the lowest eigenenergies $|j+1, j+1\rangle$ and $|j, j\rangle$ are degenerate, thus corresponding to a PSF phase with a finite pair coherence $\psi_{0,P} \neq 0$. When imposed in the TDGE, such degeneracy condition pinpoints the location of the PSF lines on a discrete set of critical chemical potentials $(\mu/U)_c^{\mathrm{PSF}}$ through the equation

$$-U_{12} - 2\,j\,(U + U_{12}) + 2\,\mu_c^{\mathrm{PSF}} = 0\,, \tag{2.33}$$

valid for any non-negative integer j. Thus, in general the ground state is given by the superposition $\alpha\,|j+1, j+1\rangle + \beta\,|j, j\rangle$, where the coefficients α and β are restricted to lie on the unit circle $|\alpha|^2 + |\beta|^2 = 1$. However, these coefficients are *undetermined* within the usual Gutzwiller ansatz, as the individual states are *inherently* $\mathbb{Z}_2$-symmetric, in contrast with the CFSF case.

The determination of α and β in the mean-field Gutzwiller theory requires the introduction of an *ad-hoc* perturbative order parameter $\psi_{0,i} = \eta > 0$ along the PSF line mimicking the tunnelling of residual background fluctuations, such that ground states with broken U(1) symmetry can be accessed. As we show in Figure 2.5(a), this turns out to uniquely fix α [orange lines] and β [light blue lines] along the PSF lines described by Eq. (2.33) *regardless* of the value of η, provided that η remains sufficiently small. In particular, concerning the PSF line separating the vacuum region from the $n_{0,d} = 2$ MI lobe, we obtain $\alpha \approx 0.858$ and $\beta \approx 0.513$, from which we derive $n_{0,d} \approx 1.47$. Similarly, for the PSF line separating the $n_{0,d} = 2$ and $n_{0,d} = 4$ MI lobes, we find $\alpha \approx 0.794$ and $\beta \approx 0.608$, which gives $n_{0,d} \approx 3.260$ in the PSF phase. In this way, we reliably obtain a PSF ground state with a well-defined value of the pair order parameter $\psi_{0,\mathrm{P}} \neq 0$.

In the QMC study of [109], α and β were found to vary with μ at fixed U_{12} and J. Analogously, the symmetry-breaking offset η makes the PSF phase line to develop a finite width, as shown in Figure 2.5(b), where the variation of $n_{0,d}$ and $\psi_{0,\mathrm{P}}$ is studied for fixed μ/U. We find that $n_{0,d}$ [light blue lines] changes continuously between the filling of the two neighbouring MI lobes, which is qualitatively consistent with the QMC results of [109], with the major difference being the size of the transition width in the chemical potential μ/U. Secondly, we also see that $\psi_{0,\mathrm{P}}$ [orange lines] behaves smoothly, vanishing identically as one enters the MI lobes and reaching a maximum in between. This reveals that the PSF-to-MI transitions are of the second order within the present approach. In general, the maximum of $\psi_{0,\mathrm{P}}$ is found to occur for a value of μ/U below the exact PSF line, becoming increasingly shifted for larger η. Also, the maximum is located where $\alpha = \beta = 1/\sqrt{2}$ [black solid line], which can be seen easily by matching
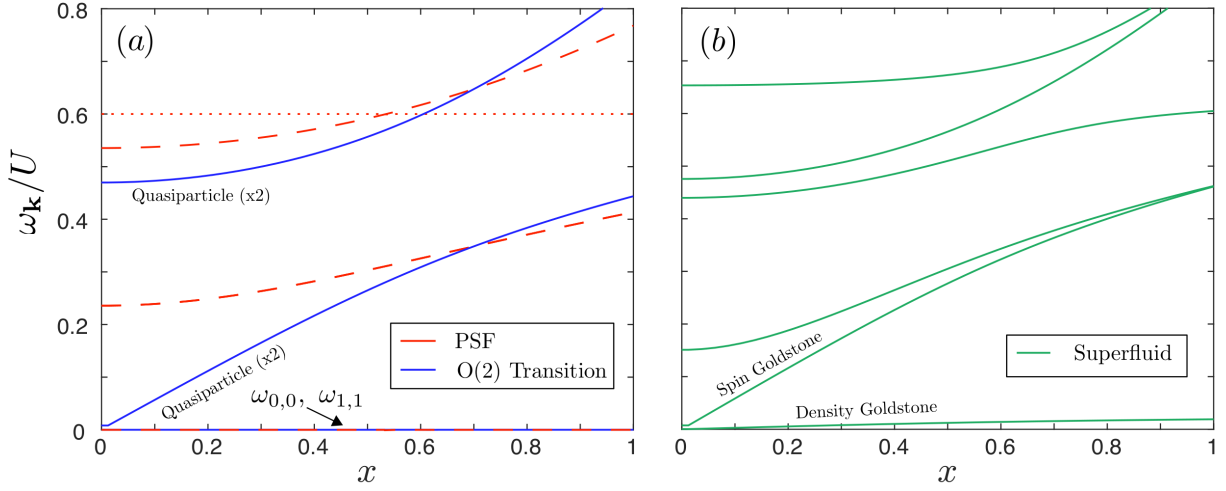
Figure 2.6: Excitation spectra (a) along the PSF-to-SF second-order transition with $n_{0,d} \approx 1.47$ and $(\mu/U)_c^{\mathrm{PSF}} = -0.35$ and (b) in the SF phase for $\mu/U \approx -0.35$ and $U_{12}/U = -0.7$ in $d = 2$. In panel (a), the hopping energies are $2\,d\,J/U = 0.08$ (red lines) and $2\,d\,(J/U)_c^{\mathrm{PSF}} \approx 0.131$ (blue lines). In the SF phase, we consider $2\,d\,J/U = 0.14$. The parentheses refer to the degeneracy of the hybridised quasiparticle bands.

the results of the two panels of Figure 2.5. However, we observe that not only α and β, but also $n_{0,d}$ and $\psi_{0,\mathrm{P}}$ are invariant with respect to the choice of the value of η if taken precisely along the PSF line ($\mu - \mu_c^{\mathrm{PSF}} = 0$). Moreover, as a function of $2\,d\,J/U$, the width of the PSF region shrinks with decreasing $2\,d\,J/U$, collapsing onto the PSF line in the strongly-interacting limit. Therefore, an infinitesimal symmetry-breaking perturbation $\eta \to 0^+$ can be safely applied for practical purposes (cfr. [124]). In the following, this limit will be assumed whenever the PSF phase is considered, in virtue of its essential insensitivity to the choice of η.

Spectrum of the PSF phase   Along the PSF line, Eq. (2.13) can be treated analytically to obtain the excitation spectrum $\omega_{\mathbf{k}}$. For the $n_{0,d} \approx 1.47$ PSF phase separating the vacuum from the $n_{0,d} = 2$ MI lobe, one obtains the implicit equation

$$
J^2(\mathbf{k}) \left[\left(8\,\beta^4 - 8\,\beta^2 + 1 \right) \mu^2 + \left(1 - 2\,\beta^2 \right)^2 U^2 + 2 \left(4\,\beta^4 - 2\,\beta^2 - 1 \right) \mu\,U - \omega_{\mathbf{k}}^2 \right]
$$
$$
+ 2\,J(\mathbf{k}) \left[\mu\,U^2 + 2\,\beta^2\,\mu^2\,U - 2 \left(\beta^2 - 1 \right) U\,\omega_{\mathbf{k}}^2 + \left(2\,\beta^2 - 1 \right) \left(\mu^2 - \omega_{\mathbf{k}}^2 \right) \mu \right]
$$
$$
+ \left(\mu^2 - \omega_{\mathbf{k}}^2 \right) \left[(\mu + U)^2 - \omega_{\mathbf{k}}^2 \right] = 0\,, \tag{2.34}
$$

which describes two distinct gapped bands, both doubly degenerate and with a mixed particle/hole characteristic $C_{i,\alpha,\mathbf{k}}$. In analogy with the CFSF phase, all the remaining excitations have a flat dispersion; in particular, the zero-energy modes $\omega_{0,0} = \omega_{1,1} = 0$ describe cost-free density fluctuations due to the formation of local particle-hole pairs within the PSF ground state predicted by Gutzwiller's mean-field theory.

Once again, the second-order phase transition from the PSF and to the SF phases is identified by the closure of the gap in the excitation spectrum. From Eq. (2.34), we find that along the $n_{0,d} \approx 1.47$ PSF line the critical hopping strength is given by

$$
2\,d \left(\frac{J}{U} \right)_c^{\mathrm{PSF}} = \frac{\mu}{U} \frac{1 + \mu/U}{\left(2 - 2\,\beta^2 \right) \mu/U - \left(1 + \mu/U \right) \left(2\,\alpha\,\beta + 1 \right)}\,. \tag{2.35}
$$

In Figure 2.6(a), we show how the excitation spectrum of the PSF phase of density $n_{0,d} \approx 1.47$ evolves as the second-order transition point $2\, d\, (J/U)_c^{\mathrm{PSF}} \approx 0.131$ is reached for $U_{12}/U = -0.7$ along the critical line at $(\mu/U)_c^{\mathrm{PSF}} = -0.35$. At the PSF-to-SF transition point, only the energy gap of the lowest quasiparticle branches vanishes, such that the band structure appears reminiscent of the MI-to-SF and CFSF-to-SF second-order tip transitions in Figure 2.2(b) and Figure 2.3(b) respectively, but with only a gapless mode being degenerate. More distinctly, the O(2)-like nature of the PSF-to-SF transition is suggested in Figure 2.6(b), where we observe that the gapless quasiparticle bands split into the Goldstone and Higgs modes active in the spin channel, while the density Goldstone mode emerges from the non-dispersive band $\omega_{0,0} = \omega_{1,1}$.

It is important to remark that the flatness of the lowest spin bands $\omega_{0,1}$ and $\omega_{1,0}$ for CFSF and density bands $\omega_{0,0}$ and $\omega_{1,1}$ for PSF is an artefact resulting from the mean-field approximation. A more careful treatment of non-local fluctuations would alter these modes to produce linear Goldstone dispersions as a result of the broken U(1) symmetry either in the spin or in the density channel, respectively.

2.3 Quantum correlations from the QGA

In this Section, we apply the QGA to calculate a range of experimentally relevant observables in two dimensions ($d = 2$): the density and spin structure factors (Subsection 2.3.1), the current response functions and associated superfluid densities (Subsection 2.3.2), the coherence function (Subsection 2.3.3), and local density and spin correlations (Subsection 2.3.4).

As a straightforward continuation of the one-component case of Chapter 1, the QGA for the two-component system relies on more structured equal-time commutation relations between the conjugate fields of the theory,

$$\left[\hat{c}_{n_1,n_2}(\mathbf{r}_1), \hat{c}_{m_1,m_2}^{\dagger}(\mathbf{r}_2) \right] = \delta_{\mathbf{r}_1,\mathbf{r}_2}\, \delta_{n_1,n_2}\, \delta_{m_1,m_2}\,, \tag{2.36}$$

as well as a different definition of the normalisation operator,

$$\hat{A}(\mathbf{r}) = \left[\hat{\mathbb{1}} - \sum_{n_1,n_2} \delta\hat{c}_{n_1,n_2}^{\dagger}(\mathbf{r})\, \delta\hat{c}_{n_1,n_2}(\mathbf{r}) \right]^{1/2}. \tag{2.37}$$

We stress that, in the same way as the Gutzwiller variables $c_{n_1,n_2}(\mathbf{r})$ assign a weight to each local configuration, the corresponding Gutzwiller operators cannot be decomposed into single-species operators without overlooking a relevant fraction of the interspecies correlations: this sharply contrasts with Bogoliubov's theory [40, 125], where the quantum fields of different species are always decoupled. It follows that the two-component QGA can take into accurate account *local* pair correlations, while quantisation allows for an approximate view on the *non-local* quantum correlations missed by mean-field theory.

In the following discussion, we will provide directly the semi-analytical predictions for the observables as provided by the QGA, while more involved and informative derivations will be briefly sketched when appropriate. For simplicity, we will assume again that the ground state of the system is the zero-temperature vacuum of the collective modes. In order to make our discussion of the QGA results consistent,

from now on we will calculate the lattice filling $n_d = \langle \hat{n}_d \rangle$ corresponding to each result by always including second-order local quantum corrections as detailed in Appendix C.2.

2.3.1 Density and spin response functions

As a first application of the QGA, we investigate the role of quantum fluctuations in the linear response dynamics of the two-component BH system to density/spin probes. The density and spin response of an ultracold system reflects the underlying correlations and collective modes of the system, and can be probed experimentally using a variety of methods, e.g. Bragg scattering or periodic modulation of the lattice depth [35, 38–40, 126, 127]. In the present case, the spin and density susceptibilities represent important tools in differentiating between the CFSF and PSF transitions, where density and spin DoF are expected to separate according to our diagnostics of the collective excitations. In general terms, we consider the effect of an external field applied at a fixed frequency ω. The local operator associated with the perturbation is denoted by $\hat{G}_{\mathbf{r}}$, while we indicate by $\hat{F}_{\mathbf{r}}$ the local operator whose linear response dynamics is under study.

Dynamical structure factors In a two-component system, the most interesting response functions are the density and the spin or magnetisation response functions, corresponding to $\hat{G}_{\mathbf{r}} = \hat{F}_{\mathbf{r}} = \hat{n}_{1,\mathbf{r}} + \hat{n}_{2,\mathbf{r}}$ and $\hat{G}_{\mathbf{r}} = \hat{F}_{\mathbf{r}} = \hat{n}_{1,\mathbf{r}} - \hat{n}_{2,\mathbf{r}}$, respectively. Such response functions are related to the density and spin structure factors of the system. Let us start from the species-resolved density response function, i.e. $\hat{G}_{\mathbf{r}} = \hat{F}_{\mathbf{r}} = \hat{n}_{i,\mathbf{r}}$, which, up to second-order in the quantum fluctuations, reads

$$\chi_{\hat{n}_i}(\mathbf{q}, \omega) = 2 \sum_{\alpha} \frac{|N_{i,\alpha,\mathbf{q}}|^2 \, \omega_{\alpha,\mathbf{q}}}{(\omega + i\,0^+)^2 - \omega_{\alpha,\mathbf{q}}^2} \tag{2.38}$$

at zero temperature. The response functions for the total density and spin channels are obtained by simple extensions of Eq. (2.38), namely

$$\chi_{\hat{n}_d}(\mathbf{q}, \omega) = 2 \sum_{\alpha} \frac{|N_{1,\alpha,\mathbf{q}} + N_{2,\alpha,\mathbf{q}}|^2 \, \omega_{\alpha,\mathbf{q}}}{(\omega + i\,0^+)^2 - \omega_{\alpha,\mathbf{q}}^2}, \tag{2.39}$$

and

$$\chi_{\hat{n}_s}(\mathbf{q}, \omega) = 2 \sum_{\alpha} \frac{|N_{1,\alpha,\mathbf{q}} - N_{2,\alpha,\mathbf{q}}|^2 \, \omega_{\alpha,\mathbf{q}}}{(\omega + i\,0^+)^2 - \omega_{\alpha,\mathbf{q}}^2}, \tag{2.40}$$

respectively. At zero temperature, the imaginary part of the response functions is proportional to the corresponding dynamical structure factors via the relation $S_{\hat{F}}(\mathbf{q}, \omega) \equiv -\text{Im}\big[\chi_{\hat{F}}(\mathbf{q}, \omega)/\pi\big]$, going under the name of Fluctuation-Dissipation Theorem (FDT) [128]. Useful information on and from the dynamical structure factors is provided by their energy momenta, also known as sum rules,

$$m_{\hat{F}}^p(\mathbf{q}) \equiv \int_0^{+\infty} d\omega \, \omega^p \, S_{\hat{F}}(\mathbf{q}, \omega). \tag{2.41}$$
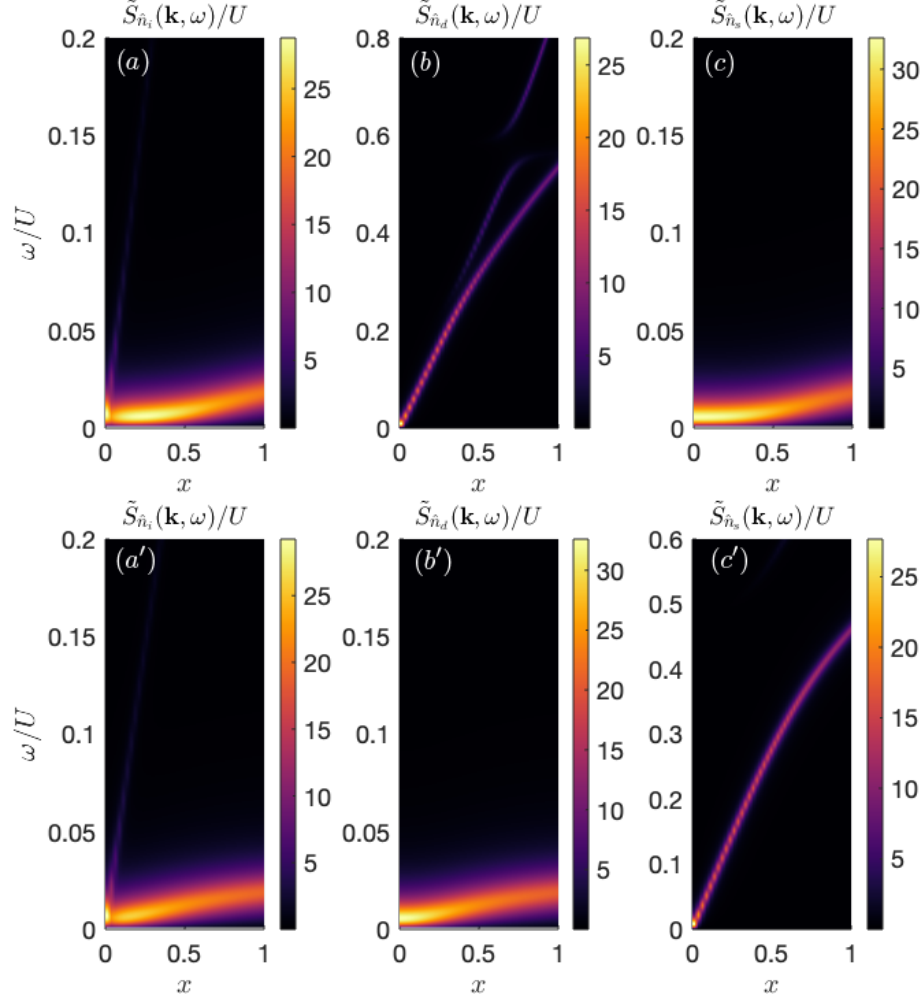
Figure 2.7: Normalised dynamical structure factors $\tilde{S}_{\hat{F}}(\mathbf{k}, \omega) = S_{\hat{F}}(\mathbf{k}, \omega)/S_{\hat{F}}(\mathbf{k})$ for (a)-(a′) the one-component density channel $\hat{F}_{\mathbf{r}} = \hat{n}_{1,\mathbf{r}}$, (b)-(b′) the total density channel $\hat{F}_{\mathbf{r}} = \hat{n}_{1,\mathbf{r}} + \hat{n}_{2,\mathbf{r}}$ and (c)-(c′) the spin channel $\hat{F}_{\mathbf{r}} = \hat{n}_{1,\mathbf{r}} - \hat{n}_{2,\mathbf{r}}$ in the SF phase in the vicinity of CFSF (a)-(c) and PSF (a′)-(c′) transitions for $d = 2$. For panels (a)-(c), the parameters are $U_{12}/U = 0.9$, $\mu/U = 0.391$, $2\,d\,J/U = 0.172$ and $n_d = 1$, see Figure 2.3(c). For (a′)-(c′) panels, the parameters are $U_{12}/U = -0.7$, $\mu/U \approx -0.35$, $2\,d\,J/U = 0.14$ and $n_d \approx 1.47$, see Figure 2.6(c).

In particular, $m^0_{\hat{F}}(\mathbf{q}) = S_{\hat{F}}(\mathbf{q})$ is the so-called static structure factor. Within our approximation in Eqs. (2.38)-(2.40), the dynamical structure factors are simply given by a sum of weighted Dirac delta functions, namely

$$S_{\hat{n}_d}(\mathbf{q}, \omega) = \sum_{\alpha} |N_{1,\alpha,\mathbf{q}} + N_{2,\alpha,\mathbf{q}}|^2 \left[\delta(\omega - \omega_{\alpha,\mathbf{q}}) - \delta(\omega + \omega_{\alpha,\mathbf{q}}) \right], \qquad (2.42)$$

$$S_{\hat{n}_s}(\mathbf{q}, \omega) = \sum_{\alpha} |N_{1,\alpha,\mathbf{q}} - N_{2,\alpha,\mathbf{q}}|^2 \left[\delta(\omega - \omega_{\alpha,\mathbf{q}}) - \delta(\omega + \omega_{\alpha,\mathbf{q}}) \right], \qquad (2.43)$$

from which the sum rules are easily determined.

Contextually to [118], the normalised dynamical structure factors $\overline{S}_{\hat{F}}(\mathbf{q}, \omega) = S_{\hat{F}}(\mathbf{q}, \omega)/S_{\hat{F}}(\mathbf{q})$ (cfr. [40]) have been analysed in the SF regime for both repulsive and attractive interspecies interactions, for which it was found that: (i) the low-momentum part of the gapped modes does not respond significantly to any of the density-type probes, in agreement with the single-component case [51, 119]; (ii) the density and spin

Goldstone modes are strongly excited by the total density and spin probes, respectively; (iii) the single-species density fluctuations are strongest on the lowest gapless branch. In [118], the density response in the PSF and CFSF regimes were also considered, although for an effective Hamiltonian including *ad-hoc* perturbative hopping processes in the strongly-interacting limit of the model.

In Figure 2.7, we show our results for the normalised dynamical structure factors in the immediate vicinity of the CFSF (a)-(c) and PSF (a′)-(c′) transitions, confirming the qualitative picture of [118] and displaying detailed signatures of the pairing phase transitions. These calculations have been performed for a total filling $\langle \hat{n}_d \rangle = 1$, including the second-order quantum corrections to the mean-field value $n_{0,d}$. Starting from panels (a)-(a′), we illustrate that single-species perturbations are sufficient for testing the proximity of the antipaired and paired phases, as $\tilde{S}_{\hat{F}}(\mathbf{q}, \omega)$ receives a dominant contribution from the lowest-lying Goldstone mode, while both the density and spin Goldstone excitations are found to have approximately the same weight in the deep SF region. More precisely, close to the CFSF (PSF) transition, the spin (density) mode (which softens at the transition) dominates the system response and enhances the amplitude of the structure factor at low energies for all momenta. Moving to the total density channel, in panel (b) we see that, despite the CFSF phase being dominated by spin fluctuations, the structure factor receives an increasing contribution by the density Goldstone mode at low momenta as the critical point is approached; as expected, the same mode controls entirely the total density response of the system close to the PSF transition, depicted in panel (b′). The situation is reversed in the case of the spin channel, considered in panels (c)-(c′): here, the projection of the structure factor over the spin Goldstone mode acts as a marker of both the CFSF and the PSF transitions, albeit on different momenta and energy ranges.

Dynamical structure factors and sum rules within the QGA

Static response and sum rules The energy moments of the dynamical structure factors allow to obtain a number of important quantities and identities that characterise the system. First of all, the uniform limit of the inverse-energy-weighted sum rule $m_{\hat{F}}^{-1}(\mathbf{q})$ gives the static response of the system to the selected perturbation. Using the QGA expressions in Eqs. (2.39)-(2.40), we obtain the relations

$$m_d^{-1}(\mathbf{q}) = \sum_\alpha \frac{(N_{1,\alpha,\mathbf{q}} + N_{2,\alpha,\mathbf{q}})^2}{\omega_{\alpha,\mathbf{q}}} \underset{\mathbf{q} \to 0}{=} \frac{\kappa}{2}, \tag{2.44}$$

$$m_s^{-1}(\mathbf{q}) = \sum_\alpha \frac{(N_{1,\alpha,\mathbf{q}} - N_{2,\alpha,\mathbf{q}})^2}{\omega_{\alpha,\mathbf{q}}} \underset{\mathbf{q} \to 0}{=} \frac{\chi}{2} \tag{2.45}$$

for the compressibility κ and the spin susceptibility χ of the two-component BH system, where the subscripts d and s are just shorthand notations for $\hat{F} = \hat{G} = \hat{n}_{d/s}$. In particular, we note that the former compressibility relation generalises the result of [51] to mixtures.

Our results for the compressibility and the spin susceptibility are shown in Figure 2.8 in the vicinity of the CFSF transition [panel (a)] and the PSF transition [panel (b)]. Notably, we find that the spin susceptibility (compressibility) diverges near the CFSF (PSF) transition. Close to the CFSF regime, this finding parallels the decreasing energy cost to produce spin excitations (see Figure 2.3), which corresponds to an increase in
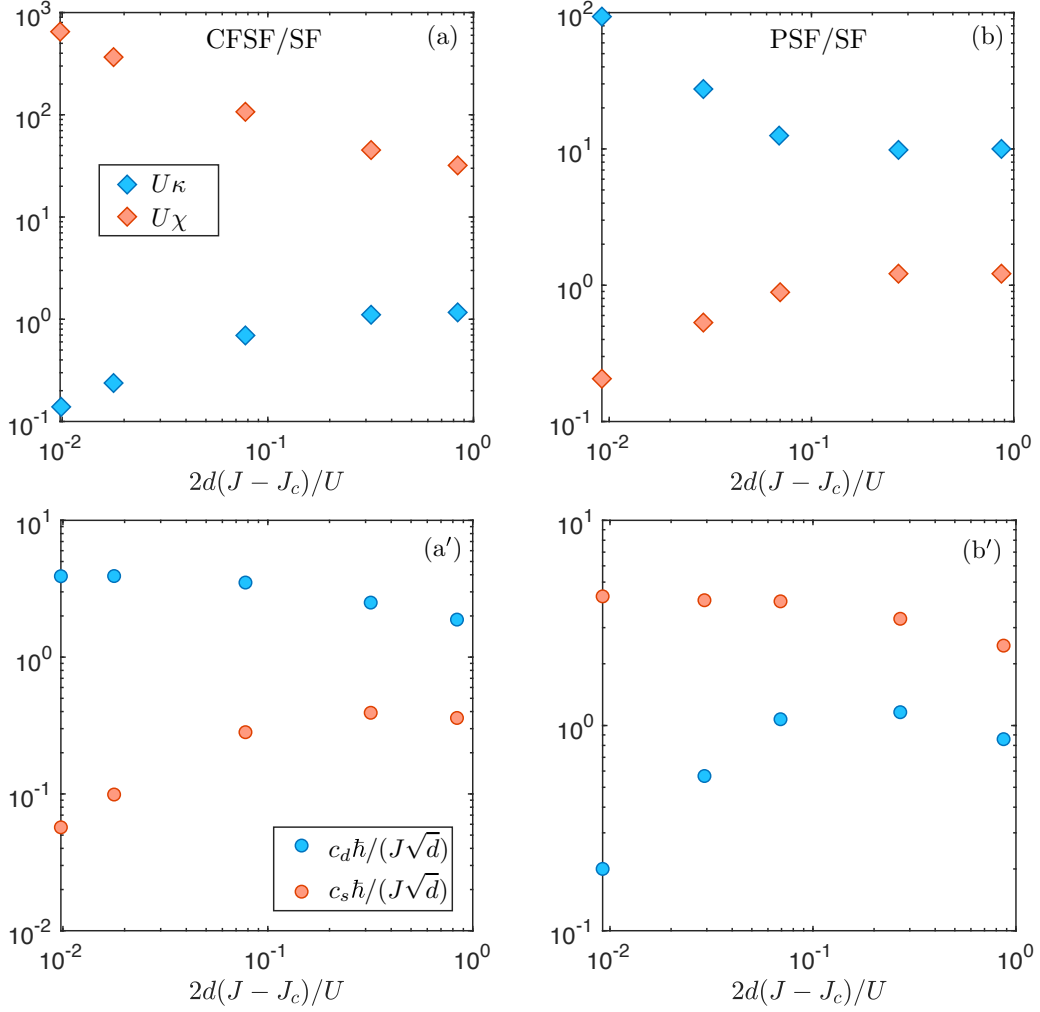
Figure 2.8: Upper panels: dependence of the compressibility (blue diamonds) and susceptibility (red diamonds) in the vicinity of the O(2) (a) CFSF and (b) PSF transitions. Lower panels: dependence of the density (blue circles) and spin (red circles) sound velocities close to the same transitions. The data in (a) and (a′) correspond to fixed $n_d = 1$ and $U_{12}/U = 0.9$, while the data in (b) and (b′) are derived for fixed $n_d \approx 1.47$ and $U_{12}/U = -0.7$. The calculations are always performed for $d = 2$.

the response of the system towards magnetic perturbations. On the other hand, in the PSF regime, the divergence of the compressibility corresponds to the decreasing energy of density excitations (see Figure 2.6), hence the increasing sensitivity of the system to density fluctuations. Additionally, we find that the compressibility (susceptibility) tends to vanish near the CFSF (PSF) transition due to the opening of a spectral gap in the density (spin) channel.

The divergence of the static response functions – which would suggest an instability of the system towards phase separation or collapse – is due to the lack of a proper inclusion of pairing quantum correlations when describing the CFSF and the PSF phases within the Gutzwiller representation: specifically, it is simply related to the presence of a zero-energy flat dispersion relation for the residual density and the spin modes, respectively. As shown in Figure 2.8(a′)-(b′), the appearance of such modes reflects into the vanishing behaviour of the spin (density) sound velocities at the CFSF (PSF) critical points.

An explicit relationship between sound velocities and static response functions can be directly uncovered by making use again of sum rules. Indeed, upon approaching the CFSF (PSF) phase, the low-momentum response function is exhausted by the spin (density) Goldstone mode, as shown in Figure 2.7. Thus, the sum rules satisfy the general relation

$$m_{d/s}^p(\mathbf{q} \to 0) \simeq \omega_{d/s,\mathbf{q}}^{p-k} \, m_{d/s}^k \simeq \left(c_{d/s} \, |\mathbf{q}| \right)^{p-k} m_{d/s}^k(\mathbf{q}) , \qquad (2.46)$$

from which a number of identities can be derived. For instance, by considering $p = 0$ and $k = -1$, one can write

$$m_d^0(\mathbf{q}, \omega) = |N_{1,d,\mathbf{q}} + N_{2,d,\mathbf{q}}|^2 \underset{\mathbf{q} \to \mathbf{0}}{=} \frac{\kappa}{2} \, c_d \, |\mathbf{q}| \qquad (2.47)$$

and

$$m_s^0(\mathbf{q}, \omega) = |N_{1,s,\mathbf{q}} - N_{2,s,\mathbf{q}}|^2 \underset{\mathbf{q} \to \mathbf{0}}{=} \frac{\chi}{2} \, c_s \, |\mathbf{q}| , \qquad (2.48)$$

which we have verified numerically and generalise the single-component identity given in [51] relating the Goldstone mode structure factor to the compressibility and the speed of sound excitations. The latter equations are moreover not independent. In fact, within the present Bogoliubov-like approach, the $p = 1$ sum rule (also referred to as *f-sum rule* in the literature) can be calculated exactly [40]: $m_{d/s}^1(\mathbf{q}) = \left\langle \left[\delta \hat{n}_{d/s}(\mathbf{q}), \left[\hat{H}_{2\mathrm{BH}}, \delta \hat{n}_{d/s}(\mathbf{q}) \right] \right] \right\rangle \propto \mathbf{q}^2$ for $|\mathbf{q}| \to 0$. From this, using relation $m_{d/s}^1(\mathbf{q}) = \omega_{d/s,\mathbf{q}}^2 \, m_{d/s}^{-1}(\mathbf{q})$, we immediately infer that $c_{d/s}^2 \propto 1/\kappa \, (1/\chi)$. Therefore, if the sound dispersion flattens, the corresponding static response must diverge.

2.3.2 Current response and superfluid components

We now investigate the role of quantum fluctuations in the linear response of the binary BH system to current probes. The response of an ultracold system to this class of perturbations reflects its superfluid properties, which are expected to be remarkably different in the CFSF and PSF phases due to a large collisionless superfluid drag between the two components [109] as a consequence of strong pair correlations.

In this Subsection, we consider the transverse (i) *intraspecies* current response with $\hat{G}_{\mathbf{r}} = \hat{F}_{\mathbf{r}} = \hat{j}_i$ and (ii) *interspecies* current response with $\hat{F}_{\mathbf{r}} = \hat{j}_1$ and $\hat{G}_{\mathbf{r}} = \hat{j}_2$, evaluated in the static limit $\omega = 0$ along the x-directed links of the square lattice (without loss of generality). Here, $\hat{j}_i$ is the current operator referred to i^{th} species taken in the uniform limit $\mathbf{q} \to \mathbf{0}$, that is

$$\hat{j}_{i,\mathbf{q}\to\mathbf{0}}^x = 2 J \lim_{\mathbf{q}\to\mathbf{0}} \sum_{\mathbf{k}} \sin\left(k_x + \frac{q_x}{2} \right) \hat{a}_{i,\mathbf{k}}^\dagger \, \hat{a}_{i,\mathbf{k}+\mathbf{q}} . \qquad (2.49)$$

Within the QGA formalism, the intra/interspecies current response functions are found to be

$$\chi_{\hat{j}_i,\hat{j}_i}^T(\mathbf{q} \to \mathbf{0}, \omega = 0) = -4 J^2 \sum_{\alpha,\beta} \sum_{\mathbf{k}} \frac{\left| U_{i,\alpha,\mathbf{k}} \, V_{i,\beta,\mathbf{k}} - U_{i,\beta,\mathbf{k}} \, V_{i,\alpha,\mathbf{k}} \right|^2}{\omega_{\alpha,\mathbf{k}} + \omega_{\beta,\mathbf{k}}} \sin^2(k_x a)$$

$$(2.50)$$

and

$$\chi^T_{\hat{j}_1,\hat{j}_2}(\mathbf{q} \to \mathbf{0}, \omega = 0) = -4\,J^2 \sum_{\alpha,\beta} \sum_{\mathbf{k}} \frac{\prod_{i=1}^2 \left(U_{i,\alpha,\mathbf{k}}\,V_{i,\beta,\mathbf{k}} - U_{i,\beta,\mathbf{k}}\,V_{i,\alpha,\mathbf{k}}\right)}{\omega_{\alpha,\mathbf{k}} + \omega_{\beta,\mathbf{k}}} \sin^2(k_x\,a)$$

(2.51)

respectively. The above equations naturally generalise the findings of [82] provided by the Bogoliubov approximation. In that case, one has only the density and spin Goldstone modes given by Eq. (2.28) and consequently the current response functions satisfy the relation $\chi^T_{\hat{j}_1,\hat{j}_1}(\mathbf{q} \to \mathbf{0}, \omega = 0) = -\chi^T_{\hat{j}_1,\hat{j}_2}(\mathbf{q} \to \mathbf{0}, \omega = 0)$ exactly. Within the QGA, due to the presence of additional excitation bands with a substantial spectral weight for strong enough interactions, the very same equality is approximately fulfilled in the deep SF phase only. Physically, the violation of the aforementioned identity reflects the breaking of Galilean invariance (cfr. [82]), which allows for a non-zero normal component of the gas contributing to superfluidity even at zero temperature, as we will discuss in the following.

We proceed to introduce the relevant superfluid quantities in the two-species BH model. For a homogeneous two-component superfluid system, the relations between the mass current densities $m_i\,\mathbf{j}_i$ of each species and the velocities of the gas components are governed by the two-fluid model originally formulated in [96] and read

$$m_1\,\mathbf{j}_1 = \rho_{n,1}\,\mathbf{v}_n + \rho_{s,1}\,\mathbf{v}_1 + \rho_{12}\,\mathbf{v}_2\,,$$

(2.52a)

$$m_2\,\mathbf{j}_2 = \rho_{n,2}\,\mathbf{v}_n + \rho_{s,2}\,\mathbf{v}_2 + \rho_{12}\,\mathbf{v}_1\,,$$

(2.52b)

where m_i is the bare mass of the ith species of the system, $\rho_{s,i}$ and $\mathbf{v}_i$ are respectively the superfluid (mass) densities and velocities for each component, ρ_{12} is the so-called drag interaction and $\rho_{n,i}$ are the normal (mass) densities of the system, which are assumed to flow both at the same velocity $\mathbf{v}_n$. The physical role of the superfluid drag, going under the name of *Andreev-Bashkin (AB) effect*, has a self-evident explanation: a superflow in one component can be driven by the collisionless drag from the superflow in the other component of the system, and vice versa. For a continuous system, by Galilean invariance Eqs. (2.52) are supplemented by a close relationship $m_i\,N_i/V = \rho_{n,i} + \rho_{s,i} + \rho_{12}$ between the normal part of the system and the superfluid densities, such that at zero temperature, where $\rho_{n,i} = 0$, the whole volume density of the system $(N_1 + N_2)/V$ participates in the superfluid flow [129]. On a lattice, the breaking of Galilean invariance requires the mass current densities to satisfy a different transformation rule in the presence of a vector potential acting as a probe, such that the density N_i/V is replaced by $-K_i/(2\,J)$, where $K_i = \left\langle \hat{K}_i \right\rangle$ is the kinetic energy density of the ith species along the direction of the phase twist induced by the vector potential [82]. In particular, we recall that the local kinetic operator acting along x-directed links of a square lattice is given by

$$\hat{K}_i^x(\mathbf{r}) = -J\left(\hat{a}^\dagger_{i,\mathbf{r}+\mathbf{e}_x}\,\hat{a}_{i,\mathbf{r}} + \text{H.c.}\right)\,.$$

(2.53)

Most importantly, we also remark that the normal component $n_{n,i}$ may *not* vanish at zero temperature on a lattice. Therefore, recovering a result derived in [106], for the

two-component BH model we obtain

$$-\frac{K_i^x}{2J} = n_{n,i} + n_{s,i} + n_{12} , \qquad (2.54)$$

where we have introduced the superfluid (normal) number densities as $n_{s(n),i} \equiv \rho_{s(n),i}/m$ and the drag $n_{12} \equiv \rho_{12}/m$ to facilitate a direct comparison with the lattice filling. The average kinetic energy density K_i^x calculated within the QGA theory reads

$$K_i^x \approx -2\,J\,|\psi_{0,i}|^2 - \frac{2\,J}{V} \sum_\alpha \sum_{\mathbf{k}} |V_{i,\alpha,\mathbf{k}}|^2 \, \cos(k_x\,a) . \qquad (2.55)$$

To quantify how the AB effect impacts on the effective mass of the gas components, we define the dimensionless parameter ξ_i^* through the equations

$$n_{n,i} + n_{s,i} \equiv -\xi_i^* \frac{K_i^x}{2\,J} , \qquad (2.56a)$$

$$n_{12} \equiv -\frac{K_i^x}{2\,J}\,(1 - \xi_i^*) , \qquad (2.56b)$$

where $\xi^* = m/m^*$ reflects the extent to which the bare mass $m \equiv (2\,J)^{-1}$ on the lattice is renormalised by the interaction between the superfluid flows. Explicitly, when $\xi_i^* > 1$ ($\xi_i^* < 1$) the renormalised effective mass is smaller (larger) than the bare mass. This extends the concept of the renormalised effective mass discussed in [81, 96] to the lattice, as Eq. (2.56b) is exactly analogous to Eq. (4) in the second work. We note that in those works translational invariance ensures that the renormalised effective mass remains always larger than the bare mass due to the guaranteed positivity of n_{12}. On a lattice, the inclusion of $n_{n,i}$ in Eq. (2.56a), which is trivially absent for a continuous superfluid at zero temperature, adds additional complexity while ensuring that the variation of ξ_i^* is due solely to the collisionless drag.

Having introduced the relevant superfluid components, we now resort to the formal results of [82] to relate them to the current-current response functions of the two-component BH model. In particular, one has

$$n_{s,i} = \frac{m}{V}\chi^T_{\hat{j}_i,\hat{j}_i}(\mathbf{q}\to\mathbf{0},\omega=0) - \frac{K_i^x}{2\,J} , \qquad (2.57)$$

$$n_{12} = \frac{m}{V}\chi^T_{\hat{j}_1,\hat{j}_2}(\mathbf{q}\to\mathbf{0},\omega=0) . \qquad (2.58)$$

A third relation provides a sum rule for the total normal fraction of the system $n_n = n_{n,1} + n_{n,2}$ as the total transverse current response function, reading

$$n_n = -\frac{m}{V}\left[\chi^T_{\hat{j}_1,\hat{j}_1}(\mathbf{q}\to\mathbf{0},\omega=0) + \chi^T_{\hat{j}_2,\hat{j}_2}(\mathbf{q}\to\mathbf{0},\omega=0) + 2\,\chi^T_{\hat{j}_1,\hat{j}_2}(\mathbf{q}\to\mathbf{0},\omega=0)\right] . \qquad (2.59)$$

From Eq. (2.59), we notice how, upon exchanging $\hat{j}_1$ with $\hat{j}_2$, opposite values of the current response functions $\chi^T_{\hat{j}_1,\hat{j}_1}(\mathbf{q}\to\mathbf{0},\omega=0) = -\chi^T_{\hat{j}_1,\hat{j}_2}(\mathbf{q}\to\mathbf{0},\omega=0)$ results in $n_n = 0$, as would be predicted by the Bogoliubov approximation, in clear contrast with the correct physics of a strongly-interacting lattice system at zero temperature. It is worth noting that all the previous relations have been historically derived through the application of either scattering theory [106] or linear response formalism [82]; with a
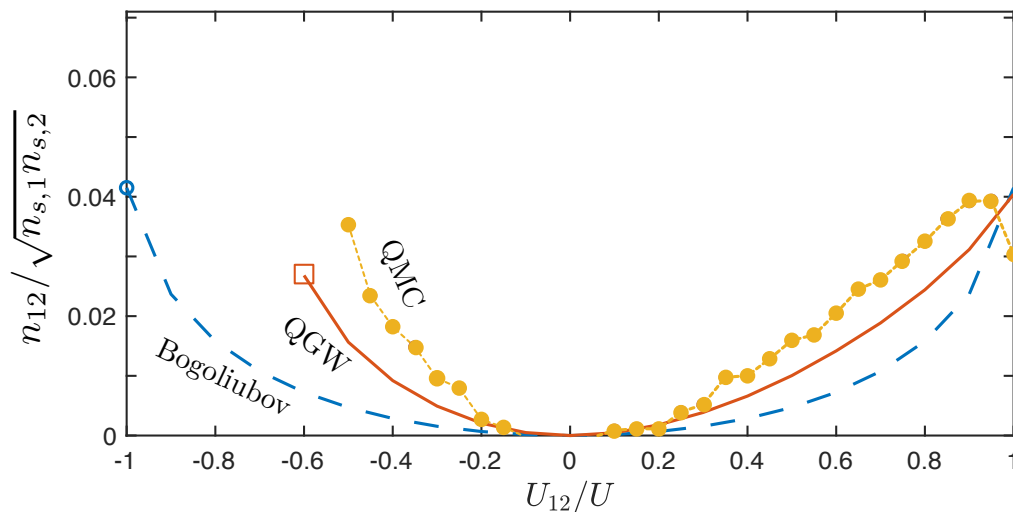
Figure 2.9: Collisionless drag versus the interspecies coupling strength U_{12}/U for fixed $n_d \approx 0.5$ and $2\,d\,J/U = 0.4$ in $d = 2$. Here, we compare the QGA prediction (orange solid line) with the Bogoliubov result from [82, 106] (light-blue dashed line) and the QMC data (yellow dotted line) from [109] evaluated on a lattice of size $V = 10^2$. The hollow square and circle symbols indicate the collapse point for the QGA and Bogoliubov results, respectively.

look to future developments, in Appendix D we propose a more modern approach to the calculation of the superfluid properties of a strongly-correlated system which exploits the power of diagrammatics and Ward identities.

It is worth mentioning that measuring the AB effect is a challenging task experimentally; however, it has been recently proposed to draw on fast response dynamics to directly access the entrainment in continuous systems [82, 130]. In light of our results, we conjecture that the same proposal could be applied in the presence of a lattice.

Superfluid regime

In the deep SF regime, the current response functions and the average kinetic energy match their expressions given by the mean-field Gutzwiller theory, namely $\chi^T_{\hat{j}_i, \hat{j}_j}(\mathbf{q} \to \mathbf{0}, \omega = 0) = 0$ and $K^x_{0,i} = -2\,J\,|\psi_{0,i}|^2$, respectively. As for the one-component case, this leads to equal superfluid and condensate densities, namely $n_{s,i} = |\psi_{0,i}|^2$, as well as a vanishing drag $n_{12} = 0$ and a trivial renormalisation of the effective mass $\xi^* \approx 1$.

At intermediate $2\,d\,J/U$, the superfluid drag was calculated using quantum Monte Carlo (QMC) simulations in [109]. The comparison of the QGA results with the Bogoliubov predictions (see [82, 106]) and the QMC data is shown in Figure 2.9, for a hopping energy equal to $2\,d\,J/U = 0.4$ and a fixed total filling $n_d \approx 0.5$. We remark here that the accuracy of our drag estimation hinges on the correct calculation of the total filling, which must include second-order quantum corrections accounted for by the QGA theory (see again Appendix C.2). For repulsive interactions, these corrections are always less than $\sim 10\%$ and therefore can be essentially neglected. By contrast, for attractive interactions quantum corrections increase for larger $|U_{12}|$ and can be as large as $\sim 25\%$ due to the diverging compressibility near the collapse transition – see panel (e) of Figure 2.4. We find that including the quantum corrections has the effect of shifting the collapse transition towards a stronger attraction U_{12} compared to

the critical point obtained by keeping the mean-field filling $n_{0,i}$. This fact restricts the calculation of the drag to well before the Bogoliubov prediction for the collapse point ($U_{12}/U \leq -1$) [82, 110].

The QGA results of Figure 2.9 [orange solid line] are obtained on the same $V = 10^2$ lattice considered in the QMC calculations of [109] [yellow dotted line]. We find that in general the drag increases for smaller lattice sizes, in contrast to the results of that work. Furthermore, we also observe that the collapse point is shifted towards less attractive U_{12} for smaller lattices. Additionally, we note that, regardless of the sign of U_{12}, the collisionless drag remains always positive in the SF regime, and consequently the renormalised effective mass is larger than the bare one. Physically, this indicates that the dressing effect of individual particle motions of one species due to the superfluid flow of the other component has a particle (rather than hole) character.

On the whole, the QGA predictions underestimate the QMC results, but qualitatively reproduce the asymmetry of the superfluid drag with respect to U_{12}. On the other hand, the Bogoliubov results [light-blue dashed line] are symmetric with respect to U_{12}, do not capture the first-order transition and lie well below the uncertainty window of the QMC points. In this regard, the QGA can be viewed as a major improvement over the standard Bogoliubov treatment of quantum fluctuations in the presence of strong correlations [82, 83, 106]. Indeed, it is well known that Bogoliubov's theory underestimates the current response functions, as it takes into account only the excitation vertices of the Goldstone modes in Eqs. (2.50)-(2.51) and neglects the contribution of all the other collective modes, which acquire a sizeable spectral weight away from the deep SF limit.

Phase transitions for $U_{12} > 0$

In this Subsection, we study the superfluid components across the various phase transitions appearing for repulsive interspecies interactions. To that end, we begin by discussing the first and second-order MI-to-SF transitions, passing to the second-order CFSF-to-SF transition in the second place.

(*Mott Insulator to Superfluid*) – In Figure 2.10(a) and Figure 2.10(b), we show the QGA results for the relevant transport quantities, which include the superfluid components, the intraspecies current response, and the average kinetic energy across the second and first-order MI-to-SF transitions of the $n_{0,d} = 2$ lobes for $U_{12}/U = 0.5$ and $U_{12}/U = 0.9$, respectively.

Qualitatively, the behaviour of the superfluid fraction exhibits a number of features in common with the QGA results for the single-component BH model [131]. Specifically, in the SF regime, the superfluid density $n_{s,i}$ [black solid line] remains always larger than the condensate fraction [black dotted line] and approaches the total density of the corresponding species in the deep SF limit. Furthermore, $n_{s,i}$ vanishes discontinuously (continuously) at the first-order (second-order) critical point and is exactly zero in the MI phase as in the single component case. Once again, this latter feature is ensured by the exact cancellation between the current response function $\chi^T_{\hat{j}_i, \hat{j}_i}$ [pink dashed line], given by Eq. (2.50), and the contribution of zero-point fluctuations to the average kinetic energy K^x_i [cyan dashed line] provided by Eq. (2.55). As expected, both the quantities tend towards zero in the strongly-interacting limit $2\,d\,J/U \to 0$. The collisionless drag [gray solid line] remains always on the order of a few percent of $n_{s,i}$, reaching the maximal value close to the MI-to-SF critical point and vanishing entirely within the MI
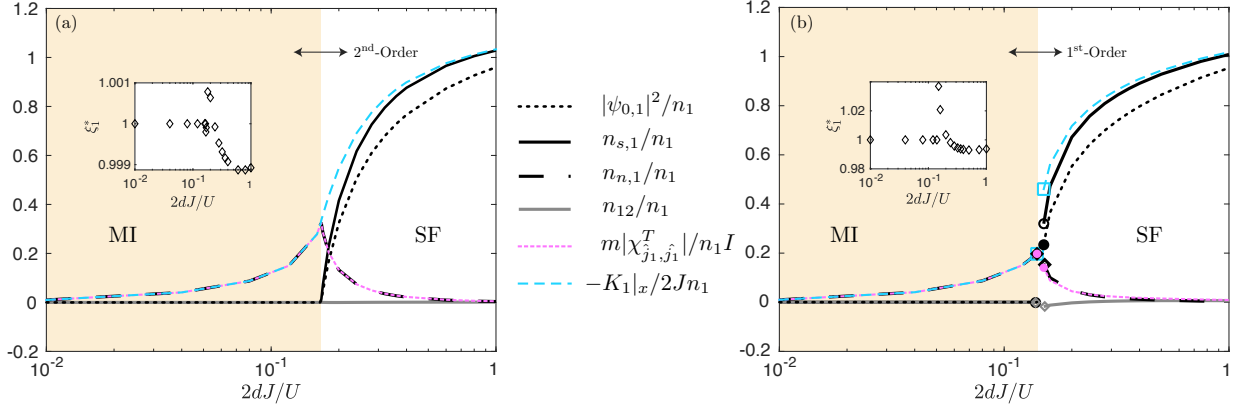
Figure 2.10: Transport quantities in two dimensions across the MI-to-SF second (left panel) and first (right panel) order transitions at fixed $\mu/U = 1.4$ and $\mu/U = 1$ for $U_{12}/U = 0.5$ and $U_{12}/U = 0.9$, corresponding to the $n_d = 2$ MI lobes in Figure 2.1(a) and Figure 2.1(b), respectively. The one-component densities n_i include the corrections of the second-order quantum fluctuations. The tan-shaded area indicates the MI region. Thick black and grey lines indicate the QGA predictions for the superfluid density $n_{s,1}$ and the (vanishingly small) superfluid drag n_{12} respectively, while the black dashed and dotted lines refer to the normal component $n_{n,1}$ and condensate fraction $|\psi_{0,1}|^2$. Pink dotted and blue dashed lines are the contributions to $n_{s,1}$ from the average kinetic energy K_i^x and the intraspecies current response function $\chi_{\hat{j}_i,\hat{j}_i}^T$, respectively. (Insets) Renormalisation of the effective mass across the MI-to-SF transitions due to the collisionless drag.

phase. Because the superfluid drag is small, the renormalisation of the effective mass is also negligible and the normal components $n_{n,i}$ [black dashed line] are dominated by the contribution of the intraspecies current response function $\chi_{\hat{j}_i,\hat{j}_i}^T$, as one can see by comparing Eqs. (2.58)-(2.59).

It is now worth commenting on the relative weight of the various excitation vertices that contribute the most to the results displayed in Figure 2.10. In the SF regime, the spin-density Goldstone vertex makes the largest contribution to the expression of $\chi_{\hat{j}_i,\hat{j}_i}^T$ in Eq. (2.50), followed by smaller terms coming from the vertex between the Goldstone and Higgs modes with density character. This is in strong contrast to the single component case, where $\chi_{\hat{j}_i,\hat{j}_i}^T$ is nearly saturated by the Goldstone-Higgs vertex, being the Goldstone mode of the density type only. Similarly, the interspecies current response $\chi_{\hat{j}_1,\hat{j}_2}^T$, and therefore the superfluid drag, is nearly saturated by the vertices involving the Goldstone modes. On the other hand, the zero-point fluctuations in the average kinetic energy K_i^x [cyan dashed line] are dominated by the contribution of the spin Goldstone mode, in addition to the mean-field effect of the order parameter $\psi_{0,i}$.

Inside the MI phase, the spectral summation of the intraspecies response $\chi_{\hat{j}_i,\hat{j}_i}^T$ is totally due to the vertices of the particle/hole excitations, while the average kinetic energy K_i^x is dominated by the contribution of the lowest particle or hole bands, depending on the chemical potential. As the MI-to-SF transition is crossed, these excitations turn into the Goldstone modes, such that the spectral content of K_i^x changes smoothly across the criticality. An analogous reasoning applies to $\chi_{\hat{j}_i,\hat{j}_i}^T$. On the other hand, we note that, interestingly, the interspecies response $\chi_{\hat{j}_1,\hat{j}_2}^T$ is not fully saturated by the vertices involving only the first few particle/hole bands, requiring also the contribution of higher-energy excitations in order to give a perfect cancellation of the superfluid drag in the MI lobe.

(*Counterflow Superfluid to Superfluid*) – The QGA results for the superfluid components, the intraspecies current response, and the average kinetic energy across the
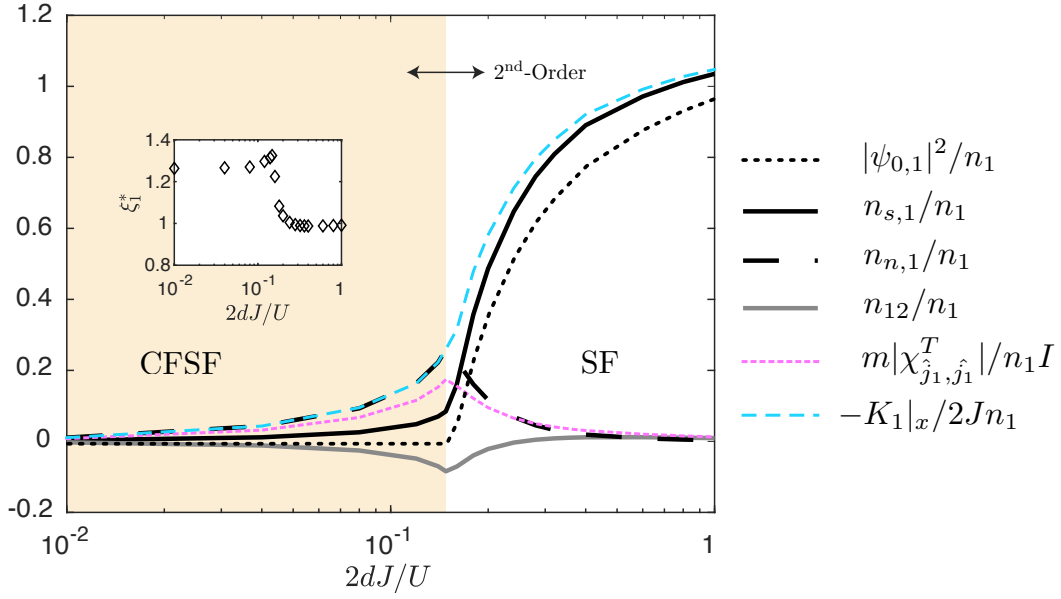
Figure 2.11: Transport quantities in two dimensions across the CFSF-to-SF second-order edge transition, traversed at fixed chemical potential $\mu/U = 0.5$ for $U_{12}/U = 0.9$, corresponding to the $n_d = 1$ CFSF lobe in Figure 2.1(b). The one-component filling n_i includes the corrections of the second-order quantum fluctuations. The tan-shaded area indicates the MI region. Thick black and grey lines indicate the QGA predictions for the superfluid density $n_{s,1}$ and the superfluid drag n_{12} respectively, while the black dashed and dotted lines refer to the normal component $n_{n,1}$ and condensate fraction $|\psi_{0,1}|^2$. Pink dotted and blue dashed lines are the contributions to $n_{s,1}$ from the average kinetic energy K_i^x and the intraspecies current response function $\chi_{\hat{j}_i,\hat{j}_i}^T$, respectively. (Inset) Renormalisation of the effective mass across the CFSF transition due to the collisionless drag.

second-order CFSF-to-SF transition of the $n_{0,d} = 1$ lobe for $U_{12}/U = 0.9$ are shown in Figure 2.11.

In the SF region close to the CFSF phase, the results are equivalent to the ones found in proximity of the MI lobe discussed previously. In the CFSF regime, we find that the superfluid drag reaches the negative saturation threshold $n_{12}/\sqrt{n_{s,1}\,n_{s,2}} = -100\%$, a result that strongly recalls the QMC calculations in [109], performed in $d = 2$ as well. Notably, we also observe that in the CFSF phase, even though the drag is saturated, the net superfluidity $n_{s,1} + n_{12} = 0$ vanishes. This mirrors the fact that counterflow superfluidity occurs when particles and holes of different species flow along counter-directed paths, such that equal and opposite current densities for each component develop [91, 109]. Importantly, within the QGA formalism this perfect balance is due *solely* to quantum fluctuations, as the mean-field Gutzwiller theory trivially predicts $n_{s,1} = n_{12} = 0$. Qualitatively speaking, such finding agrees with the statement in [118] that superfluidity in the CFSF phase arises through second-order hopping processes not seised by mean-field theory; however, the *ad-hoc* introduction of such processes performed in that work is not explicitly comprised in the O(J^2) contribution of quantum fluctuations to Eqs. (2.50)-(2.51), which is thus a genuine result of the QGA quantum theory. The collisionless drag remains large and negative across the CFSF-to-SF transition, so that the renormalised effective mass becomes significantly less than its bare value, particularly at the critical point. We remark here that the onset of a negative superfluid drag indicates that a travelling particle carries, in addition to its own bare mass, holes of the other species resulting in a reduced effective mass. As the deep SF regime is approached, the drag n_{12} changes sign leading to an increased
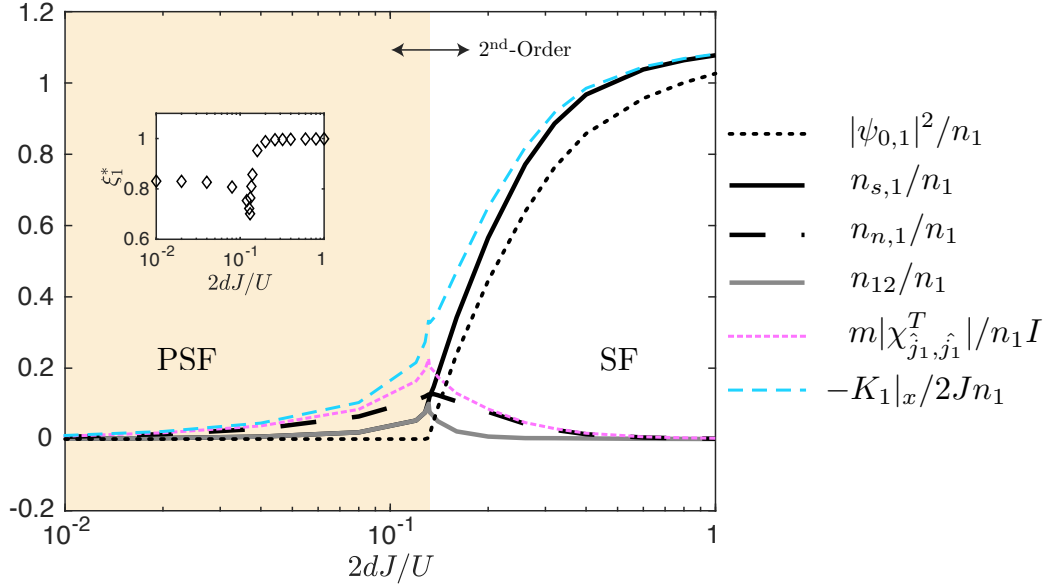
Figure 2.12: Transport quantities in two dimensions across the PSF-to-SF phase transition along the $(\mu/U)_c^{\mathrm{PSF}} = -0.35$ critical line, which separates the vacuum region from the $n_d = 2$ MI lobe for $U_{12}/U = -0.7$, see Figure 2.4(b). The one-component filling n_i include the corrections of the second-order quantum fluctuations. The tan-shaded area indicates the MI region. Thick black and grey lines indicate the QGA predictions for the superfluid density $n_{s,1}$ and the superfluid drag n_{12} respectively, while the black dashed and dotted lines refer to the normal component $n_{n,1}$ and condensate fraction $|\psi_{0,1}|^2$. Pink dotted and blue dashed lines are the contributions to $n_{s,1}$ from the average kinetic energy K_i^x and the intraspecies current response function $\chi_{\hat{j}_i,\hat{j}_i}^T$, respectively. (Inset) Renormalisation of the effective mass across the PSF transition due to the collisionless drag.

effective mass as observed before.

Further insights come from inspecting the relative weight of the various excitations vertices that contribute to the quantities shown in Figure 2.11. In the CFSF regime, the average kinetic energy K_i^x is almost saturated by the gapped hole mode with the lowest energy. Correspondingly, both the intraspecies $\chi_{\hat{j}_i,\hat{j}_i}^T$ and interspecies $\chi_{\hat{j}_1,\hat{j}_2}^T$ current response functions are dominated by the all-to-all vertices of the lowest four particle/hole bands. It is curious to observe that the spectral weight of these particle-hole excitations is sufficient to obtain the -100% saturation of the superfluid drag, even though low-energy antipair excitations are only described by the flat bands $\omega_{0,1}$, which do not contribute to the physics of fluctuations in our theory. As the transition point is crossed into the SF regime, K_i^x is saturated by the density Goldstone mode, while the response functions $\chi_{\hat{j}_i,\hat{j}_i}^T$ and $\chi_{\hat{j}_1,\hat{j}_2}^T$ get a large contribution by the vertices between the density Goldstone mode and the first gapped modes of the SF phase.

<u>*Phase transitions for $U_{12} < 0$*</u>

In this last Subsection, we study the superfluid components across the second-order PSF-to-SF transition. The analysis of the MI-to-SF critical behaviour given in the previous Subsection is found to remain valid also in the case $U_{12} < 0$, with the only difference that the physical roles of the spin and density Goldstone modes are swapped.

(*Pair Superfluid to Superfluid*) – The QGA predictions for the transport quantities across the second-order PSF-to-SF for $U_{12}/U = -0.7$ with $(\mu/U)_c^{\mathrm{PSF}} = -0.35$ and $n_{0,d} \approx 1.47$ are presented in Figure 2.12.

In the PSF regime, we find that the superfluid drag fulfils the positive saturation condition $n_{12}/\sqrt{n_{s,1}\,n_{s,2}} = +100\%$, which is again compatible with the QMC findings in [109]. Unlike the CFSF phase, however, here the saturation of the drag results in a non-zero net superfluidity $n_{s,1} + n_{12} > 0$. Physically speaking, this can be interpreted from the point of view of pairs of particles of different species following co-directed paths and resulting in pair superfluidity [109]. In analogy with the QGA description of the CFSF phase, this result can be entirely ascribed to the quantum fluctuations successfully captured by our theory. Indeed, the collisionless drag remains large and positive along the whole PSF line and through the transition into the SF phase. Consequently, the effective mass is strongly renormalised, so as to be significantly larger than the bare mass, in particular at the transition point. We note that this increase of the effective mass is much larger than in the SF and MI regimes due to the tendency of a travelling particle to transport, in addition to its own mass, particles of the other species that consequently enhance the dressing effect of the medium. We note that, as the system approaches the deep SF regime, the drag remains positive but becomes increasingly small.

We conclude by commenting again on the spectral decomposition of the various quantities shown in Figure 2.12. On the verge of the PSF side of the transition, the average kinetic energy K_i^x is strongly dominated by the lowest quasiparticle band (with hybrid spin and density character). The same observation partially applies to both the current response functions $\chi^T_{\hat{j}_i,\hat{j}_i}$ and $\chi^T_{\hat{j}_1,\hat{j}_2}$, in which the coupling between different quasiparticle bands plays a major role. As for the CFSF phase in Figure 2.11, it is surprising to verify that these gapped quasiparticle modes are sufficient to reproduce the superfluid drag saturation characteristic of the PSF phase, such that they can be regarded as the only excitations responsible for the superfluid flow of particle pairs. Once the critical point is reached and the SF phase develops, K_i^x gets a major contribution from the spin Goldstone mode, while the current response functions are saturated by the coupling of the same mode with the Higgs-like branches that occupy the high-energy part of the spectrum.

Spectral composition of the superfluid drag

2.3.3 Coherence function

To obtain a better understanding of the role of quantum fluctuations across the phase diagram, we now turn our attention to the study of equal-time correlation functions, which can also be probed experimentally using e.g. quantum gas microscopy [37, 132]. This class of observables is of particular interest in the present context of a multi-component system, as the separation between density and spin DoF close and inside the CFSF and PSF phases is expected to provide static correlations with a Janus-faced profile, depending on which excitation channel is considered.

In analysing the single-particle coherence function, we restrict ourselves to the investigation of intraspecies correlations, as the approximate description of the CFSF and PSF phases within the Gutzwiller framework [118] is expected to miss non-local coherence effects at low energy involving strongly-correlated pairs, in contrast with the results for the current response functions studied in Subsection 2.3.2.

Figure 2.13: One-body coherence function $g_i^{(1)}(\mathbf{r})$ for $d = 2$ and $U_{12}/U = 0.9$ evaluated at fixed $\mu/U = 1.4$ across the (a) MI to (b) SF first-order transition.

The normalised single-particle coherence function for the ith species is defined as

$$g_i^{(1)}(\mathbf{r}) \equiv \frac{\left\langle \hat{a}_{i,\mathbf{r}}^\dagger \, \hat{a}_{i,\mathbf{0}} \right\rangle}{\left\langle \hat{a}_{i,\mathbf{0}}^\dagger \, \hat{a}_{i,\mathbf{0}} \right\rangle} \, . \tag{2.60}$$

The QGA quantisation scheme maps the *microscopic* operator $\hat{a}_{i,\mathbf{r}}$ into the effective Bose field $\hat{\psi}_i(\mathbf{r})$, which carries both a *macroscopic* contribution due to condensation and the effect of short-range quantum correlations on the one-body coherence. Showing a close resemblance to its twin within Bogoliubov's theory, the first-order expansion of $\hat{\psi}_i(\mathbf{r})$ in terms of quantum fluctuations reads

$$\hat{\psi}_i(\mathbf{r}) \approx \psi_{0,i} + \frac{1}{\sqrt{V}} \sum_\alpha \sum_\mathbf{k} \left[U_{i,\alpha,\mathbf{k}} \, e^{i\,\mathbf{k}\cdot\mathbf{r}} \, \hat{b}_{\alpha,\mathbf{k}} + V_{i,\alpha,\mathbf{k}}^* \, e^{-i\,\mathbf{k}\cdot\mathbf{r}} \, \hat{b}_{\alpha,\mathbf{k}}^\dagger \right] , \tag{2.61}$$

where the particle (hole) amplitudes $U_{i,\alpha,\mathbf{k}}$ $(V_{i,\alpha,\mathbf{k}})$ have been introduced in Eqs. (1.24) and saturate the generalised Bogoliubov normalisation condition

$$\sum_\alpha \left(\left| U_{i,\alpha,\mathbf{k}} \right|^2 - \left| V_{i,\alpha,\mathbf{k}} \right|^2 \right) = 1 \, , \tag{2.62}$$

which encloses excitations with a finite energy only and holds throughout the phase diagram. Applying our usual evaluation protocol to Eq. (2.60), the single-particle coherence function can be recast into the form

$$g_i^{(1)}(\mathbf{r}) = \frac{\left\langle \hat{\psi}_i^\dagger(\mathbf{r}) \, \hat{\psi}_i(\mathbf{0}) \right\rangle}{\left\langle \hat{\psi}_i^\dagger(\mathbf{0}) \, \hat{\psi}_i(\mathbf{0}) \right\rangle} \approx \frac{\left| \psi_{0,i} \right|^2 + I^{-1} \sum_\alpha \sum_\mathbf{k} \left| V_{i,\alpha,\mathbf{k}} \right|^2 \cos(\mathbf{k} \cdot \mathbf{r})}{\left| \psi_{0,i} \right|^2 + I^{-1} \sum_\alpha \sum_\mathbf{k} \left| V_{i,\alpha,\mathbf{k}} \right|^2} \, , \tag{2.63}$$

which is a straightforward generalisation of the one-component result in Eq. (1.27). In the numerator of the right-hand side of Eq. (2.63), the first term reflects the long-range order of the one-body density matrix in the SF phase, while the second term reproduces the destructive interference of quantum fluctuations at finite distances, such that only the condensate fraction $\left| \psi_{0,i} \right|^2$ survives in the $\mathbf{r} \to \infty$ limit (see the relevant discussion
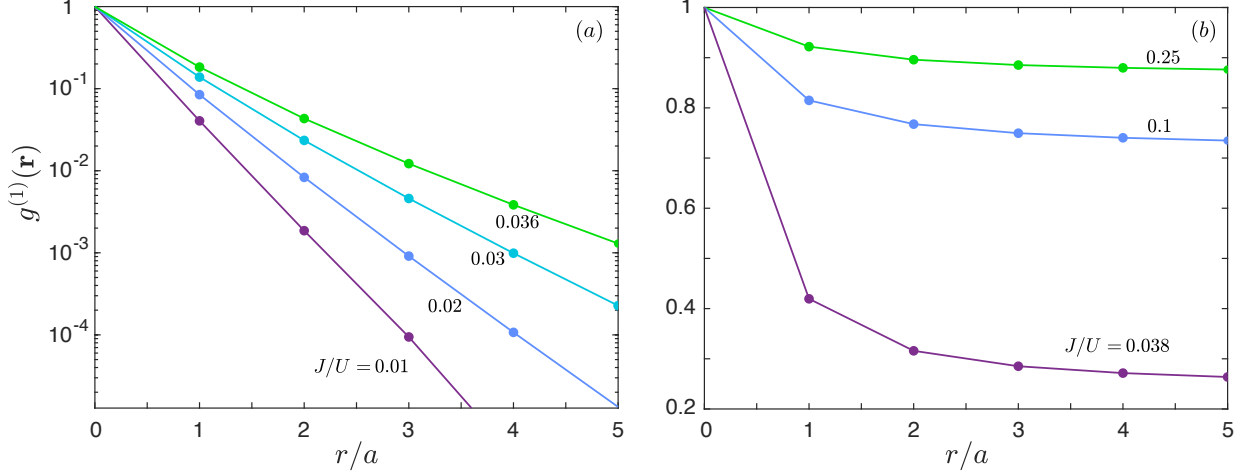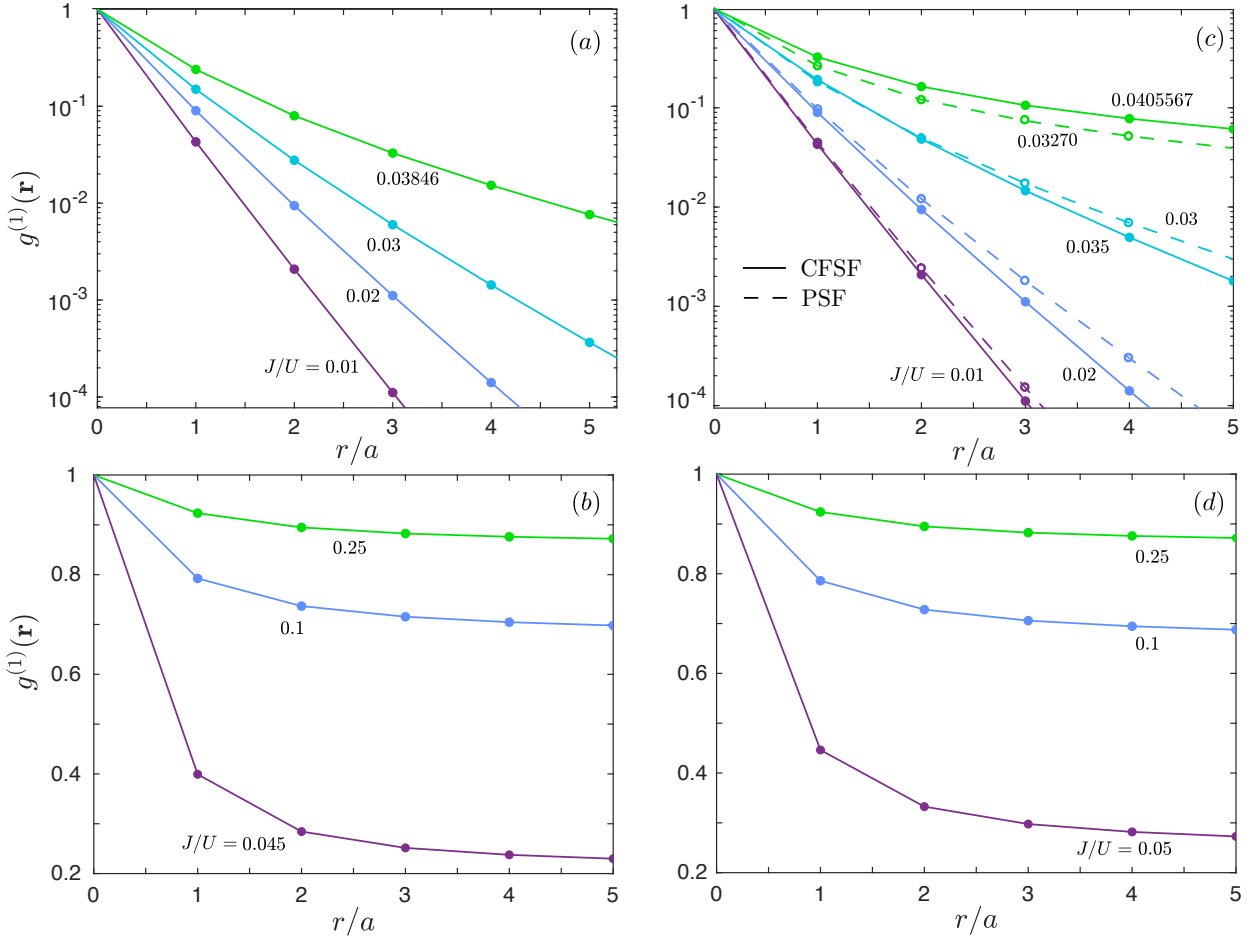
Figure 2.14: One-body coherence function $g^{(1)}(\mathbf{r})$ for $d = 2$ and $U_{12}/U = 0.9$ evaluated at fixed $\mu/U = 0.5$ (a-b) and $\mu/U \approx 0.39$ (c-d) across the edge and O(2) CFSF-to-SF transitions, respectively. In panel (c), the approaching of the PSF-to-SF transition from the PSF side is also shown for $(\mu/U)_c^{\mathrm{PSF}} = -0.35$ and $U_{12}/U = -0.7$.

in Section 2.2 of [124]).

We do not show here explicit results for the second-order MI-to-SF transition, as it presents the very same features of the one-component criticality [131]. In particular, the QGA drastically improves mean-field theory by predicting the onset of off-site coherence in the strongly-interacting regime: in the MI phase, the one-body correlations are generally suppressed exponentially as $g^{(1)}(\mathbf{r}) \sim \exp(-r/\xi)$ with a finite coherence length ξ, whereas in the SF phase $g^{(1)}(\mathbf{r})$ decays always as a power law. More generally, in the deep SF limit $(2\,d\,J/U \gg 1)$, the spectral sum in Eq. (2.63) is almost saturated by the density and spin Goldstone modes only and the behaviour of a weakly-interacting gas is recovered [83, 131]. As a strongly-correlated SF develops, the contribution of other excitation modes to the quantum depletion becomes relevant and the Bogoliubov predictions are naturally amended by the QGA.

In the two-component system, we find that the very same behaviour carries over also to the first-order MI-to-SF transition, shown in Figure 2.13 and to the second-order CFSF-to-SF transition, as well as the PSF-to-SF critical point, both illustrated in Figure 2.14. In particular, in analogy with the physics of the MI-to-SF transition in the one-component system [131], the QGA theory is able to capture the different critical

behaviours of the CFSF-to-SF transition depending on whether this is approached at integer or non-integer filling, namely across either the tip of the edge of the CFSF lobes. Upon reaching the SF phase through the edge of the CFSF lobe [Figure 2.14(a), from purple to green lines], the correlation length ξ grows monotonically but remains bounded. As soon as one enters the SF phase, the long-range behaviour of $g_i^{(1)}(\mathbf{r})$ changes abruptly into a power-law scaling [Figure 2.14(b)]. On the contrary, when approaching the SF phase at the tip of the CFSF region, the correlation length ξ diverges [Figure 2.14(c)] and a power-law dependence for $g_i^{(1)}(\mathbf{r})$ gradually sets in [Figure 2.14(d)]. In panel (c), the evolution of $g_i^{(1)}(\mathbf{r})$ along the PSF critical line is also shown, displaying an analogous behaviour.

As in the one-component case, this difference in the behaviour of $g_i^{(1)}(\mathbf{r})$ is due to the different spectral properties of the collective excitations close to the edge/tip critical points of the CFSF lobe. At the edge transition, either a particle or a hole excitation out of the four dispersive branches becomes gapless. Since our description of the short-distance coherence in the CFSF phase relies on virtual particle/hole excitations via Eq. (2.63), the exponential decay of $g_i^{(1)}(\mathbf{r})$ is ruled by the gap of the particle (hole) excitation that remains finite at the transition. On the contrary, at the tip critical point, both the lowest-energy particle and hole modes become gapless (before turning into the density and spin Goldstone modes on the SF side of the transition), giving a divergent coherence length [63]. Therefore, we speculate that the critical field theory describing the CFSF-to-SF boundary is connected to the same describing the universality classes of the MI-to-SF transition, which we have extensively discussed in Chapter 1.

2.3.4 Density and spin correlations

In this Subsection, we address the local structure of equal-time two-body correlations for both the density and spin channels, focusing on their behaviour across the quantum phase transitions of the system as determined by second-order quantum fluctuations.

Crucially, the QGA treats local and non-local observables separately. Whereas non-local two-body correlations $G_{d/s}^{(2)}(\mathbf{r} \neq \mathbf{0}) = \left\langle \hat{n}_{d/s}(\mathbf{r} \neq \mathbf{0}) \, \hat{n}_{d/s}(\mathbf{0}) \right\rangle$ are directly related to the Fourier transform of the static structure factors $S_{d/s}(\mathbf{q})$ (and then share the pathologies discussed in Subsection 2.3.1), on-site fluctuations can be always computed as expectation values of individual local operators, as shown explicitly in the following. Ultimately, the QGA is built on a local approximation of the ground state, and therefore we expect its predictions for local two-body fluctuations to be accurate even in the vicinity of phases characterised by strong pairing correlations.

With these caveats in mind, we first consider the two-body correlation function for an individual species

$$G_i^{(2)}(\mathbf{r} = \mathbf{0}) \equiv \left\langle \hat{n}_i^2(\mathbf{0}) \right\rangle \longrightarrow \left\langle \hat{\mathcal{D}}_i(\mathbf{0}) \right\rangle , \qquad (2.64)$$

where we have introduced the QGA square density operator

$$\hat{\mathcal{D}}_i(\mathbf{r}) \equiv \sum_{n_1,n_2} \left(n_1^2 \, \delta_{i,1} + n_2^2 \, \delta_{i,2} \right) \hat{c}_{n_1,n_2}^\dagger(\mathbf{r}) \, \hat{c}_{n_1,n_2}(\mathbf{r}) , \qquad (2.65)$$

which, importantly, is distinct from the square of the density operator $\hat{\mathcal{N}}_i(\mathbf{r})$. Expanding

$\hat{\mathcal{D}}_i(\mathbf{0})$ up to second-order in the fluctuations and calculating its quantum average, we obtain

$$G_i^{(2)}(\mathbf{0}) = (1 - F)\, D_{0,i} + \frac{1}{V} \sum_{\alpha} \sum_{\mathbf{k}} \sum_{n_1,n_2} \left(n_1^2\, \delta_{i,1} + n_2^2\, \delta_{i,2} \right) \left| v_{\alpha,\mathbf{k},n_1,n_2} \right|^2 , \quad (2.66)$$

at zero temperature, which extends the result (1.44a) found for the one-component BH model. Here, $D_{0,i} = \sum_{n_1,n_2} \left(n_1^2\, \delta_{i,1} + n_2^2\, \delta_{i,2} \right) \left| c_{n_1,n_2}^0 \right|^2$ is the mean-field value of the square density, while

$$F = \left\langle \hat{A}(\mathbf{0})^2 \right\rangle = \frac{1}{V} \sum_{\alpha} \sum_{\mathbf{k}} \sum_{n_1,n_2} \left| v_{\alpha,\mathbf{k},n_1,n_2} \right|^2 \quad (2.67)$$

is the control parameter of the theory, see Subsection 1.2.3 of the previous Chapter. Once more, we observe that the quantisation protocol corrects the mean-field value of local observables in a two-fold way: on the one hand, the second term of Eq. (2.66) makes a positive contribution due to quantum fluctuations; on the other hand, the quantity F, quantifying the magnitude of quantum effects, renormalises the mean-field value $D_{0,i}$.

Next, we calculate the two-body correlation function between different species $G_{12}^{(2)}(\mathbf{r} = \mathbf{0}) = \langle \hat{n}_1(\mathbf{r} = \mathbf{0})\, \hat{n}_2(\mathbf{0}) \rangle$, which is given by

$$G_{12}^{(2)}(\mathbf{0}) = \left\langle \hat{\mathcal{D}}_{12}(\mathbf{0}) \right\rangle , \quad (2.68)$$

where we have defined the composite density operator

$$\hat{\mathcal{D}}_{12}(\mathbf{r}) \equiv \sum_{n_1,n_2} n_1\, n_2\, \hat{c}_{n_1,n_2}^\dagger(\mathbf{r})\, \hat{c}_{n_1,n_2}(\mathbf{r}) . \quad (2.69)$$

We find the result

$$G_{12}^{(2)}(\mathbf{0}) = (1 - F)\, D_{0,12} + \frac{1}{V} \sum_{\alpha} \sum_{\mathbf{k}} \sum_{n_1,n_2} n_1\, n_2 \left| v_{\alpha,\mathbf{k},n_1,n_2} \right|^2 , \quad (2.70)$$

where $D_{0,12} = \sum_{n_1,n_2} n_1\, n_2 \left| c_{n_1,n_2}^0 \right|^2$ is the mean-field prediction.

Having outlined the form of single-species and pair local correlations, the on-site two-body correlation functions for the total density and spin channels can be obtained directly from

$$G_{d/s}^{(2)}(\mathbf{0}) \equiv \left\langle [\hat{n}_1(\mathbf{0}) \pm \hat{n}_2(\mathbf{0})]^2 \right\rangle = G_1^{(2)}(\mathbf{0}) + G_2^{(2)}(\mathbf{0}) \pm 2\, G_{12}^{(2)}(\mathbf{0}) . \quad (2.71)$$

For convenience, we analyse the normalised density and spin variances $g_{d/s}^{(2)}(\mathbf{0})$. Estimating the variances amounts to shifting $G_{d/s}^{(2)}(\mathbf{0})$ by $n_{d/s}^2 = \left\langle \hat{n}_{d/s} \right\rangle^2$; additionally, because $n_s = 0$ in our $\mathbb{Z}_2$-symmetric model, we always normalise the correlation functions by the squared mean density $n_d^2 = \langle \hat{n}_d \rangle^2$ to give

$$g_{d/s}^{(2)}(\mathbf{0}) \equiv \frac{G_{d/s}^{(2)}(\mathbf{0}) - n_{d/s}^2}{n_d^2} . \quad (2.72)$$
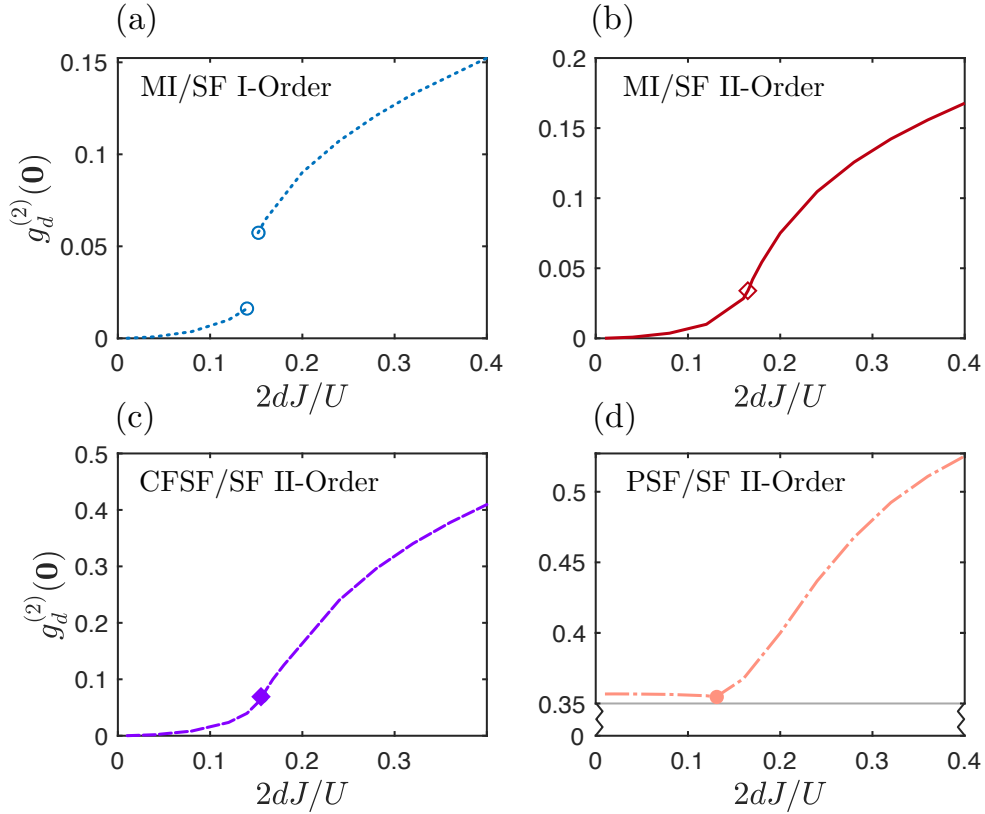
Figure 2.15: Local density-density correlation $g_d^{(2)}(\mathbf{r} = \mathbf{0})$ evaluated for $d = 2$ as a function of $2\,d\,J/U$ across (a) the first-order MI-to-SF edge transition (blue dotted lines) for $U_{12}/U = 0.9$ and $\mu/U = 1.4$ at fixed $n_d = 2$, (b) the second-order MI-to-SF edge transition (red solid line) for $U_{12}/U = 0.5$ and $\mu/U = 1$ at fixed $n_d = 2$, (c) the second-order CFSF-to-SF edge transition (purple dashed line) for $U_{12}/U = 0.9$ and $\mu/U = 0.5$ at fixed $n_d = 1$, and (d) the second-order PSF-to-SF transition (pink dashed-dotted line) for $U_{12}/U = -0.7$ and $(\mu/U)_c^{\mathrm{PSF}} = -0.35$ with $n_d = 1.47$. The point located on each curve indicates the location of the respective phase transition.

Our calculations for the density correlation $g_d^{(2)}(\mathbf{0})$ across the various phase transitions of the model are shown in Figure 2.15. In the SF region, we observe the typical antibunching $g_d^{(2)}(\mathbf{0}) < 1$ of local density fluctuations due to the on-site interaction U. Moving towards the MI phase [panels (a)-(b)], the qualitative features of density correlations are strongly reminiscent of the behaviour of a single-component BH model [131], except for the first-order MI-to-SF transition, at which the antibunching factor shows a discontinuity. In particular, in the MI region, where mean-field theory would predict $g_d^{(2)}(\mathbf{0}) = 0$, the QGA is able to account for the virtual excitation of doublon-holon pairs, which leads to the scaling $g_i^{(2)}(\mathbf{0}) \propto (J/U)^2$ at low J, in excellent agreement with perturbative calculations in the strongly-interacting limit [43, 118]. Remarkably, we observe that the CFSF phase [panel (c)] shares the same properties of the MI state in the density channel. This can be understood as a consequence of the similarity between the spectral structure of the two phases. In the CFSF phase, density fluctuations build on the lowest-lying, gapped particle/hole excitations, which have a strong density character exactly as their counterparts in the MI phase. By contrast, $g_d^{(2)}(\mathbf{0})$ exhibits a quite different behaviour across the PSF-to-SF transition. Instead of being suppressed, sizeable density fluctuations survive in the whole PSF region and saturate to a finite value at low J/U. This result clearly agrees with the physical scenario of the PSF phase
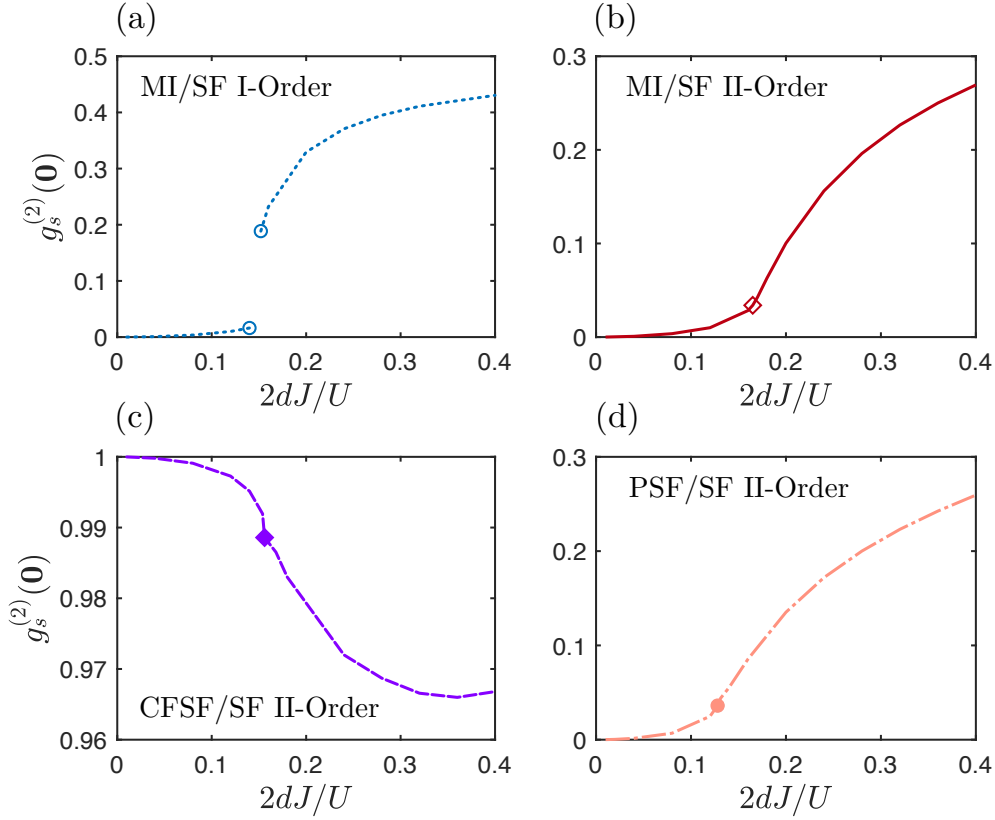
Figure 2.16: Local spin-spin correlation $g_s^{(2)}(\mathbf{r} = \mathbf{0})$ evaluated for $d = 2$ as a function of $2\,d\,J/U$ across the same phase transitions as in Figure 2.15.

[panel (d)], where the formation of local pairs is explicitly favoured, as opposed to the CFSF state, in which particles belonging to different species repel each other. However, we believe that the apparent independence of $g_d^{(2)}(\mathbf{0})$ on J/U is a by-product of the inability of our theory to incorporate dispersive pair excitations in the PSF phase.

Density and spin separation at the pairing transitions

A complementary view on two-body correlations is provided by the spin fluctuations $g_s^{(2)}(\mathbf{0})$, which are reported in Figure 2.16 along the same transition paths of Figure 2.15. Across the MI-to-SF transition [panels (a)-(b)], spin correlations mimic the behaviour of density fluctuations, meaning that the Mott interactions freezes equally both the density and spin DoF. This is not the case for the paired phases, where the density and spin channels decouple. On the one hand, despite its Mott-like character in the density channel, the CFSF phase [panel (c)] is characterised by a large $g_s^{(2)}(\mathbf{0})$, indicating that counterflow superfluidity is linked to the creation of local magnetic moments with large spin fluctuations, such as in a paramagnetic MI state [133, 134]. Notice that, however, $g_s^{(2)}(\mathbf{0}) < 1$ for finite values of J/U, signalling that the local moments possess a finite stiffness due to the particle/hole excitations of the CFSF phase. On the other hand, we find that $g_s^{(2)}(\mathbf{0})$ is strongly suppressed in the PSF phase [panel (d)], where the spin DoF interact repulsively, in analogy again with the physics of the MI-to-SF transition [90].

2.4 Digest of the results and outlook

In this Chapter, we have studied the properties of quantum fluctuations in the two-component BH model at zero temperature, considering both repulsive and attractive interspecies interactions. Expanding on the mean-field ground-state phase diagram first reported in [118], we have analysed the band structure of the model in the whole phase diagram with particular attention paid to its quantum phase transitions and the limitations intrinsic to the local nature of the Gutzwiller ansatz for the many-body wave function. In order to estimate actual quantum correlations, we have generalised to bosonic mixtures the single-component QGA framework and further proved its ability to provide a systematic and comprehensive description of both local and non-local correlations across the phase diagram of the model and, in particular, across its quantum critical regimes.

We have first illustrated that the formation of pair correlations can be directly connected to the analytical behaviour of the compressibility and spin susceptibility, which reflect the strength of critical fluctuations upon reaching the PSF and CFSF transitions, respectively. Notably, by the application of spectral sum rules [40] together with the FDT, we are able to relate the physical picture of the response functions to the sound velocities of the Goldstone modes and the static structure factors of the SF state. These results indicate that experimental probes of strongly-correlated paired phases can yield plain information on the spectral properties of the system in the quantum critical regimes.

Within the QGA, we have also studied the properties of superfluid transport, finding an interspecies collisionless drag whose origin is solely due to quantum fluctuations. In this respect, we have compared quantitatively our results to QMC predictions [109] within the SF phase over a range of interspecies couplings, and studied the matrix of superfluid components across the various phase transitions. In particular, we have observed that the drag is saturated in the vicinity of the PSF and CFSF phases, where strong pair correlations prevail over single-particle coherence. Moreover, we have offered a clear interpretation of the superfluid components in terms of multi-mode scattering processes involving the collective excitations of the system, including not only the density and spin Goldstone modes, but also the Higgs modes and those higher gapped excitations that emerge at strong interactions and whose physical meaning is less understood in the literature.

Finally, we have shown that the QGA theory gives an accurate account of the role of quantum fluctuations in equal-time few-body correlations in the whole phase diagram of the system. In particular, we have demonstrated how the critical behaviours of the one-body coherence function are analogous to those found for MI-to-SF transition in the single-component BH model. Remarkably, at the two-body level, we have also found that the CFSF/PSF phase transitions closely mirror the MI transition physics in the density/spin channels, respectively. Throughout our analysis, we have highlighted how quantum correlations closely link with the character of collective modes in distinct interaction regimes.

The generalisation of our theory to multi-component Bose/Fermi mixtures and different trapping geometries, where novel types of AB effects are predicted [111, 135], poses intriguing problems for future research. Additionally, an improvement in the description of non-local fluctuations, crucial for instance to introduce hopping-induced

correlations into the paired phases, appears possible within a cluster extension of the Gutzwiller theory (cfr. [14, 89, 136–142]). Such an extension is required, for example, to describe long-range interactions or magnetic ordering in supersolid phases where translational symmetry is spontaneously broken (cfr. [90, 143, 144]). Relaxing the $\mathbb{Z}_2$-symmetry constraint also opens exciting questions on the imbalanced two-component BH model, whose fermionic counterpart is currently the subject of intense interest in the community of ultracold atoms (cfr. [145, 146]). From a more formal perspective, the systematic way in which quantum fluctuations can be incorporated in the QGA theory raises interesting curiosities about its diagrammatic representation in quantum field theory. Conversely, such a connection might enable the translation of the comparatively sizeable literature of diagrammatic techniques into the language of QGA theory to diagnose possible issues in the method or introduce concepts already well-known in that context (cfr. the seminal works [147, 148]).

Impurity dephasing in a Bose-Hubbard environment

3

This Chapter is based on an adaptation of the following publication.

▶ <u>Fabio Caleffi</u>, M. Capone, I. de Vega, and A. Recati, *Impurity dephasing in a Bose–Hubbard model*, New Journal of Physics **23**, 033018 (15 March 2021)

3.1 Open systems in correlated environments

Understanding the dynamics of an open quantum system, i.e. a quantum system coupled to its environment, is relevant in a variety of domains including condensed-matter physics, quantum computing, quantum optics and ultracold gases [149–152]. When the open system and its environment are weakly coupled, it is often a good approximation to describe the latter as a set of harmonic oscillators linearly coupled to the system. This class of problems is well described by the so-called Caldeira-Leggett model [153], when the open system is described in terms of continuous variables, or by the spin-boson model, when it is a discrete system [154]. In any of these models, the influence of the environment on the system depends only on a single-particle spectral density, and this strongly simplifies the description of the system. The past few decades have seen the development of a large variety of methods to describe the open system dynamics in this context, including path integrals [155, 156], stochastic Schrödinger equations [157, 158], hierarchical systems of equations [159, 160] or, when computing the full dynamics of both the system and its environment, chain mapping representations [161, 162] or quantum Monte Carlo techniques [163, 164]. However, when the environment is strongly correlated or non-harmonic, the above picture may no longer be accurate and more involved approaches are required to account for the resulting non-Gaussian environment statistics. The state-of-the-art methods to numerically study these systems are based on matrix product states [165–168]; nevertheless, due to the rapid entanglement growth, these methods become highly inefficient beyond one-dimensional cases or when approaching to a critical regime.

The recent advances in locally manipulating ultracold gases in optical lattices has made such a platform ideal for the study of impurities coupled to a non-trivial bath [167, 169–173] either per se or as quantum simulators of toy models for less clean systems. In this Chapter, we analyse the pure dephasing dynamics of a two-level impurity whose environment is represented by the single-band BH model studied in Chapter 1. This problem has been recently analysed for a one-dimensional BH environment away from its critical transition [167]. Here we take a leap forward by considering a 2D BH model and characterising the impurity dynamics along the whole phase diagram, focusing on the critical regions. In the following, we will reach our goal thanks to the use of QGA, which allows us to include the relevant correlations of the bath – in particular the ones responsible for non-Gaussian effects – without being computationally demanding.

One of the main findings of our study is the strong dependence of the dephasing dynamics on the universality class of the MI-to-SF transition of the BH environment. In particular, we show that: (1) when the quantum phase transition is due to particle number change (CI critical point), the impurity dynamics is perfectly Markovian, being

the environment dynamics dominated by single particle processes, despite the strong interactions; (2) on the other hand, when the transition occurs at fixed integer density at the O(2) critical point, the spectrum of the bath contains multiple low-energy collective modes. Their presence leads to a non-Markovian dephasing dynamics, strongly affected by two-particle processes in the environment, which make the standard Gaussian statistics fail. Most importantly – in close analogy with the findings of a related work on one-dimensional quantum spin baths [174] – we find that both the short and long-time behaviour of the dephasing dynamics are precise detectors of the type of universality class of the transition.

3.2 Pure dephasing model within the QGA

3.2.1 Quantum impurity in a Bose-Hubbard bath

We consider a two-level static impurity coupled to a two-dimensional BH model, hereafter referred to as the bath. The total Hamiltonian of the system can be written as $\hat{H} \equiv \hat{H}_{\mathrm{BH}} + \hat{H}_{\mathrm{imp}} + \hat{H}_c$ with

$$
\hat{H}_{\mathrm{imp}} \equiv \frac{\omega_0}{2} \left(1 + \hat{\sigma}_z\right) ,
$$
$$
\hat{H}_c \equiv g \, \hat{\sigma}_z \, \hat{n}_{\mathbf{0}} ,
$$

(3.1)

where the impurity is assumed to be located at site $\mathbf{0}$ in correspondence of the centre of a thermodynamically large BH lattice. Following the standard derivation of spin boson models [149, 154, 175], the impurity can be modelled as a spinful particle governed by the Hamiltonian $\hat{H}_{\mathrm{imp}}$ with a resonant frequency ω_0 and is coupled to the bath density $\hat{n}_{\mathbf{0}}$ via a local interaction $\hat{H}_c$ with strength g.

We assume that initially the state of the system is separable $\rho(t = 0) = \rho_{\mathrm{BH}}^0 \otimes \rho_{\mathrm{imp}}^0$, where ρ_{BH}^0 is the zero-temperature ground state of the BH Hamiltonian $\hat{H}_{\mathrm{BH}}$ and ρ_{imp}^0 is the initial state of the impurity. As usual in the study of open quantum systems, we assume that the bath and the impurity are weakly coupled so that the bath state is not too altered with respect to ρ_{BH}^0 during its time evolution. Under such approximation, it is well-known that the impurity dynamics is fully characterised by the time correlation function of the environment coupling operator, $\hat{n}_{\mathbf{0}}$. Our goal is to estimate the latter precisely by resorting to the QGA technology, which have been already proven to be a surprisingly accurate estimator for static density correlations in Chapter 1.

3.2.2 Comprehensive review of the BH excitations within the QGA

Before proceeding, we briefly review in more detail the structure of the BH excitation spectrum $\omega_{\alpha,\mathbf{k}}$ along the phase diagram, focusing in particular on the quantum critical regimes, since its knowledge gives important insights into the dephasing dynamics of the spin impurity, as we will illustrate in Section 3.3. For convenience, in Figure 3.1 a summary of the phase diagram of the BH system in the strongly-correlated regime and of the excitation spectra in correspondence of peculiar points is shown.

In the MI incompressible phase, the two lowest excitation branches are the gapped particle and hole excitations (not shown in Figure 3.1). As the SF phase is approached along a CI transition line [blue dashed line, see panel (b)] one of the excitations
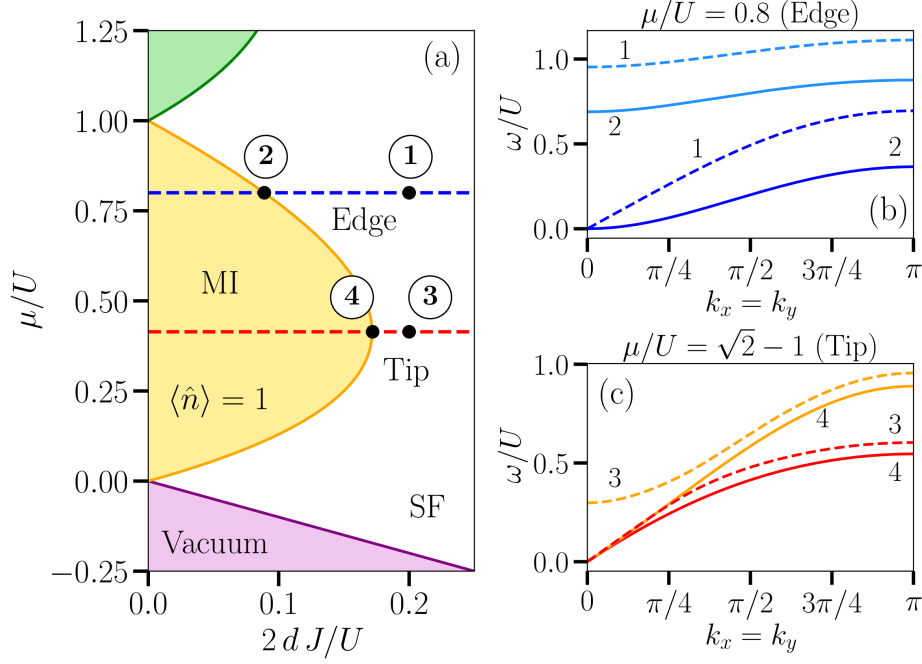
Figure 3.1: Panel (a): mean-field phase diagram of the BH model around the MI lobe with integer filling $\langle \hat{n} \rangle = 1$. The blue (red) dashed line marks the path crossing the incommensurate (commensurate) MI-to-SF transition point considered in this work. The two panels (b) and (c) at the right-hand side depict the energy dispersion at the points (1)-(4) represented in the phase diagram (a). Panel (b), represents points (1) and (2) near and within the critical point at the edge transition, in dashed and solid lines respectively. For these two points, the Goldstone and Higgs modes are represented in blue and light-blue lines respectively. Panel (c) represents points (3) and (4) near and at the critical point at the tip transition, again in dashed and solid lines respectively. Goldstone and Higgs modes are now represented in red and orange lines respectively.

becomes gapless and transforms into the gapless Goldstone mode. The low-momentum dispersion relation of the Goldstone mode becomes quadratic exactly at the transition point [see point (2)], while is linear in the SF phase (collisionless sound mode) [see point (1)]. Therefore, at the CI critical point the BH environment, although strongly-interacting, behaves as an effective free Bose gas of quasiparticles with a renormalised mass. On the other hand, crossing the transition at the fixed-density O(2) critical point [see point (4) along the red dashed line] both the lowest-energy modes, comprising the Higgs excitation, are gapless and, in sharp contrast with the CI critical region, have a linear dispersion relation. In the SF phase, only one linear gapless mode is present with a finite sound velocity [see point (3)], while the amplitude mode acquires a finite energy gap.

The QGA method provides a recipe to express operators and observables of the BH bath directly in terms of the excitations operators $\hat{b}_{\alpha,\mathbf{k}}$. In particular, the impurity dynamics due to the weak coupling with the bath is fully qualified by the time dependent density correlation function at the impurity position. Explicitly, the expression for the QGA density operator $\hat{\mathcal{N}}(\mathbf{0}, t)$ in the interaction picture can be written up to second order in the fluctuations as

$$\hat{\mathcal{N}}(\mathbf{0}, t) \approx n_0 + \delta_1 \hat{\mathcal{N}}(\mathbf{0}, t) + \delta_2 \hat{\mathcal{N}}(\mathbf{0}, t), \tag{3.2}$$

where n_0 is the mean-field density, and we separate the *one-particle*

$$\delta_1 \hat{\mathcal{N}}(\mathbf{0}, t) \equiv \frac{1}{\sqrt{V}} \sum_\alpha \sum_\mathbf{k} N_{\alpha,\mathbf{k}} \left(e^{-i\,\omega_{\alpha,\mathbf{k}}\,t}\, \hat{b}_{\alpha,\mathbf{k}} + e^{i\,\omega_{\alpha,\mathbf{k}}\,t}\, \hat{b}_{\alpha,\mathbf{k}}^\dagger \right), \qquad (3.3)$$

Spectral de-
composition
of quantised
density
fluctuations

from the *two-particle*

$$\delta_2 \hat{\mathcal{N}}(\mathbf{0}, t) \equiv \frac{1}{V} \sum_{\alpha,\beta} \sum_{\mathbf{k},\mathbf{p}} \Big[W_{\alpha,\mathbf{k}|\beta,\mathbf{p}}^* \, e^{i(\omega_{\alpha,\mathbf{k}} + \omega_{\beta,\mathbf{p}})t}\, \hat{b}_{\alpha,\mathbf{k}}^\dagger\, \hat{b}_{\beta,\mathbf{p}}^\dagger + \text{H.c.}$$
$$+ U_{\alpha,\mathbf{k}|\beta,\mathbf{p}} \, e^{i(\omega_{\alpha,\mathbf{k}} - \omega_{\beta,\mathbf{p}})t}\, \hat{b}_{\alpha,\mathbf{k}}^\dagger\, \hat{b}_{\beta,\mathbf{p}} + V_{\beta,\mathbf{p}|\alpha,\mathbf{k}} \, e^{-i(\omega_{\alpha,\mathbf{k}} - \omega_{\beta,\mathbf{p}})t}\, \hat{b}_{\alpha,\mathbf{k}}\, \hat{b}_{\beta,\mathbf{p}}^\dagger \Big]$$
$$(3.4)$$

contributions of the collective modes. The single-mode coefficient $N_{\alpha,\mathbf{k}}$ was already introduced in Eq. (1.45), while the two-mode coefficients $W_{\alpha,\mathbf{k}|\beta,\mathbf{p}}$, $U_{\alpha,\mathbf{k}|\beta,\mathbf{p}}$ and $V_{\alpha,\mathbf{k}|\beta,\mathbf{p}}$ have expressions

$$W_{\alpha,\mathbf{k}|\beta,\mathbf{p}} \equiv \sum_n (n - n_0)\, u_{\alpha,\mathbf{k},n}\, v_{\beta,\mathbf{p},n}, \qquad (3.5a)$$

$$U_{\alpha,\mathbf{k}|\beta,\mathbf{p}} \equiv \sum_n (n - n_0)\, u_{\alpha,\mathbf{k},n}^*\, u_{\beta,\mathbf{p},n}, \qquad (3.5b)$$

$$V_{\alpha,\mathbf{k}|\beta,\mathbf{p}} \equiv \sum_n (n - n_0)\, v_{\alpha,\mathbf{k},n}^*\, v_{\beta,\mathbf{p},n}. \qquad (3.5c)$$

Physically, these objects correspond to the spectral decomposition of the structure factor of density correlations projected onto the multi-branch basis of the collective modes.

It is worth noticing that the inclusion of two-particle processes due to $\delta_2\hat{n}$ into the bath description generalises the standard setting of the spin boson model [176], where the impurity polarisation $\hat{\sigma}_z$ couples only to linear contributions of the form (3.3) (see e.g. [18]). Indeed, we underline that the two-mode contributions dominate the density correlation functions in the MI phase and close to the MI-to-SF transition [131]. In the following, we will show that the very same consideration applies also to the description of the dephasing dynamics of an embedded impurity, with the only exception of the CI transition point.

3.2.3 Non-Markovianity measure of pure dephasing

Having an effective quadratic model for the BH environment at our disposal – see Eq. (1.10) –, the theoretical investigation of the pure dephasing dynamics becomes tractable in the limit in which the presence of the impurity does not perturb significantly the behaviour of the environment, i.e. when the bath-impurity coupling g is small compared to all the other energy scales of the problem. For the purpose of this study, we choose to work in such a weak coupling limit.

Using the time-convolutionless projection operator technique up to second order in the coupling constant g [149], the evolution of the density matrix of the impurity can be shown to obey a time-local master equation [177]

$$\partial_t\, \rho_\text{imp} = -i \frac{\tilde{\omega}_0}{2} [\hat{\sigma}_z, \rho_\text{imp}] + \frac{g^2}{2} \gamma(t) \left(\hat{\sigma}_z\, \rho_\text{imp}\, \hat{\sigma}_z - \rho_\text{imp} \right), \qquad (3.6)$$

where $\tilde{\omega}_0 = \omega_0 + g\,n_0$ is the impurity energy splitting renormalised by the mean local density of the BH bath n_0. As anticipated before, the dephasing rate $\gamma(t)$ is completely determined by the time-dependent correlations of the bath operator coupled to the impurity – local density fluctuations in the present case –, namely

$$\gamma(t) \equiv \mathrm{Re} \int_0^t d\tau \, \langle \hat{n}_{\mathbf{0}}(\tau) \, \hat{n}_{\mathbf{0}}(0) \rangle \,, \qquad (3.7)$$

where we have defined the notation $\langle \cdots \rangle = \mathrm{Tr}\{\cdots \rho_{\mathrm{BH}}^0\}$. We recall here that the derivation of (3.6) does not require any assumption about the statistical properties of the environment, so that in principle the rate (3.7) can account also for weak-coupling effects of non-Gaussian correlations. Now, we highlight that the integrated rate

$$\Gamma(t) \equiv \int_0^t d\tau \, \gamma(\tau) \qquad (3.8)$$

is key to understanding the dephasing dynamics, as it establishes a direct connection between the decay rate $\gamma(t)$ and the physical consequences of its non-Markovian features.

In the framework of the open quantum system formalism, Breuer-Laine-Piilo (BLP) have proposed a rigorous definition for non-Markovianity of a generic quantum channel [178]. Indeed, for the dephasing model studied in this work, the BLP non-Markovianity measure depends directly on the decoherence function $\Gamma(t)$ via the so-called Loschmidt Echo (LE) [179, 180]

$$L(t) \equiv \exp\left[-2\,g^2\,\Gamma(t)\right], \qquad (3.9)$$

driving the off-diagonal evolution of the impurity state $\rho_{imp}(t)$ [1]. In particular, the amount of non-Markovianity corresponds to the *information back-flow* [180–182]

$$\mathcal{B}_- \equiv \sum_{i,\,L(t_{i+1})>L(t_i)} \left[\sqrt{L(t_{i+1})} - \sqrt{L(t_i)}\right], \qquad (3.10)$$

where the sum is taken over the set of time intervals $[t_i, t_{i+1}]$ in which the echo increases, i.e. when $\gamma(t) < 0$. During these intervals, some of the previously lost information regarding the initial state of the impurity is temporarily recovered. Conversely, the Markovian character of the dynamics $\mathcal{B}_+$ is quantified by summing $\sqrt{L(t_{i+1})} - \sqrt{L(t_i)}$ over the time intervals in which quantum information is lost. For the sake of clarity, we point out that, for the special type of open quantum system that we consider here, all non-Markovianity measures agree in distinguishing Markovian from non-Markovian features during the decoherence dynamics [183, 184].

In the following Sections, we will describe how the non-Markovian character of the dephasing process relates to strong correlations in the BH environment, focusing on the role played by the universality classes of the MI-to-SF transition and on the importance of including non-Gaussian correlations beyond a linear coupling between the bath excitations and the impurity (two-particle contributions). In this regard, we start our analysis by illustrating how the QGA provides semi-analytical expressions

Beyond the spin boson model: bath statistics and non-Markovianity

---

[1] See Appendix E.1 for an exhaustive definition of the BLP non-Markovianity measure, as well as its calculation in the present pure dephasing model.

for the dephasing rate $\gamma(t)$ and the decoherence function $\Gamma(t)$, with a clear distinction between one-particle and non-Gaussian fluctuations.

3.2.4 QGA expressions of $\gamma(t)$ and $\Gamma(t)$ and short-time behaviour of the Loschmidt echo $L(t)$

In this Subsection, we report for completeness the explicit expressions of the relevant quantities introduced above within the QGA formalism. Inserting the expression of the QGA density operator (3.2) into the definition of the dephasing rate $\gamma(t)$, we can distinguish two contributions $\gamma(t) = \gamma_1(t) + \gamma_2(t)$. The first term is due to the linear-order part of the density field (3.3),

$$\gamma_1(t) = \text{Re} \int_0^t d\tau \left\langle \delta_1 \hat{\mathcal{N}}(\mathbf{0}, \tau) \, \delta_1 \hat{\mathcal{N}}(\mathbf{0}, 0) \right\rangle = \frac{1}{V} \sum_\alpha \sum_\mathbf{k} |N_{\alpha,\mathbf{k}}|^2 \frac{\sin(\omega_{\alpha,\mathbf{k}} \, t)}{\omega_{\alpha,\mathbf{k}}}, \quad (3.11)$$

while the second contribution is generated by the two-particle density operator (3.4), in particular

$$\begin{aligned}
\gamma_2(t) &= \text{Re} \int_0^t d\tau \left\langle \delta_2 \hat{\mathcal{N}}(\mathbf{0}, \tau) \, \delta_2 \hat{\mathcal{N}}(\mathbf{0}, 0) \right\rangle \\
&= \frac{1}{V^2} \sum_{\alpha,\beta} \sum_{\mathbf{k},\mathbf{p}} \left(\left| W_{\alpha,\mathbf{k}|\beta,\mathbf{p}} \right|^2 + W_{\alpha,\mathbf{k}|\beta,\mathbf{p}}^* \, W_{\beta,\mathbf{p}|\alpha,\mathbf{k}} \right) \frac{\sin\left[(\omega_{\alpha,\mathbf{k}} + \omega_{\beta,\mathbf{p}}) \, t \right]}{\omega_{\alpha,\mathbf{k}} + \omega_{\beta,\mathbf{p}}}
\end{aligned} \quad (3.12)$$

at zero temperature. Analogously, the decoherence function is given by $\Gamma(t) = \Gamma_1(t) + \Gamma_2(t)$ with $\Gamma_i(t) = \int_0^t d\tau \, \gamma_i(\tau)$, $i = 1, 2$. The off-diagonal elements of the impurity density matrix will evolve according to the LE, which factorises into

$$L(t) = \exp\left[-2 \, g^2 \, \Gamma(t) \right] = \exp\left[-2 \, g^2 \, \Gamma_1(t) \right] \, \exp\left[-2 \, g^2 \, \Gamma_2(t) \right]. \quad (3.13)$$

QGA anatomy of the Loschmidt echo

From Eqs. (3.11)-(3.12), we see that the expected short-time Gaussian behaviour $\exp\left[-\lambda \, g^2 \, t^2 \right]$ [185] of the LE is recovered with

$$\lambda \equiv \frac{1}{V} \sum_\alpha \sum_\mathbf{k} |N_{\alpha,\mathbf{k}}|^2 + \frac{1}{V^2} \sum_{\alpha,\beta} \sum_{\mathbf{k},\mathbf{p}} \left(\left| W_{\alpha,\mathbf{k}|\beta,\mathbf{p}} \right|^2 + W_{\alpha,\mathbf{k}|\beta,\mathbf{p}}^* \, W_{\beta,\mathbf{p}|\alpha,\mathbf{k}} \right). \quad (3.14)$$

In the following, we will show how both λ and the BLP non-Markovianity measure are not only extremely sensitive to the phase transition points, but behave differently depending on their universality class.

3.3 Numerical results

In the following, we present the numerical results obtained by computing the dephasing functions (3.11)-(3.12) and the LE $L(t)$. All the calculations have been performed on a 400×400 square lattice, made possible by the low numerical complexity of the QGA. Moreover, we have imposed periodic boundary conditions so as to make the dephasing dynamics independent of the specific position of the impurity in the BH environment and avoid boundary effects. For brevity, hereafter we will refer to the CI transition as *edge transition*, while the O(2) critical point will be indicated as *tip transition*.
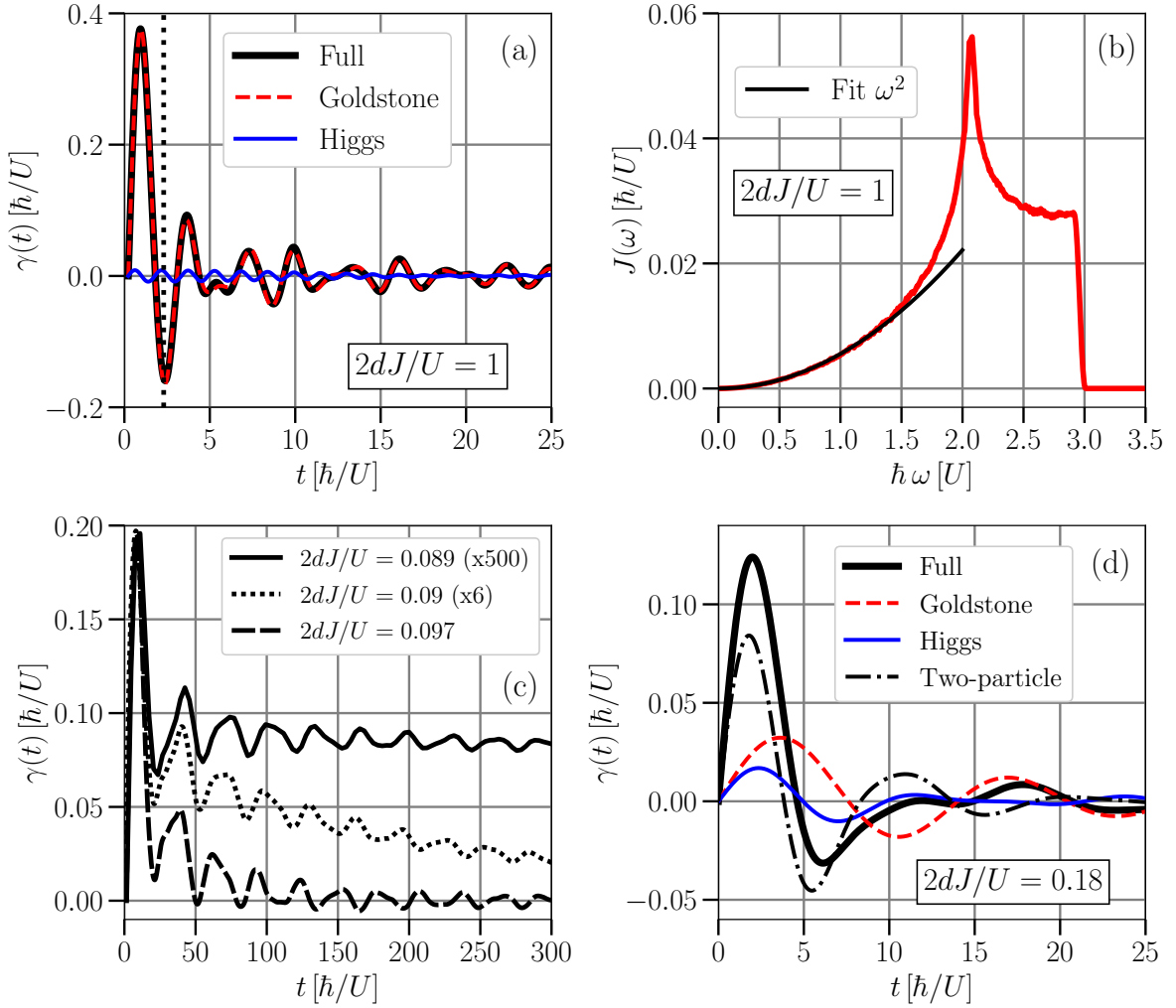
Figure 3.2: (a) Black solid line: dephasing rate $\gamma(t)$ at $2\,d\,J/U = 1$ and $\mu/U = 0.8$ in the deep SF phase. Red dashed and blue solid lines: one-particle contributions of the Goldstone and Higgs modes respectively. The vertical black dashed line highlights the time scale τ_G. (b) Red points: sampling of the spectral density $J(\omega)$ given by Eq. (3.15) for $2\,d\,J/U = 1$ and $\mu/U = 0.8$. Black solid line: ω^2 fit of $J(\omega)$ at low ω. (c) Change of $\gamma(t)$ while approaching the edge transition in the SF phase at $(2\,d\,J/U)_c^{edge} = 0.0\overline{8}$, with decreasing $2\,d\,J/U$ from bottom to top. Magnification of $\gamma(t)$ at lower $2\,d\,J/U$ is applied. (d) Black solid line: $\gamma(t)$ at $2\,d\,J/U = 0.18$ and $\mu/U = \sqrt{2} - 1$, close to the tip critical point $(2\,d\,J/U)_c^{tip} \approx 0.172$ in the SF phase. Black dashed-dotted line: fraction of $\gamma(t)$ given by two-particle contributions involving the Goldstone and Higgs modes. The colour code for the one-particle contributions is the same as in panel (a). Notice that the physical units of the dephasing rate function $\gamma(t)$ are the same of time, after restoring $\hbar$.

3.3.1 General features of dephasing in the superfluid phase

We start our analysis of the dephasing dynamics starting from the weakly-interacting limit (deep SF phase) of the BH bath. In Figure 3.2(a), we report the behaviour of the dephasing rate function $\gamma(t)$ [black solid line] for $2\,d\,J/U = 1$. As expected, in this regime the one-particle contribution from the gapless Goldstone mode [red dashed line] saturates the time evolution of $\gamma(t)$. The dephasing rate exhibits broad oscillations around zero at short times, signalling the occurrence of non-Markovian effects, simply due to the finite bandwidth of the model. Very small amplitude oscillations persist for long times, leading to an essentially constant $\Gamma(t)$ and therefore only to a partial decoherence of the impurity density matrix.

For the sake of clarity, we argue a little bit on such a result, which can be better

understood by expressing the dephasing rate $\gamma(t) = \int_0^\infty d\omega\, J(\omega) \sin(\omega t)/\omega$ [186] in terms of the one-particle spectral density

$$J(\omega) \equiv \frac{1}{V} \sum_{\alpha, \mathbf{k}} \left| N_{\alpha, \mathbf{k}} \right|^2 \delta(\omega - \omega_{\alpha, \mathbf{k}}). \tag{3.15}$$

Intrinsic non-Markovianity of the superfluid phase

This quantity for $2\,d\,J/U = 1$ is shown in Figure 3.2(b). Being the Goldstone spectrum gapless and linear at small momenta, the spectral density scales as $J(\omega) \sim \omega^d$ at low frequencies. Nevertheless, in contrast with the non-Markovianity criterion generally adopted – obtained in [182] and fixing to $d > 2$ the necessary condition for memory effects in gapless baths –, we observe that $\gamma(t)$ can assume negative values in our $d = 2$ model. The reason is that usually an environment with infinite-bandwidth modes is considered in the literature [182], resulting in a smooth cut-off of the spectral density. The finite bandwidth of the BH model excitations implies a sharp frequency cut-off of $J(\omega)$ corresponding to the Goldstone mode energy at the edge of the Brillouin zone, $\omega_{\mathrm{G},\pi}$. Correspondingly, we observe that the oscillations of $\gamma(t)$ occur on a time scale $\tau_{\mathrm{G}} = 2\,\pi/\omega_{\mathrm{G},\pi}$ [vertical dotted line in Figure 3.2(a)] set by the bandwidth of the Goldstone excitation [2].

3.3.2 Dephasing dynamics at incommensurate filling

Broadening the discussion of the previous Subsection, we first analyse the quantitative evolution of the dephasing rate $\gamma(t)$ and of the LE $L(t)$ as the BH bath becomes strongly-interacting without entering the MI phase and, on the contrary, retaining a superfluid character. Specifically, this corresponds to increasing the boson interaction U at fixed non-commensurate density and reaching the so-called Hard-Core Superfluid (HCSF) regime of the BH system. Strictly speaking, we recall here that the hard-core states of the BH system are precisely approached in the $J/U \to 0$ limit of the SF phase and coincide with the extremal points of the CI transition line. For later utility, we also mention that the quantum critical nature of the hard-core states is indeed signalled by the vanishing sound velocity of the Goldstone mode and a diverging compressibility of the BH system [3]. Typical constant-density contours in the strongly-interacting SF phase are shown in Figure 3.3.

Figure 3.4(a) shows the change in the dephasing rate $\gamma(t)$ for decreasing hopping energy $2\,d\,J/U$ at fixed density $\langle \hat{n} \rangle = 0.6$ [see the solid black line in Figure 3.3]. We observe that, upon approaching the hard-core limit $J/U \to 0$ from the deep SF phase, the order of magnitude of $\gamma(t)$ increases significantly, while the time scale of the dephasing dynamics slows down, in such a way that the profiles of $\gamma(t)$ at different values of $2\,d\,J/U$ are related by a simple scaling relation. On the other hand, the strongly-correlated SF regime still exhibits an evident non-Markovian character, as recognisable also in the oscillating behaviour of the LE $L(t)$, see Figure 3.4(b). Here, we can appreciate how non-Markovianity and the overall magnitude of $\gamma(t)$ compete in controlling the amount of dephasing of the impurity. However, at very small J/U, the

---

[2] We refer the reader to Appendix E.2 for an analytical derivation of the low-frequency scaling of $J(\omega)$ in the deep SF phase, as well as for an extensive discussion on the difference between lattice and continuous models at the level of the spectral density $J(\omega)$ and the dephasing function $\gamma(t)$.

[3] See Appendix B.2 for more detailed discussion of the essential features of the hard-core SF states in the BH system.
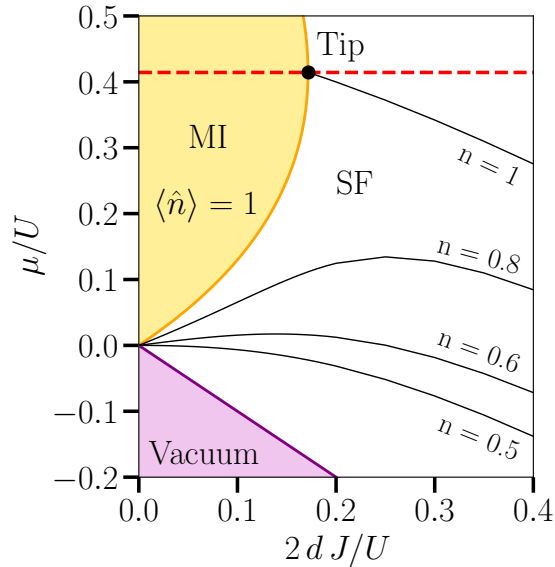
Figure 3.3: Detail of the mean-field phase diagram of the BH model [see panel (a) of Figure 3.1] showing typical constant-density lines (black solid lines) in the SF phase. Non-integer filling lines connect the HCSF regime ($J/U \ll 1$) to the deep SF phase at $J/U \gtrsim 1$.

strong enhancement of the amplitude of $\gamma(t)$ eventually wins over revival effects and drives an almost complete dephasing of the impurity state in a short time interval.

These results find an intuitive explanation in the physical properties of the HCSF state. For $t \ll 1/J$, strong bath correlations prevent the density excitations generated by the impurity from leaving a small neighbourhood of the impurity itself, therefore leading to the large and positive density correlations observed in Figure 3.4(a). However, being the phase still coherent in character, hopping process are favoured at larger times and periodically flip the sign of $\gamma(t)$ in analogy with what we observe in the deep SF regime. Therefore, the total amount of dephasing depends on whether local density correlations are sufficiently strong to overcome non-Markovian effects favoured long-range coherence.

Fast decoherence in the hard-core regime

The dependence of the dephasing rate on the lattice filling can be understood by looking at Figure 3.4(c)-(d), referring to a larger filling $\langle \hat{n} \rangle = 0.8$. In particular, we notice that the oscillation amplitude of $\gamma(t)$ and the speed of the dephasing process decrease as the bath density is increased towards the integer value $\langle \hat{n} \rangle = 1$, a necessary condition for crossing the MI-to-SF transition. In this regard, in the next Subsection we will precisely show that the proximity of the MI phase is linked with the appearance of strong non-Markovian features in the dephasing dynamics at integer bath filling. Finally, we report the remarkable fact that, upon reaching the HCSF regime, the Goldstone mode alone still provides the major contribution to $\gamma(t)$, which is essentially given by its Gaussian part $\gamma_1(t)$ (see the discussion of Subsection 3.2.4). This implies that a one-particle description of the BH bath provides a good approximation of the dephasing dynamics when the impurity is embedded in a strongly-interacting superfluid away from the MI-to-SF criticality.

In Chapter 4, we will show that the peculiar Markovian features of the HCSF regime, and similarly the edge critical region, can be ultimately ascribed to the exceptional softening of the Goldstone mode in these regions, which makes the BH bath maximally
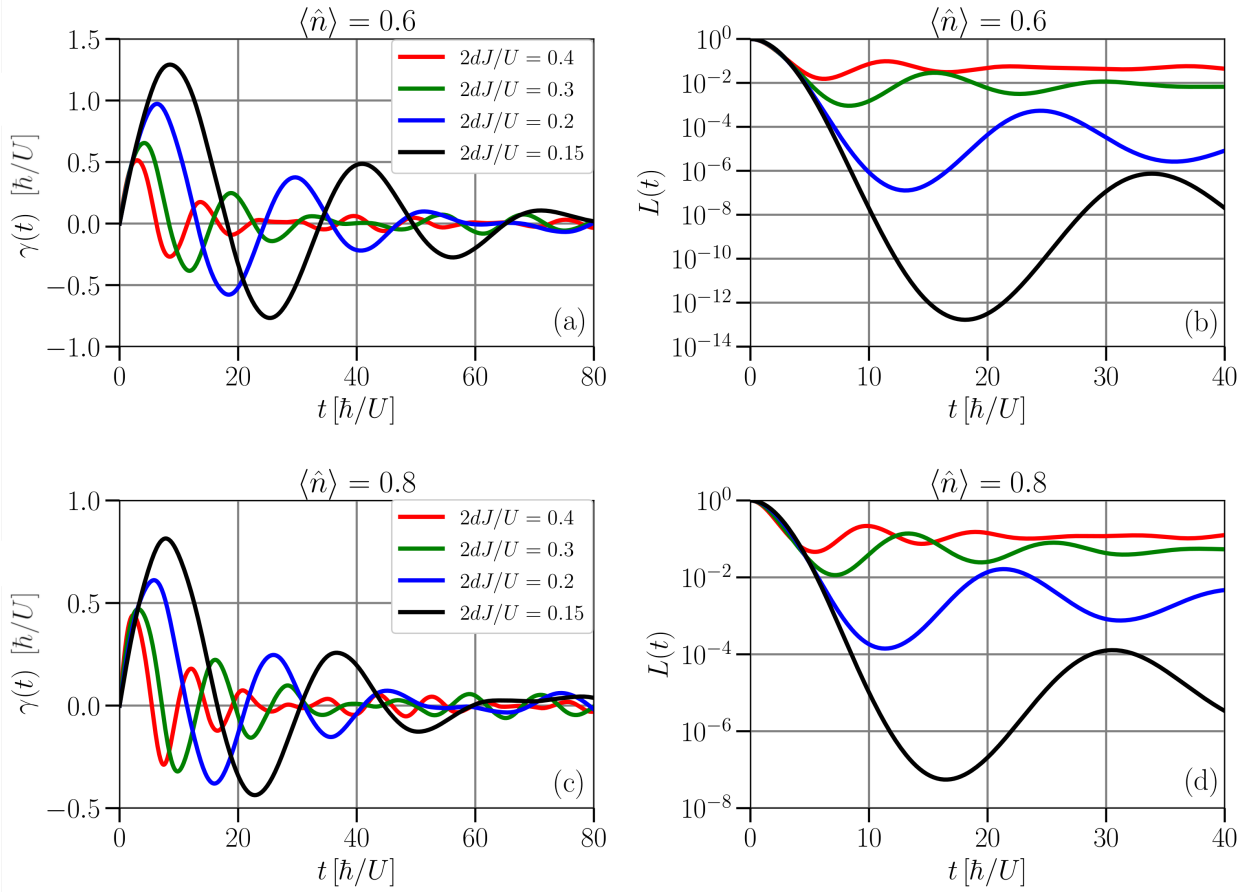
Figure 3.4: (a) Dephasing rate $\gamma(t)$ given by Eq. (3.11) at constant density $\langle \hat{n} \rangle = 0.6$ for decreasing $2\,d\,J/U$ (from red to black solid line) on approaching the HCSF regime of the SF phase. (b) Loschmidt echo $L(t)$ corresponding to the dephasing rates in panel (a). (c)-(d) Dephasing rate and Loschmidt echo for the same values of $2\,d\,J/U$ at a larger, non-integer filling $\langle \hat{n} \rangle = 0.8$.

prone to density fluctuations. In particular, we will discuss how this key aspect reflects into the coupling of a mobile impurity with the BH system and how its properties closely relate to Markovian decoherence in that scenario.

3.3.3 Dephasing dynamics across the MI-to-SF transition

Moving away from the deep SF phase and approaching the MI-to-SF critical region, the fate of the SF non-Markovian dynamics turns out to strongly depend on the type of crossed critical point. In particular, crossing the edge transition [blue dashed line in Figure 3.1] the amplitude of memory effects decreases with increasing interaction U/J until the dynamics becomes purely Markovian on the MI boundary. On the contrary, crossing the tip transition [red dashed line in Figure 3.1(a)], the non-Markovianity is even more enhanced by quantum fluctuations with respect to the deep SF phase.

In panel (c) of Figure 3.2, we display the evolution of $\gamma(t)$ for different values of $2\,d\,J/U$ upon approaching the edge transition. We observe that, close to the critical point $(2\,d\,J/U)_c^{\text{edge}} = 0.0\bar{8}$, $\gamma(t)$ becomes strictly positive, and the dynamics slows down significantly, when compared with the evolution in the deep SF regime shown in panel (a). Therefore, at the edge critical point the dephasing rate reaches a constant value $\gamma(t) \sim \eta$ at asymptotically large times. Hence, a transition from a non-Markovian to a Markovian regime occurs and, exactly at the transition point, the LE acquires the typical

exponential behaviour $L(t) \sim \exp\left(-2\,\eta\,g^2\,t\right)$ of a standard Lindblad dynamics.

The origin of such Markovian behaviour is due to the peculiar spectral properties of the BH model on the edge of the MI lobe. In particular, as illustrated in Subsection 3.2.2: (i) the Goldstone mode turns into an effective quasiparticle branch with quadratic energy dispersion; (ii) the Higgs mode keeps a finite energy gap. It follows that the strongly-correlated superfluid sitting close to the edge critical point can be described as a dilute free-boson gas with an effective mass renormalised by the vicinity of the MI phase [63, 131]. Indeed, it is easy to check that for a free Bose gas – irrespectively of the presence of a lattice – the LE decays always exponentially [4] as $L(t) \sim e^{-\beta\,t}$ for $d = 2$. As in the deep SF case, the Goldstone one-particle contribution to $\gamma(t)$ is the dominant one, with the difference that the two-particle contributions are non-negligible in the edge critical region. However, we find that such a contribution integrates to zero exactly in the time integral of the decoherence function $\Gamma(t) = \int_0^t d\tau\,\gamma(\tau)$. In this respect, the irrelevance of non-Gaussian bath correlations can be seen as a natural consequence of the effective one-particle description holding in proximity of the edge critical region.

The result is very different when approaching the commensurate transition at the tip of the MI lobe, as shown in panel (d). The dynamics appears to be always non-Markovian and the memory effects are amplified with respect to the deep SF regime. The dephasing rate $\gamma(t)$ gets a relevant contribution from the Higgs excitation and, most importantly, from the two-particle couplings [black dot-dashed line]. Specifically, the competition between the Goldstone and Higgs branches is evidently due to the closing of the Higgs gap at the tip critical point. For the same reason, one gets a sizeable contribution to the dynamics from two-particle vertex between the Goldstone and Higgs modes, encoded in the structure factors $W_{\mathrm{Gol},\mathbf{k}|\mathrm{Hig},\mathbf{p}}$ and $W_{\mathrm{Hig},\mathbf{p}|\mathrm{Gol},\mathbf{k}}$ in the two-mode part of the density operator (3.4). Decreasing further $2\,d\,J/U$ towards the critical point, non-Gaussian correlations eventually become the dominant contribution to $\gamma(t)$, since the order of magnitude of the one-particle weights $N_{\alpha,\mathbf{k}}$ is totally suppressed on the brink of the MI-to-SF transition [131].

In this respect, we want to stress that two-particle processes become the only non-vanishing contributions to density correlations when the BH environment enters the MI phase [131]. Therefore, the dephasing dynamics undergoes a substantial change across the edge transition, where the one-particle picture is abruptly replaced by non-Gaussian correlations, while at the tip transition the single-to-two particle transfer of the spectral weight of the bath fluctuations appears to be a smoother crossover.

3.3.4 Short-time decoherence process and non-Markovianity features

A concise way to visualise the previous results is provided by inspecting the dephasing dynamics from the point of view of the LE. Specifically, we focus our analysis on two complementary features of the decoherence process, namely (i) the short-time behaviour of the impurity decoherence $L(t \to 0) = \exp\left(-\lambda\,g^2\,t^2\right)$ and (ii) the estimation of the information back-flow $\mathcal{B}_-$. More precisely, we renormalise the information back-flow by the overall coherence loss as $\mathcal{R} = \mathcal{B}_-/\mathcal{B}_+$, which provides a more informative measure of non-Markovianity while changing the bath parameters [187].

Our numerical results for the short-time decoherence rate λ, given by the expres-

---

[4] We refer again the reader to Appendix E.2 for the explicit expressions of $\gamma(t)$ and $L(t)$ of a free boson gas on a lattice and on the continuum.

sion (3.14), are reported in panel (a) of Figure 3.5. Reaching the MI-to-SF critical region from the deep SF phase, the decoherence rate λ decreases as a consequence of the stronger non-Markovianity introduced by interactions in the BH bath. Reducing further the hopping energy, we observe that λ presents different behaviours depending on the type of approached transition. At the edge critical points, the decoherence rate quickly drops to a small value (decreasing by almost two orders of magnitude) upon entering the MI phase, where we find that $\lambda \propto (J/U)^2$. The first derivative of λ with respect to J/U presents a discontinuity at the critical point. Conversely, when crossing the transition at the tip of the MI lobe, λ is a smooth function of the hopping energy. We notice that the latter result nicely resembles what has been found for the impurity decoherence process in a $d = 1$ interacting quantum spin bath [174], which has a critical point of the same O(2) universality class. Therefore, as proved in the case of the static properties [131], the QGA method is able to capture strong correlation effects also in the present time-dependent scenario, beyond the one-dimensional case and without strong numerical requirements.

The time-integrated dephasing dynamics, in the form of the non-Markovianity measure $\mathcal{R}$, is even more dramatically affected by the type of critical correlations than short-time decoherence. Our numerical results for $\mathcal{R}$ across the edge and tip transitions are reported in panel (b) of Figure 3.5 with the same colour code of panel (a). In particular, for the calculation of $\mathcal{R}$ we have fixed $g/U = 10^{-3} \ll 2\,d\,J/U, \mu/U$ coherently with the weak-coupling condition.

In the deep SF limit $J/U \gg 1$, we find that both the information flows $\mathcal{B}_\pm$ tend to zero scaling as $(J/U)^{-1}$, such that their ratio $\mathcal{R}$ is a constant. This indicates that, when embedded in a weakly-interacting gas, the impurity dephases according to a fixed fraction of lost information. When approaching the strongly-interacting regime, the renormalised back-flow $\mathcal{R}$ reaches a maximal value well before the MI-to-SF transition. This suggests that, away from the critical region, the primary effect of stronger interactions is to increase the amount of information recovered by the impurity during the dynamics. In the vicinity of the critical boundary, the non-Markovianity measure $\mathcal{R}$ starts decreasing, and its behaviour depends on how the MI-to-SF is crossed.

Impurity dephasing as a sensitive probe of the bath physics

Close to the edge transition, $\mathcal{R}$ rapidly vanishes, being zero within a small window of J/U in the SF region. This result perfectly mirrors the non-Markovian to Markovian transition displayed in Figure 3.2(c) and the effective free-particle description of the CI critical point. Subsequently, the quantity $\mathcal{R}$ show a discontinuous behaviour, when entering the insulating phase. This result finds a straightforward interpretation in terms of the particle/hole excitations of the MI phase [167]. Due to their incoherent character, these modes excite doublon-holon pairs with a finite correlation length, so that density fluctuations are localised in real space. Then, when particle/hole excitations couple to the impurity, the information flowing to the BH environment remains localised in a small neighbourhood of the impurity and is likely to be restored after a short time due to another particle/hole excitation. As the amplitude of density fluctuations in the MI phase increase with J/U, the absolute value of both the information flows $\mathcal{B}_\pm$ increases accordingly; on the other hand, the renormalised back-flow $\mathcal{R}$ decrease as a consequence of the increasing BH correlation length, which prevent part of the lost information from flowing back to the impurity. However, since at the edge transition either the particle or the hole branch remains gapped, a finite correlation length still
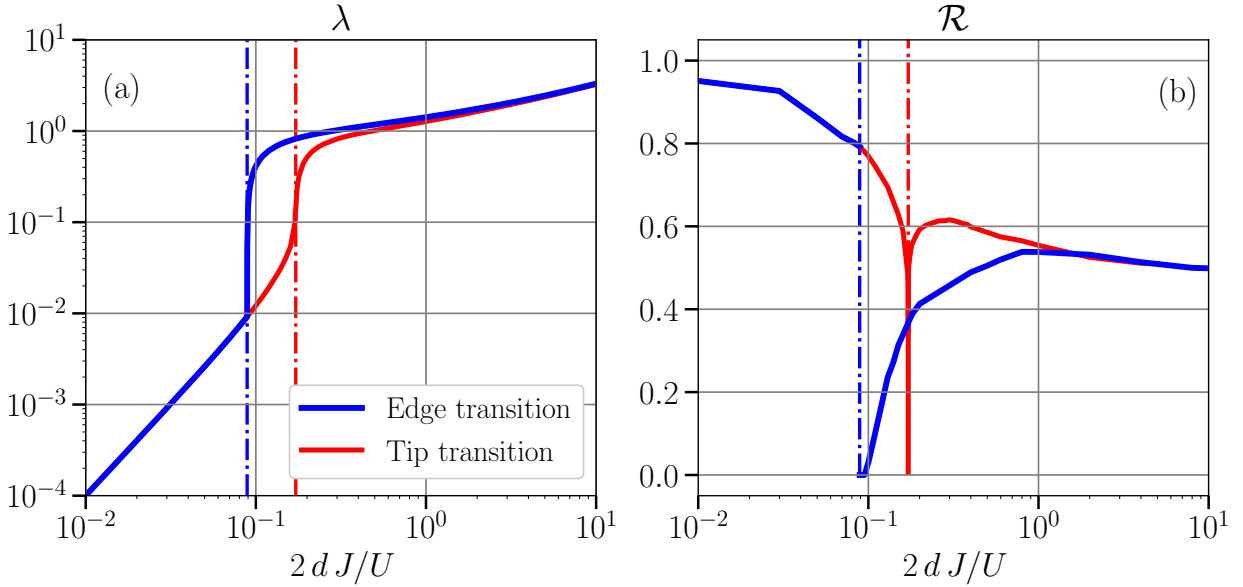
Figure 3.5: (a) Short-time decoherence rate λ as a function of the rescaled hopping energy $2\,d\,J/U$ across the edge (blue line) and tip (red line) transition points [see the phase diagram cuts in panel (a) of Figure 3.1]. (b) Normalised information back-flow $\mathcal{R} = \mathcal{B}_-/\mathcal{B}_+$ for the same parameters. In both panels, the CI and O(2) critical points are indicated by blue and red dashed-dotted lines respectively.

controls the dynamics exactly at the critical point [63, 131], before diverging in the SF phase. This discontinuous behaviour of the correlation length is at the roots of the finite jump in $\mathcal{R}$ across the non-Markovian to Markovian transition.

The behaviour is different at the tip transition. As shown before, in this regime critical fluctuations are mainly due to non-Gaussian correlations, whose main effect is to amplify the oscillation amplitude of the dephasing rate $\gamma(t)$. Therefore, the amount of total information flowing both from and to the impurity grows accordingly. Nevertheless, the renormalised backflow $\mathcal{R}$ still converges to zero at the critical point, meaning that eventually the BH environment becomes effectively Markovian at the critical point. It follows that, in contrast with the edge case, $\mathcal{R}$ is found to be a continuous function of the hopping $2\,d\,J/U$ across the tip transition, but with a very sharp and non-monotonic profile [red line in Figure 3.5(b)].

3.4 Summary and take-home messages

In this Chapter, we have presented an exhaustive account of the non-Markovian effects characterising the dephasing dynamics of an impurity embedded in a BH environment undergoing the MI-to-SF transition. Our analysis addresses the impurity problem beyond the standard formalism of open quantum systems. The two main new features are the inclusion of the effects of strong correlations (as well as critical fluctuations) in the environment and the extension of this physics beyond the one-dimensional case in a flexible and numerically cheap way made possible by the QGA formalism. Thereby, our method is, to the best of our knowledge, the first one that allows for an efficient description of an open system that is coupled to an environment undergoing a critical transition.

Strong signatures of deviation from a Markovian behaviour due to the spatial

discreteness of the lattice setup, not explicitly discussed in previous works, have been also highlighted in the interacting SF phase and related to key features of the spectral density $J(\omega)$. This suggests the idea that the very same phenomenon could take place in different lattice models whose dynamics is governed by common spectral properties. Furthermore, we have observed that the amount of non-Markovianity of the dephasing process is particularly large when approaching the tip critical region, where two-particle effects become more relevant in the physical picture and thus the environment differs more significantly from the standard spin-boson description. This opens the path for further investigations into the role of strong non-Gaussian, e.g. two-particle, correlations in relation to strong memory effects [188].

More importantly, we have found that, when the BH environment approaches the MI-to-SF criticality, the dephasing dynamics is extremely sensitive to the universality class of the transition. In this regard, we have shown that not only the deviation from Markovianity, but also the short-time behaviour of the decoherence dynamics carries strong signatures of the type of criticality approached by the environment. This remarkable result agrees with similar findings concerning interacting quantum spin baths [174], suggesting the existence of a more general rationale which goes beyond the precise nature and the dimensionality of the bath. Finally, from an experimental perspective, the sharp difference between the dephasing processes at the different MI-to-SF transitions discussed in this work identifies the study of the decoherence dynamics and, in particular, non-Markovianity measures of impurity dephasing as an unambiguous probe of the type of critical behaviour experienced by the environment.

With these conclusions in mind, in the next Chapter we will show that the open quantum system perspective of a static impurity in a complex environment has a number of features in common with its opposite realisation at equilibrium, namely the many-body physics of a mobile impurity. This will allow us to gain a deeper and comprehensive view on the behaviour of quantum impurities in strongly-interacting bosonic baths.

Lattice polarons across the superfluid-to-Mott transition | 4

This Chapter integrates the results of the paper:

▶ V. E. Colussi, <u>Fabio Caleffi</u>, C. Menotti, and A. Recati, *Lattice polarons across the superfluid to Mott insulator transition*, arXiv:2205.09857 (20 May 2022), Under consideration for publication in Physical Review Letters

with original findings referring to the following future publication:

▶ V. E. Colussi, <u>Fabio Caleffi</u>, C. Menotti, and A. Recati, *Properties of the polaron cloud in a Bose-Hubbard lattice*, In preparation (2022)

4.1 Polarons on a lattice: a brief introduction

Polarons, quasiparticles formed by a mobile impurity dressed by a cloud of excitations of the bath in which they are immersed, are ubiquitous in physics. Important examples include their emergence in quantum materials [189], superfluid helium [190], nuclear matter [191], and ultracold atomic gases [192]. In particular, this last context is of exceptional importance, as an ultracold atomic bath is usually quite clean with respect to noise or disorder sources, while both its equation of state and the impurity-bath coupling are highly tunable controllable [40, 193]. This has enabled recent pioneering measurements of polaronic quasiparticle properties [194–197], and opened new exciting perspectives for quantum simulation [198, 199]. Even more importantly, the possibility of simulating Hubbard models through ultracold atoms in optical lattices [33, 132], addressing e.g. the debated relationship between the doped Fermi-Hubbard model and high-T_c superconductivity, has posed many open questions regarding the fundamental quasiparticle properties of polarons on lattices, particularly in quantum critical regimes [115, 200–202].

Studies of impurities in quantum critical baths have already yielded valuable physical insights from both a fundamental, into polaron properties resulting from different universality classes of a phase transition, and a practical, into impurities as probes of non-trivial quantum and thermal correlations in their environment, point of view. These include the disappearance of the Bose polaron across the BEC transition [203], and the discontinuity of the energy of a Fermi polaron across the celebrated Berezinskii-Kosterlitz-Thouless transition [204]. For the particular case of a BH bath, the dynamical behaviour of a fixed impurity has been unfolded in the previous Chapter, and has been shown to reveal much information about the structure of quantum correlations of the environment, in analogy with the phenomenology of open quantum systems in spinful environments [205]. We stress once more that quantum critical regimes as those characterising the BH system are always absent in the continuum, where strong impurity-bath correlations cannot be separated from quantum chemistry effects due to few-body physics [206–212].

Although the BH model can be extended straightforwardly to include impurities, the fate of Bose polarons across the MI-to-SF transition have attracted much less attention than their fermionic counterpart and remain largely unexplored. Previous

studies have considered either a homogeneous bath [213, 214] or applications in the deep MI and SF limits only, where the standard mean-field picture applies [215–217]. In this respect, the development of the QGA offers a tempting occasion to systematically include the impact of quantum fluctuations into the description of the Bose polaron.

In this Chapter, we study the fundamental quasiparticle properties of a lattice Bose polaron throughout the whole phase diagram of the BH bath. Carrying over the QGA modelling applied to the fixed impurity case, we will develop a powerful procedure for expanding bath-impurity interactions in terms of elementary excitations to arbitrary order, extending the celebrated Fröhlich model for polarons in crystals [218]. This expansion includes both the many-band structure of the BH spectrum and non-linear interactions, which will be essential to capturing the hallmarks of the MI-to-SF transition. The spectral features of the Bose polaron will be determined within second-order perturbation theory, with the aim of describing the non-obvious effects of strong correlations of the environment at weak coupling.

4.2 Mobile impurity in a Bose-Hubbard environment

4.2.1 Lattice polaron model

We turn our attention to the complementary physical situation with respect to Chapter 3 and consider a mobile impurity coupled to a two-dimensional BH system loaded on a uniform square lattice [1] of spatial volume V. The microscopic Hamiltonian is $\hat{H} \equiv \hat{H}_{\mathrm{BH}} + \hat{H}_{\mathrm{I}} + \hat{H}_{\mathrm{IB}}$, where

$$\hat{H}_{\mathrm{I}} \equiv -J_{\mathrm{I}} \sum_{\langle \mathbf{r}, \mathbf{s} \rangle} \left(\hat{a}^{\dagger}_{I,\mathbf{r}} \, \hat{a}_{I,\mathbf{s}} + \mathrm{H.c.} \right) + z \, J_{\mathrm{I}} \sum_{\mathbf{r}} \hat{a}^{\dagger}_{I,\mathbf{r}} \, \hat{a}_{I,\mathbf{r}} \,, \tag{4.1a}$$

$$\hat{H}_{\mathrm{BH}} \equiv U_{12} \sum_{\mathbf{r}} \hat{n}_{\mathbf{r}} \, \hat{n}_{I,\mathbf{r}} \tag{4.1b}$$

are the Hamiltonian terms describing the impurity and the bath-impurity coupling, respectively. Specifically, the chemical potential term in Eq. (4.1a) shifts the bare energy of the impurity in order to endow it with the free-particle quadratic dispersion $e_{\mathbf{k}} \equiv 4 \, J \sum_{i=1}^{d} \sin^2(k_i/2)$. Here, the bosonic operators $\hat{a}_{I,\mathbf{r}}$ ($\hat{a}^{\dagger}_{I,\mathbf{r}}$) and $\hat{n}_{I,\mathbf{r}} \equiv \hat{a}^{\dagger}_{I,\mathbf{r}} \, \hat{a}_{I,\mathbf{r}}$ are defined to be the creation (destruction) and local density operators of the impurity. For simplicity, we assume that the bare mass of particles in the BH bath $m^{-1} = 2 \, J$ and the impurity mass $M^{-1} \equiv 2 \, J_{\mathrm{I}}$ are equal. In the same spirit of the impurity dephasing analysis, only weak impurity-bath couplings U_{12} will be considered, such that the impurity and bath energy scales are in general well-separated, provided the bath remains energetically stable in the presence of the impurity. Under such conditions, the back action of the impurity on the BH ground state can therefore be neglected.

4.2.2 The Bogoliubov-Fröhlich model

In this Subsection, we start analysing the polaron problem from the simplest case, that is in the limit where the quantum depletion of the BEC forming in the SF regime

---

[1] All the numerical results presented in this Chapter refer to a $d = 2$ lattice of $V = 20^2$ sites, unless otherwise specified.

is small compared to the lattice filling $\langle \hat{n} \rangle$. In this case, the density of the cloud of excitations surrounding the impurity is expected to be small relative to the density of the surrounding BEC, justifying the usual Bogoliubov expansion in powers of the BEC order parameter ψ_0. Therefore, we can safely expand the Hamiltonian (4.1) up to linear order in terms of BEC fluctuations (rather than in the density channel) to obtain the Bogoliubov form of the Fröhlich Hamiltonian routinely used in the characterisation of a mobile impurity in a weakly-interacting condensate (c.f. [219]).

Within the usual Bogoliubov approximation, one has just a single elementary excitation, the Goldstone phonon mode, such that the bath-impurity interaction takes the form [215]

$$\hat{H}_{\mathrm{IB}} \approx U_{12} \left| \psi_0 \right|^2 + \frac{U_{12}}{\sqrt{V}} \sum_{\mathbf{k}} B_{\mathbf{k}} \, e^{i\,\mathbf{k}\cdot\mathbf{r}} \left(\hat{b}_{\mathbf{k}} + \hat{b}_{-\mathbf{k}}^{\dagger} \right) \tag{4.2}$$

where

$$B_{\mathbf{k}} \equiv \psi_0 \left(U_{\mathrm{Bog},\mathbf{k}} + V_{\mathrm{Bog},\mathbf{k}} \right) \tag{4.3}$$

is the one-particle vertex function of the Goldstone mode, with the particle (hole) amplitude $U_{\mathbf{k}}$ ($V_{\mathbf{k}}$) given by

$$\left| U_{\mathrm{Bog},\mathbf{k}} \right|^2 \equiv \frac{1}{2} \left[\frac{z\,J + \varepsilon_{\mathbf{k}} + \left| \psi_0 \right|^2 U}{\omega_{\mathbf{k}}} + 1 \right], \tag{4.4a}$$

$$\left| V_{\mathrm{Bog},\mathbf{k}} \right|^2 \equiv \frac{1}{2} \left[\frac{z\,J + \varepsilon_{\mathbf{k}} + \left| \psi_0 \right|^2 U}{\omega_{\mathbf{k}}} - 1 \right]. \tag{4.4b}$$

Following the terminology of [219], we refer to the Hamiltonian (4.2) for the Bose polaron coupling as the Bogoliubov-Frölich model.

The simple theoretical approach to quantum fluctuations reviewed above can be generalised to include the interaction of the impurity with all the other excitations of the background bath, e.g. the Higgs mode in the SF state and doublon-holon modes in the MI regime. This simply amounts to replace the standard Bogoliubov expansion of the Bose field operators with the QGA lowest-order projection of the Bose field,

$$\delta_1 \hat{\psi}(\mathbf{r}) = \frac{1}{\sqrt{V}} \sum_{\alpha} \sum_{\mathbf{k}} \left[U_{\alpha,\mathbf{k}} \, e^{i\,\mathbf{k}\cdot\mathbf{r}} \, \hat{b}_{\alpha,\mathbf{k}} + V_{\alpha,\mathbf{k}} \, e^{-i\,\mathbf{k}\cdot\mathbf{r}} \, \hat{b}_{\alpha,\mathbf{k}}^{\dagger} \right], \tag{4.5}$$

which is nothing but a direct generalisation of the Bogoliubov expression to comprise the additional excitation modes α that become relevant away from the weakly-interacting limit. In what follows, we will refer to this extended representation as the QGA-Bogoliubov-Frölich model of the BH polaron, specified by the multi-branch vertex functions $B_{\alpha,\mathbf{k}} = \psi_0 \left(U_{\alpha,\mathbf{k}} + V_{\alpha,\mathbf{k}} \right)$ weighting the coupling of the impurity with one-particle condensate excitations across the phase diagram of the bath.

4.2.3 QGA representation of the polaron coupling

In order to fully characterise the properties of the coupling of the BH environment with the mobile impurity across the the phase diagram shown in Figure 4.1(a), we resort again to the QGA formalism as detailed in Chapter 3, but under a different
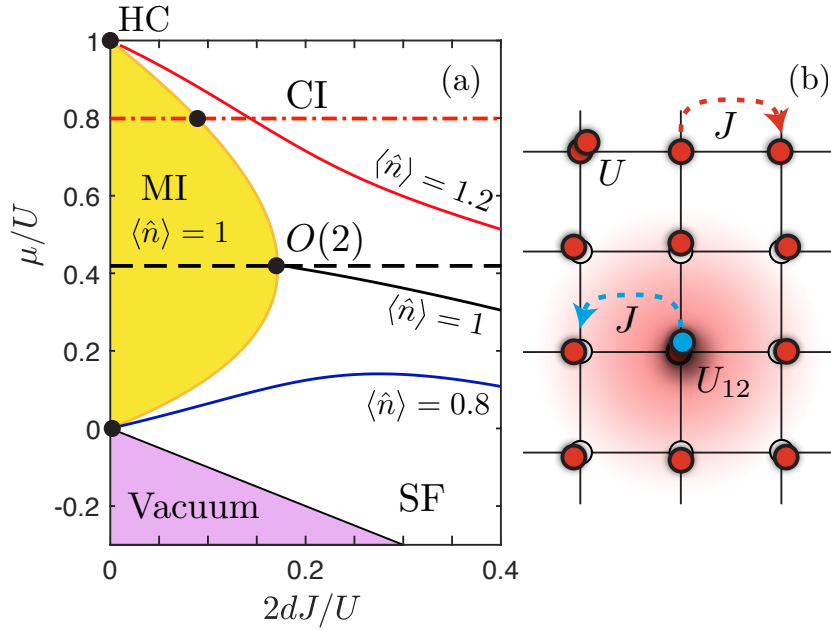
Figure 4.1: (a) Gutzwiller mean-field phase diagram of a d-dimensional BH bath around the $\langle \hat{n} \rangle = 1$ Mott lobe showing constant $\langle \hat{n} \rangle$ (solid) and μ/U (dashed and dashed-dotted) lines. The MI-to-SF transition can be crossed at the tip via the O(2) transition or at the edges via the commensurate-incommensurate (CI) transition. For increasing interaction strength U, non-integer filling lines connect the deep SF and HCSF regimes of the SF. (b) A mobile impurity with hopping energy J and coupling U_{12} to a BH bath is dressed by a cloud of excitations, producing a lattice Bose polaron.

perspective.

We open our discussion by reminding that the successful predictions of the QGA theory made so far rely on its ability to essentially capture the physics of quantum fluctuations across the diverse strongly-correlated regimes due to the MI-to-SF quantum phase transition. In turn, this is related to the accurate description of quantum correlations determined by both one- and two-body fluctuations involving the collective modes of the system, whose relative weights vary significantly upon reaching different critical regions. In the following, we will focus in particular on the roles played by low-energy excitations (Goldstone and Higgs modes) in the polaron features inside the critical SF regime and how they connect to the behaviour inside the MI phase, characterised by doublon-holon excitations.

Beyond-Fröhlich polaron model from the QGA

The polaron cloud is formed by the multi-branch spectrum of the BH excitations, which are taken into account by expanding $\hat{H}_{\mathrm{IB}}$ in powers of the operators $\hat{b}_{\alpha,\mathbf{k}}$ and $\hat{b}^{\dagger}_{\alpha,\mathbf{k}}$. In analogy with the decomposition of density correlations of Chapter 3, we find

$$\hat{H}_{\mathrm{IB}} \approx U_{12} \sum_{\mathbf{r}} \hat{n}_{\mathrm{I},\mathbf{r}} \left[n_0 + \delta_1 \hat{n}(\mathbf{r}) + \delta_2 \hat{n}(\mathbf{r}) + \dots \right] . \tag{4.6}$$

The first term in parentheses gives the mean-field energy shift $U_{12}\, n_0$, the second term

$$\delta_1 \hat{n}(\mathbf{r}) = \frac{1}{\sqrt{V}} \sum_{\alpha} \sum_{\mathbf{k}} N_{\alpha,\mathbf{k}} \left(\hat{b}_{\alpha,\mathbf{k}}\, e^{i\,\mathbf{k}\cdot\mathbf{r}} + \hat{b}^{\dagger}_{\alpha,\mathbf{k}}\, e^{-i\,\mathbf{k}\cdot\mathbf{r}} \right) , \tag{4.7}$$

corresponds to a phonon-like coupling with the impurity. At this level, the resultant Gutzwiller-Frölich model [18, 218] is already more general than any Bogoliubov expansion on top of the SF state [83, 167, 215]: in fact, not only the latter is accurate in the

deep SF regime only, but also relies solely on the excitations of the BEC, which detaches from the microscopic density channel in the presence of strong interactions. Since two-particle processes become relevant in the vicinity of the O(2) critical region [131, 220], the non-linear term should also be included,

$$\delta_2 \hat{n}(\mathbf{r}) = \frac{1}{V} \sum_{\alpha,\beta} \sum_{\mathbf{k},\mathbf{p}} \left[W_{\alpha,\mathbf{k}|\beta,\mathbf{p}} \left(\hat{b}^\dagger_{\alpha,\mathbf{k}} \hat{b}^\dagger_{\beta,\mathbf{p}} e^{-i(\mathbf{k}+\mathbf{p})\cdot\mathbf{r}} + \text{H.c.} \right) \right. \tag{4.8}$$

$$\left. + U_{\alpha,\mathbf{k}|\beta,\mathbf{p}} \, \hat{b}^\dagger_{\alpha,\mathbf{k}} \, \hat{b}_{\beta,\mathbf{p}} \, e^{i(\mathbf{p}-\mathbf{k})\cdot\mathbf{r}} + V_{\alpha,\mathbf{k}|\beta,\mathbf{p}} \, \hat{b}_{\alpha,\mathbf{k}} \, \hat{b}^\dagger_{\beta,\mathbf{p}} \, e^{i(\mathbf{k}-\mathbf{p})\cdot\mathbf{r}} \right] ,$$

yielding a *beyond*-Fröhlich model of the bath-impurity interaction. We anticipate here that, at zero temperature, only contributions weighted by the structure factors $W_{\alpha,\mathbf{k}|\beta,\mathbf{p}}$ affect the energetics of the polaron, as the other terms are associated with thermally activated excitations. Nevertheless, the vertices $U_{\alpha,\mathbf{k}|\beta,\mathbf{p}}$ and $V_{\alpha,\mathbf{k}|\beta,\mathbf{p}}$ will be shown to give a non-negligible contribution to the number of particles populating the polaron cloud, as well as to mediate quantum correlations between the polaron and the bath.

4.3 Self-energy of the Bose polaron

Physically speaking, the polaron is composed of both the impurity and the surrounding cloud of excited bath modes, producing the quasiparticle depicted in Figure 4.1(b). The dressing properties of the impurity are quantified by the self-energy

$$\Sigma(\mathbf{k},\omega) = G^{(0)}(\mathbf{k},\omega)^{-1} - G(\mathbf{k},\omega)^{-1} , \tag{4.9}$$

where $G^{(0)}(\mathbf{k},\omega)$ and $G(\mathbf{k},\omega)$ are the bare and interacting impurity Green's functions, respectively. We calculate the self-energy diagrammatically via the Dyson series, including all relevant zero-temperature diagrams up to second order in U_{12} shown in Figure 4.2. To this level of approximation within the QGA, we find

$$\Sigma(\mathbf{k},\omega) \approx U_{12} \langle \hat{n} \rangle + \Sigma_{1\text{P}}(\mathbf{k},\omega) + \Sigma_{2\text{P}}(\mathbf{k},\omega) , \tag{4.10}$$

where $\langle \hat{n} \rangle = n_0 + \langle \delta_2 \hat{n} \rangle$ includes the QGA second-order quantum corrections to the bath density, the one-particle (Gutzwiller-Fröhlich) contribution is

$$\Sigma_{1\text{P}}(\mathbf{k},\omega) \equiv \frac{U_{12}^2}{V} \sum_\alpha \sum_\mathbf{q} \frac{|N_{\alpha,\mathbf{q}}|^2}{\omega - \omega_{\alpha,\mathbf{q}} - e_{\mathbf{k}-\mathbf{q}} + i\,0^+} , \tag{4.11}$$

and the two-particle (beyond-Fröhlich) contribution is

$$\Sigma_{2\text{P}}(\mathbf{k},\omega) \equiv \frac{U_{12}^2}{2\,V^2} \sum_{\alpha,\beta} \sum_{\mathbf{q},\mathbf{q}'} \frac{\left| W_{\alpha,\mathbf{q}|\beta,\mathbf{q}'} + W_{\beta,\mathbf{q}'|\alpha,\mathbf{q}} \right|^2}{\omega - \omega_{\alpha,\mathbf{q}} - \omega_{\beta,\mathbf{q}'} - e_{\mathbf{k}-\mathbf{q}-\mathbf{q}'} + i\,0^+} . \tag{4.12}$$

Due to the vanishing of the one-particle vertices $N_{\alpha,\mathbf{k}}$ [Figure 4.2(a)] in the incompressible MI regime, we immediately notice the crucial role of direct $W_{\alpha,\mathbf{k}|\beta,\mathbf{k}'}$ and exchange $W_{\beta,\mathbf{k}'|\alpha,\mathbf{k}}$ two-particle processes [Figure 4.2(b)] – such as the excitation of particle-hole pairs – in the quantum critical regime. As we mentioned before, at zero temperature these beyond-Fröhlich effects describe only the simultaneous emission or

Two-boson vertices in the impurity self-energy
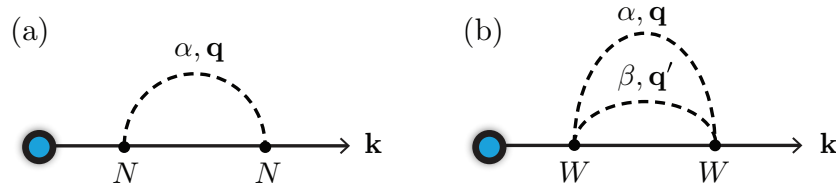
Figure 4.2: Diagrammatic representation of the interacting impurity Green's function $G(\mathbf{k}, \omega)$ at the Hartree-Fock level (up to second order in U_{12}) within the zero-temperature QGA. Panels (a)-(b) depict the one- and two-particle diagrams with QGA vertex functions $N_{\alpha,\mathbf{q}}$ and $W_{\alpha,\mathbf{q}|\beta,\mathbf{q}'}$, respectively. Full lines represent the bare impurity Green's function $G^{(0)}(\mathbf{k}, \omega)$, while dashed lines correspond to bare Green's functions $D^{(0)}(\mathbf{k}, \omega)$ of the collective modes of the BH bath.

absorption of two excitations by the impurity. This is in sharp contrast with the case of the Fermi polaron, where the equivalent processes are suppressed due to Fermi statistics [221]. For the purpose of comparison, we also report the expression for the polaron self-energy within the Fröhlich models discussed in Subsection 4.2.2,

$$\Sigma(\mathbf{k}, \omega) = U_{12} |\psi_0|^2 + \frac{U_{12}^2}{V} \sum_\alpha \sum_\mathbf{q} \frac{|B_{\alpha,\mathbf{q}}|^2}{\omega - \omega_{\alpha,\mathbf{q}} - e_{\mathbf{k}-\mathbf{q}} + i\,0^+}\,, \tag{4.13}$$

where the summation is taken over the Goldstone mode only in the case of the Bogoliubov-Frölich theory and over the entire BH multi-branch spectrum within the QGA-Bogoliubov-Frölich model.

Before proceeding further, it is interesting to notice that, considering the QGA prediction for the dynamical structure factor of the BH model

$$\begin{aligned} S_n(\mathbf{q}, \omega) = &\sum_\alpha |N_{\alpha,\mathbf{q}}|^2 \, \delta(\omega - \omega_{\alpha,\mathbf{q}}) \\ &+ \frac{1}{2V} \sum_{\alpha,\beta} \sum_\mathbf{p} |W_{\alpha,\beta\,;\,\mathbf{p},\mathbf{p}+\mathbf{q}} + W_{\beta,\alpha\,;\,\mathbf{p}+\mathbf{q},\mathbf{p}}|^2 \, \delta(\omega - \omega_{\alpha,\mathbf{p}} - \omega_{\beta,\mathbf{p}+\mathbf{q}})\,, \end{aligned} \tag{4.14}$$

we can express our result for the polaron self-energy in the suggestive form

$$\Sigma(\mathbf{k}, \omega) = \frac{U_{12}^2}{V} \sum_\mathbf{q} \int d\varepsilon \, S_n(\mathbf{q}, \varepsilon) \, G^{(0)}(\mathbf{k} + \mathbf{q}, \omega - \varepsilon)\,. \tag{4.15}$$

The above relation strongly reminds of a Bethe-Salpeter equation linking one-body correlations (left-hand side) with two-body fluctuations (right-hand side) and is evidently a natural consequence of the self-consistent character of our Hartree-Fock calculation of $\Sigma(\mathbf{k}, \omega)$.

The key properties of the lattice Bose polaron include its dispersion, stability, and coherence, which have been the subjects of numerous experimental research efforts on the continuum [196, 197, 203, 222–224] exploiting the powerful toolbox of RF interferometry [225] combined with the manipulation of Feshbach resonances [193]. In this work, we calculate the polaron dispersion by considering the self-energy on the bare mass shell ($\omega = e_\mathbf{k}$). This procedure goes under the name of Rayleigh-Schrödinger perturbation theory [18] and, when tailored for the polaron problem, is known to provide physically sound results when tailored to the polaron problem. In particular, this scheme successfully compares to more involved approaches as e.g. the Brillouin (off-shell) scheme, which require to calculate renormalised spectral properties self-consistently

and have been argued to mix perturbative orders in an uncontrolled manner [226–228]. According to the on-shell approximation, the full polaron energy dispersion reads $E_{\mathbf{k}} = e_{\mathbf{k}} + \text{Re}[\Sigma(\mathbf{k}, e_{\mathbf{k}} + i\,0^+)]$, which can be expanded at low momentum as

$$E_{\mathbf{k}} \equiv E_0 + \frac{\mathbf{k}^2}{2\,M_*} + O(k^4)\,, \tag{4.16}$$

where E_0 is the uniform shift of the polaron energy, and M_* is the polaron effective mass. Both quantities can be inferred from Eq. (4.16) via the equations

$$E_0 \equiv \text{Re}\left[\Sigma\left(\mathbf{0}, i\,0^+\right)\right] \tag{4.17}$$

and

$$\frac{M}{M_*} \equiv \frac{M}{d} \sum_{i=1}^{d} \left.\frac{\partial^2 E_{\mathbf{k}}}{\partial k_i^2}\right|_{\mathbf{k}=\mathbf{0}}\,, \tag{4.18}$$

respectively. On the other hand, the coherence and stability of the polaron are determined by the (on-shell) momentum-dependent quasiparticle residue

$$Z_{\mathbf{k}}^{-1} \equiv 1 - \left.\frac{\partial \text{Re}[\Sigma(\mathbf{k}, \omega + i\,0^+)]}{\partial \omega}\right|_{\omega = e_{\mathbf{k}}} \tag{4.19}$$

and the decay rate

$$\Gamma(\mathbf{k}) \equiv -2\,\text{Im}\left[\Sigma\left(\mathbf{k}, e_{\mathbf{k}} + i\,0^+\right)\right]\,. \tag{4.20}$$

In particular, the quasiparticle residue measures the overlap between the polaron and free impurity states, quantifying the renormalised spectral weight of the polaronic pole of the Green's function [18]. It follows that the polaron is a well-defined coherent mode provided that $\Gamma(\mathbf{k}) \ll E_{\mathbf{k}}$ and $Z_{\mathbf{k}}$ is finite.

We conclude this Section by noting that Eqs. (4.10) and (4.13) are invariant under a sign change of U_{12}, up to a possible overall shift due to the Hartree contribution, and therefore we restrict ourselves to the case $U_{12} > 0$, producing results for $U_{12}/U = 0.2$ without loss of generality at weak coupling. We also specify that we will work in units of U when considering quantities having the dimensions of energy.

4.4 Polaron energetics across the MI-to-SF transition

4.4.1 QGA description of the polaronic spectrum

First and foremost, we study in detail how the spectral properties of the polaron depend on the quantum critical behaviour of the bath. In particular, from Eqs. (4.17)-(4.18) we obtain the semi-analytical predictions

$$E_0 = U_{12}\,\langle \hat{n} \rangle - \frac{U_{12}^2}{V}\left[\sum_{\alpha}\sum_{\mathbf{q}} \frac{|N_{\alpha,\mathbf{q}}|^2}{\omega_{\alpha,\mathbf{q}} + e_{\mathbf{q}}} - \frac{1}{2V}\sum_{\alpha,\beta}\sum_{\mathbf{q},\mathbf{q}'} \frac{\left|W_{\alpha,\mathbf{q}|\beta,\mathbf{q}'} + W_{\beta,\mathbf{q}'|\alpha,\mathbf{q}}\right|^2}{\omega_{\alpha,\mathbf{q}} + \omega_{\beta,\mathbf{q}'} + e_{\mathbf{q}+\mathbf{q}'}}\right]\,, \tag{4.21}$$

and

$$\frac{M}{M_*} = 1 - \frac{1}{d}\frac{U_{12}^2}{V}\left[\sum_\alpha \sum_{\mathbf{q}} \sum_{i=1}^{d} |N_{\alpha,\mathbf{q}}|^2\, \Phi(\mathbf{q},\mathbf{0},\omega_{\alpha,\mathbf{q}}) \right. \tag{4.22}$$

$$\left. -\frac{1}{2V}\sum_{\alpha,\beta}\sum_{\mathbf{q},\mathbf{q}'}\sum_{i=1}^{d}\left|W_{\alpha,\mathbf{q}|\beta,\mathbf{q}'} + W_{\beta,\mathbf{q}'|\alpha,\mathbf{q}}\right|^2 \Phi(\mathbf{q},\mathbf{q}',\omega_{\alpha,\mathbf{q}}+\omega_{\beta,\mathbf{q}'})\right],$$

where we have defined the function

$$\Phi(\mathbf{k},\mathbf{p},\omega) = \frac{2\,M^{-1}\sin\left(k_i+p_i\right)^2}{\left(\omega+e_{\mathbf{k+p}}\right)^3} + \frac{1-\cos\left(q_i+p_i\right)}{\left(\omega+e_{\mathbf{k+p}}\right)^2}. \tag{4.23}$$

Our results for E_0 and M/M_* are shown in Figure 4.3 both at fixed chemical potential [(a)-(b)] and fixed filling [(a')-(b')] across the O(2) and CI transitions.

In general, starting from the deep SF regime and reducing the hopping J/U, the dressing effect of the bath excitations leads to a heavier polaron with energy lower than the Hartree shift $U_{12}\langle \hat{n}\rangle$, which corresponds to the limiting value in both the deep SF and MI regimes. In the former regime, the contribution of quantum fluctuations is saturated by the excitation of the gapless Goldstone mode, whereas in the latter it is solely due to the excitation of particle-hole pairs. However, as the strongly-correlated regime is approached, we observe two distinct trends depending on the universality class of the transition and the character of the underlying critical fluctuations.

Link between beyond-Fröhlich processes and Mottness
Upon crossing the O(2) phase transition, either by fixing $\langle\hat{n}\rangle = 1$ or $\mu/U = \sqrt{2}-1$, we see from Figure 4.3 that both E_0 and M/M_* reach an absolute minimum on the SF side and increase *smoothly* across the transition. Here, both the Goldstone and Higgs branches make competing contributions to the polaron cloud at the one-particle level due to the closing of the Higgs gap at the critical point. For the same reason, the beyond-Fröhlich two-particle process involving the coupling of the Goldstone and Higgs modes, encoded in the vertex $W_{\text{Gold},\mathbf{q}|\text{Hig},\mathbf{q}'}$, makes also a significant contribution to the SF side of the transition. These processes become the only non-vanishing contributions at the critical point, leading to a smooth crossover towards the Mott polaron as a consequence of the non-Gaussian statistics [2] of the bath [220]. In the MI lobe, the polaron cloud is composed by doublon-holon pairs with fixed size set by $(J/U)^2$, becoming increasingly localised in a small neighbourhood of the impurity with emission and absorption processes occurring on relatively short time scales [43, 131, 220].

The situation changes drastically when the MI boundary is crossed instead at the CI transition for fixed chemical potential, as shown in Figure 4.3(a)-(b) [red dashed-dotted line]. In this case, both E_0 and M/M_* are dominated by one-particle processes despite strong interactions, in analogy with the physical mechanism behind pure dephasing in the same region. Here, quantum fluctuations are predominantly due to the Goldstone mode, as the Higgs mode retains a sizeable gap at the transition. On the SF side of the CI point, the polaron properties are more strongly renormalised than at the O(2)

---

[2] We redirect the reader to Subsection 3.2.3 and Section 3.3 for a more detailed discussion on the relation between the order of quantum fluctuations due to the collective modes and the statistics of the BH bath. In particular, we recall that the expression "non-Gaussian" refers here to the order of the non-linear coupling of the impurity with the bath modes, made possible by the peculiar description of "Gaussian" quantum fluctuations provided by the QGA.
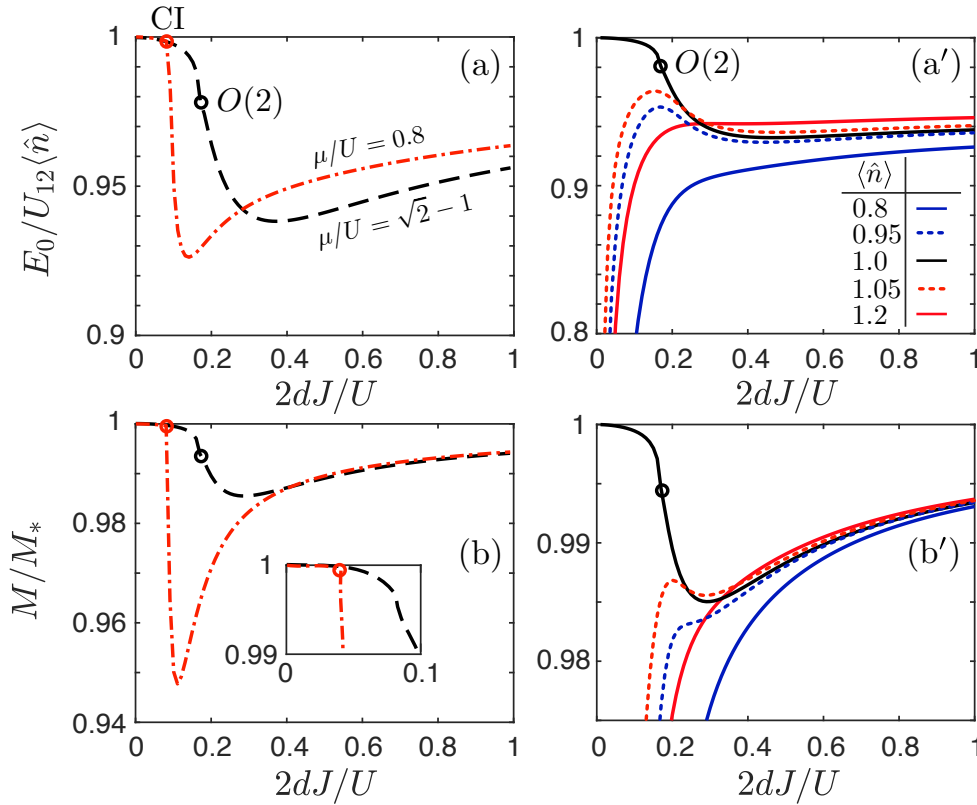
Figure 4.3: (a)-(b) Polaron spectral properties for fixed μ/U across the O(2) (black dashed) and CI (red dashed-dotted) transitions, with the non-analytic nature of the latter highlighted in the inset. (a')-(b') Polaron spectral properties for fixed $\langle \hat{n} \rangle$. The $\langle \hat{n} \rangle = 1$ line crosses O(2) critical point at $2\,d\,J/U \approx 0.172$, while the non-integer lines approach the HCSF regime, where the extremal point of the CI transition is located. The dots indicate the O(2) quantum critical points.

point, moving *sharply* towards their bare values on the MI side. At the CI point, the bath behaves as an effective free Bose gas of quasiparticles with vanishing sound speed and large compressibility [3], hence becoming softer to perturbations of the density than at the O(2) point, where the sound speed reaches a finite value and the compressibility vanishes continuously [51, 131]. Consequently, there is a stronger interplay between density fluctuations of the bath and the impurity. The non-analyticity of the polaron properties at the transition [inset Figure 4.3(b)] closely reflects the discontinuous behaviour of the single-particle coherence length at the CI transition [63, 131] due to the abrupt suppression of one-particle processes, with only two-particle processes surviving the opening of the Mott gap.

Travelling instead along lines of non-integer filling [see Figure 4.1(a)], the bath enters the regime of the HCSF state ($J/U \ll 1$) at the upper/lower margins of the MI lobes shown in Figure 4.3(a')-(b') [red and blue solid and dotted lines]. Here, as anticipated in Chapter (3), the bath becomes strongly-interacting without entering the MI phase, with the polaron cloud again dominated by one-particle excitations of the Goldstone mode, having a vanishingly small sound velocity and hence an almost quadratic dispersion. The behaviour of the HCSF as a Bose gas of strongly-renormalised quasiparticles entails a diverging compressibility [43] and, correspondingly, a divergence in E_0 and M/M_* precisely at the hard-core point located at $J/U \to 0$. As a side note, we observe that a

---

[3] See Appendix B.2 for a detailed description of the behaviour of the Goldstone sound velocity in different critical regimes of the BH model.
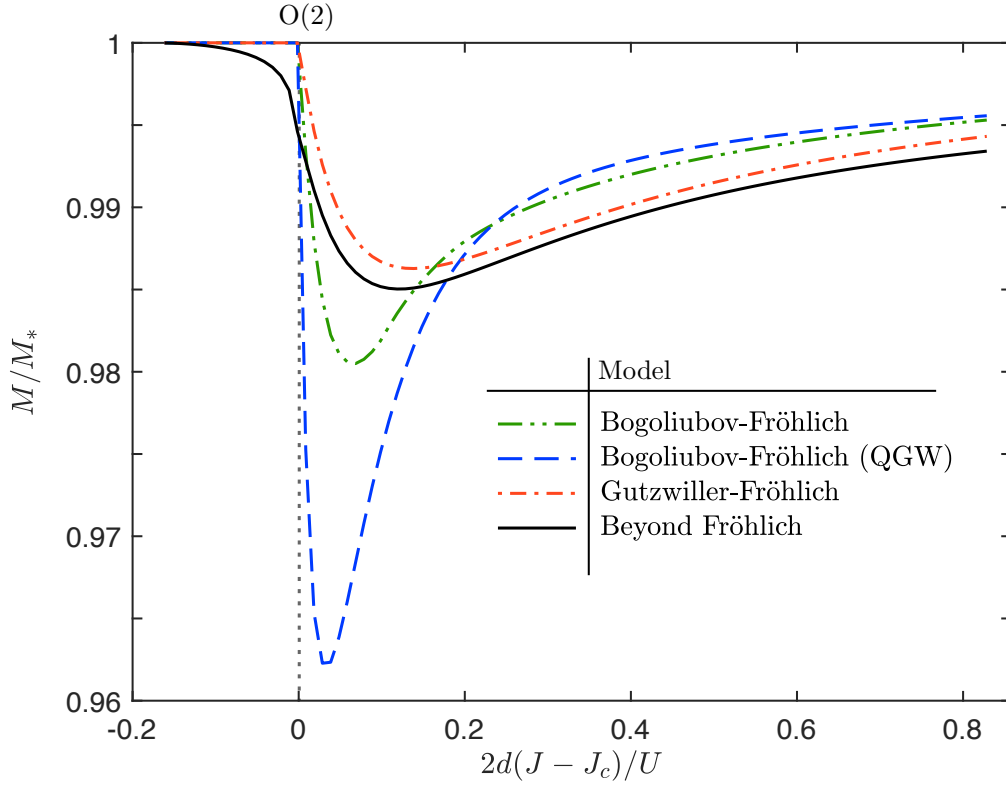
Figure 4.4: Comparison between the results for the effective mass of the polaron across the O(2) transition according to different models of the impurity-bath interaction for fixed $\langle \hat{n} \rangle = 1$. The location of the corresponding phase transitions are indicated by vertical dotted lines.

non-monotonic behaviour is found as the filling nears an integer value [dotted lines Figure 4.3(a')-(b')] in the strongly-correlated regime, due to the growing vicinity of the phase transition.

4.4.2 Comparison with the predictions of Fröhlich models

In order to appreciate more the improvement provided by the QGA theory applied to the Bose polaron, it is important to understand where the Fröhlich physical scenario suffices and the different flavours of the Bogoliubov treatment discussed in Subsection 4.2.2 can be used.

In Figure 4.4, we show a comparison between the predictions of different models of the bath-impurity interaction for the polaron effective mass M/M_* across the O(2) critical point. We immediately observe that all approaches agree in the deep SF limit, where the effective mass reaches its bare value. Near the strongly-correlated regime of the bath, the Bogoliubov-Frölich result [dot-dashed green line] starts deviating from its Gutzwiller reformulation [dashed blue line], with the latter giving a heavier effective mass as a consequence of including the contribution of a larger number of excitation branches, which encode the effect of stronger interactions. However, we point out that in general the QGA-Bogoliubov-Frölich theory tends to overestimate significantly the weight of quantum fluctuations in the strongly-interacting SF phase, even if all the excitations on top of the condensate are considered. Instead, in this regime both the Gutzwiller-Frölich model [dot-dashed red line] and its beyond-Fröhlich generalisation

[solid black line] predict a milder renormalisation of the effective mass. In particular, the difference between these two curves reflects the increased contribution of two-body processes in the quantum critical regime involving the Goldstone-Higgs vertex on the SF side and doublon-holon excitations on the MI side. Our beyond-Fröhlich approach is able to account for these processes, which yield the smooth evolution of M/M_* across the O(2) transition. On the contrary, it is clear from Figure 4.4 that all Fröhlich models provide instead a non-analytic behaviour at this point, with the effective mass dropping trivially to its bare value as a consequence of the vanishing weight of one-body vertices of the collective modes. While this non-analyticity is smeared by two-particle processes across the O(2) transition, the line of CI transitions is still well described by the Gutzwiller-Frölich model, which correctly captures the non-analytic behaviours of the polaron properties across this special type of criticality.

These findings demonstrate that the QGA treatment of the microscopic bath-impurity coupling is essential to the overall physical consistency and accuracy of the predictions presented in this work. Ultimately, the Bogoliubov scheme is reliable only in the deep superfluid regime, where the negligible depletion of the condensate justifies the corresponding expansion.

How the QGA rectifies the Bogoliubov polaron

4.5 Quasiparticle weight and polaron lifetime

The quantum critical nature of the bath can also strongly impact on the coherence and stability of the polaron, jeopardising its experimental detection. The on-shell quasiparticle residue and decay rate follow from Eqs. (4.19)-(4.20),

$$
Z_{\mathbf{k}}^{-1} = 1 + \frac{U_{12}^2}{V} \left[\sum_{\alpha} \sum_{\mathbf{q}} \frac{|N_{\alpha,\mathbf{q}}|^2}{\left(e_{\mathbf{k}} - e_{\mathbf{k}-\mathbf{q}} - \omega_{\alpha,\mathbf{q}}\right)^2} \right.
$$
$$
\left. + \frac{1}{2V} \sum_{\alpha,\beta} \sum_{\mathbf{q},\mathbf{q}'} \frac{\left|W_{\alpha,\mathbf{q}|\beta,\mathbf{q}'} + W_{\beta,\mathbf{q}'|\alpha,\mathbf{q}}\right|^2}{\left(e_{\mathbf{k}} - e_{\mathbf{k}-\mathbf{q}-\mathbf{q}'} - \omega_{\alpha,\mathbf{q}} - \omega_{\alpha,\mathbf{q}'}\right)^2} \right] ,
\tag{4.24}
$$

$$
\Gamma_{\mathbf{k}} = \frac{2\pi U_{12}^2}{V} \left[\sum_{\alpha} \sum_{\mathbf{q}} |N_{\alpha,\mathbf{q}}|^2 \, \delta(e_{\mathbf{k}} - e_{\mathbf{k}-\mathbf{q}} - \omega_{\alpha,\mathbf{q}}) \right.
\tag{4.25}
$$
$$
\left. + \frac{1}{2V} \sum_{\alpha,\beta} \sum_{\mathbf{q},\mathbf{q}'} \left|W_{\alpha,\mathbf{q}|\beta,\mathbf{q}'} + W_{\beta,\mathbf{q}'|\alpha,\mathbf{q}}\right|^2 \, \delta(e_{\mathbf{k}} - e_{\mathbf{k}-\mathbf{q}-\mathbf{q}'} - \omega_{\alpha,\mathbf{q}} - \omega_{\beta,\mathbf{q}'}) \right] ,
$$

with the latter having the form of a FGR with effective couplings set by the QGA one- and two-particle vertices. In particular, the decay rate accounts for the zero-temperature spontaneous emission of excitations from the polaron cloud, which is energetically allowed provided that $e_{\mathbf{k}} = e_{\mathbf{k}-\mathbf{q}} + \omega_{\alpha,\mathbf{q}}$ and $e_{\mathbf{k}} = e_{\mathbf{k}-\mathbf{q}-\mathbf{q}'} + \omega_{\alpha,\mathbf{q}} + \omega_{\beta,\mathbf{q}}$ are satisfied for some exchanged momenta $\mathbf{q}, \mathbf{q}'$. Moreover, it is easy to see that these events are energetically favoured for lighter impurities due to the convexity of $e_{\mathbf{k}} \sim M^{-1}$. In order to evaluate the δ-functions in Eq. (4.5) on a finite-sized lattice, we utilise their Lorentzian representation, with a width equal to $\eta = 10^{-2}$ chosen to produce results compatibly with the numerical size of the square lattice under consideration. In general,

a finer resolution of the δ-function (smaller η) implies the need of a larger lattice, which considerably increases the computational cost, particularly to resolve the beyond-Fröhlich effects. Additionally, we expect the energy conservation bounds in Eq. (4.5) to be blurred on the lattice due to an approximated representation of the δ-function.

As a secondary detail, by making use of Eq. (4.14), we notice that the polaron decay rate can also be written as

$$\Gamma_{\mathbf{k}} = \frac{2\,\pi\,U_{12}^2}{V}\sum_{\mathbf{q}}\int d\varepsilon\, S_n(\mathbf{q}, \varepsilon)\, A_0(\mathbf{k}, \varepsilon + \varepsilon_{\mathbf{k}+\mathbf{q}}) \,, \tag{4.26}$$

where $A_0(\mathbf{k}, \varepsilon) = -\mathrm{Im}[\Sigma(\mathbf{k}, \varepsilon + i\,0^+)]$ is the bare DoS of the impurity. This provides us with a straightforward interpretation of $\Gamma_{\mathbf{k}}$: it quantifies how much the dynamical structure factor of the bath, that is the spectral weight of density excitations, and the on-shell impurity states overlap in momentum-frequency space.

4.5.1 Low-energy contribution of the Goldstone mode to $\Gamma_{\mathbf{k}}$

By simple analytic manipulations, we can identify precise bounds on the impurity velocity for which the decay rate $\Gamma_{\mathbf{k}}$ gathers the contribution of soft Goldstone excitations at the one-particle level. Considering the energy conservation identity $e_{\mathbf{k}} - e_{\mathbf{k}-\mathbf{q}} = \omega_{\alpha,\mathbf{q}}$ and the limit of small $|\mathbf{q}|$, we have

$$\sum_{i=1}^{d}(\partial_{k_i} e_{\mathbf{k}})\, q_i = \sum_{i=1}^{d} v_{\mathbf{k}}^i\, q_i = \mathbf{v}_{\mathbf{k}} \cdot \mathbf{q} = c_s\,|\mathbf{q}| \,, \tag{4.27}$$

where $v_{\mathbf{k}}^i \equiv 2\,J_{\mathrm{I}}\sin(k_i)$ is the ith component of the impurity velocity and c_s is the sound velocity of the Goldstone mode as always. Now, since $c_s > 0$, the scalar product $\mathbf{v}_{\mathbf{k}} \cdot \mathbf{q}$ should be positive in order to ensure energy conservation. In particular, calling the angle between the vectors $\mathbf{v}_{\mathbf{k}}$ and $\mathbf{q}$ as θ, this results in $|\mathbf{v}_{\mathbf{k}}|\,|\mathbf{q}|\cos(\theta) > 0$, so that $-\pi/2 < \theta < \pi/2$ (modulo $2\,\pi$). In the two-dimensional case, this means that at least one component of the impurity velocity should have the same direction of the corresponding component of $\mathbf{q}$. Conversely, such a restriction on θ can be seen also a bound on the possible exchange momentum $\mathbf{q}$ that the Goldstone mode can have. The limiting value of the modulus of the impurity velocity can be obtained from the solution of Eq. (4.27), reading

$$|\mathbf{v}_{\mathbf{k}}| = -\frac{c_s}{\cos(\theta)} \longrightarrow P_{\mathrm{I}} \equiv \sqrt{\sum_{i=1}^{d}\sin(k_i)^2} = -M\frac{c_s}{\cos(\theta)} \tag{4.28}$$

Landau criterion for the polaron momentum

where P_{I} is defined to be the modulus of the impurity momentum. We highlight that this result clearly establishes a sort of Landau criterion [40, 229, 230] for the impurity velocity to generate low-energy sound excitations of the bath [231, 232]: in particular no excitation can be emitted by the polaron in the so-called *subsonic* regime $P_{\mathrm{I}} < k_c \equiv M\,c_s$. For instance, we observe that a completely delocalised polaron with $\mathbf{k} = \mathbf{0}$ cannot spontaneously decay into arbitrarily soft Goldstone modes. Remarkably, we observe that this last result does *not* change at the CI transition and in the HC limit of the system, where the Goldstone mode has a purely quadratic energy dispersion

and the energy conservation rule at low momenta changes into

$$-\frac{1}{2}\sum_{i=1}^{d}\left(\partial_{k_i}^2 e_{\mathbf{k}}\right) q_i^2 = -\frac{1}{2}\sum_{i=1}^{d}\left(z\,J_{\mathrm{I}} - e_{\mathbf{k}}^i\right) q_i^2 = G\,|\mathbf{q}|^2\,, \tag{4.29}$$

where $e_{\mathbf{k}}^i \equiv 4\,J_{\mathrm{I}}\sin\left(k_i/2\right)^2$ and $G > 0$ is the effective mass of Bose particles in the bath. Indeed, Eq. (4.29) has no solution for $\mathbf{k} = \mathbf{0}$, however energy conservation can be fulfilled for moderately large values of $|\mathbf{k}|$: for instance, if the impurity has momentum k along all the spatial directions of the lattice, we obtain $k = \arccos\left[-G/\left(d\,J_{\mathrm{I}}\right)\right]$.

The observations made above can be substantiated by explicitly calculating the contribution of the Goldstone mode to the decay rate at low momenta. In particular, we restrict again our analysis to the single-particle part

$$\Gamma_{\mathbf{k}}^{(1,\mathrm{G})} \equiv \frac{2\,\pi\,U_{12}^2}{I}\sum_{\mathbf{q}} |N_{\mathrm{G},\mathbf{q}}|^2\,\delta(e_{\mathbf{k}} - e_{\mathbf{k}-\mathbf{q}} - \omega_{\mathrm{G},\mathbf{q}})\,, \tag{4.30}$$

which to a first approximation gives a good physical intuition of polaron decoherence over the whole SF phase, in particular close to the CI transition and in the strongly-interacting SF regime. In the limit of small $|\mathbf{k}|$ and $|\mathbf{q}|$, the argument of the δ-function in Eq. (4.30) can be greatly simplified and written as

$$e_{\mathbf{k}} - e_{\mathbf{k}-\mathbf{q}} - \omega_{\mathrm{G},\mathbf{q}} \xrightarrow[\mathbf{k},\,\mathbf{q}\to\mathbf{0}]{} -\frac{\mathbf{q}^2}{2\,M} + \frac{|\mathbf{k}|\,|\mathbf{q}|\cos\left(\theta\right)}{M} - c_s\,|\mathbf{q}| \tag{4.31}$$

up to second-order in momentum. Therefore, in the thermodynamic limit we can transform the momentum sum of Eq. (4.30) into the integral form

$$\Gamma_{\mathbf{k}}^{(1,\mathrm{G})} \approx \begin{cases} \frac{U_{12}^2}{2\,\pi}\int_0^\Lambda dq\,q\int_0^{2\pi} d\theta\,|N_{\mathrm{G},\mathbf{q}}|^2\,\delta\left[-\frac{q^2}{2\,M} + \frac{k\,q\cos\left(\theta\right)}{M} - c_s\,q\right] & d = 2\,, \\[2ex] \frac{U_{12}^2}{2\,\pi}\int_0^\Lambda dq\,q^2\int_{-1}^{1} d\cos\left(\theta\right)|N_{\mathrm{G},\mathbf{q}}|^2\,\delta\left[-\frac{q^2}{2\,M} + \frac{k\,q\cos\left(\theta\right)}{M} - c_s\,q\right] & d = 3\,, \end{cases} \tag{4.32}$$

where for illustrative purposes we have considered the cases $d = 2, 3$ (while additional care would be required for $d = 1$) and we have defined $k = |\mathbf{k}|$. Λ is a suitably chosen momentum cut-off which will have no influence on the final result, as the integration of the δ-functions will be shown to fix the allowed values of q. For the sake of clarity, we also stress that $q = 0$ is not enclosed in the integration domain, since it is excluded from the excitation spectrum of the Goldstone mode as usual. In $d = 2$, we can first perform the momentum integral of the δ-function, whose argument vanishes for $q(\theta) = 2\left[k\cos\left(\theta\right) - k_c\right]$, apart from the avoided solution $q = 0$. On the other hand, in $d = 3$, we can start from the angular integral. As a result, we obtain

Semi-analytical prediction for the polaron decay rate

$$\Gamma_{\mathbf{k}}^{(1,\mathrm{G})} \approx \begin{cases} \frac{U_{12}^2\,M}{\pi}\int_0^{2\pi} d\theta\,\left|N_{\mathrm{G},\mathbf{q}(\theta)}\right|^2\,\theta\left[\cos\left(\theta\right) - \frac{k_c}{k}\right] & d = 2\,, \\[2ex] \frac{U_{12}^2\,M}{2\,\pi\,k}\int_0^\Lambda dq\,q\,|N_{\mathrm{G},\mathbf{q}}|^2\,\theta[2\left(k - k_c\right) - q] & d = 3\,. \end{cases} \tag{4.33}$$

Crucially, the theta functions appearing in the integrands above derive from the constraints $q > 0$ (for $d = 2$) and $|\cos\left(\theta\right)| \leq 1$ (for $d = 3$), combined with the identity $\frac{q}{2\,M} - \frac{k\cos\left(\theta\right)}{M} + c_s = 0$ imposed by the δ-functions. In particular, we immediately notice

that, as a consequence of $\cos(\theta) \leq 1$ and $q > 0$, in both cases we must have $k > k_c$ necessarily in order to have a finite result for $\Gamma_{\mathbf{k}}^{(1,\mathrm{G})}$. Thus, we naturally recover the Landau criterion for the impurity velocity. Consequently, Eq. (4.33) yields the final result

$$\Gamma_{\mathbf{k}}^{(1,\mathrm{G})} \approx \theta(k - k_c) \begin{cases} \frac{4\,U_{12}^2\,M\,\gamma}{\pi} \left[\sqrt{k^2 - k_c^2} - k_c \arccos\left(\frac{k_c}{k}\right) \right] & d = 2\,, \\[3mm] \frac{4\,U_{12}^2\,M\,\gamma}{3\,\pi\,k} \left(k - k_c\right)^3 & d = 3\,, \end{cases} \tag{4.34}$$

where we have used the fact that $|N_{\mathrm{G},\mathbf{q}}|^2 \approx \gamma\,q$ in the long-wavelength limit. Since $|N_{G,\mathbf{q}}|^2$ can be identified with the one-mode contribution to the static structure factor of the BH system, we can resort to the use of spectral sum rules [40, 51] to write $\gamma = \kappa\,c_s/2$, where κ is the compressibility of the BH bath [4]. For convenience, we recall here that $\kappa \sim 1/J$ in the HCSF region and $\kappa \sim 1/U$ in the deep SF regime, respectively; moreover, κ is finite on the SF side of the CI transition before jumping *discontinuously* to zero in the MI phase, in stark contrast with the case of the O(2) transition where κ tends smoothly to zero [51].

Importantly, we first observe that our approximation for the decay rate is predicted to be an increasing function of momentum. If the impurity momentum is taken slightly above the Landau threshold and c_s is finite, we have

$$\Gamma_{\mathbf{k}}^{(1,G)} \underset{k \to k_c^+}{\approx} \begin{cases} \frac{4\,U_{12}^2\,\kappa}{3\,\pi} \sqrt{2\,k_c}\,(k - k_c)^{3/2} & d = 2\,, \\[3mm] \frac{2\,U_{12}^2\,\kappa}{3\,\pi} \left(k - k_c\right)^3 & d = 3\,, \end{cases} \tag{4.35}$$

From Eq. (4.35), we deduce that in general $\Gamma_{\mathbf{k}}^{(1,\mathrm{G})} \sim (k - k_c)^{3(d-1)/2}$ for $d > 1$. Interestingly, we note that this behaviour mimics (but does not match) the momentum scaling of the energy dissipated by a heavy impurity in a weakly-interacting BEC on the continuum [229], reading $(k - k_c)^{d-1}$.

Now, we specify that the previous result is valid as long as k is of the same order of (albeit larger than) q. Since also $k - k_c$ has to be a small quantity, we must hence restrict ourselves to the case $k_c \ll 1$. This condition is always satisfied in proximity of the CI transition and in the HCSF regime (where c_s tends to zero), but can be reached also in the deep SF region for a sufficiently small M. More in detail, taking the limit $c_s \to 0$ in Eq. (4.34), we obtain

$$\Gamma_{\mathbf{k}}^{(1,G)} \approx \theta(k - k_c) \begin{cases} \frac{2\,U_{12}^2\,\kappa\,k_c}{\pi}\,k & d = 2\,, \\[3mm] \frac{2\,U_{12}^2\,\kappa\,k_c}{3\,\pi}\,k^2 & d = 3\,, \end{cases} \tag{4.36}$$

which notably recovers the same momentum scaling as on the continuum [229]. It must be noted that, for the choice $M = (2\,J)^{-1}$ adopted in this Chapter, the Landau threshold k_c vanishes identically at the CI critical point (where M remains finite), while in the

---

[4] See also Subsection 2.3.1 of Chapter 2 for a more explicit application of spectral sum rules to deduce the relationship between the static structure factor, the compressibility and the sound velocity in a superfluid state.

HCSF region k_c converges to a finite value $k_c^{\text{HC}} = (n_0 + 1)\sqrt{z\left(\langle\hat{n}\rangle - n_0\right)\left(n_0 + 1 - \langle\hat{n}\rangle\right)}$, where n_0 is the integer filling of the lower MI lobe [5]. Nevertheless, we expect that Eq. (4.36) still provides a good rule of thumb for the decay rate in the HC limit, as we will show in the following.

4.5.2 Analysis of the results

To gain an intuitive but also quantitative insight into the polaron decay, we first resort to its approximate estimation via the single-particle contribution of the Goldstone mode, as detailed in the previous Subsection. The significance of Eqs. (4.34)-(4.35) lies in the fact that both κ and c_s are strongly renormalized by the presence of the lattice: in particular, when $c_s \to 0$ on the brink of the CI critical points and in the strongly-interacting SF regime, the softening of sound excitations provide also slowly-moving polarons ($k \to 0$) with a finite lifetime and increases the number of scattering channels giving a finite contribution to $\Gamma_{\mathbf{k}}$. Also, the non-trivial interplay between κ and c_s [51] allows us to make qualitative predictions on the behaviour of $\Gamma_{\mathbf{k}}$ in those quantum critical limits where the approximation (4.34) holds: on the one hand, approaching the SF side of the CI point, where κ is finite and $k_c \to 0$, we expect $\Gamma_{\mathbf{k}}$ to reach a maximum close to the transition, before dropping to negligible values in the MI phase; on the other hand, in the HC limit where $\kappa \to \infty$ and k_c is finite, $\Gamma_{\mathbf{k}} \propto \kappa$ is expected to diverge. Due to the role of two-particle processes, the case of the $O(2)$ critical point – where both the Goldstone and Higgs modes become gapless – entails instead a completely different picture which has to be investigated numerically.

Our results for $Z_{\mathbf{k}}$ and $\Gamma_{\mathbf{k}}$ at fixed chemical potential are shown in Figure 4.5(a)-(b). As the bath crosses the O(2) transition at fixed $\mu/U = \sqrt{2}-1$, the polaron remains a well-defined object ($Z_{\mathbf{k}} \sim 1, \Gamma_{\mathbf{k}} \ll E_{\mathbf{k}}$) at all momenta. In crossing the CI transition for fixed $\mu/U = 0.8$, both quantities behave sharply, with the non-analyticity shown in the inset of Figure 4.5(b) being analogous to the one of the polaron properties associated with $\text{Re}[\Sigma(\mathbf{k}, \omega)]$ [inset Figure 4.3(b)]. At finite momenta, the polaron coherence and stability are generally weaker, undergoing a mild renormalisation across the O(2) transition while rapidly deteriorating at the CI points approaching the strongly-interacting limit $J/U \to 0$. As commented earlier, in this limit the Goldstone sound velocity c_s tends to vanish, and so does the Landau bound on the impurity momentum $k_c \to 0$: it follows that spontaneous emission of soft modes becomes energetically allowed over a wider range of impurity momenta.

In this regard, we turn now our attention to the the coherence and stability properties of the polaron along lines at fixed density, shown in Figure 4.5(c)-(d). At integer filling, the polaron remains well-defined at all momenta; on the other hand, for non-integer filling, the bath enters the regime of the HCSF, which has been recently predicted to spoil the coherence of static impurities over time [220]. In the same region, it has been also predicted that a mobile impurity is subjected to a quantum Brownian motion due to the essentially free-particle nature of the bath [233]. Indeed, we observe that the polaronic dressing of the impurity becomes so strongly renormalised so as to be orthogonal with the bare impurity state ($Z_{\mathbf{k}} \to 0$), giving rise to a bosonic instance

---

[5] We refer the interested reader to Appendix B.2 for a detailed derivation of the compressibility and sound velocity behaviours in a proximity of the CI critical point and in the HC limit of the BH system within the Gutzwiller approximation.
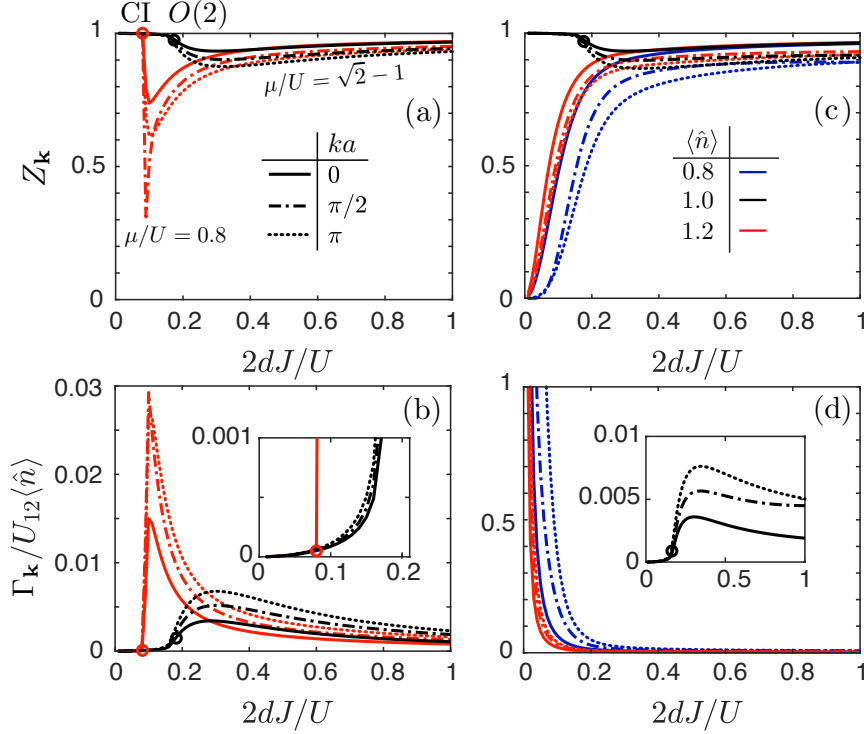
Figure 4.5: Momentum dependence of the quasiparticle residue and decay rate of the polaron for: (a)-(b) fixed μ/U across the O(2) (black) and CI (red) transitions; (c)-(d) fixed $\langle\hat{n}\rangle$ at integer filling (black) across the O(2) transition and non-integer fillings (blue, red), which suffer from an orthogonality catastrophe ($Z_\mathbf{k} \to 0$) in the HC regime. Dots indicate quantum critical points, with the non-analyticity of the decay rate across the CI transition shown in the inset of panel (c).

Orthogonality catastrophe in the hard-core regime

of Anderson's orthogonality catastrophe [234]. We recall that this effect occurs also in the continuum for a mobile impurity immersed in an ideal Bose gas due to the infinite compressibility of the bath and macroscopic polaron cloud that forms [207, 235, 236]. In the HC regime, we find also that $\Gamma_\mathbf{k} \gg E_\mathbf{k}$, signalling the breakdown of the quasiparticle description within the Rayleigh-Schrödinger scheme. This coincides with the eventual acquisition of negative values of E_0 in Figure 4.3(c) signalling also a fall in the assumption that the back action of the impurity on the bath can be neglected, as the environment becomes unstable to the presence of the impurity due to the diverging compressibility.

For the sake of clarity, we note that our numerical predictions for $\Gamma_\mathbf{k}$ never vanish for $\mathbf{k} = \mathbf{0}$, apparently contradicting Eq. (4.5) and the following discussion. This spurious effect has to be mainly attributed to the difficulty of numerically resolving the energy balance of the scattering processes that contribute to $\Gamma_\mathbf{k}$ on a lattice, a task which is affected by the intrinsic uncertainty of any δ-function representation. However, we have chosen to report our numerical results as they still grasp the expected qualitative features of the polaron decay rate, ranging from its dependence on momentum to its enhancement in proximity of the CI critical points and inside the HCSF regime, in accordance with the behaviour of $Z_\mathbf{k}$ in the same regions. Also, we point out that the numerical results for $\mathbf{k} \neq \mathbf{0}$ are well-converged for $\Gamma_\mathbf{k} \gtrsim \eta$ where $\eta \sim 1/V$ is the width of the chosen δ-function resolution.

4.6 Looking to new experimental scopes: landscape of the polaron cloud

The polaron spectral features are not the only properties that can be experimentally accessed in modern apparatuses for quantum simulations. Indeed, a number of questions posed by the community revolve around the real-space profile of the polaron, in terms of both the number of physical particles occupying the surrounding cloud of virtual excitations and effective quantum correlations between the impurity and the bath. It is important to underline that this investigation has the more general goal of understanding how the polaron dressing cloud builds up and how correlations are mediated by the collective modes, with relevant consequences on the many-body physics of polaronic matter (bipolarons). The spectroscopic tools mentioned earlier cannot be exploited to track the formation of quasiparticles and monitor the structure of the polaron cloud. Conversely, dynamical probes such as many-body Ramsey interferometry [237–239] and the use of coherent Rabi oscillations [240, 241] (although the extension to the bosonic medium is currently lacking) are well suited to this purpose, besides providing useful information on the quasiparticle residue [241, 242]. Moreover, the advent of quantum gas microscopy makes the observation of the internal structure of polaronic quasiparticles practically feasible, having successful applications to the case of magnetic impurities [145, 243].

In the following, we will give a quantitative account of the polaron cloud features by resorting to the Chevy ansatz

Chevy's ansatz for the polaron wave function

$$|\Psi(\mathbf{k})\rangle = \frac{1}{\sqrt{\Omega_{\mathbf{k}}}} \left(|\mathbf{k}\rangle |\Omega\rangle + \frac{U_{12}}{\sqrt{V}} \sum_{\alpha} \sum_{\mathbf{q}} \frac{N^*_{\alpha,-\mathbf{q}}}{e_{\mathbf{k}} - e_{\mathbf{k+q}} - \omega_{\alpha,-\mathbf{q}}} |\mathbf{k+q}\rangle |\alpha,-\mathbf{q}\rangle \right. \quad (4.37)$$

$$\left. + \frac{U_{12}}{V} \sum_{\alpha,\beta} \sum_{\mathbf{p,q}} \frac{W^*_{\alpha,\beta|\mathbf{p},-\mathbf{p}-\mathbf{q}}}{e_{\mathbf{k}} - e_{\mathbf{k+q}} - \omega_{\alpha,\mathbf{p}} - \omega_{\beta,-\mathbf{p}-\mathbf{q}}} |\mathbf{k+q}\rangle |\alpha,\mathbf{p}\,;\,\beta,-\mathbf{p}-\mathbf{q}\rangle \right)$$

for the polaron wave function for a given impurity momentum $\mathbf{k}$, which simply amounts to calculating the impurity state up to lowest-order perturbation theory in the QGA representation of the impurity-bath interaction (4.6). Here, $|\mathbf{k}\rangle$ denotes the bare impurity state, $|\alpha,\mathbf{q}\rangle$ and $|\alpha,\mathbf{q}\rangle$ are single- and two-particle states of the bath respectively and

$$\Omega_{\mathbf{k}} = 1 + \frac{U_{12}^2}{V} \left[\sum_{\alpha} \sum_{\mathbf{q}} \frac{|N_{\alpha,\mathbf{q}}|^2}{(e_{\mathbf{k}} - e_{\mathbf{k+q}} - \omega_{\alpha,\mathbf{q}})^2} \right.$$

$$\left. + \frac{1}{2V} \sum_{\alpha,\beta} \sum_{\mathbf{p,q}} \frac{\left|W_{\alpha,\beta|\mathbf{p},\mathbf{p}+\mathbf{q}} + W_{\beta,\alpha|\mathbf{p}+\mathbf{q},\mathbf{p}}\right|^2}{(e_{\mathbf{k}} - e_{\mathbf{k+q}} - \omega_{\alpha,\mathbf{p}} - \omega_{\beta,\mathbf{p}+\mathbf{q}})^2} \right] = Z_{\mathbf{k}}^{-1} \quad (4.38)$$

is the wave function normalisation factor and coincides the inverse quasiparticle residue of the polaron. Heuristic ansätze of the form have been proved to provide a remarkably reliable description of polaron physics in both bosonic and fermionic baths, embracing both certain strong-coupling regimes and a large class of beyond-Fröhlich fluctuations.
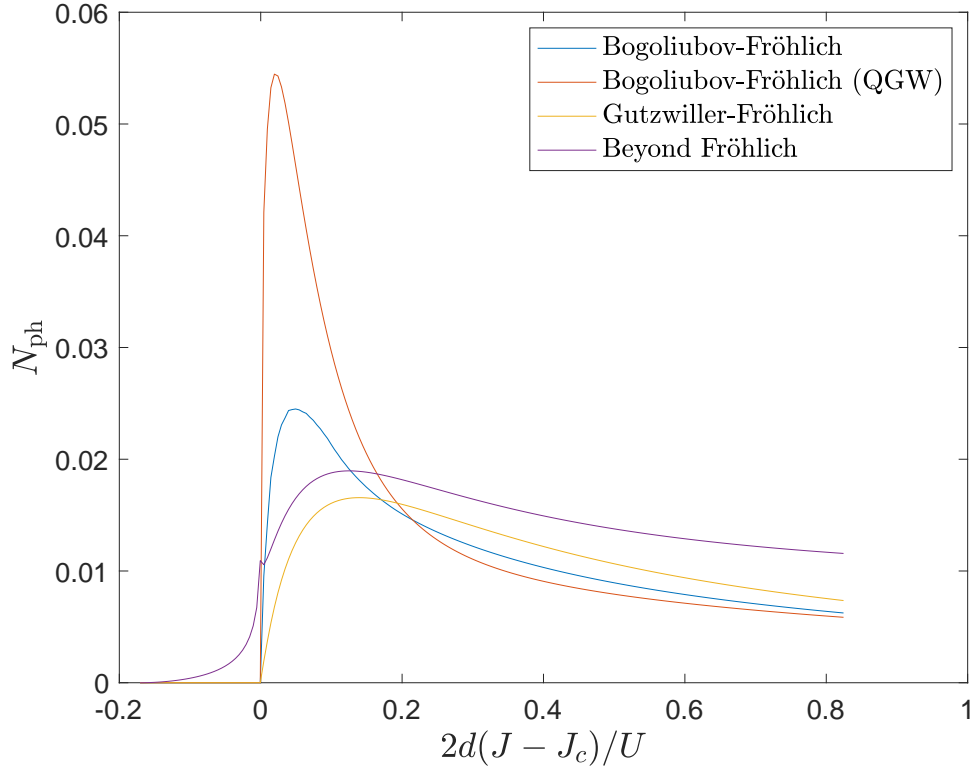
Figure 4.6: Average number of excitations of the BH bath forming the cloud of a polaron with momentum $\mathbf{k} = \mathbf{0}$ across the O(2) transition at fixed unit filling $\langle \hat{n} \rangle = 1$. Here, $2\, d\, J_c/U = \left(\sqrt{2} - 1\right)^2 \approx 0.172$ is the critical hopping energy at the tip of the $\langle \hat{n} \rangle = 1$ MI lobe. The results of the beyond-Fröhlich QGA model (purple) are compared to those of the Gutzwiller-Frölich model (yellow) and the Frölich theory within the Gutzwiller (red) and Bogoliubov (blue) approximations.

4.6.1 Number of bath excitations in the polaron cloud

The number of proper bath excitations can be estimated by introducing the total density operator of collective modes as

$$\hat{N}_{\text{ph}} \equiv \sum_{\alpha} \sum_{\mathbf{q}} \hat{b}_{\alpha,\mathbf{q}}^{\dagger}\, \hat{b}_{\alpha,\mathbf{q}} \,. \tag{4.39}$$

The expectation value of this operator over the Chevy ansatz (4.37) yields the average number of bath excitations contained in a polaron with momentum $\mathbf{k}$, namely

$$
\begin{aligned}
N_{\text{ph}}(\mathbf{k}) &\equiv \langle \Psi(\mathbf{k}) | \, \hat{n}_b \, | \Psi(\mathbf{k}) \rangle \\
&= \frac{1}{\Omega_{\mathbf{k}}} \frac{U_{12}^2}{V} \left[\sum_{\alpha} \sum_{\mathbf{q}} \frac{|N_{\alpha,\mathbf{q}}|^2}{\left(e_{\mathbf{k}} - e_{\mathbf{k}+\mathbf{q}} - \omega_{\alpha,\mathbf{q}} \right)^2} \right. \\
&\quad \left. + \frac{1}{V} \sum_{\alpha,\beta} \sum_{\mathbf{p},\mathbf{q}} \frac{\left| W_{\alpha,\beta|\mathbf{p},\mathbf{p}+\mathbf{q}} + W_{\beta,\alpha|\mathbf{p}+\mathbf{q},\mathbf{p}} \right|^2}{\left(e_{\mathbf{k}} - e_{\mathbf{k}+\mathbf{q}} - \omega_{\alpha,\mathbf{p}} - \omega_{\beta,\mathbf{p}+\mathbf{q}} \right)^2} \right] \,.
\end{aligned}
\tag{4.40}
$$

It is worth noting that, indicating the one- and two-particle contributions to the (inverse) quasiparticle residue (4.38) as $\delta Z_{n,\mathbf{k}}^{-1}$ with $n = 1$ and 2 respectively, we can rewrite

$n_{\rm ph}(\mathbf{k})$ in the form

$$N_{\rm ph}(\mathbf{k}) = Z_{\mathbf{k}} \sum_n n \, \delta Z_{n,\mathbf{k}}^{-1} \, . \tag{4.41}$$

The above alternative expression allows us to make analytical guesses on the behaviour of $N_{\rm ph}(\mathbf{k})$ in connection with special limiting values of the quasiparticle residue. The simplest example is represented by MI phase, where we obtain

$$N_{\rm ph}^{\rm MI}(\mathbf{k}) = 2 \left[1 + \delta Z_{2,\mathbf{k}}^{-1} \right]^{-1} \delta Z_{2,\mathbf{k}}^{-1} \sim (J/U)^2 \, , \tag{4.42}$$

a result confirming the expectation that only a small number of doublon-holon pairs occupy the polaron cloud on average. The other physical situation that we can grasp exactly is the HCSF regime, where $\delta Z_{1,\mathbf{k}}^{-1} \to \infty$ is the dominant contribution so as to give a vanishing quasiparticle residue and the orthogonality catastrophe. In this case, we readily obtain

$$N_{\rm ph}^{\rm HCSF}(\mathbf{k}) \approx \left[1 + \delta Z_{1,\mathbf{k}}^{-1} \right]^{-1} \delta Z_{1,\mathbf{k}}^{-1} \to 1 \, . \tag{4.43}$$

Interestingly, this result does *not* indicate that only one physical particle of the bath participates in the polaron formation, but rather that a single Goldstone mode couples to the impurity. In the next Subsection, we will show that such a long-range excitation entails an infinite number of physical particles, making the polaron cloud extending over the whole lattice and hindering the formation of a quasiparticle.

In Figure 4.6, we illustrate the behaviour of $N_{\rm ph}(\mathbf{k} = \mathbf{0})$ for a uniformly delocalised polaron across the O(2) transition of the BH bath at fixed unit filling $\langle \hat{n} \rangle = 1$. The prediction of our beyond-Frölich model [purple line] echoes the result for the quasiparticle weight $Z_{\mathbf{k}=\mathbf{0}}$ in Figure 4.5(b), to which $N_{\rm ph}(\mathbf{k} = \mathbf{0})$ is loosely related: in particular, the number of excitations forming the polaron cloud tends smoothly to zero in both the deep SF and MI limits, with a long-tailed decrease in the former case. The absolute maximum of $N_{\rm ph}(\mathbf{k} = \mathbf{0})$ is located in the strongly-correlated SF region close to the critical point $J = J_c$, where two-particle processes of the collective modes start to matter, connecting with the behaviour in the MI phase. Focusing our attention on the critical SF regime, it is worth noticing how the QGA result compares with the ones of Fröhlich models. On the one hand, the Gutzwiller-Fröhlich theory [yellow line] follows the same qualitative behaviour of the QGA predictions, but fails to account for the contribution of two-mode excitations of the bath; on the other hand, the Bogoliubov models (hinging on the coupling between the impurity and the condensate channel) [red and blue lines] overestimate the weight of quantum fluctuations in the polaron cloud, similarly to the case of the effective mass addressed in Subsection 4.4.2.

4.6.2 How many particles is the polaron made of?

Following the arguments of [192, 244], the number of bath particles contained in the impurity dressing cloud can be defined as the number of particles that must be added to the medium in order to keep its chemical potential (i.e., the medium density far away from the impurity) fixed when the impurity is injected into the system. In particular, this quantity can be proved to be given by

$$\Delta N = -\frac{\partial E_0}{\partial \mu} \tag{4.44}$$

at zero temperature. In what follows, we also consider a different estimation strategy for the number of "excess particles" in the bath due to the presence of the impurity, based on the Chevy ansatz (4.37), which remarkably agrees exactly with the result of Eq. (4.44) to lowest order in the coupling U_{12} and well approximates higher-order contributions.

We define the number of particles forming the polaron cloud by means of the variation of the bath density with respect to the BH ground state decoupled from the impurity, namely

$$\Delta N(\mathbf{k}) = V\left[\langle\Psi(\mathbf{k})|\,\hat{n}(\mathbf{r})\,|\Psi(\mathbf{k})\rangle - \langle\hat{n}(\mathbf{r})\rangle_0\right], \tag{4.45}$$

where the factor V takes care of the fact that the number of bath particles depleted or attracted by the impurity is of order $\mathrm{O}(V^{-1})$. Moreover, the spatial dependence of $\Delta N(\mathbf{k})$ has been ignored because of the translational invariance of the system, being the impurity momentum a good quantum number in the present context.

For consistency, we perform the calculation of $\Delta N(\mathbf{k};\mathbf{r})$ by expanding the bath density operator in order to include two-particle processes involved in the beyond-Fröhlich coupling with the impurity, $\hat{n}(\mathbf{r}) \to \hat{N}(\mathbf{r}) \approx n_0 + \delta_1\hat{n}(\mathbf{r}) + \delta_2\hat{n}(\mathbf{r})$. It turns out that the only non-vanishing contributions to $\Delta N(\mathbf{k})$ are those deriving from the coupling between different n-particle sectors of the Chevy wave function mediated by fluctuations in the bath operator $\hat{n}(\mathbf{r})$. In particular, up to quadratic order in U_{12} we have

$$\Delta N(\mathbf{k}) = -U_{12}\,\kappa + \frac{U_{12}^2}{V}\left[\sum_{\alpha,\beta}\sum_{\mathbf{q}}\frac{N_{\alpha,\mathbf{q}}^*\,N_{\beta,\mathbf{q}}\left(U_{\beta,\mathbf{q}|\alpha,\mathbf{q}} + V_{\beta,\mathbf{q}|\alpha,\mathbf{q}}\right)}{(e_\mathbf{k} - e_{\mathbf{k+q}} - \omega_{\alpha,\mathbf{q}})\,(e_\mathbf{k} - e_{\mathbf{k+q}} - \omega_{\beta,\mathbf{q}})} \right. \tag{4.46}$$

$$\left. + \frac{1}{V}\sum_{\alpha,\beta,\gamma}\sum_{\mathbf{p},\mathbf{q}}\frac{\left(W_{\alpha,\mathbf{p}|\beta,\mathbf{p+q}}^* + W_{\beta,\mathbf{p+q}|\beta,\mathbf{p}}^*\right)\left(W_{\gamma,\mathbf{p}|\beta,\mathbf{p+q}} + W_{\beta,\mathbf{p+q}|\gamma,\mathbf{p}}\right)\left(U_{\gamma,\mathbf{p}|\alpha,\mathbf{p}} + V_{\gamma,\mathbf{p}|\alpha,\mathbf{p}}\right)}{(e_\mathbf{k} - e_{\mathbf{k+q}} - \omega_{\alpha,\mathbf{p}} - \omega_{\beta,\mathbf{p+q}})\,(e_\mathbf{k} - e_{\mathbf{k+q}} - \omega_{\gamma,\mathbf{p}} - \omega_{\beta,\mathbf{p+q}})}\right],$$

where κ is the QGA prediction for the compressibility of the BH system, that is:

$$\kappa = 2\lim_{\mathbf{k}\to\mathbf{0}}\sum_\alpha\frac{|N_{\alpha,\mathbf{k}}|^2}{\omega_{\alpha,\mathbf{k}}} + \frac{1}{V}\sum_{\alpha,\beta}\sum_\mathbf{k}\frac{\left|W_{\alpha,\mathbf{k}|\beta,\mathbf{k}} + W_{\beta,\mathbf{k}|\alpha,\mathbf{k}}\right|^2}{\omega_{\alpha,\mathbf{k}} + \omega_{\beta,\mathbf{k}}}. \tag{4.47}$$

It is worth pointing out that the result of Eq. (4.46) coincides exactly with the outcome of diagrammatic perturbation theory at the Hartree-Fock level.

Interestingly, the compressibility term of $\Delta N(\mathbf{k})$, quantifying to which extent the bath is prone to density perturbations, depends on the sign of U_{12} and provides the mean-field result $\Delta N_{MF} = -U_{12}/U$ in the weakly-interacting limit of the BH environment. Moreover, recalling the leading order term to the polaron energy $E_0 \approx U_{12}\langle\hat{n}\rangle$, we observe that the thermodynamic definition of the number of dressing particles yields $\Delta N = -U_{12}\,\partial\langle\hat{n}\rangle/\partial\mu = -U_{12}\,\kappa$, which coincides with our result to lowest order in perturbation theory. The remaining, sub-leading contributions represent a sizeable effect of fluctuations in the critical SF phase and in the MI regime, as they strictly depend on two-particle processes of the collective modes. In this regard, we notice that $\Delta N(\mathbf{k})$ depends explicitly on the vertices $U_{\gamma,\alpha|\mathbf{k},\mathbf{k}} + V_{\gamma,\alpha|\mathbf{k},\mathbf{k}}$, which instead do not play any role in the other polaron observables at zero temperature: this suggests that the presence of the impurity leads to the creation of *thermal-like* excitations which participate in the excess number of particles but *not* in the number of excitations in the
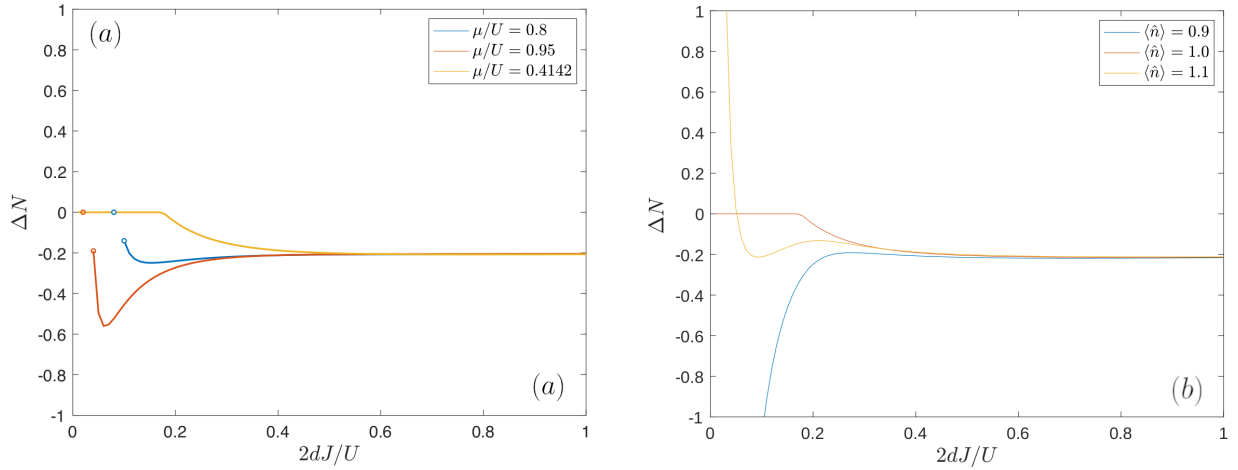
Figure 4.7: Plots of the number of physical particles forming the polaron cloud for an impurity with momentum $\mathbf{k} = \mathbf{0}$, calculated as the number of excess particles in the bath due to the presence of the impurity, see Eq. (4.45). (a) $\Delta N \equiv \Delta N(\mathbf{k} = \mathbf{0})$ along constant-μ/U lines crossing the BH phase transitions of the $\langle \hat{n} \rangle = 1$ MI lobe. (b) The same quantity plotted along constant-density lines approaching the O(2) critical point [red] and the upper (lower) hard-core point of the SF phase with respect to the $\langle \hat{n} \rangle = 1$ MI lobe [yellow (blue)].

polaron cloud.

Our results for $\Delta N \equiv \Delta N(\mathbf{k})$ in the representative case $\mathbf{k} = \mathbf{0}$ are shown in Figure 4.7. In panel (a), we illustrate how the number of excess particles changes upon crossing the MI-to-SF transition at fixed chemical potential. In the deep SF regime, all curves agree in giving the mean-field value $\Delta N(\mathbf{k} = \mathbf{0}) \approx -U_{12}\kappa \approx -U_{12}/U = 0.2$, due to the fact that the compressibility converges to U^{-1} in that limit. Decreasing the hopping energy, we find that the behaviour of ΔN is an even sharper signature of the type of approached critical point as compared to the polaron energy E_0 and effective mass M/M^* in Figure 4.3.

We first notice that ΔN is negative everywhere in the SF region along the chosen horizontal cuts of the phase diagram, suggesting that the polaron consists of a cloud of holes around the impurity as a consequence of the repulsive interaction with the bath. The O(2) critical point is crossed by the line at constant $\mu/U = \sqrt{2} - 1 \approx 0.4142$: here, we observe a smooth vanishing of ΔN, which then remain zero in the whole MI phase. This fact can be readily explained in terms of the zero-temperature excitations of the incompressible MI state: these are non-local pairs of doublon-holon excitations, which therefore do not give a net contribution to ΔN. The situation on the SF side of the transition is substantially different when crossing the CI critical points [red and blue lines]: remarkably, ΔN undergoes a finite jump to zero exactly at the transition, which therefore has the characteristics of a first-order criticality as seen from the polaron dressing cloud. Importantly, this behaviour is mirrored by the discontinuous profile of κ when doping the MI state to cross the CI transition (see Appendix B.2). Last but not least, we point out that ΔN reaches an absolute minimum in the SF regime close to the CI critical point, whose height increases as μ/U nears the hard-core points of the system, corresponding to $\mu/U = 1$ in Figure 4.7(a).

The behaviour of ΔN in the HCSF regime is the subject of panel (b) of Figure 4.7, which illustrates how the trend obtained by fixing the density to a non-integer value [yellow and blue lines] distances itself from the behaviour at constant unit filling [red
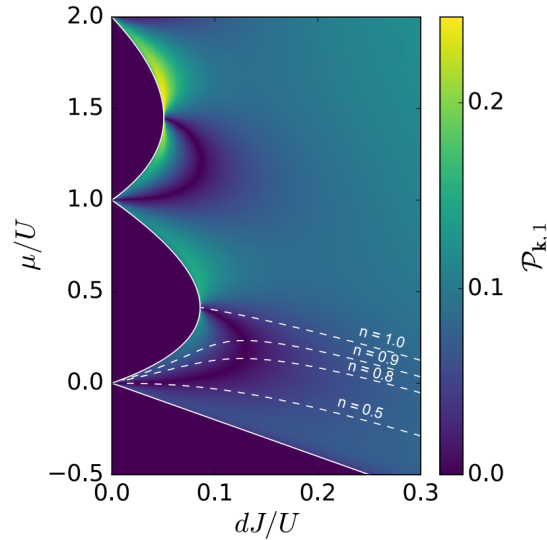
Figure 4.8: Colour plot of the spectral amplitude $\mathcal{P}_{\mathbf{k},1} \equiv |U_{\mathrm{Gol},\mathbf{k}} + V_{\mathrm{Gol},\mathbf{k}}|$ of the Goldstone mode for $\mathbf{k} \to \mathbf{0}$ in the strongly-interacting regime of the BH model. Constant density contours are shown as dashed white lines. The dark purple arcs along which $\mathcal{P}_{\mathbf{k},1} = 0$ are due to the PHS condition $U_{\mathrm{Gol},\mathbf{k}} = -V_{\mathrm{Gol},\mathbf{k}}$. The areas below the MI lobes enclosed by the arcs correspond to the regimes of hole superfluidity.

line] crossing the O(2) critical point. The former curves show that, upon approaching of the orthogonality catastrophe in the strongly-interacting SF region, ΔN reaches increasingly large values and eventually diverges at the hard-core point $J/U \to 0$, acting as a further unambiguous marker of the collapse of the polaron quasiparticle. Even more interestingly, we notice that the low-J sign ΔN strictly depends on whether, indicating as n_0 the Mott filling closest to $\langle \hat{n} \rangle$, we have $n_0 < \langle \hat{n} \rangle < n_0 + 1/2$ ($\Delta N > 0$) or $n_0 - 1/2 < \langle \hat{n} \rangle < n_0$ ($\Delta N < 0$). Specifically, the numerical results reported in Figure 4.7(b) refer to the case $n_0 = 1$. In other words, the impurity behaves as an accumulator of either particles or holes depending on the density of the strongly-correlated SF phase sitting on top of the MI state.

The relevance of this result lies in the fact that the very same density ranges of the HCSF state have been recently shown to correspond to regimes of *particle* and *hole superfluidity*, respectively [52]. Physically speaking, this means that the sign of the doping $\Delta_n = \langle \hat{n} \rangle - n_0$ with respect to the MI filling determines the particle/hole nature of the superfluidity carriers in a strongly-interacting BH system [43, 245, 246]. Hence, hole superfluidity appears to be a subtle manifestation of Mottness; indeed, in the BH phase diagram the particle-to-hole SF crossover runs along arc-shaped contours connecting the tips of the MI lobes to the lower hard-core points, which are solely determined by the PHS of the Goldstone excitation at low momenta [see Figure 4.8].

Probing superfluidity via the polaron cloud

Now, while particle superfluidity is a common feature of weakly-interacting condensates, the emergence of hole superfluidity is tied to the presence of a lattice in the form of strong local correlations and is believed to play a crucial role in the physics of high-temperature superconductors [247–249]. Yet, this appears also to be a challenging property to detect experimentally, at least to the same extent as other elusive properties as the superfluid drag, since it requires advanced techniques, as e.g. two-pulse Bragg spectroscopy [250, 251] and ARPES-like methods [252–254], which give access to the one-particle Green's function of the system. We thus hypothesise that ΔN could serve as a simpler, first-hand probe of the type of excitations involved in the superfluid

transport in order to pinpoint the location particle/hole superfluid transition. In this respect, a more in-depth analysis could include a systematic study of the relationship between the change in sign of ΔN and the hole superfluidity boundaries identified in Figure 4.8, which we leave as an open question for future studies.

4.6.3 Quantum correlations between the polaron and the bath

We introduce the impurity-bath density correlation function as given by

$$g_{\mathrm{IB}}(\mathbf{k};\mathbf{r}) = V\left[\langle \hat{n}(\mathbf{r})\,\hat{n}_{\mathrm{I}}(\mathbf{0})\rangle_{\mathbf{k}} - \langle \hat{n}(\mathbf{r})\rangle_{\mathbf{k}}\,\langle \hat{n}_{\mathrm{I}}(\mathbf{0})\rangle_{\mathbf{k}}\right] = V\,\langle \hat{n}(\mathbf{r})\,\hat{n}_{\mathrm{I}}(\mathbf{0})\rangle_{\mathbf{k}} - \langle \hat{n}(\mathbf{r})\rangle_{\mathbf{k}}\ , \quad (4.48)$$

where $\langle\cdot\rangle_{\mathbf{k}}$ is a shorthand for the notation $\langle\Psi(\mathbf{k})|\cdot|\Psi(\mathbf{k})\rangle$ and the factor V rescales the final result so as to offset the infinitesimal value of the impurity density $\langle \hat{n}_{\mathrm{I}}(\mathbf{0})\rangle = 1/V$. Here, we define the impurity density operator as

$$\hat{n}_{\mathrm{I}}(\mathbf{r}) = \frac{1}{V}\sum_{\mathbf{k},\mathbf{p}} e^{-i(\mathbf{k}-\mathbf{p})\mathbf{r}}\,\hat{c}_{\mathbf{k}}^{\dagger}\,\hat{c}_{\mathbf{p}}\ . \qquad (4.49)$$

Expanding again the bath density operator $\hat{n}_{B}(\mathbf{r})$ up to second order in the fluctuations, we obtain

$$
\begin{aligned}
g_{\mathrm{IB}}(\mathbf{k};\mathbf{r}) = \frac{1}{\Omega_{\mathbf{k}}}\frac{U_{12}}{V}\Bigg[&2\sum_{\alpha}\sum_{\mathbf{q}} \frac{|N_{\alpha,\mathbf{q}}|^{2}}{e_{\mathbf{k}} - e_{\mathbf{k}+\mathbf{q}} - \omega_{\alpha,\mathbf{q}}}\cos(\mathbf{q}\cdot\mathbf{r}) \\
&+ \frac{1}{V}\sum_{\alpha,\beta}\sum_{\mathbf{p},\mathbf{q}} \frac{\left|W_{\alpha,\mathbf{p}|\beta,\mathbf{p}+\mathbf{q}} + W_{\beta,\mathbf{p}+\mathbf{q}|\alpha,\mathbf{p}}\right|^{2}}{e_{\mathbf{k}} - e_{\mathbf{k}+\mathbf{q}} - \omega_{\alpha,\mathbf{p}} - \omega_{\beta,\mathbf{p}+\mathbf{q}}}\cos(\mathbf{q}\cdot\mathbf{r})\Bigg]\ ,
\end{aligned}
\qquad (4.50)
$$

where we have truncated the expression to first order in U_{12} for simplicity. In fact, under our weak-coupling hypothesis, we expect the net effect of the presence of the impurity to be either the bunching $[g_{\mathrm{IB}}(\mathbf{k};\mathbf{r}) > 0]$ or the antibunching $[g_{\mathrm{IB}}(\mathbf{p};\mathbf{r}) < 0]$ depending in the first place on the sign of U_{12}. However, the sign of $g_{\mathrm{IB}}(\mathbf{p};\mathbf{r})$ could also exhibit a non-trivial dependence on the impurity momentum $\mathbf{k}$, which determines the number of bath excitations scattering with the impurity.

Notably, we observe that $g_{IB}(\mathbf{p};\mathbf{r})$ can be calculated through the following convolution integral

$$g_{IB}(\mathbf{k};\mathbf{r}) = \frac{2\,U_{12}}{V}Z_{\mathbf{k}}\sum_{\mathbf{q}}\int d\varepsilon\, S_{n}(\mathbf{q},\varepsilon)\,\mathrm{Re}\Big[G_{0}\Big(\mathbf{k}+\mathbf{q},e_{\mathbf{k}}-\varepsilon+i\,0^{+}\Big)\Big]\cos(\mathbf{q}\cdot\mathbf{r}) \qquad (4.51)$$

up to first order in U_{12}, where we have directly used the identity $\Omega_{\mathbf{k}}^{-1} = Z_{\mathbf{k}}$. Furthermore, comparing the expression of $g_{IB}(\mathbf{k};\mathbf{r})$ with the impurity self-energy in Eq. (4.10), we obtain the suggestive identity

$$g_{IB}(\mathbf{k};\mathbf{0}) = \frac{2\,Z_{\mathbf{k}}}{U_{12}}\left[\mathrm{Re}\Big[\Sigma\Big(\mathbf{k},e_{\mathbf{k}}+i\,0^{+}\Big)\Big] - \langle \hat{n}_{B}\rangle\,U_{12}\right]\ , \qquad (4.52)$$

meaning that local impurity-bath correlations are given by the on-shell values of the impurity self-energy in the perturbative regime. Now, reminding that the impurity

energy is given by $E_0 = \text{Re}\big[\Sigma(\mathbf{0}, i\,0^+)\big]$, we find

$$E_0 = (U_{12}/2)\left[Z_{\mathbf{0}}^{-1}\, g_{IB}(\mathbf{0};\mathbf{0}) + 2\,\langle \hat{n}_B \rangle \right]. \tag{4.53}$$

Then, if the polaron is energetically stable ($E_0 > 0$) and $U_{12} > 0$, we deduce that $Z_{\mathbf{0}}^{-1}\, g_{IB}(\mathbf{0};\mathbf{0}) > -2\,\langle \hat{n}_B \rangle$ necessarily. At the same time, since $E_0 \leq \langle \hat{n}_B \rangle\, U_{12}$, we obtain $g_{IB}(\mathbf{0};\mathbf{0}) < 0$. Overall, we conclude that local and uniform impurity-bath correlations are bounded by the quasiparticle weight of the polaron according to $-2\,\langle \hat{n}_B \rangle\, Z_{\mathbf{0}} < g_{IB}(\mathbf{0};\mathbf{0}) \leq 0$. Physically, the negativity of $g_{IB}(\mathbf{0};\mathbf{0})$ reflects the anti-bunching fluctuations due to the repulsive impurity-bath interaction. For instance, in the deep SF and MI regimes, we predict vanishing correlations $g_{IB}(\mathbf{0};\mathbf{0}) \to 0$, as $Z_{\mathbf{0}} \to 1$ and $E_0 \to \langle \hat{n}_B \rangle\, U_{12}$ in those limits. On the other hand, in the HCSF regime, where $Z_{\mathbf{0}} \to 0$ and $E_0 \to -\infty$, $g_{IB}(\mathbf{0};\mathbf{0})$ must be a negative number, presumably diverging to $-\infty$ and thus indicating a dynamical instability of the system.

An exhaustive overview of the QGA results for $g_{IB}(\mathbf{k} = \mathbf{0};\mathbf{r})$ in the case of a uniformly delocalised polaron is shown in Figure 4.9, where we make again a distinction between fixing the chemical potential [first row] and fixing the BH bath density [second row] as different ways to reach the strongly-interacting regimes of the system. By and large, we obtain that $g_{IB}(\mathbf{k} = \mathbf{0};\mathbf{r})$ is always an exponentially decaying function of the lattice distance, whose features (like the antibunching factor and the correlation length) are however highly sensitive to the bath correlations.

When reaching the O(2) transition at constant chemical potential $\mu/U \approx 0.4142$ [see Figure 4.9(a)], the decrease of the hopping energy J/U has the effect of quenching impurity-bath correlations. In addition, we notice that, close to the critical point $2\,d\,J_c/U \approx 0.172$, non-local correlations $g_{IB}(\mathbf{k} = \mathbf{0};\mathbf{r} \neq \mathbf{0})$ change sign, signalling the existence of critical bunching correlations between the impurity and the surrounding bath particles. The same feature survives the quantum phase transition for $J < J_c$: here, $g_{IB}(\mathbf{k} = \mathbf{0};\mathbf{r})$ dies out quickly as the deep MI regime is approached. It is interesting to compare this result with the behaviour of ΔN [see Figure 4.7(a)]: notably, although doublon-holon pairs excited by the impurity in the MI phase do not participate in the number of particles forming the polaron, they still influence the shape of the polaron cloud.

Our results suggest that the previous non-local features of $g_{IB}(\mathbf{k} = \mathbf{0};\mathbf{r})$ are related to the strong interplay between the Goldstone-Higgs modes on one side and doublon-holon modes on the other side of the tip of the MI lobe: in fact, these become barely visible as the chemical potential is either lowered or increased with respect to the O(2) critical point, as show in Figure 4.9(b). However, in contrast with the case of panel (a), we observe that the values of $g_{IB}(\mathbf{k} = \mathbf{0};\mathbf{r})$ follow an evident non-monotonic behaviour when moving from the SF to the MI phases across the CI critical point [panel (b)], in which the critical point is located at $2\,d\,J_c/U \approx 0.024$. As anticipated in the theoretical discussion above, this behaviour is nothing but a consequence of the small quasiparticle weight of the polaron close to the CI transition, which indeed is quite close to the HCSF regime for the $\mu/U = 0.95$ under consideration.

This latter case is explored in more detail in panels (c)-(d) for fixed $\langle \hat{n} \rangle = 0.9$ and $\langle \hat{n} \rangle = 1.1$ respectively, in parallel with the calculation of ΔN. Here, we notice that the impurity-bath correlation function, after a first flattening with decreasing J/U, lowers again towards increasingly negative values below the hopping threshold $2\,d\,J/U \approx 0.2$.
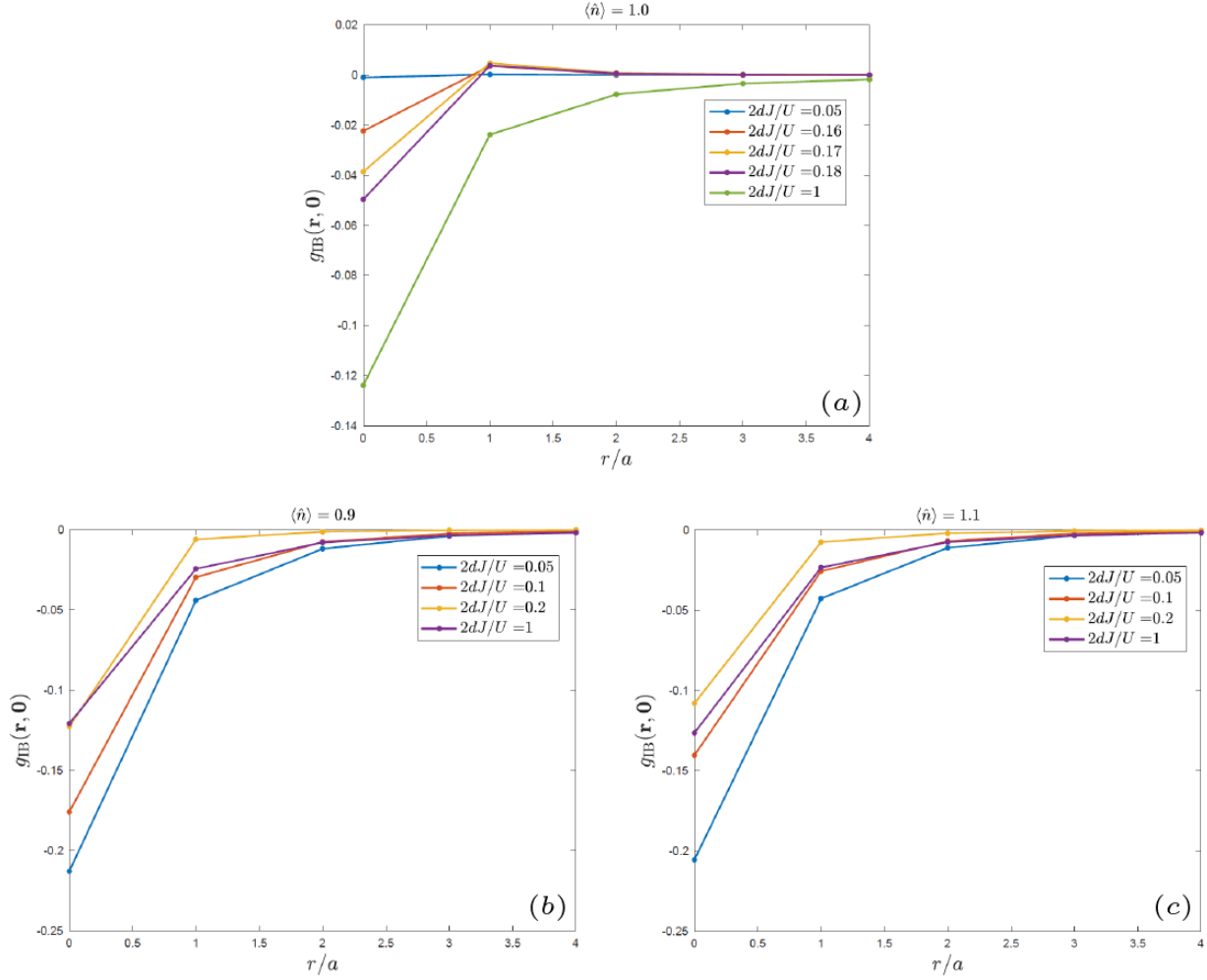
Figure 4.9: Impurity-bath density correlation function $g_{IB}(\mathbf{k} = \mathbf{0}; \mathbf{r})$ calculated at constant chemical potential [first row] and by fixing the lattice filling of the BH bath [second row] for different values of $2\,d\,J/U$ in the strongly-correlated regime. The lattice distance $\mathbf{r}$ has been taken along the x-directed links of a 2D square lattice.

Clearly, this energy scale marks the point where Mott physics have a prominent role on quantum correlations and the onset of the HCSF regime. Reducing further the hopping energy J/U, the antibunching of $g_{IB}(\mathbf{k} = \mathbf{0}; \mathbf{r})$ becomes larger and larger, and is eventually expected to diverge in the exact hard-core limit $J/U \to 0$. At the same time, we observe that the impurity-bath correlation length increases accordingly, compatibly with the result that the polaron cloud starts accommodating a macroscopic number of bath particles ΔN, see again panel (b) of Figure 4.7. Nonetheless, we notice that the increasing negativity of $g_{IB}(\mathbf{k} = \mathbf{0}; \mathbf{r})$ for $\langle \hat{n} \rangle = 1.1$ contrasts with the diverging, positive value of ΔN for the same density: in fact, the latter result could be also understood in terms of the onset of an effective *attractive* coupling between the impurity and the bath components, which would lead in principle to $g_{IB}(\mathbf{k} = \mathbf{0}; \mathbf{r}) > 0$ (bunching effect). We believe that this discrepancy is due to the truncation of result (4.50) to lowest order in the bare coupling U_{12} and that the inclusion of all the second-order terms would correctly account for the attractive effect of quantum fluctuations embodied by ΔN.

For the sake of clarity, we conclude our discussion by underscoring that the previous results should not be read as a faithful description of the polaron in the HCSF regime,

as the breakdown of the quasiparticle picture in that limit is a good indication of the fact that richer physics could emerge from more refined theoretical methods or, staying on simpler grounds, even from a resummation of the self-energy diagrams. On the other hand, the singular behaviours of $\Delta N(\mathbf{k})$ and $g_{\mathrm{IB}}(\mathbf{k}; \mathbf{0})$ can still be seen as indices of structural changes in the excitation spectrum of the bath.

4.7 Future developments

By blending standard diagrammatic techniques with the QGA theory, we have presented a beyond-Fröhlich study of the physics of a mobile impurity embedded in a BH bath throughout the entire phase diagram of the system. Crucially, we have shown how the different universality classes of the MI-to-SF phase transition are strongly reflected in the properties of the polaron via the cloud of collective modes that dress the impurity. This finding highlights the experimental potential of polarons as versatile probes of quantum correlations of a many-body environment. Moreover, we have provided both quantitative and qualitative predictions about the behaviour of numerous observables of utmost experimental interest, such as the number of bath particles composing the polaron cloud and impurity-bath correlations. Among the notable results of our analysis, we have shown that a clear-cut instance of orthogonality catastrophe occurs in the strongly-interacting superfluid regime of the bath, reflecting its behaviour as a highly compressible, effectively free Bose gas of quasiparticles. Importantly, within our perturbative treatment the bosonic lattice polaron remains a well-defined quasiparticle outside of this limit, which does not prohibit its experimental detection over large portions of the quantum critical regime. Geneally speaking, our results demonstrate how the richer phase diagram resulting from confining a many-body environment to a lattice can fundamentally alter the quasiparticle properties of polarons.

The success of the approach implemented in this work raises exciting prospects in view of investigating impurity physics on lattice systems of interest within the larger context of quantum simulation [132, 199]. Furthermore, the fine modelling of the impurity-bath interaction offered by the QGA could motivate the opening of novel research lines in the relatively young field of lattice polarons [214, 255–263], concerning in particular the study of bath-mediated interactions [264, 265] and few-body correlations [266] within the broader framework of polaronic matter physics [200, 267–270].

From a broader perspective, the many conceptual links between the polaron physics and the open dynamics of a static impurity offered by our methodology allow us to envision a unified picture of quantum impurities in strongly-correlated lattice models. In particular, we have realised that the idea of "observing the drop for probing the ocean" is particularly suited to get accurate information on static and dynamical fluctuations across distinct quantum critical regimes. In this respect, the representative examples analysed in this Thesis are those cases in which the environment excitations soften in the channel coupling with the impurity as a pure consequence of strong interactions in the presence of a lattice. This manifests in a number of interconnected phenomena, ranging from perfect Markovian decoherence to a breakdown of the quasiparticle description, which could tie in with a dynamical instability of the system and be the source of exciting new physical situations.

Collective modes and quantum correlations of the Fermi-Hubbard model

5

This Chapter is based on a synopsis of the following work under development.

▶ Fabio Caleffi, and M. Capone, *Slave boson fluctuations and collective modes from a quantum Gutzwiller ansatz*, In preparation (2022)

5.1 New handles for a time-honoured problem

Alongside the scientific effort of understanding the essence of the low-energy physics of superfluids and purely bosonic systems in general, the long-standing exploration of collective excitations in correlated electron systems finds it roots in the seminal works of Hubbard [271, 272], Landau [273], and Pines [274–276]. In his study on the celebrated model taking his name [271, 272], Hubbard identified the origin of the so-called Hubbard bands, describing quite universally the high-energy spectrum of strongly-interacting electrons, however without clarifying how delocalisation turns the Mott state into a stable coherent phase with a well-defined Fermi surface. On the other hand, starting from the reasonable assumption that weakly-interacting electrons form a gas of quasiparticles with renormalised properties adiabatically connected to the non-interacting system, Landau's theory of the Fermi liquid [29, 273, 277] has proved successful to model the opposite limit of a robust metallic state where electron interactions are regarded as a perturbation. Precisely within Landau's phenomenological framework, it was first shown by Pines and Bohm [274–276] that collective excitations arising from dynamical fluctuations of the ground state are signalled in the spectrum of response functions by a discrete number of peaks with non-trivial dispersive trends depending on the nature of the phase under analysis.

Not differently from the still hazy relationship between Mottness and the structure of quantum correlations in the strongly-interacting superfluid phases of BH models, bridging between the Fermi liquid behaviour and Mott localisation remains a hard problem for condensed matter physicists, as it usually requires expensive numerical resources to be deeply investigated. Despite extremely valuable results have been obtained thorough powerful techniques as DMFT [278] and the various implementations of the QMC method, these approaches are either intrinsically affected by finite-size effects [279] or neglect the possibly crucial role of non-local correlations. These limitations become significant drawbacks especially in the presence of a finite doping, where the formation of incommensurate magnetic phases and unconventional metallic states [280–284], competing with and/or favouring the onset of high-temperature superconductivity [285–287], makes the role of non-local effects and collective dynamics even more substantial.

The purpose of this Chapter is to extend the QGA treatment of collective modes employed in the previous Chapters in the context of BH models to the Fermi-Hubbard system at equilibrium. Although the building blocks of the fermionic QGA theory are expected to strongly resemble the Kotliar-Ruckenstein representation of SB fluctuations [288–290], our approach provides a particularly insightful and flexible route to the bosonic elementary excitations of the system and their physical interpretation, as

well as to those quantum correlations (including non-local fluctuations) determined from collective effects. Establishing an elegant connection with the spectral properties of a bosonic optical lattice, the QGA scheme will be shown to reconcile the Fermi liquid physics in the weakly-interacting regime with the development of strong correlations in striking agreement with DMFT, tracking how the Mott transition occurs at the level of both static and dynamical fluctuations. Our calculations will be carried out in the paramagnetic phase in the absence of symmetry breaking: whereas neglecting magnetic and charge ordering seems to constrain the range of validity of our results, we recall here that incommensurate instabilities are always found to be suppressed for temperatures of the same order of the bare hopping energy. Also, we clarify that, in light of the enormous theoretical and experimental progress made in recent years in the understanding of Hubbard physics (not limited to real materials), the main purpose of our study is to illustrate a simple yet effective description of the physics of collective modes in order to expose their non-obvious interplay in giving superficially well-understood physics.

5.2 A quantum Gutzwiller theory for fermions

5.2.1 The fermionic Gutzwiller approximation in a nutshell

The introduction of the Gutzwiller ansatz as a variational wave function designed for interacting fermions, as well as the evaluation scheme of approximate expectation values based on it – the so-called Gutzwiller Approximation (GA) –, dates back originally to the seminal works of M. Gutzwiller [7, 8], after which a sizeable number of papers has been devoted to the in-depth study of the working principles of the approximation [291–293] and its wide range of applications, see in particular [12, 294–298] as a non-exhaustive list of works. In this Subsection, we follow [13, 299, 300] in order to illustrate the fundamentals of the GA mean-field theory.

The time-dependent Gutzwiller wave function, defined as [299, 301]

$$|\Psi_G(t)\rangle = \bigotimes_{\mathbf{i}} \hat{P}(\mathbf{i}, t) |\Psi_0(t)\rangle \,, \tag{5.1}$$

is a site-factorised ansatz resulting from the application of the local projector $\hat{P}(\mathbf{i}, t)$, acting in the local Hilbert space of the system and depending on time-dependent variational parameters, onto a suitable Slater determinant $|\Psi_0(t)\rangle$. For the sake of simplicity, in the following we will not consider symmetry-broken states $|\Psi_0(t)\rangle$, e.g. BCS-like wave functions, or operators $\hat{P}(\mathbf{i}, t)$ that violate either charge or spin conservation, although the extension to those cases follows a similar, yet more complex derivation [13, 293, 302, 303]. The most general projector $\hat{P}(\mathbf{i}, t)$ can be written as [299, 300, 304]

$$\hat{P}(\mathbf{i}, t) \equiv \sum_{a,b} c_{ab}(\mathbf{i}, t) |a, \mathbf{i}\rangle \langle b, \mathbf{i}| \,, \tag{5.2}$$

where a, b label the local Fock states built through the annihilation (creation) fermionic operators $\hat{c}_{\mathbf{i},a}(\hat{c}^\dagger_{\mathbf{i},a})$, with a indicating both spin and orbital indices. The application of $\hat{P}(\mathbf{i}, t)$ on $|\Psi_0(t)\rangle$ can be expressed in terms of the uncorrelated local probability

distribution as

$$P_{ab}^0(\mathbf{i}, t) \equiv \langle a, \mathbf{i} | \Psi_0(t) \rangle \langle \Psi_0(t) | b, \mathbf{i} \rangle \,, \tag{5.3}$$

so that, for any expectation value $\langle \Psi_G(t) | \hat{O} \left[\hat{c}_{\mathbf{i},\sigma}, \hat{c}_{\mathbf{i},\sigma}^\dagger \right] | \Psi_G(t) \rangle$ of the operator $\hat{O}$, the result depends on the Gutzwiller variational matrix

$$\hat{P}_G(\mathbf{i}, t) \equiv \hat{c}(\mathbf{i}, t) \sqrt{\hat{P}^0(\mathbf{i}, t)} \,. \tag{5.4}$$

Specifically, the GA consists in requiring that expectation values of both local and non-local operators are reproduced exactly in the limit of infinite dimensions $d \to \infty$. This match is made possible by imposing the following constraints on $\hat{P}_G(\mathbf{i}, t)$ at any time [292, 299],

$$\mathrm{Tr}\left[\hat{P}_G^\dagger(\mathbf{i}, t) \, \hat{P}_G(\mathbf{i}, t) \right] = 1 \,, \tag{5.5a}$$

$$\begin{aligned}
\mathrm{Tr}\left[\hat{P}_G^\dagger(\mathbf{i}, t) \, \hat{P}_G(\mathbf{i}, t) \, \hat{c}_{\mathbf{i},a}^\dagger \, \hat{c}_{\mathbf{i},b} \right] &= \langle \Psi_0(t) | \, \hat{c}_{\mathbf{i},a}^\dagger \, \hat{c}_{\mathbf{i},b} | \Psi_0(t) \rangle \\
&\equiv n_{ab}^0(\mathbf{i}, t) \,,
\end{aligned} \tag{5.5b}$$

where the fermionic operators in the trace argument must be regarded in their matrix representation with respect to the local Fock basis in Eq. (5.2). The second constraint (5.5b) serves as a *gauge-fixing* condition for the Gutzwiller parameters $c_{ab}(\mathbf{i}, t)$ in order that expectation values derived by the GA correctly retrieve the same physical content of $|\Psi_0(t)\rangle$ for a non-interacting system, in close analogy with rotationally-invariant SB theories (RISB) [305, 306].

A second important actor of the GA is the wave function renormalisation matrix $\psi_{ij}(\mathbf{i}, t)$, implicitly defined by the following set of equations:

$$\begin{aligned}
\langle \Psi_G(t) | \, \hat{c}_{\mathbf{i},a} | \Psi_G(t) \rangle &= \langle \Psi_0(t) | \, \hat{P}^\dagger(\mathbf{i}, t) \, \hat{c}_{\mathbf{i},a} \, \hat{P}(\mathbf{i}, t) | \Psi_0(t) \rangle \\
&\equiv \sum_b \psi_{ab}(\mathbf{i}, t) \, \langle \Psi_0(t) | \, \hat{c}_{\mathbf{i},b} | \Psi_0(t) \rangle \,.
\end{aligned} \tag{5.6}$$

Clearly, $\psi_{ab}(\mathbf{i}, t)$ allows to rewrite the action of the annihilation operator $\hat{c}_{\mathbf{i},a}$ on the Gutzwiller wave function as a proper translation of the application of the same operator on the uncorrelated state $|\Psi_0(t)\rangle$. Under the general assumption that the operators $\hat{c}_{\mathbf{i},a}$ act on the natural orbitals a that diagonalise the one-body density matrix of the system, one can readily show that, as a consequence of the constraints (5.5), $\psi_{ab}(\mathbf{i}, t)$ acquires the simple expression [299, 300]

$$\psi_{ab}(\mathbf{i}, t) = \frac{\mathrm{Tr}\left[\hat{P}_G^\dagger(\mathbf{i}, t) \, \hat{c}_{\mathbf{i},a} \, \hat{P}_G(\mathbf{i}, t) \, \hat{c}_{\mathbf{i},b}^\dagger \right]}{\sqrt{n_b^0(\mathbf{i}, t) \left[1 - n_b^0(\mathbf{i}, t) \right]}} \,, \tag{5.7}$$

where, according to Eq. (5.5b), $n_b^0(\mathbf{i}, t)$ is the local occupation of the orbital b. In the next Sections, we will show that the renormalisation matrix $\psi_{ab}(\mathbf{i}, t)$, being related to the expectation value of hopping-type operators, has a crucial role in determining the coherence properties of the model under study.

5.2.2 Gutzwiller picture of the normal-phase Hubbard model

Let us put in action the GA toolkit and consider the case of the repulsive Fermi-Hubbard (FH) model in its paramagnetic sector. The Hubbard Hamiltonian reads

$$\hat{H} = -t \sum_{\sigma} \sum_{\langle \mathbf{i}, \mathbf{j} \rangle} \left(\hat{c}^{\dagger}_{\mathbf{i}, \sigma} \, \hat{c}_{\mathbf{j}, \sigma} + \text{H.c.} \right) + U \sum_{\mathbf{i}} \hat{n}_{\mathbf{i}, \uparrow} \, \hat{n}_{\mathbf{i}, \downarrow} - \mu \sum_{\mathbf{i}} \hat{n}_{\mathbf{i}} , \tag{5.8}$$

where t is the hopping energy, U the on-site interaction between different spin species σ and μ the chemical potential, while $\langle \mathbf{i}, \mathbf{j} \rangle$ labels all the pairs of nearest-neighboring sites and $\hat{n}_{\mathbf{i}, \sigma} = \hat{c}^{\dagger}_{\mathbf{i}, \sigma} \, \hat{c}_{\mathbf{i}, \sigma}$ is the local density operator for the spin species σ. For later purposes, we notice that the one-band Hamiltonian (5.8) is invariant under U(2) = U(1) × SU(2) gauge transformations of the fermionic operators.

The local basis of the model consists of four states, which we choose to be, in order, the empty configuration $|0\rangle$, the singly-occupied spin states $|\uparrow\rangle, |\downarrow\rangle$ and the double occupation state $|2\rangle$. Accordingly, the most general charge and spin-conserving Gutzwiller matrix has the diagonal representation $\left[\hat{P}_G(\mathbf{i}, t) \right]_{ab} = C_a(\mathbf{i}, t) \, \delta_{ab}$, where the spin is solely projected along the z direction for simplicity, although a fully SU(2)-invariant formulation poses no conceptual difficulties [307]. Indeed, full spin-rotation invariance and the inclusion of both longitudinal and transverse spin fluctuations become important in the presence of either magnetic ordering or inhomogeneous configurations [307], whose study goes beyond the scope of this work. The requirement (5.5a) acts as a normalisation condition for the Gutzwiller parameters,

$$\sum_{a} |C_a(\mathbf{i}, t)|^2 = 1 . \tag{5.9}$$

The simple structure of $\hat{P}_G(\mathbf{i}, t)$ leads to a substantial simplification in the structure of the renormalisation matrix, which is diagonal with respect to the spin index and reads [65]

$$\psi_{\sigma}(\mathbf{i}, t) = N_{\sigma}(\mathbf{i}, t) \left[C_0^*(\mathbf{i}, t) \, C_{\sigma}(\mathbf{i}, t) + C_{-\sigma}^*(\mathbf{i}, t) \, C_2(\mathbf{i}, t) \right] , \tag{5.10}$$

where we have used the general expression (5.7) and defined

$$N_{\sigma}(\mathbf{i}, t) \equiv \frac{1}{\sqrt{n_{\sigma}^0(\mathbf{i}, t) \left[1 - n_{\sigma}^0(\mathbf{i}, t) \right]}} , \tag{5.11}$$

with the spin-resolved local density is consistently expressed in terms of the Gutzwiller parameters as $n_{\sigma}^0(\mathbf{i}, t) = |C_{\sigma}(\mathbf{i}, t)|^2 + |C_2(\mathbf{i}, t)|^2$ in accordance with Eq. (5.5b).

Since the constraints (5.5) can be proven to hold during the whole stationary dynamics of the system once fixed at $t = 0$ [65, 300], we can reformulate the Fermi-Hubbard problem in terms of a time-local Gutzwiller energy functional

$$E(t) \equiv \langle \Psi_G(t) | \hat{H} | \Psi_G(t) \rangle = E_T(t) + E_{loc}(t) , \tag{5.12}$$

where we isolate a kinetic part

$$E_T(t) \equiv -t \sum_\sigma \sum_{\langle \mathbf{i},\mathbf{j} \rangle} \left[\langle \Psi_G(t) | \, \hat{c}^\dagger_{\mathbf{i},\sigma} \, \hat{c}^\dagger_{\mathbf{j},\sigma} \, | \Psi_G(t) \rangle + \text{H.c.} \right] = \langle \Psi_0(t) | \, \hat{H}_T(t) \, | \Psi_0(t) \rangle$$

(5.13)

and the energy contribution due to the on-site terms $\hat{H}_{loc}$ of the Hamiltonian (5.8),

$$E_{loc}(t) \equiv \sum_\mathbf{i} \text{Tr} \left[\hat{P}^\dagger_G(\mathbf{i}, t) \, \hat{H}_{loc}(\mathbf{i}) \, \hat{P}_G(\mathbf{i}, t) \right]$$

(5.14)

$$= U \sum_\mathbf{i} |C_2(\mathbf{i}, t)|^2 - \mu \sum_\mathbf{i} \left[|C_\uparrow(\mathbf{i}, t)|^2 + |C_\downarrow(\mathbf{i}, t)|^2 + 2 |C_2(\mathbf{i}, t)|^2 \right] .$$

The operator

$$\hat{H}_T(t) \equiv -t \sum_\sigma \sum_{\langle \mathbf{i},\mathbf{j} \rangle} \left[\psi^*_\sigma(\mathbf{i}, t) \, \psi_\sigma(\mathbf{j}, t) \, \hat{c}^\dagger_{\mathbf{i},\sigma} \, \hat{c}_{\mathbf{j},\sigma} + \text{H.c.} \right]$$

(5.15)

can be viewed as the Hamiltonian of the low-energy quasiparticles building the uncorrelated state $|\Psi_0(t)\rangle$. It is now straightforward to introduce a Lagrangian functional of the Gutzwiller DoF [13, 308] supplemented by the constraints (5.5), namely

$$\mathfrak{L}[C, C^*, |\Psi_0\rangle] \equiv \langle \Psi_G | \, i \, \partial_t - \hat{H} \, | \Psi_G \rangle$$

$$= \frac{i}{2} \left\{ \sum_\mathbf{i} \text{Tr} \left[\hat{P}^\dagger_G(\mathbf{i}, t) \, \partial_t \hat{P}_G(\mathbf{i}, t) \right] + \langle \Psi_0(t) | \, \dot{\Psi}_0(t) \rangle - \text{c.c.} \right\} - E(t)$$

$$+ \sum_\mathbf{i} \Lambda_\mathbf{i} \left\{ \text{Tr} \left[\hat{P}^\dagger_G(\mathbf{i}, t) \, \hat{P}_G(\mathbf{i}, t) \right] - 1 \right\}$$

(5.16)

$$+ \sum_\sigma \sum_\mathbf{i} m_{\mathbf{i},\sigma} \left\{ \text{Tr} \left[\hat{P}^\dagger_G(\mathbf{i}, t) \, \hat{P}_G(\mathbf{i}, t) \, \hat{c}^\dagger_{\mathbf{i},\sigma} \, \hat{c}_{\mathbf{i},\sigma} \right] - \langle \Psi_0(t) | \, \hat{c}^\dagger_{\mathbf{i},\sigma} \, \hat{c}_{\mathbf{i},\sigma} \, | \Psi_0(t) \rangle \right\}$$

$$= \frac{i}{2} \left[\sum_{\mathbf{i},a} C^*_a(\mathbf{i}) \dot{C}_a(\mathbf{i}) + \langle \Psi_0(t) | \, \dot{\Psi}_0(t) \rangle - \text{c.c.} \right] - E(t) + \sum_\mathbf{i} \Lambda_\mathbf{i} \left[\sum_a |C_a(\mathbf{i}, t)|^2 - 1 \right]$$

$$+ \sum_\sigma \sum_\mathbf{i} m_{\mathbf{i},\sigma} \left[|C_\sigma(\mathbf{i}, t)|^2 + |C_2(\mathbf{i}, t)|^2 - \langle \Psi_0(t) | \, \hat{c}^\dagger_{\mathbf{i},\sigma} \, \hat{c}_{\mathbf{i},\sigma} \, | \Psi_0(t) \rangle \right] ,$$

where the Lagrange multipliers $\Lambda_\mathbf{i}$ and $m_{\mathbf{i},\sigma}$ enforce the normalisation condition (5.5a) and the gauge-fixing identities (5.5b), respectively. Within the Lagrangian picture (5.16), the conjugate momenta of the Gutzwiller parameters $C_a(\mathbf{i}, t)$ are easily identified again with their complex conjugates $C^*_a(\mathbf{i}, t) = \partial \mathfrak{L}/\partial \dot{C}_a(\mathbf{i}, t)$. The corresponding saddle-point equations,

$$i \, \partial_t C_a(\mathbf{i}, t) = \frac{\partial E(t)}{\partial C^*_a(\mathbf{i}, t)} - \left[\Lambda_\mathbf{i} + (\delta_{a,\sigma} + \delta_{a,2}) \, m_{\mathbf{i},\sigma} \right] C_a(\mathbf{i}, t)$$

(5.17a)

$$i \, \partial_t |\Psi_0(t)\rangle = \hat{H}_T(t) |\Psi_0(t)\rangle + \sum_\sigma \sum_\mathbf{i} m_{\mathbf{i},\sigma} \, \hat{c}^\dagger_{\mathbf{i},\sigma} \, \hat{c}_{\mathbf{i},\sigma} ,$$

(5.17b)

are a paradigmatic instance of the fermionic TDGE, which have been extensively applied to a broad range of dynamical problems, from quantum quenches [296, 309]

to transport phenomena [310]. We point out that, within the above GA scheme, the variational parameters $C_a(\mathbf{i}, t)$ possess their own dynamics because of their one-to-one correspondence with the conjugate fields $C_a^*(\mathbf{i}, t)$. This makes a crucial difference with respect to previous time-dependent methods [301, 307, 311], where the dynamics of $C_a(\mathbf{i}, t)$ is driven only by the evolution of the quasiparticle state $|\Psi_0\rangle$, and is of great importance to the formal introduction of quantum fluctuations discussed in this work.

We notice also that, whereas the Hubbard-U interaction is quartic in the fermionic operators, the situation is reversed in the Lagrangian functional (5.16), where the hopping part $E_T(t)$ acts instead as an effective interaction term. Nevertheless, as a consequence of the constraints (5.5b) in common with SB approaches, the GA does not entail a perturbative description of the weakly-interacting limit $U/t \ll 1$; actually, in Section 5.5 we will show that the predictions of our theory of Gaussian fluctuations match exactly with both the non-interacting limit $U/t \to 0$ and the deep MI regime $U/t \to \infty$ in a non-obvious way.

As a first step towards the development of the fermionic QGA framework, in the following Subsection we will briefly review the stationary solution of Eqs. (5.17) for the ground state of (5.8) in its normal phase.

5.2.3 Saddle-point stationary solution of the TDGE

The GA ground state of the paramagnetic Hubbard model is readily found by searching for the lowest-energy stationary solution of Eq. (5.17a). Explicitly, assuming $C_a(\mathbf{i}, t) = C_a^0 \exp(-i\,\omega\,t)$ with C_a^0 being site-independent for each flavour a, Eq. (5.17a) translates into a set of four coupled equations in the form of a non-linear eigenvalue problem,

$$\sum_b H_{ab}^{(0)}[C, C^*]\, C_b = \Lambda\, C_a\,, \tag{5.18}$$

to be self-consistently solved such that the constraints (5.5b) are always fulfilled [65]. In more detail, the mean-field Hamiltonian matrix of the Gutzwiller parameters reads

$$H_{ab}^{(0)}[C, C^*] = [U\,\delta_{a,2} - (\mu + m)\,(\delta_{a,\uparrow} + \delta_{a,\downarrow} + 2\,\delta_{a,2})]\,\delta_{a,b} - z\,T(m)\sum_\sigma \frac{\partial\,|\psi_\sigma|^2}{\partial C_a^*} \tag{5.19}$$

where the spin index of m_σ can be dropped by paramagnetic symmetry. The calculation of the hopping part of the mean-field Gutzwiller Hamiltonian $\hat{H}^{(0)}[C, C^*]$ requires a careful evaluation of the renormalisation matrix derivatives $\partial\,|\psi_\sigma|^2/\partial C_a^*$ starting from the general formula (5.7). Following the derivation of [65], we have

$$\frac{\partial \psi_{ij}(\mathbf{i})}{\partial C_a^*(\mathbf{i})} = \frac{\partial R_{ij}(\mathbf{i})}{\partial C_a^*(\mathbf{i})}\,N_j(\mathbf{i}) + \sum_l R_{il}(\mathbf{i})\,N_l(\mathbf{i})\,M_{lj}(\mathbf{i})\frac{\partial S_{lj}(\mathbf{i})}{\partial C_a^*(\mathbf{i})}\,, \tag{5.20}$$

where we have defined

$$R_{ij}(\mathbf{i}) \equiv \mathrm{Tr}\Big[\hat{P}_G^\dagger(\mathbf{i})\,\hat{c}_{\mathbf{i},i}\,\hat{P}_G(\mathbf{i})\,\hat{c}_{\mathbf{i},j}^\dagger\Big]\,, \tag{5.21a}$$

$$M_{ij}(\mathbf{i}) \equiv \frac{1}{2} \frac{[N_i(\mathbf{i}) \, N_j(\mathbf{i})]^2}{N_i(\mathbf{i}) + N_j(\mathbf{i})} \left[1 - n_i^0(\mathbf{i}) - n_j^0(\mathbf{i}) \right] , \tag{5.21b}$$

$$S_{ij}(\mathbf{i}) \equiv \mathrm{Tr} \left\{ \hat{P}_G^\dagger(\mathbf{i}) \, \hat{P}_G(\mathbf{i}) \left[\hat{c}_{\mathbf{i},i}, \hat{c}_{\mathbf{i},j}^\dagger \right] \right\} . \tag{5.21c}$$

Thus, when applied to the paramagnetic state, Eq. (5.20) leads to

$$\frac{\partial |\psi_\sigma|^2}{\partial C_a^*} = 2 \, M_\sigma \, |\psi_\sigma|^2 \, d_a \, C_a + N_\sigma \left[\psi_\sigma^* \left(C_\sigma \, \delta_{a,0} + C_2 \, \delta_{a,-\sigma} \right) + \psi_\sigma \left(C_0 \, \delta_{a,\sigma} + C_{-\sigma} \, \delta_{a,2} \right) \right] , \tag{5.22}$$

where $d_a \equiv \delta_{a,0} + \delta_{a,-\sigma} - \delta_{a,\sigma} - \delta_{a,2}$. The factor $T(m) \equiv t \, \langle \Psi_0 | \hat{c}_{\mathbf{i},\sigma}^\dagger \, \hat{c}_{\mathbf{i}+\mathbf{e}_x,\sigma} | \Psi_0 \rangle$ descends from the expectation value of the renormalised hopping operator $\hat{H}_T(t)$ over $|\Psi_0(t)\rangle$. According to Eqs. (5.15) and (5.17b), the uncorrelated state $|\Psi_0(t)\rangle$ describes a Fermi sea formed by quasiparticles with an effective hopping $t_{eff} = t \, |\psi|^2$ and energy dispersion $E_{\mathbf{k}} = -2 \, t_{eff} \sum_{i=1}^d \cos(k_i) + m$. Ergo, the quantity $-T$ plays the role of effective hopping energy for the Gutzwiller coordinates $C_a(\mathbf{i})$ as a mean-field effect of the fermionic subsystem.

As an illustrative example, we consider the half-filling case $\mu = U/2$ at zero temperature, which admits a clean analytical solution. In this case, $m = 0$ and

$$-T \equiv -t \, \langle \Psi_0 | \hat{c}_{\mathbf{i},\sigma}^\dagger \, \hat{c}_{\mathbf{i}+\mathbf{e}_x,\sigma} | \Psi_0 \rangle = \frac{1}{(2\pi)^d \, z} \int d^d\mathbf{k} \, \theta(-E_{\mathbf{k}}) \, \varepsilon_{\mathbf{k}} = -\frac{1}{4 \, d} \left(\frac{4}{\pi} \right)^d t , \tag{5.23}$$

where $\varepsilon_{\mathbf{k}} = -2 \, t \sum_{i=1}^d \cos(k_i)$ is the free-particle energy dispersion and the MI limit $\psi_\sigma \to 0$ has been taken after performing the momentum summation. Indeed, this operation is well justified, since such a limit has the simple effect of shrinking the spectral density of quasiparticles to a delta peak around the chemical potential with infinitesimal support [1] – see Subsection 5.5.1. Correspondingly, the eigenproblem (5.18) simplifies into

$$\begin{pmatrix} 0 & -2 \, z \, T & -2 \, z \, T & 0 \\ -2 \, z \, T & -U/2 & 0 & -2 \, z \, T \\ -2 \, z \, T & 0 & -U/2 & -2 \, z \, T \\ 0 & -2 \, z \, T & -2 \, z \, T & 0 \end{pmatrix} \begin{pmatrix} C_0 \\ C_\uparrow \\ C_\downarrow \\ C_2 \end{pmatrix} = \omega \begin{pmatrix} C_0 \\ C_\uparrow \\ C_\downarrow \\ C_2 \end{pmatrix} . \tag{5.24}$$

The lowest-energy eigenvalue of Eq. (5.24) has the simple expression

$$\omega_0 = -\frac{U}{4} \left[1 + \sqrt{1 + \left(\frac{16 \, z \, T \, \psi_0}{U} \right)^2} \right] , \tag{5.25}$$

where the mean-field *quasiparticle weight* ψ_0 is spin-independent,

$$\psi_0 = \sqrt{1 - \left(\frac{U}{U_c} \right)^2} , \tag{5.26}$$

---

[1] Moreover, in Section 5.3 we will show that the effective hopping energy of the fermionic DoF does not vanish due to their coupling with doublon-holon excitations of the MI, where strictly speaking low-energy quasiparticles are replaced by spinons, which in turn are *not* expected contribute to the one-particle coherence.

and vanishes at the critical interaction $U_c = 16\,z\,T$: this is the well-known critical point of the Brinkman-Rice (BR) description of the Metal-Mott Transition (MIT) within the GA [312]. The ground state Gutzwiller parameters are

$$(C_0, C_\uparrow, C_\downarrow, C_2) = \left(\sin \frac{\theta}{2}, \cos \frac{\theta}{2}, \cos \frac{\theta}{2}, \sin \frac{\theta}{2} \right), \tag{5.27}$$

where $\theta \equiv \arccos(U/U_c)$. While in the non-interacting limit all local configurations are equally explored $C_0 = C_\sigma, C_2 = 1/2$ as expected, at the BR transition the GA predicts perfect unit filling with $C_0 = C_2 = 0$ and $C_0 = C_2 = 1/\sqrt{2}$. Thus, the Gutzwiller mean-field solution provides a trivial, site-localised depiction of the MI phase.

The full phase diagram of the paramagnetic sector of the system is shown in panel (a) of Figure 5.1. For later convenience, the $\mu - U$ projection of the phase space has been chosen in order to emphasise better the lobe-shaped region occupied by the MI state [purple area] and how it connects to the metallic phase out of PHS [black solid line]. From an experimental point of view, the chemical potential μ is hardly tunable, while doping the system is the most doable option. The situation is however reversed in our theoretical study, as fixing the density partially hides the physics of collective modes that we will discuss in the following.

5.2.4 Theory of the bosonic quantum fluctuations

In order to go beyond the GA saddle-point solution reviewed in the previous Subsections, we can adopt a similar strategy as in Chapter 1 and build a simple quantum theory of the bosonic DoF of the Gutzwiller ansatz. Once again, this corresponds to promoting the dynamical variables $C_a(\mathbf{i})$ and their conjugate momenta $C_a^*(\mathbf{i})$ to quantum bosonic fields and imposing equal-time commutation relations between them,

$$\left[\hat{C}_a(\mathbf{i}), \hat{C}_b^\dagger(\mathbf{j}) \right] = \delta_{\mathbf{i},\mathbf{j}}\,\delta_{a,b}\,. \tag{5.28}$$

As regards instead the fate of the quasiparticle state $|\Psi_0\rangle$, for the time being we neglect those fluctuations arising from the interaction between the fermionic excitations and the bosonic DoF $\hat{C}_a(\mathbf{i})$, the discussion of which is postponed to Section 5.3. Before proceeding, we remark that, although the QGA workflow that we apply here has strong similarities with the study of Gaussian fluctuations around SB mean-field theories, it has the crucial advantage of providing a more transparent view on the collective modes of the system, how they affect different observables and, ultimately, how they relate to the properties of low-energy quasiparticles.

Retaining only a mean-field description of the quasiparticle Fermi sea $|\Psi_0\rangle$, the Hamiltonian of the Gutzwiller fields $\hat{C}_a(\mathbf{i})$ is readily found to be

Hamiltonian of the QGA bosonic modes

$$\begin{aligned} \hat{\mathcal{H}}_{\mathrm{B}} \equiv &- T \sum_\sigma \sum_{\langle \mathbf{i},\mathbf{j} \rangle} \left[\hat{\psi}_\sigma^\dagger(\mathbf{i})\,\hat{\psi}_\sigma(\mathbf{j}) + \mathrm{H.c.} \right] + U \sum_{\mathbf{i}} \hat{C}_2^\dagger(\mathbf{i})\,\hat{C}_2(\mathbf{i}) \\ &- (\mu + m) \sum_{\mathbf{i}} \left[\hat{C}_\uparrow^\dagger(\mathbf{i})\,\hat{C}_\uparrow(\mathbf{i}) + \hat{C}_\downarrow^\dagger(\mathbf{i})\,\hat{C}_\downarrow(\mathbf{i}) + 2\,\hat{C}_2^\dagger(\mathbf{i})\,\hat{C}_2(\mathbf{i}) \right], \end{aligned} \tag{5.29}$$

where $\hat{\psi}_\sigma(\mathbf{i})$ is the quantised counterpart of the renormalisation matrix (5.10) and the physical significance of the quasiparticle hopping energy $-T$ is now evident. It is worth

observing that the quantum Gutzwiller Hamiltonian (5.29) strongly resembles the $\mathbb{Z}_2$-symmetric binary BH model examined in Chapter 2, restricted to the hard-core limit so as to mimic the Pauli blockade for particles having the same spin and with the interspecies interaction mapping to U. In next Sections, we will show that the link between the two models, far from being a mere artefact of the QGA, sheds a novel light on the physical meaning of the collective modes of the FH system. Moreover, quantum correlations that are known to develop in one model will serve as terms of comparison for physical expectations in the other.

Considering the usual QGA partitioning of the bosonic operators,

$$\hat{C}_a(\mathbf{i}) = \hat{A}(\mathbf{i})\, C_a^0 + \delta\hat{C}_a(\mathbf{i})\,, \tag{5.30}$$

and assuming that the Hamiltonian (5.29) refers to a homogeneous system, it is convenient to work in momentum space by writing

$$\delta\hat{C}_a(\mathbf{j}) \equiv \frac{1}{\sqrt{V}} \sum_{\mathbf{k}\in \mathrm{BZ}} e^{i\mathbf{k}\cdot\mathbf{j}}\, \delta\hat{\gamma}_a(\mathbf{k})\,. \tag{5.31}$$

where V is the lattice volume. Inserting Eq. (5.31) in $\hat{\mathcal{H}}_{\mathrm{B}}$ and expanding the operators up to quadratic order in the fluctuations, we obtain

$$\hat{\mathcal{H}}_{\mathrm{B}}^{(2)} = E_0 + \frac{1}{2}\sum_{\mathbf{k}} \left[\delta\hat{\underline{\gamma}}^\dagger(\mathbf{k}), -\delta\hat{\underline{\gamma}}(-\mathbf{k})\right]\, \hat{\mathcal{L}}_{\mathbf{k}} \begin{bmatrix} \delta\hat{\underline{\gamma}}(\mathbf{k}) \\ \delta\hat{\underline{\gamma}}^{\bar{\dagger}}(-\mathbf{k}) \end{bmatrix}\,, \tag{5.32}$$

where E_0 coincides with the mean-field variational energy of the ground state (apart from a constant shift). The calculation of the 4×4 blocks of the pseudo-Hermitian matrix $\hat{\mathcal{L}}_{\mathbf{k}}$ is provided by second-order derivatives of the energy functional (5.12) with respect to the Gutzwiller parameters. Specifically, using the same notation as in Chapter 1, we have

$$
\begin{aligned}
(\mathbf{H_k})_{ab} \equiv &\left[-\omega_0 - (\mu + m)\left(\delta_{a,\uparrow} + \delta_{a,\downarrow}\right) + U\,\delta_{a,2}\right]\delta_{a,b} \\
&- z\,T\,\psi_0 \sum_\sigma \left[\left(\frac{\partial^2 \psi_\sigma}{\partial C_a^*\, \partial C_b}\right)_0 + \left(\frac{\partial^2 \psi_\sigma^*}{\partial C_a^*\, \partial C_b}\right)_0\right] \\
&- T_{\mathbf{k}} \sum_\sigma \left[\left(\frac{\partial \psi_\sigma^*}{\partial C_a^*}\right)_0 \left(\frac{\partial \psi_\sigma}{\partial C_b}\right)_0 + \left(\frac{\partial \psi_\sigma^*}{\partial C_b}\right)_0 \left(\frac{\partial \psi_\sigma}{\partial C_a^*}\right)_0\right]\,,
\end{aligned}
\tag{5.33a}
$$

$$
\begin{aligned}
(\mathbf{K_k})_{ab} \equiv &- z\,T\,\psi_0 \sum_\sigma \left[\left(\frac{\partial^2 \psi_\sigma}{\partial C_a^*\, \partial C_b^*}\right)_0 + \left(\frac{\partial^2 \psi_\sigma^*}{\partial C_a^*\, \partial C_b^*}\right)_0\right] \\
&- T_{\mathbf{k}} \sum_\sigma \left[\left(\frac{\partial \psi_\sigma^*}{\partial C_a^*}\right)_0 \left(\frac{\partial \psi_\sigma}{\partial C_b^*}\right)_0 + (a \leftrightarrow b)\right]\,,
\end{aligned}
\tag{5.33b}
$$

where the subscript 0 refers to the equilibrium value and $T_{\mathbf{k}} = (T/t)\,\varepsilon_{\mathbf{k}}$ is the effective free dispersion of the bosonic DoF. We highlight once more that the ground state energy ω_0, set by the saddle-point evolution of the Gutzwiller parameters C_a^0, appears in the diagonal elements of (1.12a) as a consequence of the normalisation operator $\hat{A}(\mathbf{i})$ and, shifting the diagonal elements of $\hat{\mathcal{L}}_{\mathbf{k}}$, assures a gapless spectrum for density and spin excitations in the metallic phase. While the first-order derivatives of the renormalisation

factor ψ_σ can be straightforwardly deduced from a generalisation of Eq. (5.20), the calculation of the second-order derivatives in Eqs. (5.33) requires further analytical manipulations [65], with the results

$$\left(\frac{\partial \psi_{ij}}{\partial C_a^* \partial C_b}\right)_0 \tag{5.34a}$$

$$= \frac{\partial^2 R_{ij}}{\partial C_a^* \partial C_b} N_j + \sum_l \left(R_{il}\, M_{lj} \frac{\partial^2 S_{lj}}{\partial C_a^* \partial C_b} + \frac{\partial R_{il}}{\partial C_a^*} M_{lj} \frac{\partial S_{lj}}{\partial C_b} + \frac{\partial R_{il}}{\partial C_b} M_{lj} \frac{\partial S_{lj}}{\partial C_a^*} + R_{il}\, \mathcal{E}_{lj} \right),$$

$$\left(\frac{\partial \psi_{ij}}{\partial C_a^* \partial C_b^*}\right)_0 = \sum_l \left(\frac{\partial R_{il}}{\partial C_a^*} M_{lj} \frac{\partial S_{lj}}{\partial C_b^*} + \frac{\partial R_{il}}{\partial C_b^*} M_{lj} \frac{\partial S_{lj}}{\partial C_a^*} + R_{il}\, \mathcal{F}_{lj} \right), \tag{5.34b}$$

where we have defined

$$\mathcal{E}_{ij} \equiv \frac{(N_i N_j)^2}{N_i + N_j} \sum_l \left[\frac{\partial S_{il}}{\partial C_a^*} \frac{\partial S_{lj}}{\partial C_b} + (a \leftrightarrow b)^* \right] \left(\frac{1}{4} + M_{il}\, S_{lj} \frac{N_i N_j + N_i N_l + N_j N_l}{(N_i N_l N_j)^2} \right), \tag{5.35a}$$

$$\mathcal{F}_{ij} \equiv \frac{(N_i N_j)^2}{N_i + N_j} \sum_l \left[\frac{\partial S_{il}}{\partial C_a^*} \frac{\partial S_{lj}}{\partial C_b^*} + (a \leftrightarrow b) \right] \left(\frac{1}{4} + M_{il}\, S_{lj} \frac{N_i N_j + N_i N_l + N_j N_l}{(N_i N_l N_j)^2} \right), \tag{5.35b}$$

with substantial simplifications in the present case.

As in the case of the BH model, the diagonalisation of the Hamiltonian of Gaussian bosonic fluctuations can be achieved by a suitable Bogoliubov rotation of the Gutzwiller operators,

$$\delta \hat{\gamma}_c(\mathbf{k}) = \sum_\alpha u_{\alpha,\mathbf{k},c}\, \hat{b}_{\alpha,\mathbf{k}} + \sum_\alpha v_{\alpha,-\mathbf{k},c}^*\, \hat{b}_{\alpha,-\mathbf{k}}^\dagger, \tag{5.36}$$

recasting the quadratic form (5.32) into the diagonal expression

$$\hat{\mathcal{H}}_{\mathrm{B}}^{(2)} = E_0 + \sum_\alpha \sum_{\mathbf{k}} \omega_{\alpha,\mathbf{k}}\, \hat{b}_{\alpha,\mathbf{k}}^\dagger \hat{b}_{\alpha,\mathbf{k}}, \tag{5.37}$$

which provides a quadratic model for the bosonic excitations of the system under a mean-field decoupling the interaction with the fermionic quasiparticles.

In the same way as the Hamiltonian of the bosonic DoF $\hat{\mathcal{H}}_{\mathrm{B}}$ has been constructed, we can employ a similar quantisation strategy to improve the calculation of arbitrary expectation values by the inclusion of operator-valued quantum fluctuations. In more detail, the calculation of the expectation value of a generic observable $\left\langle \hat{O}\left[\hat{c}_{\mathbf{i},\sigma}, \hat{c}_{\mathbf{i},\sigma}^\dagger\right] \right\rangle$ overlaps significantly with the bosonic QGA protocol, except for the first step concerning the conversion of an observable into the Gutzwiller DoF. In particular:

- if the observable is a one-particle correlator of the form $\hat{O} = \hat{c}_{\mathbf{i},\sigma}^\dagger(t)\, \hat{c}_{\mathbf{j},\sigma}(t')$, one has to take into account both the renormalisation fields $\psi_\sigma(\mathbf{i}, t)$ and the contribution of the fermionic quasiparticles, in analogy with the calculation of the hopping energy (5.13), hence $\mathsf{O}[C_a, C_a^*] = \psi_\sigma^*(\mathbf{i}, t)\, \psi_\sigma(\mathbf{j}, t') \langle \Psi_0 | \hat{c}_{\mathbf{i},\sigma}^\dagger(t)\, \hat{c}_{\mathbf{j},\sigma}(t') | \Psi_0 \rangle$;
- for any other observable given by higher-order propagators such as charge or spin correlations, only the expression of $\mathsf{O}[C_a, C_a^*]$ in terms of the Gutzwiller parameters is needed, since $\hat{O}\left[\hat{c}_{\mathbf{i},\sigma}, \hat{c}_{\mathbf{i},\sigma}^\dagger\right]$ can be always recast into the product of

two-body local operators.

In Section 5.4, we apply the procedure outlined above to familiar quantities, such as the Green's function of the theory and equal-time correlations, as well as charge and spin susceptibilities. Selected results for such quantities at zero temperature are then presented extensively in Section 5.5.

As underlined in Chapter 1, the last step of the complete QGA evaluation protocol outlined in Subsection 1.2.4 is at the roots of the most relevant feature of the QGA, which is the introduction of non-trivial quantum correlations beyond the single-particle sector of the collective modes. In fact, the order-by-order expansion of any operator in terms of the quantum fluctuations $\delta \hat{C}_a(\mathbf{i})$ enables a systematic inclusion of multi-mode vertices involving more than one excitation $\hat{b}_{\alpha,\mathbf{k}}$. Importantly, we find that two-mode correlations are of key importance in controlling both local and non-local fluctuations, also via the non-linearity introduced by the normalisation operator $\hat{A}(\mathbf{i})$ in Eq. (5.30). In this sense, the case of charge correlations offers an instructive example of the role of non-quadratic fluctuations, see the derivation sketched in Subsection 5.4.2 and the discussion of Subsection 5.5.2. Even more interestingly, our quantisation procedure provides novel insights into the physical role of multi-mode correlations (and collective effects in general) when the coupling between the bosonic modes and the fermionic species is reintegrated into the theory. This crucial point is tackled in Section 5.3, where we will discuss in detail how bosonic quantum fluctuations modify the attributes of low-energy quasiparticles.

For the sake of clarity, we point out again that the inclusion of quadratic fluctuations only does not produce any change in the phase diagram of the system, which retains essentially its mean-field shape [see Figure 5.1(a)]. However, the addition of fluctuations beyond second order in the $\delta \hat{C}_a$'s appears as a well-posed problem and is supposed to describe the back-action of fluctuations onto the stationary state: this would allow to construct a fully self-consistent theory of quantum fluctuations with respect to the GA constraints (5.5).

5.2.5 Bosonic excitation spectrum

Since the main focus of our study revolves around the properties of the collective modes and how their spectral features mould quantum correlations, we dedicate this Subsection to a preliminary discussion of the structure of the many-body excitation spectrum of the normal-phase Hubbard model as determined by diagonalisation of the bosonic Hamiltonian (5.37) in $d = 2$. As regards the metallic state, we report the analytical expressions of the eigenenergies $\omega_{\alpha,\mathbf{k}}$ for the half-filled lattice only, for which we retrieve the findings of [65] complemented by some original observations. As anticipated before, we notably find close analogies between the excitation spectrum of fermionic collective excitations and the normal modes of the binary BH mixture analysed in Chapter 2.

The metallic phase [panels (b)-(c) of Figure 5.1] is characterised by three different excitation modes, two of which are acoustic excitations. One of the latter modes is the so-called Landau's zero sound [red solid lines] associated with density fluctuations and displays the well-known dispersion relation predicted by Fermi liquid theory [29,
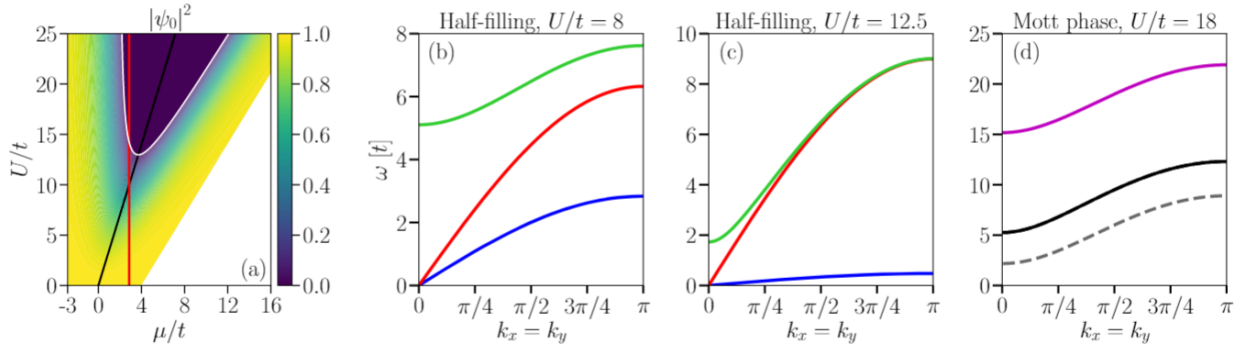
Figure 5.1: (a) Phase diagram of the paramagnetic Hubbard model within Gutzwiller mean-field theory for $d = 2$. The colour map refers to the value of the quasiparticle weight $|\psi_0|^2$, hence the MI lobe coincides with the dark purple region. The white area corresponds to a completely filled lattice. Black solid line: points at PHS. Red solid line: phase diagram cut at constant $\mu/t = 3$ crossing the doping-driven MIT, taken as a reference for Figure 5.4-5.6. (b)-(c) Excitation spectrum of the collective modes at half filling for $U/t = 8$ and $U/t = 12.5$ respectively, in the metallic phase. The MIT occurs at $U/t \approx 12.97$. Blue solid line: spin sound dispersion (5.39). Red solid line: Landau's density mode (5.38). Green solid line: Hubbard optical branch (5.40). (d) Energy spectrum of the MI at $U/t = 18$. Black solid line: dispersion relation of the degenerate doublon-holon excitations in the PH-symmetric case. Pink solid (gray dashed) line: doublon (holon) excitation branch for $\mu/t = 3$, in absence of PHS.

301] at Particle-Hole Symmetry (PHS) [see the black solid line in Figure 5.1(a)],

$$\omega_{d,\mathbf{k}} = \underbrace{\frac{U_c}{4}(1+u)\sqrt{u(2-u)}}_{\sqrt{z}\,c_d}\sqrt{1 - 16\,T_{\mathbf{k}}/U_c}\,, \qquad (5.38)$$

where we have introduced the rescaled interaction parameter $u \equiv U/U_c$. Formally speaking, $\omega_{d,\mathbf{k}}$ can be interpreted as the Goldstone mode related to in-phase oscillations of the quasiparticle weight spinor $(\psi_\uparrow, \psi_\downarrow)$. It is worth highlighting that, in the PHS case (5.38), the zero sound velocity c_d increases monotonously with the interaction u and reaches a finite value at the transition point $u = 1$ [see Figure 5.1(c)]; on the contrary, c_d converges to zero at any other point of the doping-driven MIT [see e.g. the red solid line in Figure 5.1(a)].

Energy spectrum of the FH collective modes   The second acoustic mode of the metallic phase can be identified with longitudinal spin fluctuations, as the corresponding eigenstates $(u_{s,\mathbf{k},a}, v_{s,\mathbf{k},a})$ have non-zero components in the single-spin sectors $a = \uparrow, \downarrow$ only. Alongside density fluctuations, this excitation is akin to the Goldstone mode associated with out-of-phase oscillations of the quasiparticle weight spinor or, rephrased differently, the spontaneous breaking of SU(2) invariance in the ground state of bosons. Differently from the Landau mode, the bandwidth of the spin branch [blue solid lines]

$$\omega_{s,\mathbf{k}} = \frac{U_c}{4}(1-u)\sqrt{u(2+u)}\sqrt{1 - 16\,T_{\mathbf{k}}/U_c} \qquad (5.39)$$

has a non-monotonic dependence with respect to u and always vanishes at the MIT, compatibly the naive expectation that spin fluctuations in the paramagnetic MI have zero energy cost due to the formation of local magnetic moments.

At half filling, a more clear-cut fingerprint of the MIT can be identified in the

behaviour of the third excitation mode [green solid lines], having energy dispersion

$$\omega_{h,\mathbf{k}} = \frac{U_c}{2}\sqrt{1 - 16\, u^2\, T_{\mathbf{k}}/U_c}\,. \tag{5.40}$$

This optical mode, which is generally deemed as the main responsible for the high-energy features of the system [299, 313], is directly linked to the Hubbard-U interaction and indeed acquires a non-zero bandwidth at finite u, while its excitation gap softens when moving from weak to strong interactions. Upon approaching the MIT at PHS, $\omega_{h,\mathbf{k}}$ becomes gapless and degenerate with the zero sound mode, suggesting that the spectral weight of density excitations is progressively transferred to high-energy states. In Figure 5.1(c) we observe that, for large enough U, the zero sound branch and the *Hubbard mode* start becoming degenerate at large momenta and coincide exactly at the critical point only. In Section 5.5.1, we are going to show that this gradual overlap mechanism manifests explicitly in the structure of the different modal contributions to the local DoS. In the most general case, upon reaching the MI boundary out of PHS, $\omega_{h,\mathbf{k}}$ keeps a finite energy gap, such that the Hubbard mode (5.40) remains always detached from the Landau branch (5.38).

As the system undergoes the MIT [panel (d) of Figure 5.1], the QGA theory provides a more accurate representation of the spectral properties of the MI as compared to the shallow picture of the BR mean-field theory. The zero sound and Hubbard modes are replaced by the (gapped) doublon and holon excitation branches

$$\omega^{\mathrm{MI}}_{\mathrm{P/H},\mathbf{k}} = \frac{U}{2}\sqrt{1 - 16\, T_{\mathbf{k}}/U} \pm \left(\frac{U}{2} - \mu\right) \tag{5.41}$$

with quadratic dispersion at low $\mathbf{k}$ and vanishing bandwidth with increasing U/t. Under the PHS condition $\mu = U/2$, the doublon-holon bands (5.41) are degenerate [black solid line] and become both gapless at the MIT; on the contrary, in the non-symmetric case [violet and gray lines] the lowest-lying excitation has either particle or hole character depending on the chemical potential and is the only branch becoming gapless at the MIT. Interestingly and not surprisingly, we observe that these behaviours strongly remind of the structure of the incoherent excitations characterising the bosonic MI phases explored in the previous Chapters.

5.3 Effective boson-mediated interaction between the quasiparticles

Up to this point, we have looked into how our method captures the proper collective excitations of the system by constructing the Hamiltonian (5.29) of the quantised fluctuations $\delta\hat{C}_a(\mathbf{i})$, while low-energy quasiparticles have been decoupled from the bosonic modes and averaged out over the mean-field state $|\Psi_0\rangle$. In other words, we have drawn two independent portraits for the bosonic and fermionic excitations of the system, taking into account only their mutual feedback at the mean-field level. Hence, it is natural to wonder (i) what is the net effect of reintroducing the coupling between the bosonic and fermionic components and (ii) how the correlations between the latter are modified by their own collective behaviour. The idea of mapping the FH system into an effective model for quasiparticles coupled to auxiliary quantised modes is not

new [296, 314–317] and has been mainly explored in the case of slave spin theories. However, in what follows we will propose a simple treatment of the coupling between fermions and bosonic excitations whose advantage is to make the role of collective modes in building the quasiparticle interaction vertices emerge more clearly.

Pair hopping model of the boson-quasiparticle coupling
We start our analysis by adopting a similar quantisation strategy as in Subsection 5.2.4 and, omitting the chemical potential term $m \sum_{\sigma,\mathbf{i}} \hat{c}^\dagger_{\mathbf{i},\sigma} \hat{c}_{\mathbf{i},\sigma}$, rewriting the Hamiltonian of quasiparticles (5.15) as

$$\hat{\mathcal{H}}_{\mathrm{F}} \equiv -t \sum_{\sigma} \sum_{\langle \mathbf{i},\mathbf{j} \rangle} \left[\hat{\psi}^\dagger_\sigma(\mathbf{i}) \, \hat{\psi}_\sigma(\mathbf{j}) \, \hat{c}^\dagger_{\mathbf{i},\sigma} \, \hat{c}_{\mathbf{j},\sigma} + \mathrm{H.c.} \right] , \qquad (5.42)$$

which describes a two-point coupling between fermions and bosonic modes involved in hopping processes. Thanks to the QGA technology developed so far, we are now able to re-express such interactions in terms of the proper excitations of the system by expanding the operator $\hat{\psi}_\sigma(\mathbf{i})$ with respect to quantum fluctuations.

To lowest order, the pair-hopping Hamiltonian (5.42) turns into

$$\mathcal{H}^{(1)}_{\mathrm{F}} = -\sum_{\sigma} \sum_{\mathbf{i}} \sum_{\mathbf{j}(\mathbf{i})} \left\{ t_{eff} \, \hat{c}^\dagger_{\mathbf{i},\sigma} \, \hat{c}_{\mathbf{j},\sigma} + t \, \psi_0 \left[\delta_1 \hat{\psi}^\dagger_\sigma(\mathbf{i}) + \delta_1 \hat{\psi}_\sigma(\mathbf{j}) \right] \hat{c}^\dagger_{\mathbf{i},\sigma} \, \hat{c}_{\mathbf{j},\sigma} \right\} , \quad (5.43)$$

where $\mathbf{j}(\mathbf{i})$ labels the z nearest-neighboring sites of $\mathbf{i}$. In the expression above, the object $\delta_1 \hat{\psi}_\sigma(\mathbf{i})$ is a spinful variant of the QGA Bose field, not dissimilar to the operator (2.61) in the case of the binary BH model. More precisely, we have

$$\delta_1 \hat{\psi}_\sigma(\mathbf{i}) \equiv \frac{1}{\sqrt{V}} \sum_{\alpha,\mathbf{k}} \left[U^\sigma_{\alpha,\mathbf{k}} \, e^{i\,\mathbf{k}\cdot\mathbf{i}} \, \hat{b}_{\alpha,\mathbf{k}} + \left(V^\sigma_{\alpha,\mathbf{k}} \right)^* e^{-i\,\mathbf{k}\cdot\mathbf{i}} \, \hat{b}^\dagger_{\alpha,\mathbf{k}} \right] , \qquad (5.44)$$

where we have introduced the spin-resolved particle (hole) amplitudes $U^\sigma_{\alpha,\mathbf{k}}$ $\left(V^\sigma_{\alpha,\mathbf{k}} \right)$, the properties of which will be further explored in Subsection 5.4.1. Inserting the expression (5.44) of the operator $\delta_1 \hat{\psi}_\sigma(\mathbf{i})$ into Eq. (5.43), we obtain a linear coupling of the fermionic fields with the bosonic modes, hence we can integrate out the latter so as to obtain an effective dynamical interaction between the quasiparticles mediated by the single-boson propagator $D^{(1)}_\alpha(\mathbf{k},\omega) = -i\,\mathcal{T}_{t-t'} \left\langle \hat{b}_{\alpha,\mathbf{k}}(t) \, \hat{b}^\dagger_{\alpha,\mathbf{k}}(t') \right\rangle$. If we neglect retardation effects and take the static limit

$$D^{(1)}_\alpha(\mathbf{k},\omega) = \frac{1}{\omega - \omega_{\alpha,\mathbf{k}}} \simeq -\frac{1}{\omega_{\alpha,\mathbf{k}}} , \qquad (5.45)$$

Effective non-local interaction between quasiparticles
we obtain a time-local Hamiltonian equipped with a *long-range* interaction,

$$\begin{aligned}
\hat{\mathcal{H}}^{(1)}_{\mathrm{F}} \approx \psi^2_0 \sum_{\sigma} \sum_{\mathbf{k}} \varepsilon_{\mathbf{k}} \, \hat{c}^\dagger_{\mathbf{k}\sigma} \, \hat{c}_{\mathbf{k}\sigma} - \frac{\psi^2_0}{2\,V} \sum_{\sigma,\sigma'} \sum_{\alpha} \sum_{\mathbf{k},\mathbf{k}',\mathbf{q}} \frac{1}{\omega_{\alpha,\mathbf{q}}} \\
\times \left[\left(U^\sigma_{\alpha,\mathbf{q}} U^{\sigma'}_{\alpha,\mathbf{q}} + V^\sigma_{\alpha,\mathbf{q}} V^{\sigma'}_{\alpha,\mathbf{q}} \right) \left(\varepsilon_{\mathbf{k}} \, \varepsilon_{\mathbf{k}'-\mathbf{q}} + \varepsilon_{\mathbf{k}'} \, \varepsilon_{\mathbf{k}+\mathbf{q}} \right) \right. \\
\left. + \left(U^\sigma_{\alpha,\mathbf{q}} V^{\sigma'}_{\alpha,\mathbf{q}} + V^\sigma_{\alpha,\mathbf{q}} U^{\sigma'}_{\alpha,\mathbf{q}} \right) \left(\varepsilon_{\mathbf{k}} \, \varepsilon_{\mathbf{k}'} + \varepsilon_{\mathbf{k}'-\mathbf{q}} \, \varepsilon_{\mathbf{k}+\mathbf{q}} \right) \right] \\
\times \hat{c}^\dagger_{\mathbf{k}\sigma} \, \hat{c}^\dagger_{\mathbf{k}'\sigma'} \, \hat{c}_{\mathbf{k}'-\mathbf{q}\sigma'} \, \hat{c}_{\mathbf{k}+\mathbf{q}\sigma} ,
\end{aligned} \qquad (5.46)$$

where the symbol of complex conjugation for the bosonic particle (hole) amplitudes
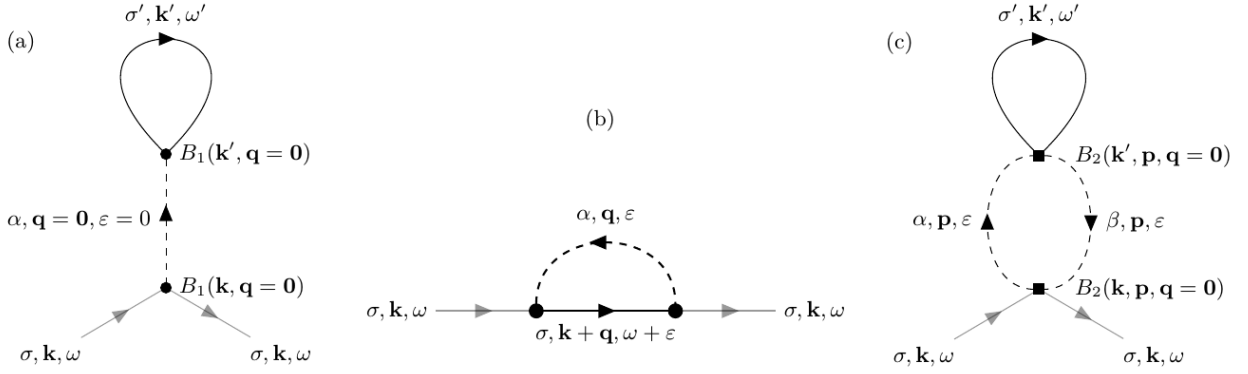
Figure 5.2: (a)-(b) Hartree and Fock terms of $\Sigma_{\mathrm{F}}^{(1)}(\mathbf{k}, \omega)$ respectively, generated by one-boson exchange processes. For the sake of simplicity, we reported only the Fock diagram with counterpropagating quasiparticle and bosonic propagators. (c) Next-order Hartree term contributing to $\Sigma_{\mathrm{F}}^{(1)}(\mathbf{k}, \omega)$, accounting for the two-boson exchange interaction. The symbol $\bullet$ in panels (a)-(b) corresponds to the one-boson interaction vertex $B_1(\mathbf{k}, \mathbf{q}) \equiv \psi_0 \left(U_{\alpha, \mathbf{q}}\, \varepsilon_{\mathbf{k+q}} + V_{\alpha, \mathbf{q}}\, \varepsilon_{\mathbf{k}}\right)$, while the symbol $\blacksquare$ in panel (c) stand for the two-boson Hartree vertex $B_2(\mathbf{k}, \mathbf{p}, \mathbf{q}) = U_{\alpha, \mathbf{p-q}}\, V_{\beta, \mathbf{p+q}}\, \varepsilon_{\mathbf{k+p+q}}$.

has been omitted, as the latter are always real quantities in the present setting.

Since we aim at estimating only the mean impact of the one-boson effective interaction (5.46) on the properties of quasiparticles, we proceed heuristically by calculating the Hartree-Fock approximation of the corresponding self-energy $\Sigma_{\mathrm{F}}^{(1)}(\mathbf{k}, \omega)$, for which we obtain

$$
\Sigma_{\mathrm{F}}^{(1)}(\mathbf{k}, \omega) \simeq \underbrace{4\, z\, T\, \psi_0^2 \sum_\alpha \frac{\left(U_{\alpha, \mathbf{0}} + V_{\alpha, \mathbf{0}}\right)^2}{\omega_{\alpha, \mathbf{0}}} \varepsilon_{\mathbf{k}}}_{Hartree} \tag{5.47}
$$

$$
+ \frac{\psi_0^2}{V} \sum_\alpha \sum_{\mathbf{q}} \frac{1}{\omega_{\alpha, \mathbf{q}}} \Big[\left(U_{\alpha, \mathbf{q}}\, U_{\alpha, \mathbf{q}} + V_{\alpha, \mathbf{q}}\, V_{\alpha, \mathbf{q}}\right)\left(\varepsilon_{\mathbf{k}}^2 + \varepsilon_{\mathbf{k+q}}^2\right)
$$

$$
+ 2 \left(U_{\alpha, \mathbf{q}}\, V_{\alpha, \mathbf{q}} + V_{\alpha, \mathbf{q}}\, U_{\alpha, \mathbf{q}}\right) \varepsilon_{\mathbf{k}}\, \varepsilon_{\mathbf{k+q}}\Big]\, F(E_{\mathbf{k+q}}) ,
$$

where $F(\omega)$ is the Fermi-Dirac distribution. Remarkably, we find numerically that the Hartree diagram of $\Sigma_{\mathrm{F}}^{(1)}(\mathbf{k}, \omega)$ is always much larger than the exchange term [Figure 5.2(a-b)], as a consequence of the fact that bosonic vertices of the form $\left(U_{\alpha, \mathbf{q}}^\sigma\right)^n \left(V_{\alpha, \mathbf{q}}^\sigma\right)^m / \omega_{\alpha, \mathbf{q}}$ are always peaked around $\mathbf{q} = \mathbf{0}$ for each mode α, especially on the brink of the MIT. It follows that the coupling between quasiparticles and bosonic modes induces, for the most part, a uniform effect on the quasiparticle correlations within the simplifications made so far. Also, the static approximation of the propagator $D_\alpha^{(1)}(\mathbf{q}, \omega)$ turns out to be a negligible bias for our calculation, as including a fully dynamical interaction contributes only a marginal modification to the exchange diagram of $\Sigma_{\mathrm{F}}^{(1)}(\mathbf{k}, \omega)$. Therefore, these observations allow for a good approximation of the quasiparticle self-energy through its Hartree term only,

$$
\Sigma_{\mathrm{F}}^{(1)}(\mathbf{k}, \omega) \simeq 4\, z\, T\, \psi_0^2 \sum_\alpha \frac{\left(U_{\alpha, \mathbf{0}} + V_{\alpha, \mathbf{0}}\right)^2}{\omega_{\alpha, \mathbf{0}}} \varepsilon_{\mathbf{k}} , \tag{5.48}
$$

where the spin index has been dropped for simplicity. The semi-analytical result (5.48) conveys a very intuitive physical interpretation of the effective interaction (5.46). In

fact, noticing that $\Sigma_{\mathrm{F}}^{(1)}(\mathbf{k}, \omega) \propto \varepsilon_{\mathbf{k}}$, this is responsible for a *positive* shift of the hopping energy,

$$\frac{\Delta t_1}{t} = 4\,z\,T\,\psi_0^2 \sum_\alpha \frac{(U_{\alpha,\mathbf{0}} + V_{\alpha,\mathbf{0}})^2}{\omega_{\alpha,\mathbf{0}}} > 0 \,, \qquad (5.49)$$

via the Dyson equation $\omega - (1 + \Delta t_1/t)\,\varepsilon_{\mathbf{k}} \equiv G_0^{-1}(\mathbf{k}, \omega) - \Sigma_{\mathrm{F}}^{(1)}(\mathbf{k}, \omega)$ for the quasiparticle Green's function. Loosely speaking, expression (5.49) is a signature of the fact that bosonic fluctuations tend to strengthen the coherence of the quasiparticles at lowest order.

As a matter of fact, we realise however that the previous derivation is meaningful in the metallic phase only, as the self-energy $\Sigma_{\mathrm{F}}^{(1)}(\mathbf{k}, \omega) \propto \psi_0^2$ vanishes identically in the MI, thus masking the fate of the boson-fermion coupling beyond the MIT. This shortcoming has to be attributed to the reduced order of quantum correlations encompassed by the Hamiltonian (5.43). As pointed out in Section 5.4.2, the regime of strong interactions requires to take a deeper look into multi-mode bosonic correlations, which are expected to overcome the weight of linear-order fluctuations for sufficiently strong U/t. Analogously, we have to expand the quasiparticle Hamiltonian (5.42) to the next order for improving our description of the residual fermionic correlations across the MI region. Indeed, a number of recent works [134, 318, 319] have proposed that the paramagnetic MI can be understood as a quantum spin liquid where the hopping of spinons (the leftover fermionic DOF) is crucially determined by their coupling to doublon-holon pairs, namely two-particle excitations. In the following, we will give substantial support to this speculation by means of our analysis of higher-order collective fluctuations.

Going beyond the first-order interaction (5.43), the second-order expansion of the operator $\hat{\psi}_\sigma^\dagger(\mathbf{i})\,\hat{\psi}_\sigma(\mathbf{j})$ enriches the quasiparticle Hamiltonian with two-boson coupling terms via two different contributions. The first one is given by substituting both the renormalisation fields in the product $\hat{\psi}_\sigma^\dagger(\mathbf{i})\,\hat{\psi}_\sigma(\mathbf{j})$ by their first-order expansions as $\delta_1\hat{\psi}_\sigma^\dagger(\mathbf{i})\,\delta_1\hat{\psi}_\sigma(\mathbf{j})$. Inserting the expression of $\delta_1\hat{\psi}_\sigma(\mathbf{i})$ given by Eq. (5.44), we obtain the result

$$
\begin{aligned}
\hat{\mathcal{H}}_{\mathrm{F}}^{(2)} = \hat{\mathcal{H}}_{\mathrm{F}}^{(1)} & \\
+ \frac{1}{V} \sum_\sigma \sum_{\alpha,\beta} \sum_{\mathbf{k},\mathbf{p},\mathbf{q}} & \varepsilon_{\mathbf{k}+\mathbf{q}} \Big[U_{\alpha,\mathbf{k}}^\sigma U_{\beta,\mathbf{p}}^\sigma\,\hat{b}_{\alpha,\mathbf{k}}^\dagger\,\hat{b}_{\beta,\mathbf{p}} + U_{\alpha,\mathbf{k}}^\sigma V_{\beta,\mathbf{p}}^\sigma\hat{b}_{\alpha,\mathbf{k}}^\dagger\,\hat{b}_{\beta,-\mathbf{p}}^\dagger \qquad (5.50) \\
& + V_{\alpha,\mathbf{k}}^\sigma U_{\beta,\mathbf{p}}^\sigma\,\hat{b}_{\alpha,-\mathbf{k}}\,\hat{b}_{\beta,\mathbf{p}} + V_{\alpha,\mathbf{k}}^\sigma V_{\beta,\mathbf{p}}^\sigma\,\hat{b}_{\alpha,-\mathbf{k}}\,\hat{b}_{\beta,-\mathbf{p}}^\dagger \Big]\,\hat{c}_{\mathbf{q},\sigma}^\dagger\,\hat{c}_{\mathbf{k}-\mathbf{p}+\mathbf{q},\sigma} \,.
\end{aligned}
$$

The other contribution comes from expanding each operator $\hat{\psi}_\sigma(\mathbf{i})$ up to quadratic products of the fluctuations $\delta\hat{C}_a^\dagger(\mathbf{i})\,\delta\hat{C}_b(\mathbf{i})$, resulting in

$$\hat{\mathcal{H}}_{\mathrm{F}}^{(2)} \equiv -t\,\psi_0 \sum_\sigma \sum_{\langle \mathbf{i},\mathbf{j} \rangle} \left\{ \left[\delta_2\hat{\psi}_\sigma^\dagger(\mathbf{i}) + \delta_2\hat{\psi}_\sigma(\mathbf{j})\right] \hat{c}_{\mathbf{i},\sigma}^\dagger\,\hat{c}_{\mathbf{j},\sigma} + \mathrm{H.c.} \right\} \,, \qquad (5.51)$$

where the notation $\delta_2\hat{\psi}_\sigma(\mathbf{i})$ indicates the second-order expansion of $\hat{\psi}_\sigma(\mathbf{i})$. Although the right-hand side of Eq. (5.51) is of the same order of Eq. (5.50), we always find that the expectation values comprising the operator $\delta_2\hat{\psi}_\sigma(\mathbf{i})$ are appreciable only in the strongly-interacting metallic phase and, however, negligible relative to averages

incorporating the first-order expansion $\delta_1 \hat{\psi}_\sigma(\mathbf{i})$ [131]. Therefore, being the operator (5.51) also proportional to the square root of the quasiparticle weight ψ_0 – which is rather small or zero for strong enough interactions –, we neglect its effect on the effective boson-quasiparticle interaction.

Now, the integration of bosons in (5.50) yields two distinct terms. The lowest-order one is simply given by the mean-field decoupling of the right-hand side of $\hat{\mathcal{H}}_{\mathrm{F}}^{(2)}$ with respect to the bosonic ground state and reads

$$\hat{\mathcal{H}}_{\mathrm{F}}^{(2,1)} = \frac{1}{V} \sum_\sigma \sum_\alpha \sum_{\mathbf{k},\mathbf{q}} \left| V_{\alpha,\mathbf{q}}^\sigma \right|^2 \varepsilon_{\mathbf{k}+\mathbf{q}} \, \hat{c}_{\mathbf{k},\sigma}^\dagger \, \hat{c}_{\mathbf{k},\sigma} \,, \tag{5.52}$$

at zero temperature. Using the fact that $V_{\alpha,\mathbf{k}}^\sigma$ is always an even function of $\mathbf{k}$, it is straightforward to verify that $\hat{\mathcal{H}}_{\mathrm{F}}^{(2,1)}$ yields an additional positive shift of the hopping energy,

$$\Delta t_{2,1} \equiv -\frac{1}{z \, V} \sum_\alpha \sum_\mathbf{q} |V_{\alpha,\mathbf{q}}|^2 \, \varepsilon_\mathbf{q} > 0 \,. \tag{5.53}$$

In the second place, as our theory takes advantage of Wick's theorem for splitting higher-order correlators of the modes $\hat{b}_{\alpha,\mathbf{k}}$, the next-order term derives from integrating out the quadratic moments of (5.50) at the price of calculating two-particle propagators of the kind $D^{(2)} = -i \, \mathcal{T}_{t-t'} \left\langle \hat{b}_{\alpha,\mathbf{k}}(t) \, \hat{b}_{\beta,\mathbf{p}}(t) \, \hat{b}_{\gamma,\mathbf{k}'}^\dagger(t') \, \hat{b}_{\delta,\mathbf{p}'}^\dagger(t') \right\rangle$. In this way, neglecting the frequency dependence of $D^{(2)}$ as before, we obtain a straightforward correction to the effective time-local interaction (5.46),

$$\begin{aligned} \hat{\mathcal{H}}_{\mathrm{F}}^{(2)} \approx{} & \hat{\mathcal{H}}_{\mathrm{F}}^{(1)} + \hat{\mathcal{H}}_{\mathrm{F}}^{(2,1)} \\ & - \frac{1}{V^2} \sum_{\sigma,\sigma'} \sum_{\alpha,\beta} \sum_{\mathbf{k},\mathbf{k}',\mathbf{p},\mathbf{q}} \frac{1}{\omega_{\alpha,\mathbf{p}} + \omega_{\beta,\mathbf{p}-\mathbf{q}}} \left(U_{\alpha,\mathbf{p}}^2 \, V_{\beta,\mathbf{p}-\mathbf{q}}^2 \, \varepsilon_{\mathbf{k}+\mathbf{p}} \, \varepsilon_{\mathbf{k}'+\mathbf{p}-\mathbf{q}} \right. \\ & \left. + U_{\alpha,\mathbf{p}} \, U_{\beta,\mathbf{p}-\mathbf{q}} \, V_{\alpha,\mathbf{p}} \, V_{\beta,\mathbf{p}-\mathbf{q}} \, \varepsilon_{\mathbf{k}+\mathbf{p}} \, \varepsilon_{\mathbf{k}'-\mathbf{p}} \right) \hat{c}_{\mathbf{k}\sigma}^\dagger \, \hat{c}_{\mathbf{k}'\sigma'}^\dagger \, \hat{c}_{\mathbf{k}'-\mathbf{q}\sigma'} \, \hat{c}_{\mathbf{k}+\mathbf{q}\sigma} \,. \end{aligned} \tag{5.54}$$

Consistently with the physical arguments leading to Eq. (5.48), the two-boson Hartree diagram generated by $\hat{\mathcal{H}}_{\mathrm{F}}^{(2)}$ [see Figure 5.2(c)] implies another simple renormalisation of the quasiparticle energy dispersion, such that the full hopping shift due to boson-mediated interactions becomes

$$\begin{aligned} \frac{\Delta t_\Sigma}{t} &\equiv \frac{\Delta t_1 + \Delta t_{2,2}}{t} \\ &= 4 \, z \, T \, \psi_0^2 \sum_\alpha \frac{(U_{\alpha,\mathbf{0}} + V_{\beta,\mathbf{0}})^2}{\omega_{\alpha,\mathbf{0}}} + \frac{2 \, T}{z \, t^2 \, V} \sum_{\alpha,\beta,\mathbf{k}} \frac{(U_{\alpha,\mathbf{k}} \, V_{\beta,\mathbf{k}} + U_{\beta,\mathbf{k}} \, V_{\alpha,\mathbf{k}})^2}{\omega_{\alpha,\mathbf{k}} + \omega_{\beta,\mathbf{k}}} \, \varepsilon_\mathbf{k}^2 > 0 \,. \end{aligned} \tag{5.55}$$

Importantly and not accidentally, Δt_Σ turns out to be identical (apart from a constant) to the static and uniform hopping susceptibility for the bosonic excitations of the system (see Appendix C.3 a more detailed discussion).

Kinetic effect of two-particle bosonic correlations

Due to the inclusion of higher-order bosonic correlations, the overall hopping renormalisation $\Delta t = \Delta t_{2,1} + \Delta t_\Sigma$ is now generally finite even in the MI, where quantum fluctuations are triggered by the hopping of the doublon-holon pairs described by our theory. Moreover, we observe that order-by-order interaction channels have the global effect of enhancing the coherence of the underlying quasiparticles. Interestingly, these

results exhibit a remarkable agreement with those recent works proposing the doublon-holon binding mechanism as an essential feature of the MIT [319, 320]. Also, within our physical scenario, the onset of the MI phase is associated with a peculiar separation between charge and magnetic degrees of freedom, with the latter replacing Fermi quasiparticles in the form of gapless spin excitations whose renormalized dispersion lifts the huge degeneracy of local moments (see again [134, 318]). Notably, our simple treatment of collective modes recovers such non-trivial physics with an original focus on the kind of correlations involved. Also, we point out that the identification of the residual fermionic excitations in the MI region with spin fluctuations provides a natural explanation for the finiteness of the hopping renormalisation Δt in the absence of Fermi quasiparticles. Actually, from the perspective of the one-body propagator (5.68), the quasiparticle weight $|\psi_0|^2$ can be regarded as the only well-defined marker of a Fermi liquid. A formal calculation of the feedback of Δt on $|\psi_0|^2$ would require to solve the TDGE self-consistently with respect to quantum fluctuations, a task that goes well beyond the scope of this work.

5.4 Quantum fluctuations in relevant observables

In the previous Sections, we have developed a quantum theory of the bosonic collective excitations on top of the Gutzwiller mean-field state and developed a consistent procedure for systematically including quantum fluctuations into the computation of a generic observable. In addition, we have explored the possibility of reincluding the effect of the coupling between bosons and fermionic quasiparticles as an effective interaction between the latter.

In the following, we will put these concepts into practice through the explicit evaluation of both one- and two-body correlations of interest, in order to highlight the ability of our method to deal with non-trivial quantum fluctuations. For illustrative purposes, we limit our semi-analytical calculations to zero temperature only as done in the previous Chapters.

5.4.1 Green's function

The first example of quantum correlation that we can easily determine through our quantum theory is the Green's function

$$
\begin{aligned}
G_{\sigma\sigma'}(\mathbf{i},\mathbf{j};t) &\equiv -i\left\langle T_t\left[\hat{c}_{\mathbf{i},\sigma}(t)\,\hat{c}^\dagger_{\mathbf{j},\sigma'}\right]\right\rangle_G \\
&= -i\,\theta(t)\left\langle\hat{c}_{\mathbf{i},\sigma}(t)\,\hat{c}^\dagger_{\mathbf{j},\sigma'}\right\rangle_G + i\,\theta(-t)\left\langle\hat{c}^\dagger_{\mathbf{j},\sigma'}\,\hat{c}_{\mathbf{i},\sigma}(t)\right\rangle_G,
\end{aligned}
\tag{5.56}
$$

where $\langle\cdot\rangle_G$ labels the average over the Gutzwiller ansatz (5.1). Under the GA, Eq. (5.56) becomes

$$
\begin{aligned}
G_{\sigma\sigma'}(\mathbf{i},\mathbf{j};t) =\ &-i\,\theta(t)\,\psi_\sigma(\mathbf{i},t)\,\psi^*_{\sigma'}(\mathbf{j})\left\langle\hat{c}_\sigma(\mathbf{i},t)\,\hat{c}^\dagger_{\sigma'}(\mathbf{j})\right\rangle_0 \\
&+i\,\theta(-t)\,\psi^*_{\sigma'}(\mathbf{j})\,\psi_\sigma(\mathbf{i},t)\left\langle\hat{c}^\dagger_{\sigma'}(\mathbf{j})\,\hat{c}_\sigma(\mathbf{i},t)\right\rangle_0,
\end{aligned}
\tag{5.57}
$$

where now the average symbol $\langle\cdot\rangle_0$ refers to the fermionic state $|\Psi_0\rangle$. After promoting the renormalisation fields $\psi_\sigma(\mathbf{i},t)$ to operators, expanding up to second-order in the

fluctuations and averaging over the bosonic ground state, we obtain

$$
\begin{aligned}
G_{\sigma\sigma'}(\mathbf{i}, \mathbf{j}; t) = & -i\,\theta(t)\,\psi_{0,\sigma}\,\psi_{0,\sigma'}^*\,\left\langle \hat{c}_\sigma(\mathbf{i}, t)\,\hat{c}_{\sigma'}^\dagger(\mathbf{j}) \right\rangle_0 \\
& + i\,\theta(-t)\,\psi_{0,\sigma'}^*\,\psi_{0,\sigma}\,\left\langle \hat{c}_{\sigma'}^\dagger(\mathbf{j})\,\hat{c}_\sigma(\mathbf{i}, t) \right\rangle_0 \\
& - i\,\theta(t)\,\left\langle \delta_1\hat{\psi}_\sigma(\mathbf{i}, t)\,\delta_1\hat{\psi}_{\sigma'}^\dagger(\mathbf{j}) \right\rangle \left\langle \hat{c}_\sigma(\mathbf{i}, t)\,\hat{c}_{\sigma'}^\dagger(\mathbf{j}) \right\rangle_0 \\
& + i\,\theta(-t)\,\left\langle \delta_1\hat{\psi}_{\sigma'}^\dagger(\mathbf{j})\,\delta_1\hat{\psi}_\sigma(\mathbf{i}, t) \right\rangle \left\langle \hat{c}_{\sigma'}^\dagger(\mathbf{j})\,\hat{c}_\sigma(\mathbf{i}, t) \right\rangle_0 .
\end{aligned}
\tag{5.58}
$$

where $\delta_1\hat{\psi}_\sigma(\mathbf{i}, t)$ is the very same Bose field operator defined in Eq. (5.44). Inspecting the Hamiltonian (5.29), we clearly recognise that the operator (5.44) controls the one-body coherence of the bosonic DoF hopping on the lattice as it occurs in the QGA description of BH models: in fact, it annihilates (creates) a collective excitation $(\alpha, \mathbf{k})$ according to the particle (hole) amplitudes $U_{\alpha,\mathbf{k}}^\sigma$ ($V_{\alpha,\mathbf{k}}^\sigma$). Specularly, we can physically identify the object (5.44) with quantised fluctuations of the quasiparticle weight of fermionic excitations. For completeness, we specify that the operator expansion (5.44) and the spectral weights $U_{\alpha,\mathbf{k}}^\sigma$ ($V_{\alpha,\mathbf{k}}^\sigma$) follow directly from evaluating first-order derivatives of the renormalisation matrix (5.10) with respect to fluctuations. More explicitly, we have

$$
\begin{aligned}
U_{\gamma,\mathbf{k}}^\sigma \equiv & \, N_\sigma \sum_a \left[\left(C_a^0\right)^* u_{\gamma,\mathbf{k},a+\sigma} + C_a^0\, v_{\gamma,\mathbf{k},a-\sigma} \right] \\
& + \psi_0\,M_\sigma \sum_a d_a \left[\left(C_a^0\right)^* u_{\gamma,\mathbf{k},a} + C_a^0\, v_{\gamma,\mathbf{k},a} \right] ,
\end{aligned}
\tag{5.59a}
$$

$$
\begin{aligned}
V_{\gamma,\mathbf{k}}^\sigma \equiv & \, N_\sigma \sum_a \left[\left(C_a^0\right)^* u_{\gamma,\mathbf{k},a-\sigma} + C_a^0\, v_{\gamma,\mathbf{k},a+\sigma} \right] \\
& + \psi_0\,M_\sigma \sum_a d_a \left[C_a^0\, u_{\gamma,\mathbf{k},a} + \left(C_a^0\right)^* v_{\gamma,\mathbf{k},a} \right] ,
\end{aligned}
\tag{5.59b}
$$

where the notation $a \pm \sigma$ stands for the local state a from which a particle with spin σ has been added (removed).

Here we open a formal, yet insightful parenthesis on the particle statistics encoded in the Bose field $\delta_1\hat{\psi}_\sigma(\mathbf{i})$. For $U/t \gg 1$, the bosonic particle-hole amplitudes are numerically found to fulfil the sum rule

$$
\sum_\alpha \left[U_{\alpha,\mathbf{k}}^\sigma \left(U_{\alpha,\mathbf{k}}^{\sigma'}\right)^* - \left(V_{\alpha,\mathbf{k}}^\sigma\right)^* V_{\alpha,\mathbf{k}}^{\sigma'} \right] \approx 1 - \langle \hat{n} \rangle ,
\tag{5.60}
$$

where $\langle \hat{n} \rangle$ is the lattice filling. Additionally, the very same equality is always valid at PHS. Thus, we can readily show that the operator (5.44) satisfies the commutation relation

$$
\left[\delta_1\hat{\psi}_\sigma(\mathbf{i}), \delta_1\hat{\psi}_{\sigma'}^\dagger(\mathbf{j}) \right] \approx \delta_{\mathbf{i},\mathbf{j}}\,(1 - \langle \hat{n} \rangle)
\tag{5.61}
$$

in the same regime. It is interesting to notice that the above relation strongly resembles the commutation rule $[\hat{S}_-, \hat{S}_+] = -\hat{S}_z$ between the lowering ($\hat{S}_-$) and raising ($\hat{S}_+$) spin operators under the mapping $\hat{S}_z \to \langle \hat{n} \rangle - 1$. This analogy establishes an intriguing connection between our QGA treatment of SB fluctuations and slave spin representations [314, 316, 321], providing also a justification for the physically sound description of the large-U physics offered by the latter. Indeed, in this limit $\delta_1\hat{\psi}_\sigma(\mathbf{i})$ mimics the behaviour of a hard-core boson field, reflecting the effective spin statistics

of the underlying physical particles.

Starting from Eq. (5.58), we first define the Green's function of the bosonic DoF as

$$G^{\mathrm{B}}_{\sigma\sigma'}(\mathbf{i},\mathbf{j};t) \equiv -i\,\psi_{0,\sigma}\,\psi^*_{0,\sigma'} - i\,\theta(t)\left\langle \delta_1\hat{\psi}_\sigma(\mathbf{i},t)\,\delta_1\hat{\psi}^\dagger_{\sigma'}(\mathbf{j})\right\rangle - i\,\theta(-t)\left\langle \delta_1\hat{\psi}^\dagger_{\sigma'}(\mathbf{j})\,\delta_1\hat{\psi}_\sigma(\mathbf{i},t)\right\rangle.$$
(5.62)

Therefore, considering the Green's function of the fermionic quasiparticles

$$G_0(\mathbf{i},\mathbf{j};t) \equiv \delta_{\sigma,\sigma'}\left[-i\,\theta(t)\left\langle \hat{c}_\sigma(\mathbf{i},t)\,\hat{c}^\dagger_\sigma(\mathbf{j})\right\rangle_0 + i\,\theta(-t)\left\langle \hat{c}^\dagger_\sigma(\mathbf{j})\,\hat{c}_\sigma(\mathbf{i},t)\right\rangle_0\right],$$
(5.63)

it is easy to see that the full Green's function of the theory (5.58) factorises into

$$G_{\sigma\sigma'}(\mathbf{i},\mathbf{j};t) = i\,\delta_{\sigma,\sigma'}\,G_0(\mathbf{i},\mathbf{j};t)\,G^{\mathrm{B}}_{\sigma\sigma}(\mathbf{i},\mathbf{j};t).$$
(5.64)

Whereas the mean-field decoupling between fermionic and bosonic excitations leads to a simple renormalisation of the quasiparticle Green's function $G_0(\mathbf{i},\mathbf{j};t)$ in real space, the momentum-frequency structure of $G_{\sigma\sigma'}(\mathbf{i},\mathbf{j};t)$ is less trivial and results from the convolution between the Fourier transforms of the individual propagators (5.62)-(5.63), namely

$$G_0(\mathbf{k},\omega) = \frac{1}{\omega - E_{\mathbf{k}}}$$
(5.65)

and

$$G^{\mathrm{B}}_{\sigma\sigma'}(\mathbf{k},\omega) = -2\,\pi\,i\,V\,|\psi_0|^2\,\delta(\omega)\,\delta_{\mathbf{k},0} + \sum_\alpha\left[\frac{U^\sigma_{\alpha,\mathbf{k}}\left(U^{\sigma'}_{\alpha,\mathbf{k}}\right)^*}{\omega - \omega_{\alpha,\mathbf{k}}} - \frac{\left(V^\sigma_{\alpha,\mathbf{k}}\right)^* V^{\sigma'}_{\alpha,\mathbf{k}}}{\omega + \omega_{\alpha,\mathbf{k}}}\right].$$
(5.66)

At finite temperatures, the final result for the momentum-frequency resolution of the Green's function reads

$$G_{\sigma\sigma'}(\mathbf{k},\omega) = \delta_{\sigma\sigma'}\left(\frac{|\psi_0|^2}{\omega - E_{\mathbf{k}}} + \frac{1}{V}\sum_\alpha\sum_{\mathbf{p}}\left\{\frac{\left|U^\sigma_{\alpha,\mathbf{k}-\mathbf{p}}\right|^2\left[B(\omega_{\alpha,\mathbf{k}-\mathbf{p}}) + F(-E_{\mathbf{p}})\right]}{\omega - \omega_{\alpha,\mathbf{k}-\mathbf{p}} - E_{\mathbf{p}}}\right.\right.$$
$$\left.\left.+ \frac{\left|V^\sigma_{\alpha,\mathbf{k}-\mathbf{p}}\right|^2\left[B(\omega_{\alpha,\mathbf{k}-\mathbf{p}}) + F(E_{\mathbf{p}})\right]}{\omega + \omega_{\alpha,\mathbf{k}-\mathbf{p}} - E_{\mathbf{p}}}\right\}\right),$$
(5.67)

where $B(\omega)$ is the Bose distribution. Taking the zero temperature limit, Eq. (5.62) specialises into

QGA prediction for the Green's function

$$G_{\sigma\sigma'}(\mathbf{k},\omega) =$$
$$\delta_{\sigma,\sigma'}\left\{\frac{|\psi_0|^2}{\omega - E_{\mathbf{k}}} + \frac{1}{V}\sum_{\alpha,\mathbf{p}}\left[\frac{\left|U^\sigma_{\alpha,\mathbf{k}-\mathbf{p}}\right|^2\theta(\mathbf{p} > \mathbf{k}_F)}{\omega - \omega_{\alpha,\mathbf{k}-\mathbf{p}} - E_{\mathbf{p}}} + \frac{\left|V^\sigma_{\alpha,\mathbf{k}-\mathbf{p}}\right|^2\theta(\mathbf{p} < \mathbf{k}_F)}{\omega + \omega_{\alpha,\mathbf{k}-\mathbf{p}} - E_{\mathbf{p}}}\right]\right\},$$
(5.68)

where $\mathbf{k}_F$ indicates the Fermi surface momenta.

Eq. (5.68) is the first key result of the present Chapter. Despite its simplicity, the structure of $G_{\sigma\sigma'}(\mathbf{k},\omega)$ offers an intuitive visualisation of the elementary excitations steering one-body correlations. We first observe that the physical meaning of the

bosonic particle-hole amplitudes $U^\sigma_{\alpha,\mathbf{k}}$ ($V^\sigma_{\alpha,\mathbf{k}}$) is now self-explanatory: they tune the spectral weights according to which the collective modes are excited in the particle (hole) channel above (below) the Fermi sea. Furthermore, we note that the poles of $G_{\sigma\sigma'}(\mathbf{k}, \omega)$ can be identified with a non-obvious combination between a quasiparticle excitation $E_\mathbf{p}$ and the ensemble of bosonic modes $\pm\omega_{\alpha,\mathbf{k}-\mathbf{p}}$, resulting in an overall fermionic mode dressed by bosonic excitations. On the other hand, in the MI $E_\mathbf{p} \to 0$ and quantum correlations can be entirely described in terms of doublon-holon excitations having energy spectra (5.41). We anticipate here that the semi-analytical transparency of our result proves to be a powerful tool in pinpointing the contributions of different excitations to the local DoS, as we will show in Subsection 5.5.1.

5.4.2 Equal-time charge correlations

In Subsection 5.2.4, we have argued that the QGA is particularly convenient for the calculation of two-body propagators. In fact, the latter can be completely expressed in terms of the Gutzwiller operators $\hat{C}_a(\mathbf{i})$ and the bosonic excitations of the system, which are the main ingredients of our quantum theory. We illustrate now how this advantageous feature of the QGA makes the calculation of equal-time correlations a straightforward operation as in the case of BH models.

As a typical application to quantum fluctuations beyond the one-particle level, we consider the normalised pair (or charge) correlation function

$$g(\mathbf{i}) \equiv \frac{\langle \hat{n}(\mathbf{i})\, \hat{n}(\mathbf{0}) \rangle - \langle \hat{n}(\mathbf{i}) \rangle \langle \hat{n}(\mathbf{0}) \rangle}{\langle \hat{n}(\mathbf{i}) \rangle \langle \hat{n}(\mathbf{0}) \rangle}\,. \tag{5.69}$$

Applying the usual quantisation procedure and exploiting translational invariance, Eq. (5.69) assumes the form

$$g(\mathbf{i}) = \begin{cases} \left\langle \hat{\mathcal{D}}(\mathbf{0}) \right\rangle \Big/ \left\langle \hat{\mathcal{N}}(\mathbf{0}) \right\rangle^2 - 1 & \mathbf{i} = \mathbf{0}\,, \\ \left\langle \hat{\mathcal{N}}(\mathbf{i})\, \hat{\mathcal{N}}(\mathbf{0}) \right\rangle \Big/ \left\langle \hat{\mathcal{N}}(\mathbf{0}) \right\rangle^2 - 1 & \mathbf{i} \neq \mathbf{0}\,, \end{cases} \tag{5.70}$$

where the QGA density $\hat{\mathcal{N}}(\mathbf{i})$ and square density $\hat{\mathcal{D}}(\mathbf{i})$ operators are now defined as

$$\hat{\mathcal{N}}(\mathbf{i}) \equiv \sum_a n_a\, \hat{C}^\dagger_a(\mathbf{i})\, \hat{C}_a(\mathbf{i})\,, \tag{5.71a}$$

$$\hat{\mathcal{D}}(\mathbf{i}) \equiv \sum_a n_a^2\, \hat{C}^\dagger_a(\mathbf{i})\, \hat{C}_a(\mathbf{i})\,, \tag{5.71b}$$

respectively, where n_a indicates the number of particles in the local Fock state $|a, \mathbf{i}\rangle$. As done in the previous Chapters, the expectation values of Eqs. (5.70) are evaluated by expanding the operators (5.70) up to fourth order in the fluctuations $\delta\hat{C}_a(\mathbf{i})$, with special care for the off-site correlator. As a final result, after defining the single-excitation

$$N_{\alpha,\mathbf{k}} \equiv \sum_c n_c\, C^0_c\, (u_{\alpha,\mathbf{k},c} + v_{\alpha,\mathbf{k},c}) \tag{5.72}$$

and two-excitation

$$W_{\alpha,\mathbf{k}|\beta,\mathbf{p}} \equiv \sum_c (n_c - n_0)\, u_{\alpha,\mathbf{k},c}\, v_{\beta,\mathbf{p},c} \tag{5.73}$$

structure factors of the collective modes in the charge channel, we obtain closed-form expressions for on-site

$$g(\mathbf{i} = \mathbf{0}) = \frac{D_0 + 1/V \sum_{\alpha,\mathbf{k},c} \left(n_c^2 - D_0\right) \left|v_{\alpha,\mathbf{k},c}\right|^2}{\left[n_0 + 1/V \sum_{\alpha,\mathbf{k},c} \left(n_c - n_0\right) \left|v_{\alpha,\mathbf{k},c}\right|^2\right]^2} - 1\,, \tag{5.74}$$

and non-local

$$
\begin{aligned}
g(\mathbf{i} \neq \mathbf{0}) = {} & \frac{1/V \sum_{\alpha,\mathbf{k}} \left|N_{\alpha,\mathbf{k}}\right|^2 \cos\left(\mathbf{k} \cdot \mathbf{i}\right)}{\left[n_0 + 1/V \sum_{\alpha,\mathbf{k},c} \left(n_c - n_0\right) \left|v_{\alpha,\mathbf{k},c}\right|^2\right]^2} + \\
& + \frac{1/V^2 \sum_{\alpha,\beta,\mathbf{k},\mathbf{p}} \left|W_{\alpha,\mathbf{k}|\beta,\mathbf{p}} + W_{\beta,\mathbf{p}|\alpha,\mathbf{k}}\right|^2 \cos\left[(\mathbf{k} + \mathbf{p}) \cdot \mathbf{i}\right]}{2 \left[n_0 + 1/V \sum_{\alpha,\mathbf{k},c} \left(n_c - n_0\right) \left|v_{\alpha,\mathbf{k},c}\right|^2\right]^2}\,,
\end{aligned}
\tag{5.75}
$$

charge correlations at zero temperature.

A few remarks on the above results are in order. As long as non-local charge correlations (5.75) are concerned, our approach entails a clean separation of those fluctuations due to individual collective modes from correlations due to two-mode vertices. This outcome suggests a close relationship between *non-local* two-body correlations and the excitation of multiple bosonic modes. On the contrary, within our theory multi-mode processes do not participate superficially in *local* correlations, which however are strongly affected by the non-linearity introduced by the normalisation operator $\hat{A}(\mathbf{i})$, which is believed to give the lowest-order feedback of quantum fluctuations onto the mean-field predictions n_0 and D_0.

In Subsection 5.5.2, we will show that all the types of higher-order fluctuations pointed out before share a common physical side, as they turn out to have a significant weight close to and beyond the MIT. This is immediately evident in the case of non-local correlations (5.75), as the single-mode structure factors (5.72) weighing *linear-order* density fluctuations are known to vanish identically in the MI state [51, 131].

5.4.3 Charge and spin susceptibilities

Linear response theory within the GA framework [65, 308] addresses the calculation of n-particle propagators by adding suitable perturbations to the Hamiltonian of the system and determining the properties of RPA-type fluctuations for each kind of response. By contrast, our approach is able to access many-body correlations directly by means of its built-in quantum formalism, so that the spectral features of a given response channel are calculated more efficiently and up to arbitrary orders in the fluctuations. In this regard, we show below how the flexibility of our method applies to the estimation of the proper susceptibilities of the system.

Charge and magnetic response functions in momentum-frequency space are formally defined by

$$\chi_c(\mathbf{q}, \omega) \equiv -i \int dt\, e^{i\left(\omega + i\, 0^+\right)t} \sum_{\mathbf{i}} e^{-i\,\mathbf{q}\,\mathbf{i}} \left\langle \left[\hat{\mathcal{N}}(\mathbf{i}, t), \hat{\mathcal{N}}(\mathbf{0}, 0)\right] \right\rangle\,, \tag{5.76}$$

and

$$\chi_s(\mathbf{q},\omega) \equiv -i \int dt\, e^{i(\omega+i\,0^+)t} \sum_{\mathbf{i}} e^{-i\,\mathbf{q}\,\mathbf{i}} \left\langle \left[\hat{S}_z(\mathbf{i},t), \hat{S}_z(\mathbf{0},0) \right] \right\rangle, \qquad (5.77)$$

respectively, where the infinitesimal frequency shift $\omega \to \omega + i\,0^+$ regularises the results at large negative times. Here we define the QGA spin operator as

$$\hat{S}_z(\mathbf{i}) \equiv \frac{1}{2}\left[\hat{\mathcal{N}}_\uparrow(\mathbf{i}) - \hat{\mathcal{N}}_\downarrow(\mathbf{i}) \right] = \sum_a s_a\, \hat{C}_a^\dagger(\mathbf{i})\, \hat{C}_a(\mathbf{i}), \qquad (5.78)$$

where

$$\hat{\mathcal{N}}_\sigma(\mathbf{i}) \equiv \sum_a n_{a,\sigma}\, \hat{C}_a^\dagger(\mathbf{i})\, \hat{C}_a(\mathbf{i}) \qquad (5.79)$$

is the spin-resolved density operator, with $n_{a,\sigma} = \delta_{a,\sigma} + \delta_{a,2}$ indicating the number of particles with spin σ in the local state $|a,\mathbf{i}\rangle$, such that $s_a = \left(n_{a,\uparrow} - n_{a,\downarrow}\right)/2$. Operatively, we proceed by unfolding the density and spin operators up to second order in the quantised modes $\hat{b}_{\alpha,\mathbf{k}}$ as usual and switching to the interaction picture

$$\hat{b}_{\alpha,\mathbf{k}} \longrightarrow \hat{b}_{\alpha,\mathbf{k}}(t) \equiv e^{-i\,\omega_{\alpha,\mathbf{k}}\,t}\, \hat{b}_{\alpha,\mathbf{k}}. \qquad (5.80)$$

At zero temperature, the final expression of the charge susceptibility reads

$$\chi_c(\mathbf{q},\omega) = 2 \underbrace{\sum_\alpha \frac{|N_{\alpha,\mathbf{q}}|^2\, \omega_{\alpha,\mathbf{q}}}{(\omega + i\,0^+)^2 - \omega_{\alpha,\mathbf{q}}^2}}_{\chi_c^{[1]}(\mathbf{q},\omega)} + \frac{2}{V} \underbrace{\sum_{\alpha,\beta,\mathbf{k}} \frac{\mathcal{W}_{\alpha,\mathbf{k}|\beta,\mathbf{k}+\mathbf{q}}\left(\omega_{\alpha,\mathbf{k}} + \omega_{\beta,\mathbf{k}+\mathbf{q}}\right)}{(\omega + i\,0^+)^2 - \left(\omega_{\alpha,\mathbf{k}} + \omega_{\beta,\mathbf{k}+\mathbf{q}}\right)^2}}_{\chi_c^{[2]}(\mathbf{q},\omega)},$$

$$(5.81)$$

where we have defined the two-mode spectral weights

$$\mathcal{W}_{\alpha,\mathbf{k}|\beta,\mathbf{p}} \equiv \left| W_{\alpha,\mathbf{k}|\beta,\mathbf{p}} \right|^2 + W_{\alpha,\mathbf{k}|\beta,\mathbf{p}}\, W_{\beta,\mathbf{p}|\alpha,\mathbf{k}}^*, \qquad (5.82)$$

attached to direct (W^2) and exchange ($W \cdot W$) scattering vertices between pairs of collective modes in the charge channel. A similar result holds also for the spin susceptibility $\chi_s(\mathbf{q},\omega)$, which is calculated explicitly in Appendix C.3. Similarly to the result for non-local pair correlations, we observe that the QGA provides a clear visualisation of the single-mode $\left(\chi^{[1]}\right)$ and two-mode $\left(\chi^{[2]}\right)$ bosonic correlations contributing to the susceptibilities. Moreover, since our approach accounts for the full momentum-frequency structure of $\chi_{c(s)}(\mathbf{q},\omega)$, we are also in the position of characterising dynamical correlations with the minimum numerical effort, as well as without any initial assumption on the dynamics of specific observables [301].

In the same spirit, we have at our disposal a simple way for estimating the reducible vertex functions or two-particle self-energies, defined through the celebrated Bethe-Salpeter equations

$$\Gamma_c(\mathbf{q},\omega) = \chi_0(\mathbf{q},\omega)^{-1} - \chi_c(\mathbf{q},\omega)^{-1}, \qquad (5.83a)$$

$$\Gamma_s(\mathbf{q},\omega) = \left[\chi_0(\mathbf{q},\omega)/4\right]^{-1} - \chi_s(\mathbf{q},\omega)^{-1}, \qquad (5.83b)$$

where $\chi_0(\mathbf{q},\omega)$ $(\chi_0/4)$ denotes the charge (spin) susceptibility of the quasiparticles,

given by the Lindhard function

$$
\begin{aligned}
\chi_0(\mathbf{q}, \omega) &\equiv -\frac{2\,i}{V} \int \frac{d\nu}{2\,\pi} \sum_{\mathbf{k}} G_0(\mathbf{k} + \mathbf{q}, \nu)\, G_0(\mathbf{k}, \nu - \omega) \\
&= \frac{2}{V} \sum_{\mathbf{k}} \frac{F(E_{\mathbf{k}}) - F(E_{\mathbf{k}+\mathbf{q}})}{\omega + E_{\mathbf{k}} - E_{\mathbf{k}+\mathbf{q}}} \,.
\end{aligned}
\tag{5.84}
$$

In view of benchmarking our predictions, we restrict ourselves to the analysis of static response measures as the compressibility

$$
\kappa = -\chi_c(\mathbf{q} \to \mathbf{0}, \omega = 0)
\tag{5.85}
$$

and the uniform spin susceptibility

$$
\chi = -\chi_s(\mathbf{q} \to \mathbf{0}, \omega = 0)\,.
\tag{5.86}
$$

According to Eq. (5.81), the collective modes linked to density or spin fluctuations could be regarded as the main actors of the dynamical response of the system. This physical scenario is however incomplete: indeed, a sizeable modification to the vertex functions (5.83) comes into play when taking into account the quasiparticle hopping renormalisation Δt given by the coupling with the bosonic modes, as we discuss now in depth.

5.4.4 Renormalisation of the response functions

In practical terms, the most evident consequence of the hopping renormalisation Δt is to induce a change in the density (spin) susceptibility of fermions: without loss of generality, this can be rewritten as

$$
\chi_0'(\mathbf{k}, \omega) = \frac{\chi_0(\mathbf{k}, \omega)}{1 - \delta\Gamma(\mathbf{k}, \omega)\, \chi_0(\mathbf{k}, \omega)}\,,
\tag{5.87}
$$

where we have defined the vertex shift $\delta\Gamma(\mathbf{k}, \omega)$ produced by interactions. Accordingly, making the substitution $\chi_0(\mathbf{k}, \omega) \to \chi_0'(\mathbf{k}, \omega)$ into the Bethe-Salpeter equations, the reducible vertex functions acquire a net shift

$$
\begin{aligned}
\Gamma_{c(s)}'(\mathbf{k}, \omega) &= \Gamma_{c(s)}(\mathbf{k}, \omega) + \delta\Gamma_{c(s)}(\mathbf{k}, \omega) \\
&= \Gamma_{c(s)}(\mathbf{k}, \omega) + \delta\Gamma_{c(s)}^{(1)}(\mathbf{k}, \omega) + \delta\Gamma_{c(s)}^{(2)}(\mathbf{k}, \omega)\,,
\end{aligned}
\tag{5.88}
$$

where, for later convenience, we distinguish between the contributions due to first-order $\delta\Gamma_{c(s)}^{(1)}(\mathbf{k}, \omega)$ and second-order $\delta\Gamma_{c(s)}^{(2)}(\mathbf{k}, \omega)$ quantum fluctuations. Notice that the above equations allow the possibility that the coupling of fermions with the bosonic modes generates an either repulsive or attractive channel for the quasiparticles depending on the exchanged momentum (energy) $\mathbf{k}$ (ω).

Let us now unfold Eqs. (5.87)-(5.88) when applied to the computation of the compressibility (5.85) and the magnetic response (5.86), which can be treated semi-analytically. Recalling the definition of the quasiparticle susceptibility (5.84) and taking

into account the hopping shift Δt, we obtain

$$\chi_0'(\mathbf{k} \to \mathbf{0}, \omega = 0) = -\mathcal{A}_0 \left| \psi_0^2 + \Delta t/t \right|^{-1}, \tag{5.89}$$

where $\mathcal{A}_0$ is the value of the quasiparticle DoS at the chemical potential. From Eq. (5.87), it follows that

$$\delta\Gamma_c^{(i)}(\mathbf{k} \to \mathbf{0}, 0) = \frac{1}{4}\delta\Gamma_s^{(i)}(\mathbf{k} \to \mathbf{0}, 0) = \frac{|\psi_0^2 + \Delta t_i/t| - \psi_0^2}{\mathcal{A}_0}, \tag{5.90}$$

Charge/spin vertex shift from the boson-quasiparticle coupling

where the index $i = 1, 2$ refers to the order of quantum fluctuations included. Finally, the renormalised compressibility κ' and spin susceptibility χ' can be found by recalculating $\chi_{c(s)}(\mathbf{k}, \omega)$ according to the Bethe-Salpeter equations (5.83) after either (i) replacing $\chi_0(\mathbf{k}, \omega)$ with the right-hand side of Eq. (5.89) or (ii) modifying the reducible vertex functions according to Eq. (5.90). As a result, we obtain

$$\kappa' = -\left[\chi_0^{-1}(\mathbf{k} \to \mathbf{0}, 0) - \Gamma_c'(\mathbf{k} \to \mathbf{0}, 0)\right]^{-1} = \left[\psi_0^2/\mathcal{A}_0 + \Gamma_c'(\mathbf{k} \to \mathbf{0}, 0)\right]^{-1}, \tag{5.91a}$$

$$\chi' = -\left[4\,\chi_0^{-1}(\mathbf{k} \to \mathbf{0}, 0) - \Gamma_s'(\mathbf{k} \to \mathbf{0}, 0)\right]^{-1} = \left[4\,\psi_0^2/\mathcal{A}_0 + \Gamma_s'(\mathbf{k} \to \mathbf{0}, 0)\right]^{-1}. \tag{5.91b}$$

The significant deviations in κ and χ due to the boson-quasiparticle coupling are discussed in detail in Secs. 5.5.3-5.5.4. We anticipate here that, as a remarkable outcome of our simple Hartree-Fock calculations, the effective quasiparticle interaction (5.54) brings about a finite spin susceptibility across the whole phase diagram of the model, compatibly the prediction that the normal-phase Hubbard model cannot experience magnetic ordering as it undergoes the Mott localisation [278]. It is important to underline that our findings are a genuine product of the quantum formalism hereby developed and cannot be accessed by linear response theory, which does not cover the higher-order coupling channels inherently encoded in the effective interaction $\hat{\mathcal{H}}_{\mathrm{F}}^{(2)}$.

5.5 Results for the 2D paramagnetic Hubbard model

We now proceed to present the numerical results obtained by the application of our approach to the ground state of the Hubbard model (5.8) in its normal phase for a 2D square lattice at zero temperature. All the numerical results reported hereafter have been obtained for a 60×60 lattice in order to avoid possible finite size effects.

5.5.1 How collective modes shape the DoS

The DoS of the system $A_\sigma(\mathbf{k}, \omega)$ can be derived straightforwardly from the Green's function through the well-known relation $A_\sigma(\mathbf{k}, \omega) = -2\,\mathrm{Im}\big[G_{\sigma\sigma}(\mathbf{k}, \omega + i\,0^+)\big]$. From
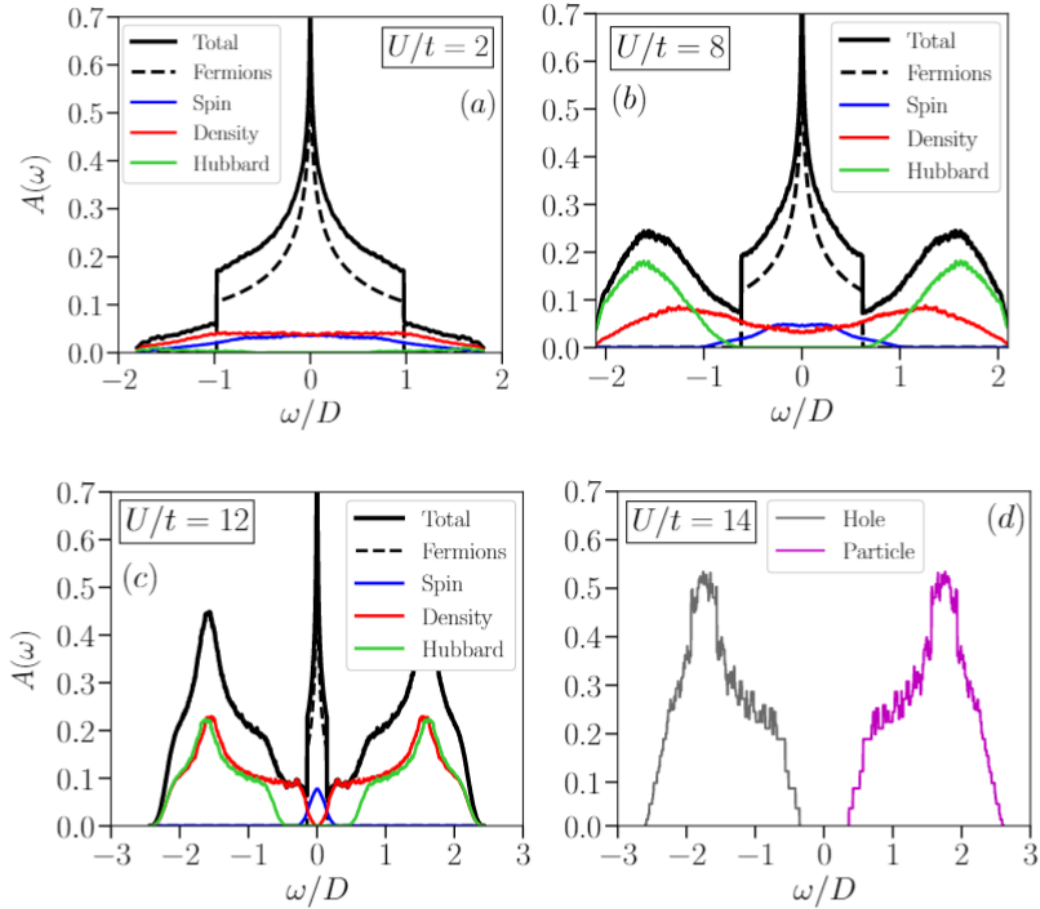
Figure 5.3: Local DoS $A_\sigma(\omega)$ of the paramagnetic Hubbard model for (a) $U/t = 2$, (b) $U/t = 8$, (c) $U/t = 12$, (d) $U/t = 14$ (MI) at PHS. The frequency integral of $A_\sigma(\omega)$ is normalised to 1 as usual. The MIT takes place at the mean-field critical point $U_c = 16\,z\,T \simeq 12.97\,t$. The energy scale is fixed by the non-interacting half bandwidth $D = z\,t$. For panels from (a) to (c), the DoS is split into the contributions of: fermionic quasiparticles (black dotted lines), Landau's density mode (red solid lines), spin sound mode (blue solid lines) and Hubbard optical mode (green solid lines). The overall DoS is highlighted by a black solid line. In panel (d), the DoS of doublon (holon) excitations is identified by a violet (gray) solid line.

Eq. (5.68), at zero temperature we obtain

$$A_\sigma(\mathbf{k}, \omega) = |\psi_0|^2\, \delta(\omega - E_\mathbf{k}) + \frac{1}{V} \sum_\alpha \sum_{\mathbf{p} > \mathbf{k_F}} \left| U^\sigma_{\alpha, \mathbf{k-p}} \right|^2 \delta(\omega - \omega_{\alpha, \mathbf{k-p}} - E_\mathbf{p})$$
$$+ \frac{1}{V} \sum_\alpha \sum_{\mathbf{p} < \mathbf{k_F}} \left| V^\sigma_{\alpha, \mathbf{k-p}} \right|^2 \delta(\omega + \omega_{\alpha, \mathbf{k-p}} - E_\mathbf{p}) \,. \tag{5.92}$$

As a by-product of the key result (5.68), Eq. (5.92) provides a transparent interpretation of the spectral structure of the DoS, since we can distinguish unambiguously between different contributions due to the fermionic quasiparticles and their coupling with the collective modes of the system. In particular, this can serve the purpose of giving a precise identity to the kind of excitations moulding the so-called *Hubbard bands*, as we discuss in the following.

Figure 5.3 shows our numerical results for the (normalised) local DoS $A_\sigma(\omega) = 1/V \sum_\mathbf{k} A_\sigma(\mathbf{k}, \omega)$ across the MIT at PHS ($\mu = U/2$). For clarity, we decompose the total DoS [solid black line] into the fraction due to the quasiparticles [black dotted line] and

the contribution due to the bosonic modes [coloured solid lines].

For weak interactions [panel (a)], the DoS of quasiparticles starts losing spectral weight in favour of low-energy energy states covered by the Landau mode [red solid line] and spin excitations [blue solid line], whereas the weight of the Hubbard optical mode [green solid line] is almost negligible. Moreover, we observe that the DoS tails are mostly controlled by the zero sound mode and extend to energies beyond the non-interacting bandwidth $D = z\,t$. It follows that the high-energy properties of the weakly-interacting lattice can be essentially traced back to density fluctuations.

Moving to intermediate values of U/t [panel (b)], the structure of $A_\sigma(\omega)$ becomes more complex. While charge excitations are pushed to higher energies but still contribute to the population of low-energy states, a significant part of the spectral weight of quasiparticles is already transferred to energy states accessed by the Hubbard optical mode, whose spectral weight is non-zero exactly above the effective bandwidth $D_{eff} = D\,|\psi_0|^2$ subtending the quasiparticle DoS. Interestingly, both the excitations contribute to the formation of the Hubbard bands, which now appear as well-formed high-energy features. On the other hand, we observe that most part of the spectral fraction due to spin fluctuations is always enclosed by the quasiparticle DoS, a feature hinting at the Landau damping of spin excitations due to their strong coupling with the quasiparticle/quasihole continuum predicted by Fermi liquid theory [73, 277].

On the brink of the MIT [panel (c)], the DoS is almost saturated by the Hubbard bands, whose weight is now equally distributed to the density and Hubbard optical modes. At low energies, the quasiparticle DoS and the Hubbard bands are connected by a small pocket of states which are excited by the Landau mode only. Following the discussion of Section 5.2.5, this peculiar separation of energy scales closely reflects the progressive degeneracy of the zero sound and Hubbard branches, which at half filling develops at high-energy first [see panel (c) of Figure 5.1] and, for increasing U/t, moves towards $\omega = 0$, until the MIT occurs. Also, we may be tempted to identify low-energy density excitations as those states that bridge the gap between the quasiparticle DoS and the Hubbard bands and are responsible for transferring spectral weight from one to the others. It is worth mentioning that the threshold $U/t \simeq 6$ after which we observe a first clear-cut separation between the quasiparticle peak and the Hubbard bands tallies approximately with the same region where DMFT-NRG [322] and DΓA [323] calculations spot the formation of a well-defined pseudogap of $A_\sigma(\omega)$ at intermediate values of ω (upon a suitable rescaling of the MIT critical point with respect to the Gutzwiller prediction for U_c).

Finally, once the system enters the MI [panel (d)], $A_\sigma(\omega)$ splits completely into the two Hubbard bands corresponding to doublon and holon excitations, separated by a finite gap U and extending over bandwidths proportional to t/U, as expected by the well-known picture of DMFT calculations [278, 324].

5.5.2 Charge correlations

The QGA result for the local charge correlation $g(\mathbf{0})$ given by Eq. (5.74) at PHS is shown as a black solid line in the panel (a) of Figure 5.4. Our prediction well matches with both the value $g(\mathbf{0}) = 1/2$ of a non-interacting gas and the complete suppression of density fluctuations for $U/t \gg 1$ in the deep MI, where $g(\mathbf{0}) = 0$. In the metallic phase, the antibunching $g(\mathbf{0}) < 1/2$ due to the repulsive on-site interaction decreases slower
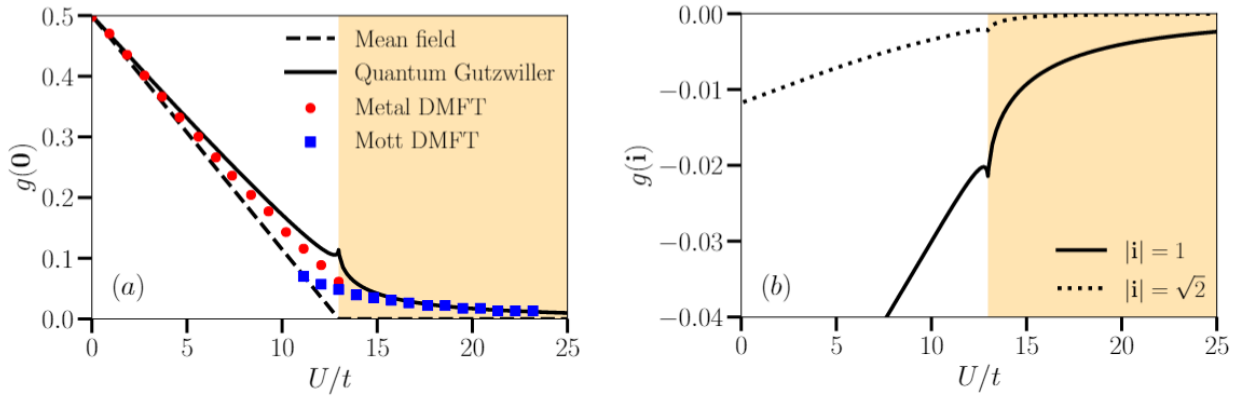
Figure 5.4: (a) On-site charge correlation $g(\mathbf{0})$ as a function of U/t at PHS. The white (orange-shaded) area indicates the metallic (MI) region. Black solid line: QGA. Black dashed line: mean-field GA. Red dots: DMFT metallic solution. Blue squares: DMFT insulating solution. In order to compare our results with the DMFT data, the critical interaction of the latter has been rescaled by a factor U_c/U_c^{DMFT} so as to make the position of the MIT point within the two approaches coincide. (b) Non-local charge correlation function $g(\mathbf{i})$ for $|\mathbf{i}| = 1$ (solid line) and $|\mathbf{i}| = \sqrt{2}$ (dotted line) as a function of U/t at PHS.

Charge fluctuations benchmarked against DMFT

than the outcome of the mean-field GA [black dashed line] upon approaching the MIT critical point. Indeed, while mean-field theory predicts a perfect antibunching of $g(\mathbf{0})$ at the MIT and beyond, the QGA result is able to account for the virtual excitation of doublon-holon pairs contributing to density fluctuations. In this respect, our method improves significantly the BR picture of the MIT [312] thanks to an accurate representation of the spectral features of the MI. Remarkably, we find that both in the weakly-interacting limit and for sufficiently strong U/t our prediction for local density fluctuations perfectly coincides with both the metallic [red dots] and insulating [blue squares] DMFT solutions, while close to the transition point our approach gives a qualitatively different result. In particular, we find that $g(\mathbf{0})$ slightly increases close to the metallic side of the MIT, showing a non-analytic behaviour across the critical point.

This peculiar behaviour finds a simple explanation in the spectral properties of the collective modes characterising the PH-symmetric MIT. In fact, the critical softening of the Hubbard mode (5.40) and its degeneracy with the zero sound excitation (5.38) make this special point to host two different coherent modes with eigenvectors scaling as $\left(\underline{u}_{\alpha,\mathbf{k}}, \underline{v}_{\alpha,\mathbf{k}}\right) \sim |\mathbf{k}|^{-1/2}$ at low $\mathbf{k}$. This singularity propagates to the structure factors of charge correlations in the expression of $g(\mathbf{i})$ and is at the roots of the cusp-like profile displayed in Figure 5.4. Therefore, the absence of gapped collective excitations appears to be the factor behind the enhancement of density fluctuations, analogous to critical opalescence [325], close to the PH-symmetric MIT. By contrast, approaching the doping-driven MIT, the Hubbard mode (5.40) retains a finite gap and an incoherent character. As a consequence, the corresponding spectral weights do not lose regularity at low $\mathbf{k}$ and a monotonous, smooth decrease of $g(\mathbf{0})$ occurs (not shown).

These findings underscore how *local* density fluctuations across the MIT are controlled by the precise spectral properties of the *non-local* quantum fluctuations accounted by our quantum theory. Nevertheless, we cannot exclude that our predictions, having their origin in a mean-field state, could overestimate the amplitude of quantum fluctuations for critically strong interactions and simply offer a qualitatively different view on local fluctuations with respect to the DMFT scenario. Also, the non-analytic

behaviour of $g(\mathbf{0})$ across the MIT could be read as a marker of the substantial back action that self-consistent fluctuations would have on the saddle-point solution around the MIT.

On an equal footing, the predictive power of our method with respect to non-local quantum fluctuations can be further explored by looking at off-site charge correlations (5.75). In panel (b) of Figure 5.4 we report the results of the QGA calculations of $g(|\mathbf{i}| = 1)$ [solid line] and $g\left(|\mathbf{i}| = \sqrt{2}\right)$ [dotted line] as functions of U/t at PHS, for which we notice again the (inverted) peaked profile of density fluctuations at the MIT point. These curves successfully reproduce the suppression of non-local charge correlations for increasing U/t caused by the Mott localisation and still predict the survival of zero-point fluctuations due to virtual doublon-holon pairs propagating in the insulating phase. This significant outcome brings further support to our approach as a simple but powerful tool for interpolating between weak and strong interactions in the description of non-trivial quantum correlations.

Non-local charge correlations from the QGA

5.5.3 Compressibility

Panel (a) of Figure 5.5 shows the behaviour of the compressibility as a function of U/t at PHS. The QGA prediction of κ as derived directly from the bosonic response function (5.85) [black dashed line] is a monotonous, decreasing function of U/t and converges continuously to zero at the MIT, signalling the suppression of uniform density fluctuations. While this result is well-known in the literature, the spectral decomposition of Eq. (5.81) makes room for a simple anatomy of those excitations that contribute the most to the compressibility. Differently from the equal-time correlations examined in Subsection 5.5.2, we find that κ is dominated by the single-mode contribution $\chi_c^{[1]}$ for all values of U/t, while the two-mode part $\chi_c^{[2]}$ is nearly negligible.

However, whereas multi-mode effects encased by the *bare* susceptibility $\chi_c(\mathbf{0}, 0)$ are unimportant, a significant contribution comes indirectly from the interaction of the quasiparticles with the bosonic modes themselves, renormalising the charge vertex function. In Figure 5.5(a), the black dotted line indicates the corrected compressibility κ' taking into account only the single-boson part $\delta\Gamma_c^{(1)}(\mathbf{q}, \omega)$ of the charge vertex shift (5.90), while the black solid line includes the full shift $\delta\Gamma_c(\mathbf{q}, \omega)$ comprising two-boson scattering processes. We observe that the main effect of boson-mediated interactions is to suppress the compressibility in the metallic phase, suggesting that $\delta\Gamma_c^{(1)}(\mathbf{q}, \omega)$ acts as an additional repulsive channel for the quasiparticles. Such suppression is maximal in the regime of moderately strong U/t and, remarkably, is even more enhanced by the two-boson correlations encoded in $\delta\Gamma_c^{(2)}(\mathbf{q}, \omega)$. Notice that, consistently with physical expectations, the non-interacting limit of κ and the MI incompressibility are not touched by its renormalisation κ', which can be regarded as a non-perturbative effect with respect to the interaction U/t.

The analogous results for the compressibility out of PHS are reported in Figure 5.5(b), where κ is calculated along the constant chemical potential line $\mu/t = 3$ crossing the doping-driven MIT [for reference, see the red solid line in Figure 5.1(a)]. Here, we still find a similar suppression of charge fluctuations induced by the boson-quasiparticle coupling, with some qualitative differences: while the single-boson channel renormalises κ at low U/t, two-boson couplings give a major correction in the strongly-interacting regime. In addition, we observe that κ reaches a finite value
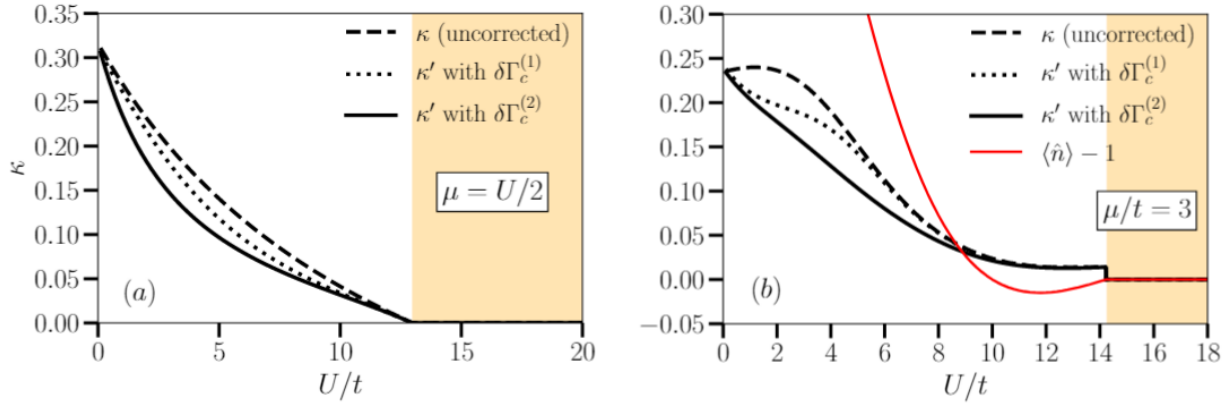
Figure 5.5: (a) Compressibility κ as a function of U/t at PHS. The white (orange-shaded) area identifies the metallic (MI) region. Dashed line: QGA prediction as given by Eq. (5.81), omitting the charge vertex shift due to the boson-quasiparticle coupling. Dotted line: correction of κ due to the lowest-order vertex shift $\delta\Gamma_c^{(1)}(\mathbf{q}, \omega)$. Solid line: correction due to the full vertex shift $\delta\Gamma_c(\mathbf{q}, \omega) = \delta\Gamma_c^{(1)}(\mathbf{q}, \omega) + \delta\Gamma_c^{(2)}(\mathbf{q}, \omega)$. (b) The analogous plot of κ across the doping-driven MIT at constant chemical potential $\mu/t = 3$. The red solid line is the density deviation from half filling.

on the metallic side of the MIT, eventually jumping to zero for $U > U_c$, a feature that evidently distinguish the doping-driven MIT from the PH-symmetric case.

This anomalous behaviour can be understood by inspecting the low-$\mathbf{q}$ structure of the bare susceptibility $\chi_c^{[1]}(\mathbf{q}, \omega)$, which is solely determined by the zero sound mode $(d, \mathbf{q})$. In the expression

$$\kappa = -\chi_c^{[1]}(\mathbf{q} \to \mathbf{0}, \omega = 0) = \frac{2\,|N_{\mathrm{d},\mathbf{q}\to\mathbf{0}}|^2}{\omega_{\mathrm{d},\mathbf{q}\to\mathbf{0}}}, \tag{5.93}$$

the density structure factor is found to scale linearly with momentum as $|N_{\mathrm{d},\mathbf{q}\to\mathbf{0}}|^2 \sim \gamma\,|\mathbf{q}|$, so that $\kappa = 2\gamma/c_d$. Now, the structure factor slope γ is always a vanishing quantity at the MI boundary; on the other hand, the zero sound velocity c_d is finite only at the PH-symmetric MIT, while it goes to zero as fast as γ for all the other critical points. Therefore, while at PHS the vanishing spectral weight of charge excitations is not accompanied by a decrease in the sound velocity, the doped MI exhibits density fluctuations whose velocity is as small as their spectral weight. Such mechanism justifies the discontinuity of κ at the doping-driven MIT that we observe in Figure 5.5(b). It is also interesting to notice that the finite jump of κ is mirrored by a discontinuity in the first-order derivative of the lattice filling across the MIT [red solid line], meaning that the dilute gas of either particles or holes doping the MI forms a compressible metallic state. Notably, these observations make the physics of the doping-driven MIT quite similar to that of the CI-type transitions in BH models: not surprisingly, this analogy is an insightful result of the QGA mapping between the collective modes of the Fermi sea and the density/spin excitations of the binary BH model, see Subsection 5.2.4.

Connection with the collective response of BH systems

5.5.4 Spin susceptibility

A similar analysis as for the compressibility predictions can be applied to the static-uniform spin susceptibility (5.86), the numerical results of which are reported in Figure 5.6 with the same colour code of Figure 5.5.

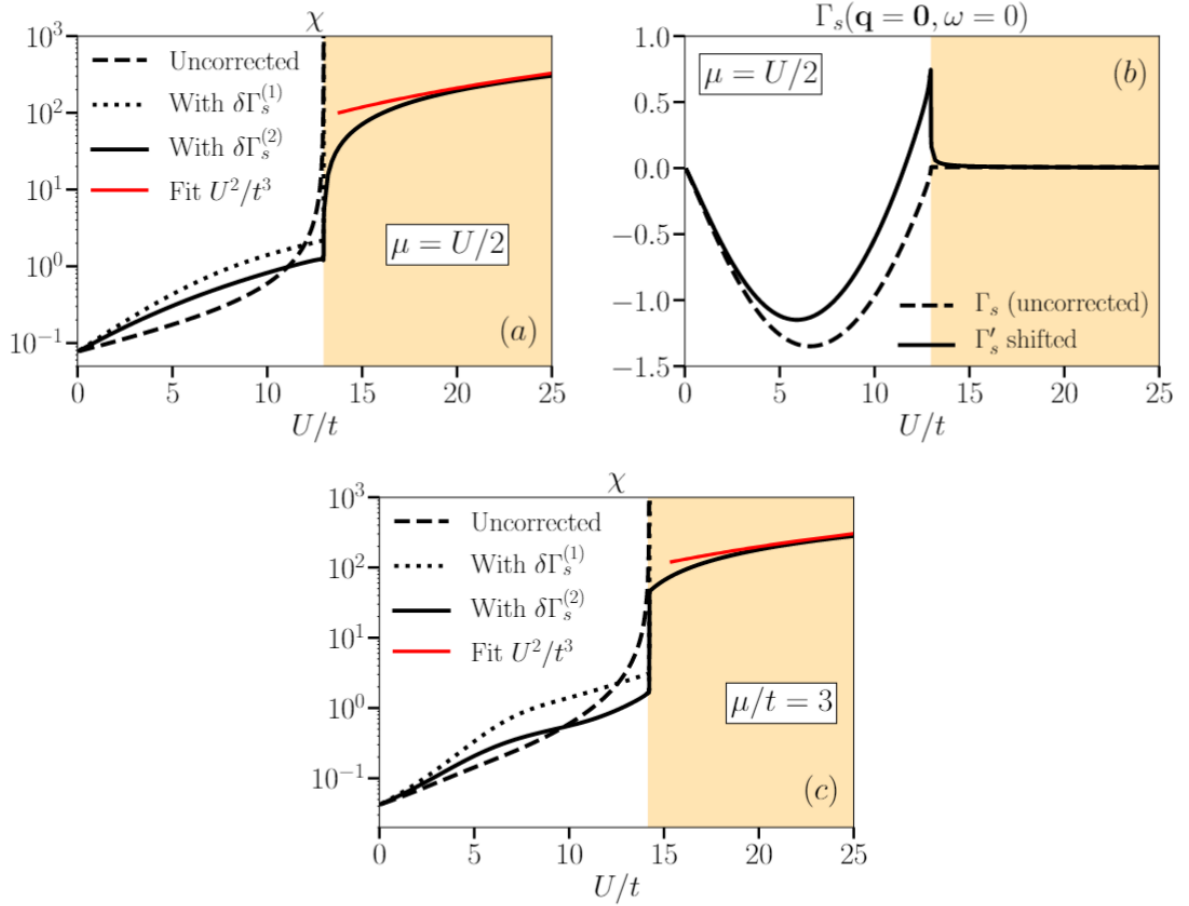At PHS [panel (a)], the QGA estimation for χ based on the bare susceptibility

Figure 5.6: (a) Static-uniform spin susceptibility χ as a function of U/t at PHS. The white (orange-shaded) area indicates the metallic (MI) region. Dashed line: QGA prediction as given by Eq. (5.86), neglecting the spin vertex shift due to the boson-quasiparticle coupling. Dotted line: correction of χ due to the lowest-order vertex shift $\delta\Gamma_s^{(1)}(\mathbf{q},\omega)$. Solid line: correction due to the full vertex shift $\delta\Gamma_s(\mathbf{q},\omega) = \delta\Gamma_s^{(1)}(\mathbf{q},\omega) + \delta\Gamma_s^{(2)}(\mathbf{q},\omega)$. Red solid line: fit of the curve U^2/t^3 against the numerical data in the deep MI. (b) Vertex function of the spin channel $\Gamma_s(\mathbf{q},\omega)$ in the static-uniform limit at PHS. (c) Spin susceptibility χ across the doping-driven MIT at constant chemical potential $\mu/t = 3$. The line style code of panels (b)-(c) is the same of panel (a).

of Eq. (5.86) is a monotonous, increasing function of U/t – the so-called Stoner enhancement of the magnetic response – and diverges as $1/(U_c - U)$ at the MIT point, thus behaving as a footprint of the formation of local magnetic moments on the verge of the insulating phase. This result is in qualitative agreement with popular GA + RPA approximate schemes [29, 307]; however, whereas a critical divergence is known to be a typical feature of the local spin susceptibility $\chi_s(\omega) \equiv 1/V \sum_{\mathbf{q}} \chi_s(\mathbf{q},\omega)$, the static-uniform response χ is correctly predicted by DMFT to have a finite value across the whole phase diagram of the paramagnetic Hubbard model [278].

Nonetheless, the apparent failure of our quantum theory in capturing the right physics of χ through the baseline Eq. (5.86) is perfectly counterbalanced by considering again the effect of the reducible vertex shift $\delta\Gamma_s(\mathbf{q},\omega)$, which in the present case takes an even more crucial role.

In Figure 5.6(a), we observe that the single-boson vertex shift $\delta\Gamma_F^{(1)}(\mathbf{q},\omega)$ not only leads to an increase in the magnetic response for intermediate interactions, but also eliminates the susceptibility divergence at the critical point. This outcome reproduces recent calculations based on an improvement of linear response theory around the

GA [65], but still contrasts with precision approaches as DMFT. In fact, the spin susceptibility is still divergent in the MI, as the first-order quasiparticle self-energy $\Sigma_\mathrm{F}^{(1)}(\mathbf{q}, \omega)$ – responsible for the vertex renormalisation – decrease proportionally to quasiparticle weight $|\psi_0|^2$, see Section 5.3. Then, we deduce that one-boson correlations, although sufficient to regularise χ on the metallic side of the MIT, do not account for all the relevant magnetic fluctuations at strong interactions.

This issue is solved by the higher-order contributions to the full spin vertex shift $\delta\Gamma_s(\mathbf{q}, \omega)$. Such correction ultimately yields the expected result: in the metallic phase, two-boson scattering processes are responsible for a general decrease of the magnetic response, which is then found to be continuous across the MIT and increases monotonously for $U > U_c$. Most importantly, we obtain that χ scales according to a power law U^2/t^3 – see the curve fitting [red solid line] in Figure 5.6(a). Such an energy scale is not a coincidence, as it naturally emerges from the close relationship between the quasiparticle self-energy $\Sigma_\mathrm{F}(\mathbf{q}, \omega)$ and kinetic correlations of doublon-holon pairs on top of the MI, whose excitation probability is exactly proportional to $(t/U)^2$ as suggested by strong-coupling perturbation theory.

Spin vertex renormalisation across the MIT

The above considerations gain further insights from the inspection of the spin vertex $\Gamma_s(\mathbf{q} \to \mathbf{0}, \omega = 0)$, reported in panel (b) of Figure 5.6. Here, we observe that the *bare* vertex as given by Eq. (5.83b) is always negative in the metallic phase and zero after the MIT, indicating that the effective interaction between magnetic DoF is at least only attractive. As boson-quasiparticle interactions are admitted, the corrected vertex $\Gamma'_s(\mathbf{0}, 0)$ undergoes a sign flip in the metallic region close to the MI boundary. Thereafter, $\Gamma'_s(\mathbf{0}, 0)$ reaches its maximum at the MIT and is a non-vanishing, decreasing function of U/t in the insulating phase, thus preventing the magnetic moments from behaving independently and developing a diverging magnetic response. We can understand this result by linking the attractive-to-repulsive transition of the effective spin coupling to the activation of the so-called superexchange mechanism for $U/t \gg 1$ – associated to the U^2/t^3 scaling of χ – and the onset of weak antiferromagnetic fluctuations, in striking agreement with the predictions of DMFT [278]. Under this perspective, going beyond a mean-field picture of the boson-fermion coupling correctly restores higher-order hopping processes that lend a finite stiffness to spin excitations in the MI phase [134, 319]. As a last remark, we stress that the non-trivial behaviour of $\Gamma'_s(\mathbf{0}, 0)$ mirrors again the non-perturbative character of the quantum correlations embraced by the QGA in the strongly-interacting regime.

For the sake of completeness, in Figure 5.6(c) we show the U/t-dependence of the spin susceptibility out of PHS for $\mu/t = 3$. Interestingly, in correspondence of the doping-driven MIT χ displays the same discontinuity feature characterising the compressibility, in contrast again with the PH-symmetric case shown in Figure 5.6(a). Despite this analogy, it is important to observe that, differently from the compressibility, the continuity of the spin susceptibility across the MIT depends exclusively on the multi-mode bosonic correlations carried by the vertex shift $\delta\Gamma_s(\mathbf{q}, \omega)$ and cannot be explained in terms of individual collective modes only.

We conclude this Subsection by noting that the stabilisation of low-energy spin excitations in the MI as a mere effect of multi-boson fluctuations has a strong resemblance to the emergence of a dispersionful spin (density) sound mode in the CFSF (PSF) phase of the two-component BH model as a consequence of high-order hopping processes, a problem that we addressed in Chapter 2. In the same way, we believe that the spin vertex

renormalisation due to the doublon-holon binding should translate into a well-defined spin wave branch of the MI phase in a refined formulation of the QGA.

5.5.5 Comparison with other approaches

In order to emphasise more the relevance of our results, it is worth commenting on the relationship of the fermionic QGA theory with alternative methods addressing the study of quantum correlations from the standpoint of the fundamental excitation modes in strongly-correlated electron systems.

As mentioned earlier, our approach to fluctuations of the SB type has a number of features in common with recently proposed methods [65, 308] relying on the application of linear response theory to the TDGE equations (5.17); this scheme, particularly suited for the calculation of response functions, is known to include fluctuations of the RPA class [301, 307, 311] and is expected to give comparable results with our method for a class of quantities in which only quadratic fluctuations are regarded. For instance, this is the case of charge and magnetic susceptibilities truncated to the single-mode sector of the bosonic modes, e.g. the $\chi^{[1]}$ contribution to Eq. (5.81). However, since linear response theory does not treat the $\delta \hat{C}_a$'s as fully quantised excitations, RPA fluctuations above the GA cannot account for higher-order quantum correlations governed by the collective modes of the theory, which are pivotal for an accurate description of the strongly-correlated regime. From a more general point of view, the quantum theory proposed here provides a simpler and more intuitive route to the computation of dynamical correlations, as the linear response formalism requires to recompute the spectral properties of fluctuations for each desired perturbation channel [65, 307]. The practical simplicity of our approach finds its clearest example in the calculation of the Green's function of the system, see Section 5.4.1.

Recalling the discussion of Subsection 1.2.5, as the mean-field GA is known to be equivalent to the saddle-point solution of SB theories [288, 289, 292], we expect our analysis to have strong similarities also to including quantum fluctuations within slave particle methods [49, 314, 326, 327], as long as second-order fluctuations are concerned. One important difference from these approaches, shared with the bosonic formulation of the QGA, is however the way in which the observables are computed: in particular, we never rely on the reconstruction of the original fermionic operators $\hat{c}_{\mathbf{i},\sigma}$ through the *overall* Gutzwiller coordinates $\hat{C}_a(\mathbf{i})$. In fact, from the very beginning, the only dynamical variables of the theory are the fluctuation operators $\delta \hat{C}_a(\mathbf{i})$ and $\delta \hat{C}_a^\dagger(\mathbf{i})$, which are not subjected to any constraint because of our convenient choice for the normalisation operator $\hat{A}$. Strictly speaking, a fully self-consistent approach would demand the extension of the gauge-fixing constraints (5.5b) to comprise the effect of fluctuations, a task that we do not pursue here given the small quantum corrections that we find for the lattice filling $\langle \hat{n} \rangle$ (see Appendix C.2 for additional details).

We also underline that, to the best of our knowledge, there are no available slave particle calculations that provide a quantitative understanding of the physics of collective modes resembling our findings. In this respect, Gaussian expansions of SB theories have seen only a few applications to the computation of arbitrary two-particle correlations and quasiparticles vertices in general strongly-correlated systems [313, 328–330]. Finally, we remind here that the path integral formulation of SB theories with respect to quantum fluctuations is known to be a highly elaborate task with

respect to both the normal ordering of the bosonic operators and the continuum limit of functional integrals [331, 332]. The complexity of such procedure has hindered practical calculations of dynamical quantities within that formalism.

Concerning the predictive power of our method, we have shown how the QGA can account accurately for both local and non-local correlations and successfully compares to the results of DMFT [278]. The latter represents the state-of-the-art approach to the study of strongly-correlated systems, as it is able to provide a robust quantitative view on local quantum fluctuations and non-perturbative dynamical properties stemming from strong correlations. On the other hand, DMFT and its cluster extensions [324, 333–335] are not guaranteed to correctly reproduce non-local effects, which usually require ad-hoc improving schemes as e.g. diagrammatic extensions of the theory [336–338]. From this perspective, the QGA theory is intended to be a complementary tool with respect to the locally exact scenario of DMFT: in fact, it takes its fundamental steps from including directly non-local fluctuations on top of a variational local ansatz (5.1), at the price of an approximate description of quantum effects at all scales. It must be also noted that the aforementioned approaches based on DMFT lean on a self-consistent calculation of one-body correlation functions, which can be directly probes by experimental protocols such as photoemission measurements. However, other experimental techniques are centred around two-particle quantities such as the charge and spin response functions, which are probed i.e. in neutron scattering experiments. By and large, computing two-particle correlations is more challenging because of the need to accurately including vertex corrections [278, 339], which are indeed among the non-local objects accessible by the QGA. Furthermore, the minimal numerical complexity of our method – which only requires the diagonalisation of the Hamiltonian (5.32) and allows for large lattice sizes – makes our results competitive with more accurate but computationally demanding techniques. In this regard, going beyond the realm of equilibrium configurations, the study of time-dependent problems (e.g., quantum quenches and relaxation dynamics) appears to be a straightforward generalisation of our approach. This is as an advantageous feature as compared e.g. to QMC methods, which can hardly treat dynamical processes for reasonably long times sufficiently close to the thermodynamic limit.

5.6 Summary and prospects

In this Chapter, we have introduced a novel approach to the study of collective modes and quantum correlations in strongly-correlated fermionic systems based on a QGA-inspired representation of SB fluctuations. The theory has been benchmarked in the simple yet non-trivial case of the paramagnetic Hubbard model: by virtue of its flexibility, the QGA has been shown to account accurately for both local and non-local correlations throughout the phase diagram of the model and across the MIT. Similarly to its bosonic implementation, the method provides semi-analytical insights into the role played by different collective excitations within a large class of observables, ranging from the local DoS to non-local charge correlations. Most importantly, we have shown how the predictions for charge and spin correlations benefit from the ability of our approach to include higher-order correlations involving the bosonic modes of the system. In particular, we have shown that the two-body coupling between spinons and doublon-holon excitations yields an elegant rationale for the finite spin susceptibility

of the paramagnetic MI.

Under an efficient implementation of the Gutzwiller approximation for more complex fermionic configurations (see e.g. [340]), the generality of our approach paves the way for exciting applications as, for example, the spectral properties of symmetry-broken phases, the exploration of non-local correlations in Hund's correlated metals, a feasible description of bipartite entanglement in analogy with SB approaches [50] and the impact of strong interactions on the excitations of topological insulators [341]. Additionally, our semi-analytical view on quantum correlations appears particularly suited to exploring the realm of out-of-equilibrium phenomena (e.g., quantum quenches), with a special eye to open questions regarding the relationship between quantum fluctuations and the relaxation dynamics of quasiparticles [296, 309]. On the other hand, the simple treatment of two-body correlations offered by the present method could stimulate novel research lines within the recent investigation of non-perturbative properties of strongly-correlated systems hinging on two-particle physics [323, 342–345]. Furthermore, in the direction of improving the accuracy of short-range quantum correlations, a cluster extension of the theory [14, 89, 136, 137, 140] appears to be a doable task to be addressed in a future work. It is finally worth observing that our Lagrangian-based approach towards quantum fluctuations can be generalised to other correlated wave functions, provided that there exists a suitable analytical or computational scheme to optimise the classical dynamics of the ansatz parameters.

Concluding remarks and outlook $\Big|$ 6

Going through a global overview of the solutions offered by the QGA to the problems addressed in the previous Chapter, we can fully appreciate that the most prominent virtue of the QGA consists in giving a transparent illustration of how the collective modes assemble quantum correlations. The semi-analytical structure of the method, in conjunction with its practical simplicity, make it a potentially valuable tool for deriving original predictions or interpolating exact numerical/experimental data in hardly accessible regimes, especially from the viewpoint of non-local correlations. In this regard, we have collected several important insights and results, which we summarise as follows. In the case of the one-component BH model, we have gained:

- ▶ a clear distinction between the different universality classes of the MI-to-SF transition in the BH model from the point of view of non-local fluctuations;
- ▶ a semi-analytical prediction for the superfluid density of the BH model;
- ▶ a strikingly accurate estimation of two-particle correlations in quantum-critical regime;
- ▶ a physically sound prediction for the Higgs mode lifetime at the O(2) transition.

Generalising our analysis to the binary BH mixture, we have successfully tested our method on:

- ▶ capturing elusive non-local effects as the so-called superfluid drag;
- ▶ describing the spin-charge separation taking place at the pairing phase transitions of the system, from the point of view of both response functions and static correlations.

Concerning the application of our approach to bosonic impurity models, we have shown that:

- ▶ both the dephasing dynamics of a static impurity and the spectral properties of a Bose polaron are sharply sensitive probes of the different BH critical regimes;
- ▶ there is a close relation between strong correlations and rechoerence effects in the dephasing dynamics;
- ▶ the Bose polaron experiences an orthogonality catastrophe in the strongly-interacting SF phase appearing upon doping the MI state;
- ▶ the QGA provides possibly valuable predictions for the fundamental features of the Bose polaron cloud.

Last but not least, extending the QGA to the analysis of collective modes in a FH paramagnet, we have achieved:

- ▶ a thorough description of the excitation spectrum of the bosonic modes of the system across the MIT;
- ▶ a transparent view on how elementary excitations are related to the behaviour of the DoS and two-particle correlations;
- ▶ a simple yet effective theory of the coupling between bosonic modes and fermionic quasiparticles, including its physical role in two-particle observables.

As mentioned at an early stage, we have all elements to believe that suitable improvements of the QGA would significantly broaden its range of applicability and strengthen its physical accuracy. In particular, our methodological outlook includes

a suitable cluster extensions (which would allow for an exact description of short range correlations e.g. in bipartite configurations) and providing the theory with a self-consistent structure (linking quantum fluctuations with the saddle-point dynamics). Additionally, the elasticity of the QGA theory could be further put under scrutiny along a number of different directions. Aside from a systematic application to the analysis of non-linear collective effects, intriguing questions regard also the relationship between quantum fluctuations incorporated by the QGA and the physical information encoded in diagrammatic representations of many-body correlators. This cross-examination of the theory would probably reveal the reasons behind its quantitative success and, at the same time, the missing ingredients behind its non-negligible drawbacks. On the same footing, the idea of using the QGA as an efficient method for entanglement estimation in high dimensions appears as an instructive objective to pursue. Last but not least, we remind here that the fundamental postulate of the QGA is the quantisation of a set of Lagrangian coordinates constructed via the variational principle. The generalisation of a similar strategy to different ansätze for the many-body wave function, or even the design of an alternative quantisation procedure are also stimulating topics that would deserve a deeper exploration.

Turning our attention to the most outstanding problems in condensed matter physics, the improvements and test-beds proposed above acquire even more importance if we consider the amount of open questions left by the literature on the importance of collective effects in the presence of increasingly complex interactions and controlled dynamical phenomena, made possible by the high parametric tunability in ultracold atomic physics and quantum simulation science. From interacting topological physics to bipolaronic correlations, we speculate that the QGA could give a substantial contribution to the understanding of the nature of quantum fluctuations in these scenarios.

Broadening further our perspective on the physical relevance of our results, through the QGA we have made some steps towards a sort of unified picture of the bosonic degrees of freedom of the Hubbard model, of their physical essence and, more generally, of their relation to Mottness, while keeping in mind the inherent limitations of our method. In particular, we have identified interesting parallelisms between the excitation spectra of BH and FH models, in addition to giving a physical interpretation of the fermionic MI state in light of the physics of strongly-interacting bosonic species. Understanding the universal features of Mott physics and how it impacts on the surrounding coherent phases, as well as on the behaviour of quantum impurities, is a highly debated problem to which the QGA attempts to give a first (partial) answer in terms of the elementary excitations as fundamental players.

The success of our approach to collective modes in many-body systems at equilibrium motivates us to consider its extension to complex instances of an open quantum system. In the following Part of the Thesis, we will take advantage of modern implementations of many-body physics for quantum fluids of light to examine the fate of Mott-type correlations in the presence of strong dissipative effects. In particular, we will show how these elements, bringing the Hubbard physics out of the equilibrium realm, enlarges the number of ingredients concurring to Mottness and, correspondingly, contributes to the creation of a novel class of strongly-correlated states.

Part II

Towards a Theory of Quantum Fluctuations in a Driven-Dissipative Fluid of Light

Introduction | 1

Subsections 1.2.1 and 1.2.2 of the present Chapter take free inspiration from the following publications:

▶ M. Wouters, I. Carusotto, *Excitations in a nonequilibrium Bose-Einstein condensate of exciton polaritons*, Physical Review Letters **99**, 140402 (3 October 2007)

▶ M. Wouters, I. Carusotto, *Excitations and superfluidity in non-equilibrium Bose–Einstein condensates of exciton–polaritons*, Superlattices and Microstructures **43**, 524-527 (2008)

Moreover, part of the contents of Subsections 1.2.2 and 1.2.3 is included in the following work under construction.

▶ <u>Fabio Caleffi</u>, M. Capone, I. Carusotto, *Phase diagram of a non-equilibrium Bose-Einstein condensate of exciton-polaritons*, Project under definition (2022)

1.1 Superfluids out of equilibrium and where to find them

From a historical perspective, by virtue of the seminal work of Bogoliubov [5, 346, 347], the discourse on collective modes in quantum many-body theory is strongly entangled with the phenomenon of superfluidity, which can be regarded as the most celebrated collective effect having its roots in the long-range behaviour of the excitation spectrum. More importantly, superfluidity is one of the most fascinating manifestations of macroscopic quantum coherence in interacting condensed matter systems and is the key to a number of remarkable effects, ranging for example from the generation of dissipationless flows around defects [348–352] to quantised circulations and persistent currents [353–357]. First motivated by its discovery in liquid helium [358–360], the physics of superfluid matter has been later extended to comprise the phenomena of BEC [6] and the Bardeen-Cooper-Schrieffer (BCS) collective state of fermions [346, 361, 362], which is responsible for the superconductive behaviour of a wide class of materials.

Macroscopic coherence and superfluidity are not restricted to systems close to thermodynamic equilibrium, such as Bose liquids, superconductors and ultracold atomic gases. It has also been recently observed in contexts quite far from equilibrium, where the system is found in a steady state realised by a dynamical balance of drive and loss processes. Within this broad research area, a prominent role in the study of non-equilibrium superfluidity is played by semiconductor microcavities [363–366], which have been also among the first condensed matter routes to the study of BEC physics and quantum correlations in bosonic systems [367–370]. These systems allow for the possibility of coupling light quanta with the bosonic collective modes of semiconducting materials, also known as excitons: this leads to the formation of microcavity EP, quasiparticles with hybrid light-matter features. Aside from the physically inspiring feature of providing photons with an effective mass, the enormous interest attracted by these physical entities is motivated by the possibility of manipulating many-body interactions by changing the driving power of polaritons and the energy detuning

between photons and excitons, as well as of accurately probing the matter component of the steady state by measuring the properties of the emitted light. An additional advantage of semiconductor microcavities is that they can host clean realisations of BEC and superfluidity with relatively large critical temperatures [363], only limited by the dipole interactions between excitons and photons in semiconductor devices such as GaAs. Other materials, such as GaN, have been shown to allow for polariton lasing at room temperature [371, 372], an outstanding result that has promoted numerous technological efforts aiming at the creation of innovative stages for polariton superfluidity and correlated bosonic physics in general. Quantum collective effects at such high temperatures are believed to be suitable for actual device applications, e.g. in quantum storage and computation, in addition to the transport of light-matter pulses without destructive losses over macroscopic distances.

Even if many-body interactions are typically weak in EP systems, in some notable cases they can lead to unexpected strong-correlation effects, see e.g. [373]. However, several ways to boost polariton-polariton interactions have been proposed over the last decade, see for example [374], motivated also by the lively interest stirred by the first experimental observation of BEC in a semiconductor device [367]. In this regard, condensation of EP's in a flat-band system has been recently reported in [375] and has opened a new line of research focusing on the interplay between frustration and interaction out of equilibrium. More generally, the possibility of exploiting EP-inspired systems governed by the effective GPE dynamics of light propagation in non-linear media for quantum simulation purposes has been extensively addressed in [376–378].

In parallel with the progress in controlling light-matter interactions in semiconductor structures to realise quantum fluids of light [41], the scientific community has also seen great advances in the fields of quantum non-linear optics and cavity QED. This has encouraged proposals to study many-body physics by the manipulation of strongly-correlated photons. At first, theoretical and experimental setups based on arrays of coupled resonators were considered, where trapped photons were assumed to interact with either real or artificial atoms. Along this direction, pioneering studies have suggested the realisation of quantum phase transitions of the Mott-superfluid type qualifying the well-known Jaynes-Cummings-Hubbard (JCH) model under the mean-field approximation [379–381]. These first works have been followed soon by a number of studies investigating more specific features and simulations avenues, including beyond-mean-field effects [382], strongly-interacting polaritons in photonic crystals [383], propagation of photonic and atomic excitations [384], the design of spin models [385–387], and fractional quantum Hall physics [388]. More recently, the out-of-equilibrium phases of driven-dissipative BH models – realised via coherently-pumped arrays of non-linear cavities – has gathered much interest, motivated by the prospect of synthesising equilibrium-like quantum states, as well as by the occurrence of peculiar bistability phenomena and modulational instabilities in the steady state [19, 22, 389, 390].

These early proposals have laid the foundations of a novel research line of quantum simulation science, built on the variety of physical phenomena taking place in hybrid light-matter systems. To mention a few of such seminal works without trying to be exhaustive, we refer the reader to studies exploring entanglement generation [387, 391–393], multi-component models and the emergence of solitonic behaviours [394, 395], the strong-coupling theory of the JCH model [396], and applications in quantum

information processing [397]. With particular reference to the technological developments concerning cavity QED resonators, these have found their state-of-the-art implementation in Circuit Quantum Electodynamics (C-QED) platforms [398], which benefit from broadly-tunable coupling strengths and low decoherence rates. Other technologies such as photonic crystal structures and open cavity configurations have also been explored [399, 400]. More recently, it has been also proposed to couple superconducting circuits with nitrogen-vacancy centres as a promising alternative in the quantum simulation toolbox [401–403]. By and large, the possibility of efficiently measuring correlation functions of photonic states, the integrability of the proposed platforms with additional on-chip optical components, and the intriguing perspective of operating even at room temperatures have made quantum simulation within the cavity QED framework a quickly evolving and thriving field at the frontier of many-body physics [404, 405].

Independently of the class of systems and devices where they are realised, properties which characterise driven-dissipative quantum gases are fundamentally different compared to those of superfluids or more general coherent phases at thermal equilibrium, and thus offer the exciting opportunity to investigate unprecedented physical phenomena, as well as brand-new types of quantum coherence and critical behaviours. This second Part of the Thesis is aimed at providing a non-comprehensive theoretical description of these properties in two distinct examples of quantum fluids of light. In the present Chapter, we will restrict ourselves to the case of weak interactions and the physics of EP superfluids, with special attention devoted to their collective excitations in different dissipative regimes. In the next Chapter, we will take a leap towards the realm of strong correlations and analyse quantum fluctuations in a driven-dissipative C-QED system of hard-core bosons: here, the superfluid state shares the phase diagram with a normal phase characterised by Mott-like correlations via a quantum phase transition of the stationary state. Such an insulating regime will be shown to strongly differ from the antibunched mixed state identified in [22] as a key consequence of the non-Markovian pumping scheme adopted in our system. More in detail, we will also discuss in detail which features of out-of-equilibrium superfluidity are affected by the compresence of strong interactions and dissipations.

1.2 The case study of exciton-polariton condensates

1.2.1 Exciton-polariton coherence in a nutshell

The schematic picture of the experimental realisation of a EP condensate is sketched in Figure 1.1. Upon injecting light at high energy, free-charge carriers are first generated from the semiconductor material composing the microcavity. High-energy polaritons are subsequently cooled down by phonon emission, which leads to the creation of an incoherent gas of excitons in the quantum well [Figure 1.1(a)] whose energy accumulates on top of the lower polariton branch (LP), also known as the bottleneck region [see the orange points in Figure 1.1(b)]. This intermediate state acts as a reservoir for the EP condensate: polariton-polariton collisions drive the scattering of polaritons from the bottleneck region to the bottom of the LP branch. When the stimulated scattering rate overcomes dissipative losses, the EP field becomes coherent and a fully-fledged BEC appears.
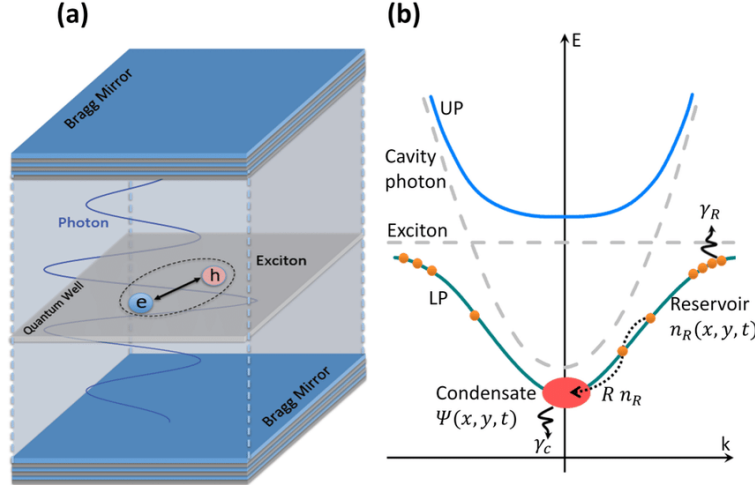
(a) **(b)**

Figure 1.1: Panel (a): illustration of the semiconductor microcavity setting leading to a coupling between excitonic excitations and photons insides a quantum well. Panel (b): sketch of the driving mechanism pumping the reservoir polaritons from the bottleneck region (orange points) into the condensate mode (red ellipse) at the bottom of the LP band (solid green line). The grey dashed lines indicate the excitonic and cavity photon bands, hybridising into the LP and the UP (upper polariton band, blue solid line). Notice that the cavity photons are responsible for giving the effective mass of EP's in the LP band.

In the following, we proceed to review a simple yet effective mean-field model of the EP setting, which also illustrates some of the basic physical principles behind the development of quantum coherence in a driven-dissipative system. In particular, we highlight that such a theoretical formulation is inspired by the classical treatment of laser operation [406], and closely resembles the theory of atomic lasers developed in [407]. The main advantage of the model consists in the fact that it does not involve the specifics of the microscopic physics of polaritons, and therefore can be used to describe the out-of-equilibrium dynamics independently of details of the pumping scheme. Only three assumptions are required to hold in order to provide the model with physical consistency: i) a single state of the LP branch is macroscopically occupied, so that it can be described by a classical field; ii) the state of the reservoir is fully determined by the spatial polariton density $n_{\mathrm{R}}(\mathbf{r}, t)$. This second assumption requires that relaxation processes are fast enough to ensure local equilibrium of the polariton reservoir in the bottleneck region, and that quantum coherence forming between the reservoir and the condensate decays on a sufficiently fast timescale compared to the EP condensate lifetime.

1.2.2 Mean-field theory and elementary excitations

Under the assumptions outlined in the previous Subsection, the condensate dynamics is to a first approximation described by a generalised GPE for the macroscopic EP coherent field including amplification and loss terms,

$$i \frac{\partial \psi(\mathbf{r}, t)}{\partial t} = \left\{ -\frac{\nabla^2}{2\, m_{\mathrm{LP}}} + \frac{i}{2} \left[R(n_{\mathrm{R}}) - \gamma \right] + g\, |\psi(\mathbf{r}, t)|^2 + 2\, \tilde{g}\, n_{\mathrm{R}}(\mathbf{r}, t) \right\} \psi(\mathbf{r}, t) \quad (1.1)$$

where m_{LP} is the effective mass of the LP branch, γ is the condensate loss rate and g is the strength of the polariton-polariton interaction within the condensate. The stimulated scattering of reservoir polaritons into the condensate mode is encoded in the term $R(n_{\mathrm{R}})$, which is defined to be a monotonically growing function depending on the

details of the driving mechanism, while the mean-field interaction experienced by the condensate polaritons due to elastic collisions with the reservoir components is given by the term $2\,\tilde{g}\,n_{\mathrm{R}}(\mathbf{r}, t)$, where $\tilde{g}$ is generally different from g. For clarity, we emphasise that the GPE (1.1) requires that density and phase fluctuations of the condensate field are small. Strictly speaking, this regime is reached for pumping powers well above the condensation threshold: in the following Subsection, we will see how the violation of this assumption manifests in the dynamical behaviour of the system at the level of its elementary excitations.

The dynamics of the condensate is coupled to the Boltzmann diffusion equation for the density of reservoir polaritons, reading

$$i\frac{\partial n_{\mathrm{R}}(\mathbf{r}, t)}{\partial t} = P - \gamma_{\mathrm{R}}\, n_{\mathrm{R}}(\mathbf{r}, t) - R(n_{\mathrm{R}})\,|\psi(\mathbf{r}, t)|^2 + D_{\mathrm{R}}\,\nabla^2 n_{\mathrm{R}}(\mathbf{r}, t)\,. \qquad (1.2)$$

Polaritons are pumped in the reservoir with a continuous and uniform pumping rate P, and relax according to the damping rate γ_{R}. The so-called hole-burning effect due to the scattering of reservoir polaritons into the condensate is taken into account by the term $R(n_{\mathrm{R}})\,|\psi(\mathbf{r}, t)|^2$, which evidently establish the coupling between reservoir polaritons and the condensate field; reservoir polaritons are also assumed to undergo spatial diffusion in relation to a diffusion constant D_{R}.

By inspection of Eqs. (1.1)-(1.2), the stationary state of the system can be easily found by means of the ansatz

$$\psi(\mathbf{r}, t) = \psi_0\, e^{-i\,\tilde{\mu}\, t}\,, \qquad (1.3a)$$

$$n_{\mathrm{R}}(\mathbf{r}, t) = n_{\mathrm{R}}^0\,. \qquad (1.3b)$$

For small P, no condensate is present ($\psi_0 = 0$) and the reservoir density is given by $n_{\mathrm{R}}^0 = P/\gamma_{\mathrm{R}}$. This incoherent solution is dynamically stable as long as the effective pumping of polaritons at the bottom of the LP branch is overcome by losses, namely $R(n_{\mathrm{R}}^0) < \gamma$. The lasing threshold $P = P_{\mathrm{thr}}$ corresponds to the value of n_{R}^0 which guarantees equilibrium between amplification and losses: when the pumping rate P is further increased above the threshold, a condensate appears. Stationarity imposes the net gain $R(n_{\mathrm{R}}^0) - \gamma$ to vanish, a condition that fixes the reservoir density to the equilibrium value $n_{\mathrm{R}}^0 = n_{\mathrm{R}}^{\mathrm{thr}}$. Correspondingly, the condensate density is given by $\rho_c = |\psi_0|^2 = (P - P_{\mathrm{thr}})\,/\gamma$, while the parametric oscillation of the order parameter has the frequency $\tilde{\mu} = \mu + 2\,\tilde{g}\,n_{\mathrm{R}}^{\mathrm{thr}}$, with $\mu = g\,\rho_c$ being the usual mean-field shift of the condensate chemical potential due to interactions.

The generality of the mean-field model of Eqs. (1.1)-1.2 has the crucial advantage of taking into account the multi-mode nature of the spatially extended polariton field and describing its coherent dynamics on the same footing: these features are essential to a robust study of the elementary excitations of the condensate. In close analogy with the linearisation of the TDGE in Eq. (2.12) of Chapter 2, the excitation spectrum of the driven-dissipative EP system can be obtained by expanding Eqs. (1.1)-1.2 around the stationary state solution in terms of linear fluctuations. Thanks to the translational invariance of the system, fluctuations of the condensate field and reservoir density can be decomposed as

$$\psi(\mathbf{r}, t) = \psi_0 \left[u_{\mathbf{k}}\, e^{i(\mathbf{k}\cdot\mathbf{r} - \omega\, t)} + v_{\mathbf{k}}^*\, e^{-i(\mathbf{k}\cdot\mathbf{r} - \omega\, t)} \right] e^{-i\,\mu\, t}\,, \qquad (1.4a)$$

$$n(\mathbf{r}, t) = n_{\mathrm{R}}^0 \left[w_{\mathbf{k}}\, e^{i(\mathbf{k}\cdot\mathbf{r} - \omega\, t)} + \text{c.c.} \right]. \tag{1.4b}$$

Substituting the above expansions into the equations of motion (1.1)-1.2 and keeping terms up to linear order, we readily obtain the eigenvalue equation

$$\hat{\mathcal{L}}_{\mathbf{k}} \begin{pmatrix} u_{\mathbf{k}} \\ v_{\mathbf{k}} \\ w_{\mathbf{k}} \end{pmatrix} = \omega \begin{pmatrix} u_{\mathbf{k}} \\ v_{\mathbf{k}} \\ w_{\mathbf{k}} \end{pmatrix}, \tag{1.5}$$

where the generalised Bogoliubov matrix $\hat{\mathcal{L}}_{\mathbf{k}}$ has the form

$$\hat{\mathcal{L}}_{\mathbf{k}} \equiv \begin{bmatrix} f_{\mathbf{k}} + \mu & \mu & \frac{2\,\gamma\,\mu}{\alpha\,\gamma_{\mathrm{R}}} + i\frac{\beta\,\gamma}{2} \\ -\mu & -f_{\mathbf{k}} - \mu & -\frac{2\,\gamma\,\mu}{\alpha\,\gamma_{\mathrm{R}}} + i\frac{\beta\,\gamma}{2} \\ -i\,\alpha\,\gamma_{\mathrm{R}} & -i\,\alpha\,\gamma_{\mathrm{R}} & -i\,(\eta\,\gamma_{\mathrm{R}} + D_{\mathbf{k}}) \end{bmatrix}, \tag{1.6}$$

and the standard Hartree-Fock value $\tilde{g} = 2\,g$ has been considered. Here, $\alpha = \frac{P_{\mathrm{thr}}}{P} - 1$ is the relative deviation of the pumping rate from the lasing threshold, the coefficient $\beta = n_{\mathrm{R}}^0\, R'(n_{\mathrm{R}}^0)/R(n_{\mathrm{R}}^0)$ characterises the dependence of the amplification rate $R(n_{\mathrm{R}}^0)$ on the reservoir density, $\eta = 1 + \alpha\,\beta$ can be regarded as the effective pumping rate on the condensate mode. Moreover, we have defined $f_{\mathbf{k}} = (2\,m_{\mathrm{LP}})^{-1}\,\mathbf{k^2}$ as the free-particle dispersion of polaritons and $D_{\mathbf{k}} = D_{\mathrm{R}}\,\mathbf{k^2}$. Quite remarkably, we note that the excitation spectrum does not depend on the precise value of the scattering rate $R(n_{\mathrm{R}}^0)$ of the reservoir polaritons into the condensate mode, but only the relative pumping rate α and the effective exponent β do matter via η, as we will discuss in more detail in the following. The excitation spectrum can be straightforwardly determined by calculating the solutions of the equation $\det\!\left(\hat{\mathcal{L}}_{\mathbf{k}} - \omega\,\mathbb{1} \right) = 0$, whose unfolded expression is

$$\omega^3 + i\,(\eta\,\gamma_{\mathrm{R}} + D_{\mathbf{k}})\left(\omega^2 - \omega_{\mathrm{Bog},\mathbf{k}}^2 \right) - \left[\omega_{\mathrm{Bog},\mathbf{k}}^2 + (\eta - 1)\,\gamma\,\gamma_{\mathrm{R}} \right]\omega + 4\,i\,\gamma\,\mu\,f_{\mathbf{k}} = 0. \tag{1.7}$$

In the previous equation, $\omega_{\mathrm{Bog},\mathbf{k}}$ is the usual Bogoliubov dispersion of the Goldstone mode at equilibrium, reading

$$\omega_{\mathrm{Bog},\mathbf{k}} \equiv \sqrt{f_{\mathbf{k}}\,(f_{\mathbf{k}} + 2\,\mu)} \tag{1.8}$$

with sound velocity

$$c_{s,\mathrm{Bog}} \equiv \sqrt{\frac{\mu}{m_{\mathrm{LP}}}} \tag{1.9}$$

in the long-wavelength limit.

Typical examples of the dispersion of the elementary excitations are shown in Figure 1.2, where the momentum is rescaled by the healing length of the condensate $\xi = (2\,m_{\mathrm{LP}}\,\mu)^{-1/2}$. As the onset of a BEC entails a spontaneous breaking of a U(1) symmetry, the excitation spectrum always involves a Goldstone branch whose dispersion $\omega_{\mathrm{Gol}}(\mathbf{k})$ vanishes at low momenta. Physically, this mode can be understood as an arbitrarily soft rotation of the condensate phase across the sample: one can readily verify that the generator $(1, -1, 0)^T$ of global phase rotations is indeed an eigenvector of $\hat{\mathcal{L}}_{\mathbf{k}=\mathbf{0}}$ with a zero eigenvalue.

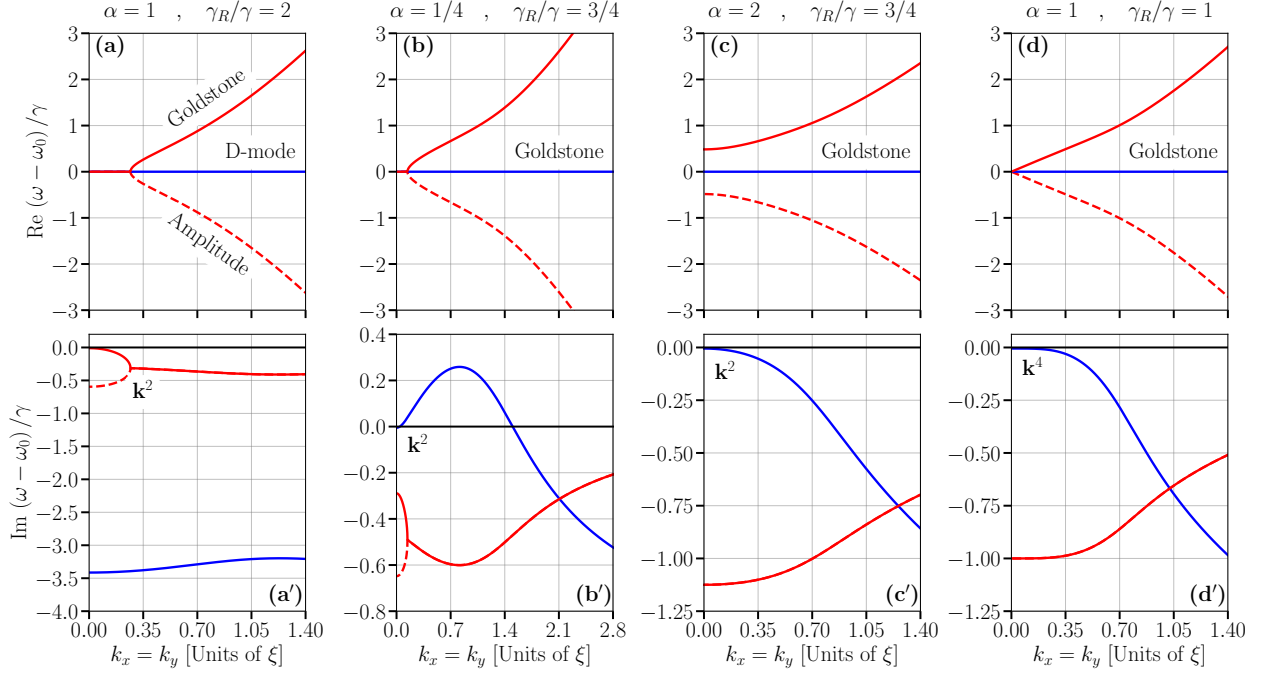Let us analyse the different parametric cases in more detail, starting from the

Figure 1.2: Selected examples of the energy spectrum of the collective modes of an EP condensate in a 2D quantum well. The upper panels show the real part of the excitation energies, while the lower panels refer to the imaginary parts or damping rates of the excitations. For all the panels, common parameters of the system are $\mu/\gamma = P_{\mathrm{thr}}/\gamma = \beta = 1$ and $D_{\mathrm{R}}/\gamma = 5 \cdot 10^{-4}$. The healing length of the condensate is equal to $\xi \approx 14.02$ for panels (b)-(b′) and $\xi \approx 6.97$ otherwise.

physically most relevant regime $\gamma \ll \gamma_{\mathrm{R}}$ where the reservoir state is able to follow adiabatically the condensate dynamics. The dispersion for this case is shown in Figure 1.2(a)-(a′): in stark contrast with the linear dispersion of the propagating sound mode in equilibrium BEC's [40], an unconventional feature of the Goldstone mode [red solid line] in the present out-of-equilibrium context is its diffusive and non-propagating behaviour at low $|\mathbf{k}|$: specifically, the real part of the spectrum is dispersionless and equal to zero, while the imaginary part behaves quadratically with momentum. This fundamental result was among the first indications of the universal character of the Goldstone diffusivity, which is indeed a generic fact in non-equilibrium phase transitions, not only under a coherent drive as in pattern-forming systems [408, 409], but also in the case of incoherent pumping. It is important to notice that such a diffusive behaviour is not due to the spatial diffusion of reservoir polaritons, and would be present even when $D_{\mathrm{R}} = 0$. The value $D_{\mathrm{R}}/\gamma = 5 \cdot 10^{-4}$ chosen to produce the numerical results of Figure 1.2 has been suggested by experimental studies on CdTe quantum well samples [410].

An analytical explanation of the diffusive behaviour can be straightforwardly derived by adiabatically eliminating the dispersionless and strongly damped reservoir mode – referred to as *D-mode* in the Figure 1.2(a)-(a′) –, whose imaginary energy is close to $\Gamma_{\mathrm{D}}(\mathbf{k}) \approx -\eta \gamma_{\mathrm{R}}$. Taking for simplicity $D_{\mathrm{R}} = 0$, the two branches of the condensate excitations [red lines] turn out to have the approximate dispersion

$$\omega_{\mathrm{Gol}}(\mathbf{k}) \approx -i\frac{\Gamma}{2} \pm \sqrt{\omega_{\mathrm{Bog},\mathbf{k}}^2 - \frac{\Gamma^2}{4}} \ . \tag{1.10}$$

The non-equilibrium nature of the above excitations is quantified by the effective

damping rate

$$\Gamma \equiv \frac{(\eta - 1)\,\gamma}{\eta}\,, \tag{1.11}$$

which interestingly vanishes in correspondence of the condensation threshold ($\eta = 1$) and tends to the bare loss rate γ for high pumping intensities $\alpha \gg 1$. The upper branch coincides with the Goldstone mode discussed before, while the lower branch with a negative excitation energy is related to modulations of the condensate density. For low $|\mathbf{k}|$ in the diffusive regime, the latter mode is damped with a finite rate given by Γ. From Eq. (1.10), we immediately obtain a prediction for the width in momentum space $\Delta\mathbf{k}_{\text{diff}}$ where the Goldstone real dispersion is flat, and phase excitations are diffusive. In particular, we have

$$|\Delta\mathbf{k}_{\text{diff}}\,\xi|^2 \approx \sqrt{1 + \frac{\Gamma^2}{4\,\mu^2}} - 1 = \sqrt{1 + \left(\frac{\beta\,\gamma^2}{2\,P_{\text{thr}}\,g\,\eta}\right)^2} - 1\,. \tag{1.12}$$

Outside this region, the excitation modes (1.10) overlap with the standard Bogoliubov dispersion of an equilibrium condensate. It is worth observing that, however, the sound-like behaviour is observable provided that $|\Delta\mathbf{k}_{\text{diff}}| \ll \xi^{-1}$, with ξ being the healing length of the condensate. By a simple calculation, we find that this condition corresponds to the requirement $\gamma^2/\gamma_{\text{R}} \ll g\,n_{\text{R}}^0\,\eta/\beta$, meaning that the condensate damping rate should not be comparable with the energy scale of the interaction with the reservoir.

In the analysis of [411], it was first observed that the situation becomes more complex when the condensate and reservoir decay rates have comparable magnitudes and the reservoir cannot be adiabatically eliminated from the dynamical description of the system. For moderate values of η, the most significant feature is the incommensurate dynamical instability $\text{Im}(\omega) > 0$ of the D-mode branch that is visible in Figure 1.2(b′): this indicates that the homogeneous state is no longer dynamically stable, and a spatial modulation has to appear in the density profile of the condensate. The origin of the instability can be traced back to the repulsive interaction between the condensate and the reservoir polaritons: a local depletion of the reservoir density $n_{\text{R}}(\mathbf{r}, t)$ creates a potential well which attracts the condensate polaritons, making the depletion in the local reservoir density even larger. In particular, we find that this scenario is possible only for $\gamma/\gamma_{\text{R}} < 2\,\eta$, so that the effect of reservoir-condensate interactions is able to overcome the tendency of density modulations to relax down as previously discussed.

Quite remarkably, the dynamical instability of the hybridised Goldstone mode due to polariton interactions does not exhaust the physics of the EP condensate in the anti-adiabatic regime: in fact, by exploring further the parameter space of the system and studying the possible solutions of the eigenvalue equation (1.7), we find that the interplay between pumping and losses can result in a wider range of physical scenarios [see in particular panels (c)-(c′) and (d)-(d′) of Figure 1.2], which we will discuss extensively in the following Subsection.

1.2.3 Phase diagram of the excitations

On the basis of the structure of the Goldstone mode in the long-wavelength limit, we can construct a schematic phase diagram of EP condensates in terms of the dissipative
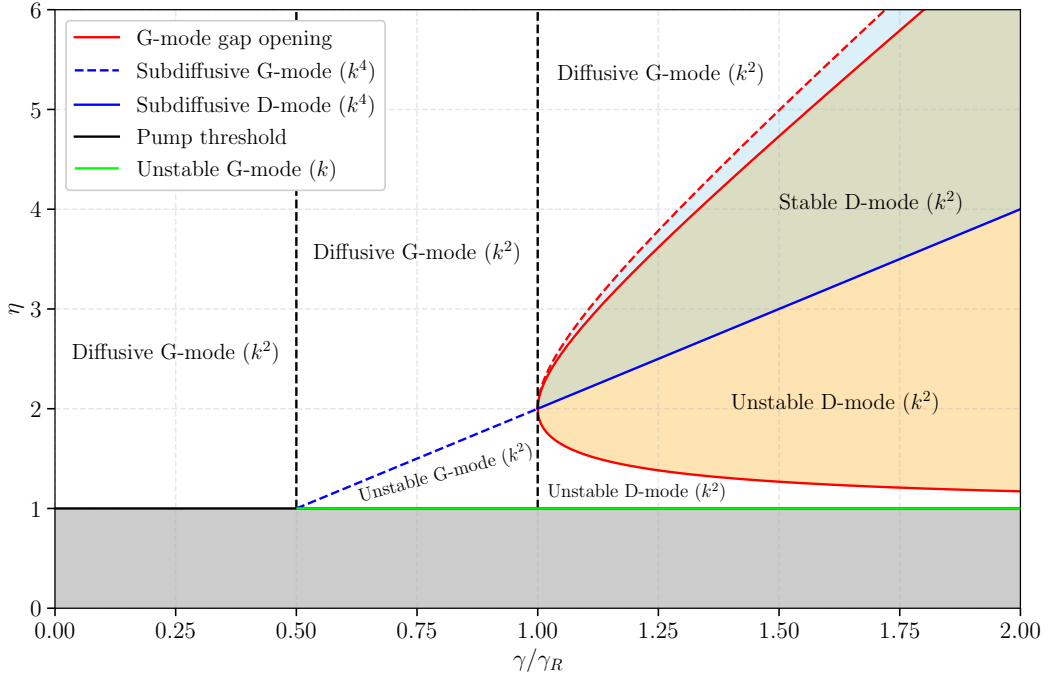
Figure 1.3: Phase diagram based on the structure of the excitation spectrum of a EP condensate. Blue shaded area: stable and diffusive D-mode. Orange shaded area, $2\,\gamma/\gamma_{\mathrm{R}}\left(1-\sqrt{1-\gamma_{\mathrm{R}}/\gamma}\right)<\eta<2\,\gamma/\gamma_{\mathrm{R}}\left(1+\sqrt{1-\gamma_{\mathrm{R}}/\gamma}\right)$: gap opening region. Blue solid line, $\eta=2\,\gamma/\gamma_{\mathrm{R}}$: stable and subdiffusive Goldstone mode. Green solid line, $\eta\to1^{+}$: unstable and superdiffusive Goldstone mode.

energy scales of the problem (the effective pumping η and the loss ratio $\gamma/\gamma_{\mathrm{R}}$), shown in Figure 1.3. The following discussion will be of great importance to establish a deeper parallelism between the out-of-equilibrium excitations of a EP system and quantum fluctuations of the driven-dissipative fluid of light that we will study in the next Chapter.

The upper left corner of the phase diagram is entirely occupied by the regime of the standard diffusive *G-mode*, a term by which we indicate the only excitation with a non-trivial positive-energy dispersion in real space [solid red lines in the first row of Figure 1.2]. Notably, we discover that this region comprises not only the adiabatic limit $\gamma/\gamma_{\mathrm{R}}\leq1/2$, but also those states that are stabilised at sufficiently large pumping η when the loss ratio $\gamma/\gamma_{\mathrm{R}}$ is larger. Therefore, the G-mode can still have a diffusive character when the effective pumping is strong enough to win over the anti-adiabaticity of the loss dynamics, thus limiting the amount of phase/amplitude fluctuations in the condensate. In general, by straightforward analytical manipulations of Eq. (1.7), we find that the diffusive coefficient of the Goldstone mode has the expression

$$D = \frac{\mu}{m_{\mathrm{LP}}\,\Gamma}\left(1-\frac{2\,\gamma}{\eta\,\gamma_{\mathrm{R}}}\right) = \left[\Gamma^{-1}-\frac{2}{(\eta-1)\,\gamma_{\mathrm{R}}}\right]c_{s,\mathrm{Bog}}^{2} \qquad (1.13)$$

and is interestingly given by a renormalisation of the Bogoliubov sound velocity due to the balance between effective pumping on the condensate mode and reservoir losses.

Richer situations arise when $\gamma/\gamma_{\mathrm{R}}>1/2$ and $\eta\lesssim4\,\gamma/\gamma_{\mathrm{R}}-1$. Specifically, we can identify a stability region for $\eta>2\,\gamma/\gamma_{\mathrm{R}}$ and an instability region otherwise, where the imaginary part of the Goldstone dispersion becomes positive over a finite

range of momenta (including the unstable configuration discussed in the previous Subsection).

Let us first consider the case $1/2 < \gamma/\gamma_R < 1$. Here, the stable diffusive G-mode survives down to $\eta = 2\,\gamma/\gamma_R$ [blue dashed line], below which it becomes unstable developing a negative diffusive coefficient, see Eq. (1.13). In particular, we notice that this corresponds to $\Gamma > (\eta - 1)\,\gamma_R/2$, meaning that the effective lifetime of the condensate mode is smaller than the one of reservoir polaritons. For $\gamma/\gamma_R > 1$, the dissipative dynamics of the condensate and the polariton reservoir are more strongly related to each other, such that the D-mode comes into play to determine the coherent excitations of the system. Starting from the region of the diffusive G-mode and lowering η, phase excitations hybridise with the dissipative mode and a stable form of the diffusive D-mode takes the role of the Goldstone branch [blue shaded area between the red dashed line and the blue solid line]. Most interestingly, the hybridisation in the excitation spectrum preempts the opening of a gap in the G-mode dispersion [Figure 1.2(c)-(c′)], which occurs in the effective pumping range $2\,\gamma/\gamma_R \left(1 - \sqrt{1 - \gamma_R/\gamma}\right) < \eta < 2\,\gamma/\gamma_R \left(1 + \sqrt{1 - \gamma_R/\gamma}\right)$ [orange shaded area between the red solid lines]. In particular, the energy gap reads

$$\Delta_{\mathrm{gap}} = \pm\frac{\eta}{2}\left[\frac{4\,(\eta - 1)}{\eta^2}\frac{\gamma}{\gamma_R} - 1\right]^{1/2}\gamma_R = \pm\left[\frac{4\,\Gamma}{\eta\,\gamma_R} - 1\right]^{1/2}|\Gamma_{\mathrm{gap}}(\mathbf{k} = \mathbf{0})|$$
$$= \pm\left[\frac{2\,\Gamma}{|\Gamma_{\mathrm{gap}}(\mathbf{k} = \mathbf{0})|} - 1\right]^{1/2}|\Gamma_{\mathrm{gap}}(\mathbf{k} = \mathbf{0})|\,, \tag{1.14}$$

where

$$\Gamma_{\mathrm{gap}}(\mathbf{k} = \mathbf{0}) = -i\frac{\eta\,\gamma_R}{2} \tag{1.15}$$

is the damping rate of the G-mode and amplitude branches at $\mathbf{k} = \mathbf{0}$. In particular, it is worth noting that the energy gap is set by the reservoir loss rate γ_R and vanishes for $\Gamma < |\Gamma_{\mathrm{gap}}(\mathbf{k} = \mathbf{0})|/2$, namely when the effective pumping on the condensate mode is at least an order of magnitude slower than the dissipative dynamics of the reservoir. The line $\eta = 2\,\gamma/\gamma_R$ separating stable and unstable regimes is the bisector of this area [blue solid line]: this strongly supports the idea that the gap opening phenomenon is tightly related to the appearance of the diffusive D-mode. Furthermore, we emphasise that an energy gap in the long-wavelength limit could be interpreted in terms of relaxation oscillations of the EP lasing state [412, 413]. Eventually, for sufficiently low η, the excitation gap closes, such that the unstable D-mode described in [411] is recovered.

It is worth discussing in more detail what happens on the stability threshold $\eta = 2\,\gamma/\gamma_R$. Here, the diffusive coefficient D vanishes identically, providing the Goldstone dispersion with a different power-law dependence on momentum. In particular, it turns out that the Goldstone propagation is *stable and subdiffusive* with $\Gamma_{\mathrm{Gol}}(\mathbf{k}) \sim -i\,\mathcal{D}\,\mathbf{k}^4$ [Figure 1.2(d)-(d′)]. The precise nature of this peculiar instance of the Goldstone mode is once again determined by the loss ratio γ/γ_R: if $1/2 < \gamma/\gamma_R < 1$, it is the standard G-mode branch; for $\gamma/\gamma_R > 1$, this is replaced by the hybridised D-mode. The subdiffusion coefficient $\mathcal{D}$ can be determined analytically with the result

$$\mathcal{D} = \frac{1}{\Gamma}\left(\frac{1}{4\,m_{\mathrm{LP}}^2} + \frac{D_{\mathrm{R}}\,c_{s,\mathrm{Bog}}^2}{\eta\,\gamma_{\mathrm{R}}}\right) = \frac{1}{4\,m_{\mathrm{LP}}^2\,\Gamma}\left(1 + \frac{4\,D_{\mathrm{R}}\,\mu^2}{\eta\,\gamma_{\mathrm{R}}}\right) \approx \left(4\,m_{\mathrm{LP}}^2\,\Gamma\right)^{-1}, \quad (1.16)$$

and mainly hinges on the lifetime of the condensate mode Γ^{-1}.

Importantly, the line $\eta = 2\,\gamma/\gamma_{\mathrm{R}}$ is not the only set of parameters for which the Goldstone diffusivity breaks down into a different pattern of propagation. This is also the case of the limit $\eta \to 1^+$ [green solid line], namely on top of the gain threshold in the presence of an extremely dilute condensate. Here, the G-mode branch develops an *unstable superdiffusive* behaviour $\Gamma_{\mathrm{Gol}}(\mathbf{k}) \sim i\,C\,|\mathbf{k}|$, whose dispersion is controlled by the renormalised sound velocity

$$C^2 = \left(\frac{2\,\gamma}{\eta\,\gamma_{\mathrm{R}}} - 1\right) c_{s,\mathrm{Bog}}^2. \qquad (1.17)$$

More in detail, the superdiffusivity of the Goldstone mode is effective only on sufficiently large spatial scales, namely

$$|\mathbf{k}_{\mathrm{superdiff}}\,\xi|^2 \ll \frac{(\eta - 1)\,\Gamma\,\gamma}{2\left(\frac{2\gamma}{\gamma_R} - 1\right)\mu^2} = \frac{\left(\beta\,\gamma^2\right)^2}{2\left(\frac{2\gamma}{\gamma_R} - 1\right)(P_{\mathrm{thr}}\,g)^2}. \qquad (1.18)$$

However, such a critical type of instability is found to occur in the anti-adiabatic regime $\gamma/\gamma_{\mathrm{R}} > 1/2$ only. When $\eta = 1$ exactly, the sound velocity disappears proportionally to the condensate order parameter, and we recover the on-threshold spectrum given by

$$\omega_{\mathrm{Gol/Amp}}^{\mathrm{thr}} = \pm\omega_{\mathrm{Bog},\mathbf{k}} \to f_{\mathbf{k}}, \qquad (1.19a)$$

$$\omega_{\mathrm{D}}^{\mathrm{thr}} = -i\left(\gamma_{\mathrm{R}} + D_{\mathbf{k}}\right). \qquad (1.19b)$$

for the Goldstone/amplitude and D-mode branches respectively.

The overall structure of the excitation spectrum is closely reflected by the one-body dynamical correlations of the EP condensate. For brevity, our results for these quantities are examined in Appendix F.1, as they provide a particularly insightful basis for comparison with quantum fluctuations in the driven-dissipative photonic lattice that will be the subject of the next Chapter. In particular, most of the physics of EP condensates introduced before will be shown to encompass also the phenomenology of strongly-correlated superfluid regimes, whereas unprecedented properties and manifestations of quantum coherence due to the compresence of dissipation and strong interactions will require a more comprehensive analysis of quantum fluctuations out of equilibrium.

The present Chapter is based on selected results discussed in the following upcoming publication.

▶ Fabio Caleffi, M. Capone, and I. Carusotto, *Collective excitations of a strongly-correlated non-equilibrium photon fluid across the Mott/superfluid phase transition*, In preparation (2022)

2.1 Driven-dissipative photonic lattice: a paradigmatic model

We consider a d-dimensional array of optical cavities modelled by a BH Hamiltonian,

$$\hat{H}_{\mathrm{BH}} \equiv -J \sum_{\langle \mathbf{r}, \mathbf{s} \rangle} \hat{a}_{\mathbf{r}}^{\dagger} \hat{a}_{\mathbf{s}} + \sum_{\mathbf{r}} \left(\omega_c \, \hat{a}_{\mathbf{r}}^{\dagger} \hat{a}_{\mathbf{r}} + U \, \hat{a}_{\mathbf{r}}^{\dagger} \hat{a}_{\mathbf{r}}^{\dagger} \hat{a}_{\mathbf{r}} \, \hat{a}_{\mathbf{r}} \right) , \tag{2.1}$$

where $\hat{a}_{\mathbf{r}} \left(\hat{a}_{\mathbf{r}}^{\dagger} \right)$ is the bosonic annihilation (creation) operator of a photon in the cavity at site $\mathbf{r}$, J tunnelling (or hopping) rate between the cavities, ω_c is the natural frequency of each cavity, and U is the energy scale of the Kerr non-linearity, which has the same second-quantised form of a Hubbard interaction.

The first building block of the driven-dissipative dynamics of the BH array is given by the Rabi coupling of each cavity with an external Two-Level Emitters (TLE), which is pumped incoherently via a Markovian source with rate Γ_p. The Hamiltonian of the TLE's and their coupling with the cavities are ruled by

$$\hat{H}_{\mathrm{em}} \equiv \omega_{\mathrm{at}} \sum_{\mathbf{r}} \hat{\sigma}_{\mathbf{r}}^{+} \hat{\sigma}_{\mathbf{r}}^{-} + \Omega \sum_{\mathbf{r}} \left(\hat{a}_{\mathbf{r}}^{\dagger} \hat{\sigma}_{\mathbf{r}}^{-} + \mathrm{H.c.} \right) , \tag{2.2}$$

where $\hat{\sigma}_{\mathbf{r}}^{\pm}$ is the rising (lowering) operator in the pseudospin space of one TLE. We emphasise here that the coupling with the two-level atoms makes a simple realisation of a non-Markovian driving protocol for the photonic lattice [414]. Contextually, a suitable extension of the same scheme has been shown to ideally provide a high-fidelity stabilisation of the BH phase diagram [20], at least in the limit of low dimensions.

The dynamics of photon pumping and leakage processes, along with the unitary evolution of the system, is described by the Lindblad equation for the full density matrix of the system,

$$\partial_t \hat{\rho} = -i \left[\hat{H}, \hat{\rho} \right] + \frac{1}{2} \sum_{\mathbf{r}} \left\{ \Gamma_l \, \mathcal{D}[\hat{a}_{\mathbf{r}}; \hat{\rho}] + \gamma \, \mathcal{D}[\hat{\sigma}_{\mathbf{r}}^{-}; \hat{\rho}] + \Gamma_p \, \mathcal{D}[\hat{\sigma}_{\mathbf{r}}^{+}; \hat{\rho}] \right\} , \tag{2.3}$$

where $\hat{H} \equiv \hat{H}_{\mathrm{BH}} + \hat{H}_{\mathrm{em}}$, and

$$\mathcal{D}\left[\hat{O}; \hat{\rho} \right] \equiv 2 \, \hat{O} \, \hat{\rho} \, \hat{O}^{\dagger} - \left\{ \hat{O}^{\dagger} \hat{O}, \hat{\rho} \right\} \tag{2.4}$$

is the so-called *dissipator* associated with the operator $\hat{O}$. Here, Γ_l denotes the radiative loss rate of the cavities, while γ is the photon leakage rate of the TLE's. A pictorial
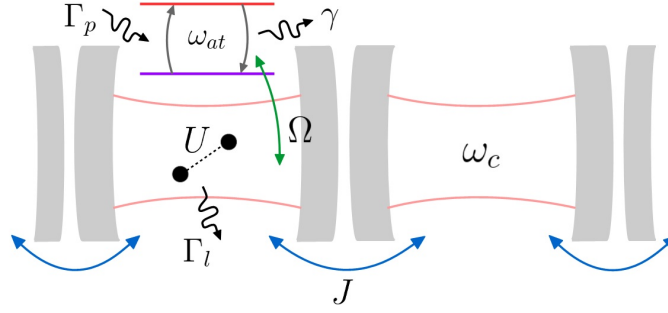
Figure 2.1: Schematic illustration of the driven-dissipative photonic system under study. Each cavity is subject to non-Markovian pumping via the Rabi drive Ω involving a TLE, while the coupling with the environment produces incoherent photon leakage at a rate Γ_l.

sketch of the model setting is provided in Figure 2.1.

2.2 Mean-field theory of the stationary state

2.2.1 Gutzwiller approximation of the Lindblad dynamics

Since we aim at encompassing a non-trivial description of the strongly-interacting limit of the driven-dissipative photonic lattice, we take inspiration from our research efforts at equilibrium and study the Non-Equilibrium Stationary State (NESS) of the model within the Gutzwiller mean-field approximation [19, 22, 390], which consists in a site-factorised ansatz for the density matrix,

$$\hat{\rho} = \bigotimes_{\mathbf{r}} \sum_{n,m} \sum_{\sigma,\sigma'} c_{n,m,\sigma,\sigma'}(\mathbf{r}) \left| n, \sigma \right\rangle_{\mathbf{r}} \left\langle m, \sigma' \right|_{\mathbf{r}} . \tag{2.5}$$

Here, $\left| n, \sigma \right\rangle_{\mathbf{r}}$ denotes the global quantum state of a single cavity-TLE pair, with the former occupied by n photons and the latter having the polarisation $\sigma = \pm 1$, and $c_{n,m,\sigma,\sigma'}(\mathbf{r})$ is the corresponding density matrix coefficient. Clearly, $c_{n,m,\sigma,\sigma'}(\mathbf{r})$ factorises into the usual Gutzwiller wave function weights as $c_{n,m,\sigma,\sigma'}(\mathbf{r}) = c^*_{m,\sigma'}(\mathbf{r}) c_{n,\sigma}(\mathbf{r})$ whenever the density matrix describes a pure BH state.

Inserting the ansatz (2.5) and adopting the vectorised representation of $\hat{\rho}$ (also known as Choi-Jamiolkowski isomorphism [415, 416]), the Lindblad equation turns into a set of mutually coupled dynamical equations for the density matrix elements,

$$i \, \partial_t \, \vec{c}(\mathbf{r}) = \hat{L}[\vec{c}(\mathbf{r})] \cdot \vec{c}(\mathbf{r}) . \tag{2.6}$$

More precisely, the Eqs. (2.6) have the form of a set of generalised GPE's which allow to find an approximate solution to the non-equilibrium evolution of the system at the price of introducing non-linearities in the dynamics. More precisely, the Lindblad

superoperator $\hat{L}[\vec{c}(\mathbf{r})]$ has the expression

$$
\begin{aligned}
L_{n,m,\sigma,\sigma'}^{n',m',\mu,\mu'}[\vec{c}(\mathbf{r})] \equiv -J &\left[\left(\sqrt{n'+1}\,\delta_{n,n'+1}\,\delta_{m,m'}\,\delta_{\sigma,\mu}\,\delta_{\sigma',\mu'} - \sqrt{m'}\,\delta_{n,n'}\,\delta_{m,m'-1}\,\delta_{\sigma,\mu}\,\delta_{\sigma,\mu} \right) \sum_{\mathbf{s}(\mathbf{r})} \psi(\mathbf{s}) \right. \\
&\left. + \left(\sqrt{n'}\,\delta_{n,n'-1}\,\delta_{m,m'}\,\delta_{\sigma,\mu}\,\delta_{\sigma',\mu'} - \sqrt{m'+1}\,\delta_{n,n'}\,\delta_{m,m'+1}\,\delta_{\sigma,\mu}\,\delta_{\sigma',\mu'} \right) \sum_{\mathbf{s}(\mathbf{r})} \psi^{*}(\mathbf{s}) \right] \\
&+ \left\{ \omega_{c}\left(n'-m'\right) + U\left[n'\left(n'-1\right) - m'\left(m'-1\right)\right] + \omega\,\frac{\mu-\mu'}{2} \right\} \delta_{n,n'}\,\delta_{m,m'}\,\delta_{\sigma,\mu}\,\delta_{\sigma',\mu'} \\
&+ \Omega\left(\sqrt{n'+1}\,\delta_{n,n'+1}\,\delta_{m,m'}\,\delta_{\sigma,-1}\,\delta_{\sigma,-\mu}\,\delta_{\sigma',\mu'} - \sqrt{m'}\,\delta_{n,n'}\,\delta_{m,m'-1}\,\delta_{\sigma',1}\,\delta_{\sigma,\mu}\,\delta_{\sigma',-\mu'} \right. \\
&\left. + \sqrt{n'}\,\delta_{n,n'-1}\,\delta_{m,m'}\,\delta_{\sigma,1}\,\delta_{\sigma,-\mu}\,\delta_{\sigma',\mu'} - \sqrt{m'+1}\,\delta_{n,n'}\,\delta_{m,m'+1}\,\delta_{\sigma',-1}\,\delta_{\sigma,\mu}\,\delta_{\sigma',-\mu'} \right) \\
&+ i\,\Gamma_{l}\left[\sqrt{n'\,m'}\,\delta_{n,n'-1}\,\delta_{m,m'-1}\,\delta_{\sigma,\mu}\,\delta_{\sigma',\mu'} - \frac{1}{2}\left(n'+m'\right)\delta_{n,n'}\,\delta_{m,m'}\,\delta_{\sigma,\mu}\,\delta_{\sigma',\mu'} \right] \\
&+ i\,\gamma\left(\delta_{\sigma,-1}\,\delta_{\sigma',-1}\,\delta_{n,n'}\,\delta_{m,m'}\,\delta_{\sigma,-\mu}\,\delta_{\sigma',-\mu'} - \frac{2+\mu+\mu'}{4}\,\delta_{n,n'}\,\delta_{m,m'}\,\delta_{\sigma,\mu}\,\delta_{\sigma',\mu'} \right) \\
&+ i\,\Gamma_{p}\left(\delta_{\sigma,1}\,\delta_{\sigma',1}\,\delta_{n,n'}\,\delta_{m,m'}\,\delta_{\sigma,-\mu}\,\delta_{\sigma',-\mu'} - \frac{2-\mu-\mu'}{4}\,\delta_{n,n'}\,\delta_{m,m'}\,\delta_{\sigma,\mu}\,\delta_{\sigma',\mu'} \right),
\end{aligned}
\tag{2.7}
$$

where the notation $\mathbf{s}(\mathbf{r})$ labels the nearest-neighbouring sites of $\mathbf{r}$ and

$$
\psi(\mathbf{r}) \equiv \mathrm{Tr}(\hat{\rho}\,\hat{a}_{\mathbf{r}}) = \sum_{n}\sum_{\sigma} \sqrt{n+1}\,c_{n+1,n,\sigma,\sigma}(\mathbf{r}) \tag{2.8}
$$

is the condensation order parameter. The mean-field NESS of the system is determined by numerically propagating Eq. (2.7) in real time through a fourth-order Runge-Kutta algorithm, until convergence to the homogeneous solution $\hat{\rho}_0 = \hat{\rho}(t \to \infty) = \vec{c}_0$.

Besides the order parameter value, other local expectations values are straightforwardly evaluated through the following formulas,

$$
n(\mathbf{r}) \equiv \mathrm{Tr}(\hat{\rho}\,\hat{n}_{\mathbf{r}}) = \sum_{n}\sum_{\sigma} n\,c_{n,n,\sigma,\sigma}(\mathbf{r}), \tag{2.9}
$$

$$
\Delta n^{2}(\mathbf{r}) \equiv \mathrm{Tr}\left\{ \hat{\rho}\left[\hat{n}_{\mathbf{r}} - n(\mathbf{r})\right]^{2} \right\} = \sum_{n}\sum_{\sigma} n^{2}\,c_{n,n,\sigma,\sigma}(\mathbf{r}) - n(\mathbf{r})^{2}, \tag{2.10}
$$

$$
S_{z}(\mathbf{r}) \equiv \frac{1}{2}\mathrm{Tr}(\hat{\rho}\,\hat{\sigma}_{\mathbf{r}}^{z}) = \frac{1}{2}\sum_{n}\sum_{\sigma} \sigma\,c_{n,n,\sigma,\sigma}(\mathbf{r}), \tag{2.11}
$$

$$
S_{-}(\mathbf{r}) \equiv \frac{1}{2}\mathrm{Tr}(\hat{\rho}\,\hat{\sigma}_{\mathbf{r}}^{-}) = \frac{1}{2}\sum_{n} c_{n,n,1,-1}(\mathbf{r}), \tag{2.12}
$$

providing respectively the cavity density/filling, the photon density variance, the pseudospin and order parameter of the emitter coupled to the cavity at site $\mathbf{r}$. Moreover, we can easily estimate the purity

$$
P \equiv \mathrm{Tr}\left(\hat{\rho}^{2}\right) = \sum_{n,m}\sum_{\sigma,\sigma'} \left|c_{n,m,\sigma,\sigma'}\right|^{2} \tag{2.13}
$$

and the von-Neumann entropy

$$
S \equiv -\mathrm{Tr}[\hat{\rho}\,\ln(\hat{\rho})] = -\sum_{i} \lambda_{i}\,\ln(\lambda_{i}) \tag{2.14}
$$

of the NESS, where we have made the hypothesis of a uniform steady state under our local approximation of $\hat{\rho}$. In particular, we notice that the purity P is identical to the Frobenius norm of the density matrix. In Eq. (2.14), the summation runs over the eigenvalues of the density matrix λ_i.

We wish to emphasise that the ansatz (2.5) entails a non-perturbative description of the local Rabi coupling in (2.2), namely it properly accounts for the local correlations between the cavities and the TLE's and therefore allows to capture the physics of the so-called ultrastrong coupling limit $\Omega \gtrsim \sqrt{\Gamma_p \Gamma_l}$, also known as the C-QED regime. In this Chapter, we consider the hard-core limit of our model ($U/J \to \infty$), which represents a simple yet prototypical scenario of the physics of strong photon correlations that we want to address in this work. Moreover, we choose to set the TLE frequency to $\omega_{\mathrm{at}} = \omega_c - z\,J$ (with $z = 2\,d$), in order that the gain of photons is strongest at the bottom of the cavity band ($\mathbf{k} = \mathbf{0}$). This ensures that the spatially homogeneous condensate underlying our mean-field calculation is not affected by spurious fragmentation effects at finite $\mathbf{k}$ [417].

2.2.2 Phase diagram of the hard-core stationary state

Having outlined our mean-field approach to the driven-dissipative dynamics of $\hat{\rho}$ and the specific physical setting that we will address in the remainder of this Chapter, we devote the present Subsection to analyse in detail the mean-field properties of the out-of-equilibrium phase diagram of the system, with particular emphasis on the quantum phase transition and crossovers between the different NESS configurations. From now on, the pumping rate Γ_p will be set as the unit of energy for the sake of simplicity.

In Figure 2.2(a), we show a projection of the hard-core phase diagram of the NESS in the (J, Ω) space for $\Gamma_l/\Gamma_p = 5 \cdot 10^{-2}$ and $\gamma/\Gamma_p = 10^{-3}$. Within our mean-field analysis, the landscape of the possible states of the system consists of two phases, depending on whether the U(1) symmetry of the BH lattice is broken or not. We first notice that the symmetric state – which we anticipate to have an insulating character – occupies the whole region below the so-called *lasing threshold* $\Gamma_{\mathrm{em}}/\Gamma_l = 1$, where $\Gamma_{\mathrm{em}} \equiv 4\,\Omega^2/\Gamma_p$ is the effective emission rate of the TLE's with respect to the BH lattice [1]: in fact, a necessary condition in order to have a significant population in the symmetry-broken phase is that photon pumping overcomes the leakage rate Γ_l. For fixed Ω, the quantum phase transition responsible for symmetry breaking occurs for a sufficiently large value of $z\,J$; in particular, the general trend is such that the symmetric state is more and more robust against hopping processes, so that the critical point is shifted to larger values of the hopping energy.

As regards the lobe-shaped region of the symmetry-broken state, we can distinguish between two different regimes, namely above and below the tip of the lobe respectively. In the following, we will further characterise the properties of the NESS phases according to these two opposite situations, which we refer to as the weak-coupling ($\Gamma_{\mathrm{em}}/\Gamma_l \sim 1$) [Figure 2.2(b)] and the strong-coupling ($\Gamma_{\mathrm{em}}/\Gamma_l \gtrsim 1$) [Figure 2.2(c)]

---

[1] Rigorously speaking, $\Gamma_{\mathrm{em}} = 4\,\Omega^2/\Gamma_p$ is the effective pumping rate of the TLE's in the perturbative limit $\Omega \ll \Gamma_p$ (see [20, 414] as applicable references), nevertheless such a quantity remarkably provides a good rule of thumb for the same energy scale in the strong-coupling limit as well, see Eq. (2.18) and the subsequent discussion.
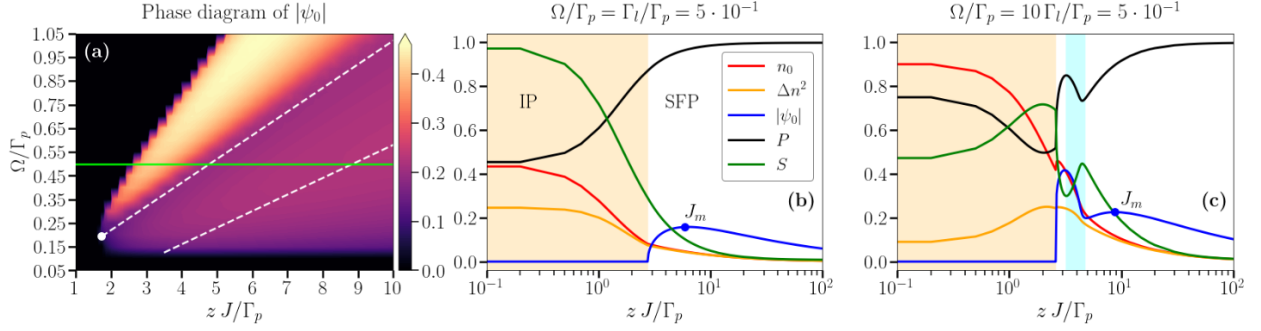
Figure 2.2: Panel (a): mean-field phase diagram of the NESS of the driven-dissipative hard-core photonic lattice for $\Gamma_l/\Gamma_p = 5 \cdot 10^{-2}$ and $\gamma/\Gamma_p = 10^{-3}$. The green line corresponds to the horizontal cut at $\Omega/\Gamma_p = 5 \cdot 10^{-1}$ illustrated in panel (c). The white point marks the position of the tip of the SFP lobe, while the white dashed lines enclose the region of hole superfluidity. Panel (b): mean-field behaviour of the NESS observables across the I-to-SF transition at constant $\Omega/\Gamma_p = \Gamma_l/\Gamma_p = 5 \cdot 10^{-1}$ and $\gamma/\Gamma_p = 10^{-3}$ in the weak-coupling regime. Panel (c): horizontal cut of the mean-field phase diagram in panel (a) at constant $\Omega/\Gamma_p = 5 \cdot 10^{-1}$ in the strong-coupling regime. Colour code of the lines in panels (b)-(c): density [red]; density variance [orange]; photon order parameter [blue]; purity [black]; entropy [green]. The white (orange-shaded) area indicates the SFP (IP) region, while the cyan-shaded stripe marks the values of zJ for which a dynamical instability due to the Goldstone mode appears (see Subsection 2.5.1).

regimes. More precisely, this distinction will be of particular importance to understand the low-J properties of the superfluid phase.

Insulating phase & out-of-equilibrium quantum phase transition

We start our analysis by considering different horizontal cuts at constant Ω across the phase diagram shown in Figure 2.2(a).

Mott-like state of photons

Below a critical value of the hopping J_c, the NESS is found in an Insulating Phase (IP) with vanishing order parameter $\psi_0 = 0$. More precisely, for a large enough Rabi coupling $\Omega \gg \sqrt{\Gamma_p \Gamma_l}$ and $J \lesssim J_c$ [Figure 2.2(c)], the local density n_0 [red solid line] reaches a value close to 1, in such a way that the cavity array hosts an almost pure Mott-like state [25, 414] as highlighted by the large purity [black solid line] of the NESS. Correspondingly, the local density variance [orange solid line] and the entropy [green solid line] are frozen in the same limit. It is important to notice that stabilisation of a robust MI state is a peculiar result of the joint outcome of strong local interactions and continuous pumping of photons.

Indeed, more general studies [414, 418] have shown that at $J = 0$ the driven-dissipative dynamics ruled by the master equation (2.3) is always able to stabilise an insulating NESS if the TLE frequency ω_{at} is set to be resonant with the $N \to N + 1$ transition of the Hubbard lattice, where N is the total number of photons in the cavities. The resulting weakly mixed state is dominated by the $N + 1$ photon state, while the emitters are stuck in the excited $\sigma = 1$ state, thus forming an efficient reservoir for the BH system. This situation requires a fine tuning of the parameters for a generic vale of N; however, the case $N = 1$ turns out to admit more relaxed constraints, namely

$$\frac{\Gamma_{\mathrm{em}}}{\Gamma_l} \gg 1 \,, \tag{2.15a}$$

$$\frac{\Gamma_{\mathrm{em}}\Gamma_p^2}{\Gamma_l U^2} \ll 1 \,, \tag{2.15b}$$

Whereas the condition (2.15b) is always satisfied in our hard-core setting, the inequal-

ity (2.15a) clearly loosens in the weak-coupling regime $\Gamma_{\mathrm{em}}/\Gamma_l \sim 1$: here, the NESS is an insulating mixed state at low density characterised by relatively large density fluctuations and a sizeable entropy [see Figure 2.2(b)].

While the state at $J = 0$ is per se interesting, its structure undergoes a gradual change by turning on the photon tunnelling J: this plays against the stabilisation of a pure MI state and affects the effective pumping of photons into the cavities with contrasting outcomes depending on $\Gamma_{\mathrm{em}}/\Gamma_l$, as we discuss now in more detail.

U(1)
symmetry
breaking by
incommen-
surability

Increasing the cavity bandwidth $z\,J$ towards values comparable to Γ_p, lost photons are repumped less efficiently. At strong coupling [Figure 2.2(c)], this leads to a substantial decrease in both the local density n_0 and the purity of the NESS, alongside an increase of local density fluctuations and entropy generation. Notably, the situation changes significantly at weak coupling [Figure 2.2(b)], where the onset of photon tunnelling lowers density fluctuations and purifies the NESS. At the critical point J_c, the system undergoes a second-order dynamical phase transition [419] to a Superfluid Phase (SFP), developing a finite order parameter displaying limit cycles $\psi_0 = |\psi_0|\,e^{-i\,\omega_0\,t}$ and with modulus scaling as $|\psi_0| \sim \sqrt{J - J_c}$ [420].

We stress that, in the present context, the formation of a coherent delocalised phase is not due to a competition between the hopping J and local interactions as it happens usually in strongly-correlated systems: instead, it crucially results from the incommensurability between the kinetic energy of photons propagating across the lattice and the emission rate Γ_p. This effect translates into a smaller effective pumping and a stronger competition between photon gain and losses as $z\,J$ reaches the critical point. In this respect, we point out that the I-to-SF transition occurs only for a hole-dominated fluid, namely for $n_0 < 1/2$, with the critical value of n_0 decreasing for increasing Γ_l. This fact is not only related to the inherent competition between pumping and losses caused by the increase of J, but finds also an explanation in the energy gained by the system through the formation of a condensate, as we will show more explicitly in the next paragraph.

More quantitative insights on the energy scales involved in the development of coherence inside the IP and in the breaking of U(1) symmetry can be obtained by an exact derivation of the NESS density matrix $\vec{c}_0$. Formally, this calculation amounts to simply determine the unique eigenvector of $\hat{L}[\vec{c}(\mathbf{r})]$ with vanishing eigenvalue, which corresponds to our mean-field approximation of the IP state. As a final result, we find that the density matrix consists of five independent coefficients only, having expressions

$$(c_0)_{0,1,1,-1} = \frac{z\,J\,\Gamma_l}{\Gamma_p\,\Omega} + i\,\frac{(\Gamma_p + \Gamma_l + \gamma)\,\Gamma_l}{2\,\Gamma_p\,\Omega}\,, \tag{2.16a}$$

$$(c_0)_{0,0,-1,-1} = \frac{\gamma}{\Gamma_p}\,c_{0,0,1,1} + \frac{(\Gamma_l + \gamma)\,\Gamma_l}{\Gamma_p^2}\,, \tag{2.16b}$$

$$(c_0)_{0,0,1,1} = \frac{\gamma}{\Gamma_p} + \frac{\Gamma_p\,\Gamma_l}{4\,\Omega^2}\left[\left(\frac{2\,\Omega}{\Gamma_p}\right)^2 + \left(1 + \frac{\Gamma_l + \gamma}{\Gamma_p}\right)^2 + \left(\frac{2\,z\,J}{\Gamma_p}\right)^2\right]\,, \tag{2.16c}$$

$$(c_0)_{1,1,-1,-1} = \frac{\Gamma_l + \gamma}{\Gamma_p}\,, \tag{2.16d}$$

$$(c_0)_{1,1,1,1} = 1\,, \tag{2.16e}$$

to be normalised by the trace $\mathrm{Tr}(\hat{\rho}) = \sum_n \sum_\sigma (c_0)_{n,n,\sigma,\sigma}$. Now, assuming to work in the limit $\gamma \ll \Gamma_p$, so that the TLE's are most of the time in their excited state $\sigma = 1$, and under the realistic condition $\Gamma_l \ll \Gamma_p$, the order of magnitude of the critical value of the photon bandwidth $z\,J_c$ can be straightforwardly obtained by imposing

$$\frac{(c_0)^{J=J_c}_{0,0,1,1}}{(c_0)^{J=J_c}_{1,1,1,1}} \simeq 1 \,, \tag{2.17}$$

namely that the probability of a cavity to be either occupied or empty is about the same. From this condition, we get

$$\frac{z\,J_c}{\Gamma_p} \simeq \frac{1}{2}\sqrt{\frac{\Gamma_{\mathrm{em}}}{\Gamma_l} - 1} \,, \tag{2.18}$$

which is in good agreement with the location of the I-to-SF boundary for a moderately large Ω. Importantly, we note that the critical point exists as long as $\Gamma_{\mathrm{em}}/\Gamma_l \geq 1$, which coincides exactly the lasing condition introduced before. Instructive information can be also extracted from the off-diagonal element $(c_0)_{0,1,1,-1}$, which quantifies the degree of quantum coherence in the IP. Comparing its (unnormalised) modulus at $J = 0$ with the value at $J = J_c$, we find

$$\left|(c_0)^{J=0}_{0,1,1,-1}\right| = \frac{(\Gamma_p + \Gamma_l + \gamma)\,\Gamma_l}{2\,\Gamma_p\,\Omega} < \left|(c_0)^{J=J_c}_{0,1,1,-1}\right| \simeq \sqrt{\frac{\Gamma_l}{\Gamma_p}} \tag{2.19}$$

where the inequality holds compatibly with the usual hypothesis $\Gamma_p \gg \Gamma_l, \gamma$ and, not surprisingly, when the lasing condition is fulfilled. Therefore, coherence in the IP state develops upon increasing the hopping and is determined by the photon leakage rate Γ_l only at the critical point, as we will also observe more explicitly in Subsection 2.5.1. This result hints once more at the key role played by different dissipation mechanisms in building coherence in the system, a feature that we will address more closely in the following paragraph.

Superfluid phase

Inside the SFP, the local density n_0 is still an overall decreasing function of J, which therefore acts similarly to a chemical potential for the system. Indeed, we find that the limit-cycle frequency shows only a little deviation from the mean-field hard-core energy at equilibrium [2], that is $\omega_0 \approx z\,J\,(2\,n_0 - 1) + \omega_c$, meaning that the condensate energy is lowered at large J by depleting photons [see Figure 2.3(a)]. Incidentally, we notice that, in the case of the hard-core lattice, the mean-field shift of the energy due to interactions is solely due to the hopping and reads $\Delta\mu = 2\,z\,J\,n_0$. Quite the opposite, the condensate density $\rho_c = |\psi_0|^2$ is generally a non-monotonic function of J, depending on the *gain ratio* $g \equiv \Gamma_{\mathrm{em}}/\Gamma_p$, see Figure 2.3(b). Interestingly, we notice that a non-monotonic behaviour of the order parameter is a property in common with other dissipative phase transitions, e.g. those appearing in spin chains [421, 422]. In these systems, complexity in the mean-field properties of the order parameter is usually a clue to the presence of subtle phenomena due to quantum fluctuations, not evident at

---

[2] We direct the reader to Appendix F.2 for a review of the mean-field description of hard-core bosons on a lattice.
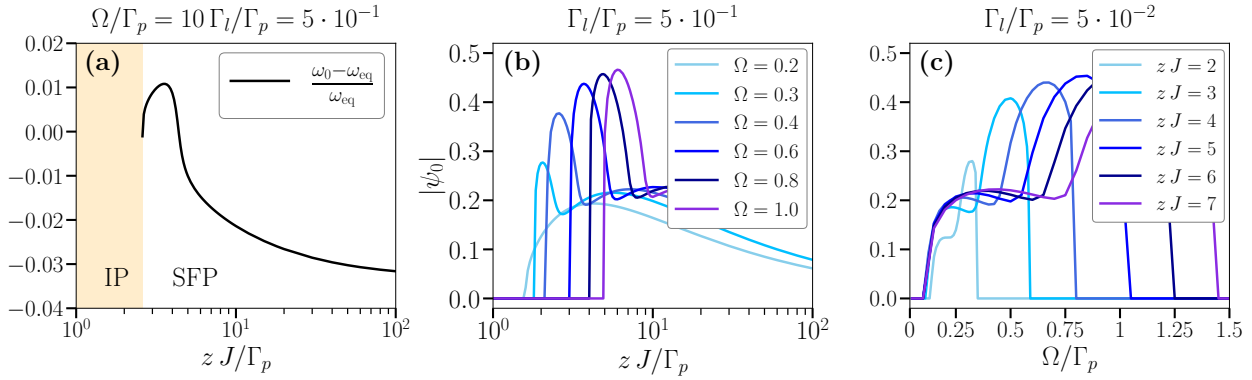
In panels (b)-(c), the values of Ω and $z\,J$ are implicitly taken in units of Γ_p.

Figure 2.3: Panel (a): J-dependence of the relative deviation of the limit-cycle frequency of the SFP order parameter from its equilibrium value $\omega_{\mathrm{eq}} = z\,J\,(2\,n_0 - 1) + \omega_c$ for $\Omega/\Gamma_p = 5 \cdot 10^{-1}$, $\Gamma_l/\Gamma_p = 5 \cdot 10^{-2}$ and $\gamma/\Gamma_p = 10^{-3}$. The white (orange-shaded) area indicates the SFP (IP) region. Panel (b): J-dependence of the order parameter of the SFP for different constant values of Ω, ranging from the weak-coupling regime (light-blue line) to the strong-coupling limit (purple line), corresponding to distinct horizontal cuts of the phase diagram shown in Figure 2.2(a). Panel (c): Ω-dependence of the order parameter of the SFP for increasing constant values of J, corresponding to distinct vertical cuts of the same phase diagram.

Non-monotonicity of the condensate density

the level of the superficial NESS structure; in the next Sections, we will show that these observations apply also to our specific case.

In the weak-coupling regime $g \sim 1$ (namely, below the tip of the SFP lobe) [Figure 2.2(b)], ρ_c shows a maximum for $J = J_m$, after which it saturates n_0 realising an extremely pure and dilute condensate. Analogously to n_0, both density fluctuations Δn^2 and the entropy S decrease monotonically, their maximum being located at the critical point. This situation can be understood as follows. For $J < J_m$, where $\partial \rho_c / \partial n_0 < 0$, local losses Γ_l start having a strong influence on the dissipative dynamics and favour quantum coherence at the same time: since the condensate density increases despite the photon leakage, the NESS can be classified as an instance of *hole superfluid* [43, 52]. For $J > J_m$, the large bandwidth $z\,J$ overcomes the effect of all dissipative effects, so that cavity photons form a dilute *particle superfluid*, which is also almost pure given the narrowing of the pumping rate Γ_p as compared to J.

Interestingly, in the strong-coupling regime $g \gtrsim 1$ [Figure 2.2(c)], a second maximum of ρ_c develops close to the critical point for $J_c < J < J_m$, mirrored by a sharp peak in the NESS purity. In this hopping range, the Rabi coupling Ω is large enough to pump photons in high-energy states overlapping with the would-be hard-core state at equilibrium with $0 < \omega_c < z\,J$. A notable signature of this physics is, besides a marked entropy suppression, the particle character of the superfluid state in this region. Furthermore, the maximal value of the condensate density is remarkably close to its equilibrium value $\rho_c = \Delta n^2 / n_0$. In addition, we notice that the height of the intruding maximum of ρ_c and the resulting degree of non-monotonicity appear to depend on the gain ratio g: the stronger is the coupling with the TLE, the higher and wider is the peak in the order parameter. For completeness, we highlight in advance that the hopping region connecting the first maximum of ρ_c to the dilute limit [cyan-shaded area in Figure 2.2(c)] is of particular importance, as it hides a dynamical instability of low-energy excitations for $\Omega \sim \Gamma_p$, see the following Subsection 2.5.1.

For completeness, we point out that the J-dependence of ρ_c and all the other mean-field quantities is quite similar to their Ω-dependence when crossing the SFP

lobe at fixed J, as explicitly shown in Figure 2.3(c). Here, we observe that decreasing Ω has the same effect of increasing J and, in particular, the "weak-coupling" type of behaviour corresponds to small fixed values of J, sufficiently close to the tip of the SFP lobe. This additional result confirms the physical picture of the hopping as a mechanism opposing to pumping and viceversa and, most importantly, substantiate our diagnosis of the SFP non-monotonic properties in terms of particle/hole superfluidity. In fact, rigorously speaking, the precise character of the superfluid carriers is related to the sign of $\mathfrak{s} = \text{sgn}(\partial \rho_c / \partial n_0)$ evaluated at fixed J [43, 423]. Nonetheless, in our system we find that $\mathfrak{s}$ does *not* change if calculated at fixed Ω for the same values of J, as considered in the main discussion above. Putting these comments into perspective, we remark that the knowledge of the particle/hole character of a superfluid state is of key importance in order to address the problem of the stability of non-linear phenomena, such as standing and propagating solitons [245, 246], that could be possibly realised in our driven-dissipative setting [424–428].

Signatures of particle/hole superfluidity

2.3 Theory of Bogoliubov fluctuations

2.3.1 Collective modes

Taking advantage of the close analogy that we have identified between the Gutzwiller-Lindblad equations (2.6) and the well-known GPE equation, we can take inspiration from linear response methods at equilibrium [51, 52] – reviewed in Chapter 2 of Part I – and consider small oscillations of the density around the NESS configuration of the form

$$\vec{c}(\mathbf{r}, t) = \vec{c}_0(t) + \delta \vec{c}(\mathbf{r}, t) = \hat{U}(t) \left[\vec{c}_0 + \vec{u}_{\mathbf{k}} \, e^{i(\mathbf{k} \cdot \mathbf{r} - \omega_{\mathbf{k}} t)} + \vec{v}_{\mathbf{k}}^* \, e^{-i(\mathbf{k} \cdot \mathbf{r} - \omega_{\mathbf{k}}^* t)} \right] \hat{U}^\dagger(t) , \quad (2.20)$$

where the unitary operator $\hat{U}(t) \equiv \exp \left[-i \left(\hat{n} + \hat{\sigma}_z / 2 \right) \omega_0 \, t \right]$ rotates the density matrix in the reference frame of limit cycles (if present) and $\vec{u}_{\mathbf{k}} \, (\vec{v}_{\mathbf{k}})$ weighs a particle (hole) excitation with energy $\omega_{\mathbf{k}} \, (-\omega_{\mathbf{k}}^*)$. We note that Eq. (2.20) is a direct generalisation of the approach introduced in [19] to the case of incoherent pumping and naturally incorporate those local correlations in the TLE-cavity unit of the system naturally accounted by the Gutzwiller approximation. Linearising the equations of motion (2.6) with respect to the $\delta \vec{c}$'s, one obtains a Bogoliubov-de Gennes system of equations,

$$\hat{\mathcal{L}}_{\mathbf{k}} \begin{pmatrix} \vec{u}_{\mathbf{k}} \\ \vec{v}_{\mathbf{k}} \end{pmatrix} = \omega_{\mathbf{k}} \begin{pmatrix} \vec{u}_{\mathbf{k}} \\ \vec{v}_{\mathbf{k}} \end{pmatrix} , \quad (2.21)$$

Bogoliubov-Lindblad equations of the collective excitations

where the non-Hermitian superoperator $\hat{\mathcal{L}}_{\mathbf{k}} \equiv \text{diag}\left(\hat{A}_{\mathbf{k}}, -\hat{A}_{\mathbf{k}}^* \right)$ has a block-diagonal structure because of the relation $\vec{v}_{\mathbf{k}} = \left(\vec{u}_{\mathbf{k}} \right)^T$, due to the built-in Hermiticity of the density matrix, resulting in the identity $c_{n,m,\sigma,\sigma'}(\mathbf{r}, t) = c_{m,n,\sigma',\sigma}^*(\mathbf{r}, t)$. The matrix

elements of the upper diagonal block of $\hat{\mathcal{L}}_{\mathbf{k}}$ are given by:

$$
\begin{aligned}
A_{n,m,\sigma,\sigma'}^{n',m',\mu,\mu'}(\mathbf{k}) &\equiv L_{n,m,\sigma,\sigma'}^{n',m',\mu,\mu'}[\vec{c}_0] \\
&+ \varepsilon_{\mathbf{k}} \left[\left(\sqrt{n}\,(c_0)_{n-1,m,\sigma,\sigma'} - \sqrt{m+1}\,(c_0)_{n,m+1,\sigma,\sigma'} \right) \sqrt{n'}\,\delta_{n'-1,m'}\,\delta_{\mu,\mu'} \right. \\
&\left. + \left(\sqrt{n+1}\,(c_0)_{n+1,m,\sigma,\sigma'} - \sqrt{m}\,(c_0)_{n,m-1,\sigma,\sigma'} \right) \sqrt{n'+1}\,\delta_{n'+1,m'}\,\delta_{\mu,\mu'} \right] \\
&- \omega_0 \left(n - m + \frac{\sigma - \sigma'}{2} \right) \delta_{n,n'}\,\delta_{m,m'}\,\delta_{\sigma,\mu}\,\delta_{\sigma',\mu'}\,,
\end{aligned}
$$
(2.22)

where $\varepsilon_{\mathbf{k}} = -2\,J \sum_{a=1}^d \cos(k_a)$ is again the free-particle dispersion on a lattice.

The eigenvalue equation (2.21) is among the main results of this Chapter and provides the energy spectra of the proper many-body excitations $\omega_{\alpha,\mathbf{k}}$ of the NESS, in addition to information on their role in quantum observables as we will show in the next Subsection. Notice that, as a byproduct of the global U(1) invariance of the ansatz (2.5), there is a single zero-energy eigenmode $\omega_{\alpha=0,\mathbf{k}} = 0$ degenerate with the NESS [44], namely $(u_{n,m,\sigma,\sigma'}, v_{n,m,\sigma,\sigma'}) = \left[(c_0)_{n,m,\sigma,\sigma'}, (c_0)_{n,m,\sigma,\sigma'}^* \right]$. Also, the non-vanishing eigenvalues of $\hat{\mathcal{L}}_{\mathbf{k}}$ can be grouped into anti-conjugate pairs, $\omega_{\alpha,\mathbf{k}} = \pm\omega'_{\alpha,\mathbf{k}} + i\,\omega''_{\alpha,\mathbf{k}}$, since $\mathrm{Re}\left[\mathrm{Tr}(\hat{A}_{\mathbf{k}}) \right] = 0$; indeed, this is intimately related to the fact that the unitary evolution of the system traces back to the Hamiltonian commutator in Eq. (2.3). However, a less intuitive relation holds between positive- and negative-energy eigenvectors. It is important to observe that, within our notation (2.20), the NESS is a stable state if $\mathrm{Im}(\omega_{\alpha,\mathbf{k}}) < 0$ for each excitation mode $(\alpha, \mathbf{k})$: a violation of such inequality indicates that the uniform NESS is dynamically unstable to a different ordering of photons on the lattice.

2.3.2 Fluctuations of observables

One of the main advantages of our formalism concerns a quantitative estimation of how active the NESS collective excitations are in different perturbation channels. This analysis will prove useful to understand e.g. the particle/hole and phase/amplitude characters of the low-energy collective modes across the phase diagram of the NESS.

As a first example, let us consider the density channel. Inserting the density matrix expansion (2.20) into the expression of Eq. (2.9), we find that linear density fluctuations due to the $(\alpha, \mathbf{k})$ excitation behave as

$$
\begin{aligned}
n(\mathbf{r}) &= \sum_n \sum_\sigma n \left[(c_0)_{n,n,\sigma,\sigma} + u_{\alpha,\mathbf{k},n,n,\sigma,\sigma}\,e^{i\,\mathbf{k}\cdot\mathbf{r}} + v_{\alpha,\mathbf{k},n,n,\sigma,\sigma}^*\,e^{-i\,\mathbf{k}\cdot\mathbf{r}} \right] \\
&= n_0 + \left(N_{\alpha,\mathbf{k}}\,e^{i\,\mathbf{k}\cdot\mathbf{r}} + \text{c.c.} \right),
\end{aligned}
$$
(2.23)

where we have introduced the density spectral weight

$$
N_{\alpha,\mathbf{k}} \equiv \sum_n \sum_\sigma n\,u_{\alpha,\mathbf{k},n,n,\sigma,\sigma}\,.
$$
(2.24)

Similarly, we can examine the fluctuations of the order parameter, given by

$$\psi(\mathbf{r}) = \sum_n \sum_\sigma \sqrt{n+1} \left[(c_0)_{n+1,n,\sigma,\sigma} + u_{\alpha,\mathbf{k},n+1,n,\sigma,\sigma} \, e^{i\,\mathbf{k}\cdot\mathbf{r}} + v^*_{\alpha,\mathbf{k},n+1,n,\sigma,\sigma} \, e^{-i\,\mathbf{k}\cdot\mathbf{r}} \right]$$

$$= \psi_0 + U_{\alpha,\mathbf{k}} \, e^{i\,\mathbf{k}\cdot\mathbf{r}} + V^*_{\alpha,\mathbf{k}} \, e^{-i\,\mathbf{k}\cdot\mathbf{r}}, \tag{2.25}$$

where

$$U_{\alpha,\mathbf{k}} \equiv \sum_n \sum_\sigma \sqrt{n+1} \, u_{\alpha,\mathbf{k},n+1,n,\sigma,\sigma} \tag{2.26}$$

and

$$V_{\alpha,\mathbf{k}} \equiv \sum_n \sum_\sigma \sqrt{n+1} \, v_{\alpha,\mathbf{k},n+1,n,\sigma,\sigma} = \sum_n \sum_\sigma \sqrt{n+1} \, u_{\alpha,\mathbf{k},n,n+1,\sigma,\sigma} \tag{2.27}$$

are generalisations of the particle/hole amplitudes (2.17) of fluctuations in the one-body bosonic field to the present non-equilibrium setting. We point out that, whereas particle and hole fluctuations of the density matrix are related by simple transposition $\vec{v}_\mathbf{k} = (\vec{u}_\mathbf{k})^T$, we cannot identify an obvious PHS condition for the excitations of the photon field, since $|U_{\alpha,\mathbf{k}}| \neq |V_{\alpha,\mathbf{k}}|$ in principle. This is due to the fact that $u_{\alpha,\mathbf{k},n,m,\sigma,\sigma'} \neq u^*_{\alpha,\mathbf{k},m,n,\sigma',\sigma}$ in general, meaning that either particle or hole fluctuations of the density matrix are not individually bound to be Hermitian.

Using Eq. (2.25), we can also estimate the spectral contribution of each excitation mode to amplitude and phase perturbations of the order parameter. To lowest order, upon writing the order parameter as $\psi(\mathbf{r}) = |\psi(\mathbf{r})| \exp[i\,\varphi(\mathbf{r})]$, the former kind of fluctuations reads

$$\delta \, |\psi(\mathbf{r})| \approx \delta \left\{ |\psi(\mathbf{r})| \cos \left[\varphi(\mathbf{r}) \right] \right\} = \frac{1}{2} \, \delta \left[\psi(\mathbf{r}) + \text{c.c.} \right] = \frac{1}{2} \left(U_{\alpha,\mathbf{k}} + V_{\alpha,\mathbf{k}} \right) e^{i\,\mathbf{k}\cdot\mathbf{r}} + \text{c.c.}, \tag{2.28}$$

while phase fluctuations are approximately captured by

$$\delta\varphi(\mathbf{r}) \approx \frac{\delta \left\{ |\psi(\mathbf{r})| \sin \left[\varphi(\mathbf{r}) \right] \right\}}{|\psi(\mathbf{r})|} = \frac{1}{2\,i\,|\psi(\mathbf{r})|} \delta \left[\psi(\mathbf{r}) - \text{c.c.} \right] \propto \frac{1}{2\,i} \left(U_{\alpha,\mathbf{k}} - V_{\alpha,\mathbf{k}} \right) e^{i\,\mathbf{k}\cdot\mathbf{r}} + \text{c.c.} \tag{2.29}$$

2.4 Response functions and quantum correlations

2.4.1 Generalised linear response theory

Let us consider a generic perturbation in the momentum-frequency channel $(\mathbf{k}, \omega)$ represented by the operator $\hat{F}_\mathbf{r}$,

$$\hat{H}_\mathrm{P}(t) \equiv \sum_\mathbf{r} \left[V_{\mathbf{k},\omega} \, e^{i(\mathbf{k}\cdot\mathbf{r} - \omega\,t)} \hat{F}_\mathbf{r} + V^*_{\mathbf{k},\omega} \, e^{-i(\mathbf{k}\cdot\mathbf{r} - \omega\,t)} \hat{F}^\dagger_\mathbf{r} \right]. \tag{2.30}$$

Gaussian fluctuations induced by such perturbation can be evaluated by considering its contribution at linear order to the dynamical equations of quantum fluctuations (2.21), which simply generalise into

$$\omega \begin{pmatrix} \vec{u}_\mathbf{k} \\ \vec{v}_\mathbf{k} \end{pmatrix} = \hat{\mathcal{L}}_\mathbf{k} \begin{pmatrix} \vec{u}_\mathbf{k} \\ \vec{v}_\mathbf{k} \end{pmatrix} + \hat{W}_{\mathbf{k},\omega} \begin{pmatrix} \vec{c}_0 \\ (\vec{c}_0)^* \end{pmatrix}, \tag{2.31}$$

where $\hat{W}_{\mathbf{k},\omega} \equiv \mathrm{diag}(\hat{w}_{\mathbf{k}}, -\hat{w}_{\mathbf{k}}^*)$, with the matrix blocks $\hat{w}_{1,\mathbf{k},\omega} \sim V_{\mathbf{k},\omega}$ and $\hat{w}_{2,\mathbf{k},\omega} \sim V_{\mathbf{k},\omega}^*$ given by the Lindbladian terms corresponding the perturbation operators $\hat{F}_{\mathbf{r}}$ and $\hat{F}_{\mathbf{r}}^\dagger$ respectively. By inverting Eq. (2.31), we obtain a convoluted extension of the original Bogoliubov-de Gennes eigenvalue problem,

$$
\begin{pmatrix} \vec{u}_{\mathbf{k}} \\ \vec{v}_{\mathbf{k}} \end{pmatrix} = \left(\omega \, \hat{\mathbb{1}} - \hat{\mathcal{L}}_{\mathbf{k}} \right)^{-1} \begin{pmatrix} \hat{w}_{1,\mathbf{k},\omega} & 0 \\ 0 & -\hat{w}_{2,\mathbf{k},\omega} \end{pmatrix} \begin{pmatrix} \vec{c}_0 \\ (\vec{c}_0)^* \end{pmatrix} .
\tag{2.32}
$$

As a final step, we can make use of the spectral decomposition of $\hat{\mathcal{L}}_{\mathbf{k}}$ and rewrite Eq. (2.32) as

$$
\begin{aligned}
\begin{pmatrix} \vec{u}_{\mathbf{k}} \\ \vec{v}_{\mathbf{k}} \end{pmatrix} &= \sum_\alpha \begin{pmatrix} \vec{u}_{\alpha,\mathbf{k}} \\ \vec{v}_{\alpha,\mathbf{k}} \end{pmatrix} \frac{1}{\omega - \omega_{\alpha,\mathbf{k}}} \begin{pmatrix} \vec{x}_{\alpha,\mathbf{k}} \\ \vec{y}_{\alpha,\mathbf{k}} \end{pmatrix}^\dagger \begin{pmatrix} \hat{w}_{1,\mathbf{k},\omega} & 0 \\ 0 & -\hat{w}_{2,\mathbf{k},\omega} \end{pmatrix} \begin{pmatrix} \vec{c}_0 \\ (\vec{c}_0)^* \end{pmatrix} \\
&= \hat{R} \cdot \hat{\Omega}(\omega) \cdot \left[\hat{R}^{-1} \cdot \hat{W}_{\mathbf{k},\omega} \cdot \begin{pmatrix} \vec{c}_0 \\ (\vec{c}_0)^* \end{pmatrix} \right] ,
\end{aligned}
\tag{2.33}
$$

where $(\vec{x}_{\alpha,\mathbf{k}}, \vec{y}_{\alpha,\mathbf{k}})$ is the left eigenvector of $\hat{\mathcal{L}}_{\mathbf{k}}$ associated with the excitation mode $(\alpha, \mathbf{k})$, $\hat{\Omega}_{\alpha\beta}(\omega) = \delta_{\alpha,\beta}/\left(\omega - \omega_{\alpha,\mathbf{k}} \right)$ and the matrix $\hat{R}$ gathers the right eigenvectors of $\hat{\mathcal{L}}_{\mathbf{k}}$ on its columns. After carrying out the calculation of the right-hand side of Eq. (2.33), the linear response function for a given observable $\hat{O}(\mathbf{r}, t)$ is directly provided by the corresponding linear expansion in terms of the fluctuation amplitudes $(\underline{u}_{\mathbf{k}}, \underline{v}_{\mathbf{k}})$ as given by the result of Eq. (2.33).

2.4.2 Density fluctuations from the Bragg response

As a first illustrative example, let us consider a Bragg perturbation

$$
\hat{H}_{\mathrm{Bragg}}(t) \equiv \sum_{\mathbf{r}} V_{\mathbf{k},\omega} \cos \left(\mathbf{k} \cdot \mathbf{r} - \omega \, t \right) \hat{n}_{\mathbf{r}} .
\tag{2.34}
$$

This Hamiltonian perturbation produces a modulation in the photon density according to the identity $\delta \langle \hat{n}_{\mathbf{r}} \rangle = \rho_{\mathbf{k},\omega} \, e^{i(\mathbf{k} \cdot \mathbf{r} - \omega \, t)} + \text{c.c.}$, where $\rho_{\mathbf{k},\omega} = \chi_n(\mathbf{k}, \omega) \, V_{\mathbf{k},\omega}$ with $\chi_n(\mathbf{k}, \omega)$ being defined as the density response function. In this case, Eq. (2.32) specialises into

$$
\begin{pmatrix} \vec{u}_{\mathbf{k}} \\ \vec{v}_{\mathbf{k}} \end{pmatrix} = \frac{1}{2} \sum_\alpha \begin{pmatrix} \vec{u}_{\alpha,\mathbf{k}} \\ \vec{v}_{\alpha,\mathbf{k}} \end{pmatrix} \frac{1}{\omega - \omega_{\alpha,\mathbf{k}}} \begin{pmatrix} \vec{x}_{\alpha,\mathbf{k}} \\ \vec{y}_{\alpha,\mathbf{k}} \end{pmatrix}^\dagger \begin{bmatrix} \vec{\mathcal{N}}_0 \\ -\left(\vec{\mathcal{N}}_0 \right)^* \end{bmatrix} V_{\mathbf{k},\omega} ,
\tag{2.35}
$$

where $(\mathcal{N}_0)_{n,m,\sigma,\sigma'} = (n - m) \, (c_0)_{n,m,\sigma,\sigma'}$. The density fluctuation amplitude $\rho_{\mathbf{k},\omega} \equiv N_{\mathbf{k}}$ is given by contracting the left-hand side of Eq. (2.35) by a tensor with elements

$n\, \delta_{n,n'}\, \delta_{m,m'}\, \delta_{n,m}\, \delta_{\sigma,\mu}\, \delta_{\sigma',\mu'}\, \delta_{\sigma,\sigma'}$ in both the $\vec{u}_{\mathbf{k}}$ and $\vec{v}_{\mathbf{k}}$ sectors, hence

$$
\begin{aligned}
2\,\rho_{\mathbf{k},\omega} &= \sum_{\alpha} \frac{N_{\alpha,\mathbf{k}}}{\omega - \omega_{\alpha,\mathbf{k}}} \begin{pmatrix} \vec{x}_{\alpha,\mathbf{k}} \\ \vec{y}_{\alpha,\mathbf{k}} \end{pmatrix}^{\dagger} \begin{bmatrix} \vec{\mathcal{N}}_9 \\ -\left(\vec{\mathcal{N}}_0\right)^{*} \end{bmatrix} V_{\mathbf{k},\omega} \\
&= \sum_{\alpha} \frac{N_{\alpha,\mathbf{k}} \left[\vec{x}^{*}_{\alpha,\mathbf{k}} \cdot \vec{\mathcal{N}}_0 - \vec{y}^{*}_{\alpha,\mathbf{k}} \cdot \left(\vec{\mathcal{N}}_0\right)^{*} \right]}{\omega - \omega_{\alpha,\mathbf{k}}} V_{\mathbf{k},\omega} \\
&= 2 \underbrace{\sum_{\alpha} \frac{N_{\alpha,\mathbf{k}} \left(\vec{x}^{*}_{\alpha,\mathbf{k}} \cdot \vec{\mathcal{N}}_0 \right)}{\omega - \omega_{\alpha,\mathbf{k}}} V_{\mathbf{k},\omega}}_{\chi_n(\mathbf{k},\omega)} \,.
\end{aligned}
\tag{2.36}
$$

Therefore, we observe that the density spectral weight $N_{\alpha,\mathbf{k}}$ sets directly the strength of the dynamical density response of the system in the NESS. We remark that, since the analytic continuation of $\chi_n(\mathbf{k},\omega)$ can be identified with the two-particle Green's function of the system, a suitable manipulation of its Fourier transform provides the lowest-order estimation of spatial and temporal density correlations, as we will discuss in Subsection 2.4.5.

2.4.3 Normal and anomalous components of the Green's function

A particularly insightful quantity is the response of cavity photons to an external classical field. This probe can be modelled as a particle-hole perturbation (coherent drive) on the BH lattice and has been also the focus of recent experimental efforts targeting the dynamical properties of the driven-dissipative MI state [25]. The very same object can be identified with the retarded Green's function of the NESS, for which our calculations give a simple semi-analytical result that we discuss in this Subsection.

Similarly to the case of a density perturbation, we start our derivation by studying the response of the photon field to a perturbation creating a particle (removing a hole) with a given momentum in the NESS, namely

$$
\hat{H}_{\mathrm{p}}(t) \equiv \frac{1}{2} \sum_{\mathbf{r}} \left[\eta_{\mathbf{k},\omega}\, e^{i(\mathbf{k}\cdot\mathbf{r} - \omega\, t)}\, \hat{a}^{\dagger}_{\mathbf{r}} + \eta^{*}_{\mathbf{k},\omega}\, e^{-i(\mathbf{k}\cdot\mathbf{r} - \omega\, t)}\, \hat{a}_{\mathbf{r}} \right]\,,
\tag{2.37}
$$

which breaks the U(1) symmetry of the model explicitly and therefore is coupled to fluctuations of the order parameter $\psi(\mathbf{r})$. The linear response equations corresponding to the perturbation (2.37) have the form

$$
\begin{pmatrix} \vec{u}_{\mathbf{k}} \\ \vec{v}_{\mathbf{k}} \end{pmatrix} = \frac{1}{2} \sum_{\alpha} \begin{pmatrix} \vec{u}_{\alpha,\mathbf{k}} \\ \vec{v}_{\alpha,\mathbf{k}} \end{pmatrix} \frac{1}{\omega - \omega_{\alpha,\mathbf{k}}} \begin{pmatrix} \vec{x}_{\alpha,\mathbf{k}} \\ \vec{y}_{\alpha,\mathbf{k}} \end{pmatrix}^{\dagger} \begin{bmatrix} \vec{\mathcal{P}}_0 \\ -\left(\vec{\mathcal{Q}}_0\right)^{*} \end{bmatrix} \eta_{\mathbf{k},\omega}\,,
\tag{2.38}
$$

where we have defined the vectorised matrices

$$
\left(\mathcal{P}_0\right)_{n,m,\sigma,\sigma'} = \sqrt{n}\,\left(c_0\right)_{n-1,m,\sigma,\sigma'} - \sqrt{m+1}\,\left(c_0\right)_{n,m+1,\sigma,\sigma'}
\tag{2.39}
$$

and

$$
\left(\mathcal{Q}_0\right)_{n,m,\sigma,\sigma'} = \sqrt{n+1}\,\left(c_0\right)_{n+1,m,\sigma,\sigma'} - \sqrt{m}\,\left(c_0\right)_{n,m-1,\sigma,\sigma'}\,.
\tag{2.40}
$$

Now, the previous expression allows us to calculate two different types of response functions, either in the (i) particle or in the (ii) hole channel.

The first kind of response requires to determine the *particle* fluctuation amplitude $U_{\alpha,\mathbf{k}}$ defined in Eq. (2.26): this is given by contracting both the sides of Eq. (2.38) by an operator with tensor components $\sqrt{n+1}\,\delta_{n+1,n'}\,\delta_{n,m'}\,\delta_{n,m+1}\,\delta_{\sigma,\mu}\,\delta_{\sigma',\mu'}\,\delta_{\sigma,\sigma'}$ in the $\vec{u}_{\mathbf{k}}$ sector and $\sqrt{n+1}\,\delta_{n,n'}\,\delta_{n+1,m'}\,\delta_{n,m-1}\,\delta_{\sigma,\mu}\,\delta_{\sigma',\mu'}\,\delta_{\sigma,\sigma'}$ in the $\vec{v}_{\mathbf{k}}$ sector. As a result, we obtain

$$
\begin{aligned}
2\,\Psi_{\mathbf{k},\omega} &= \sum_\alpha \frac{U_{\alpha,\mathbf{k}}}{\omega - \omega_{\alpha,\mathbf{k}}} \begin{pmatrix} \vec{x}_{\alpha,\mathbf{k}} \\ \vec{y}_{\alpha,\mathbf{k}} \end{pmatrix}^\dagger \left[\begin{array}{c} \vec{\mathcal{P}}_0 \\ -\left(\vec{\mathcal{Q}}_0\right)^* \end{array} \right] \eta_{\mathbf{k},\omega} \\
&= \sum_\alpha \frac{U_{\alpha,\mathbf{k}} \left[\vec{x}_{\alpha,\mathbf{k}}^* \cdot \vec{\mathcal{P}}_0 - \vec{y}_{\alpha,\mathbf{k}}^* \cdot \left(\vec{\mathcal{Q}}_0\right)^* \right]}{\omega - \omega_{\alpha,\mathbf{k}}} = \\
&= 2 \underbrace{\sum_\alpha \frac{U_{\alpha,\mathbf{k}} \left(\vec{x}_{\alpha,\mathbf{k}}^* \cdot \vec{\mathcal{P}}^0 \right)}{\omega - \omega_{\alpha,\mathbf{k}}}}_{G_R(\mathbf{k},\omega)} \eta_{\mathbf{k},\omega}\,,
\end{aligned}
\tag{2.41}
$$

where $\Psi_{\mathbf{k},\omega}$ is the order parameter variation. Physically speaking, the response of the order parameter to the perturbation (2.37) in the particle channel can be interpreted as the normal component of the retarded Green's function of cavity photons [51, 74]. More explicitly, the explicit expression of our prediction for the Green's function is

$$
G_R(\mathbf{k},\omega) \equiv \sum_\alpha \frac{Z_{\alpha,\mathbf{k}}}{\omega - \omega_{\alpha,\mathbf{k}}} = {\sum_\alpha}' \left[\frac{Z_{\alpha,\mathbf{k}}}{\omega - \omega_{\alpha,\mathbf{k}}} + \frac{Y_{\alpha,\mathbf{k}}^*}{\omega + \omega_{\alpha,\mathbf{k}}^*} \right]\,,
\tag{2.42}
$$

which has been written in a more symmetric form in the last equality. Here, we have defined the quasiparticle

$$
Z_{\alpha,\mathbf{k}} \equiv U_{\alpha,\mathbf{k}} \left(\vec{x}_{\alpha,\mathbf{k}}^* \cdot \vec{\mathcal{P}}_0 \right)
\tag{2.43}
$$

and quasihole

$$
Y_{\alpha,\mathbf{k}} \equiv V_{\alpha,\mathbf{k}} \left(\vec{y}_{\alpha,\mathbf{k}}^* \cdot \vec{\mathcal{P}}_0^* \right)
\tag{2.44}
$$

weights, while the summation on the right-hand side of Eq. (2.42) is restricted to excitations with positive real energy.

The second type of dynamical fluctuations which can be drawn out of Eq. (2.41) encodes the response of the order parameter in the hole channel. This corresponds to extracting the *hole* amplitude $V_{\alpha,\mathbf{k}}$ from the right-hand side of Eq. (2.38) in the same way as outlined above for the normal component. The final result of this procedure is the retarded anomalous component of the Green's function, having the expression

$$
\Delta_R(\mathbf{k},\omega) \equiv \sum_\alpha \frac{\overline{Z}_{\alpha,\mathbf{k}}}{\omega - \omega_{\alpha,\mathbf{k}}} = {\sum_\alpha}' \left[\frac{\overline{Z}_{\alpha,\mathbf{k}}}{\omega - \omega_{\alpha,\mathbf{k}}} + \frac{\overline{Y}_{\alpha,\mathbf{k}}^*}{\omega + \omega_{\alpha,\mathbf{k}}^*} \right]\,,
\tag{2.45}
$$

where we have introduced the anomalous quasiparticle $\overline{Z}_{\alpha,\mathbf{k}} = (V_{\alpha,\mathbf{k}}/U_{\alpha,\mathbf{k}})\,Z_{\alpha,\mathbf{k}}$ and quasihole $\overline{Y}_{\alpha,\mathbf{k}} = (U_{\alpha,\mathbf{k}}/V_{\alpha,\mathbf{k}})\,Y_{\alpha,\mathbf{k}}$ weights. As one could expect by physical intuition, anomalous correlations play a major role in the SF phase of the NESS and, in analogy with the case of EP condensates [429], can be exploited for directly probing the excitation spectrum of the system, as we will discuss more in depth in the following

Subsections 2.4.4 and 2.5.2.

Applying the concepts of Keldysh field theory [430], the simplest object provided by the retarded Green's function is the DoS of the NESS, reading

$$A(\mathbf{k}, \omega) \equiv -\frac{1}{\pi} \text{Im}[G_R(\mathbf{k}, \omega)] = -\frac{1}{\pi} \sum_{\alpha} \frac{\omega''_{\alpha,\mathbf{k}} Z'_{\alpha,\mathbf{k}} + \left(\omega - \omega'_{\alpha,\mathbf{k}}\right) Z''_{\alpha,\mathbf{k}}}{\left(\omega - \omega'_{\alpha,\mathbf{k}}\right)^2 + \left(\omega''_{\alpha,\mathbf{k}}\right)^2} \tag{2.46}$$

where the symbols $'$ and $''$ indicate real and imaginary parts respectively. It is worth noticing that the DoS is not a plain sum of Lorentz distributions centred around the poles of the Green's function (as it would happen at equilibrium), but in principle could get a finite contribution from the principal value of the propagator, which is an odd function of ω with respect to $\omega'_{\alpha,\mathbf{k}}$ and therefore behaves as a sort of Fano resonance of the collective mode. Indeed, this is due to the fact that the quasiparticle weight $Z_{\alpha,\mathbf{k}}$ can generically acquire a complex value out of equilibrium, since it quantifies no longer the overlap of a collective mode with a single-particle excitation of the NESS, but depends on the spectral decomposition of the Lindbladian in a non-trivial way [431]. In particular, this is inherently connected to the fact that right and left eigenvectors are not related by simple conjugation, meaning that the creation and destruction of an elementary excitation on top of the stationary state are not inverse processes. For the same reason, we anticipate here that also the sign of $A(\mathbf{k}, \omega)$ could also display an exceptional behaviour when the NESS is far from being an equilibrium configuration of the system, as we will show in detail in the first part of Subsection 2.5.2. In this respect, we notice that the local DoS $A(\omega) \equiv V^{-1} \sum_{\mathbf{k}} A(\mathbf{k}, \omega)$ satisfies the sum rule

DoS negativity

$$\int d\omega \, A(\omega) = 1 - 2 \langle \hat{n} \rangle \tag{2.47}$$

as a consequence of the commutation relation between hard-core bosonic operators. This automatically implies that $A(\mathbf{k}, \omega) < 0$ for some values of $(\mathbf{k}, \omega)$ at least for $n_0 > 1/2$.

2.4.4 Probing photonic states: transmittivity and reflectivity of the cavities

Along the same conceptual lines of the previous Subsection, an alternative quantum description of the driving of a cavity photon mode by an incident coherent light beam can be obtained by resorting to the so-called *input-output theory* [432, 433] for optical cavities [434]. In particular, the Hamiltonian term describing the external driving of a standard two-sided cavity by an incident field of amplitude $E_{\text{in}}(\mathbf{r}, t)$ is akin to the perturbation of Eq. (2.37) and can be written in $\mathbf{k}$-space as

$$\hat{H}_{\text{drive}}(t) \equiv i \sum_{\mathbf{k}} \left[\gamma_{\text{f},\mathbf{k}} \, \tilde{E}_{\text{in}}(\mathbf{k}, t) \, \hat{a}^{\dagger}_{\mathbf{k}} - \gamma^*_{\text{f},\mathbf{k}} \, \tilde{E}^*_{\text{in}}(\mathbf{k}, t) \, \hat{a}_{\mathbf{k}} \right] , \tag{2.48}$$

where $\tilde{E}_{\text{in}}(\mathbf{k}, t)$ is the Fourier transform of $E_{\text{in}}(\mathbf{r}, t)$ and $\gamma_{\text{f},\mathbf{k}}$ is the transmission amplitude of the front mirror of the cavity. In the following, we will also denote the transmission amplitude of the back mirror by $\gamma_{\text{b},\mathbf{k}}$. We remark that these coefficients are physically linked with the radiative damping Γ_l by the simple relation $2\Gamma_l = |\gamma_{\text{f},\mathbf{k}}|^2 + |\gamma_{\text{b},\mathbf{k}}|^2$. For the sake of simplicity, we will assume that the cavity has a fully

symmetric geometry such that the transmission amplitudes read $\left|\gamma_{\mathrm{f/b},\mathbf{k}}\right| = \sqrt{\Gamma_l}$ and are independent of momentum. We also recall here that $\gamma_{\mathrm{f/b},\mathbf{k}}$ can be usually extracted from transmission and reflection measurements on the unloaded cavity.

The finite transmittivity of the front and the back mirrors of the cavity is responsible for the re-emission of light with an amplitude proportional to the intra-cavity field $\langle \hat{a}_{\mathbf{k}} \rangle$. By means of the boundary conditions set by the two cavity mirrors, in the linear-response regime the reflected and transmitted fields can be related to the intra-cavity field within the input-output framework as [41, 435]

$$\tilde{E}_{\mathrm{T}}(\mathbf{k}, \omega) = T(\mathbf{k}, \omega)\, \tilde{E}_{\mathrm{in}}(\mathbf{k}, \omega) \tag{2.49a}$$

$$\tilde{E}_{\mathrm{R}}(\mathbf{k}, \omega) = R(\mathbf{k}, \omega)\, \tilde{E}_{\mathrm{in}}(\mathbf{k}, \omega) \tag{2.49b}$$

respectively. In the above equations, we have introduced the transmittivity

$$T(\mathbf{k}, \omega) \equiv -i\, \gamma_{\mathrm{f},\mathbf{k}}\, \gamma_{\mathrm{b},\mathbf{k}}^*\, G_R(\mathbf{k}, \omega) \tag{2.50}$$

and reflectivity

$$R(\mathbf{k}, \omega) \equiv 1 - i\, \left|\gamma_{\mathrm{f},\mathbf{k}}\right|^2 G_R(\mathbf{k}, \omega) = 1 + \left(\frac{\gamma_{\mathrm{f},\mathbf{k}}}{\gamma_{\mathrm{b},\mathbf{k}}}\right)^* T(\mathbf{k}, \omega) \tag{2.51}$$

functions, which can be measured via well-established experimental tools and represent the most direct access to the excitation spectra and one-body correlations of the photonic state, as they are entirely determined by the retarded Green's function $G_R(\mathbf{k}, \omega)$. For later convenience, we can write the expression of the reflectivity modulus as

$$|R(\mathbf{k}, \omega)|^2 = \left[1 - \pi\left|\gamma_{\mathrm{f},\mathbf{k}}\right|^2 A(\mathbf{k}, \omega)\right]^2 + \left|\gamma_{\mathrm{f},\mathbf{k}}\right|^4 \mathrm{Re}[G_R(\mathbf{k}, \omega)]^2 \simeq 1 - 2\pi\left|\gamma_{\mathrm{f},\mathbf{k}}\right|^2 A(\mathbf{k}, \omega), \tag{2.52}$$

where in the last equality we have made the assumptions $\left|\gamma_{\mathrm{f},\mathbf{k}}\right|^2 A(\mathbf{k}, \omega) \ll 1$ and $\left|\gamma_{\mathrm{f},\mathbf{k}}\right|^2 \mathrm{Re}[G_R(\mathbf{k}, \omega)]^2 \ll A(\mathbf{k}, \omega)$, which we will also consider when analysing our numerical results under proper conditions.

Importantly, it must be noted that the standard sum rule

$$|T(\mathbf{k}, \omega)|^2 + |R(\mathbf{k}, \omega)|^2 = 1 + 2\left|\gamma_{\mathrm{f},\mathbf{k}}\right|^2 \left\{\Gamma_l\, |G_R(\mathbf{k}, \omega)|^2 + \mathrm{Im}[G_R(\mathbf{k}, \omega)]\right\} \overset{?}{=} 1 \tag{2.53}$$

is fulfilled only if $\Gamma_l\, |G_R(\mathbf{k}, \omega)|^2 = -\mathrm{Im}[G_R(\mathbf{k}, \omega)] = \pi A(\mathbf{k}, \omega)$. Whereas this condition is satisfied in many common situations (e.g. a damped oscillator), it could be instead largely violated in the presence of peculiar out-of-equilibrium effects, for instance when the NESS is characterised by spontaneous energy emission. In Subsection (2.5.2), we will show that this is not only the case of the SFP, where the $\mathbf{k} = \mathbf{0}$ lasing state naturally amplifies both $T(\mathbf{k}, \omega)$ and $R(\mathbf{k}, \omega)$, but remarkably also of the IP, for which we uncover an anomalous behaviour of the response functions as a consequence of the population inversion phenomenon. Indeed, since we know that $A(\mathbf{k}, \omega) < 0$ for some specific values of $(\mathbf{k}, \omega)$ across the whole IP, we obtain that $|R(\mathbf{k}, \omega)|^2 > 1$ from Eq. (2.52) and that Eq. (2.53) is always violated in this regime.

We conclude this Subsection by introducing a third useful response function of
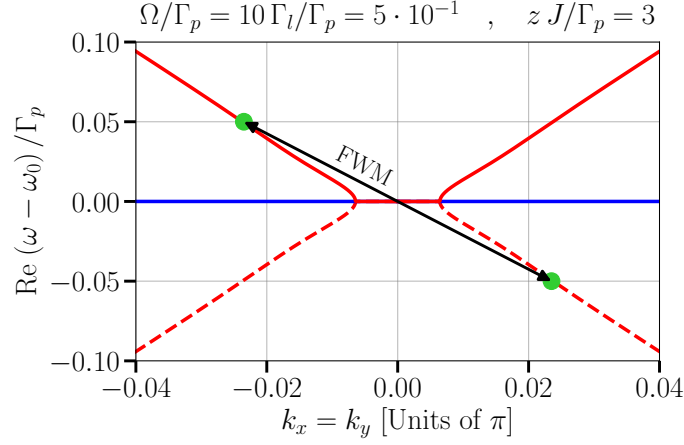
Figure 2.4: Pictorial sketch of the FWM measurement protocol. The coloured lines represent the collective excitations of the SFP, see the subsequent Figure 2.6. The black arrows illustrate the scattering process from which the FWM signal is generated: the system is perturbed at $(\mathbf{k}, \omega)$ (lower green dot) and its response is probed at $(-\mathbf{k}, -\omega)$.

interest in the SFP, going under the name of Four-Wave Mixing (FWM) signal, which has been proven useful to attain a solid experimental evidence of the amplitude excitation branch in EP condensates, given its rather weak luminescence in the transmittivity channel [429]. The physical process underlying the measurement protocol of the FWM response is sketched in Figure 2.4. Elementary excitations are created on top of the condensate by injecting extra photons with a probe laser beam with a finite momentum $\mathbf{k}$ and tuned at a frequency ω. The response of the system is then observed via the coherent light emission at an opposite wave vector $-\mathbf{k}$ and energy $2\omega_0 - \omega$: the existence of a coherent coupling between the frequencies ω and $2\omega_0 - \omega$ (located symmetrically around the effective chemical potential ω_c) and the momenta $\pm\mathbf{k}$ from the fact that the elementary excitations of the condensate consist of a coherent superposition of plane waves at $(\mathbf{k}, \omega)$ and $(-\mathbf{k}, 2\omega_0 - \omega)$: this can be in turn interpreted as a clue of the existence of anomalous correlations in the system. Indeed, it turns out that the FWM signal is simply provided by the retarded anomalous propagator,

$$F(\mathbf{k}, \omega) \equiv -i\,\gamma_{\mathrm{f},\mathbf{k}}\,\gamma_{\mathrm{b},\mathbf{k}}^{*}\,\Delta_R(\mathbf{k}, \omega) \tag{2.54}$$

which has been shown to couple positive- and negative-energy modes of the system, see Eq. (2.45) and the comments below.

2.4.5 A recipe for computing quantum correlation functions

For the purpose of estimating actual expectation values from the linear response formalism developed in the previous Subsections, it is instructive to compare our result for the retarded Green's function (2.42) with its general Källén-Lehmann spectral representation in terms of the eigenstates of the Lindblad superoperator [436, 437],

$$
\begin{aligned}
G_R(\mathbf{k}, \omega) &= \sum_\alpha \left[\frac{\langle I|\,\hat{a}_{\mathbf{k}}\,|r_\alpha\rangle\,\langle l_\alpha|\,\hat{a}_{\mathbf{k}}^\dagger\,|\rho_0\rangle}{\omega - \omega_{\alpha,\mathbf{k}}} - \frac{\left(\langle I|\,\hat{a}_{\mathbf{k}}^\dagger\,|r_\alpha\rangle\,\langle l_\alpha|\,\hat{a}_{\mathbf{k}}\,|\rho_0\rangle\right)^*}{\omega + \omega_{\alpha,\mathbf{k}}^*} \right] = \\
&= \sum_\alpha \frac{\langle I|\,\hat{a}_{\mathbf{k}}\,|r_\alpha\rangle\,\langle l_\alpha|\,\hat{a}_{\mathbf{k}}^\dagger\,|\rho_0\rangle - \left(\langle I|\,\hat{a}_{\mathbf{k}}^\dagger\,|\bar{r}_\alpha\rangle\,\langle \bar{l}_\alpha|\,\hat{a}_{\mathbf{k}}\,|\rho_0\rangle\right)^*}{\omega - \omega_{\alpha,\mathbf{k}}},
\end{aligned}
\tag{2.55}
$$

where $|\rho_0\rangle$ is the NESS eigenvector, $\langle\rho_0|$ is the vectorised identity matrix (namely, the left eigenvector associated with the NESS) and $|\bar{r}_\alpha\rangle$ $\left(|\bar{l}_\alpha\rangle\right)$ is defined to be the *dual* eigenvector of $|r_\alpha\rangle$ $(|l_\alpha\rangle)$, in the sense that that their eigenvalues have opposite real parts $\omega_{\alpha,\mathbf{k}} = -\overline{\omega}^*_{\alpha,\mathbf{k}}$ for each $\mathbf{k}$. Contrasting the expression of the quasiparticle weight $Z_{\alpha,\mathbf{k}}$ with the numerator of the right-hand side of Eq. (2.55), we can readily infer a one-to-one correspondence between the eigenstates of the Gutzwiller-Lindblad superoperator of quantum fluctuations $\hat{\mathcal{L}}_\mathbf{k}$ and the (approximate) $\mathbf{k}$-projections of the actual Lindbladian right/left eigenvectors, namely

$$
\begin{aligned}
(|r_\alpha\rangle, |l_\alpha\rangle)_\mathbf{k} &\longrightarrow (u_{\alpha,\mathbf{k},n,m,\sigma,\sigma'}, x_{\alpha,\mathbf{k},n,m,\sigma,\sigma'}) \ , \\
\left(|\bar{r}_\alpha\rangle, |\bar{l}_\alpha\rangle\right)_\mathbf{k} &\longrightarrow \left(v^*_{\alpha,\mathbf{k},n,m,\sigma,\sigma'}, y^*_{\alpha,\mathbf{k},n,m,\sigma,\sigma'}\right) \ ,
\end{aligned}
\tag{2.56}
$$

hence

$$
\begin{aligned}
\langle I|\hat{a}_\mathbf{k}|r_\alpha\rangle &= \left(\langle I|\hat{a}^\dagger_\mathbf{k}|\bar{r}_\alpha\rangle\right)^* = U_{\alpha,\mathbf{k}} \ , \\
\langle I|\hat{a}^\dagger_\mathbf{k}|r_\alpha\rangle &= (\langle I|\hat{a}_\mathbf{k}|\bar{r}_\alpha\rangle)^* = V_{\alpha,\mathbf{k}} \ , \\
\langle l_\alpha|\hat{a}_\mathbf{k}|\rho_0\rangle &= \vec{x}^*_{\alpha,\mathbf{k}} \cdot \vec{\mathcal{P}}^\dagger_{0,2} \ , \\
\left(\langle\bar{l}_\alpha|\hat{a}_\mathbf{k}|\rho_0\rangle\right)^* &= \vec{x}^*_{\alpha,\mathbf{k}} \cdot \vec{\mathcal{P}}_{0,2} \ , \\
\langle l_\alpha|\hat{a}^\dagger_\mathbf{k}|\rho_0\rangle &= \left(\langle\bar{l}_\alpha|\hat{a}^\dagger_\mathbf{k}|\rho_0\rangle\right)^* = \vec{x}^*_{\alpha,\mathbf{k}} \cdot \vec{\mathcal{P}}_{0,1} \ ,
\end{aligned}
\tag{2.57}
$$

where we have introduced the matrices

$$
(\mathcal{P}_{0,1})_{n,m,\sigma,\sigma'} = \sqrt{n}\,(c_0)_{n-1,m,\sigma,\sigma'}
\tag{2.58}
$$

and

$$
(\mathcal{P}_{0,2})_{n,m,\sigma,\sigma'} = \sqrt{m+1}\,(c_0)_{n,m+1,\sigma,\sigma'}
\tag{2.59}
$$

such that $\vec{\mathcal{P}}_0 = \vec{\mathcal{P}}_{0,1} - \vec{\mathcal{P}}_{0,2}$.

From Gaussian fluctuations to expectation values

Having a direct mapping relating Gaussian fluctuations around the NESS to single-particle expectation values at our disposal, we are now in the position of calculating the expression of any one-body correlation function within our Gutzwiller approximation. In particular, in this study we consider the coherence function, having the general representation [437]

$$
g_1(\mathbf{r}, t) \equiv \frac{1}{V}\sum_\alpha\sum_\mathbf{k} \langle I|\hat{a}^\dagger_\mathbf{k}|r_\alpha\rangle\,\langle l_\alpha|\hat{a}_\mathbf{k}|\rho_0\rangle\, e^{i\left(\mathbf{k}\cdot\mathbf{r}-\omega_{\alpha,\mathbf{k}}t\right)}
\tag{2.60}
$$

for $t > 0$, while complex conjugation of the same formula gives the behaviour of $g_1(\mathbf{r}, t)$ at negative times. Consequently, using Eqs. (2.57), our prediction for the coherence function reads

$$
g_1(\mathbf{r}, t) = \frac{1}{V}\sum_\alpha\sum_\mathbf{k} V_{\alpha,\mathbf{k}}\left(\vec{x}^*_{\alpha,\mathbf{k}}\cdot\vec{\mathcal{P}}^\dagger_{0,2}\right)e^{i\left(\mathbf{k}\cdot\mathbf{r}-\omega_{\alpha,\mathbf{k}}t\right)} \ ,
\tag{2.61}
$$

which is correctly controlled by the hole amplitude of the collective excitations as expected from the expression of the retarded Green's function (2.42). The very same procedure can be applied to the calculation of the pair correlation function, whose

spectral decomposition for $t > 0$ is given by:

$$g_2(\mathbf{r}, t) \equiv \frac{1}{V} \sum_\alpha \sum_\mathbf{k} \langle I|\hat{n}_\mathbf{k}|r_\alpha\rangle \langle l_\alpha|\hat{n}_\mathbf{k}|\rho_0\rangle \, e^{i(\mathbf{k}\cdot\mathbf{r} - \omega_{\alpha,\mathbf{k}}\, t)} \tag{2.62}$$

which, translated into our linear-response language, has the form:

$$g_2(\mathbf{r}, t) = \frac{1}{V} \sum_\alpha \sum_\mathbf{k} N_{\alpha,\mathbf{k}} \left(\underline{x}_{\alpha,\mathbf{k}}^* \cdot \underline{C}_1^0 \right) e^{i(\mathbf{k}\cdot\mathbf{r} - \omega_{\alpha,\mathbf{k}}\, t)} \tag{2.63}$$

where we have defined $(\mathcal{N}_{0,1})_{n,m,\sigma,\sigma'} = n\,(c_0)_{n,m,\sigma,\sigma'}$.

For the sake of simplicity, in Subsection 2.5.3 we will restrict our discussion of quantum correlations to the coherence function in the IP, that we present both as an ideal probe of local fluctuations in this exotic phase and as a proof of the physical consistency of the calculation recipe outlined above.

2.5 Making the theory work: numerics of quantum fluctuations

2.5.1 Excitation spectrum of elementary excitations

We now proceed to give a detailed account of the excitation spectrum of the NESS across the I-to-SF transition, restricting ourselves to the most relevant modes at low energy. The remaining excitations correspond to all the possible local excitations of the system, with energies proportional to suitable combinations of ω_c and ω_{at} and damping rates $\omega_{\alpha,\mathbf{k}}''$ given by large fractional values of Γ_p.

Insulating phase   The IP excitation spectrum [Figure 2.5] consists of two dispersive branches $\omega_\pm(\mathbf{k}) = \pm\,\varepsilon_{\mathrm{ph}}(\mathbf{k}) - i\,\Gamma_{\mathrm{ph}}(\mathbf{k})$ [red solid/dotted lines] and a purely dissipative local mode $\omega_\mathrm{D} = -i\,\Gamma_\mathrm{D}$ [blue solid line], to which we will refer as the *D-mode* consistently with the spectrum of EP systems discussed in the previous Chapter. The former bands correspond to distinct quasiparticle (quasihole) excitations respectively $(U_{-,\mathbf{k}} = V_{+,\mathbf{k}} = 0)$, while the latter excites density fluctuations only. Specifically, we find $|U_{+,\mathbf{k}}| = |V_{-,\mathbf{k}}| \approx |N_{\mathrm{D},\mathbf{k}}| \approx 1/\sqrt{2}$.

Deep in the IP, the quasiparticle damping $\Gamma_{\mathrm{ph}}(\mathbf{k})$ has a gapped, quadratic dispersion [see Figure 2.5(a')-(d')] which extends up to the energy scale of the effective pumping rate Γ_{em}, such that non-local excitations benefit from a longer lifetime due to hopping fluctuations. As the hopping reaches the lasing threshold J_c, the damping of the dissipative mode Γ_D converges to the energy scale of cavity losses Γ_l, while the Liouvillian gap $\Gamma_{\mathrm{ph}}(\mathbf{0})$ vanishes proportionally to $J_c - J$ as expected from quantum field theory [430]: this substantiates the physical picture of long-lived quasiparticles/holes as precursors of the non-equilibrium I-to-SF transition. The hopping has a dramatic effect also on the quasiparticle energy dispersion, which is well fitted by $\varepsilon_{\mathrm{ph}}(\mathbf{k}) \approx (1 - 2\,n_0)\,\varepsilon_\mathbf{k} + \omega_c$ and is characterised by a density-dependent bandwidth. Specifically, when $n_0 > 1/2$ at small J, $\varepsilon_{\mathrm{ph}}(\mathbf{k})$ displays an *inverted* profile with minimal gap at $\mathbf{k} = \boldsymbol{\pi}$ [Figure 2.5(a)-(b)], while a standard quadratic dispersion is found for $n_0 < 1/2$ at larger J [Figure 2.5(d)]. Eventually, $\varepsilon_{\mathrm{ph}}(\mathbf{0}) \to \omega_0$ at the transition point, which therefore can be identified as an authentic finite-frequency criticality [408, 420].

These results find an intuitive explanation in the aforementioned commensurability

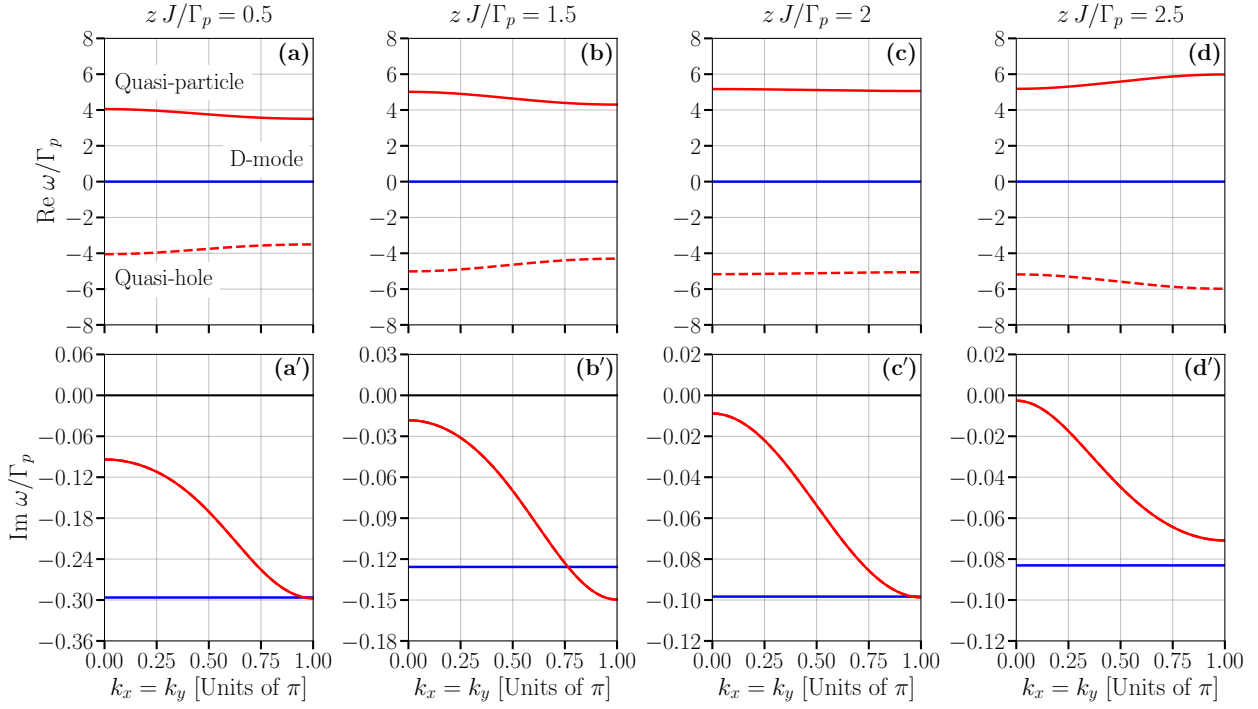*Quasiparticle modes of the insulating state*

Figure 2.5: Excitation spectrum of the collective modes of the IP for $\Omega/\Gamma_p = 5 \cdot 10^{-1}$, $\Gamma_l/\Gamma_p = 5 \cdot 10^{-2}$ and $\gamma/\Gamma_p = \cdot 10^{-3}$. Columns from left to right correspond to increasing values of the hopping J, in particular: (a)-(a') $z J/\Gamma_p = 0.5$; (b)-(b') $z J/\Gamma_p = 1.5$; (c)-(c') $z J/\Gamma_p = 2$; (d)-(d') $z J/\Gamma_p = 2.5$. The I-to-SF critical point is located at $z J_c/\Gamma_p \approx 2.62$. The upper panels show the real part of the excitation energies $\omega'_{\alpha,\mathbf{k}}$, while the lower panels display the imaginary part $\omega''_{\alpha,\mathbf{k}}$. Red solid lines: quasiparticle branch. Red dashed lines: quasihole branch. Blue solid line: D-mode branch. The black solid line in the lower panels highlights the stability threshold $\text{Im}(\omega) = 0$.

effect due to the combination of strong interactions and dissipation. For $n_0 > 1/2$, photon pumping is efficient enough to prevent holes from moving around the hard-core lattice by refilling them: thus, local particle-hole excitations are energetically favoured, despite their shorter lifetime. By contrast, in the opposite case the IP becomes hole-dominated and non-local fluctuations are more likely to be excited. Importantly, there always exists a value of J for which $n_0 = 1/2$, such that the band $\varepsilon_{\text{ph}}(\mathbf{k})$ is completely flat, see Figure 2.5(c). Later on, we will show that this PHS point plays a special role in the dynamical correlations of the IP.

Finally, we point out that the change in the energy scale of the D-mode ω_{D} is also a litmus paper of the link between the weakening of effective pumping due to J and the development of coherence in the system: in fact, we see that $\Gamma_{\text{D}} \sim \Gamma_{\text{em}}$ for $J \ll \Gamma_p$ and monotonically reaches values of the order of Γ_l right before the I-to-SF transition point.

Superfluid phase   As the onset of the SFP corresponds to a spontaneous breaking of U(1) symmetry, for $J > J_c$ the quasiparticle mode $\omega_+(\mathbf{k})$ is replaced by a Goldstone branch $\omega_{\text{G}}(\mathbf{k})$ whose energy vanishes in the long-wavelength limit [40, 408]. Physically, this mode can be understood as a slow rotation of the photonic condensate phase across the cavity array. Starting from this general premise, let us now analyse the spectral properties of the different SFP regimes in more detail, starting from the low-hopping region $J \lesssim J_m$. From now on, for the sake of additionally comparing our results with the excitation spectrum of EP condensates reviewed in the previous Chapter,

the lattice momentum will be rescaled by the healing length of the SF state, reading $\xi = \pi / [2 \arcsin{(n_0)}]$ to a first approximation [3].

For this case, a typical example of the excitation spectrum is shown in Figure 2.6(a)-(a′). Differently from the linear dispersion of sound modes [4] in equilibrium superfluids [83], the Goldstone mode [red solid line] shows here a diffusive and non-propagating behaviour for small $|\mathbf{k}|$: while the excitation energy flattens out to zero over a sphere of momenta whose radius $|\Delta\mathbf{k}_{\mathrm{diff}}|$ scales with Γ_l, the damping rate vanishes with a quadratic dispersion. This finding is in broad agreement with previous works addressing the elementary excitations of out-of-equilibrium condensates [411, 438–440] and, importantly, extends the domain of the Goldstone mode diffusivity to driven-dissipative phase transitions driven by strong interactions. In addition to the Goldstone branch, we find also the corresponding conjugate or *ghost* mode $\omega_{\mathrm{A}}(\mathbf{k})$ at negative energy [red dotted line], which ensues from the quasihole mode of the IP and is connected with damped fluctuations of the condensate density [411, 440], see also the dashed red line in panel (B.1) of Figure 2.10. Additionally, we notice that the D-branch $\omega_{\mathrm{D}}(\mathbf{k}) \sim -i\,\Gamma_l$ [blue solid line] starts acquiring a non-trivial dispersion and retains a strong density character [see Figure 2.10(A.1)]. The relationship between the latter mode and the Goldstone branch is pivotal to grasping the physics of the deep SFP, as we show in the following.

Goldstone mode diffusivity

For $J \lesssim J_m$, there is a clear separation of energy scales between the Goldstone damping $\Gamma_{\mathrm{G}}(\mathbf{k})$ and $\omega_{\mathrm{D}}(\mathbf{k})$, reaching its maximum at constant Ω when the NESS significantly overlaps with the hard-core state at equilibrium in the strong-coupling regime $g \gg 1$. Crucially, increasing the hopping reduces the damping gap between the two branches. This is closely reflected by the behaviour of their relative phase character $|U_{\alpha,\mathbf{k}} - V_{\alpha,\mathbf{k}}|$ [see panels (C.1)-(C.2) of Figure 2.10]: as J increases towards J_m, part of the Goldstone spectral weight is gradually transferred to the D-mode, starting from finite $|\mathbf{k}|$. For later convenience, we highlight that the particle/hole amplitudes of the excitation modes are all equal and satisfy $|U_{\alpha,\mathbf{k}}| = |V_{\alpha,\mathbf{k}}|$ in the diffusive window of the BZ: this means that the non-equilibrium superfluid state, in spite of its non-trivial particle-hole character depending on J, is characterised by an emergent PHS on long-range spatial scales. Such a symmetry is then gradually broken by the Goldstone and ghost branches only as the momentum is increased, with the two excitations acquiring predominantly a particle and a hole character, respectively. This feature will be further addressed in the forthcoming Subsection 2.5.2 in relation to its impact on the dynamical response function of the superfluid NESS.

Emergent particle-hole symmetry of gapless modes

The above situation breaks at the boundary between particle and hole superfluidity $J = J_m$. In fact, this hopping value marks the point at which the diluteness of the condensate here, the condensate diluteness stems from the fact that pumping and loss processes occur on comparable effective time scales, such that the dissipative dynamics of the TLE's cannot be adiabatically separated from that of the BH lattice. Hence, as the large photon bandwidth zJ is compensated by a low density, the coherent dynamics of the photon fluid in the limit $J > J_m$ interweaves with low-energy dissipative processes, which therefore take full part in phase diffusion across the whole system. Similarly

Anti-adiabaticity and dissipative Goldstone hybridisation

---

[3] We refer the interested reader to Appendix F.2 for additional details on the derivation of the healing length in the case of hard-core bosons within mean-field theory.

[4] See again Appendix F.2 for a concise description of the Bogoliubov-Goldstone mode of hard-core bosons on a lattice at equilibrium.
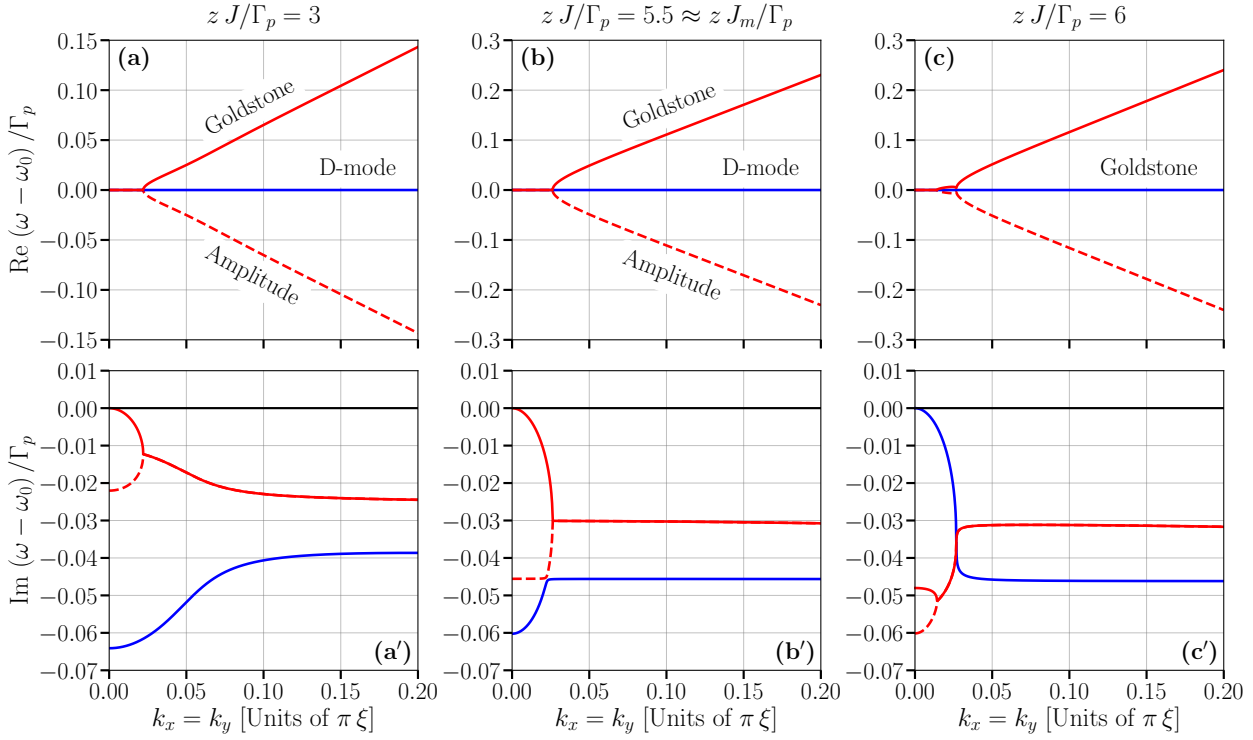
Figure 2.6: Excitation spectrum of the collective modes of the SFP for $\Omega/\Gamma_p = 3 \cdot 10^{-1}$, $\Gamma_l/\Gamma_p = 5 \cdot 10^{-2}$ and $\gamma/\Gamma_p = \cdot 10^{-3}$. Columns from left to right correspond to increasing values of the hopping J, in particular: (a)-(a') $z\,J/\Gamma_p = 3$; (b)-(b') $z\,J/\Gamma_p = 5.5 \approx z\,J_m/\Gamma_p$; (c)-(c') $z\,J/\Gamma_p = 6$. The upper panels show the real part of the excitation energies $\omega'_{\alpha,\mathbf{k}}$, while the lower panels display the imaginary part $\omega''_{\alpha,\mathbf{k}}$. Red solid lines: Goldstone branch (at low J only). Red dashed lines: amplitude branch (at low J only). Blue solid line: D-mode/Goldstone branch (depending on the value of J, see the main text discussion). The black solid line in the lower panels highlights the stability threshold $\mathrm{Im}(\omega) = 0$. The expression $\omega - \omega_0$ indicates that the excitation energy is calculated with respect to the limit-cycle frequency ω_0. The healing length of the system is $\xi \approx 3.4, 4.7, 4.9$ (units of lattice spacing) from left to right, respectively.

to what happens in a EP condensate at low pumping intensity, this translates into a cross-hybridisation of the D-mode $\omega_D(\mathbf{k})$ with the Goldstone branch $\Gamma_G(\mathbf{k})$ at small momenta, leaving the structure of the real energy spectrum unaltered. Interestingly, we note that such a band crossing takes place also at the level of the fluctuation amplitudes, see in particular the comparison between panels (A.2)-(A.3) and (B.2)-(B.3) of Figure 2.10. More precisely, we notice that, upon increasing the hopping J, the D-mode gradually loses its density character and acquires the same amplitude character of the ghost mode in the diffusive regime just on the brink of the anti-adiabatic crossover. As a side note, we point out that such a regime of our hard-core setting does not admit a simple GPE description of the lasing state, which would involve a mean-field approximation of the Rabi coupling resembling the semi-classical theory of atomic lasing [407, 441]. Indeed, the key advantage of our Gutzwiller approach consists in fully incorporating local fluctuations due to the strong interactions felt by photons despite their diluteness.

Comparison with exciton-polariton condensates   It is important to highlight that the TLE loss rate γ turns out to have little effect on the spectral properties discussed previously: increasing γ/Γ_l has the simple outcome of spoiling population inversion in the IP and shifting the lasing threshold J_c to larger values, as one can derive from Eq. (2.17). It is instructive to compare this result with what happens in a EP condensate when losses are faster than those of reservoir
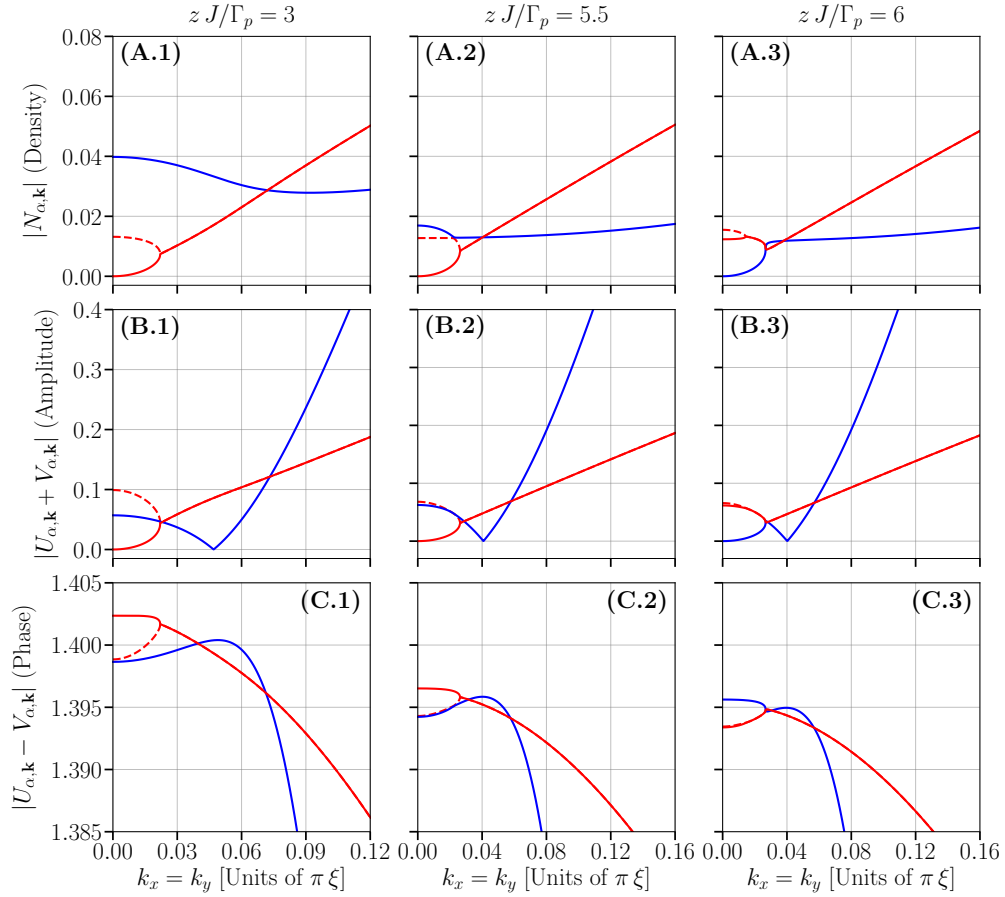
Figure 2.7: Spectral amplitudes of the collective modes of the SFP with respect to different excitation channels for the same parameters of Figure 2.6. Columns from left to right correspond to increasing values of the hopping J, in particular: (a)-(a$'$) $z\,J/\Gamma_p = 3$; (b)-(b$'$) $z\,J/\Gamma_p = 5.5 \approx z\,J_m/\Gamma_p$; (c)-(c$'$) $z\,J/\Gamma_p = 6$. Rows from top to bottom: modulus of the density fluctuation $N_{\alpha,\mathbf{k}}$ and amplitude/phase fluctuation $U_{\alpha,\mathbf{k}} \pm V_{\alpha,\mathbf{k}}$ amplitudes for each collective mode.

polaritons [5], set by the equivalent of γ: in that context, the Goldstone mode strongly entangles with the dissipative channels as well, but the condensate is prone to a dynamical instability due to the repulsive interaction with the reservoir [411, 442]. By contrast, in the present case phase excitations are always stable and the Goldstone hybridisation with dissipative processes always takes place for a sufficiently large J, independently of the ratio γ/Γ_l. This suggests a different physical origin for our instance of the Goldstone hybridisation: more precisely, we argue that the Rabi-type coupling with the TLE's, accurately accounted by our approach to fluctuations, is key to a stable mixing of dissipation and coherent dynamics at large J. However, we report that an incommensurate instability of the $\omega_{\mathrm{G/A}}(\mathbf{k})$ branches appears in the ultrastrong-coupling regime $g \gg 1$ for intermediate values of J [Figure 2.8] corresponding to the cyan-shaded area in Figure 2.2(c). In particular, we find that the Goldstone energy at the momentum for which the instability $\Gamma_{\mathrm{G/A}}(\mathbf{k})$ is maximal scales linearly with the Rabi coupling Ω, signalling that this is the mechanism responsible for pattern formation. Once again, we interpret this feature as a direct consequence of the competition between photon interactions and effective pumping: as long as J is sufficiently small to allow for having a sizeable density in the system, the condensate will tend to arrange itself into the most convenient pattern to accommodate fast injected photons. We speculate that

Dynamical instabilities of the Goldstone mode

---

[5] See Section 1.2.2 of the previous Chapter.

$$\Omega/\Gamma_p = 20 \; \Gamma_l/\Gamma_p = 1 \quad , \quad z\,J/\Gamma_p = 6.5$$
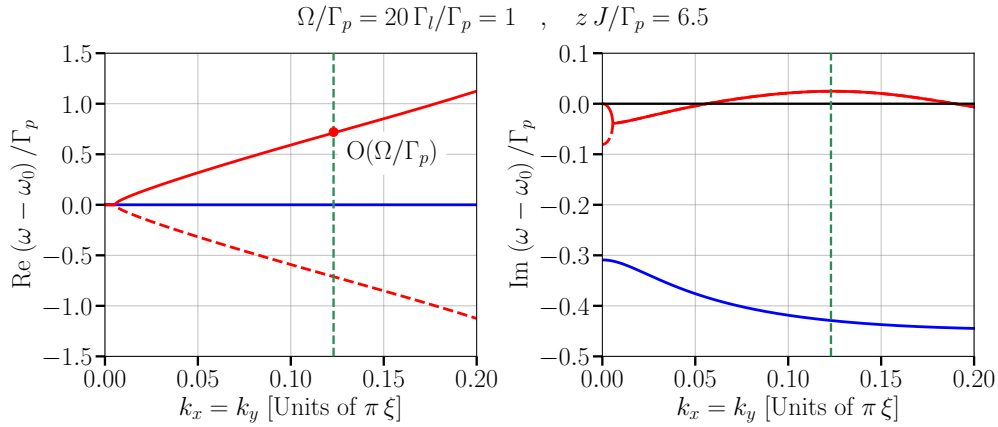
Figure 2.8: Excitation spectrum of the SF state stabilised for $\Omega/\Gamma_p = 1$, $\Gamma_l/\Gamma_p = 5 \cdot 10^{-2}$ and $\gamma/\Gamma_p = \cdot 10^{-3}$ with the hopping energy $z\,J/\Gamma_p = 6.5$, inside the equivalent of the cyan-shaded area in Figure 2.2(c). The dashed green line indicates the incommensurate momentum for which the NESS is maximally unstable. The healing length of the system is $\xi \approx 2.2$ (units of lattice spacing).

this modulational instability can be associated with the onset of strong short-range correlations, in analogy with the physics of the one-dimensional system considered in [389].

2.5.2 Density of states and dynamical response functions

Insulating phase

Density of states of the IP First-hand information on the behaviour of dynamical correlations in the IP is provided by the DoS, which we calculate both in the full $(\mathbf{k}, \omega)$ space [Figure 2.9] and in its local projection $A(\omega)$ [Figure 2.10] for completeness.

Janus-faced behaviour of the insulating state

Looking at the general features DoS for different values of J, we immediately notice that, in striking contrast to equilibrium cases, $A(\mathbf{k}, \omega)$ is neither a symmetric nor a strictly positive function, as it receives a major contribution from the quasiparticle branch $\varepsilon_+(\mathbf{k})$ only and assumes negative values (N-DoS) below a specific energy scale ω_* [black horizontal lines in Figure 2.9]. Our results demonstrate that this phenomenology, already observed in the presence of two-body losses and Markovian pumping [420, 431, 443], is pretty universal and extends to the strongly-interacting non-Markovian system considered in the Thesis. Physically speaking, the N-DoS is a genuine non-equilibrium signature of the pumping-induced *population inversion* taking place in the deep IP and is also a manifestation of *energy gain*, a condition which is conventionally associated with optical amplification [444, 445] but, at the same time, competes with the onset of coherence in our system. From these observations, we draw a complex, Janus-faced portrait of the IP state: not only it can allow for a positive gain with respect to light emission *despite* the absence of long-range coherence – as we will discuss in a short while –, but also it displays a non-equilibrium facet which is solely due to many-body excitations and does *not* emerge at the level of the (almost pure) NESS. We conclude this preliminary discussion by observing that the frequency scale ω_* converges exactly to the critical limit-cycle frequency ω_0; this supports the interpretation of ω_* as an effective chemical potential for quasiparticles, since it separates positive- and negative-weight states. We clarify here that ω_* exhibits only a weak dependence on the hopping J
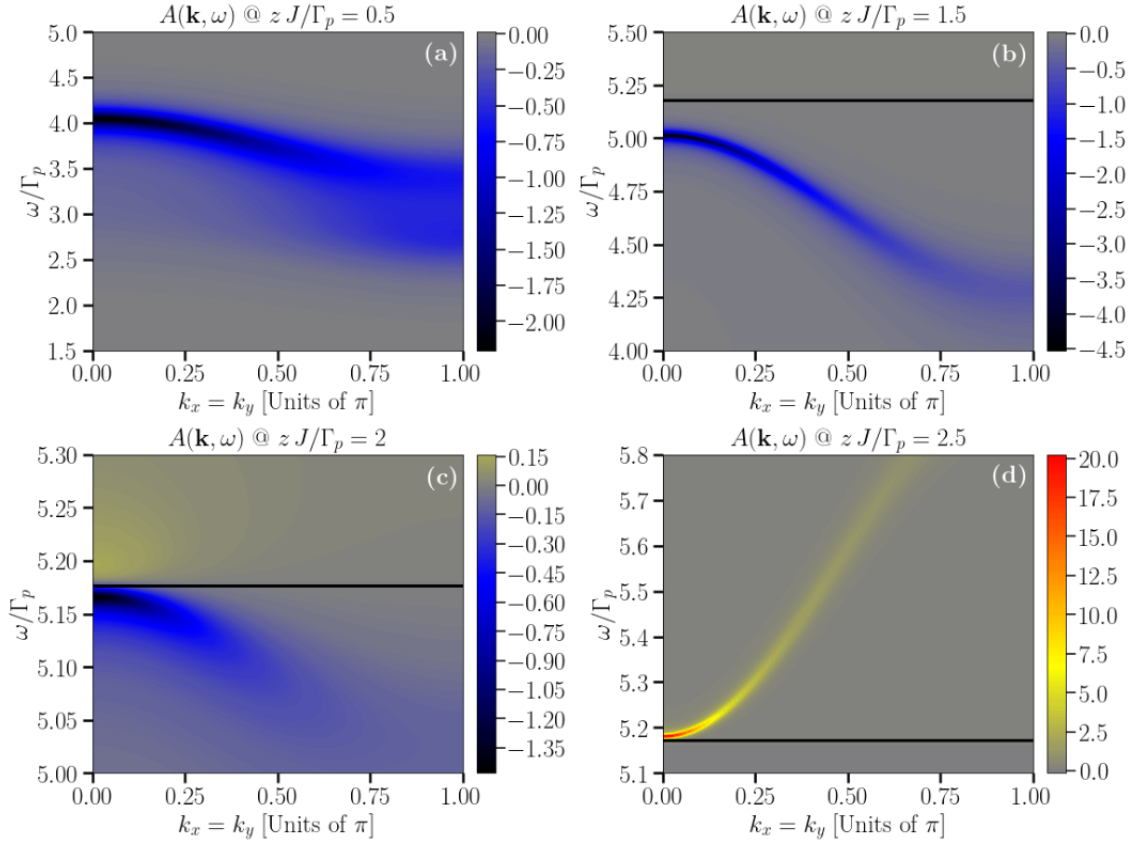
Figure 2.9: Profile of the DoS of the IP in momentum-frequency space across the IP for constant $\Omega/\Gamma_p = 5 \cdot 10^{-1}$, $\Gamma_l/\Gamma_p = 5 \cdot 10^{-2}$, $\gamma/\Gamma_p = 5 \cdot 10^{-3}$ and the same hopping values considered in Figure 2.5, in particular: (a) $zJ/\Gamma_p = 0.5$; (b) $zJ/\Gamma_p = 1.5$; (c) $zJ/\Gamma_p = 2$; (d) $zJ/\Gamma_p = 2.5$. The colour scale is normalised so as to make 0 correspond to the grey tone.

according to our Gutzwiller approach to Gaussian fluctuations, a subtle property that conversely has been found by DMFT calculations [443] in diverse driven-dissipative models.

Let us now describe in detail the behaviour of the DoS upon approaching the I-to-SF transition, keeping an eye on Eq. (2.46) as a quantitative reference. In the Mott-like regime at low J [Figure 2.9(a)], most part of $A(\mathbf{k}, \omega)$ lies well below the frequency scale ω_* and has a dual profile depending on the momentum of quasiparticle excitations. In particular, whereas the N-DoS reaches its minimal value at low momenta, it covers a wider range of states at the border of the BZ, where it splits into two peaks. This behaviour can be elegantly explained in terms of the crucial role played by the quasiparticle weight $Z_{+,\mathbf{k}}$ in the DoS expression (2.46). The real part of $Z_{+,\mathbf{k}}$, associated with the Lorentzian component of $A(\mathbf{k}, \omega)$, is *negative* and gives a leading contribution for non-local quasiparticle states, which explains the well-visible peak of the DoS at small momenta. By contrast, the imaginary part of $Z_{+,\mathbf{k}}$, which instead weighs the *odd* resonance of quasiparticle modes, favours localised states and yields the corresponding double-peaked profile of the DoS for $|\mathbf{k}| \approx \pi$. However, since we always have $|Z'_{+,\mathbf{k}}| > |Z''_{+,\mathbf{k}}|$ at small J, the latter contribution is never sufficiently large to flip the DoS sign in the Mott-like regime. Therefore, we realise that both the negativity of $Z'_{+,\mathbf{k}}$ and a significant imaginary component $Z''_{+,\mathbf{k}}$ strongly relate to the appearance of population inversion and, more generally, hint at the strong non-equilibrium character of the NESS. Summarising this physics at the level of the local DoS [Figure 2.10], $A(\omega)$
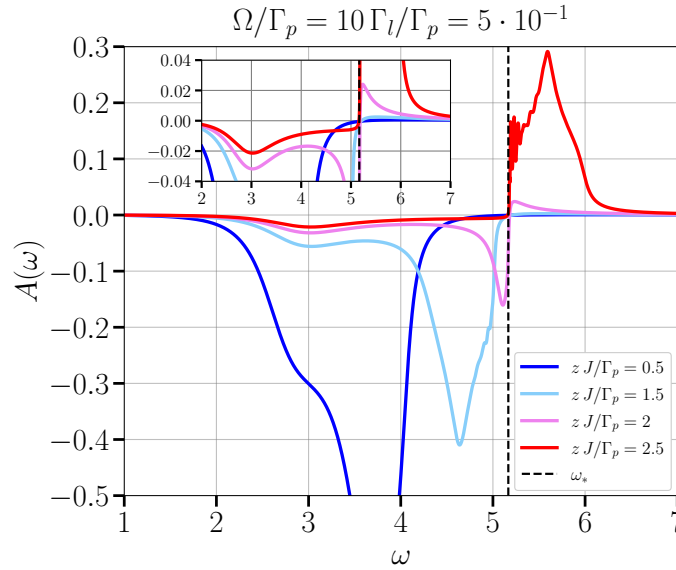
Figure 2.10: Profile of the local as a function of frequency across the IP for constant $\Omega/\Gamma_p = 5 \cdot 10^{-1}$, $\Gamma_l/\Gamma_p = 5 \cdot 10^{-2}$, $\gamma/\Gamma_p = 5 \cdot 10^{-3}$ and the same hopping values considered in Figure 2.9.

is a negative-valued distribution, with a bimodal structure paralleling the momentum dependence of the underlying correlations.

As J increases [Figure 2.9(b)], population inversion is progressively lost: this manifests into the quasiparticle band nearing the frequency threshold ω_* starting from non-local states at $\mathbf{k} = \mathbf{0}$. In particular, as anticipated before, we notice that states lying above ω_* acquire a significant positive weight. Once again, we can quantitatively understand this mechanism from the point of view of the quasiparticle weight. Moving towards the PHS point at $n_0 = 1/2$, both the components of $Z_{+,\mathbf{k}}$ decrease in amplitude towards comparable values and become flat in momentum. Thus, precisely at the PHS point [see Figure 2.9(c)], the DoS has the shape of a Fano resonance around the quasiparticle energy $\omega_{+,\mathbf{k}} \approx \omega_*$, determined by the imaginary part of $Z_{+,\mathbf{k}}$ [see also the pink curve in Figure 2.10]. Increasing further J towards the I-to-SF transition, the real part of the quasiparticle weight becomes large and positive for states for which $\omega > \omega_*$, while the imaginary component remains a vanishingly small number and gives the residual N-DoS below ω_*. Ultimately, the DoS becomes strictly non-negative exactly before the critical point $J = J_c$ [Figure 2.9(d)]. Here, the whole spectral weight has been transferred above the effective chemical potential ω_* [red curve in Figure 2.10]: then, this frequency scale can be rigorously identified with the critical energy of delocalised quasiparticle excitations, which are then free to condense.

Looking globally at our result, the fine features of the momentum-frequency dependence of DoS upon approaching the I-to-SF critical point can be seen as a good indication of the *quantumness* of the quantum phase transition characterising the current driven-dissipative setting, in contrast to other out-of-equilibrium systems where the order parameter noise encoded in $G_R(\mathbf{k}, \omega)$ is frequency-independent at low energy and the critical behaviour of can be regarded as classical [430, 446]. In this sense, it is clear that the energy-dependent gain of the incoherent non-Markovian pumping scheme considered here is of crucial importance in giving dynamical correlations a non-trivial energy-dependent structure.
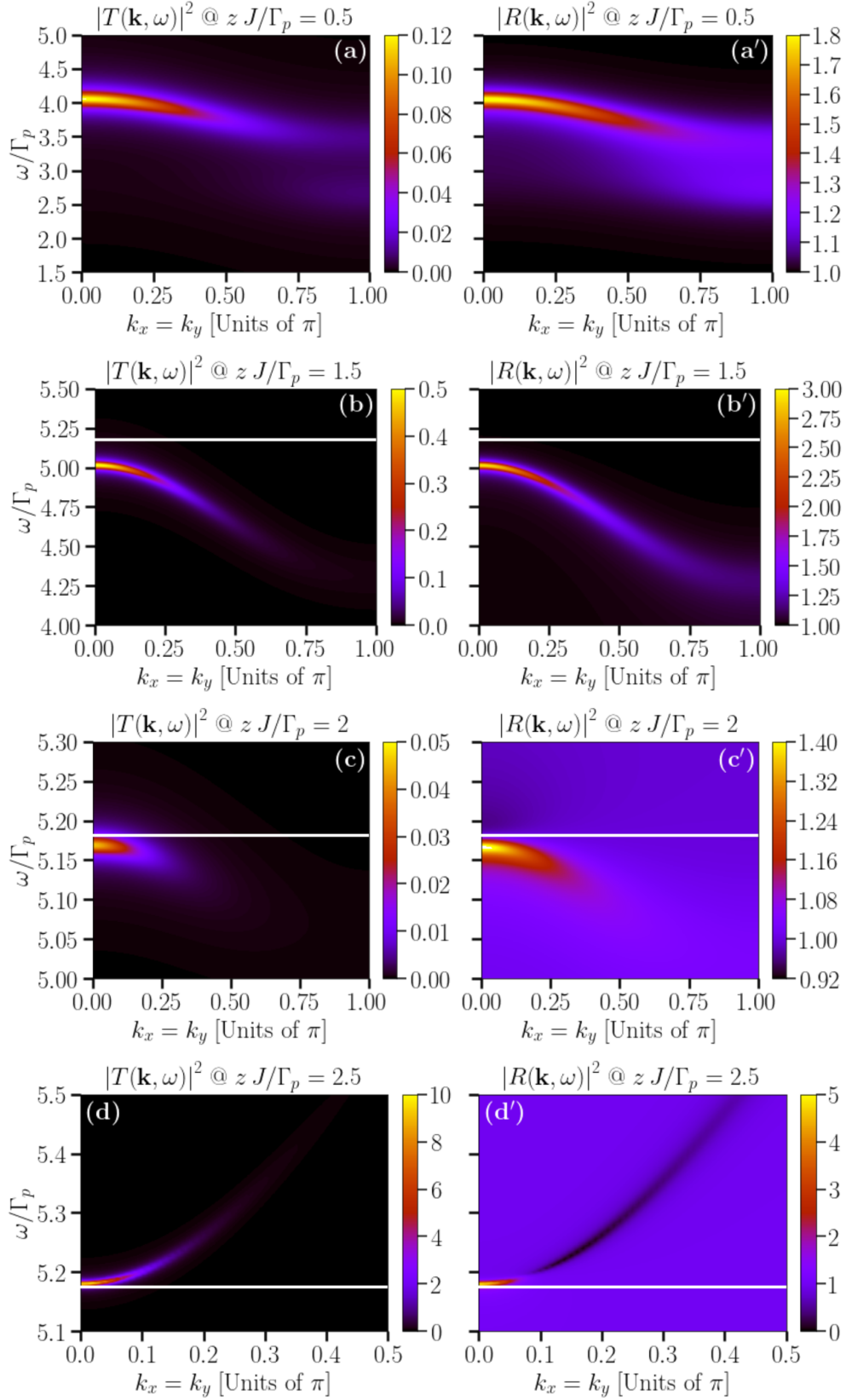
Figure 2.11: Transmittivity and reflectivity signals of optical cavities in the IP regime for the same parameters of Figure 2.5, with increasing values of the hopping J from top to bottom. Left panels: contour plots of the transmittivity signal. Right panels: reflectivity signals.

One-body dynamical response of the IP By virtue of Eqs. (2.52)-(2.53), we immediately realise that the N-DoS phenomenon has a dramatic impact on the transmittivity and reflectivity spectra. In the following, we will illustrate that these observables can be regarded as the most clear-cut fingerprints of the exceptional properties of the normal phase of the NESS.

In the deep IP regime [Figure 2.11(a)-(a′)], the transmittivity signal is always significantly larger than the bare transmission amplitude $\tau = \gamma_f \, \gamma_b^* = \Gamma_l$ in correspondence of the quasiparticle branch, but never exceeds the threshold $|T(\mathbf{k}, \omega)|^2 = 1$. The situation is remarkably different in the reflectivity channel: here, the output signal displays a positive gain with $|R(\mathbf{k}, \omega)|^2 > 1$ and echoes the same out-of-equilibrium spectral features of quasiparticle excitations described in the previous paragraphs. While this result is a clear consequence of Eq. (2.52), it uncovers more explicitly the Janus-faced nature of the IP. In fact, although behaving as an insulator from the point of view of the excitation spectrum and lacking long-range coherence, its dynamical response strongly resembles the one of a typical lasing state, with the fundamental difference that light amplification occurs on a broad range of momenta and frequencies in the present case, not restricted to the region of momenta where coherence eventually develops at the I-to-SF transition.

Light amplification in the insulating way

As the hopping J is increased towards the PHS point at $n_0 = 1/2$ and beyond, we observe two qualitative trends coming into play [Figure 2.11(b)-(b′)]. Similarly to the DoS, most of the contribution of the quasiparticle branch to response functions shifts to lower and lower momenta; at the same time, the intensities of *both* $|T(\mathbf{k}, \omega)|^2$ and $|R(\mathbf{k}, \omega)|^2$ change non-monotonically and reach values larger than 1 above a certain value of J. Quantitatively, this behaviour is the consequence of a two-fold change in the Green's function of cavity photons. First, increasing J has the prime effect of reducing the width $\Gamma_+(\mathbf{k})$ of the quasiparticle spectrum, thus sharpening the N-DoS peak. In the second place, the modulus of $\text{Re}[G_R(\mathbf{k}, \omega)]$, which has a pole precisely on the quasiparticle branch and quantifies nothing but the strength of perturbations of the order parameter around $\psi_0 = 0$, becomes uniformly larger with the hopping. As a result, $|T(\mathbf{k}, \omega)|^2$ and $|R(\mathbf{k}, \omega)|^2$ get an increasing contribution from the natural increase of the amplitude of quantum fluctuations due to the hopping.

Close to the point where $n_0 = 1/2$ [Figure 2.11(c)-(c′)], population inversion has been partially lost and the morphology of the $|R(\mathbf{k}, \omega)|^2$ spectrum starts differing from that of $|T(\mathbf{k}, \omega)|^2$. In particular, while the latter develops a well-visible peak at the condensation point $(\mathbf{k} = \mathbf{0}, \omega_*)$, the former follows the usual behaviour of a Fano resonance around the effective chemical potential ω_*: in particular, we find that the value of $|R(\mathbf{k}, \omega)|^2$ is above (below) 1 for $\omega < \omega_*$ ($\omega > \omega_*$). Making the aforementioned approximation $|R(\mathbf{k}, \omega)|^2 \simeq 1 - 2\pi \, |\gamma_{f,\mathbf{k}}|^2 \, A(\mathbf{k}, \omega)$, we can readily link the Fano resonance to the sign flip of the DoS across $\omega = \omega_*$.

In proximity of the I-to-SF critical point [Figure 2.11(d)-(d′)], most of the DoS acquires a positive weight and covers only states above ω_*, while $\text{Re}[G_R(\mathbf{k}, \omega)]$ diverges at the same frequency scale, marking the occurrence of condensation. This second effect is the dominant one and manifests in the rapidly growing peaks of $|T(\mathbf{k}, \omega)|^2$ and $|R(\mathbf{k}, \omega)|^2$ at low momenta. The only remaining signature of the competition between the presence of states with a positive but finite DoS and the development of coherence, affecting respectively the first and second contributions to the right-hand side of Eq. (2.52), is a residual dark resonance of $|R(\mathbf{k}, \omega)|^2$ at higher energies, which eventually fades out on

the brink of the I-to-SF transition.

Superfluid phase

Density of states of the SFP As for the case of the IP, we start our analysis of dynamical correlations in the SFP by looking at the DoS. In Figure 2.12(b), we report the typical form of $A(\mathbf{k}, \omega)$ in the symmetry-broken phase, including the anti-adiabatic limit of the model. On the whole, the DoS gets a non-negligible contribution from the Goldstone branch only and exhibits a butterfly-shaped structure analogous to that of EP condensates [see Figure F.1 in Appendix F.1], however with a crucial discrepancy with respect to the latter systems. On the one hand, states at $\omega > 0$ have a non-vanishing and positive distribution in the range of diffusive momenta $\Delta \mathbf{k}_{\mathrm{diff}}$, which is peaked around $(\mathbf{k} = \mathbf{0}, \omega = 0)$ because of condensation, such that it connects continuously to the DoS of quasiparticle excitations of the critical IP [see Figure 2.9(d)]; on the other hand, states belonging to the ghost branch at $\omega < 0$ have a negative weight which mirrors exactly $A(\mathbf{k}, \omega > 0)$. More precisely, we note that this specular symmetry is an indirect consequence of the PHS relating the Goldstone and amplitude excitations at low momenta. This feature is explicitly shown in Figure 2.12(a), where we plot the particle-hole character $\mathcal{C}_{\alpha, \mathbf{k}}$ of the SFP excitations, see the definition of Eq. (2.20). In particular, we point out that all the collective modes are completely symmetric at low momenta.

For the sake of clarity, we remark that the odd behaviour of the DoS around $\omega = 0$ is a genuine product of the Goldstone diffusivity out of equilibrium and must not be confused with the well-known DoS structure of positive/negative-norm modes in an interacting bosonic system at equilibrium [6]: in particular, we find that an essential ingredient for the functional form of the DoS in the SFP is again the imaginary component of the quasiparticle weight of the Goldstone mode $Z''_{\mathrm{Gol}, \mathbf{k}} < 0$, which is negligible everywhere but in the sphere of diffusive momenta as expected. Hence, we find that the DoS is well-approximated by the expression

$$A(\mathbf{k}, \omega) = -\frac{1}{\pi} \frac{Z''_{\mathrm{Gol}, \mathbf{k}}\, \omega}{\omega^2 + \left(\omega''_{\mathrm{Gol}, \mathbf{k}}\right)^2}\,, \qquad (2.64)$$

Low-energy DoS of a out-of-equilibrium superfluid

from which we can extract also a prediction for the local DoS at low frequency by analytical integration. In d dimensions, we obtain

$$A(\omega) = -\frac{1}{\pi} \frac{\Omega_d}{(2\,\pi)^d} \frac{Z''_{\mathrm{Gol}}}{\sqrt{D}} \arctan\left(\frac{\sqrt{D}\,\Lambda_D}{\omega}\right)\,, \qquad (2.65)$$

where we have assumed $Z''_{\mathrm{Gol}, \mathbf{k}} \approx Z''_{\mathrm{Gol}}$, D is the Goldstone diffusion coefficient and Λ_D is a momentum cut-off enclosing the diffusive regime where $\omega''_{\mathrm{Gol}, \mathbf{k}} \approx D\, \mathbf{k}^2$. Notably, the static limit of the local DoS reads $A(\omega \to 0) \sim Z''_{\mathrm{Gol}}/\sqrt{D}$ and provides direct information on the diffusion coefficient. We remind here that $\omega''_{\mathrm{Gol}, \mathbf{k}}$ and $Z''_{\mathrm{Gol}, \mathbf{k}}$ refer to the hybridised D-mode becoming gapless in the anti-adiabatic regime of the SFP, see Subsection 2.5.1.

---

[6] See e.g. the QGA prediction for the Green's function of the BH model in Eq. (B.28) of Appendix B.3.
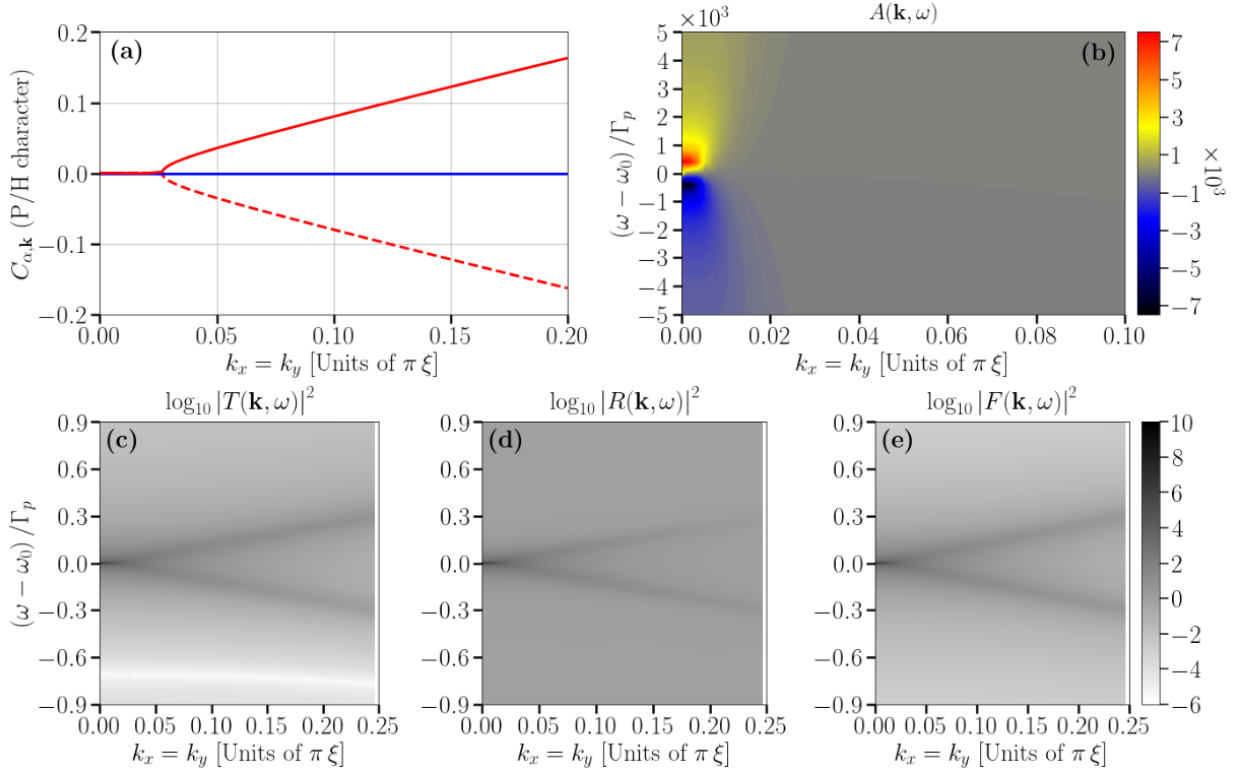
Figure 2.12: Panel (a): particle-hole character $C_{\alpha,\mathbf{k}}$ of the collective modes of the SFP. Panel (b): typical profile of the DoS in the SFP. Panels (c)-(e): behaviour of the transmittivity, reflectivity and FWM signals in the SFP, respectively. All the panels refer to the representative case of the SF state at $zJ/\Gamma_p = 6$ for $\Omega/\Gamma_p = 5 \cdot 10^{-1}$, $\Gamma_l/\Gamma_p = 5 \cdot 10^{-2}$ and $\gamma/\Gamma_p = 10^{-3}$, see the excitation spectra in Figure 2.6(c)-(c').

One-body dynamical response of the SFP The very same symmetry that governs the DoS behaviour at low energy reflects in the response functions of the photon field, whose profiles are shown in Figure 2.12(c)-(e) for the same value of J as the DoS. Differently from the case of EP condensates, the signals of the upper and lower branches have equally strong intensities in the transmittivity and the reflectivity spectra, with a weak asymmetry appearing when the PHS of the excitations is increasingly broken at large momenta. Thus, the inherent symmetry properties of the hard-core NESS make the $T(\mathbf{k}, \omega)$, $R(\mathbf{k}, \omega)$ and $F(\mathbf{k}, \omega)$ as equally sensitive probes of the low-energy excitations of the superfluid state of the photon fluid. A secondary property of the transmittivity spectrum is the appearance of a dark resonance for $\omega < 0$ [see Figure 2.12(c)], well below the signal of the ghost mode, which moves to larger energies and acquires a broader dispersion as J increases. For this reason, we interpret this feature as the effect of the destructive interference between the amplitude mode and the Goldstone/D-mode branches at the level of the Green's function, postponing a deeper understanding of such finer aspects to a more detailed study of the SFP dynamical behaviour.

It is interesting to notice that, however, neither of the one-body response functions reveal unambiguously the occurrence of the dissipative Goldstone hybridisation occurring at large J. Since the spectral contribution to density fluctuations of the D-mode $\omega_D(\mathbf{k})$ has been previously shown to drastically change across the anti-adiabatic crossover [see the first row of Figure 2.7], we theorise that more general dynamical observables probing two-body correlations of the SFP – better known as intensity
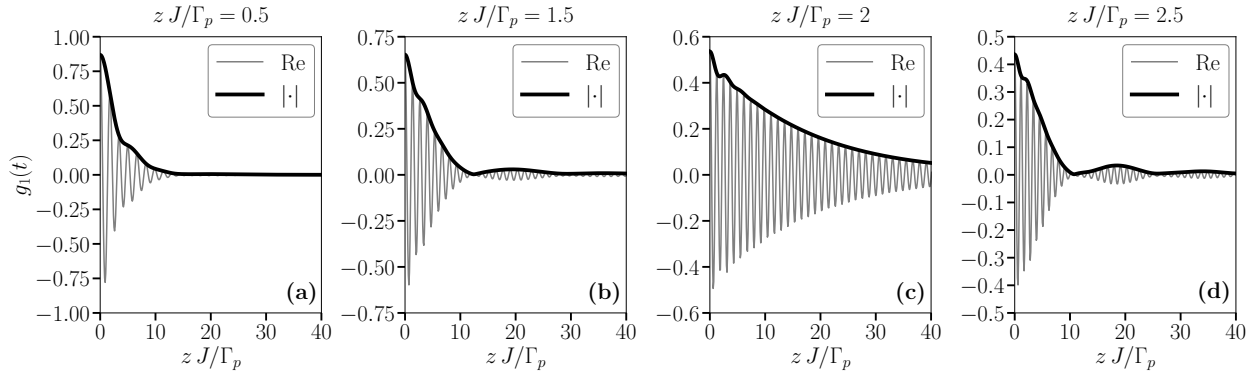
Figure 2.13: Change in the dynamics of the coherence function behaviour across the IP for constant $\Omega/\Gamma_p = 5 \cdot 10^{-1}$, $\Gamma_l/\Gamma_p = 5 \cdot 10^{-2}$, $\gamma/\Gamma_p = 5 \cdot 10^{-3}$ and the same hopping values considered in Figure 2.5. From left to right: (a) $z\,J/\Gamma_p = 0.5$; (b) $z\,J/\Gamma_p = 1.5$; (c) $z\,J/\Gamma_p = 2$; (d) $z\,J/\Gamma_p = 2.5$. Thin solid line: real part of $g_1(t)$. Thick solid line: modulus of $g_1(t)$.

correlations in the present quantum optical context – could be the ideal targets of measurement protocols aimed at detecting the spectral properties of the hybridised Goldstone mode. Since the Gutzwiller approximation is known to underestimate pair correlations at the level of Gaussian fluctuations (a shortcoming cured by the QGA), such a topic goes beyond the scope of the present work, and we leave it as an open problem for future investigations.

2.5.3 Quantum correlations: local photon coherence in the insulating phase

The DoS profile and dynamical response functions are not the only one-body features that distinguishes the IP from a strongly-correlated normal phase at equilibrium. In this Subsection, we show that also the local coherence function $g_1(t) \equiv g_1(\mathbf{0}, t)$ can provide accurate information on the quasiparticle/hole excitations of the IP and, most interestingly, how quantum coherence develops in the system. It is important to underline that, as per Eq. (2.61), a measurement of $g_1(t)$ probes the entity of local *hole* excitations, which have been actually the target of recent theoretical works and experiments in C-QED devices [25, 447, 448]. More in detail, we recall that $V_{\alpha, \mathbf{k}} \neq 0$ for the quasihole branch only in the IP: we therefore deduce that the excitations of such regimes can be clearly distinguished not only in terms of their particle/hole characters, but also depending on the type of quantum correlations that they elicit in the system.

In Figure 2.13, we show our predictions for the local coherence function in the IP corresponding to the same values of J in Figure 2.5 and, as we now discuss, to three different regimes of quasihole propagation. As a first detail, it must be noticed that $g_1(t=0)$ is exactly equal to the mean-field density of photons n_0, a sum rule that contributes to give physical consistency to our results.

At sufficiently low J with $n_0 > 1/2$ [panel (a)], $g_1(t)$ is an oscillatory function with damping time $\tau \sim \Gamma_{\rm em}^{-1} \approx \Gamma_{\rm ph}^{-1}(\mathbf{k})$ and whose period $\mathcal{T}$ is set by hopping fluctuations of photons back and forth to their lattice positions. This common form of coherence damping can be schematically understood as the excitation of a single unstable energy state, namely the lowest-energy hole mode $\omega_-(\boldsymbol{\pi})$ in the present scenario. As seen in Subsection 2.5.1, increasing J [panel (b)] has the effect of spatially spreading quasihole excitations: this leads to a flattening of $\varepsilon_-(\mathbf{k})$ as it gradually moves above the lasing frequency ω_*. As a consequence, the amplitude of $g_1(t)$ displays a beating behaviour,

A zoo of correlations: hole dynamics in the insulating state

due to the constructive interference of coherent oscillations at different momenta. On the other hand, the long-time decay is substantially controlled by the Liouvillian gap $\tau \sim \Gamma_{\mathrm{ph}}^{-1}(\mathbf{0})$. Because of the compensation between J and n_0 in fixing the bandwidth of quasihole excitations, we find that this behaviour is the one dominating the IP until the critical point $J = J_c$ is reached [panel (d)]. A remarkably different case is represented by the region in which $n_0 \approx 1/2$ [panel (c)]: here, all the quasihole modes have essentially the same energy and spectral weight in the expression of $g_1(t)$. As regards the DoS, we observe that this reflects into a power-law behaviour $A(\omega) \sim (\omega - \omega_*)^{-\nu}$ for frequencies above the lasing frequency ω_*, a clear signature of spectral accumulation [see the inset of Figure 2.10]. Accordingly, the beating dynamics of $g_1(t)$ changes into the damped power-law behaviour $\exp\left[\Gamma_{\mathrm{ph}}(\mathbf{0})\,t\right]/t^{1-\nu}$, which well fits the thick black line in panel (c). We conclude by mentioning that the decay time of coherent fluctuations $\tau \sim \Gamma_{\mathrm{ph}}^{-1}(\mathbf{0})$ eventually diverges with the closure of the Liouvillian gap at the I-to-SF transition, and therefore could serve as an additional indicator of the onset of long-range order in future experimental protocols, as prefigured as in [23, 419].

Interestingly, the results discussed above indicate that the IP can host a wide variety of one-body dynamical correlations on long time scales, despite the absence of a source of coherence (such as e.g. a condensate) and in the presence of strong dissipation mechanisms. For this reason, the IP can be definitely regarded as an *unconventional* normal state, with respect to both the excitation spectrum and observable quantum correlations. We emphasise once more that a crucial ingredient of such anomalous insulating physics resides in its out-of-equilibrium genesis, in turn made possible by the engineering of strong photon interactions in a C-QED setting.

2.6 Overview of the results

Although in this Chapter we have proposed a straightforward scheme to gain information on the NESS and excitation modes of a driven-dissipative fluid of light, our results have turned out to be unexpectedly rich in new physics, most of which is due to the dichotomy between the stationary state and its excitations that we have emphasised throughout our discussion.

Looking at the phase space explored by the NESS, we have shown that the system can be found either in an insulating or in a superfluid state, depending solely on the competition between the incoherent pumping and the hopping energy of cavity photons as a consequence of the presence of strong photon interactions. The two phases are separated by a second-order quantum phase transition, which can be driven by changing either the cavity hopping or the Rabi coupling between the cavities and the TLE's. Thanks to the flexibility of the Gutzwiller approximation, which embodies the strong-coupling regime, we have remarkably found that the superfluid order parameter is a non-monotonic function of the system parameters: explaining this feature in terms of particle/hole superfluidity, we have hypothesised that the balance between unitary and dissipative dynamics could be the key to stabilise novel types of superfluid states. A salient feature of the mean-field picture of the NESS is also the possibility of realising extremely pure states, the most interesting of which is the Mott-like phase forming at low hopping.

Our analysis of quantum fluctuations reveals however that the "surface" properties

of the NESS do not tell the whole story about the out-of-equilibrium physics of the system. Part of this information is encoded in the excitation spectrum of the collective modes: among the other results, we have found that the structure of the diffusive Goldstone mode, a universal footprint of non-equilibrium superfluids, makes the classification of the symmetry-broken states even more complex. In particular, a cross-hybridisation between phase excitations of the condensate and dissipative modes occurs in the dilute limit of the system, where there is no adiabatic separation between the cavity dynamics and the TLE's. Disclosing the quantum behaviour of the insulating phase has instead required the introduction of additional tools, including the calculation of linear response functions, in addition to designing a procedure to predict the expression of actual expectation values based on Gaussian fluctuations. This theoretical work has allowed us to appreciate what we termed the Janus-faced character of the driven-dissipative insulator: this state, despite having a gapped spectrum and exponentially decaying correlations, displays a striking dynamical response entirely due to the energy gain necessary to the very existence of the insulating state. Specifically, the transmittivity and reflectivity of the cavities in the insulating state have been shown to exceed the gain threshold well before the quantum phase transition, implying the remarkable fact that the cavity array can amplify an incident light probe without being in a lasing state.

In summary, we have illustrated how our simple linear response theory of quantum fluctuations based on the Gutzwiller approximation for the Lindblad dynamics generalises the Bogoliubov treatment of out-of-equilibrium condensates to the study of generic driven-dissipative photonic system on a lattice. Similarly to the QGA, the efficacy of our approach hinges on a detailed diagnosis of the collective modes. Even though our results are the product of a relatively strong approximation for non-local fluctuations, they strongly hint at exciting new physics, potentially not limited to the field of strongly-correlated light fluids, which certainly deserves a deeper inspection by more accurate methods.

Conclusions and future perspectives 3

In this second Part of the Thesis, we have introduced and provided the first many-body solution to a paradigmatic model for a driven-dissipative fluid of light loaded on a lattice of coupled optical cavities in the presence of non-Markovian pumping. This peculiar system has been a fruitful occasion to tackle the problem of identifying the relationship between the collective many-body excitations of a strongly-correlated system and the intrinsic non-equilibrium features of its stationary state when dissipation mechanisms are in action. Building on a Gutzwiller analysis of the excitation spectrum and Gaussian fluctuations, particularly relevant results of our work are:

- ▶ a global understanding of the excitation spectrum of the steady state across the insulator-to-superfluid transition of the system;
- ▶ a characterisation of the interplay between coherence and different dissipation channels in determining the low-energy structure of the Goldstone mode of the symmetry-broken phase;
- ▶ the uncovering of the paradoxical nature of the insulating state, which is shown to support light amplification despite the absence of long-range coherence;
- ▶ a scheme for calculating actual quantum averages starting from our derivation of $\mathbb{C}$-valued fluctuations.

Thanks to the high tunability of our model, our findings pave the way for a more general understanding of the spectral properties of the unprecedented quantum phases hosted by lattice systems driven out of equilibrium and could find a direct experimental validation through state-of-the-art C-QED engineering. Apart from being relevant for the purpose of quantum-simulating equilibrium-lake phases, such a line of research could be also an additional opportunity to cross-fertilise the languages of the condensed matter and quantum optics communities, in order to answer those multidisciplinary questions that currently arise from cutting-edge platforms of many-body physics, ranging from trapped ions [449] to optical cavities [450] and superconducting circuits [3, 42, 398, 451] and novel polariton systems [452].

To this end, numerous extensions of the present work could be possibly studied in the next future. These comprise the analysis of the whole phase diagram of the model (beyond the hard-core limit) and hence the characterisation of additional gapped modes in the SFP, a detailed study of the (potentially multiple) critical points of the I-to-SF transition. From a methodological perspective, these and other future developments could take into account improved versions of the Gutzwiller ansatz for the density matrix (e.g. a cluster solution [15–17, 421, 453]) in order to give an identity to the dynamical instabilities appearing in the SF state at strong coupling. In this regard, we cannot also exclude that describing short-range correlations exactly could radically change the phase diagram and expose other dynamical instabilities [421]. Turning our attention to open questions of a wider scope, we believe that the prospect of stabilising novel bosonic states which are hardly realisable at equilibrium (e.g. hole superfluids) poses other intriguing subjects of discussion. Analogously, the application of our method to more general driven-dissipative models (e.g. those proposed with the aim of stabilising the whole BH phase diagram [20]) is also a doable task in the same

spirit of our investigation.

Limiting ourselves to the specific case of systems under non-Markovian dissipation, our study mainly focuses on dynamical response properties, which provides information on how *dissipation* takes place in the system. While we are confident that our observations would not be qualitatively affected by the inclusion of quantum effects beyond linear response, the investigation of genuine *quantum correlations* appears to be an exciting research perspective to pursue in order to scrutinize the relation between actual quantum fluctuations and dissipation phenomena, with special attention paid to the *quantumness* of the I-to-SF transition. Future studies might address these questions in analogous driven-dissipative settings by means of the quantum trajectory technique [16, 454] specialised to the framework of the QGA theory in order to keep track of the dynamical effects of collective modes. Furthermore, our approach can represent a powerful tool for complementing the insights of powerful yet more demanding precision methods as B-DMFT [443, 455].

Recalling the aforementioned cross-fertilisation of physical ideas, we conclude this survey of final remarks with a comment on a most interesting feature of out-of-equilibrium superfluidity which is not completely grasped by our approach, that is the dissipative hybridisation of the Goldstone mode in the deep SFP. It is important to notice that this manifestation of anti-adiabaticity establishes a direct connection between our system and the so-called type-B lasers [456–459]: indeed, the working principle of these devices is based on a small number of atomic emitters whose dynamics occurs precisely on a timescale comparable to the leakage of cavity photons. In this scenario, it has been proposed [413] that the lasing dynamics of photons could mediate an effective interaction (time-evolving with the limit-cycle frequency) between the emitting centres, leading to a novel kind of light-induced time crystal. For this reason, we expect that a similar situation could take place in the dilute regime of our model. In this regard, we also envisage that crucial information on this physics could come from the theoretical and experimental analysis of those observables that could directly detect different morphologies of the Goldstone mode, e.g. intensity fluctuations of the cavity field.

APPENDIX

A

Spectral properties of the pseudo-Hermitian operator $\hat{\mathcal{L}}_{\mathbf{k}}$

The present Appendix takes free inspiration from Secs. 6.1.3. and 6.1.4. of [44].

A.1 Spectral decomposition

Since $\hat{\mathcal{L}}_{\mathbf{k}}$ is not a Hermitian operator, its eigenbasis is not orthogonal according to the Euclidean norm (in contrast with the case of BCS theory for interacting fermions). In order to write $\hat{\mathcal{L}}_{\mathbf{k}}$ in diagonal form, the knowledge of the eigenvectors is then not sufficient a priori. One generally proceeds according to the following theorem.

Theorem A.1.1 *Let $\hat{M}$ be a diagonalisable but not necessarily Hermitian operator. It follows that the diagonal form of $\hat{M}$ can be written as*

$$\hat{M} = \sum_{\alpha} m_{\alpha} \left| m_{\alpha}^{R} \right\rangle \left\langle m_{\alpha}^{L} \right| \tag{A.1}$$

where $\left| m_{\alpha}^{R} \right\rangle$ is the right eigenvector of $\hat{M}$ with eigenvalue m_{α},

$$\hat{M} \left| m_{\alpha}^{R} \right\rangle = m_{\alpha} \left| m_{\alpha}^{R} \right\rangle \tag{A.2}$$

and $\left\langle m_{\alpha}^{L} \right|$ is the corresponding left eigenvector with the same eigenvalue, namely

$$\left\langle m_{\alpha}^{L} \right| \hat{M} = \left\langle m_{\alpha}^{L} \right| m_{\alpha} \, , \tag{A.3}$$

or equivalently

$$\hat{M}^{\dagger} \left| m_{\alpha}^{L} \right\rangle = m_{\alpha}^{*} \left| m_{\alpha}^{L} \right\rangle \, . \tag{A.4}$$

$\left| m_{\alpha}^{L} \right\rangle$ *is then called the adjoint eigenvector of* $\left| m_{\alpha}^{R} \right\rangle$. *The normalisation of the left and right eigenvectors is such that* $\left\langle m_{\alpha}^{L} \middle| m_{\beta}^{R} \right\rangle = \delta_{\alpha,\beta}$.

We apply the above proposition to $\hat{\mathcal{L}}_{\mathbf{k}}$. Picking Section 1.2.2 of Part I as a reference, the right eigenvectors with eigenvalues $\omega_{\alpha,\mathbf{k}}$ can be readily identified with

$$\left| m_{\alpha}^{R} \right\rangle = \begin{pmatrix} \underline{u}_{\alpha,\mathbf{k}} \\ \underline{v}_{\alpha,\mathbf{k}} \end{pmatrix} \, . \tag{A.5}$$

Up to a normalisation factor $\mathcal{M}_{\alpha,\mathbf{k}}$, the left eigenvector can be shown to read

$$\left| m_{\alpha}^{L} \right\rangle = \mathcal{M}_{\alpha,\mathbf{k}} \begin{pmatrix} \underline{u}_{\alpha,\mathbf{k}} \\ -\underline{v}_{\alpha,\mathbf{k}} \end{pmatrix} \, . \tag{A.6}$$

The normalisation condition imposes that $\mathcal{M}_{\alpha,\mathbf{k}}^* \left(\underline{u}_{\alpha,\mathbf{k}}^* \cdot \underline{u}_{\alpha,\mathbf{k}} - \underline{v}_{\alpha,\mathbf{k}}^* \cdot \underline{v}_{\alpha,\mathbf{k}} \right) = 1$, which is a simple instance of the so-called *Minkowski norm*. If the quantity between round brackets matches the natural Bogoliubov norms ± 1, then the normalisation condition imposes $\mathcal{M}_{\alpha,\mathbf{k}} = \pm 1$ respectively. More generally, we can group the eigenvectors of $\hat{\mathcal{L}}_{\mathbf{k}}$ into three families:

- the $+$ family, such that $\left(\underline{u}_{\alpha,\mathbf{k}}^* \cdot \underline{u}_{\alpha,\mathbf{k}} - \underline{v}_{\alpha,\mathbf{k}}^* \cdot \underline{u}_{\alpha,\mathbf{k}} \right) = 1$, also known as *positive-norm* modes;
- the $-$ family, such that $\left(\underline{u}_{\alpha,\mathbf{k}}^* \cdot \underline{u}_{\alpha,\mathbf{k}} - \underline{v}_{\alpha,\mathbf{k}}^* \cdot \underline{v}_{\alpha,\mathbf{k}} \right) = -1$, also known as *negative-norm* modes;
- the 0 family, such that $\left(\underline{u}_{\alpha,\mathbf{k}}^* \cdot \underline{u}_{\alpha,\mathbf{k}} - \underline{v}_{\alpha,\mathbf{k}}^* \cdot \underline{v}_{\alpha,\mathbf{k}} \right) = 0$.

From Theorem A.1.1 we realise that there is a duality between the eigenvectors of the $+$ and $-$ family. Specifically, each positive-norm mode $\left(\underline{u}_{\alpha,\mathbf{k}}, \underline{v}_{\alpha,\mathbf{k}} \right)$ with eigenvalue $\omega_{\alpha,\mathbf{k}}$ can be paired with a negative-norm mode having right eigenvector $\left(\underline{v}_{\alpha,\mathbf{k}}^*, \underline{u}_{\alpha,\mathbf{k}}^* \right)$ and eigenvalue $-\omega_{\alpha,\mathbf{k}}^*$. It is important to note that the denomination "+ family" refers to the sign of the eigenvector norm and *not* to the sign of the eigenvalue.

The only member of the 0 family is the eigenvector $\left[\underline{c}^0, \left(\underline{c}^0 \right)^* \right]$, which represents a global phase rotation of the ground state with vanishing energy. As a by-product, it is easy to see that $\left(\underline{c}^0 \right)^* \cdot \underline{u}_{\alpha,\mathbf{k}} = \left(\underline{c}^0 \right)^* \cdot \underline{v}_{\alpha,\mathbf{k}} = 0$, which guarantees the orthogonality of quantum fluctuations with respect to the ground state.

A.2 Commutation relations

The commutation relations for the QGA fluctuation operators $\delta \hat{c}_n(\mathbf{r})$ can be identified a posteriori once the right eigenvectors $\left(\underline{u}_{\alpha,\mathbf{k}}, \underline{v}_{\alpha,\mathbf{k}} \right)$ of $\hat{\mathcal{L}}_{\mathbf{k}}$ and the exact form of the Bogoliubov rotation (1.15) are determined. Exploiting the fact that the operators $\hat{b}_{\alpha,\mathbf{k}}$, $\hat{b}_{\alpha,\mathbf{k}}^\dagger$ satisfy the Bose statistics, we obtain

$$\left[\delta \hat{c}_n(\mathbf{r}), \delta \hat{c}_m^\dagger(\mathbf{s}) \right] = \frac{1}{V} \sum_{\alpha,\mathbf{k}} e^{i\mathbf{k}\cdot(\mathbf{r}-\mathbf{s})} \left(u_{\alpha,\mathbf{k},n} u_{\alpha,\mathbf{k},m}^* - v_{\alpha,-\mathbf{k},n}^* v_{\alpha,-\mathbf{k},m} \right) . \tag{A.7}$$

A well-known property of pseudo-Hermitian matrices of the same form as $\hat{\mathcal{L}}_{\mathbf{k}}$ is the sum rule [44]

$$\sum_\alpha \left(u_{\alpha,\mathbf{k},n} u_{\alpha,\mathbf{k},m}^* - v_{\alpha,-\mathbf{k},n}^* v_{\alpha,-\mathbf{k},m} \right) = \delta_{n,m} - c_b^0 \left(c_m^0 \right)^* , \tag{A.8}$$

which formally follows from the fact that the ground state eigenvector $\left[\underline{c}^0, \left(\underline{c}^0 \right)^* \right]$, being a zero-energy eigenvector of $\hat{\mathcal{L}}_{\mathbf{k}}$, can be always projected out of the spectral decomposition of the quadratic form (1.10) when considering only excitations with finite positive energy. Inserting the expression (A.8) into Eq. (A.7), we obtain the expected quasi-bosonic commutation relations (1.19).

B

Gutzwiller theory of the Bose-Hubbard model: exact results

The first three Sections of this Appendix are partially based on well-known results reported in [43, 51].

B.1 MI-to-SF critical boundary

The location of the quantum phase transition between the MI and SF phases can be determined from the disappearance of the energy gap in the MI excitation spectrum, which corresponds to the condition $\omega_{P,\mathbf{0}} = 0$ and/or $\omega_{H,\mathbf{0}} = 0$ depending on the chemical potential μ. In this way, we recover the critical hopping value

$$2\,d\left(\frac{J}{U}\right)_c^{\mathrm{MI}} = \frac{(n_0 - \mu/U)\,(1 - n_0 + \mu/U)}{1 + \mu/U}\,, \tag{B.1}$$

where n_0 is the filling of the MI lobe under consideration. The maximal value of the critical hopping for each MI lobe, given by

$$2\,d\left(\frac{J}{U}\right)_c^{\mathrm{MI,tip}} = \left(\sqrt{n_0 + 1} - \sqrt{n_0}\right)^2\,, \tag{B.2}$$

corresponds to the tip of the Mott lobes, namely the O(2) transition points, having the chemical potentials

$$\left(\frac{\mu}{U}\right)_c^{\mathrm{MI,tip}} = \sqrt{n_0\,(n_0 + 1)} - 1\,. \tag{B.3}$$

At the O(2) critical point, the Goldstone and Higgs branches have the gapless excitation energies

$$\omega_{\mathrm{Gol/Hig},\mathbf{k}}^{\mathrm{tip}} = \left[\sqrt{n_0\,(n_0 + 1)}\,(z\,J + \varepsilon_{\mathbf{k}})\,U + \frac{1}{4}\,(z\,J + \varepsilon_{\mathbf{k}})^2\right]^{1/2} \pm \frac{\varepsilon_{\mathbf{k}}}{2}\,. \tag{B.4}$$

For small $|\mathbf{k}|$, the two branches are degenerate with the sound velocity

$$c_s^{\mathrm{tip}} = [n_0\,(n_0 + 1)]^{1/4}\,\sqrt{\left(\frac{J}{U}\right)_c^{\mathrm{MI,tip}} U}\,. \tag{B.5}$$

B.2 Acoustic features of the Goldstone mode in the SF phase

B.2.1 Derivation of the Gutzwiller sound velocity equation

In order to work out the sound velocity c_s of the Goldstone mode, we consider the diagonalisation problem of the QGA Hamiltonian (1.10) and perform a low-$\mathbf{k}$ expansion of the Bogoliubov coefficients, as well as of the corresponding excitation spectrum,

$$\underline{u}_{\alpha,\mathbf{k}} = \underline{u}_{\alpha,\mathbf{k}}^{(0)} + \underline{u}_{\alpha,\mathbf{k}}^{(1)} + \underline{u}_{\alpha,\mathbf{k}}^{(2)} + \cdots\,, \tag{B.6a}$$

$$v_{\alpha,\mathbf{k}} = \underline{v}_{\alpha,\mathbf{k}}^{(0)} + \underline{v}_{\alpha,\mathbf{k}}^{(1)} + \underline{v}_{\alpha,\mathbf{k}}^{(2)} + \cdots , \tag{B.6b}$$

$$\omega_{\alpha,\mathbf{k}} = \omega_{\alpha,\mathbf{k}}^{(0)} + \omega_{\alpha,\mathbf{k}}^{(1)} + \omega_{\alpha,\mathbf{k}}^{(2)} + \cdots , \tag{B.6c}$$

where the superscripts indicate the **k** orders. The zeroth-order contributions to the previous system of equations satisfies the relation

$$\omega_{\alpha,\mathbf{k}}^{(0)} \begin{pmatrix} \underline{u}_{\alpha,\mathbf{k}}^{(0)} \\ \underline{v}_{\alpha,\mathbf{k}}^{(0)} \end{pmatrix} = \begin{pmatrix} \boldsymbol{H_0} & \boldsymbol{K_0} \\ -\boldsymbol{K_0^*} & -\boldsymbol{H_0^*} \end{pmatrix} \begin{pmatrix} \underline{u}_{\alpha,\mathbf{k}}^{(0)} \\ \underline{v}_{\alpha,\mathbf{k}}^{(0)} \end{pmatrix} , \tag{B.7}$$

whose only lowest-energy solution in the SF phase is given by

$$u_{\text{Gol},\mathbf{k},n}^{(0)} = \left(n + \frac{\partial \omega_0}{\partial \mu} \right) c_n^0 , \tag{B.8a}$$

$$v_{\text{Gol},\mathbf{k},n}^{(0)} = -u_{\text{Gol},\mathbf{k},n}^{(0)} , \tag{B.8b}$$

$$\omega_{\text{Gol},\mathbf{k}}^{(0)} = 0 , \tag{B.8c}$$

and therefore corresponds to the Goldstone excitation as expected. In turn, the first-order terms are ruled by the equation

$$\omega_{\alpha,\mathbf{k}}^{(1)} \begin{pmatrix} \underline{u}_{\alpha,\mathbf{k}}^{(0)} \\ \underline{v}_{\alpha,\mathbf{k}}^{(0)} \end{pmatrix} = \begin{pmatrix} \boldsymbol{H_0} & \boldsymbol{K_0} \\ -\boldsymbol{K_0^*} & -\boldsymbol{H_0^*} \end{pmatrix} \begin{pmatrix} \underline{u}_{\alpha,\mathbf{k}}^{(1)} \\ \underline{v}_{\alpha,\mathbf{k}}^{(1)} \end{pmatrix} . \tag{B.9}$$

Taking into account the identity

$$\sum_m \left(H_0^{nm} + K_0^{nm} \right) \frac{\partial c_m^0}{\partial \mu} = \left(n + \frac{\partial \omega_0}{\partial \mu} \right) c_n^0 \tag{B.10}$$

the first-order solution can be written as

$$u_{\text{Gol},\mathbf{k},n}^{(1)} = v_{\text{Gol},\mathbf{k},n}^{(1)} = \omega_{\text{Gol},\mathbf{k}}^{(1)} \frac{\partial c_n^0}{\partial \mu} \tag{B.11}$$

Making use of the above results in the second-order equation

$$\omega_{\alpha,\mathbf{k}}^{(1)} \begin{pmatrix} \underline{u}_{\alpha,\mathbf{k}}^{(1)} \\ \underline{v}_{\alpha,\mathbf{k}}^{(1)} \end{pmatrix} + \omega_{\alpha,\mathbf{k}}^{(2)} \begin{pmatrix} \underline{u}_{\alpha,\mathbf{k}}^{(0)} \\ \underline{v}_{\alpha,\mathbf{k}}^{(0)} \end{pmatrix} = \begin{pmatrix} \boldsymbol{H_0} & \boldsymbol{K_0} \\ -\boldsymbol{K_0} & -\boldsymbol{H_0} \end{pmatrix} \begin{pmatrix} \underline{u}_{\alpha,\mathbf{k}}^{(2)} \\ \underline{v}_{\alpha,\mathbf{k}}^{(2)} \end{pmatrix} + \begin{pmatrix} \boldsymbol{H_k^{(2)}} & \boldsymbol{K_k^{(2)}} \\ -\boldsymbol{K_k^{(2)}} & -\boldsymbol{H_k^{(2)}} \end{pmatrix} \begin{pmatrix} \underline{u}_{\alpha,\mathbf{k}}^{(0)} \\ \underline{v}_{\alpha,\mathbf{k}}^{(0)} \end{pmatrix} \tag{B.12}$$

(where we have ignored the complex conjugation symbols in the lower matrix block for simplicity), multiplying both the sides of the equations by $\left(\underline{u}_{\alpha,\mathbf{k}}^{(0)}, -\underline{v}_{\alpha,\mathbf{k}}^{(0)} \right)$ from the left side and observing that

$$\underline{u}_{\text{Gol},\mathbf{k}}^{(0)} \cdot \underline{u}_{\mathbf{k}}^{(0)} - \underline{v}_{\mathbf{k}}^{(0)} \cdot \underline{v}_{\mathbf{k}}^{(0)} = 0 , \tag{B.13}$$

we readily obtain

$$\sum_n \left(u_{\text{Gol},\mathbf{k},n}^{(0)} - v_{\text{Gol},\mathbf{k},n}^{(0)} \right) \frac{\partial c_n^0}{\partial \mu} = \frac{\partial \langle \hat{n} \rangle}{\partial \mu} \equiv \kappa , \tag{B.14}$$

where κ is the mean-field predictions for the compressibility. Combining this result with Eq. (B.12), we derive the general formula

$$c_s = \sqrt{\frac{2\,J}{\kappa}}\,|\psi_0| \tag{B.15}$$

for the Goldstone sound velocity.

B.2.2 Behaviour of the sound-velocity in the BH strongly-correlated regimes

In the deep SF limit $(J \gg U)$, $|\psi_0| \approx \sqrt{\langle \hat{n} \rangle_{MF}}$ and $\kappa \approx U^{-1}$. Thus, we recover the well-known Bogoliubov expression for the sound velocity on a lattice, namely

$$c_{s,\mathrm{Bog}} = \sqrt{2\,J\,U\,\langle \hat{n} \rangle_{MF}}\,. \tag{B.16}$$

In the opposite limit $(J \ll U)$, the SF phase with fractional density $n_0 < \langle \hat{n} \rangle < n_0 + 1$ is confined in the region between the MI lobes with filling n_0 and $n_0 + 1$. For $J/U \to 0$, the chemical potential of the system is evidently a linear function of the density, namely

$$\mu^{(J \to 0)} = \mu_-(J) + [\mu_+(J) - \mu_-(J)]\,(\langle \hat{n} \rangle_{MF} - n_0)\,, \tag{B.17}$$

where $\mu_\pm(J)$ is the parametric equation of the upper/lower MI boundary, respectively. Using Eq. (B.1), we obtain

$$\mu_\pm^{(J \to 0)}(J) = U\,n_0 \pm z\,J\,(n_0 + 1)\,, \tag{B.18}$$

from which we deduce that

$$\kappa^{(J \to 0)} = [2\,z\,J\,(n_0 + 1)]^{-1}\,, \tag{B.19}$$

implying that the compressibility diverges in the HCSF limit of the system, as expected. Now, using the thermodynamic relation $\partial E_{\mathrm{BH}}/\partial \langle \hat{n} \rangle = \mu$ for the energy density E_{BH} and the mean-field condition $E_{\mathrm{BH},\pm} = U\,n_0\,(n_0 \pm 1)\,/2$ holding at the MI boundary, we get

$$E_{\mathrm{BH}}^{(J \to 0)} = U\,n_0 \left(\langle \hat{n} \rangle - \frac{n_0 + 1}{2} \right) - z\,J\,(n_0 + 1)\,(\langle \hat{n} \rangle_{MF} - n_0)\,(n_0 + 1 - \langle \hat{n} \rangle_{MF})\,. \tag{B.20}$$

From the previous equation, we can easily extract the order parameter value in the strongly-interacting SF regime by means of

$$\left| \psi_0^{(J \to 0)} \right|^2 = -\frac{1}{z}\frac{\partial E_{\mathrm{BH}}}{\partial J} = (n_0 + 1)\,(\langle \hat{n} \rangle_{MF} - n_0)\,(n_0 + 1 - \langle \hat{n} \rangle_{MF})\,, \tag{B.21}$$

from which we finally obtain the sound velocity

$$c_s^{(J \to 0)} = -\frac{1}{z}\frac{\partial E_{\mathrm{BH}}}{\partial J} = 2\,J\,(n_0 + 1)\,\sqrt{z\,(\langle \hat{n} \rangle_{MF} - n_0)\,(n_0 + 1 - \langle \hat{n} \rangle_{MF})}\,, \tag{B.22}$$

which reaches its minimal value for half-integer densities $\langle \hat{n} \rangle_{MF} = n_0 + 1/2$. This behaviour mirrors qualitatively the one of hard-core bosons in 1D, where the sound velocity has the exact expression $c_s^{\mathrm{HC}} = 2\,J\sin\left(\pi\,\langle \hat{n} \rangle\right)$, see e.g. [460] and also the mean-field treatment of the case $n_0 = 0$ in Section F.2 of the Appendix.

Upon approaching the MI boundary, c_s goes to zero everywhere except for the O(2) critical points, where it converges to the value of Eq. (B.5). This behaviour can be understood by considering the critical properties of the order parameter $|\psi_0|$ and the compressibility κ. In fact, the latter quantity
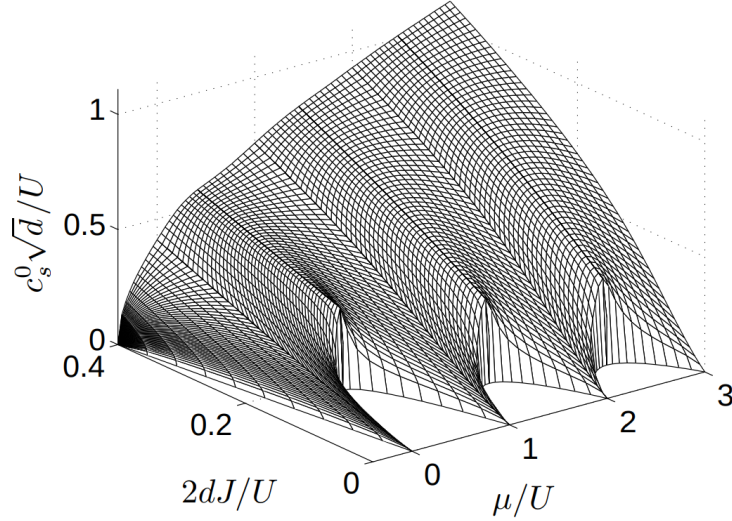
Figure B.1: Surface plot of the sound velocity as a function of the hopping energy $2\,d\,J/U$ and the chemical potential in the strongly-correlated regime of the BH model. The flat white regions correspond to the MI lobes of the phase diagram. The figure has been taken and adapted from [51].

goes continuously to zero proportionally to the condensate density $\rho_c = |\psi_0|^2$ only at the tip of the MI lobes, thus explaining the respective finite value of c_s; on the other hand, κ reaches a finite value on the brink of the CI transition points, hence the vanishing sound velocity of the SF formed by doping the MI phase.

To conclude, in Figure B.1 we provide an illustrative summary of the sound velocity properties in the strongly-interacting and quantum critical regimes discussed before.

B.3 Excitation spectrum and Green's function in the MI phase

In the MI phase, the mean-field Gutzwiller parameters have the simple analytical form $c_n^{0,\mathrm{MI}} = \delta_{n,n_0}$ pinned at the MI filling n_0. Consequently, the blocks of the pseudo-Hermitian $\hat{\mathcal{L}}_{\mathbf{k}}$ of fluctuations simplify into

$$H_{\mathrm{MI},\mathbf{k}}^{nm} = \left[\frac{U}{2}\,n\,(n-1) - \mu\,n - \omega_0\right]\delta_{n,m} + \varepsilon_{\mathbf{k}}\left[n_0\,\delta_{n+1,n_0}\,\delta_{m+1,n_0} + (n_0+1)\,\delta_{n-1,n_0}\,\delta_{m-1,n_0}\right]\,, \quad \text{(B.23a)}$$

$$K_{\mathrm{MI},\mathbf{k}}^{nm} = \varepsilon_{\mathbf{k}}\,\sqrt{n_0\,(n_0+1)}\,\left(\delta_{n+1,n_0}\,\delta_{m-1,n_0} + \delta_{n-1,n_0}\,\delta_{m+1,n_0}\right)\,. \quad \text{(B.23b)}$$

It follows that the QGA eigenvalue problem reduces to the diagonalisation of 2×2 matrices that couple $u_{\alpha,\mathbf{k},n_0+1}$ to $v_{\alpha,\mathbf{k},n_0-1}$ and $u_{\alpha,\mathbf{k},n_0-1}$ to $v_{\alpha,\mathbf{k},n_0+1}$, respectively. The former pair of Bogoliubov coefficients correspond to the particle branch of the MI phase, while the latter is related to the hole branch. Overall, the excitation spectrum of these two modes is given the analytical formula

$$\omega_{\mathrm{P/H},\mathbf{k}} = \frac{1}{2}\sqrt{U^2 + 4\,\varepsilon_{\mathbf{k}}\,U\left(n_0 + \frac{1}{2}\right) + \varepsilon_{\mathbf{k}}^2} \pm \left[U\left(n_0 - \frac{1}{2}\right) - \mu + \frac{\varepsilon_{\mathbf{k}}}{2}\right]\,, \quad \text{(B.24)}$$

which is good agreement with results obtained by applying the Hubbard-Stratonovich transformation [64] and the Schwinger boson approach [47]. In particular, by writing Eq. (B.24) as

$\omega_{\mathrm{P/H},\mathbf{k}} = \Delta_{\mathrm{P/H}} + m_{\mathrm{P/H}}^{-1}\,\mathbf{k}^2/2$, we can extract the particle/hole energy gaps

$$\Delta_{\mathrm{P/H},\mathbf{k}} = \omega_{\mathrm{P/H},\mathbf{0}} = \frac{1}{2}\sqrt{U^2 - 4\,z\,J\,U\left(n_0 + \frac{1}{2}\right) + (z\,J)^2} \pm \left[U\left(n_0 - \frac{1}{2}\right) - \mu - \frac{z\,J}{2}\right], \qquad (\text{B.25})$$

as well as their effective masses,

$$\frac{m}{m_{\mathrm{P/H}}} = \frac{1}{2}\left[\frac{(2\,n_0 + 1)\,U - z\,J}{\Delta_{\mathrm{P}} + \Delta_{\mathrm{H}}} \pm 1\right]. \qquad (\text{B.26})$$

Besides particle/hole excitations, the other branches of the MI spectrum are dispersionless with energies

$$\omega_{\mathrm{MI},\lambda} = \frac{U}{2}\left[\lambda\,(\lambda - 1) - n_0\,(n_0 - 1)\right] - \mu\,(\lambda - n_0), \qquad (\text{B.27})$$

where λ is a non-negative integer number different from n_0 and $n_0 \pm 1$. The eigenvectors of these modes are given by $u_{\alpha,\mathbf{k},n} = \delta_{n,\lambda}$ to $v_{\alpha,\mathbf{k},n} = 0$, such that they do not contribute to quantum correlations in the MI.

Analogously to the calculation of the Green's function of the QGA bosonic fields in the FH model – see Eqs. (5.62) and (5.66) –, our second-order prediction for the Green's function of the BH model reads

$$G_{\mathrm{BH}}(\mathbf{k}, \omega) = -2\,\pi\,i\,V\,|\psi_0|^2\,\delta(\omega)\,\delta_{\mathbf{k},0} + \sum_{\alpha}\left[\frac{|U_{\alpha,\mathbf{k}}|^2}{\omega - \omega_{\alpha,\mathbf{k}}} - \frac{|V_{\alpha,\mathbf{k}}|^2}{\omega + \omega_{\alpha,\mathbf{k}}}\right]. \qquad (\text{B.28})$$

In the MI phase, the Green's function acquires the simple expression

$$G_{\mathrm{BH}}^{\mathrm{MI}}(\mathbf{k}, \omega) = \frac{|U_{\mathrm{P},\mathbf{k}}|^2}{\omega - \omega_{\mathrm{P},\mathbf{k}}} - \frac{|V_{\mathrm{H},\mathbf{k}}|^2}{\omega + \omega_{\mathrm{H},\mathbf{k}}}, \qquad (\text{B.29})$$

where we have used the fact that doublon (holon) modes are weighted by the particle (hole) fluctuation amplitude only, since $U_{\mathrm{H},\mathbf{k}} = 0$ and $V_{\mathrm{P},\mathbf{k}} = 0$ identically. Therefore, we observe that the squared hole amplitude $|V_{\mathrm{H},\mathbf{k}}|^2$ can be interpreted as the quasiparticle residue of hole excitations, as we also mention in Subsection 1.3.1 of Part I. The numerical results discussed throughout the main body of the Thesis show that the QGA offers a particularly accurate description of the MI physics. In what follows, we show that the reason for this success has to be attributed to the analytical structure of the self-energy of the MI state as predicted by the QGA.

We start our discussion by the explicit calculation of the MI self-energy via the Dyson equation $\Sigma_{\mathrm{BH}}^{\mathrm{MI}}(\mathbf{k}, \omega) = \left[G_{\mathrm{BH}}^{(0)}(\mathbf{k}, \omega)\right]^{-1} - \left[G_{\mathrm{BH}}^{\mathrm{MI}}(\mathbf{k}, \omega)\right]^{-1}$, where $\left[G_{\mathrm{BH}}^{(0)}(\mathbf{k}, \omega)\right]^{-1} = \omega - \varepsilon_{\mathbf{k}}$ is the non-interacting Green's function of bosons on the lattice, yielding the result

$$\Sigma_{\mathrm{BH}}^{\mathrm{MI}}(\mathbf{k}, \omega) = \omega - \varepsilon_{\mathbf{k}} + \mu + \frac{\omega_{\mathrm{P},\mathbf{k}}\,\omega_{\mathrm{H},\mathbf{k}} + (\omega_{\mathrm{P},\mathbf{k}} - \omega_{\mathrm{H},\mathbf{k}})\,\omega - \omega^2}{Z_{\mathrm{H},\mathbf{k}}\,(\omega_{\mathrm{P},\mathbf{k}} + \omega_{\mathrm{H},\mathbf{k}}) + \omega_{\mathrm{H},\mathbf{k}} + \omega}, \qquad (\text{B.30})$$

where we have renamed $Z_{\mathrm{H},\mathbf{k}} \equiv |V_{\mathrm{H},\mathbf{k}}|^2$ for the sake of simplicity and used the Bogoliubov identity $|U_{\mathrm{P},\mathbf{k}}|^2 - |V_{\mathrm{H},\mathbf{k}}|^2 = 1$ valid in the MI phase. Let us first analyse the behaviour of $\Sigma_{\mathrm{BH}}^{\mathrm{MI}}(\mathbf{k}, \omega)$ at small momenta and frequencies, that is when both the particle and hole gaps $\Delta_{\mathrm{P}}, \Delta_{\mathrm{H}}$ are finite. In particular, we make a distinction between the so-called ω-limit (uniform limit $\mathbf{q} = \mathbf{0}$ taken before $\omega \to 0$) and the

q-limit (static limit $\omega = 0$ taken before $\mathbf{q} \to \mathbf{0}$). In the former case, we obtain

$$\Sigma_{\text{BH}}^{\text{MI}}(\mathbf{k} = \mathbf{0}, \omega \to 0) \simeq \frac{\Delta_{\text{P}} \Delta_{\text{H}}}{Z_{\text{H},\mathbf{0}} (\Delta_{\text{P}} + \Delta_{\text{H}}) + \Delta_{\text{H}}} \tag{B.31}$$
$$+ \left\{ 1 + \frac{\Delta_{\text{P}} - \Delta_{\text{H}}}{Z_{\text{H},\mathbf{0}} (\Delta_{\text{P}} + \Delta_{\text{H}}) + \Delta_{\text{H}}} - \frac{\Delta_{\text{P}} \Delta_{\text{H}}}{[Z_{\text{H},\mathbf{0}} (\Delta_{\text{P}} + \Delta_{\text{H}}) + \Delta_{\text{H}}]^2} \right\} \omega + \text{O}\left(\omega^2\right),$$

revealing that the self-energy scales linearly at low frequency. In the **q**-limit case, we derive

$$\Sigma_{\text{BH}}^{\text{MI}}(\mathbf{k} \to \mathbf{0}, \omega = 0) \simeq \frac{\Delta_{\text{P}} \Delta_{\text{H}}}{Z_{\text{H},\mathbf{0}} (\Delta_{\text{P}} + \Delta_{\text{H}}) + \Delta_{\text{H}}} + \text{O}\left(k^4\right). \tag{B.32}$$

indicating that the MI self-energy has weak dependence on momentum at low energy, the leading-order term being in powers of $\mathbf{k}^4$. More precisely, at lowest order we have

$$\Sigma_{\text{BH}}^{\text{MI}}(\mathbf{k} \to \mathbf{0}, \omega = 0) \simeq \frac{z}{2} \left[\left(\frac{J}{U}\right)_c^{\text{MI}} - \frac{J}{U} \right] \left[1 - \frac{J}{24 (1 + \mu)} \sum_{i=1}^{d} k_i^4 \right] + \text{O}\left(k^6\right) \tag{B.33}$$

It is important to notice that the non-quadratic dependence on momentum of $\Sigma_{\text{BH}}^{\text{MI}}(\mathbf{k} \to \mathbf{0}, \omega = 0)$ predicted by the QGA can be read as a consequence of the fundamentally *quasi-local* nature of the MI phase and is the reason behind the following relation relating the non-local quasiparticle weight of hole excitations with the corresponding effective mass,

$$Z_{\text{H},\mathbf{0}} = \frac{m}{Z_{\text{H}}}. \tag{B.34}$$

Additionally, we highlight that the quartic-order coefficient $J/ [24 (1 + \mu)]$ in (B.33) is always smaller than about 10^{-3} in $d = 3$, decreases with $1/d$ as the dimensionality of the system is increased at fixed $z J$ and, evidently, vanishes in the large-filling limit $\mu \to \infty$. These observations provide further quantitative support to the QGA as a reliable theory of quantum correlations in the MI regime. Finally, we also notice that the overall factor in front of the lowest-order terms in Eq. (B.33) vanishes at the MI-to-SF boundary, thus giving an almost dispersionless self-energy at the critical point just before the onset of one-body coherence.

Rigorously speaking, the calculation of the quasiparticle residues and effective masses of particle/-hole excitations requires the evaluation of the MI self-energy on the respective poles in momentum space [18]. In particular, focusing again on the hole mode for illustrative purposes, we have

$$\frac{m}{m_{\text{H}}} = \left[1 - \frac{\partial \Sigma_{\text{BH}}^{\text{MI}}(\mathbf{k}, \omega)}{\partial \omega} \bigg|_{\mathbf{k}=\mathbf{0}, \, \omega = \Delta_{\text{H}}} \right]^{-1} \left[1 + 2 m \frac{\partial \Sigma_{\text{BH}}^{\text{MI}}(\mathbf{k}, \omega_{\text{H},\mathbf{k}})}{\partial \mathbf{k}^2} \bigg|_{\mathbf{k}=\mathbf{0}} \right]$$
$$= Z_{\text{H},\mathbf{0}} \left[1 + 2 m \frac{\partial \Sigma_{\text{BH}}^{\text{MI}}(\mathbf{k}, \omega_{\text{H},\mathbf{k}})}{\partial \mathbf{k}^2} \bigg|_{\mathbf{k}=\mathbf{0}} \right], \tag{B.35}$$

where the last equality is the result of a straightforward calculation based on Eq. (B.30). Let us then evaluate the second factor on the right-hand side of Eq. (B.35). The partial derivative of the MI self-energy with respect to $\mathbf{k}^2$ evaluated at the holon pole $\omega_{\text{H},\mathbf{k}}$ reads

$$\frac{\partial \Sigma_{\text{BH}}^{\text{MI}}(\mathbf{k}, \omega_{\text{H}}(\mathbf{k}))}{\partial \mathbf{k}^2} = -\frac{1}{2 m} + \frac{1}{|Z_{\text{H},\mathbf{k}}|^2} \frac{\partial}{\partial \mathbf{k}^2} \left[\frac{\mathbf{k}^2}{2 m_{\text{H}}^*} + \text{O}\left(k^4\right) \right]. \tag{B.36}$$

Therefore, it is easy to observe that

$$\left.\frac{\partial \Sigma_{\mathrm{BH}}^{\mathrm{MI}}(\mathbf{k}, \omega_{\mathrm{H},\mathbf{k}})}{\partial \mathbf{k}^2}\right|_{\mathbf{k}=0} = 0\,, \tag{B.37}$$

exactly, hence Eq. (B.35) leads to the expected relation (B.34). In conclusion, the MI self-energy scales with k^4 also around the particle/hole poles of the Green's function. In more detail, the corresponding momentum derivative turns out to have the simple quadratic structure

$$\frac{\partial \Sigma_{\mathrm{BH}}^{\mathrm{MI}}(\mathbf{k}, \omega_{\mathrm{H},\mathbf{k}})}{\partial \mathbf{k}^2} \simeq \frac{1}{4}\frac{2 + m_{\mathrm{H}}/m}{(2\,n_0 + 1)\,U - z\,J}\frac{\mathbf{k}^2}{2\,m^2} + \mathrm{O}\!\left(k^4\right) \tag{B.38}$$

at low momenta, displaying an analytic behaviour across the MI-to-SF transition.

B.4 Additional details on the derivation of non-Gaussian fluctuations

In this Appendix Section, we briefly sketch the construction of the third-order extension of the QGA theory that we have applied to the special case of the decay processes of the collective modes in Section 1.4 of Part I.

The third-order contributions of the quantised fluctuations to the QGA Hamiltonian of the BH model descend from the expansion of both the hopping operator and the local terms. More explicitly,

$$
\begin{aligned}
\hat{H}_{\mathrm{QGA}}^{(3)} &= \hat{H}_1^{(3)} + \hat{H}_2^{(3)} + \hat{H}_3^{(3)} = \\
&= -J\sum_{\mathbf{r},s(\mathbf{r})}\left[\delta_1\hat{\psi}^\dagger(\mathbf{r})\,\delta_2\hat{\psi}(\mathbf{s}) + \delta_2\hat{\psi}^\dagger(\mathbf{r})\,\delta_1\hat{\psi}(\mathbf{s})\right] - J\sum_{\mathbf{r},s(\mathbf{r})}\left[\psi_0^*(\mathbf{r})\,\delta_3\hat{\psi}(\mathbf{s}) + \delta_3\hat{\psi}^\dagger(\mathbf{r})\,\psi_0(\mathbf{s})\right] \\
&\quad - \frac{1}{2}\sum_{\mathbf{r}}\sum_{n}\left[H_n\,c_n^0\,\delta\hat{c}_n^\dagger(\mathbf{r})\sum_{m}\delta\hat{c}_m^\dagger(\mathbf{r})\,\delta\hat{c}_m(\mathbf{r}) + \mathrm{H.c.}\right],
\end{aligned}
\tag{B.39}
$$

where the third-order expansion of the Bose-field $\delta_3\,\hat{\psi}(\mathbf{r})$ reads

$$\delta_3\hat{\psi}(\mathbf{r}) \equiv -\frac{1}{2}\sum_n\sqrt{n}\,c_n^0\,\delta\hat{c}_{n-1}^\dagger(\mathbf{r})\sum_m\delta\hat{c}_m^\dagger(\mathbf{r})\,\delta\hat{c}_m(\mathbf{r}) - \frac{1}{2}\sum_m\delta\hat{c}_m^\dagger(\mathbf{r})\,\delta\hat{c}_m(\mathbf{r})\sum_n\sqrt{n}\left(c_{n-1}^0\right)^*\delta\hat{c}_n(\mathbf{r}) \tag{B.40}$$

and the symbol $s(\mathbf{r})$ labels the nearest-neighbouring sites around $\mathbf{r}$, while the third line of Eq. (B.39) is due to the expansion of the normalisation operator $\hat{A}(\mathbf{r})$. Considering a homogeneous system and playing with the Bogoliubov rotation of the Gutzwiller fluctuation operators $\hat{c}_n(\mathbf{r})$, a lengthy but straightforward calculation provides the following intermediate expression,

$$
\begin{aligned}
\hat{H}_{\mathrm{QGA}}^{(3)} &= \frac{1}{\sqrt{V}}\sum_{\mathbf{k},\mathbf{p}}\sum_{\alpha}\left\{\varepsilon_{\mathbf{k}}\,U_{\alpha,\mathbf{k}}\,\hat{b}_{\alpha,\mathbf{k}}^\dagger\sum_m\sqrt{m}\,\delta\hat{c}_{m-1}^\dagger(\mathbf{p})\,\delta\hat{c}_m(\mathbf{k}+\mathbf{p})\right. \\
&\quad + \varepsilon_{\mathbf{k}}\,V_{\alpha,\mathbf{k}}\,\hat{b}_{\alpha,-\mathbf{k}}\sum_m\sqrt{m}\,\delta\hat{c}_{m-1}^\dagger(\mathbf{p})\,\delta\hat{c}_m(\mathbf{k}+\mathbf{p}) \\
&\quad \left.+\frac{1}{2}\left[\psi_0\,(z\,J - 2\,\varepsilon_{\mathbf{k}})\,(U_{\alpha,\mathbf{k}} + V_{\alpha,\mathbf{k}}) + \frac{U}{2}\,(N_{\alpha,\mathbf{k}} - D_{\alpha,\mathbf{k}})\right]\hat{b}_{\alpha,\mathbf{k}}^\dagger\sum_m\delta\hat{c}_m^\dagger(\mathbf{p})\,\delta\hat{c}_m(\mathbf{k}+\mathbf{p})\right\} \\
&\quad + \mathrm{h.c.}\,,
\end{aligned}
\tag{B.41}
$$

where the spectral weight

$$D_{\alpha,\mathbf{k}} \equiv \sum_n n^2 \left[\left(c_n^0 \right)^* u_{\alpha,\mathbf{k},n} + c_n^0 \, v_{\alpha,\mathbf{k},n} \right]$$

(B.42)

weighs linear-order quantum fluctuations in the double-density channel in the same way as $N_{\alpha,\mathbf{k}}$ does in the density channel, see Eq. (1.45). Let us then focus on those terms of $\hat{H}_{QGA}^{(3)}$ that are responsible for the decay processes involving the collective modes of the quadratic QGA theory. In particular, the related vertices are given by combinations of two creation operators $\hat{b}_{\alpha,\mathbf{k}}^\dagger$ and one annihilation operator $\hat{b}_{\beta,\mathbf{p}}$. Therefore, isolating all the relevant contributions to Eq. (B.41) and performing the appropriate algebra, we obtain the decay interaction Hamiltonian

$$
\begin{aligned}
\hat{H}_{\mathrm{QGA}}^{(3)} &= \frac{1}{2\sqrt{V}} \sum_{\alpha,\beta,\gamma} \sum_{\mathbf{k},\mathbf{p}} \left\{ \left[\psi_0 \left(z\,J - 2\,\varepsilon_{\mathbf{k}} \right) \left(U_{\alpha,\mathbf{k}} + V_{\alpha,\mathbf{k}} \right) + \frac{U}{2} \left(N_{\alpha,\mathbf{k}} - D_{\alpha,\mathbf{k}} \right) \right] E_{\mathbf{p},\mathbf{k}-\mathbf{p}}^{\beta,\gamma} \right. \\
&\quad + \left[\psi_0 \left(z\,J - 2\,\varepsilon_{\mathbf{k}-\mathbf{p}} \right) \left(U_{\alpha,\mathbf{k}-\mathbf{p}} + V_{\alpha,\mathbf{k}-\mathbf{p}} \right) + \frac{U}{2} \left(N_{\alpha,\mathbf{k}-\mathbf{p}} - D_{\alpha,\mathbf{k}-\mathbf{p}} \right) \right] F_{\mathbf{p},\mathbf{k}}^{\beta,\alpha} \\
&\quad + \left[\psi_0 \left(z\,J - 2\,\varepsilon_{\mathbf{p}} \right) \left(U_{\alpha,\mathbf{p}} + V_{\alpha,\mathbf{p}} \right) + \frac{U}{2} \left(N_{\alpha,\mathbf{p}} - D_{\alpha,\mathbf{p}} \right) \right] G_{\mathbf{k},\mathbf{k}-\mathbf{p}}^{\alpha,\gamma} \\
&\quad + 2 \left[\varepsilon_{\mathbf{k}} \, U_{\alpha,\mathbf{k}} \, \underline{E}_{\mathbf{p},\mathbf{k}-\mathbf{p}}^{\beta,\gamma} + \varepsilon_{\mathbf{k}-\mathbf{p}} \, U_{\gamma,\mathbf{k}-\mathbf{p}} \, \overline{F}_{\mathbf{p},\mathbf{k}}^{\beta,\alpha} + \varepsilon_{\mathbf{p}} \, U_{\beta,\mathbf{p}} \, \overline{G}_{\mathbf{k},\mathbf{k}-\mathbf{p}}^{\alpha,\gamma} \right. \\
&\quad \left. \left. + \varepsilon_{\mathbf{k}} \, V_{\alpha,\mathbf{k}} \, \overline{E}_{\mathbf{p},\mathbf{k}-\mathbf{p}}^{\beta,\gamma} + \varepsilon_{\mathbf{k}-\mathbf{p}} \, V_{\gamma,\mathbf{k}-\mathbf{p}} \left(\overline{F}_{\mathbf{k},\mathbf{p}}^{\alpha,\beta} \right)^* + \varepsilon_{\mathbf{p}} \, V_{\beta,\mathbf{p}} \left(\overline{G}_{\mathbf{k}-\mathbf{p},\mathbf{k}}^{\gamma,\alpha} \right)^* \right] \right\} \hat{b}_{\beta,\mathbf{p}}^\dagger \, \hat{b}_{\gamma,\mathbf{k}-\mathbf{p}}^\dagger \, \hat{b}_{\alpha,\mathbf{k}} \\
&\equiv \frac{1}{2\sqrt{V}} \sum_{\alpha,\beta,\gamma} \sum_{\mathbf{k},\mathbf{p}} H_{\alpha,\beta,\gamma}(\mathbf{k},\mathbf{p}) \, \hat{b}_{\beta,\mathbf{p}}^\dagger \, \hat{b}_{\gamma,\mathbf{k}-\mathbf{p}}^\dagger \, \hat{b}_{\alpha,\mathbf{k}} \,,
\end{aligned}
$$

(B.43)

yielding the desired Hamiltonian operator of Eq. (1.46). For the sake of conciseness, in the previous expression we have defined the following two-mode structure factors,

$$E_{\mathbf{k},\mathbf{p}}^{\alpha,\beta} \equiv \sum_n u_{\alpha,\mathbf{k},n}^* \, v_{\beta,\mathbf{p},n}^* \,,$$

(B.44a)

$$F_{\mathbf{k},\mathbf{p}}^{\alpha,\beta} \equiv \sum_n u_{\alpha,\mathbf{k},n}^* \, u_{\beta,\mathbf{p},n} \,,$$

(B.44b)

$$G_{\mathbf{k},\mathbf{p}}^{\alpha,\beta} \equiv \sum_n v_{\alpha,\mathbf{k},n} \, v_{\beta,\mathbf{p},n}^* \,,$$

(B.44c)

$$\underline{E}_{\mathbf{k},\mathbf{p}}^{\alpha,\beta} \equiv \sum_n \sqrt{n} \, u_{\alpha,\mathbf{k},n}^* \, v_{\beta,\mathbf{p},n-1}^* \,,$$

(B.44d)

$$\overline{E}_{\mathbf{k},\mathbf{p}}^{\alpha,\beta} \equiv \sum_n \sqrt{n} \, u_{\alpha,\mathbf{k},n-1}^* \, v_{\beta,\mathbf{p},n}^* \,,$$

(B.44e)

$$\overline{F}_{\mathbf{k},\mathbf{p}}^{\alpha,\beta} \equiv \sum_n \sqrt{n} \, u_{\alpha,\mathbf{k},n-1}^* \, u_{\beta,\mathbf{p},n} \,,$$

(B.44f)

$$\overline{G}_{\mathbf{k},\mathbf{p}}^{\alpha,\beta} \equiv \sum_n \sqrt{n} \, v_{\alpha,\mathbf{k},n-1} \, v_{\beta,\mathbf{p},n}^* \,.$$

(B.44g)

C

Local quantum corrections and other specifics of the QGA

C.1 Assessing the method through sum rules and commutations

In studying how one-body correlations are captured by the QGA in the comprehensive case of the two-component BH model, we have pointed out that the structure of the particle (hole) amplitudes $U_{i,\alpha,\mathbf{k}}$ $(V_{i,\alpha,\mathbf{k}})$ is strictly related to the bosonic statistics of the collective excitations, since

$$\left[\delta_1\hat{\psi}_i(\mathbf{r}), \delta_1\hat{\psi}_i^\dagger(\mathbf{s})\right] = \frac{1}{V}\sum_{\mathbf{k}} e^{i\,\mathbf{k}\cdot(\mathbf{r}-\mathbf{s})}\sum_\alpha \left(\left|U_{i,\alpha,\mathbf{k}}\right|^2 - \left|V_{i,\alpha,\mathbf{k}}\right|^2\right) = \delta_{\mathbf{r},\mathbf{s}}\,, \tag{C.1}$$

where we have used the Bose field expansion (2.61) and the last equality is verified provided that

$$\sum_\alpha \left(\left|U_{i,\alpha,\mathbf{k}}\right|^2 - \left|V_{i,\alpha,\mathbf{k}}\right|^2\right) = 1\,. \tag{C.2}$$

In practice, we find that the previous identity is numerically satisfied if a sufficiently large number of excitation branches are included into the α-summation. In the following, we show that we can apply similar arguments to the quantised pair/antipair fields defined in Eqs. (2.5a)-(2.5b) and utilise sum rules given by commutation relations of the form (C.1) as benchmarks of the QGA description in different quantum phases.

The quantised pair and antipair fields read

$$\hat{\psi}_{\mathrm{P}}(\mathbf{r}) \equiv \sum_{n_1,n_2} \sqrt{n_1\,n_2}\,\hat{c}^\dagger_{n_1-1,n_2-1}(\mathbf{r})\,\hat{c}_{n_1,n_2}(\mathbf{r}) - \hat{\psi}_1(\mathbf{r})\,\hat{\psi}_2(\mathbf{r}) \tag{C.3}$$

and

$$\hat{\psi}_{\mathrm{C}}(\mathbf{r}) \equiv \sum_{n_1,n_2} \sqrt{n_1(n_2+1)}\,\hat{c}^\dagger_{n_1-1,n_2+1}(\mathbf{r})\,\hat{c}_{n_1,n_2}(\mathbf{r}) - \hat{\psi}_1(\mathbf{r})\,\hat{\psi}_2^\dagger(\mathbf{r}) \tag{C.4}$$

respectively. Including first-order fluctuations only, the pairing fields can be expanded as

$$\hat{\psi}_{\mathrm{P}}(\mathbf{r}) \approx \psi_{0,\mathrm{P}} + \delta_1\hat{\psi}_{\mathrm{P}}(\mathbf{r})\,, \tag{C.5a}$$

$$\hat{\psi}_{\mathrm{C}}(\mathbf{r}) \approx \psi_{0,\mathrm{C}} + \delta_1\hat{\psi}_{\mathrm{C}}(\mathbf{r}), \tag{C.5b}$$

where the mean-field quantities $\psi_{0,\mathrm{P}}$ and $\psi_{0,\mathrm{C}}$ are respectively the pair and antipair order parameters given by Eqs. (2.5), while fluctuations are encoded in the operators

$$\delta_1\hat{\psi}_{\mathrm{P}}(\mathbf{r}) \equiv \sum_{n_1,n_2} \sqrt{n_1\,n_2}\left[c^0_{n_1,n_2}\,\delta\hat{c}^\dagger_{n_1-1,n_2-1}(\mathbf{r}) + \left(c^0_{n_1-1,n_2-1}\right)^*\delta\hat{c}_{n_1,n_2}(\mathbf{r})\right]$$
$$- \psi_{0,2}\,\delta_1\hat{\psi}_1(\mathbf{r}) - \psi_{0,1}\,\delta_1\hat{\psi}_2(\mathbf{r})\,, \tag{C.6a}$$

$$\delta_1\hat{\psi}_{\mathrm{C}}(\mathbf{r}) \equiv \sum_{n_1,n_2} \sqrt{n_1(n_2+1)} \left[c^0_{n_1,n_2} \, \delta\hat{c}^\dagger_{n_1-1,n_2+1}(\mathbf{r}) + \left(c^0_{n_1-1,n_2+1} \right)^* \delta\hat{c}_{n_1,n_2}(\mathbf{r}) \right]$$
$$- \psi_{0,2}\,\delta_1\hat{\psi}_1(\mathbf{r}) - \psi_{0,1}\,\delta_1\hat{\psi}_2^\dagger(\mathbf{r}) \,. \tag{C.6b}$$

Recasting the $\delta\hat{c}$'s into the basis of collective modes, we can rewrite the first-order expansions (C.6) in the compact, suggestive form

$$\delta_1\hat{\psi}_{\mathrm{P/C}}(\mathbf{r}) = \frac{1}{\sqrt{I}} \sum_\alpha \sum_{\mathbf{k}} \left[U_{\mathrm{P/C},\alpha,\mathbf{k}} \, e^{i\,\mathbf{k}\cdot\mathbf{r}} \, \hat{b}_{\alpha,\mathbf{k}} + V^*_{\mathrm{P/C},\alpha,\mathbf{k}} \, e^{-i\,\mathbf{k}\cdot\mathbf{r}} \, \hat{b}^\dagger_{\alpha,\mathbf{k}} \right]$$
$$- \psi_{0,2}\,\delta_1\hat{\psi}_1(\mathbf{r}) - \psi_{0,1}\,\delta_1\hat{\psi}_2^\dagger(\mathbf{r}) \,, \tag{C.7}$$

where the *two-body* particle (hole) amplitudes $U_{\mathrm{P/C},\alpha,\mathbf{k}} \left(V_{\mathrm{P/C},\alpha,\mathbf{k}} \right)$ are explicitly given by

$$U_{\mathrm{P},\alpha,\mathbf{k}} \equiv \sum_{n_1,n_2} \sqrt{n_1 n_2} \left[\left(c^0_{n_1-1,n_2-1} \right)^* u_{\alpha,\mathbf{k},n_1,n_2} + c^0_{n_1,n_2}\, v_{\alpha,\mathbf{k},n_1-1,n_2-1} \right], \tag{C.8a}$$

$$U_{\mathrm{C},\alpha,\mathbf{k}} \equiv \sum_{n_1,n_2} \sqrt{n_1(n_2+1)} \left[\left(c^0_{n_1-1,n_2+1} \right)^* u_{\alpha,\mathbf{k},n_1,n_2} + c^0_{n_1,n_2}\, v_{\alpha,\mathbf{k},n_1-1,n_2+1} \right], \tag{C.8b}$$

$$V_{\mathrm{P},\alpha,\mathbf{k}} \equiv \sum_{n_1,n_2} \sqrt{n_1 n_2} \left[\left(c^0_{n_1,n_2} \right)^* u_{\alpha,\mathbf{k},n_1-1,n_2-1} + c^0_{n_1-1,n_2-2}\, v_{\alpha,\mathbf{k},n_1,n_2} \right], \tag{C.8c}$$

$$V_{\mathrm{C},\alpha,\mathbf{k}} \equiv \sum_{n_1,n_2} \sqrt{n_1(n_2+1)} \left[\left(c^0_{n_1,n_2} \right)^* u_{\alpha,\mathbf{k},n_1-1,n_2+1} + c^0_{n_1-1,n_2+2}\, v_{\alpha,\mathbf{k},n_1,n_2} \right], \tag{C.8d}$$

in analogy with Eqs. (2.17). Recalling the above discussion on the completeness relation concerning the one-body Bose fields (C.1), a natural question that arises from the decompositions in Eqs. (C.6) is whether they reproduce the two-body canonical commutators

$$\left[\hat{a}_{1,\mathbf{r}}\, \hat{a}_{2,\mathbf{r}}, \hat{a}^\dagger_{1,\mathbf{s}}\, \hat{a}^\dagger_{2,\mathbf{s}} \right] = \delta_{\mathbf{r},\mathbf{s}} \left(1 + \hat{n}_{d,\mathbf{r}} \right), \tag{C.9a}$$

$$\left[\hat{a}_{1,\mathbf{r}}\, \hat{a}^\dagger_{2,\mathbf{r}}, \hat{a}^\dagger_{1,\mathbf{s}}\, \hat{a}_{2,\mathbf{s}} \right] = -\delta_{\mathbf{r},\mathbf{s}}\, \hat{n}_{s,\mathbf{r}}, \tag{C.9b}$$

where density $\hat{n}_{d,\mathbf{r}}$ and spin $\hat{n}_{s,\mathbf{r}}$ operators were defined in Section 2.2.1 of Part I. Inserting the QGA expression of the pairing fields (C.7), the lowest-order estimation of the commutation rules (C.9) reads

$$\left[\delta_1\hat{\psi}_{\mathrm{P/C}}(\mathbf{r}), \delta_1\hat{\psi}^\dagger_{\mathrm{P/C}}(\mathbf{s}) \right] = \frac{1}{V} \sum_{\mathbf{k}} e^{i\,\mathbf{k}\cdot(\mathbf{r}-\mathbf{s})} \sum_\alpha \left(\left| U_{\alpha,\mathrm{P/C},\mathbf{k}} \right|^2 - \left| V_{\alpha,\mathrm{P/C},\mathbf{k}} \right|^2 \right). \tag{C.10}$$

Notably, we discover numerically that, due to the only approximate description of the excitation spectrum of the CFSF and PSF phases, with particular reference to the flat bands describing antipairing and pairing excitations in Figure 2.3 and Figure 2.6 respectively, the above canonical relations are not satisfied on average in the strongly-interacting regime, namely

$$\left[\delta_1\hat{\psi}_{\mathrm{P}}(\mathbf{r}), \delta_1\hat{\psi}^\dagger_{\mathrm{P}}(\mathbf{s}) \right] \neq \delta_{\mathbf{r},\mathbf{s}} \left(1 + \langle \hat{n}_{d,\mathbf{r}} \rangle \right), \tag{C.11}$$

and likewise for the antipair Bose field, while a perfect match is found towards the deep SF regime. We speculate that the violation of the sum rules (C.9) is therefore due to the missing spectral contribution of those low-energy modes which are not grasped by our basic QGA theory.
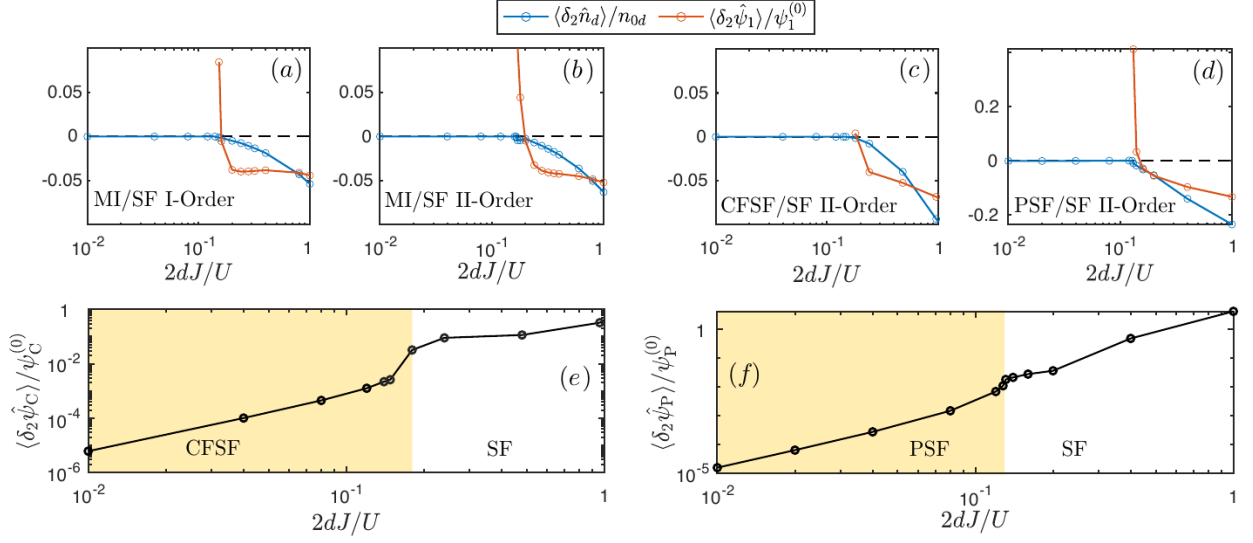
Figure C.1: (a)-(d) Quantum corrections to the total density and the one-body order parameter of the binary BH model across its quantum phase transitions. (a) First-order MI-to-SF transition for $U_{12}/U = 0.9$ and $n_d = 2$. (b) Second-order MI-to-SF transition for $U_{12}/U = 0.5$ and $n_d = 2$. (c) CFSF-to-SF transition for $U_{12}/U = 0.9$ and $n_d = 1$. (d) PSF-to-SF transition for $U_{12}/U = -0.7$ and $n_d \approx 1.47$. (e) Quantum correction to the CFSF order parameter for fixed total density $n_d = 1$ at $U_{12}/U = 0.9$ and along the $\mu/U = 0.5$ line within the CFSF phase. (f) Quantum correction to the PSF order parameter for fixed total density $n_d \approx 1.47$ at $U_{12}/U = -0.7$ and along the $(\mu/U)_c^{\text{PSF}} = -0.35$ critical line within the PSF phase.

C.2 Quantum corrections to local observables

Although in the main body of the Thesis we devote most of our attention to the study of non-local quantum correlations in different forms, the QGA allows also for a simple estimation of quantum corrections to local observables, which have been extensively explored in Sections 1.3.3, 2.3.4 and Subsections 5.4.2, 5.5.2 of Part I in the case of charge and/or spin correlations within the BH and FH models, respectively. In this Appendix Section, we give a more detailed account of quantum corrections to the local density and the order parameters of the BH models addressed in the present Thesis, with particular emphasis on the critical regimes. A similar formal discussion applies to the case of the FH model, for which we always find small quantum corrections to the lattice filling, and therefore we do not explicitly discuss here.

Let us consider again the case of the two-component BH model as an illustrative example. By expanding the local Gutzwiller operators up to second order in the fluctuations, we find that their average can be always written as the sum of two terms as

$$\left\langle \hat{\mathcal{N}}_i(\mathbf{r}) \right\rangle = n_{0,i} + \left\langle \delta_2 \hat{\mathcal{N}}_i(\mathbf{r}) \right\rangle , \tag{C.12a}$$

$$\left\langle \hat{\mathcal{D}}_i(\mathbf{r}) \right\rangle = D_{0,i} + \left\langle \delta_2 \hat{\mathcal{D}}_i(\mathbf{r}) \right\rangle , \tag{C.12b}$$

$$\left\langle \hat{\psi}_i(\mathbf{r}) \right\rangle = \psi_{0,i} + \left\langle \delta_2 \hat{\psi}_i(\mathbf{r}) \right\rangle , \tag{C.12c}$$

$$\left\langle \hat{\psi}_{\text{P}}(\mathbf{r}) \right\rangle = \psi_{0,\text{P}} + \left\langle \delta_2 \hat{\psi}_{\text{P}}(\mathbf{r}) \right\rangle , \tag{C.12d}$$

$$\left\langle \hat{\psi}_{\text{C}}(\mathbf{r}) \right\rangle = \psi_{0,\text{C}} + \left\langle \delta_2 \hat{\psi}_{\text{C}}(\mathbf{r}) \right\rangle . \tag{C.12e}$$

The second-order corrections appearing on the right-hand side of Eqs. (C.12) are given by

$$\left\langle \delta_2 \hat{\mathcal{N}}_i(\mathbf{r}) \right\rangle = -F\, n_{0,i} + \sum_{n_1,n_2} (n_1\, \delta_{i,1} + n_2\, \delta_{i,2}) \left\langle \delta \hat{c}^\dagger_{n_1,n_2}(\mathbf{r})\, \delta \hat{c}_{n_1,n_2}(\mathbf{r}) \right\rangle, \tag{C.13a}$$

$$\left\langle \delta_2 \hat{\mathcal{D}}_i(\mathbf{r}) \right\rangle = -F\, d_{0,i} + \sum_{n_1,n_2} \left(n_1^2\, \delta_{i,1} + n_2^2\, \delta_{i,2}\right) \left\langle \delta \hat{c}^\dagger_{n_1,n_2}(\mathbf{r})\, \delta \hat{c}_{n_1,n_2}(\mathbf{r}) \right\rangle, \tag{C.13b}$$

$$\left\langle \delta_2 \hat{\psi}_1(\mathbf{r}) \right\rangle = -F\, \psi_{0,1} + \sum_{n_1,n_2} \sqrt{n_1}\, \langle \delta \hat{c}^\dagger_{n_1-1,n_2}(\mathbf{r})\, \delta \hat{c}_{n_1,n_2}(\mathbf{r}) \rangle, \tag{C.13c}$$

$$\left\langle \delta_2 \hat{\psi}_2(\mathbf{r}) \right\rangle = -F\, \psi_{0,2} + \sum_{n_1,n_2} \sqrt{n_2}\, \langle \delta \hat{c}^\dagger_{n_1,n_2-1}(\mathbf{r})\, \delta \hat{c}_{n_1,n_2}(\mathbf{r}) \rangle, \tag{C.13d}$$

$$\left\langle \delta_2 \hat{\psi}_\mathrm{P}(\mathbf{r}) \right\rangle_c = -F\, \psi_{0,\mathrm{P}} + \sum_{n_1,n_2} \sqrt{n_1\, n_2}\, \langle \delta \hat{c}^\dagger_{n_1-1,n_2-1}(\mathbf{r})\, \delta \hat{c}_{n_1,n_2}(\mathbf{r}) \rangle$$
$$- \left[\psi_{0,2}\, \langle \delta_2 \hat{\psi}_1(\mathbf{r}) \rangle + \psi_{0,1}\, \langle \delta_2 \hat{\psi}_2(\mathbf{r}) \rangle \right], \tag{C.13e}$$

$$\left\langle \delta_2 \hat{\psi}_\mathrm{C}(\mathbf{r}) \right\rangle_c = -F\, \psi_{0,\mathrm{C}} + \sum_{n_1,n_2} \sqrt{n_1(n_2+1)}\, \langle \delta \hat{c}^\dagger_{n_1-1,n_2+1}(\mathbf{r})\, \delta \hat{c}_{n_1,n_2}(\mathbf{r}) \rangle$$
$$- \left[\psi_{0,2}^*\, \langle \delta_2 \hat{\psi}_1(\mathbf{r}) \rangle + \psi_{0,1}\, \langle \delta_2 \hat{\psi}_2^\dagger(\mathbf{r}) \rangle \right], \tag{C.13f}$$

where F is the control parameter of the QGA theory (see Subsection 1.2.3 of Part I) and the symbol $\langle \cdot \rangle_c$ on the left hand-side of Eqs. (C.13e)-(C.13f) emphasises that one-body correlations are subtracted on the right-hand side so that only genuine pairing/antipairing quantum fluctuations are retained, in accordance with Eqs. (2.5). At zero temperature, the expectation values of Eqs. (C.13) can be evaluated straightforwardly by a generalisation of the following two examples,

$$\left\langle \delta_2 \hat{\mathcal{N}}_i(\mathbf{r}) \right\rangle = -F\, n_{0,i} + \frac{1}{V} \sum_\alpha \sum_\mathbf{k} \sum_{n_1,n_2} (n_1\, \delta_{i,1} + n_2\, \delta_{i,2}) \left| v_{\alpha,\mathbf{k},n_1,n_2} \right|^2, \tag{C.14}$$

$$\left\langle \delta_2 \hat{\psi}_i(\mathbf{r}) \right\rangle = -F\, \psi_{0,i} + \frac{1}{V} \sum_\alpha \sum_\mathbf{k} \sum_{n_1,n_2} \left(\delta_{i,1} \sqrt{n_1}\, v_{\alpha,\mathbf{k},n_1-1,n_2} + \delta_{i,2} \sqrt{n_2}\, v_{\alpha,\mathbf{k},n_1,n_2-1} \right) v_{\alpha,\mathbf{k},n_1,n_2}. \tag{C.15}$$

from which we obtain self-contained expressions for the one-species filling and the one-body order parameter corrected by quantum fluctuations,

$$\left\langle \hat{\mathcal{N}}_i(\mathbf{r}) \right\rangle = (1-F)\, n_{0,i} + \frac{1}{V} \sum_\alpha \sum_\mathbf{k} \sum_{n_1,n_2} (n_1\, \delta_{i,1} + n_2\, \delta_{i,2}) \left| v_{\alpha,\mathbf{k},n_1,n_2} \right|^2, \tag{C.16}$$

$$\left\langle \hat{\psi}_1(\mathbf{r}) \right\rangle = (1-F)\, \psi_{0,1} + \frac{1}{V} \sum_\alpha \sum_\mathbf{k} \sum_{n_1,n_2} \sqrt{n_1}\, v_{\alpha,\mathbf{k},n_1-1,n_2}\, v_{\alpha,\mathbf{k},n_1,n_2}. \tag{C.17}$$

It is interesting to observe that, within the QGA formalism, quantum-corrected local observables are always given by the sum of two distinct terms, one given by quantum fluctuations only and the other, proportional to the mean-field average, deriving exclusively from the normalisation operator via the expectation value $\left\langle \hat{A}^2(\mathbf{r}) \right\rangle$ defining the control parameter F. This result makes more explicit the physical role of $\hat{A}(\mathbf{r})$, which accounts for the feedback of quantum fluctuations onto the Gutzwiller ground state. Along these lines, we also remark that this contribution is of key importance in giving

accurate predictions for the local density and spin correlations presented in Subsection 2.3.4 of Part I.

The relative quantum corrections to the total density and the one-body order parameters for the two-component BH model are shown in Figure C.1(a)-(d) for fixed total filling n_d. In the deep CFSF, PSF and MI phases, quantum fluctuations are always small. This remains true also near the transition points, whereas the corrections grow in correspondence of the phase separation or collapse point $|U_{12}/U| \sim 1$. It is worth noticing that, in Figure C.1(a)-(d), the corrections to the one-body order parameters appear to diverge on the brink of the phase transitions. We expect that the self-consistent inclusion of these effects into the phase diagram description would shift the CFSF, PSF and MI boundaries towards larger hopping energies in agreement with the results of quantum Monte Carlo simulations [54, 131]. Additionally, the quantum corrections to the CFSF and PSF order parameters are shown in Figure C.1(e)-(f) for fixed n_d and across the respective phase transitions to the SF regime. In the deep CFSF and PSF phases, these corrections are small, which indicates that the effect of fluctuations in these phases within the QGA picture is minimal. The corrections remain of the order of $O(10^{-1})$ across the transitions and then monotonically increase in the weakly-interacting limit $J/U \gg 1$. However, we note that the amplitude of relative quantum corrections is amplified by the fact that both $\psi_{0,\mathrm{C}}$ and $\psi_{0,\mathrm{P}}$ decrease rapidly in the deep SF regime – see panels (c) of Figure 2.1 and Figure 2.4 in the main body of the Thesis as terms of comparison.

C.3 Details on the calculation of response functions

This Appendix Section is devoted to a detailed review of the linear response formalism (c.f. [70]) applied to the QGA quantum theory, with particular reference to the binary BH system and the FH model studied in Chapters 2 and 5 of Part I respectively. For this purpose, we derive the relevant expressions for the density, spin and current response functions; in particular, the latter objects are the basic quantities from which the superfluid components of the BH model are calculated in Section 2.3.2 of Part I.

C.3.1 Linear response formalism

Let us suppose that a Hermitian, time-dependent perturbation is applied to the Hamiltonian of the system at time $t = 0$,

$$\hat{H}(t) \equiv \hat{H}_0 + \theta(t)\,\hat{G}(t)\,, \tag{C.18}$$

and define $\left|\psi_n^N\right\rangle$ as the nth eigenstate of $\hat{H}_0$ with a total number of particles equal to N. For $t < 0$, the system is in the many-body ground state $\left|\psi_0^N\right\rangle$, then its time-evolved state is given by $|\psi(t)\rangle = \hat{U}(t)\left|\psi_0^N\right\rangle$, where $\hat{U}(t)$ is the evolution operator with boundary condition $\hat{U}(0) = 1$. Assuming that the energy scale of the perturbation $\hat{G}(t)$ is sufficiently small with respect to those of $\hat{H}_0$, $\hat{U}(t)$ can be approximated by the Born approximation of the solution to the equation $i\,\partial_t\hat{U}(t) = \hat{H}(t)\,\hat{U}(t)$, namely

$$\hat{U}(t) \approx e^{-i\,\hat{H}_0\,t} - i\int_0^t d\tau\, e^{-i\,\hat{H}_0(t-\tau)}\,\hat{G}(\tau)\,e^{-i\,\hat{H}_0\,\tau}\,. \tag{C.19}$$

Now, we wish to calculate the time evolution of some observable $\left\langle\hat{F}(t)\right\rangle$, which we determine within the Heisenberg picture via the relation $\hat{F}(t) = e^{i\,\hat{H}_0\,t}\,\hat{F}\,e^{-i\,\hat{H}_0\,t}$. Evaluating $\left\langle\hat{F}(t)\right\rangle$ using Eq. (C.19), we

find

$$\left\langle \hat{F}(t) \right\rangle = \left\langle \psi_0^N \left| \hat{U}^\dagger(t)\, \hat{F}\, \hat{U}(t) \right| \psi_0^N \right\rangle \approx \left\langle \hat{F} \right\rangle_{\text{eq}} - i \int_0^t d\tau \left\langle \psi_0^N \left| \left[\hat{G}(\tau), \hat{F}(t-\tau) \right] \right| \psi_0^N \right\rangle, \tag{C.20}$$

where the "eq" subscript indicates the equilibrium expectation value. The kernel of the above integral is known as the time-domain response function

$$\chi_{\hat{F},\hat{G}}(t) = -i\theta(t) \left\langle \psi_0^N \left| \left[\hat{F}(t), \hat{G}(0) \right] \right| \psi_0^N \right\rangle. \tag{C.21}$$

In frequency space, we have

$$\chi_{\hat{F},\hat{G}}(\omega) = \lim_{\varepsilon \to 0^+} \int_{-\infty}^{\infty} dt\, e^{-\eta t}\, e^{i\omega t}\, \chi_{\hat{F},\hat{G}}(t), \tag{C.22}$$

where the infinitesimal regularisation parameter $\eta \to 0^+$ ensures that at $t = -\infty$ the system is governed by the unperturbed Hamiltonian $\hat{H}_0$. Written in terms of the perturbation operator and the probed observable, we obtain the general expression

$$\chi_{\hat{F},\hat{G}}(\omega) = -i \lim_{\varepsilon \to 0^+} \int_0^{\infty} dt\, e^{-\varepsilon t}\, e^{i\omega t} \left\langle \left[\hat{F}(t), \hat{G}(0) \right] \right\rangle. \tag{C.23}$$

In the following Subsections, we proceed to specialise Eq. (C.23) to the insightful cases of the density and current response functions of the two-component BH model under the QGA quantum theory, see Subsections 2.3.1 and 2.3.2 of Part I. We additionally devote some space to sketch the derivation of the spin susceptibility of the FH model, discussed in Subsection 5.4.3 of Part I.

C.3.2 Density and spin response functions

As a standard yet relevant case of study, we are interested in the linear response of the $\mathbf{q}$-component of the density operator

$$\hat{n}_{i,\mathbf{q}} = \sum_{\mathbf{k}} \hat{a}_{i,\mathbf{k}-\mathbf{q}}^\dagger \hat{a}_{i,\mathbf{k}} \tag{C.24}$$

for the ith species under the same type of density perturbation. Therefore, we set $\hat{F} = \hat{G} = \delta\hat{n}_{i,\mathbf{q}}$ with $\delta\hat{n}_{i,\mathbf{q}} = \hat{n}_{i,\mathbf{q}} - \langle \hat{n}_{i,\mathbf{q}} \rangle_{\text{eq}}$, where the equilibrium contribution vanishes in a uniform system but at $\mathbf{q} = \mathbf{0}$. The density-density response function is given by rephrasing Eq. (C.23) into

$$\chi_{\hat{n}_i}(\mathbf{q}, \omega) = -i \lim_{\varepsilon \to 0^+} \int_0^{\infty} dt\, e^{-\varepsilon t}\, e^{i\omega t}\, \langle [\delta\hat{n}_{i,\mathbf{q}}(t), \delta\hat{n}_{i,-\mathbf{q}}(0)] \rangle. \tag{C.25}$$

In order to evaluate this object within the QGA formalism, we apply the usual quantisation procedure to the expectation value in Eq. (C.25), which is mapped into

$$\langle [\delta\hat{\rho}_{i,\mathbf{q}}(t), \delta\hat{\rho}_{i,-\mathbf{q}}(0)] \rangle \longrightarrow \sum_{\mathbf{r}} e^{-i\mathbf{q}\cdot\mathbf{r}} \left[\left\langle \left[\delta_1\hat{\mathcal{N}}_i(\mathbf{r}, t), \delta_1\hat{\mathcal{N}}_i(\mathbf{0}, 0) \right] \right\rangle + \left\langle \left[\delta_2\hat{\mathcal{N}}_i(\mathbf{r}, t), \delta_2\hat{\mathcal{N}}_i(\mathbf{0}, 0) \right] \right\rangle \right], \tag{C.26}$$

by expanding the Gutzwiller density operator $\hat{\mathcal{N}}_i(\mathbf{r}, t)$ up to second order in the fluctuations. Here, $\delta_1\hat{\mathcal{N}}_i(\mathbf{r}, t)$ and $\delta_2\hat{\mathcal{N}}_i(\mathbf{r}, t)$ are respectively the first- and second-order expansions of the QGA density operator in terms of the collective modes operators, see e.g. Eqs. (3.3)-(3.4), whose time dependence is controlled by the interaction picture of the QGA Hamiltonian. Therefore, evaluating the commutator

in Eq. (C.26), we readily obtain

$$\chi_{\hat{n}_i}(\mathbf{q},\omega) = 2\sum_{\alpha}\frac{|N_{i,\alpha,\mathbf{q}}|^2\,\omega_{\alpha,\mathbf{q}}}{(\omega + i\,0^+)^2 - \omega_{\alpha,\mathbf{q}}^2} + \frac{1}{V}\sum_{\alpha,\beta}\sum_{\mathbf{k}}\frac{\left|W_{i;\,\alpha,\mathbf{k}|\beta,\mathbf{k}+\mathbf{q}} + W_{i;\,\beta,\mathbf{k}+\mathbf{q}|\alpha,\mathbf{k}}\right|^2\left(\omega_{\alpha,\mathbf{k}} + \omega_{\beta,\mathbf{k}+\mathbf{q}}\right)}{(\omega + i\,0^+)^2 - \left(\omega_{\alpha,\mathbf{k}} + \omega_{\beta,\mathbf{k}+\mathbf{q}}\right)^2},$$

(C.27)

where the two-mode structure factors $W_{i;\,\alpha,\mathbf{k}|\beta,\mathbf{p}}$ introduced in Eq. (3.5a) have been suitably generalised to the multi-component case.

The response function for the total density can be derived by simply summing the individual spectral weight appearing in Eq. (C.27) over the bosonic/spin species, depending on the system under consideration. This leads to the results of Eqs. (2.39) and (5.81). A similar procedure applies to the calculation of the spin susceptibility, for which we now outline the main derivation steps in the case of the FH model for the sake of completeness. The QGA spin operator defined in Eq. (5.78) can be expanded up to second-order in the operators of the collective modes as

$$\hat{S}_z(\mathbf{i}) \approx s_0 + \frac{1}{\sqrt{V}}\sum_{\alpha,\mathbf{k}}S_{\alpha,\mathbf{k}}\left(\hat{b}_{\alpha,\mathbf{k}} + \hat{b}_{\alpha,\mathbf{k}}^\dagger\right)$$
$$+ \frac{1}{V}\sum_{\alpha,\beta,\mathbf{k},\mathbf{p}}\left[\overline{U}_{\alpha,\mathbf{k}|\beta,\mathbf{p}}\,e^{-i(\mathbf{k}-\mathbf{p})\cdot\mathbf{i}}\,\hat{b}_{\alpha,\mathbf{k}}^\dagger\,\hat{b}_{\beta,\mathbf{p}} + \overline{V}_{\alpha,\mathbf{k}|\beta,\mathbf{p}}\,e^{i(\mathbf{k}-\mathbf{p})\cdot\mathbf{i}}\,\hat{b}_{\alpha,\mathbf{k}}\,\hat{b}_{\beta,\mathbf{p}}^\dagger\right.$$
$$\left. + \left(\overline{W}_{\alpha,\mathbf{k}|\beta,\mathbf{p}}\,e^{-i(\mathbf{k}+\mathbf{p})\cdot\mathbf{i}}\,\hat{b}_{\alpha,\mathbf{k}}^\dagger\,\hat{b}_{\beta,\mathbf{p}}^\dagger + \text{h.c.}\right)\right],$$

(C.28)

where the mean-field magnetisation s_0 vanishes in the paramagnetic sector of the system, and we have defined the one-mode

$$S_{\alpha,\mathbf{k}} \equiv \sum_n s_c\left[\left(C_a^0\right)^* u_{\alpha,\mathbf{k},c} + C_a^0\,v_{\beta,\mathbf{p},c}\right]$$

(C.29)

and two-mode

$$\overline{W}_{\alpha,\mathbf{k}|\beta,\mathbf{p}} \equiv \sum_n (s_c - s_0)\,u_{\alpha,\mathbf{k},c}\,v_{\beta,\mathbf{p},c}\,,$$

(C.30a)

$$\overline{U}_{\alpha,\mathbf{k}|\beta,\mathbf{p}} \equiv \sum_c (s_c - s_0)\,u_{\alpha,\mathbf{k},c}^*\,u_{\beta,\mathbf{p},c}\,,$$

(C.30b)

$$\overline{V}_{\alpha,\mathbf{k}|\beta,\mathbf{p}} \equiv \sum_c (s_c - s_0)\,v_{\alpha,\mathbf{k},c}^*\,v_{\beta,\mathbf{p},c}\,,$$

(C.30c)

fluctuation amplitudes in the spin channel. Therefore, in analogy with the charge susceptibility (5.81), for the magnetic response function we readily obtain

$$\chi_s(\mathbf{q},\omega) = 2\underbrace{\sum_{\alpha}\frac{S_{\alpha,\mathbf{q}}^2\,\omega_{\alpha,\mathbf{q}}}{(\omega + i\,0^+)^2 - \omega_{\alpha,\mathbf{q}}^2}}_{\chi_s^{[1]}(\mathbf{q},\omega)} + \frac{2}{V}\underbrace{\sum_{\alpha,\beta}\sum_{\mathbf{k}}\frac{\overline{\mathcal{W}}_{\alpha,\mathbf{k}|\beta,\mathbf{k}+\mathbf{q}}\left(\omega_{\alpha,\mathbf{k}} + \omega_{\beta,\mathbf{k}+\mathbf{q}}\right)}{(\omega + i\,0^+)^2 - \left(\omega_{\alpha,\mathbf{k}} + \omega_{\beta,\mathbf{k}+\mathbf{q}}\right)^2}}_{\chi_s^{[2]}(\mathbf{q},\omega)},$$

(C.31)

where

$$\overline{\mathcal{W}}_{\alpha,\mathbf{k}|\beta,\mathbf{p}} \equiv \overline{W}_{\alpha,\mathbf{k}|\beta,\mathbf{p}}^2 + \overline{W}_{\alpha,\mathbf{k}|\beta,\mathbf{p}}\,\overline{W}_{\beta,\mathbf{p}|\alpha,\mathbf{k}}^*\,.$$

(C.32)

C.3.3 Current response functions

Current operator As a starting ground, we determine the species-resolved local current operators by resorting to the continuity equation, which is given by

$$\nabla_{\mathbf{r}} \hat{j}_{i,\mathbf{r}} = -\frac{\partial \hat{n}_{i,\mathbf{r}}}{\partial t} = i \left[\hat{n}_{i,\mathbf{r}}, \hat{H}_{2\mathrm{BH}} \right] . \tag{C.33}$$

where the operator $\nabla_{\mathbf{r}}$ has to be regarded in its lattice definition. Inserting the BH Hamiltonian (2.1) on the right-hand side of Eq. (C.33), one finds

$$\hat{j}_{i,\mathbf{r}} = i J \sum_{j=1}^{d} \left(\hat{a}_{i,\mathbf{r}+\mathbf{e}_j}^{\dagger} \hat{a}_{i,\mathbf{r}} - \mathrm{h.c.} \right) \mathbf{e}_j . \tag{C.34}$$

For later convenience, we introduce the current operator acting along a specific direction of the square lattice, for instance the x-directed links, for which we have

$$\hat{j}_{i,\mathbf{r}}|_x = i J \left(\hat{a}_{i,\mathbf{r}+\mathbf{e}_x}^{\dagger} \hat{a}_{i,\mathbf{r}} - \mathrm{h.c.} \right) . \tag{C.35}$$

In momentum space, the unidirectional current operator Eq. (C.35) transforms into

$$\hat{j}_{i,\mathbf{q}}|_x = i J \sum_{\mathbf{k}} \left[e^{-i k_x a} - e^{i(k_x + q_x)} \right] \hat{a}_{i,\mathbf{k}}^{\dagger} \hat{a}_{i,\mathbf{k}+\mathbf{q}} , \tag{C.36}$$

which in the uniform limit $\mathbf{q} \to \mathbf{0}$ becomes

$$\hat{j}_{i,\mathbf{q}\to\mathbf{0}}|_x = 2 J \sum_{\mathbf{k}} \sin(k_x) \hat{a}_{i,\mathbf{k}}^{\dagger} \hat{a}_{i,\mathbf{k}} . \tag{C.37}$$

The uniform current operator derived above is the fundamental object by which we estimate the relevant current response functions in the following.

Intraspecies response First, we consider the case where both the probe and the response operators correspond to the same current species $\hat{j}_{i,\mathbf{q}}$. Let us take the momentum vector $\mathbf{q}$ to lie on the y-directed axis, then the longitudinal and transverse components of the current operator are given by $\hat{j}_{i,\mathbf{q}}|_y$ and $\hat{j}_{i,\mathbf{q}}|_x$, respectively. Here, we consider only the $\mathbf{q}$-limit ($\omega = 0$ followed by $\mathbf{q} \to \mathbf{0}$) of the transverse response function [79, 80], which represents the paramagnetic contribution to the individual superfluid components discussed in Subsection 2.3.2 of Part I. More explicitly, we have

$$\chi_{\hat{j}_i,\hat{j}_i}^{T}(q_x = 0, q_y \to 0, \omega = 0) = -i \lim_{\varepsilon \to 0^+} \int_0^\infty dt \, e^{-\varepsilon t} \left\langle \left[\hat{j}_{i,\mathbf{q}\to\mathbf{0}}|_x(t), \hat{j}_{i,\mathbf{q}\to\mathbf{0}}|_x(0) \right] \right\rangle . \tag{C.38}$$

The QGA quantisation of the uniform current operator $\hat{j}_{i,\mathbf{q}\to\mathbf{0}}(t)|_x$ is found to be

$$\hat{j}_{i,\mathbf{q}\to\mathbf{0}}|_x = 2 J \sum_{\alpha,\beta} \sum_{\mathbf{k}} \left[U_{i,\alpha,\mathbf{k}}^* \hat{b}_{\alpha,\mathbf{k}}^{\dagger} + V_{i,\alpha,\mathbf{k}} \hat{b}_{\alpha,-\mathbf{k}} \right] \left[U_{i,\beta,\mathbf{k}} \hat{b}_{\beta,\mathbf{k}} + V_{i,\beta,\mathbf{k}}^* \hat{b}_{\beta,-\mathbf{k}}^{\dagger} \right] \sin(k_x a) , \tag{C.39}$$

in which remarkably the presence of the condensate plays no role as the bare current vertex $\sin(k_x a)$ vanishes at $\mathbf{k} = \mathbf{0}$. Next, on the right-hand side of Eq. (C.38) we insert a resolution of the identity

operator in terms of the complete basis of the excited states of the system in order to obtain

$$\chi^T_{\hat{j}_i,\hat{j}_i}(q_x = 0, q_y \to 0, \omega = 0) = -i \lim_{\varepsilon \to 0^+} \int_0^\infty dt \, e^{-\varepsilon t} \sum_{N,n>0} \left[\left\langle \psi_0^N \left| \hat{\jmath}_i |_x(t) \right| \psi_n^N \right\rangle \left\langle \psi_n^N \left| \hat{\jmath}_i |_x(0) \right| \psi_0^N \right\rangle - \text{c.c.} \right].$$
(C.40)

Therefore, we immediately recognise that only expectation values of the kind $\left\langle \psi_0^N \left| \hat{b}_{\alpha,\mathbf{k}} \, \hat{b}_{\beta,\mathbf{p}} \right| \psi_n^{N+2} \right\rangle$ and $\left\langle \psi_0^N \left| \hat{b}_{\alpha,\mathbf{k}} \, \hat{b}_{\beta,\mathbf{p}} \right| \psi_n^{N+2} \right\rangle$ provide a finite result. More precisely, the second-order expansion of $\hat{\jmath}_{i,\mathbf{q} \to \mathbf{0}}(t)|_x$ generating such contributions can be written in the symmetric form

$$\sum_{\alpha,\beta} \sum_{\mathbf{k}} U_{i,\alpha,\mathbf{k}} \, V_{i,\beta,\mathbf{k}} \, \sin(k_x a) \, \hat{b}_{\alpha,\mathbf{k}} \, \hat{b}_{\beta,\mathbf{k}} = \frac{1}{2} \sum_{\alpha,\beta} \sum_{\mathbf{k}} \left[U_{i,\alpha,\mathbf{k}} \, V_{i,\alpha,\mathbf{k}} - U_{i,\beta,\mathbf{k}} \, V_{i,\alpha,\mathbf{k}} \right] \sin(k_x a) \, \hat{b}_{\alpha,\mathbf{k}} \, \hat{b}_{\beta,\mathbf{k}},$$
(C.41)

where we have used the fact that the particle (hole) amplitudes $U_{i,\alpha,\mathbf{k}}$ ($V_{i,\alpha,\mathbf{k}}$) are even functions of momentum in our system. Plugging the right-hand side of Eq. (C.41) back into the linear response function (C.40) and computing the time integral, we find

$$\chi^T_{\hat{j}_i,\hat{j}_i}(q_x = 0, q_y \to 0, \omega = 0) = -4 \, J^2 \frac{2^2}{4} \sum_{\alpha,\beta} \sum_{\mathbf{k}} \frac{\left| U_{i,\alpha,\mathbf{k}} \, V_{i,\beta,\mathbf{k}} - U_{i,\beta,\mathbf{k}} \, V_{i,\alpha,\mathbf{k}} \right|^2}{\omega_{\alpha,\mathbf{k}} + \omega_{\beta,\mathbf{k}}} \sin^2(k_x a). \quad \text{(C.42)}$$

In the above equation, although the numerical factors cancel each other, we have chosen to write them explicitly in order to emphasise their origin. The factor of $1/4$ arises from the symmetrisation of the current operator in Eq. (C.41); one factor of 2 descends from the inner product $\left\langle \psi_0^N \left| \hat{b}_{\alpha,\mathbf{k}} \, \hat{b}_{\beta,\mathbf{p}} \right| \psi_n^{N+2} \right\rangle$ (appearing twice), while the other factor of 2 comes from the complex conjugate term in Eq. (C.40).

Interspecies response   Now, we consider the case in which the probe observable is the current of one particle species while we measure the linear response of the current of the other species, in the transverse direction and in the **q**-limit as before. This corresponds to the off-diagonal response function

(C.43)

The calculation of $\chi^T_{\hat{j}_1,\hat{j}_2}(q_x = 0, q_y \to 0, \omega = 0)$ can be performed analogously to the intraspecies case by considering the current operator (C.39) for both the particle flavours. The final result is

$$\chi^T_{\hat{j}_1,\hat{j}_2}(q_x = 0, q_y \to 0, \omega = 0) = -4 \, J^2 \sum_{\alpha,\beta} \sum_{\mathbf{k}} \frac{\prod_{i=1}^2 \left(U_{i,\alpha,\mathbf{k}} \, V_{i,\beta,\mathbf{k}} - U_{i,\beta,\mathbf{k}} \, V_{i,\alpha,\mathbf{k}} \right)}{\omega_{\alpha,\mathbf{k}} + \omega_{\beta,\mathbf{k}}} \sin^2(k_x a),$$
(C.44)

where we have neglected the conjugation of the particle (hole) amplitudes $U_{i,\alpha,\mathbf{k}}$ ($V_{i,\alpha,\mathbf{k}}$) for simplicity, as they turn out to be always real in the present case.

It is instructive to briefly comment on how Eq. (C.44) fundamentally differs from the equivalent result of [82] within the Bogoliubov approximation. In the first place, the expression of $\chi^T_{\hat{j}_1,\hat{j}_2}(q_x = 0, q_y \to 0, \omega = 0)$ in that work contains an additional factor of $1/2$. This is due to the fact that the particle (hole) amplitudes $U_{i,\alpha,\mathbf{k}}$ ($V_{i,\alpha,\mathbf{k}}$) for the spin and density Goldstone modes are each normalised to one in [82], whereas in the present case the normalisation of quantum fluctuations is given by the sum over all the excitation branches of the spectrum (see the relative discussion in the Appendix Section C.1), which typically takes more than two branches to saturate numerically. Furthermore, the two results differ by a minus sign. When only the Goldstone branches are considered in the QGA, one finds that the U's and V's for the density Goldstone mode differ by a minus sign between the two species, whereas they are identical for the spin mode. This leads to an overall

minus sign when only these two branches are considered in Eq. (C.44). However, we notice that the normalisation condition is far from being saturated if limited to the Goldstone modes, so a good agreement with the Bogoliubov result is expected only in the weakly-interacting regime of the model. These remarks resolve the apparent discrepancies between the Bogoliubov and QGA predictions.

A diagrammatic route to the Andreev-Bashkin effect

D.1 Ward identities in absence of anomalous correlations

Our starting point is the most generic diagrammatic formulation of Ward identities [18, 461], which basically link one-body correlations with the two-body channel by means of conservation rules. The Ward relations can be written in three different forms, depending on whether two-particle correlations are expressed in terms of either (1) the two-leg vertex functions or (2) the four-leg (ir)reducible vertices. The latter form is the one which we will focus on, as it establishes a more intuitive connection between response functions and the one-body self-energy.

In the present Appendix, we choose for simplicity to restrict ourselves to the case of a multi-component system in absence of anomalous correlations. This assumption excludes automatically those superfluid/superconducting states that exhibit anomalous pairing correlations, such as the SF and PSF phases explored in Chapters 1 and 2 of Part I, whereas off-diagonal normal correlations are fully encompassed by the description. An extension of the theory comprising the contribution of anomalous correlations (modifying the zoo of vertex functions) has been initiated in several past works (see e.g. [462–464] as representatives), which however never gave a global answer to the problem of characterising quantum correlations contributing to the superfluid components of a strongly-correlated system. Nevertheless, our calculations limited to normal phases will show that questioning the relevance of anomalous correlations in interacting quantum fluids unveils their close relationship with the phenomenon of superfluidity, hinting that the latter does not necessarily depend on the existence of condensation in the system.

Let us consider a multi-component system on a lattice and a scalar observable with momentum-space operator

$$\hat{\rho}(\mathbf{q}) \equiv \sum_{a,b} \sum_{\mathbf{k}} \lambda^0_{\mathbf{k},\mathbf{k}+\mathbf{q},a,b} \, \hat{a}^\dagger_{\mathbf{k},a} \, \hat{a}_{\mathbf{k}+\mathbf{q},b} \tag{D.1}$$

associated with the generalised current operator

$$\hat{\boldsymbol{J}}(\mathbf{q}) \equiv \sum_{a,b} \sum_{\mathbf{k}} \boldsymbol{\lambda}_{\mathbf{k},\mathbf{k}+\mathbf{q},a,b} \, \hat{a}^\dagger_{\mathbf{k},a} \, \hat{a}_{\mathbf{k}+\mathbf{q},b} \,. \tag{D.2}$$

Introducing the two-leg vertex functions [18], the Ward identities read

$$
\begin{aligned}
& -\omega \, \Lambda^0_{ab}(\mathbf{k}, \varepsilon; \mathbf{k}+\mathbf{q}, \varepsilon+\omega; \mathbf{q}, \omega) + \mathbf{q} \cdot \boldsymbol{\Lambda}_{ab}(\mathbf{k}, \varepsilon; \mathbf{k}+\mathbf{q}, \varepsilon+\omega; \mathbf{q}, \omega) \\
& = \sum_c \left[\lambda^0_{\mathbf{k},\mathbf{k}+\mathbf{q},c,b} \, G^{-1}_{ac}(\mathbf{k}, \varepsilon) - \lambda^0_{\mathbf{k},\mathbf{k}+\mathbf{q},a,c} \, G^{-1}_{cb}(\mathbf{k}+\mathbf{q}, \varepsilon+\omega) \right] \,.
\end{aligned}
\tag{D.3}
$$

where $\Lambda^0_{ab}(\mathbf{k}, \varepsilon; \mathbf{k}+\mathbf{q}, \varepsilon+\omega; \mathbf{q}, \omega)$ and $\boldsymbol{\Lambda}_{ab}(\mathbf{k}, \varepsilon; \mathbf{k}+\mathbf{q}, \varepsilon+\omega; \mathbf{q}, \omega)$ are the vertex functions for the scalar and current channels respectively, while $G_{ab}(\mathbf{k}, \varepsilon)$ is the Green's function matrix. Introducing the (ir)reducible vertex functions $\Gamma_{\alpha,\beta;\gamma,\delta}(\mathbf{k}, \varepsilon; \mathbf{p}+\mathbf{q}, \nu+\omega; \mathbf{p}, \nu; \mathbf{k}+\mathbf{q}, \varepsilon+\omega)$ (Γ^0), Eq. (D.3) translates
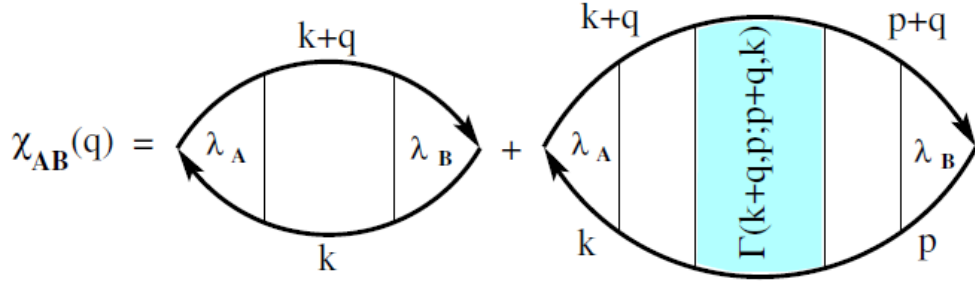
Figure D.1: Compact diagrammatic representation of a generic response function in absence of anomalous correlations. The first diagram corresponds to the dressed bubble diagram $\chi^{I}_{\alpha\beta}(\mathbf{q}, \omega)$, while the second gathers two-particle correlations given by the reducible vertex Γ.

into [18]

$$
\pm \frac{i}{V} \sum_{\mathbf{p}} \sum_{\gamma,\delta} \int \frac{d\nu}{2\pi} \Gamma^0_{a,\gamma;\delta,b}(\mathbf{k}, \varepsilon; \mathbf{p} + \mathbf{q}, \nu + \omega; \mathbf{p}, \nu; \mathbf{k} + \mathbf{q}, \varepsilon + \omega)
$$

$$
\times \sum_{c} \left[\lambda^0_{\mathbf{p},\mathbf{p}+\mathbf{q},\delta,c} G_{c\gamma}(\mathbf{p} + \mathbf{q}, \nu + \omega) - \lambda^0_{\mathbf{p},\mathbf{p}+\mathbf{q},c,\gamma} G_{\delta c}(\mathbf{p}, \nu) \right] \tag{D.4}
$$

$$
= \sum_{c} \left[\lambda^0_{\mathbf{k},\mathbf{k}+\mathbf{q},a,c} \Sigma_{cb}(\mathbf{k} + \mathbf{q}, \varepsilon + \omega) - \lambda^0_{\mathbf{k},\mathbf{k}+\mathbf{q},c,b} \Sigma_{ac}(\mathbf{k}, \varepsilon) \right],
$$

or equivalently

$$
\pm \frac{i}{V} \sum_{\mathbf{p}} \sum_{\gamma,\delta} \int \frac{d\nu}{2\pi} \Gamma_{a,\gamma;\delta,b}(\mathbf{k}, \varepsilon; \mathbf{p} + \mathbf{q}, \nu + \omega; \mathbf{p}, \nu; \mathbf{k} + \mathbf{q}, \varepsilon + \omega)
$$

$$
\times \sum_{c,d} G_{\delta c}(\mathbf{p}, \nu) G_{d\gamma}(\mathbf{p} + \mathbf{q}, \nu + \omega) \left[-\omega \lambda^0_{\mathbf{p},\mathbf{p}+\mathbf{q},c,d} + \mathbf{q} \cdot \boldsymbol{\lambda}_{\mathbf{p},\mathbf{p}+\mathbf{q},c,d} \right] \tag{D.5}
$$

$$
= \sum_{c} \left[\lambda^0_{\mathbf{k},\mathbf{k}+\mathbf{q},a,c} \Sigma_{cb}(\mathbf{k} + \mathbf{q}, \varepsilon + \omega) - \lambda^0_{\mathbf{k},\mathbf{k}+\mathbf{q},c,b} \Sigma_{ac}(\mathbf{k}, \varepsilon) \right],
$$

where $\Sigma_{ab}(\mathbf{k}, \varepsilon)$ is the self-energy matrix and the $\pm$ sign holds for bosonic (fermionic) species.

D.1.1 Application to the density-current channel

Let us now focus specifically on the density-current channel. In this case, we have

$$
\lambda^0_{\mathbf{k},\mathbf{p},a,b} = \delta_{a,b} \tag{D.6}
$$

and

$$
\lambda^x_{\mathbf{k},\mathbf{p},a,b} = i J_{ab} \left(e^{-i k_x} - e^{i p_x} \right), \tag{D.7}
$$

where J_{ab} is the hopping matrix relating different species and x stands for a generic lattice dimension. Making the hypothesis that the hopping is diagonal in the orbital subspace (namely, it does not involve

interspecies exchanges by e.g. Raman transitions), we obtain that Eq. (D.5) specialises into

$$\pm \frac{i}{V} \sum_{\mathbf{p}} \sum_{\gamma,\delta} \int \frac{d\nu}{2\pi} \Gamma_{a,\gamma;\delta,b}(\mathbf{k},\varepsilon;\mathbf{p}+\mathbf{q},\nu+\omega;\mathbf{p},\nu;\mathbf{k}+\mathbf{q},\varepsilon+\omega)$$

$$\times \sum_c G_{\delta c}(\mathbf{p},\nu) G_{c\gamma}(\mathbf{p}+\mathbf{q},\nu+\omega) \left[-\omega + \mathbf{q}\cdot\boldsymbol{\lambda}_{\mathbf{p},\mathbf{p}+\mathbf{q},c,c}\right] \tag{D.8}$$

$$= \Sigma_{ab}(\mathbf{k}+\mathbf{q},\varepsilon+\omega) - \Sigma_{ab}(\mathbf{k},\varepsilon)\,.$$

For later convenience, we also introduce the general diagrammatic expressions of the intraspecies

$$\chi_{\alpha\alpha}(\mathbf{q},\omega) = \pm \frac{i}{V} \sum_{\mathbf{k}} \int \frac{d\nu}{2\pi} \lambda_{\mathbf{k},\mathbf{k}+\mathbf{q},\alpha,\alpha}\,\lambda_{\mathbf{k}+\mathbf{q},\mathbf{k},\alpha,\alpha}\, G_{\alpha\alpha}(\mathbf{k},\nu)\, G_{\alpha\alpha}(\mathbf{k}+\mathbf{q},\nu+\omega)$$

$$- \frac{1}{V^2} \sum_{\mathbf{k},\mathbf{p}} \sum_{\beta,\gamma,\delta,\zeta} \int \frac{d\nu\,d\varepsilon}{(2\pi)^2} \lambda_{\mathbf{k},\mathbf{k}+\mathbf{q},\alpha,\alpha}\,\lambda_{\mathbf{p}+\mathbf{q},\mathbf{p},\alpha,\alpha}\, G_{\alpha\beta}(\mathbf{k}+\mathbf{q},\varepsilon+\omega)\, G_{\zeta\alpha}(\mathbf{k},\varepsilon) \tag{D.9}$$

$$\times \Gamma_{\beta,\gamma;\delta,\zeta}(\mathbf{k}+\mathbf{q},\varepsilon+\omega;\mathbf{p},\nu;\mathbf{p}+\mathbf{q},\nu+\omega;\mathbf{k},\varepsilon)\, G_{\alpha\gamma}(\mathbf{p},\nu)\, G_{\delta\alpha}(\mathbf{p}+\mathbf{q},\nu+\omega)$$

and interspecies

$$\chi_{\alpha\alpha'}(\mathbf{q},\omega) = \pm \frac{i}{V} \sum_{\mathbf{k}} \int \frac{d\nu}{2\pi} \lambda_{\mathbf{k},\mathbf{k}+\mathbf{q},\alpha,\alpha}\,\lambda_{\mathbf{k}+\mathbf{q},\mathbf{k},\alpha',\alpha'}\, G_{\alpha'\alpha}(\mathbf{k},\nu)\, G_{\alpha\alpha'}(\mathbf{k}+\mathbf{q},\nu+\omega)$$

$$- \frac{1}{V^2} \sum_{\mathbf{k},\mathbf{p}} \sum_{\beta,\gamma,\delta,\zeta} \int \frac{d\nu\,d\varepsilon}{(2\pi)^2} \lambda_{\mathbf{k},\mathbf{k}+\mathbf{q},\alpha,\alpha}\,\lambda_{\mathbf{p}+\mathbf{q},\mathbf{p},\alpha',\alpha'}\, G_{\alpha\beta}(\mathbf{k}+\mathbf{q},\varepsilon+\omega)\, G_{\zeta\alpha}(\mathbf{k},\varepsilon) \tag{D.10}$$

$$\times \Gamma_{\beta,\gamma;\delta,\zeta}(\mathbf{k}+\mathbf{q},\varepsilon+\omega;\mathbf{p},\nu;\mathbf{p}+\mathbf{q},\nu+\omega;\mathbf{k},\varepsilon)\, G_{\alpha'\gamma}(\mathbf{p},\nu)\, G_{\delta\alpha'}(\mathbf{p}+\mathbf{q},\nu+\omega)$$

response functions, where we have omitted the superscripts of the bare vertices λ for simplicity.

At this point, we split our analysis into two analytical routes, namely the ω-limit (taking $\mathbf{q}=0$) and the $\mathbf{q}$-limit (with $\omega=0$) of Eq. (D.8). The former calculation will provide us with insightful information on non-local and dynamical density correlations, while the latter limit will lead to a straightforward calculation of the superfluid density components.

D.2 ω-limit

By a suitable manipulation of Eq. (D.8) and making use of Eqs. (D.9)-(D.10), we derive the following equation for the density response functions,

$$-\omega \sum_{\beta} \left[\chi^0_{\alpha\beta}(\mathbf{q}=0,-\omega) - \chi^{\bar{V},0}_{\alpha\beta}(\mathbf{q}=0,-\omega) \right]$$

$$= \pm \frac{i}{V} \sum_{\mathbf{k}} \sum_{a,b} \int \frac{d\varepsilon}{2\pi} G_{\alpha a}(\mathbf{k},\varepsilon+\omega)\, G_{b\alpha}(\mathbf{k},\varepsilon) \left[\Sigma_{ab}(\mathbf{k},\varepsilon+\omega) - \Sigma_{ab}(\mathbf{k},\varepsilon) \right], \tag{D.11}$$

where $\chi^0_{\alpha\beta}(\mathbf{q},\omega)$ denotes the density response matrix and $\chi^{\bar{V},0}_{\alpha\beta}(\mathbf{q},\omega)$ stands for the first terms on the right-hand side of Eqs. (D.9)-(D.10), namely the dressed bubble diagram of the response functions (without vertex corrections). The right-hand side of Eq. (D.11) can be decrypted by resorting to the Dyson equation $\hat{\Sigma}(\mathbf{k},\omega) = \hat{G}_0^{-1}(\mathbf{k},\omega) - \hat{G}^{-1}(\mathbf{k},\omega)$, with $\hat{G}_0(\mathbf{k},\omega)$ being the non-interacting Green's

function matrix. It follows that

$$
- \omega \sum_{\beta} \left[\chi^0_{\alpha\beta}(\mathbf{q} = \mathbf{0}, -\omega) - \chi^{\not{V},0}_{\alpha\beta}(\mathbf{q} = \mathbf{0}, -\omega) \right]
$$
$$
= \pm \frac{i}{V} \sum_{\mathbf{k}} \sum_{c} \int \frac{d\varepsilon}{2\pi} \left[\omega \, G_{\alpha c}(\mathbf{k}, \varepsilon + \omega) \, G_{c\alpha}(\mathbf{k}, \varepsilon) + G_{\alpha\alpha}(\mathbf{k}, \varepsilon + \omega) - G_{\alpha\alpha}(\mathbf{k}, \varepsilon) \right] .
$$
(D.12)

The previous equation can be further simplified by (i) observing that the last two terms on the right-hand side cancel each other when integrated over the frequency domain, (ii) in addition to considering the following identity,

$$
\chi^{\not{V},0}_{\alpha\beta}(\mathbf{q} = \mathbf{0}, \omega) = \pm \frac{i}{V} \sum_{\mathbf{k}} \int \frac{d\varepsilon}{2\pi} G_{\alpha\beta}(\mathbf{k}, \varepsilon + \omega) \, G_{\beta\alpha}(\mathbf{k}, \varepsilon) .
$$
(D.13)

As a result, we obtain

$$
\sum_{\beta} \chi^0_{\alpha\beta}(\mathbf{q} = \mathbf{0}, \omega) = \sum_{\beta} \chi^{\not{V},0}_{\alpha\beta}(\mathbf{q} = \mathbf{0}, \omega) - \sum_{\beta} \chi^{\not{V},0}_{\alpha\beta}(\mathbf{q} = \mathbf{0}, -\omega) .
$$
(D.14)

Physically speaking, Eq. (D.14) states that the uniform limit of the overall density response of species α is an odd function of frequency and, notably, *implicitly* independent of vertex corrections and can be expressed in terms of dressed bubble diagrams only. However, we emphasise that implicit independence does not imply the absolute irrelevance of vertex correlations, as we know that the self-energy *explicitly* depends on them through the celebrated Bethe-Salpeter equations [18, 461]. We additionally notice that the static limit of Eq. (D.14) yields

$$
\sum_{\beta} \chi^0_{\alpha\beta}(\mathbf{q} = \mathbf{0}, \omega \to 0) = 0 ,
$$
(D.15)

indicating that the total contribution of diagonal and off-diagonal correlations in the density channel offset each other.

In order to have a grasp of the connection between the QGA theory of quantised fluctuations and our diagrammatic analysis of density fluctuations, let us consider the QGA prediction for the intraspecies Green's function of a bosonic system, whose non-degenerate part (excluding the contribution of a condensate) reads

$$
G_{\alpha\alpha}(\mathbf{k}, \varepsilon) = \sum_{i} \left[\frac{P_{\alpha,i,\mathbf{k}}}{\varepsilon - \omega_i(\mathbf{k})} - \frac{H_{\alpha,i,\mathbf{k}}}{\varepsilon + \omega_i(\mathbf{k})} \right] ,
$$
(D.16)

where $\omega_i(\mathbf{k})$ denotes the i-th elementary excitation of the system, with particle and hole weights given by $P_{i,\mathbf{k}} \equiv |U_{\alpha,i,\mathbf{k}}|^2$ and $H_{i,\mathbf{k}} \equiv |V_{\alpha,i,\mathbf{k}}|^2$ respectively. Supposing that the dressed bubble diagram has vanishing off-diagonal components $\chi^{\not{V},0}_{\alpha\beta}(\mathbf{q} = \mathbf{0}, \omega) = 0$ (as e.g. in the MI phase of the binary BH model), from Eq. (D.14) we readily obtain

$$
- \sum_{\beta} \left[\chi^0_{\alpha\beta}(\mathbf{q} = \mathbf{0}, -\omega) - \delta_{\alpha,\beta} \, \chi^{\not{V},0}_{\alpha\beta}(\mathbf{q} = \mathbf{0}, -\omega) \right] = \chi^{\not{V},0}_{\alpha\alpha}(\mathbf{q} = \mathbf{0}, \omega)
$$
$$
= \frac{2}{V} \sum_{\mathbf{k}} \sum_{i,j} \left(H_{\alpha,i,\mathbf{k}} H_{\alpha,j,\mathbf{k}} \frac{\omega_j(\mathbf{k}) - \omega_i(\mathbf{k})}{\omega^2 - [\omega_j(\mathbf{k}) - \omega_i(\mathbf{k})]^2} + H_{\alpha,i,\mathbf{k}} P_{\alpha,j,\mathbf{k}} \frac{\omega_j(\mathbf{k}) + \omega_i(\mathbf{k})}{\omega^2 - [\omega_j(\mathbf{k}) + \omega_i(\mathbf{k})]^2} \right) .
$$
(D.17)

at zero temperature. Therefore, we find the remarkable fact that the QGA generally involves *finite* vertex corrections to the non-local density response function. Moreover, Eq. (D.17) give a clear interpretation of vertex corrections in terms of scattering processes between multiple collective modes, in accordance with the semi-analytical intuitions discussed in the main body of the Thesis. It is worth emphasising however that this result should be handled gingerly. We know that the QGA is *not* a self-consistent theory, as it does not entail a closed-form relation between the one- and two-particle sectors of quantum correlations. For this reason, the calculation made above has to be intended as a possible way to estimate the amount of vertex corrections that the QGA is able to account for, as well as to find a qualitative relationship between response functions and one-body features.

D.3 Superfluid drag from the q-limit

Taking the **q**-limit of the Ward identities provides a relation between the static current response functions $\chi^x_{\alpha\beta}(-\mathbf{q}, \omega = 0)$ and the self-energy matrix. Analogously to the case of the ω-limit, we can rewrite such a relation as

$$
\begin{aligned}
q_x \sum_\beta & \left[\chi^x_{\alpha\beta}(-\mathbf{q}, \omega = 0) - \chi^{\Gamma,x}_{\alpha\beta}(-\mathbf{q}, \omega = 0) \right] \\
& = \pm \frac{i}{V} \sum_\mathbf{k} \sum_{c \neq \alpha} \int \frac{d\varepsilon}{2\pi} \lambda^x_{\mathbf{k+q},\mathbf{k},\alpha,\alpha} \left\{ \left[\varepsilon_{c,\mathbf{k}} - \varepsilon_{c,\mathbf{k+q}} \right] G_{\alpha c}(\mathbf{k+q}, \varepsilon) \, G_{c\alpha}(\mathbf{k}, \varepsilon) \right. \\
& \left. \qquad\qquad\qquad\qquad\qquad\qquad + G_{\alpha\alpha}(\mathbf{k+q}, \varepsilon) - G_{\alpha\alpha}(\mathbf{k}, \varepsilon) \right\},
\end{aligned}
\tag{D.18}
$$

where $\varepsilon_{\alpha,\mathbf{k}}$ is the free-particle dispersion of species α. Taking the uniform limit $\mathbf{q} \to \mathbf{0}$, we immediately realise that

$$
\begin{aligned}
& q_x \chi^{\Gamma,x}_{\alpha\beta}(\mathbf{q} \to \mathbf{0}, \omega = 0) \\
& = \mp \frac{i}{V} \lim_{\mathbf{q} \to \mathbf{0}} \sum_\mathbf{k} \sum_{c \neq \alpha} \int \frac{d\varepsilon}{2\pi} \lambda^x_{\mathbf{k+q},\mathbf{k},\alpha,\alpha} \left[\varepsilon_{c,\mathbf{k}} - \varepsilon_{c,\mathbf{k+q}} \right] G_{\alpha c}(\mathbf{k+q}, \varepsilon) \, G_{c\alpha}(\mathbf{k}, \varepsilon).
\end{aligned}
\tag{D.19}
$$

Hence, after integrating by parts the remaining terms on the right-hand side of Eq. (D.18) and observing that the kinetic energy density of species α is exactly given by

$$
K_{\alpha,x} = \mp \frac{i}{V} \sum_\mathbf{k} \int \frac{d\omega}{2\pi} \left(\nabla_\mathbf{k} \, \lambda^x_{\mathbf{k},\mathbf{k},\alpha,\alpha} \right) G_{\alpha\alpha}(\mathbf{k}, \omega),
\tag{D.20}
$$

we can easily recast Eq. (D.18) into the suggestive form

$$
\sum_\beta \chi^x_{\alpha\beta}(\mathbf{q} \to \mathbf{0}, \omega = 0) = K_{\alpha,x}.
\tag{D.21}
$$

Recalling Eq. (2.59) in the Thesis, we can formally identify the left-hand side of Eq. (D.21) with the normal component of species α, namely

$$
\rho_{n,\alpha} = -K_{\alpha,x}.
\tag{D.22}
$$

The previous relation is the main result of our derivation, as it uniquely determines the superfluid components of a generic system without anomalous correlations. In particular, recovering the definition of superfluid density $\rho_{s,\alpha}$ and indicating the total superfluid drag of species α with

$\rho_{d,\alpha} \equiv \sum_{\beta \neq \alpha} \chi_{\alpha\beta}^{x}(\mathbf{q} \to \mathbf{0}, \omega = 0)$ according to Eqs. (2.57)-(2.58) in the Thesis, we obtain

$$\rho_{d,\alpha} = K_{\alpha,x} - \chi_{\alpha\beta}^{x}(\mathbf{q} \to \mathbf{0}, \omega = 0) = -\rho_{s,\alpha} . \tag{D.23}$$

The physical meaning of this last equation is evident: in presence of any type of normal correlations only, the superfluid density of the system is 100% saturated by the superfluid drag. This highly non-trivial result perfectly describes our results for CFSF phase of the binary BH model (see the discussion of Subsection 2.3.2 of Part I) and, less importantly, the MI regime. More generally, our result shows that the superfluid flow of a given species cannot be driven by the drag only, since this can be finite only in the presence of a finite superfluid density of the same species. However, this conclusion does not exclude exotic situations in which $\rho_{d,\alpha} = 0$ but $\chi_{\alpha\beta}^{x}(\mathbf{q} \to \mathbf{0}, \omega = 0) \neq 0$ for some $\beta \neq \alpha$, a condition that has been addressed only recently and goes under the name of Borromean superfluidity [111].

Pure dephasing theory and non-Markovianity

E.1 Breuer-Laine-Piilo non-Markovianity measure

The definition of the Breuer-Laine-Piilo (BLP) measure [178] derives from considering non-Markovian those systems in which a back-flow of information from the environment to the open system occurs during the dynamics. This information recovery is formally identified by an increase in the distinguishability of pairs of evolving quantum states of the system.

In detail, a system is non-Markovian if there is a pair of system initial states $\rho_S^{(1)}(0)$ and $\rho_S^{(2)}(0)$, such that for certain times $t > 0$ their distinguishability grows, namely

$$\sigma\left[\rho_S^{(1)}(0), \rho_S^{(2)}(0); t\right] \equiv \frac{d}{dt}\mathcal{D}\left[\rho_S^{(1)}(t), \rho_S^{(2)}(t)\right] > 0\,, \tag{E.1}$$

where $\sigma\left[\rho_S^{(1)}, \rho_S^{(2)}; t\right]$ is called the *information flux* at time t and

$$\mathcal{D}\left[\rho_S^{(1)}(t), \rho_S^{(2)}(t)\right] \equiv \frac{1}{2}\left\|\rho_S^{(1)}(t) - \rho_S^{(2)}(t)\right\|_1 \equiv \frac{1}{2}\mathrm{Tr}\left\{\sqrt{\left[\rho_S^{(1)}(t) - \rho_S^{(2)}(t)\right]^\dagger \left[\rho_S^{(1)}(t) - \rho_S^{(2)}(t)\right]}\right\} \tag{E.2}$$

is defined to be the distinguishability of $\rho_S^{(1)}$ and $\rho_S^{(2)}$. Since density matrices are Hermitian, we have that

$$\mathcal{D}\left[\rho_S^{(1)}(t), \rho_S^{(2)}(t)\right] = \frac{1}{2}\mathrm{Tr}\left\{\sqrt{\left[\rho_S^{(1)}(t) - \rho_S^{(2)}(t)\right]^2}\right\} = \frac{1}{2}\sum_i |\lambda_i|\,, \tag{E.3}$$

where λ_i are the eigenvalues of the matrix $\rho_S^{(1)} - \rho_S^{(2)}$. The physical interpretation of the trace distance (E.2) is that it is related to the maximum probability of distinguishing between two quantum states. In an open quantum system, this probability in general tends to decrease in time, as the system information is lost to the environment, except when the dynamics is non-Markovian. In this case, the system regains part of the previously lost information. According to the BLP criterion, the amount of non-Markovianity of a quantum process Λ can be quantified through the measure

$$\mathcal{B}_-(\Lambda) \equiv \max_{\rho_{1,2}(0)} \int_{\sigma>0} dt\, \sigma\left[\rho_S^{(1)}(0), \rho_S^{(2)}(0); t\right]\,, \tag{E.4}$$

which reflects the maximum amount of information that can flow back to the system for a given process. As proven in [465], for all finite-dimensional quantum systems the evaluation of (E.4) can be optimised by considering initial states $\rho_S^{(1)}(0)$ and $\rho_S^{(2)}(0)$ that are orthogonal and lie on the boundary of the subset of physical states.

In the case of the two-level impurity undergoing pure dephasing studied in this paper, the open system dynamics is driven by the master equation (3.6), which allows for a simple rewriting in the vector

representation of the density matrix,

$$\frac{d}{dt}\begin{pmatrix} \rho_{11} \\ \rho_{12} \\ \rho_{21} \\ \rho_{22} \end{pmatrix} = \begin{pmatrix} 0 & 0 & 0 & 0 \\ 0 & -g^2\gamma(t) & 0 & 0 \\ 0 & 0 & -g^2\gamma(t) & 0 \\ 0 & 0 & 0 & 0 \end{pmatrix} \begin{pmatrix} \rho_{11} \\ \rho_{12} \\ \rho_{21} \\ \rho_{22} \end{pmatrix}, \tag{E.5}$$

where we have defined $\rho_{ij} = \mathrm{Tr}_S\{\rho_S(t)|i\rangle\langle j|\}$, with $|i\rangle = |1\rangle, |2\rangle$ standing for the two possible states of the impurity, and neglected the unitary evolution terms set by the renormalised transition frequency $\tilde{\omega}_0$. The analytical integration of (E.5) yields

$$\rho_S(t) = \phi_t[\rho_S(0)] = \begin{pmatrix} \rho_{11}(0) & \rho_{12}(0)\sqrt{L(t)} \\ \rho_{21}(0)\sqrt{L(t)} & \rho_{22}(0) \end{pmatrix}, \tag{E.6}$$

where ϕ_t is the dynamical map of the system density matrix associated to the pure dephasing dynamics. The function

$$L(t) = \exp\left[-2\,g^2\int_0^t d\tau\,\gamma(\tau)\right] \tag{E.7}$$

coincides with the so-called *Loschmidt echo* [180], defined as $L(t) = |\langle\psi(t)|\,\psi_0(t)\rangle|^2$, where $|\psi_0(t)\rangle$ is the bath ground state evolved according to its own Hamiltonian, while $|\psi(t)\rangle$ is the time-evolved bath state in presence of the open system. Indeed, the off-diagonal matrix elements of the system density matrix ρ_S are given by $\sqrt{L(t)}$ exactly.

Choosing two initial states that are orthogonal and lie on the Bloch sphere of the two-level system

$$\rho_S^{(1)}(0) = \frac{1}{2}\begin{pmatrix} 1 & 1 \\ 1 & 1 \end{pmatrix} \qquad \rho_S^{(2)}(0) = \frac{1}{2}\begin{pmatrix} 1 & -1 \\ -1 & 1 \end{pmatrix}, \tag{E.8}$$

we find that the trace distance (E.2) reads

$$\mathcal{D}\left[\rho_S^{(1)}, \rho_S^{(2)}\right] = \frac{1}{2}\left\|\rho_S^{(1)}(t) - \rho_S^{(2)}(t)\right\|_1 = \left\|\begin{pmatrix} 0 & \sqrt{L(t)} \\ \sqrt{L(t)} & 0 \end{pmatrix}\right\|_1 = \sqrt{L(t)}. \tag{E.9}$$

Therefore, we obtain that the distinguishability rate is given by

$$\sigma\left[\rho_S^{(1)}, \rho_S^{(2)}; t\right] = \frac{d\mathcal{D}\left[\rho_S^{(1)}, \rho_S^{(2)}\right]}{dt} = -g^2\,\gamma(t)\sqrt{L(t)} \tag{E.10}$$

and $\sigma\left[\rho_S^{(1)}, \rho_S^{(2)}; t\right] > 0$ for some t when the dephasing rate $\gamma(t)$ is negative, leading to non-Markovian dynamics. Finally, it is straightforward to deduce that the non-Markovianity measure (E.4) is provided by the values of the Loschmidt echo $L(t)$ at the boundaries of those time intervals $[t_i, t_{i+1}]$ over which $\gamma(t) < 0$, namely

$$\mathcal{B}_- = \int_{\sigma>0} dt\,\sigma\left[\rho_S^{(1)}(0), \rho_S^{(2)}(0); t\right] = -g^2\int_{\gamma<0} dt\,\gamma(t)\sqrt{L(t)} = \sum_i\left[\sqrt{L(t_{i+1})} - \sqrt{L(t_i)}\right] \tag{E.11}$$

by the definition of $L(t)$. On an equal footing, we can also quantify the amount of information that

flows from the open system to the environment by defining a Markovianity measure

$$\mathcal{B}_+ = \int_{\sigma<0} dt\, \sigma\left[\rho_S^{(1)}(0), \rho_S^{(2)}(0); t\right] = -g^2 \int_{\gamma>0} dt\, \gamma(t)\, \sqrt{L(t)}, \tag{E.12}$$

which takes into account time periods for which $\gamma(t) > 0$.

E.2 Dephasing dynamics in free and weakly-interacting bosonic baths

The free boson spectrum on the continuum is the Galilean quadratic dispersion relation

$$\varepsilon_{0,\mathbf{k}} = \frac{\mathbf{k}^2}{2\,m}, \tag{E.13}$$

so that the spectral function of density correlations scales as

$$J_0(\omega) \sim \int d^d\mathbf{k}\, \delta(\omega - \varepsilon_{0,\mathbf{k}}) \sim \omega^{(d-2)/2} \tag{E.14}$$

at small frequencies in d dimensions. It follows that the dephasing rate and decoherence function behave as

$$\gamma_0(t) = \int d\omega\, \frac{J_0(\omega)\, \sin(\omega\, t)}{\omega} \sim t^{(2-d)/2} \tag{E.15}$$

and

$$\Gamma_0(t) = \int d\omega\, \frac{J_0(\omega)\,[1 - \cos(\omega\, t)]}{\omega^2} \sim t^{(4-d)/2} \tag{E.16}$$

respectively at large times, suggesting that free bosons lead to total dephasing $\exp[-\Gamma_0(t \to \infty)] = 0$ if $d < 4$. Indeed, the asymptotic behaviour of the dephasing rate $\gamma_0(t) \sim const.$ in $d = 2$ resembles the Markovian behaviour that we observe at the edge transition described in Figure 3.2(c), where an effective free-particle description of the superfluid phase holds [63, 131]. A similar result applies to the case of lattice free bosons, for which the spatial discretisation introduces only a small, fast-oscillating modulation of $\gamma_0(t)$.

As regards the case of a weakly-interacting gas either on the continuum or on a lattice, within the Bogoliubov approximation the single-particle spectral amplitude of density fluctuations reads $N_{\mathrm{Bog},\mathbf{k}} = \sqrt{\rho_0}\,(u_{\mathbf{k}} + v_{\mathbf{k}})$, where ρ_0 is the condensate density and $u_{\mathbf{k}}$ ($v_{\mathbf{k}}$) is the particle (hole) excitation amplitude of the Goldstone mode. Since $|N_{\mathrm{Bog},\mathbf{k}}|^2 \sim |\mathbf{k}|$ at small momenta, we obtain that the low-energy behaviour of the spectral density is controlled by the spatial dimension only,

$$J_{\mathrm{Bog}}(\omega) = \int d^d\mathbf{k}\, |N_{\mathrm{Bog},\mathbf{k}}|^2\, \delta(\omega - \omega_{Bog,\mathbf{k}}) \sim \omega^d, \tag{E.17}$$

apart from subdominant corrections depending on the concavity of the Goldstone spectrum $\omega_{\mathrm{Bog},\mathbf{k}}$. Eq. (E.17) leads to

$$\gamma_{\mathrm{Bog}}(t) = \int d\omega\, \frac{J_{\mathrm{Bog}}(\omega)\, \sin(\omega\, t)}{\omega} \sim t^{-d} \tag{E.18}$$

and

$$\Gamma_{\mathrm{Bog}}(t) = \int d\omega\, \frac{J_{\mathrm{Bog}}(\omega)\,[1 - \cos(\omega\, t)]}{\omega^2} \sim t^{1-d} \tag{E.19}$$

for large times. Therefore, a weakly-interacting bath induces only a partial dephasing of the impurity
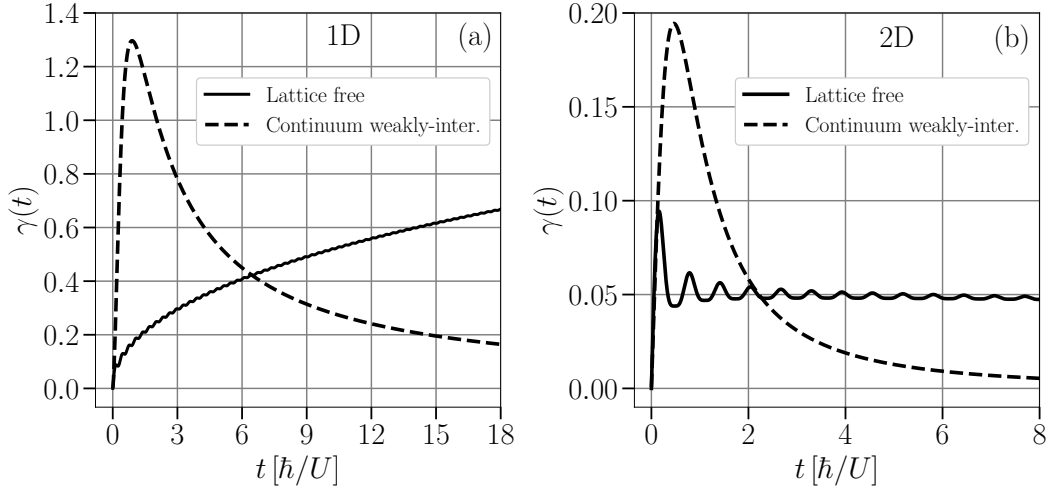
Figure E.1: (a) Dephasing rate $\gamma(t)$ for a 1D bath of lattice free bosons (solid line) and weakly-interacting bosons on the continuum (dashed line). Notice the $\sqrt{t}$ growth for free particles and the t^{-1} decay for weak interactions. (b) The same quantities calculated for $d = 2$. Notice the constant-value asymptotics of $\gamma(t)$ in presence of free bosons and the t^{-2} decay for weak interactions.

state, namely $\exp\left[-\Gamma_{\mathrm{Bog}}(t \to \infty)\right] \neq 0$, at least for $d > 1$.

Most importantly, the frequency dependence of $J_{\mathrm{Bog}}(\omega)$ on the continuum assures that non-Markovian effects do not occur in any dimension. For instance, for a $d = 1$ gas we find

$$J_{\mathrm{Bog}}^{\mathrm{1D,cont.}}(\omega) = \sqrt{2\,m}\rho_0 \sqrt{\frac{\sqrt{(\rho_0\,U)^2 + \omega^2} - \rho_0\,U}{(\rho_0\,U)^2 + \omega^2}} \sim \sqrt{\frac{m\,\rho_0}{U}}\,\omega \quad \text{for } \omega \to 0 \qquad (\mathrm{E.20})$$

which is a monotonous smooth function of ω. On the other hand, for weakly-interacting bosons loaded on a one-dimensional lattice, the spectral density

$$J_{\mathrm{Bog}}^{\mathrm{1D,latt.}}(\omega) = \sqrt{\frac{1}{J}}\rho_0 \sqrt{\frac{\sqrt{(\rho_0\,U)^2 + \omega^2} - \rho_0\,U}{(\rho_0\,U)^2 + \omega^2}} \frac{1}{\sqrt{1 - \frac{1}{4\,J}\left[\sqrt{(\rho_0\,U)^2 + \omega^2} - \rho_0\,U\right]}} \qquad (\mathrm{E.21})$$

$$\sim \sqrt{\frac{\rho_0}{2\,J\,U}}\,\omega \quad \text{for } \omega \to 0$$

presents a van Hove singularity where the dispersion relation of the Goldstone mode reaches a stationary point, namely at the boundary of the Brillouin zone $k = \pi$, where $\omega = \sqrt{2\,J\,(2\,J + 2\,\rho_0\,U)}$. This change in the high-energy structure of $J_{\mathrm{Bog}}(\omega)$ is a genuine effect of the absence of full Galilean invariance due to spatial discreteness inherent to the lattice: in fact, the lattice setting introduces an additional energy scale fixed by the bandwidth of the Goldstone excitation, approximately proportional to the hopping energy J in the weakly-interacting limit $J/U \gg 1$. Consequently, passing from the continuum to the lattice, in the superfluid phase the dephasing function $\gamma(t)$ acquires an oscillating behaviour whose period is set by the hopping time scale, as we observe e.g. in the 2D result shown in Figure 3.2(a). On the other hand, the amplitude of the oscillations of $\gamma(t)$ at large times is always controlled by the power-law decay (E.18) seen on the continuum.

Table E.1 summarises the previous discussion and reports the expressions of $J(\omega)$ and $\gamma(t)$ for the most relevant cases and limits. For the sake of completeness, Figure E.1 reports the behaviour of

the dephasing rate $\gamma(t)$ for a bath of free (weakly-interacting) bosons loaded on a square lattice (on the continuum), to be compared with our results for the critical SF phase of the BH bath at the edge transition. Finally, Table E.2 displays the long-time behaviour of the decoherence function $\Gamma(t)$ and of the Loschmidt echo $L(t)$ for the same reference cases.

Table E.1: In the case of free bosons loaded on a 1D lattice, the dephasing rate behaves as $\gamma_0(t) = t\left[\sin\left(2\,J\,t\right)J_1(2\,J\,t) + \cos\left(2\,J\,t\right)J_0(2\,J\,t)\right] \sim \sqrt{t}$ on a coarse-grained time scale (i.e. for $t \gg 1/J$), modulated by small oscillations due to the lattice discretisation [see Figure E.1(a)]. Here, $J_\alpha(z)$ denotes the Bessel function of order α. Therefore, in the long-time limit, the pure dephasing dynamics in a free-boson environment is insensitive to the spatial discretisation due to the lattice. We report the same dynamical behaviour for $d > 1$.

Bosonic state	$\mathbf{J}(\omega)$	$\mathbf{\gamma(t) = d\Gamma(t)/dt}$
Continuum free	$\omega^{(d-2)/2}$	$t^{(2-d)/2}$ for $0 < d < 4$
Lattice free (1D)	$\left[\frac{\omega}{J}\left(1 - \frac{\omega}{4\,J}\right)\right]^{-1/2}$	$t\left[\sin\left(2\,J\,t\right)J_1(2\,J\,t) + \cos\left(2\,J\,t\right)J_0(2\,J\,t)\right]$
Lattice free	$\omega^{(d-2)/2}$ for $\omega \ll J$	$t^{(2-d)/2}$ for $0 < d < 4$
Continuum weakly-interacting	$\left[\left(\rho_0\,U\right)^2 + \omega^2\right]^{-1/2}\left[\sqrt{\left(\rho_0\,U\right)^2 + \omega^2} - \rho_0\,U\right]^{d/2}$	t^{-d} for $t \gg m$
Lattice weakly-interacting (1D)	$\sqrt{\dfrac{\sqrt{(\rho_0\,U)^2+\omega^2}-\rho_0\,U}{(\rho_0\,U)^2+\omega^2}}\dfrac{1}{\left\{1-\frac{1}{4\,J}\left[\sqrt{(\rho_0\,U)^2+\omega^2}-\rho_0\,U\right]\right\}^{1/2}}$	t^{-1} for $t \gg 1/J$
Lattice weakly-interacting	$\left[\left(\rho_0\,U\right)^2 + \omega^2\right]^{-1/2}\left[\sqrt{\left(\rho_0\,U\right)^2 + \omega^2} - \rho_0\,U\right]^{d/2}$	t^{-d} for $t \gg 1/J$

Table E.2

Bosonic state	**$\Gamma(t)$**	**$L(t)$**
Continuum free	$t^{(4-d)/2}$ for $0 < d < 4$	$\exp\left[-\beta\, t^{(4-d)/2}\right]$ for $0 < d < 4$
Lattice free (1D)	$t^{3/2}$	$\exp\left(-\beta\, t^{3/2}\right)$
Lattice free	$t^{(4-d)/2}$ for $0 < d < 4$	$\exp\left[-\beta\, t^{(4-d)/2}\right]$ for $0 < d < 4$
Continuum weakly-interacting	$\begin{array}{ll}\ln(t) & \text{for} \quad d = 1 \\ t^{1-d} & \text{for} \quad d > 1\end{array}$ for $t \gg m$	$\begin{array}{ll}t^{-\alpha} & \text{with} \quad \alpha > 0 \quad \text{for} \quad d = 1 \\ \exp\left(-\beta\, t^{1-d}\right) & \text{for} \quad d > 1\end{array}$ for $t \gg m$
Lattice weakly-interacting (1D)	$\ln(t)$ for $t \gg 1/J$	$t^{-\alpha}$ with $\alpha > 0$ for $t \gg 1/J$
Lattice weakly-interacting	t^{1-d} for $t \gg 1/J$	$\exp\left[-\beta\, t^{1-d}\right]$ for $t \gg 1/J$

F

Driven-dissipative photonic systems: addenda

F.1 Exciton-polariton condensates: one-body dynamical correlations

The first section of the Appendix is dedicated to a brief discussion of the DoS and one-body dynamical response of the out-of-equilibrium EP condensates reviewed in Chapter 1 of Part II. Their calculation does not involve more effort than the derivation of response functions in the case of the driven-dissipative photonic lattice, detailed in Section 2.4 of Part II. More precisely, the one-body dynamical correlations of the system can be entirely extracted from the retarded Green's function of the EP steady state: the normal propagator is found to be

$$G_R(\mathbf{k}, \omega) = \sum_\alpha \frac{x^*_{\alpha,\mathbf{k}} \, u_{\alpha,\mathbf{k}}}{\omega - \omega_{\alpha,\mathbf{k}}} , \qquad (F.1)$$

where $x_{\alpha,\mathbf{k}}$ is the first component of the left eigenvector $\left(x_{\alpha,\mathbf{k}}, y_{\alpha,\mathbf{k}}, z_{\alpha,\mathbf{k}}\right)^T$ of the generalised Bogoliubov matrix $\hat{\mathcal{L}}_\mathbf{k}$ associated with the collective mode $(\alpha, \mathbf{k})$, while the anomalous one reads

$$\mathcal{G}_R(\mathbf{k}, \omega) = \sum_\alpha \frac{y^*_{\alpha,\mathbf{k}} \, u_{\alpha,\mathbf{k}}}{\omega - \omega_{\alpha,\mathbf{k}}} . \qquad (F.2)$$

F.1.1 Density of states

Typical profiles of the DoS of the EP steady state are shown in Figure F.1, limited to the cases where the system is dynamically stable. When the Goldstone mode coincides with the diffusive G-branch [first panel from the left], the DoS has the same bimodal structure exhibited by the driven-dissipative hard-core lattice [see Figure 2.12(b) in the main body of the Thesis], with the only qualitative discrepancy being the asymmetry between the weights of positive- and negative-energy states in the present case. This is due to the fact that, differently from the excitations of the hard-core gas, the collective modes of a weakly-interacting condensate have a predominantly particle nature. The sign flip of the DoS at the frequency $\omega = \omega_0$ is again a consequence of the imaginary part of the quasiparticle residue of the Goldstone mode $\mathrm{Im}\left(x^*_{\alpha,\mathbf{k}} \, u_{\alpha,\mathbf{k}}\right)$. Interestingly, while the DoS profile does not change appreciably with the appearance of the hybridised Goldstone mode in the driven-dissipative hard-core lattice, the situation is quite different in a EP condensate when the lowest-lying excitation is the diffusive D-mode [central panel]. Here, the out-of-equilibrium character of the system is more evident, since negative-energy states acquire a positive spectral weight for large momenta. Also, the DoS acquires an elongated shape along the momentum axis and its width decreases significantly, in agreement with the essentially flat energy dispersion of the D-mode [see panel (c) in Figure 1.2 in the main body of the Thesis]. Both these effects are brought to their extremal instance when the Goldstone mode has a subdiffusive behaviour in the long-wavelength limit [last panel from left]: in this case, the DoS is strictly positive and perfectly symmetric around $\omega = \omega_0$, with a sharp profile extending over a relatively wide range of momenta.
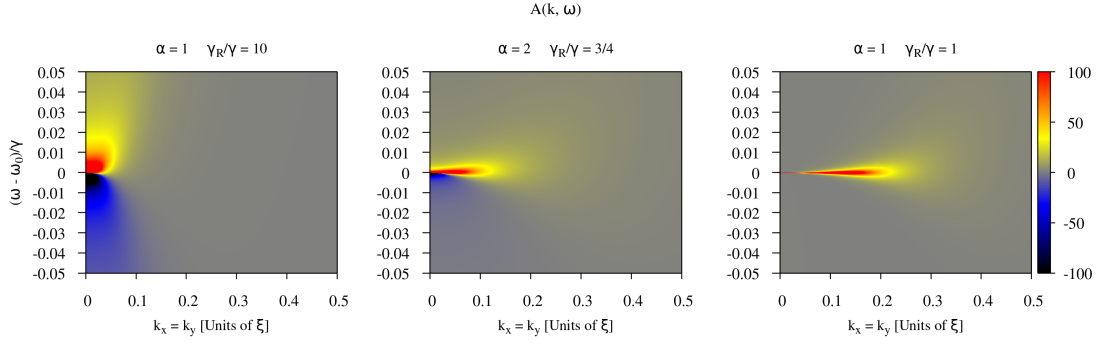
Figure F.1: Colour plots of the density of states of a EP condensate for the same parameters of Figure 1.2 in the main body of the Thesis. In particular, common parameters of the system for all the panels are $\mu/\gamma = P_{thr}/\gamma = \beta = 1$ and $D_R/\gamma = 5 \cdot 10^{-4}$. The healing length of the condensate is $\xi \approx 6.97$. Panels from left to right refer to the case of (i) the standard diffusive G-mode, (ii) the stable diffusive D-mode, (iii) the subdiffusive G/D-mode.
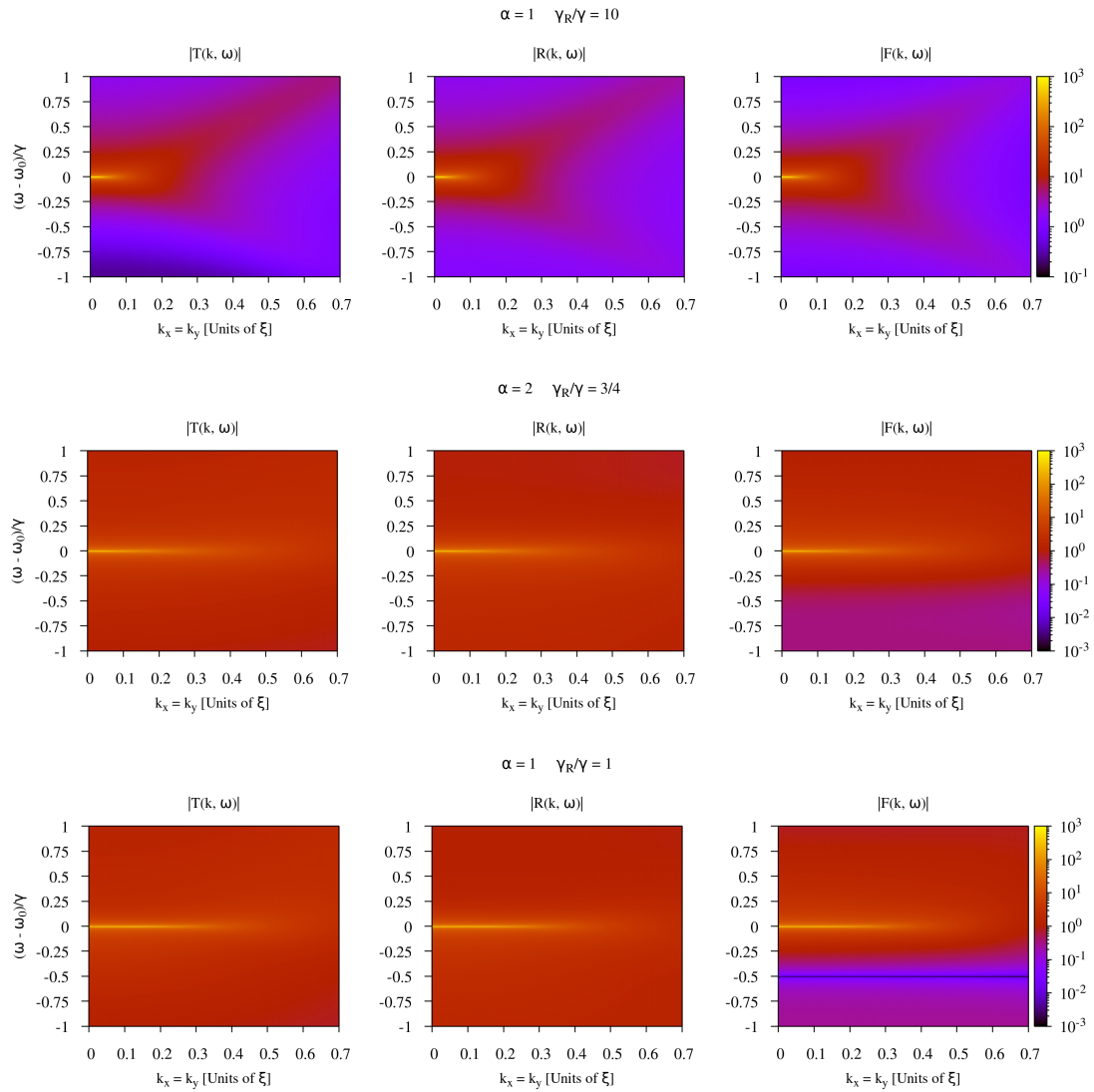
Figure F.2: Colour plots of the transmittivity (first column), reflectivity (second column) and FWM (third column) response of a EP condensate for the same parameters of Figure 1.2 in the main body of the Thesis. In particular, common parameters of the system for all the panels are $\mu/\gamma = P_{thr}/\gamma = \beta = 1$ and $D_R/\gamma = 5 \cdot 10^{-4}$. The healing length of the condensate is $\xi \approx 6.97$. As in Figure F.1, panels from left to right refer to the case of (i) the standard diffusive G-mode, (ii) the stable diffusive D-mode, (iii) the subdiffusive G/D-mode.

F.1.2 Response functions

The symmetry considerations made for the DoS apply also to the one-body response functions, which we display in Figure F.2. When the Goldstone mode is the standard diffusive G-mode [first row], we recover the transmittivity and reflectivity spectra extensively studied in [429]. In particular, we observe that both the signals are particularly sensitive to the Goldstone branch at positive energies, while the dispersion of the amplitude/ghost mode is barely visible. On the other hand, the FWM response is able to resolve both the excitation branches, as expected. It is worth noticing also the dark resonance present in the transmittivity signal, which strongly resembles the one found in the analogous response of the driven-dissipative hard-core lattice, see panel (a) of Figure 2.12 in the main body of the Thesis. Once more, the structure of one-body correlations undergoes a drastic change when the Goldstone mode hybridises with the D-mode branch. Whether the latter excitation is diffusive or subdiffusive, the response functions exhibit a sharp peak at $\omega = \omega_0$ with a flat dispersion at low momentum. A more curious hallmark of the Goldstone hybridisation is the presence of a dark resonance in the FWM spectrum, right at the energy scale of the reservoir loss rate γ_R. Interestingly, this feature does not have a counterpart in the anomalous response of the strongly-interacting photon gas, see panel (d) of Figure 2.12.

F.2 Mean-field theory and collective excitations of the hard-core Bose gas

F.2.1 Holstein-Primakoff mapping

In the hard-core limit $U/J \to \infty$, the BH model (2.1) can be recast into the Hamiltonian of a XXZ model through the Holstein-Primakoff mapping of hard-core bosons to spin operators $\hat{\tau}_{\mathbf{r}}^i$. In particular, under the identifications $\hat{a}_{\mathbf{r}} \to \hat{\tau}_{\mathbf{r}}^-$ and $\hat{n}_{\mathbf{r}} \to (\hat{\tau}_{\mathbf{r}}^z + 1)/2$, we obtain

$$\hat{H}_{\text{BH}} = -J \sum_{\langle \mathbf{r},\mathbf{s} \rangle} \hat{\tau}_{\mathbf{r}}^+ \hat{\tau}_{\mathbf{s}}^- + \frac{\bar{U}}{4} \sum_{\langle \mathbf{r},\mathbf{s} \rangle} \hat{\tau}_{\mathbf{r}}^z \hat{\tau}_{\mathbf{s}}^z + \frac{2\,\omega_c + z\,\bar{U}}{4} \sum_{\mathbf{r}} (\hat{\tau}_{\mathbf{r}}^z + 1) \,, \tag{F.3}$$

where we have also included a nearest-neighbour interaction term with energy scale $\bar{U}$ for the sake of generality. More in detail, this is exactly the non-local repulsive coupling that emerges from second-order perturbation theory on top of the hard-core and MI states of the model when one considers a very large but finite value of the Hubbard energy U: in this case, $\bar{U} \propto t^2/U$. The equations of motion of the spin operators can be readily found via the Heisenberg equation, yielding

$$i\,\dot{\hat{\tau}}_{\mathbf{r}}^z = -2\,J \sum_{\mathbf{s}(\mathbf{r})} \left(\hat{\tau}_{\mathbf{r}}^+ \hat{\tau}_{\mathbf{s}}^- - \text{h.c.} \right) \,, \tag{F.4}$$

$$i\,\dot{\hat{\tau}}_{\mathbf{r}}^- = J\,\hat{\tau}_{\mathbf{r}}^z \sum_{\mathbf{s}(\mathbf{r})} \hat{\tau}_{\mathbf{s}}^- + \frac{\bar{U}}{2}\,\hat{\tau}_{\mathbf{r}}^- \sum_{\mathbf{s}(\mathbf{r})} \hat{\tau}_{\mathbf{s}}^z + \frac{2\,\omega_c + z\,\bar{U}}{2}\,\hat{\tau}_{\mathbf{r}}^- \,. \tag{F.5}$$

F.2.2 Mean-field theory

Within the mean-field approximation, we consider the average values of the operators appearing in Eqs. (F.4)-(F.5) and decouple those fields that act on different sites. Renaming $\langle \hat{\tau}_{\mathbf{r}}^z \rangle \to 2\,n(\mathbf{r}) - 1$ and $\langle \hat{\tau}_{\mathbf{r}}^- \rangle \to \psi(\mathbf{r})$ (which stands for the photonic order parameter), we have

$$i\,\dot{n}(\mathbf{r}) = -J \sum_{\mathbf{s}(\mathbf{r})} \left[\psi^*(\mathbf{r})\,\psi(\mathbf{s}) - \text{c.c.} \right] \,, \tag{F.6}$$

$$i\,\dot\psi(\mathbf{r}) = 2\,J\,n(\mathbf{r})\sum_{\mathbf{s(r)}}\psi(\mathbf{s}) + \bar U\,\psi(\mathbf{r})\sum_{\mathbf{s(r)}}n(\mathbf{s}) - J\sum_{\mathbf{s(r)}}\psi(\mathbf{s}) + \omega_c\,\psi(\mathbf{r})\,,\tag{F.7}$$

which can be regarded as the GPE's for the hard-core regime. Let us now assume that the stationary state of the system is provided by a uniform ansatz for the density $n(\mathbf{r}) = n_0$ and for the order parameter $\psi(\mathbf{r}) = \psi_0\,e^{-i\,\omega\,t}$. Therefore, we are left with only one equation,

$$\omega\,\psi_0 = z\,J\,(2\,n_0 - 1)\,\psi_0 + z\,\bar U\,n_0\,\psi_0 + \omega_c\,\psi_0\,,\tag{F.8}$$

providing the oscillation frequency of the order parameter,

$$\omega = z\,J\,(2\,n_0 - 1) + z\,\bar U\,n_0 + \omega_c\,,\tag{F.9}$$

which can be also regarded as the effective chemical potential of a quantum degenerate gas [40]. In particular, we point out that the mean-field energy shift due to hard-core interactions reads $\Delta\mu = z\left(2\,J + \bar U\right)n_0$. Notice also that a special property of the hard-core regime is the coupling between the density and the order parameter fields. A noteworthy consequence of this fact is the exact relation $|\psi(\mathbf{r})|^2 = n(\mathbf{r})\,[1 - n(\mathbf{r})]$ valid within mean-field theory at equilibrium, meaning that the order parameter modulus is the geometric average of the particle and hole densities. Moreover, this suggests that the hard-core state is *inherently* particle-hole symmetric [52, 131] (at least at the mean-field level).

Taking advantage of the identity $|\psi_0|^2 = n_0\,(1 - n_0)$, we can calculate the optimal value of n_0 through the minimisation of the mean-field energy

$$E_{\mathrm{BH}}/V = -z\,J\,|\psi_0|^2 + \frac{z\,\bar U\,n_0^2}{2} + \omega_c\,n_0\,,\tag{F.10}$$

where V is the lattice volume. In particular, we obtain

$$n_0 = \frac{z\,J - \omega_c}{z\left(2\,J + \bar U\right)}\,,\tag{F.11}$$

so that

$$|\psi_0|^2 = \frac{(z\,J - \omega_c)\left[z\left(J + \bar U\right) + \omega_c\right]}{z^2\left(2\,J + \bar U\right)^2}\,.\tag{F.12}$$

From the mean-field energy shift $\Delta\mu$ we can also derive the healing length of the system. This can be obtained by calculating the momentum for which the single-particle kinetic energy matches $\Delta\mu$ [40], namely

$$\varepsilon_{\mathbf{k}(\xi)} = \Delta\mu\,.\tag{F.13}$$

Considering momenta lying on the diagonals of the square lattice for simplicity, we have

$$2\,z\,J\,\sin\left(\frac{\pi}{2\,\xi}\right)^2 = \Delta\mu\,,\tag{F.14}$$

whose solution can be readily shown to be

$$\xi = \frac{\pi}{2\,\arcsin\left(\sqrt{n_0}\right)}\tag{F.15}$$

and depends on the lattice filling only. It is instructive to compare our result for the healing length of the hard-core gas with the one of a weakly-interacting condensate, reading

$$\xi = \frac{\pi}{2\,\arcsin\left(\sqrt{\frac{\rho_c\,U}{2\,z\,J}}\right)}\,,\tag{F.16}$$

which is controlled by the ratio J/U, as well as by the condensate density $\rho_c = |\psi_0|^2$. On the continuum, Eq. (F.16) transforms into

$$\xi = \sqrt{\frac{z}{4\,m\,\rho_c\,U}}\,.\tag{F.17}$$

F.2.3 Collective excitations at equilibrium

The elementary excitations on top of the mean-field hard-core state determined before can be accessed by considering small-amplitude fluctuations around the condensate order parameter and the density as follows,

$$n(\mathbf{r}) = n_0\left[1 + w_{\mathbf{k}}\,e^{i(\mathbf{k}\cdot\mathbf{r}-\omega_{\mathbf{k}}t)} + w_{\mathbf{k}}^*\,e^{-i(\mathbf{k}\cdot\mathbf{r}-\omega_{\mathbf{k}}t)}\right]\,,\tag{F.18}$$

$$\psi(\mathbf{r}) = \psi_0\left[1 + u_{\mathbf{k}}\,e^{i(\mathbf{k}\cdot\mathbf{r}-\omega_{\mathbf{k}}t)} + v_{\mathbf{k}}^*\,e^{-i(\mathbf{k}\cdot\mathbf{r}-\omega_{\mathbf{k}}t)}\right]e^{-i\,\omega\,t}\,.\tag{F.19}$$

Inserting the linearised fields (F.18)-(F.19) into the GPE's (F.6)-(F.7), we obtain the eigenvalue equation

$$\begin{pmatrix} (1-2\,n_0)\,\varepsilon_{\mathbf{k}} + z\,\bar{U}\,n_0 + \omega_c & 0 & \left[2\,z\,J + \bar{U}(\mathbf{k})\right]n_0 \\ 0 & (2\,n_0-1)\,\varepsilon_{\mathbf{k}} - z\,\bar{U}\,n_0 - \omega_c & -\left[2\,z\,J + \bar{U}(\mathbf{k})\right]n_0 \\ (1-n_0)\,[z\,J + \varepsilon_{\mathbf{k}}] & -(1-n_0)\,[z\,J + \varepsilon_{\mathbf{k}}] & 0 \end{pmatrix}\begin{pmatrix} u_{\mathbf{k}} \\ v_{\mathbf{k}} \\ w_{\mathbf{k}} \end{pmatrix} = \omega_{\mathbf{k}}\begin{pmatrix} u_{\mathbf{k}} \\ v_{\mathbf{k}} \\ w_{\mathbf{k}} \end{pmatrix}\,,\tag{F.20}$$

where we have defined $\bar{U}(\mathbf{k}) = 2\,\bar{U}\sum_{a=1}^{d}\cos(k_a)$. The eigenvalues $\omega_{\mathbf{k}}$ provide the energy spectrum of the collective modes of the hard-core state, the most relevant of which is the Goldstone branch

$$\omega_{\text{Gol}}^{\text{HC}}(\mathbf{k}) = \sqrt{\frac{\left(z\,\bar{U} + 2\,\omega_c\right)^2}{z^2\left(2\,J + \bar{U}\right)^2}\,[z\,J + \varepsilon_{\mathbf{k}}]^2 + 2\,|\psi_0|^2\left[2\,z\,J + \bar{U}(\mathbf{k})\right][z\,J + \varepsilon_{\mathbf{k}}]}\,,\tag{F.21}$$

which is an acoustic excitation with sound velocity [466]

$$c_s^{\text{HC}} = \sqrt{2\,z\,J\left(2\,J + \bar{U}\right)}\,|\psi_0| = \sqrt{2\,z\,J\left(2\,J + \bar{U}\right)n_0\,(1-n_0)} = \sqrt{\frac{2\,J\,(z\,J - \omega_c)\left[z\left(J + \bar{U}\right) + \omega_c\right]}{z\left(2\,J + \bar{U}\right)}}\,.\tag{F.22}$$

To conclude, we notice that the sound velocity becomes imaginary (signalling a dynamical instability of the ground state) for $\omega_c < -z\left(J + \bar{U}\right)$ and $\omega_c > z\,J$.

Bibliography

[1] F. Caleffi, 'Quantum fluctuations beyond the Gutzwiller approximation in the Bose-Hubbard model', MA thesis (University of Trento, 2018).

[2] S. D. Jenkins and J. Ruostekoski, 'Controlled manipulation of light by cooperative response of atoms in an optical lattice', Phys. Rev. A **86**, 031602 (2012).

[3] Y. Ye, Z.-Y. Ge, Y. Wu, S. Wang, M. Gong, Y.-R. Zhang, Q. Zhu, R. Yang, S. Li, F. Liang, J. Lin, Y. Xu, C. Guo, L. Sun, C. Cheng, N. Ma, Z. Y. Meng, H. Deng, H. Rong, C.-Y. Lu, C.-Z. Peng, H. Fan, X. Zhu, and J.-W. Pan, 'Propagation and localization of collective excitations on a 24-qubit superconducting processor', Phys. Rev. Lett. **123**, 050502 (2019).

[4] E. Baldini, M. A. Sentef, S. Acharya, T. Brumme, E. Sheveleva, F. Lyzwa, E. Pomjakushina, C. Bernhard, M. van Schilfgaarde, F. Carbone, A. Rubio, and C. Weber, 'Electron-phonon-driven three-dimensional metallicity in an insulating cuprate', Proceedings of the National Academy of Sciences **117**, 6409–6416 (2020).

[5] N. N. Bogoliubov, 'On the theory of superfluidity', J. Phys. (USSR) **11**, 23–32 (1947).

[6] V. A. Zagrebnov and J.-B. Bru, 'The Bogoliubov model of weakly imperfect Bose gas', Physics Reports **350**, 291–434 (2001).

[7] M. C. Gutzwiller, 'Effect of correlation on the ferromagnetism of transition metals', Phys. Rev. Lett. **10**, 159–162 (1963).

[8] M. C. Gutzwiller, 'Correlation of electrons in a narrow s band', Phys. Rev. **137**, A1726–A1735 (1965).

[9] F. Gebhard, 'Gutzwiller correlated wave functions in finite dimensions d: A systematic expansion in $1/d$', Phys. Rev. B **41**, 9452–9473 (1990).

[10] D. S. Rokhsar and B. G. Kotliar, 'Gutzwiller projection for bosons', Phys. Rev. B **44**, 10328–10332 (1991).

[11] W. Krauth, M. Caffarel, and J.-P. Bouchaud, 'Gutzwiller wave function for a model of strongly interacting bosons', Phys. Rev. B **45**, 3137–3140 (1992).

[12] G. Wang, Y. Qian, G. Xu, X. Dai, and Z. Fang, 'Gutzwiller density functional studies of FeAs-based superconductors: Structure optimization and evidence for a three-dimensional Fermi surface', Phys. Rev. Lett. **104**, 047002 (2010).

[13] M. Sandri, M. Capone, and M. Fabrizio, 'Finite-temperature Gutzwiller approximation and the phase diagram of a toy model for V_2O_3', Phys. Rev. B **87**, 205108 (2013).

[14] U. R. Fischer and B. Xiong, 'Many-site coherence revivals in the extended Bose-Hubbard model and the Gutzwiller approximation', Phys. Rev. A **84**, 063635 (2011).

[15] H. Deng, H. Dai, J. Huang, X. Qin, J. Xu, H. Zhong, C. He, and C. Lee, 'Cluster Gutzwiller study of the Bose-Hubbard ladder: Ground-state phase diagram and many-body Landau-Zener dynamics', Phys. Rev. A **92**, 023618 (2015).

[16] W. Casteels, R. M. Wilson, and M. Wouters, 'Gutzwiller Monte Carlo approach for a critical dissipative spin model', Phys. Rev. A **97**, 062107 (2018).

[17] D. Huybrechts and M. Wouters, 'Dynamical hysteresis properties of the driven-dissipative Bose-Hubbard model with a Gutzwiller Monte Carlo approach', Phys. Rev. A **102**, 053706 (2020).

[18]G. D. Mahan, *Many-particle physics* (Springer Science & Business Media, 2013).

[19]A. Le Boité, G. Orso, and C. Ciuti, 'Steady-state phases and tunneling-induced instabilities in the driven dissipative Bose-Hubbard model', Phys. Rev. Lett. **110**, 233601 (2013).

[20]J. Lebreuilly, A. Biella, F. Storme, D. Rossini, R. Fazio, C. Ciuti, and I. Carusotto, 'Stabilizing strongly correlated photon fluids with non-Markovian reservoirs', Phys. Rev. A **96**, 033828 (2017).

[21]J. M. Fink, A. Dombi, A. Vukics, A. Wallraff, and P. Domokos, 'Observation of the photon-blockade breakdown phase transition', Phys. Rev. X **7**, 011012 (2017).

[22]A. Le Boité, G. Orso, and C. Ciuti, 'Bose-Hubbard model: Relation between driven-dissipative steady states and equilibrium quantum phases', Phys. Rev. A **90**, 063821 (2014).

[23]T. Fink, A. Schade, S. Höfling, C. Schneider, and A. Imamoglu, 'Signatures of a dissipative phase transition in photon correlation measurements', Nature Physics **14**, 365–369 (2017).

[24]P. Roushan, C. Neill, J. Tangpanitanon, V. M. Bastidas, A. Megrant, R. Barends, Y. Chen, Z. Chen, B. Chiaro, A. Dunsworth, A. Fowler, B. Foxen, M. Giustina, E. Jeffrey, J. Kelly, E. Lucero, J. Mutus, M. Neeley, C. Quintana, D. Sank, A. Vainsencher, J. Wenner, T. White, H. Neven, D. G. Angelakis, and J. Martinis, 'Spectroscopic signatures of localization with interacting photons in superconducting qubits', Science **358**, 1175–1179 (2017).

[25]R. Ma, B. Saxberg, C. Owens, N. Leung, Y. Lu, J. Simon, and D. I. Schuster, 'A dissipatively stabilized Mott insulator of photons', Nature **566**, 51–57 (2019).

[26]P. W. Anderson, 'The resonating valence bond state in la2cuo4 and superconductivity', Science **235**, 1196–1198 (1987).

[27]P. A. Lee, N. Nagaosa, and X.-G. Wen, 'Doping a mott insulator: physics of high-temperature superconductivity', Rev. Mod. Phys. **78**, 17–85 (2006).

[28]C. Castellani, C. Di Castro, D. Feinberg, and J. Ranninger, 'New model hamiltonian for the metal-insulator transition', Phys. Rev. Lett. **43**, 1957–1960 (1979).

[29]D. Vollhardt, 'Normal ^{3}He: an almost localized Fermi liquid', Rev. Mod. Phys. **56**, 99–120 (1984).

[30]E. Gull, O. Parcollet, and A. J. Millis, 'Superconductivity and the pseudogap in the two-dimensional hubbard model', Phys. Rev. Lett. **110**, 216405 (2013).

[31]A. S. Darmawan, Y. Nomura, Y. Yamaji, and M. Imada, 'Stripe and superconducting order competing in the hubbard model on a square lattice studied by a combined variational monte carlo and tensor network method', Phys. Rev. B **98**, 205132 (2018).

[32]M. P. A. Fisher, P. B. Weichman, G. Grinstein, and D. S. Fisher, 'Boson localization and the superfluid-insulator transition', Phys. Rev. B **40**, 546–570 (1989).

[33]D. Jaksch, C. Bruder, J. I. Cirac, C. W. Gardiner, and P. Zoller, 'Cold bosonic atoms in optical lattices', Phys. Rev. Lett. **81**, 3108–3111 (1998).

[34]M. Greiner, O. Mandel, T. Esslinger, T. W. Hänsch, and I. Bloch, 'Quantum phase transition from a superfluid to a mott insulator in a gas of ultracold atoms', Nature **415**, 39–44 (2002).

[35]T. Stöferle, H. Moritz, C. Schori, M. Köhl, and T. Esslinger, 'Transition from a strongly interacting 1D superfluid to a Mott insulator', Phys. Rev. Lett. **92**, 130403 (2004).

[36]S. Fölling, F. Gerbier, A. Widera, O. Mandel, T. Gericke, and I. Bloch, 'Spatial quantum noise interferometry in expanding ultracold atom clouds', Nature **434**, 481–484 (2005).

[37]W. S. Bakr, J. I. Gillen, A. Peng, S. Fölling, and M. Greiner, 'A quantum gas microscope for detecting single atoms in a Hubbard-regime optical lattice', Nature **462**, 74–77 (2009).

[38]P. T. Ernst, S. Götze, J. S. Krauser, K. Pyka, D.-S. Lühmann, D. Pfannkuche, and K. Sengstock, 'Probing superfluids in optical lattices by momentum-resolved Bragg spectroscopy', Nature Physics **6**, 56–61 (2009).

[39]M. Endres, T. Fukuhara, D. Pekker, M. Cheneau, P. Schauß, C. Gross, E. Demler, S. Kuhr, and I. Bloch, 'The Higgs amplitude mode at the two-dimensional superfluid/Mott insulator transition', Nature **487**, 454–458 (2012).

[40]L. P. Pitaevskii and S. Stringari, *Bose-Einstein condensation and superfluidity* (Oxford Science Publications, New York, 2016).

[41]I. Carusotto and C. Ciuti, 'Quantum fluids of light', Rev. Mod. Phys. **85**, 299–366 (2013).

[42]I. Carusotto, A. A. Houck, A. J. Kollár, P. Roushan, D. I. Schuster, and J. Simon, 'Photonic materials in circuit quantum electrodynamics', Nature Physics **16**, 268–279 (2020).

[43]K. V. Krutitsky, 'Ultracold bosons with short-range interaction in regular optical lattices', Physics Reports **607**, 1–101 (2016).

[44]Y. Castin, in *Coherent atomic matter waves*, edited by R. Kaiser, C. Westbrook, and F. David (EDP Sciences and Springer-Verlag, 2001), pp. 1–136.

[45]I. Carusotto and Y. Castin, 'Condensate statistics in one-dimensional interacting bose gases: exact results', Phys. Rev. Lett. **90**, 030401 (2003).

[46]K. Sheshadri, H. R. Krishnamurthy, R. Pandit, and T. V. Ramakrishnan, 'Superfluid and insulating phases in an interacting-boson model: Mean-field theory and the RPA', Europhysics Letters (EPL) **22**, 257–263 (1993).

[47]D. van Oosten, P. van der Straten, and H. T. C. Stoof, 'Quantum phases in an optical lattice', Phys. Rev. A **63**, 053601 (2001).

[48]C. Menotti and N. Trivedi, 'Spectral weight redistribution in strongly correlated bosons in optical lattices', Phys. Rev. B **77**, 235120 (2008).

[49]D. B. M. Dickerscheid, D. van Oosten, P. J. H. Denteneer, and H. T. C. Stoof, 'Ultracold atoms in optical lattices', Phys. Rev. A **68**, 043623 (2003).

[50]I. Frérot and T. Roscilde, 'Entanglement entropy across the superfluid-insulator transition: A signature of bosonic criticality', Phys. Rev. Lett. **116**, 190401 (2016).

[51]K. V. Krutitsky and P. Navez, 'Excitation dynamics in a lattice Bose gas within the time-dependent Gutzwiller mean-field approach', Phys. Rev. A **84**, 033602 (2011).

[52]M. Di Liberto, A. Recati, N. Trivedi, I. Carusotto, and C. Menotti, 'Particle-hole character of the Higgs and Goldstone modes in strongly interacting lattice bosons', Phys. Rev. Lett. **120**, 073201 (2018).

[53]B. Capogrosso-Sansone, N. V. Prokof'ev, and B. V. Svistunov, 'Phase diagram and thermodynamics of the three-dimensional Bose-Hubbard model', Phys. Rev. B **75**, 134302 (2007).

[54]B. Capogrosso-Sansone, Ş. G. Söyler, N. Prokof'ev, and B. Svistunov, 'Monte Carlo study of the two-dimensional Bose-Hubbard model', Phys. Rev. A **77**, 015602 (2008).

[55]Y. Kato and N. Kawashima, 'Quantum monte carlo method for the bose-hubbard model with harmonic confining potential', Phys. Rev. E **79**, 021104 (2009).

[56]L. Pollet and N. Prokof'ev, 'Higgs mode in a two-dimensional superfluid', Phys. Rev. Lett. **109**, 010401 (2012).

[57]K. Byczuk and D. Vollhardt, 'Correlated bosons on a lattice: Dynamical mean-field theory for Bose-Einstein condensed and normal phases', Phys. Rev. B **77**, 235106 (2008).

[58]W.-J. Hu and N.-H. Tong, 'Dynamical mean-field theory for the Bose-Hubbard model', Phys. Rev. B **80**, 245110 (2009).

[59]P. Anders, E. Gull, L. Pollet, M. Troyer, and P. Werner, 'Dynamical mean-field theory for bosons', New Journal of Physics **13**, 075013 (2011).

[60]K. Sengupta and N. Dupuis, 'Mott-insulator–to–superfluid transition in the Bose-Hubbard model: A strong-coupling approach', Phys. Rev. A **71**, 033629 (2005).

[61]A. Ran çon and N. Dupuis, 'Nonperturbative renormalization group approach to the Bose-Hubbard model', Phys. Rev. B **83**, 172501 (2011).

[62]Y. Ohashi, M. Kitaura, and H. Matsumoto, 'Itinerant-localized dual character of a strongly correlated superfluid bose gas in an optical lattice', Phys. Rev. A **73**, 033617 (2006).

[63]S. Sachdev, *Quantum phase transitions*, 2nd ed. (Cambridge University Press, 2011).

[64]S. D. Huber, B. Theiler, E. Altman, and G. Blatter, 'Amplitude mode in the quantum phase model', Phys. Rev. Lett. **100**, 050404 (2008).

[65]M. Fabrizio, 'Quantum fluctuations beyond the Gutzwiller approximation', Phys. Rev. B **95**, 075156 (2017).

[66]D. Pekker and C. Varma, 'Amplitude/Higgs modes in condensed matter physics', Annual Review of Condensed Matter Physics **6**, 269–297 (2015).

[67]D. Podolsky and S. Sachdev, 'Spectral functions of the Higgs mode near two-dimensional quantum critical points', Phys. Rev. B **86**, 054508 (2012).

[68]D. Podolsky, A. Auerbach, and D. P. Arovas, 'Visibility of the amplitude (Higgs) mode in condensed matter', Phys. Rev. B **84**, 174522 (2011).

[69]C. Cohen-Tannoudji, J. Dupont-Roc, and G. Grynberg, *Photons and atoms: Introduction to quantum electrodynamics* (Wiley-VCH Verlag GmbH & Co. KGaA, Weinheim, Germany, 1997).

[70]J.-P. Blaizot and G. Ripka, *Quantum theory of finite systems* (The Massachusetts Institute of Technology Press, Cambridge, Massachusetts, 1986).

[71]A. Griffin, 'Conserving and gapless approximations for an inhomogeneous Bose gas at finite temperatures', Phys. Rev. B **53**, 9341–9347 (1996).

[72]Y. Castin and R. Dum, 'Low-temperature Bose-Einstein condensates in time-dependent traps: Beyond the $U(1)$ symmetry-breaking approach', Phys. Rev. A **57**, 3008–3021 (1998).

[73]L. D. Landau, E. M. Lifshitz, and L. P. Pitaevskii, *Course of theoretical physics: Statistical physics, Part 2*, Vol. 9 (Pergamon Press, Oxford, New York, 1980).

[74]S. Stringari, 'Quantum fluctuations and Gross-Pitaevskii theory', Journal of Experimental and Theoretical Physics **127**, 844–850 (2018).

[75]T. P. Polak and T. K. Kopeć, 'Quantum rotor description of the Mott-insulator transition in the Bose-Hubbard model', Phys. Rev. B **76**, 094503 (2007).

[76]M. Capone, M. Civelli, S. S. Kancharla, C. Castellani, and G. Kotliar, 'Cluster-dynamical mean-field theory of the density-driven Mott transition in the one-dimensional Hubbard model', Phys. Rev. B **69**, 195105 (2004).

[77]T. Maier, M. Jarrell, T. Pruschke, and M. H. Hettler, 'Quantum cluster theories', Rev. Mod. Phys. **77**, 1027–1080 (2005).

[78]C. Berthod, T. Giamarchi, S. Biermann, and A. Georges, 'Breakup of the Fermi surface near the Mott transition in low-dimensional systems', Phys. Rev. Lett. 97, 136401 (2006).

[79]D. J. Scalapino, S. R. White, and S. C. Zhang, 'Superfluid density and the Drude weight of the Hubbard model', Phys. Rev. Lett. 68, 2830–2833 (1992).

[80]D. J. Scalapino, S. R. White, and S. Zhang, 'Insulator, metal, or superconductor: The criteria', Phys. Rev. B 47, 7995–8007 (1993).

[81]J. Nespolo, G. E. Astrakharchik, and A. Recati, 'Andreev–Bashkin effect in superfluid cold gases mixtures', New Journal of Physics 19, 125005 (2017).

[82]D. Romito, C. Lobo, and A. Recati, 'Linear response study of collisionless spin drag', Phys. Rev. Research 3, 023196 (2021).

[83]A. M. Rey, K. Burnett, R. Roth, M. Edwards, C. J. Williams, and C. W. Clark, 'Bogoliubov approach to superfluidity of atoms in an optical lattice', Journal of Physics B: Atomic, Molecular and Optical Physics 36, 825–841 (2003).

[84]O. A. Prośniak, M. Łącki, and B. Damski, 'Critical points of the three-dimensional Bose-Hubbard model from on-site atom number fluctuations', Scientific Reports 9, 8687 (2019).

[85]S. T. Beliaev, 'Energy spectrum of a non-ideal Bose gas', Sov. Phys. JETP 34, 299 (1958).

[86]S. Beliaev, 'Application of the methods of quantum field theory to a system of bosons', Zh. Eksp. Teor. Fiz. 34, 417 (1958).

[87]E. Altman and A. Auerbach, 'Oscillating superfluidity of bosons in optical lattices', Phys. Rev. Lett. 89, 250404 (2002).

[88]A. Recati and F. Piazza, 'Breaking of Goldstone modes in a two-component Bose-Einstein condensate', Phys. Rev. B 99, 064505 (2019).

[89]D.-S. Lühmann, 'Cluster Gutzwiller method for bosonic lattice systems', Phys. Rev. A 87, 043619 (2013).

[90]E. Altman, W. Hofstetter, E. Demler, and M. D. Lukin, 'Phase diagram of two-component bosons on an optical lattice', New Journal of Physics 5, 113–113 (2003).

[91]A. Kuklov, N. Prokof'ev, and B. Svistunov, 'Commensurate two-component bosons in an optical lattice: Ground state phase diagram', Phys. Rev. Lett. 92, 050402 (2004).

[92]A. B. Kuklov and B. V. Svistunov, 'Counterflow superfluidity of two-species ultracold atoms in a commensurate optical lattice', Phys. Rev. Lett. 90, 100401 (2003).

[93]A. Isacsson, M.-C. Cha, K. Sengupta, and S. M. Girvin, 'Superfluid-insulator transitions of two-species bosons in an optical lattice', Phys. Rev. B 72, 184507 (2005).

[94]A. Hubener, M. Snoek, and W. Hofstetter, 'Magnetic phases of two-component ultracold bosons in an optical lattice', Phys. Rev. B 80, 245109 (2009).

[95]A. Hu, L. Mathey, I. Danshita, E. Tiesinga, C. J. Williams, and C. W. Clark, 'Counterflow and paired superfluidity in one-dimensional Bose mixtures in optical lattices', Phys. Rev. A 80, 023619 (2009).

[96]A. Andreev and E. Bashkin, 'Three-velocity hydrodynamics of superfluid solutions', JETP 42, 164 (1976).

[97]M. A. Alpar, S. A. Langer, and J. A. Sauls, 'Rapid postglitch spin-up of the superfluid core in pulsars', The Astrophysical Journal 282, 533–541 (1984).

[98]O. Sjöberg, 'On the Landau effective mass in asymmetric nuclear matter', Nuclear Physics A 265, 511–516 (1976).

[99] M. Borumand, R. Joynt, and W. Klu źniak, 'Superfluid densities in neutron-star matter', Phys. Rev. C **54**, 2745–2750 (1996).

[100] M. Baldo, J. Cugnon, A. Lejeune, and U. Lombardo, 'Proton and neutron superfluidity in neutron star matter', Nuclear Physics A **536**, 349–365 (1992).

[101] N. Chamel, 'Two-fluid models of superfluid neutron star cores', Monthly Notices of the Royal Astronomical Society **388**, 737–752 (2008).

[102] S. B. Chung, H. Bluhm, and E.-A. Kim, 'Stability of half-quantum vortices in $p_x + i\,p_y$ superconductors', Phys. Rev. Lett. **99**, 197002 (2007).

[103] S. B. Chung, D. F. Agterberg, and E.-A. Kim, 'Fractional vortex lattice structures in spin-triplet superconductors', New Journal of Physics **11**, 085004 (2009).

[104] J. Garaud, K. A. H. Sellin, J. Jäykkä, and E. Babaev, 'Skyrmions induced by dissipationless drag in U(1)×U(1) superconductors', Phys. Rev. B **89**, 104508 (2014).

[105] D. V. Fil and S. I. Shevchenko, 'Nondissipative drag of superflow in a two-component Bose gas', Phys. Rev. A **72**, 013616 (2005).

[106] J. Linder and A. Sudbø, 'Calculation of drag and superfluid velocity from the microscopic parameters and excitation energies of a two-component Bose-Einstein condensate in an optical lattice', Phys. Rev. A **79**, 063610 (2009).

[107] L. Parisi, G. E. Astrakharchik, and S. Giorgini, 'Spin dynamics and Andreev-Bashkin effect in mixtures of one-dimensional Bose gases', Phys. Rev. Lett. **121**, 025302 (2018).

[108] V. Karle, N. Defenu, and T. Enss, 'Coupled superfluidity of binary Bose mixtures in two dimensions', Phys. Rev. A **99**, 063627 (2019).

[109] K. Sellin and E. Babaev, 'Superfluid drag in the two-component Bose-Hubbard model', Phys. Rev. B **97**, 094517 (2018).

[110] D. Contessi, D. Romito, M. Rizzi, and A. Recati, 'Collisionless drag for a one-dimensional two-component Bose-Hubbard model', Phys. Rev. Research **3**, L022017 (2021).

[111] E. Blomquist, A. Syrwid, and E. Babaev, 'Borromean supercounterfluidity', Phys. Rev. Lett. **127**, 255303 (2021).

[112] J. Catani, L. De Sarlo, G. Barontini, F. Minardi, and M. Inguscio, 'Degenerate Bose-Bose mixture in a three-dimensional optical lattice', Phys. Rev. A **77**, 011603 (2008).

[113] B. Gadway, D. Pertot, R. Reimann, and D. Schneble, 'Superfluidity of interacting bosonic mixtures in optical lattices', Phys. Rev. Lett. **105**, 045303 (2010).

[114] T. Fukuhara, P. Schauß, M. Endres, S. Hild, M. Cheneau, I. Bloch, and C. Gross, 'Microscopic observation of magnon bound states and their dynamics', Nature **502**, 76–79 (2013).

[115] P. A. Lee, N. Nagaosa, and X.-G. Wen, 'Doping a Mott insulator: Physics of high-temperature superconductivity', Rev. Mod. Phys. **78**, 17–85 (2006).

[116] P. Ao and S. T. Chui, 'Binary Bose-Einstein condensate mixtures in weakly and strongly segregated phases', Phys. Rev. A **58**, 4836–4840 (1998).

[117] P. Chen and M.-F. Yang, 'Quantum phase transitions in a two-species hard-core boson Hubbard model in two dimensions', Phys. Rev. B **82**, 180510 (2010).

[118] T. Ozaki, I. Danshita, and T. Nikuni, 'Bose-Bose mixtures in an optical lattice: First-order superfluid-insulator transition and elementary excitations', arXiv **1210**, 01370 (2012).

[119]S. D. Huber, E. Altman, H. P. Büchler, and G. Blatter, 'Dynamical properties of ultracold bosons in an optical lattice', Phys. Rev. B **75**, 085106 (2007).

[120]D. Yamamoto, T. Ozaki, C. A. R. Sá de Melo, and I. Danshita, 'First-order phase transition and anomalous hysteresis of Bose gases in optical lattices', Phys. Rev. A **88**, 033624 (2013).

[121]I. Morera, G. E. Astrakharchik, A. Polls, and B. Juliá-Díaz, 'Quantum droplets of bosonic mixtures in a one-dimensional optical lattice', Phys. Rev. Research **2**, 022008 (2020).

[122]R. Kraus, K. Biedroń, J. Zakrzewski, and G. Morigi, 'Superfluid phases induced by dipolar interactions', Phys. Rev. B **101**, 174505 (2020).

[123]Y. Machida, I. Danshita, D. Yamamoto, and K. Kasamatsu, 'Quantum droplet of a two-component Bose gas in an optical lattice near the Mott insulator transition', Phys. Rev. A **105**, L031301 (2022).

[124]A. J. Leggett, *Quantum liquids: Bose condensation and Cooper pairing in condensed-matter systems* (Oxford university press, 2006).

[125]C. J. Pethick and H. Smith, *Bose-Einstein condensation in dilute gases*, 2nd ed. (Cambridge University Press, 2008).

[126]D. van Oosten, D. B. M. Dickerscheid, B. Farid, P. van der Straten, and H. T. C. Stoof, 'Inelastic light scattering from a Mott insulator', Phys. Rev. A **71**, 021601 (2005).

[127]U. Bissbort, S. Götze, Y. Li, J. Heinze, J. S. Krauser, M. Weinberg, C. Becker, K. Sengstock, and W. Hofstetter, 'Detecting the amplitude mode of strongly interacting lattice bosons by Bragg scattering', Phys. Rev. Lett. **106**, 205303 (2011).

[128]K. Sturm, 'Dynamic structure factor: an introduction', Zeitschrift für Naturforschung A **48**, 233–242 (1993).

[129]A. J. Leggett, 'On the superfluid fraction of an arbitrary many-body system at T = 0', Journal of Statistical Physics **93**, 927–941 (1998).

[130]F. Carlini and S. Stringari, 'Spin drag and fast response in a quantum mixture of atomic gases', Phys. Rev. A **104**, 023301 (2021).

[131]F. Caleffi, M. Capone, C. Menotti, I. Carusotto, and A. Recati, 'Quantum fluctuations beyond the Gutzwiller approximation in the Bose-Hubbard model', Phys. Rev. Research **2**, 033276 (2020).

[132]C. Gross and I. Bloch, 'Quantum simulations with ultracold atoms in optical lattices', Science **357**, 995–1001 (2017).

[133]M. E. Pezzoli, F. Becca, M. Fabrizio, and G. Santoro, 'Local moments and magnetic order in the two-dimensional Anderson-Mott transition', Phys. Rev. B **79**, 033111 (2009).

[134]S. Zhou, L. Liang, and Z. Wang, 'Dynamical slave-boson mean-field study of the Mott transition in the Hubbard model in the large-z limit', Phys. Rev. B **101**, 035106 (2020).

[135]A. Syrwid, E. Blomquist, and E. Babaev, 'Dissipationless vector drag – Superfluid spin Hall effect', Phys. Rev. Lett. **127**, 100403 (2021).

[136]P. Fazekas and K. Penc, 'Generalized Gutzwiller ansatz for the half-filled Hubbard chain', International Journal of Modern Physics B **2**, 1021–1034 (1988).

[137]P. Fazekas, 'Variational study of the pair hopping model', International Journal of Modern Physics B **3**, 1765–1781 (1989).

[138]K. Suthar, H. Sable, R. Bai, S. Bandyopadhyay, S. Pal, and D. Angom, 'Supersolid phase of the extended Bose-Hubbard model with an artificial gauge field', Phys. Rev. A **102**, 013320 (2020).

[139]S. Mondal, A. Kshetrimayum, and T. Mishra, 'Two-body repulsive bound pairs in a multibody interacting Bose-Hubbard model', Phys. Rev. A **102**, 023312 (2020).

[140]M. Malakar, S. Ray, S. Sinha, and D. Angom, 'Phases and collective modes of bosons in a triangular lattice at finite temperature: A cluster mean field study', Phys. Rev. B **102**, 184515 (2020).

[141]K. Suthar, R. Kraus, H. Sable, D. Angom, G. Morigi, and J. Zakrzewski, 'Staggered superfluid phases of dipolar bosons in two-dimensional square lattices', Phys. Rev. B **102**, 214503 (2020).

[142]K. Suthar, P. Kaur, S. Gautam, and D. Angom, 'Spin-orbit-coupling-driven superfluid states in optical lattices at zero and finite temperatures', Phys. Rev. A **104**, 043320 (2021).

[143]S. Baier, M. J. Mark, D. Petter, K. Aikawa, L. Chomaz, Z. Cai, M. Baranov, P. Zoller, and F. Ferlaino, 'Extended Bose-Hubbard models with ultracold magnetic atoms', Science **352**, 201–205 (2016).

[144]V. W. Scarola and S. Das Sarma, 'Quantum phases of the extended Bose-Hubbard Hamiltonian: Possibility of a supersolid state of cold atoms in optical lattices', Phys. Rev. Lett. **95**, 033003 (2005).

[145]J. Koepsell, J. Vijayan, P. Sompet, F. Grusdt, T. A. Hilker, E. Demler, G. Salomon, I. Bloch, and C. Gross, 'Imaging magnetic polarons in the doped Fermi-Hubbard model', Nature **572**, 358–362 (2019).

[146]J. Koepsell, D. Bourgund, P. Sompet, S. Hirthe, A. Bohrdt, Y. Wang, F. Grusdt, E. Demler, G. Salomon, C. Gross, and I. Bloch, 'Microscopic evolution of doped Mott insulators from polaronic metal to Fermi liquid', Science **374**, 82–86 (2021).

[147]J. Gavoret and P. Nozières, 'Structure of the perturbation expansion for the Bose liquid at zero temperature', Annals of Physics **28**, 349–399 (1964).

[148]Y. A. Nepomnyashchii and A. A. Nepomnyashchii, 'Infrared divergence in field theory of a Bose system with a condensate', Sov. Phys. - JETP (Engl. Transl., United States) **48** (1978).

[149]H.-P. Breuer and F. Petruccione, *The theory of open quantum systems* (Oxford University Press, Oxford, 2002).

[150]I. de Vega and D. Alonso, 'Dynamics of non-Markovian open quantum systems', Rev. Mod. Phys. **89**, 015001 (2017).

[151]A. Rivas and S. F. Huelga, 'Time evolution in open quantum systems', in *Open quantum systems. An introduction* (Springer Berlin, Heidelberg, 2011), pp. 19–31.

[152]Á. Rivas, S. F. Huelga, and M. B. Plenio, 'Quantum non-markovianity: characterization, quantification and detection', Reports on Progress in Physics **77**, 094001 (2014).

[153]A. Caldeira and A. Leggett, 'Path integral approach to quantum Brownian motion', Physica A: Statistical Mechanics and its Applications **121**, 587–616 (1983).

[154]A. J. Leggett, S. Chakravarty, A. T. Dorsey, M. P. A. Fisher, A. Garg, and W. Zwerger, 'Dynamics of the dissipative two-state system', Rev. Mod. Phys. **59**, 1–85 (1987).

[155]W. Strunz, 'Stochastic path integrals and open quantum systems', Phys. Rev. A **54**, 2664 (1996).

[156]N. Makri, 'Quantum dissipative dynamics: A numerically exact methodology', The Journal of Physical Chemistry A **102**, 4414–4427 (1998).

[157]L. Diósi, N. Gisin, and W. T. Strunz, 'Non-Markovian quantum state diffusion', Phys. Rev. A **58**, 1699–1712 (1998).

[158]D. Alonso and I. de Vega, 'Multiple-time correlation functions for non-Markovian interaction: Beyond the quantum regression theorem', Phys. Rev. Lett. **94**, 200403 (2005).

[159] Y. Tanimura, 'Real-time and imaginary-time quantum hierarchal Fokker-Planck equations', The Journal of Chemical Physics **142**, 144110 (2015).

[160] C.-Y. Hsieh and J. Cao, 'A unified stochastic formulation of dissipative quantum dynamics. I. Generalized hierarchical equations', The Journal of Chemical Physics **148**, 014103 (2018).

[161] J. Prior, A. W. Chin, S. F. Huelga, and M. B. Plenio, 'Efficient simulation of strong system-environment interactions', Phys. Rev. Lett. **105**, 050404 (2010).

[162] I. de Vega and M.-C. Bañuls, 'Thermofield-based chain-mapping approach for open quantum systems', Phys. Rev. A **92**, 052116 (2015).

[163] L. Mühlbacher, C. J. C. Escher, and J. Ankerhold, 'Real-time Monte-Carlo simulations for dissipative tight-binding systems and time local master equations', Chemical Physics **322**, Real-time dynamics in complex quantum systems in honour of Phil Pechukas, 200–209 (2006).

[164] L. Pollet, 'Recent developments in quantum Monte Carlo simulations with applications for cold gases', Reports on Progress in Physics **75**, 094501 (2012).

[165] U. Schollwöck, 'The density-matrix renormalization group', Rev. Mod. Phys. **77**, 259–315 (2005).

[166] U. Schollwöck, 'The density-matrix renormalization group in the age of matrix product states', Annals of Physics **326**, 96–192 (2011).

[167] F. Cosco, M. Borrelli, J. J. Mendoza-Arenas, F. Plastina, D. Jaksch, and S. Maniscalco, 'Bose-Hubbard lattice as a controllable environment for open quantum systems', Phys. Rev. A **97**, 040101 (2018).

[168] M. Bramberger and I. De Vega, 'Dephasing dynamics of an impurity coupled to an anharmonic environment', Phys. Rev. A **101**, 012101 (2020).

[169] M. Streif, A. Buchleitner, D. Jaksch, and J. Mur-Petit, 'Measuring correlations of cold-atom systems using multiple quantum probes', Phys. Rev. A **94**, 053634 (2016).

[170] A. Kantian, U. Schollwöck, and T. Giamarchi, 'Lattice-assisted spectroscopy: A generalized scanning tunneling microscope for ultracold atoms', Phys. Rev. Lett. **115**, 165301 (2015).

[171] M. T. Mitchison, T. H. Johnson, and D. Jaksch, 'Probing the dynamic structure factor of a neutral Fermi superfluid along the BCS-BEC crossover using atomic impurity qubits', Phys. Rev. A **94**, 063618 (2016).

[172] G. L. Giorgi, S. Longhi, A. Cabot, and R. Zambrini, 'Quantum probing topological phase transitions by non-Markovianity', Annalen der Physik **531**, 1900307 (2019).

[173] S. Vardhan, G. De Tomasi, M. Heyl, E. J. Heller, and F. Pollmann, 'Characterizing time irreversibility in disordered fermionic systems by the effect of local perturbations', Phys. Rev. Lett. **119**, 016802 (2017).

[174] D. Rossini, T. Calarco, V. Giovannetti, S. Montangero, and R. Fazio, 'Decoherence induced by interacting quantum spin baths', Phys. Rev. A **75**, 032333 (2007).

[175] G.-L. Ingold, 'Path integrals and their application to dissipative quantum systems', in *Coherent evolution in noisy environments* (Springer Berlin, Heidelberg, 2002), pp. 1–53.

[176] A. Recati, P. O. Fedichev, W. Zwerger, J. von Delft, and P. Zoller, 'Atomic quantum dots coupled to a reservoir of a superfluid Bose-Einstein condensate', Phys. Rev. Lett. **94**, 040404 (2005).

[177] R. Doll, D. Zueco, M. Wubs, S. Kohler, and P. Hänggi, 'On the conundrum of deriving exact solutions from approximate master equations', Chemical Physics **347**, 243–249 (2008).

[178] H.-P. Breuer, E.-M. Laine, and J. Piilo, 'Measure for the degree of non-Markovian behavior of quantum processes in open systems', Phys. Rev. Lett. **103**, 210401 (2009).

[179] M. J. W. Hall, J. D. Cresser, L. Li, and E. Andersson, 'Canonical form of master equations and characterization of non-Markovianity', Phys. Rev. A **89**, 042120 (2014).

[180] P. Haikka, J. Goold, S. McEndoo, F. Plastina, and S. Maniscalco, 'Non-Markovianity, Loschmidt echo, and criticality: A unified picture', Phys. Rev. A **85**, 060101 (2012).

[181] P. Haikka, S. McEndoo, G. De Chiara, G. M. Palma, and S. Maniscalco, 'Quantifying, characterizing, and controlling information flow in ultracold atomic gases', Phys. Rev. A **84**, 031602 (2011).

[182] P. Haikka, T. H. Johnson, and S. Maniscalco, 'Non-Markovianity of local dephasing channels and time-invariant discord', Phys. Rev. A **87**, 010103 (2013).

[183] H.-P. Breuer, E.-M. Laine, J. Piilo, and B. Vacchini, 'Colloquium: Non-Markovian dynamics in open quantum systems', Rev. Mod. Phys. **88**, 021002 (2016).

[184] T. J. G. Apollaro, S. Lorenzo, C. Di Franco, F. Plastina, and M. Paternostro, 'Competition between memory-keeping and memory-erasing decoherence channels', Phys. Rev. A **90**, 012310 (2014).

[185] A. Peres, 'Stability of quantum motion in chaotic and regular systems', Phys. Rev. A **30**, 1610–1615 (1984).

[186] U. Weiss, *Quantum dissipative systems* (World Scientific, 2011).

[187] F. Cosco and S. Maniscalco, 'Memory effects in a quasiperiodic Fermi lattice', Phys. Rev. A **98**, 053608 (2018).

[188] N. Lambert, S. Ahmed, M. Cirio, and F. Nori, 'Modelling the ultra-strongly coupled spin-boson model with unphysical modes', Nature Communications **10**, 3721 (2019).

[189] C. Franchini, M. Reticcioli, M. Setvin, and U. Diebold, 'Polarons in materials', Nature Reviews Materials **6**, 560–586 (2021).

[190] J. Bardeen, G. Baym, and D. Pines, 'Effective interaction of He^3 atoms in dilute solutions of He^3 in He^4 at low temperatures', Phys. Rev. **156**, 207–221 (1967).

[191] M. Kutschera and W. Wójcik, 'Proton impurity in the neutron matter: A nuclear polaron problem', Phys. Rev. C **47**, 1077–1085 (1993).

[192] F. Scazza, M. Zaccanti, P. Massignan, M. M. Parish, and J. Levinsen, 'Repulsive Fermi and Bose polarons in quantum gases', Atoms **10**, 10.3390/atoms10020055 (2022).

[193] C. Chin, R. Grimm, P. Julienne, and E. Tiesinga, 'Feshbach resonances in ultracold gases', Rev. Mod. Phys. **82**, 1225–1286 (2010).

[194] A. Schirotzek, C.-H. Wu, A. Sommer, and M. W. Zwierlein, 'Observation of fermi polarons in a tunable fermi liquid of ultracold atoms', Phys. Rev. Lett. **102**, 230402 (2009).

[195] S. Nascimbène, N. Navon, K. J. Jiang, L. Tarruell, M. Teichmann, J. McKeever, F. Chevy, and C. Salomon, 'Collective oscillations of an imbalanced fermi gas: axial compression modes and polaron effective mass', Phys. Rev. Lett. **103**, 170402 (2009).

[196] M.-G. Hu, M. J. Van de Graaff, D. Kedar, J. P. Corson, E. A. Cornell, and D. S. Jin, 'Bose polarons in the strongly interacting regime', Phys. Rev. Lett. **117**, 055301 (2016).

[197] N. B. Jørgensen, L. Wacker, K. T. Skalmstang, M. M. Parish, J. Levinsen, R. S. Christensen, G. M. Bruun, and J. J. Arlt, 'Observation of attractive and repulsive polarons in a Bose-Einstein condensate', Phys. Rev. Lett. **117**, 055302 (2016).

[198] I. Bloch, J. Dalibard, and S. Nascimbène, 'Quantum simulations with ultracold quantum gases', Nature Physics **8**, 267–276 (2012).

[199] I. M. Georgescu, S. Ashhab, and F. Nori, 'Quantum simulation', Rev. Mod. Phys. **86**, 153–185 (2014).

[200] A. S. Alexandrov and N. F. Mott, 'Bipolarons', Reports on Progress in Physics **57**, 1197–1288 (1994).

[201] A. S. Alexandrov, 'Unconventional pairing symmetry of layered superconductors caused by acoustic phonons', Phys. Rev. B **77**, 094502 (2008).

[202] J. P. F. LeBlanc, A. E. Antipov, F. Becca, I. W. Bulik, G. K.-L. Chan, C.-M. Chung, Y. Deng, M. Ferrero, T. M. Henderson, C. A. Jiménez-Hoyos, E. Kozik, X.-W. Liu, A. J. Millis, N. V. Prokof'ev, M. Qin, G. E. Scuseria, H. Shi, B. V. Svistunov, L. F. Tocchio, I. S. Tupitsyn, S. R. White, S. Zhang, B.-X. Zheng, Z. Zhu, and E. Gull (Simons Collaboration on the Many-Electron Problem), 'Solutions of the two-dimensional Hubbard model: Benchmarks and results from a wide range of numerical algorithms', Phys. Rev. X **5**, 041041 (2015).

[203] Z. Z. Yan, Y. Ni, C. Robens, and M. W. Zwierlein, 'Bose polarons near quantum criticality', Science **368**, 190–194 (2020).

[204] R. Alhyder and G. M. Bruun, 'Mobile impurity probing a two-dimensional superfluid phase transition', Phys. Rev. A **105**, 063303 (2022).

[205] D. Rossini, T. Calarco, V. Giovannetti, S. Montangero, and R. Fazio, 'Decoherence induced by interacting quantum spin baths', Phys. Rev. A **75**, 032333 (2007).

[206] Y. E. Shchadilova, R. Schmidt, F. Grusdt, and E. Demler, 'Quantum dynamics of ultracold Bose polarons', Phys. Rev. Lett. **117**, 113002 (2016).

[207] S. M. Yoshida, S. Endo, J. Levinsen, and M. M. Parish, 'Universality of an impurity in a Bose-Einstein condensate', Phys. Rev. X **8**, 011024 (2018).

[208] J. Levinsen, M. M. Parish, and G. M. Bruun, 'Impurity in a Bose-Einstein condensate and the Efimov effect', Phys. Rev. Lett. **115**, 125302 (2015).

[209] A. Christianen, J. I. Cirac, and R. Schmidt, 'Chemistry of a light impurity in a Bose-Einstein condensate', Phys. Rev. Lett. **128**, 183401 (2022).

[210] A. Christianen, J. I. Cirac, and R. Schmidt, 'Bose polaron and the Efimov effect: A Gaussian-state approach', Phys. Rev. A **105**, 053302 (2022).

[211] M. Sun, H. Zhai, and X. Cui, 'Visualizing the Efimov correlation in Bose polarons', Phys. Rev. Lett. **119**, 013401 (2017).

[212] L. A. P. Ardila and S. Giorgini, 'Impurity in a Bose-Einstein condensate: Study of the attractive and repulsive branch using quantum Monte Carlo methods', Phys. Rev. A **92**, 033612 (2015).

[213] F. Grusdt, A. Shashi, D. Abanin, and E. Demler, 'Bloch oscillations of bosonic lattice polarons', Phys. Rev. A **90**, 063610 (2014).

[214] M. Bruderer, A. Klein, S. R. Clark, and D. Jaksch, 'Polaron physics in optical lattices', Phys. Rev. A **76**, 011605 (2007).

[215] D. Benjamin and E. Demler, 'Variational polaron method for Bose-Bose mixtures', Phys. Rev. A **89**, 033615 (2014).

[216] Y. Kato, K. A. Al-Hassanieh, A. E. Feiguin, E. Timmermans, and C. D. Batista, 'Novel polaron state for single impurity in a bosonic Mott insulator', EPL (Europhysics Letters) **98**, 46003 (2012).

[217] S. Dutta and E. J. Mueller, 'Variational study of polarons and bipolarons in a one-dimensional Bose lattice gas in both the superfluid and the Mott-insulator regimes', Phys. Rev. A **88**, 053601 (2013).

[218] H. Fröhlich, 'Electrons in lattice fields', Advances in Physics **3**, 325–361 (1954).

[219] F. Grusdt and E. Demler, 'New theoretical approaches to Bose polarons', Quantum Matter at Ultralow Temperatures **191**, 325 (2015).

[220] F. Caleffi, M. Capone, I. de Vega, and A. Recati, 'Impurity dephasing in a Bose-Hubbard model', New Journal of Physics **23**, 033018 (2021).

[221] R. Combescot, A. Recati, C. Lobo, and F. Chevy, 'Normal state of highly polarized Fermi gases: Simple many-body approaches', Phys. Rev. Lett. **98**, 180402 (2007).

[222] J. Catani, G. Lamporesi, D. Naik, M. Gring, M. Inguscio, F. Minardi, A. Kantian, and T. Giamarchi, 'Quantum dynamics of impurities in a one-dimensional Bose gas', Phys. Rev. A **85**, 023623 (2012).

[223] M. G. Skou, T. G. Skov, N. B. Jørgensen, K. K. Nielsen, A. Camacho-Guardian, T. Pohl, G. M. Bruun, and J. J. Arlt, 'Non-equilibrium quantum dynamics and formation of the Bose polaron', Nature Physics **17**, 731–735 (2021).

[224] M. G. Skou, K. K. Nielsen, T. G. Skov, A. M. Morgen, N. B. Jørgensen, A. Camacho-Guardian, T. Pohl, G. M. Bruun, and J. J. Arlt, 'Life and death of the Bose polaron', arXiv **2204**, 01424 (2022).

[225] C. J. Vale and M. Zwierlein, 'Spectroscopic probes of quantum gases', Nature Physics **17**, 1305–1315 (2021).

[226] T. Rice, 'The effects of electron-electron interaction on the properties of metals', Annals of Physics **31**, 100–129 (1965).

[227] Y. Zhang and S. Das Sarma, 'Quasiparticle effective-mass divergence in two-dimensional electron systems', Phys. Rev. B **71**, 045322 (2005).

[228] S. Ahn and S. Das Sarma, 'Anisotropic fermionic quasiparticles', Phys. Rev. B **103**, 045303 (2021).

[229] G. E. Astrakharchik and L. P. Pitaevskii, 'Motion of a heavy impurity through a Bose-Einstein condensate', Phys. Rev. A **70**, 013608 (2004).

[230] A. Novikov and M. Ovchinnikov, 'A diagrammatic calculation of the energy spectrum of quantum impurity in degenerate Bose-Einstein condensate', Journal of Physics A: Mathematical and Theoretical **42**, 135301 (2009).

[231] F. Grusdt, G. E. Astrakharchik, and E. Demler, 'Bose polarons in ultracold atoms in one dimension: Beyond the Fröhlich paradigm', New Journal of Physics **19**, 103035 (2017).

[232] F. Grusdt, K. Seetharam, Y. Shchadilova, and E. Demler, 'Strong-coupling Bose polarons out of equilibrium: Dynamical renormalization-group approach', Phys. Rev. A **97**, 033612 (2018).

[233] A. Lampo, S. H. Lim, M. Á. García-March, and M. Lewenstein, 'Bose polaron as an instance of quantum Brownian motion', Quantum **1**, 30 (2017).

[234] P. W. Anderson, 'Infrared catastrophe in Fermi gases with local scattering potentials', Phys. Rev. Lett. **18**, 1049–1051 (1967).

[235] N.-E. Guenther, R. Schmidt, G. M. Bruun, V. Gurarie, and P. Massignan, 'Mobile impurity in a Bose-Einstein condensate and the orthogonality catastrophe', Phys. Rev. A **103**, 013317 (2021).

[236] J. Sun, O. Rambow, and Q. Si, 'Orthogonality catastrophe in Bose-Einstein condensates', arXiv **04**, 04590 (2004).

[237] J. Goold, T. Fogarty, N. Lo Gullo, M. Paternostro, and T. Busch, 'Orthogonality catastrophe as a consequence of qubit embedding in an ultracold Fermi gas', Phys. Rev. A **84**, 063632 (2011).

[238] M. Knap, A. Shashi, Y. Nishida, A. Imambekov, D. A. Abanin, and E. Demler, 'Time-dependent impurity in ultracold fermions: Orthogonality catastrophe and beyond', Phys. Rev. X **2**, 041020 (2012).

239 W. E. Liu, J. Levinsen, and M. M. Parish, 'Variational approach for impurity dynamics at finite temperature', Phys. Rev. Lett. **122**, 205301 (2019).

240 H. S. Adlong, W. E. Liu, F. Scazza, M. Zaccanti, N. D. Oppong, S. Fölling, M. M. Parish, and J. Levinsen, 'Quasiparticle lifetime of the repulsive Fermi polaron', Phys. Rev. Lett. **125**, 133401 (2020).

241 M. M. Parish and J. Levinsen, 'Quantum dynamics of impurities coupled to a Fermi sea', Phys. Rev. B **94**, 184303 (2016).

242 M. Cetina, M. Jag, R. S. Lous, I. Fritsche, J. T. M. Walraven, R. Grimm, J. Levinsen, M. M. Parish, R. Schmidt, M. Knap, and E. Demler, 'Ultrafast many-body interferometry of impurities coupled to a fermi sea', Science **354**, 96–99 (2016).

243 G. Ji, M. Xu, L. H. Kendrick, C. S. Chiu, J. C. Brüggenjürgen, D. Greif, A. Bohrdt, F. Grusdt, E. Demler, M. Lebrat, and M. Greiner, 'Coupling a mobile hole to an antiferromagnetic spin background: Transient dynamics of a magnetic polaron', Phys. Rev. X **11**, 021022 (2021).

244 P. Massignan, M. Zaccanti, and G. M. Bruun, 'Polarons, dressed molecules and itinerant ferromagnetism in ultracold Fermi gases', Reports on Progress in Physics **77**, 034401 (2014).

245 C. Wu, H.-d. Chen, J.-p. Hu, and S.-C. Zhang, 'Vortex configurations of bosons in an optical lattice', Phys. Rev. A **69**, 043609 (2004).

246 K. V. Krutitsky, J. Larson, and M. Lewenstein, 'Dark solitons near the Mott-insulator–superfluid phase transition', Phys. Rev. A **82**, 033618 (2010).

247 S. Trotzky, L. Pollet, F. Gerbier, U. Schnorrberger, I. Bloch, N. V. Prokof'ev, B. Svistunov, and M. Troyer, 'Suppression of the critical temperature for superfluidity near the Mott transition', Nature Physics **6**, 998–1004 (2010).

248 S. Badoux, W. Tabis, F. Laliberté, G. Grissonnanche, B. Vignolle, D. Vignolles, J. Béard, D. A. Bonn, W. N. Hardy, R. Liang, N. Doiron-Leyraud, L. Taillefer, and C. Proust, 'Change of carrier density at the pseudogap critical point of a cuprate superconductor', Nature **531**, 210–214 (2016).

249 C. Giannetti, F. Cilento, S. D. Conte, G. Coslovich, G. Ferrini, H. Molegraaf, M. Raichle, R. Liang, H. Eisaki, M. Greven, A. Damascelli, D. van der Marel, and F. Parmigiani, 'Revealing the high-energy electronic excitations underlying the onset of high-temperature superconductivity in cuprates', Nature Communications **2**, 353 (2011).

250 A. Brunello, F. Dalfovo, L. Pitaevskii, and S. Stringari, 'How to measure the Bogoliubov quasiparticle amplitudes in a trapped condensate', Phys. Rev. Lett. **85**, 4422–4425 (2000).

251 J. M. Vogels, K. Xu, C. Raman, J. R. Abo-Shaeer, and W. Ketterle, 'Experimental observation of the Bogoliubov transformation for a Bose-Einstein condensed gas', Phys. Rev. Lett. **88**, 060402 (2002).

252 T.-L. Dao, A. Georges, J. Dalibard, C. Salomon, and I. Carusotto, 'Measuring the one-particle excitations of ultracold fermionic atoms by stimulated Raman spectroscopy', Phys. Rev. Lett. **98**, 240402 (2007).

253 T.-L. Dao, I. Carusotto, and A. Georges, 'Probing quasiparticle states in strongly interacting atomic gases by momentum-resolved Raman photoemission spectroscopy', Phys. Rev. A **80**, 023627 (2009).

254 J. T. Stewart, J. P. Gaebler, and D. S. Jin, 'Using photoemission spectroscopy to probe a strongly interacting Fermi gas', Nature **454**, 744–747 (2008).

255 H. Fehske, J. Loos, and G. Wellein, 'Lattice polaron formation: Effects of nonscreened electron-phonon interaction', Phys. Rev. B **61**, 8016–8025 (2000).

256 E. Cappelluti and S. Ciuchi, 'Magnetic and lattice polaron in the Holstein $t - J$ model', Phys. Rev. B **66**, 165102 (2002).

[257] E. Cappelluti, S. Ciuchi, and S. Fratini, 'Polaronic features in the optical properties of the Holstein $t-J$ model', Phys. Rev. B **76**, 125111 (2007).

[258] A. Privitera and W. Hofstetter, 'Polaronic slowing of fermionic impurities in lattice Bose-Fermi mixtures', Phys. Rev. A **82**, 063614 (2010).

[259] H. Tajima, J. Takahashi, S. I. Mistakidis, E. Nakano, and K. Iida, 'Polaron problems in ultracold atoms: Role of a Fermi sea across different spatial dimensions and quantum fluctuations of a Bose medium', Atoms **9**, 18 (2021).

[260] S. Bour, D. Lee, H.-W. Hammer, and U.-G. Meißner, 'Ab initio lattice results for Fermi polarons in two dimensions', Phys. Rev. Lett. **115**, 185301 (2015).

[261] H. Hu, A.-B. Wang, S. Yi, and X.-J. Liu, 'Fermi polaron in a one-dimensional quasiperiodic optical lattice: The simplest many-body localization challenge', Phys. Rev. A **93**, 053601 (2016).

[262] R. Liu, Y.-R. Shi, and W. Zhang, 'Non-gaussian variational approach to fermi polarons in one- and two-dimensional lattices', Phys. Rev. A **102**, 033305 (2020).

[263] A. Vashisht, M. Richard, and A. Minguzzi, 'Bose polaron in a quantum fluid of light', SciPost Phys. **12**, 8 (2022).

[264] M. Will, G. E. Astrakharchik, and M. Fleischhauer, 'Polaron interactions and bipolarons in one-dimensional Bose gases in the strong coupling regime', Phys. Rev. Lett. **127**, 103401 (2021).

[265] A. Petković and Z. Ristivojevic, 'Mediated interaction between polarons in a one-dimensional Bose gas', Phys. Rev. A **105**, L021303 (2022).

[266] P. Naidon, 'Two impurities in a Bose–Einstein condensate: From Yukawa to Efimov attracted polarons', Journal of the Physical Society of Japan **87**, 043002 (2018).

[267] A. S. Alexandrov, 'A bipolaron Bose liquid in high-T_c superconductors', in *Polarons and bipolarons in high-T_c superconductors and related materials*, edited by E. K. H. Salje, A. S. Alexandrov, and W. Y. Liang (Cambridge University Press, 1995), pp. 26–44.

[268] M. Capone, P. Carta, and S. Ciuchi, 'Dynamical mean field theory of polarons and bipolarons in the half-filled Holstein model', Phys. Rev. B **74**, 045106 (2006).

[269] A. Camacho-Guardian, L. A. Peña Ardila, T. Pohl, and G. M. Bruun, 'Bipolarons in a Bose-Einstein condensate', Phys. Rev. Lett. **121**, 013401 (2018).

[270] L. A. P. Ardila, 'Ultra-dilute gas of polarons in a Bose-Einstein condensate', Atoms **10**, 29 (2022).

[271] J. Hubbard, 'Electron correlations in narrow energy bands', Proceedings of the Royal Society of London. Series A. Mathematical and Physical Sciences **276**, 238–257 (1963).

[272] J. Hubbard, 'Electron correlations in narrow energy bands III. An improved solution', Proceedings of the Royal Society of London. Series A. Mathematical and Physical Sciences **281**, 401–419 (1964).

[273] L. D. Landau, 'The theory of a Fermi liquid', Sov. Phys. JETP, 920 (1956).

[274] D. Bohm and D. Pines, 'A collective description of electron interactions: I. Magnetic interactions', Phys. Rev. **82**, 625–634 (1951).

[275] D. Pines and D. Bohm, 'A collective description of electron interactions: II. Collective vs individual particle aspects of the interactions', Phys. Rev. **85**, 338–353 (1952).

[276] D. Bohm and D. Pines, 'A collective description of electron interactions: iii. coulomb interactions in a degenerate electron gas', Phys. Rev. **92**, 609–625 (1953).

[277] P. Nozières and P. Pines, *Theory of quantum liquids*, 1st ed. (Westview Press, 1999).

[278] A. Georges, G. Kotliar, W. Krauth, and M. J. Rozenberg, 'Dynamical mean-field theory of strongly correlated fermion systems and the limit of infinite dimensions', Rev. Mod. Phys. **68**, 13–125 (1996).

[279] D. Bormann, T. Schneider, and M. Frick, 'Finite-size effects in the two-dimensional negative-U hubbard model', Europhysics Letters (EPL) **14**, 101–106 (1991).

[280] B. I. Shraiman and E. D. Siggia, 'Spiral phase of a doped quantum antiferromagnet', Phys. Rev. Lett. **62**, 1564–1567 (1989).

[281] H. J. Schulz, 'Incommensurate antiferromagnetism in the two-dimensional Hubbard model', Phys. Rev. Lett. **64**, 1445–1448 (1990).

[282] S. A. Kivelson, E. Fradkin, and V. J. Emery, 'Electronic liquid-crystal phases of a doped Mott insulator', Nature **393**, 550–553 (1998).

[283] G. Seibold and J. Lorenzana, 'Magnetic fluctuations of stripes in the high temperature cuprate superconductors', Phys. Rev. Lett. **94**, 107006 (2005).

[284] C.-C. Chang and S. Zhang, 'Spin and charge order in the doped Hubbard model: Long-wavelength collective modes', Phys. Rev. Lett. **104**, 116402 (2010).

[285] J. Lorenzana and G. Seibold, 'Metallic mean-field stripes, incommensurability, and chemical potential in cuprates', Phys. Rev. Lett. **89**, 136401 (2002).

[286] J. Lorenzana and G. Seibold, 'Dynamics of metallic stripes in cuprates', Phys. Rev. Lett. **90**, 066404 (2003).

[287] P. Corboz, T. M. Rice, and M. Troyer, 'Competing states in the t-J model: Uniform d-wave state versus stripe state', Phys. Rev. Lett. **113**, 046402 (2014).

[288] G. Kotliar and A. E. Ruckenstein, 'New functional integral approach to strongly correlated Fermi systems: The Gutzwiller approximation as a saddle point', Phys. Rev. Lett. **57**, 1362–1365 (1986).

[289] T. Li, P. Wölfle, and P. J. Hirschfeld, 'Spin-rotation-invariant slave-boson approach to the Hubbard model', Phys. Rev. B **40**, 6817–6821 (1989).

[290] R. Frésard and P. Wölfle, 'Unified slave boson representation of spin and charge degrees of freedom for strongly correlated fermi systems', International Journal of Modern Physics B **06**, 685–704 (1992).

[291] W. Metzner and D. Vollhardt, 'Correlated lattice fermions in $d = \infty$ dimensions', Phys. Rev. Lett. **62**, 324–327 (1989).

[292] J. Bünemann and F. Gebhard, 'Equivalence of Gutzwiller and slave-boson mean-field theories for multiband Hubbard models', Phys. Rev. B **76**, 193104 (2007).

[293] C. Attaccalite and M. Fabrizio, 'Properties of Gutzwiller wave functions for multiband models', Phys. Rev. B **68**, 155117 (2003).

[294] J. Bünemann, W. Weber, and F. Gebhard, 'Multiband Gutzwiller wave functions for general on-site interactions', Phys. Rev. B **57**, 6896–6916 (1998).

[295] J. Bünemann, F. Gebhard, K. Radnóczi, and P. Fazekas, 'Gutzwiller variational theory for the Hubbard model with attractive interaction', Journal of Physics: Condensed Matter **17**, 3807–3814 (2005).

[296] M. Schirò and M. Fabrizio, 'Quantum quenches in the Hubbard model: time-dependent mean-field theory and the role of quantum fluctuations', Phys. Rev. B **83**, 165105 (2011).

[297] N. Lanatà, Y. Yao, C.-Z. Wang, K.-M. Ho, and G. Kotliar, 'Phase diagram and electronic structure of praseodymium and plutonium', Phys. Rev. X **5**, 011008 (2015).

[298] S. Peng, H. Weng, and X. Dai, 'RTGW2020: A powerful implementation of DFT + Gutzwiller method', arXiv **2111**, 09166 (2021).

[299] M. Schirò and M. Fabrizio, 'Time-dependent mean field theory for quench dynamics in correlated electron systems', Phys. Rev. Lett. **105**, 076401 (2010).

[300] M. Fabrizio, 'The out-of-equilibrium time-dependent Gutzwiller approximation', in *New materials for thermoelectric applications: Theory and experiment*, edited by V. Zlatic and A. Hewson, NATO Science for Peace and Security Series B: Physics and Biophysics New Materials for Thermoelectric Applications: Theory and Experiment (Springer Netherlands, 2013), pp. 247–273.

[301] G. Seibold and J. Lorenzana, 'Time-dependent Gutzwiller approximation for the Hubbard model', Phys. Rev. Lett. **86**, 2605–2608 (2001).

[302] G. Mazza and M. Fabrizio, 'Dynamical quantum phase transitions and broken-symmetry edges in the many-body eigenvalue spectrum', Phys. Rev. B **86**, 184303 (2012).

[303] M. Sandri and M. Fabrizio, 'Nonequilibrium dynamics in the antiferromagnetic Hubbard model', Phys. Rev. B **88**, 165113 (2013).

[304] M. Fabrizio, 'Gutzwiller description of non-magnetic Mott insulators: dimer lattice model', Phys. Rev. B **76**, 165110 (2007).

[305] F. Lechermann, A. Georges, G. Kotliar, and O. Parcollet, 'Rotationally invariant slave-boson formalism and momentum dependence of the quasiparticle weight', Phys. Rev. B **76**, 155102 (2007).

[306] A. Isidori and M. Capone, 'Rotationally invariant slave bosons for strongly correlated superconductors', Phys. Rev. B **80**, 115120 (2009).

[307] G. Seibold, F. Becca, P. Rubin, and J. Lorenzana, 'Time-dependent Gutzwiller theory of magnetic excitations in the Hubbard model', Phys. Rev. B **69**, 155113 (2004).

[308] J. Bünemann, M. Capone, J. Lorenzana, and G. Seibold, 'Linear-response dynamics from the time-dependent Gutzwiller approximation', New Journal of Physics **15**, 053050 (2013).

[309] M. Sandri, M. Schirò, and M. Fabrizio, 'Linear ramps of interaction in the fermionic Hubbard model', Phys. Rev. B **86**, 075122 (2012).

[310] G. Mazza, A. Amaricci, M. Capone, and M. Fabrizio, 'Electronic transport and dynamics in correlated heterostructures', Phys. Rev. B **91**, 195124 (2015).

[311] G. Seibold, F. Becca, and J. Lorenzana, 'Inhomogeneous Gutzwiller approximation with random phase fluctuations for the Hubbard model', Phys. Rev. B **67**, 085108 (2003).

[312] W. F. Brinkman and T. M. Rice, 'Application of Gutzwiller's variational method to the metal-insulator transition', Phys. Rev. B **2**, 4302–4304 (1970).

[313] V. H. Dao and R. Frésard, 'Collective modes in the paramagnetic phase of the Hubbard model', Phys. Rev. B **95**, 165127 (2017).

[314] L. de' Medici, A. Georges, and S. Biermann, 'Orbital-selective Mott transition in multiband systems: slave-spin representation and dynamical mean-field theory', Phys. Rev. B **72**, 205124 (2005).

[315] S. D. Huber and A. Rüegg, 'Dynamically generated double occupancy as a probe of cold atom systems', Phys. Rev. Lett. **102**, 065301 (2009).

[316] A. Rüegg, S. D. Huber, and M. Sigrist, 'Z_2-slave-spin theory for strongly correlated fermions', Phys. Rev. B **81**, 155118 (2010).

[317] S. R. Hassan and L. de' Medici, 'Slave spins away from half filling: Cluster mean-field theory of the Hubbard and extended Hubbard models', Phys. Rev. B **81**, 035106 (2010).

[318]S. Zhou, Y. Wang, and Z. Wang, 'Doublon-holon binding, Mott transition, and fractionalized antiferromagnet in the Hubbard model', Phys. Rev. B **89**, 195119 (2014).

[319]P. Prelovšek, J. Kokalj, Z. Lenarčič, and R. H. McKenzie, 'Holon-doublon binding as the mechanism for the Mott transition', Phys. Rev. B **92**, 235155 (2015).

[320]R. G. Leigh and P. Phillips, 'Origin of the Mott gap', Phys. Rev. B **79**, 245120 (2009).

[321]R. Yu and Q. Si, '$U(1)$ slave-spin theory and its application to Mott transition in a multiorbital model for iron pnictides', Phys. Rev. B **86**, 085104 (2012).

[322]R. Bulla, 'Zero temperature metal-insulator transition in the infinite-dimensional Hubbard model', Phys. Rev. Lett. **83**, 136–139 (1999).

[323]T. Schäfer, G. Rohringer, O. Gunnarsson, S. Ciuchi, G. Sangiovanni, and A. Toschi, 'Divergent precursors of the Mott-Hubbard transition at the two-particle level', Phys. Rev. Lett. **110**, 246405 (2013).

[324]H. Park, K. Haule, and G. Kotliar, 'Cluster dynamical mean field theory of the Mott transition', Phys. Rev. Lett. **101**, 186403 (2008).

[325]C. Walsh, P. Sémon, G. Sordi, and A.-M. S. Tremblay, 'Critical opalescence across the doping-driven Mott transition in optical lattices of ultracold atoms', Phys. Rev. B **99**, 165151 (2019).

[326]R. Raimondi and C. Castellani, 'Lower and upper Hubbard bands: a slave-boson treatment', Phys. Rev. B **48**, 11453–11456 (1993).

[327]S. Florens and A. Georges, 'Quantum impurity solvers using a slave rotor representation', Phys. Rev. B **66**, 165111 (2002).

[328]R. Frésard, H. Ouerdane, and T. Kopp, 'Slave bosons in radial gauge: A bridge between path integral and Hamiltonian language', Nuclear Physics B **785**, 286–306 (2007).

[329]R. Frésard and V. H. Dao, 'Charge instabilities of the extended attractive Hubbard model on the cubic lattice', Modern Physics Letters B **34**, 2040050 (2020).

[330]D. Riegler, M. Klett, T. Neupert, R. Thomale, and P. Wölfle, 'Slave-boson analysis of the two-dimensional Hubbard model', Phys. Rev. B **101**, 235137 (2020).

[331]E. Arrigoni and G. C. Strinati, 'Beyond the Gutzwiller approximation in the slave-boson approach: Inclusion of fluctuations with the correct continuum limit of the functional integral', Phys. Rev. Lett. **71**, 3178–3181 (1993).

[332]E. Arrigoni and G. C. Strinati, 'Correct continuum limit of the functional-integral representation for the four-slave-boson approach to the Hubbard model: Paramagnetic phase', Phys. Rev. B **52**, 2428–2462 (1995).

[333]M. Potthoff, M. Aichhorn, and C. Dahnken, 'Variational cluster approach to correlated electron systems in low dimensions', Phys. Rev. Lett. **91**, 206402 (2003).

[334]O. Parcollet, G. Biroli, and G. Kotliar, 'Cluster dynamical mean field analysis of the Mott transition', Phys. Rev. Lett. **92**, 226402 (2004).

[335]Y. Z. Zhang and M. Imada, 'Pseudogap and Mott transition studied by cellular dynamical mean-field theory', Phys. Rev. B **76**, 045108 (2007).

[336]A. Toschi, A. A. Katanin, and K. Held, 'Dynamical vertex approximation: A step beyond dynamical mean-field theory', Phys. Rev. B **75**, 045118 (2007).

[337]G. Rohringer, H. Hafermann, A. Toschi, A. A. Katanin, A. E. Antipov, M. I. Katsnelson, A. I. Lichtenstein, A. N. Rubtsov, and K. Held, 'Diagrammatic routes to nonlocal correlations beyond dynamical mean field theory', Rev. Mod. Phys. **90**, 025003 (2018).

[338]L. Del Re, M. Capone, and A. Toschi, 'Dynamical vertex approximation for the attractive Hubbard model', Phys. Rev. B **99**, 045137 (2019).

[339]H. Hafermann, E. G. C. P. van Loon, M. I. Katsnelson, A. I. Lichtenstein, and O. Parcollet, 'Collective charge excitations of strongly correlated electrons, vertex corrections, and gauge invariance', Phys. Rev. B **90**, 235105 (2014).

[340]N. Lanatà, H. U. R. Strand, X. Dai, and B. Hellsing, 'Efficient implementation of the Gutzwiller variational method', Phys. Rev. B **85**, 035133 (2012).

[341]J. C. Budich, B. Trauzettel, and G. Sangiovanni, 'Fluctuation-driven topological Hund insulators', Phys. Rev. B **87**, 235104 (2013).

[342]P. Thunström, O. Gunnarsson, S. Ciuchi, and G. Rohringer, 'Analytical investigation of singularities in two-particle irreducible vertex functions of the Hubbard atom', Phys. Rev. B **98**, 235107 (2018).

[343]P. Chalupa, P. Gunacker, T. Schäfer, K. Held, and A. Toschi, 'Divergences of the irreducible vertex functions in correlated metallic systems: Insights from the Anderson impurity model', Phys. Rev. B **97**, 245136 (2018).

[344]F. Krien, E. G. C. P. van Loon, M. I. Katsnelson, A. I. Lichtenstein, and M. Capone, 'Two-particle Fermi liquid parameters at the Mott transition: Vertex divergences, Landau parameters, and incoherent response in dynamical mean-field theory', Phys. Rev. B **99**, 245128 (2019).

[345]M. Reitner, P. Chalupa, L. Del Re, D. Springer, S. Ciuchi, G. Sangiovanni, and A. Toschi, 'Attractive effect of a strong electronic repulsion: The physics of vertex divergences', Phys. Rev. Lett. **125**, 196403 (2020).

[346]N. N. Bogoliubov, *Lectures on quantum statistics*, Lectures on Quantum Statistics Volume 2 (Gordon and Breach, 1970).

[347]N. N. Bogolubov and J. N. N. Bogolubov, *Introduction to quantum statistical mechanics* (World Scientific, Jan. 1982).

[348]T. Frisch, Y. Pomeau, and S. Rica, 'Transition to dissipation in a model of superflow', Phys. Rev. Lett. **69**, 1644–1647 (1992).

[349]I. Carusotto and C. Ciuti, 'Probing microcavity polariton superfluidity through resonant Rayleigh scattering', Phys. Rev. Lett. **93**, 166401 (2004).

[350]A. Amo, J. Lefrère, S. Pigeon, C. Adrados, C. Ciuti, I. Carusotto, R. Houdré, E. Giacobino, and A. Bramati, 'Superfluidity of polaritons in semiconductor microcavities', Nature Physics **5**, 805–810 (2009).

[351]G. Nardin, G. Grosso, Y. Léger, B. Piętka, F. Morier-Genoud, and B. Deveaud-Plédran, 'Hydrodynamic nucleation of quantized vortex pairs in a polariton quantum fluid', Nature Physics **7**, 635–641 (2011).

[352]D. Sanvitto, S. Pigeon, A. Amo, D. Ballarini, M. D. Giorgi, I. Carusotto, R. Hivet, F. Pisanello, V. G. Sala, P. S. S. Guimaraes, R. Houdré, E. Giacobino, C. Ciuti, A. Bramati, and G. Gigli, 'All-optical control of the quantum flow of a polariton condensate', Nature Photonics **5**, 610–614 (2011).

[353]W. F. Vinen, 'The detection of single quanta of circulation in liquid helium II', Proceedings of the Royal Society of London. Series A, Mathematical and Physical Sciences **260**, 218–236 (1961).

[354]J. D. Reppy and D. Depatie, 'Persistent currents in superfluid helium', Phys. Rev. Lett. **12**, 187–189 (1964).

355C. Ryu, M. F. Andersen, P. Cladé, V. Natarajan, K. Helmerson, and W. D. Phillips, 'Observation of persistent flow of a Bose-Einstein condensate in a toroidal trap', Phys. Rev. Lett. 99, 260401 (2007).

356M. Wouters and V. Savona, 'Superfluidity of a nonequilibrium Bose-Einstein condensate of polaritons', Phys. Rev. B 81, 054508 (2010).

357A. Ramanathan, K. C. Wright, S. R. Muniz, M. Zelan, W. T. Hill, C. J. Lobb, K. Helmerson, W. D. Phillips, and G. K. Campbell, 'Superflow in a toroidal Bose-Einstein condensate: An atom circuit with a tunable weak link', Phys. Rev. Lett. 106, 130401 (2011).

358L. P. Pitaevskii, '50 years of Landau's theory on superfluidity', Journal of Low Temperature Physics 87, 127–135 (1992).

359A. J. Leggett, 'Superfluidity', Rev. Mod. Phys. 71, S318–S323 (1999).

360L. P. Kadanoff, 'Slippery wave functions', Journal of Statistical Physics 152, 805–823 (2013).

361N. N. Bogoliubov, V. V. Tolmachov, and D. V. Širkov, 'A new method in the theory of superconductivity', Fortschritte der Physik 6, 605–682 (1958).

362R. Haag, 'The mathematical structure of the Bardeen-Cooper-Schrieffer model', Il Nuovo Cimento 25, 287–299 (1962).

363A. Imamoglu, R. J. Ram, S. Pau, and Y. Yamamoto, 'Nonequilibrium condensates and lasers without inversion: Exciton-polariton lasers', Phys. Rev. A 53, 4250–4253 (1996).

364L. S. Dang, D. Heger, R. André, F. Bœuf, and R. Romestain, 'Stimulation of polariton photoluminescence in semiconductor microcavity', Phys. Rev. Lett. 81, 3920–3923 (1998).

365P. Senellart and J. Bloch, 'Nonlinear emission of microcavity polaritons in the low density regime', Phys. Rev. Lett. 82, 1233–1236 (1999).

366P. G. Savvidis, J. J. Baumberg, R. M. Stevenson, M. S. Skolnick, D. M. Whittaker, and J. S. Roberts, 'Angle-resonant stimulated polariton amplifier', Phys. Rev. Lett. 84, 1547–1550 (2000).

367J. Kasprzak, M. Richard, S. Kundermann, A. Baas, P. Jeambrun, J. M. J. Keeling, F. M. Marchetti, M. H. Szymańska, R. André, J. L. Staehli, V. Savona, P. B. Littlewood, B. Deveaud, and L. S. Dang, 'Bose-Einstein condensation of exciton polaritons', Nature 443, 409–414 (2006).

368R. Balili, V. Hartwell, D. Snoke, L. Pfeiffer, and K. West, 'Bose-Einstein condensation of microcavity polaritons in a trap', Science 316, 1007–1010 (2007).

369H. Deng, G. S. Solomon, R. Hey, K. H. Ploog, and Y. Yamamoto, 'Spatial coherence of a polariton condensate', Phys. Rev. Lett. 99, 126403 (2007).

370D. Sarchi and V. Savona, 'Spectrum and thermal fluctuations of a microcavity polariton Bose-Einstein condensate', Phys. Rev. B 77, 045304 (2008).

371J. Baumberg, S. Christopoulos, G. B. H. von Högersthal, A. Grundy, P. Lagoudakis, A. Kavokin, G. Christmann, R. Butté, E. Feltin, J.-F. Carlin, N. Grandjean, D. Solnyshkov, and G. Malpuech, 'Room temperature polariton lasing and BEC in semiconductor microcavities', in Conference on Lasers and Electro-Optics/Quantum Electronics and Laser Science Conference and Photonic Applications Systems Technologies (2008).

372A. Das, P. Bhattacharya, J. Heo, A. Banerjee, and W. Guo, 'Polariton Bose-Einstein condensate at room temperature in an Al(Ga)N nanowire-dielectric microcavity with a spatial potential trap', Proceedings of the National Academy of Sciences 110, 2735–2740 (2013).

373M. Bamba, A. Imamo ğlu, I. Carusotto, and C. Ciuti, 'Origin of strong photon antibunching in weakly nonlinear photonic molecules', Phys. Rev. A 83, 021802 (2011).

[374] I. Carusotto, T. Volz, and A. Imamoğlu, 'Feshbach blockade: Single-photon nonlinear optics using resonantly enhanced cavity polariton scattering from biexciton states', EPL (Europhysics Letters) 90, 37001 (2010).

[375] F. Baboux, L. Ge, T. Jacqmin, M. Biondi, E. Galopin, A. Lemaître, L. Le Gratiet, I. Sagnes, S. Schmidt, H. E. Türeci, A. Amo, and J. Bloch, 'Bosonic condensation and disorder-induced localization in a flat band', Phys. Rev. Lett. 116, 066402 (2016).

[376] Y. Lai and H. A. Haus, 'Quantum theory of solitons in optical fibers. I. Time-dependent Hartree approximation', Phys. Rev. A 40, 844–853 (1989).

[377] Y. Lai and H. A. Haus, 'Quantum theory of solitons in optical fibers. II. Exact solution', Phys. Rev. A 40, 854–866 (1989).

[378] P.-É. Larré and I. Carusotto, 'Propagation of a quantum fluid of light in a cavityless nonlinear optical medium: General theory and response to quantum quenches', Phys. Rev. A 92, 043802 (2015).

[379] D. G. Angelakis, M. F. Santos, and S. Bose, 'Photon-blockade-induced Mott transitions and XY spin models in coupled cavity arrays', Phys. Rev. A 76, 031805 (2007).

[380] M. J. Hartmann, F. G. S. L. Brandão, and M. B. Plenio, 'Strongly interacting polaritons in coupled arrays of cavities', Nature Physics 2, 849–855 (2006).

[381] A. D. Greentree, C. Tahan, J. H. Cole, and L. C. L. Hollenberg, 'Quantum phase transitions of light', Nature Physics 2, 856–861 (2006).

[382] D. Rossini and R. Fazio, 'Mott-insulating and glassy phases of polaritons in 1D arrays of coupled cavities', Phys. Rev. Lett. 99, 186401 (2007).

[383] N. Na, S. Utsunomiya, L. Tian, and Y. Yamamoto, 'Strongly correlated polaritons in a two-dimensional array of photonic crystal microcavities', Phys. Rev. A 77, 031803 (2008).

[384] M. I. Makin, J. H. Cole, C. D. Hill, A. D. Greentree, and L. C. L. Hollenberg, 'Time evolution of the one-dimensional Jaynes-Cummings-Hubbard Hamiltonian', Phys. Rev. A 80, 043842 (2009).

[385] M. J. Hartmann, F. G. S. L. Brandão, and M. B. Plenio, 'Effective spin systems in coupled microcavities', Phys. Rev. Lett. 99, 160501 (2007).

[386] D. G. Angelakis and A. Kay, 'Weaving light-matter qubits into a one way quantum computer', New Journal of Physics 10, 023012 (2008).

[387] J. Cho, D. G. Angelakis, and S. Bose, 'Heralded generation of entanglement with coupled cavities', Phys. Rev. A 78, 022323 (2008).

[388] J. Cho, D. G. Angelakis, and S. Bose, 'Fractional quantum Hall state in coupled cavities', Phys. Rev. Lett. 101, 246809 (2008).

[389] R. M. Wilson, K. W. Mahmud, A. Hu, A. V. Gorshkov, M. Hafezi, and M. Foss-Feig, 'Collective phases of strongly interacting cavity photons', Phys. Rev. A 94, 033801 (2016).

[390] M. Biondi, G. Blatter, H. E. Türeci, and S. Schmidt, 'Nonequilibrium gas-liquid transition in the driven-dissipative photonic lattice', Phys. Rev. A 96, 043809 (2017).

[391] M. X. Huo, Y. Li, Z. Song, and C. P. Sun, 'Atomic entanglement versus visibility of photon interference for quantum criticality of a hybrid system', Phys. Rev. A 77, 022103 (2008).

[392] E. K. Irish, 'Ground-state entanglement in a coupled-cavity model', Phys. Rev. A 80, 043825 (2009).

[393] S. M. Giampaolo and F. Illuminati, 'Long-distance entanglement in many-body atomic and optical systems', New Journal of Physics 12, 025019 (2010).

[394] M. J. Hartmann, F. G. S. L. Brandão, and M. B. Plenio, 'A polaritonic two-component Bose-Hubbard model', New Journal of Physics 10, 033011 (2008).

[395] M. Paternostro, G. S. Agarwal, and M. S. Kim, 'Solitonic behaviour in coupled multi atom–cavity systems', New Journal of Physics 11, 013059 (2009).

[396] S. Schmidt and G. Blatter, 'Strong coupling theory for the Jaynes-Cummings-Hubbard model', Phys. Rev. Lett. 103, 086403 (2009).

[397] E. S. Kyoseva, D. G. Angelakis, and L. C. Kwek, 'A single-interaction step implementation of a quantum search in coupled micro-cavities', EPL (Europhysics Letters) 89, 20005 (2010).

[398] A. A. Houck, H. E. Türeci, and J. Koch, 'On-chip quantum simulation with superconducting circuits', Nature Physics 8, 292–299 (2012).

[399] A. Majumdar, A. Rundquist, M. Bajcsy, V. D. Dasika, S. R. Bank, and J. Vučkovi ć, 'Design and analysis of photonic crystal coupled cavity arrays for quantum simulation', Phys. Rev. B 86, 195312 (2012).

[400] G. Lepert, M. Trupke, M. J. Hartmann, M. B. Plenio, and E. A. Hinds, 'Arrays of waveguide-coupled optical cavities that interact strongly with atoms', New Journal of Physics 13, 113002 (2011).

[401] T. Hümmer, G. M. Reuther, P. Hänggi, and D. Zueco, 'Nonequilibrium phases in hybrid arrays with flux qubits and nitrogen-vacancy centers', Phys. Rev. A 85, 052320 (2012).

[402] W. L. Yang, Z.-q. Yin, Z. X. Chen, S.-P. Kou, M. Feng, and C. H. Oh, 'Quantum simulation of an artificial Abelian gauge field using nitrogen-vacancy-center ensembles coupled to superconducting resonators', Phys. Rev. A 86, 012307 (2012).

[403] J.-B. You, W. L. Yang, Z.-Y. Xu, A. H. Chan, and C. H. Oh, 'Phase transition of light in circuit-QED lattices coupled to nitrogen-vacancy centers in diamond', Phys. Rev. B 90, 195112 (2014).

[404] C. Noh and D. G. Angelakis, 'Quantum simulations and many-body physics with light', Reports on Progress in Physics 80, 016401 (2016).

[405] M. J. Hartmann, 'Quantum simulation with interacting photons', Journal of Optics 18, 104005 (2016).

[406] W. E. Lamb, 'Theory of an optical maser', Phys. Rev. 134, A1429–A1450 (1964).

[407] B. Kneer, T. Wong, K. Vogel, W. P. Schleich, and D. F. Walls, 'Generic model of an atom laser', Phys. Rev. A 58, 4841–4853 (1998).

[408] M. C. Cross and P. C. Hohenberg, 'Pattern formation outside of equilibrium', Rev. Mod. Phys. 65, 851–1112 (1993).

[409] M. Wouters and I. Carusotto, 'Goldstone mode of optical parametric oscillators in planar semiconductor microcavities in the strong-coupling regime', Phys. Rev. A 76, 043807 (2007).

[410] M. T. Portella-Oberli, V. Ciulin, S. Haacke, J.-D. Ganière, P. Kossacki, M. Kutrowski, T. Wojtowicz, and B. Deveaud, 'Diffusion, localization, and dephasing of trions and excitons in CdTe quantum wells', Phys. Rev. B 66, 155305 (2002).

[411] M. Wouters and I. Carusotto, 'Excitations in a nonequilibrium Bose-Einstein condensate of exciton polaritons', Phys. Rev. Lett. 99, 140402 (2007).

[412] K. J. Weingarten, B. Braun, and U. Keller, 'In situ small-signal gain of solid-state lasers determined from relaxation oscillation frequency measurements', Opt. Lett. 19, 1140–1142 (1994).

[413] A. M. Yacomotti, Z. Denis, A. Biella, and C. Ciuti, 'Quantum density matrix theory for a laser without adiabatic elimination of the population inversion: Transition to lasing in the class-B limit', arXiv 2205, 13473 (2022).

[414]A. Biella, F. Storme, J. Lebreuilly, D. Rossini, R. Fazio, I. Carusotto, and C. Ciuti, 'Phase diagram of incoherently driven strongly correlated photonic lattices', Phys. Rev. A **96**, 023839 (2017).

[415]M.-D. Choi, 'Completely positive linear maps on complex matrices', Linear Algebra and its Applications **10**, 285–290 (1975).

[416]A. Jamiołkowski, 'Linear transformations which preserve trace and positive semidefiniteness of operators', Reports on Mathematical Physics **3**, 275–278 (1972).

[417]E. J. Mueller, T.-L. Ho, M. Ueda, and G. Baym, 'Fragmentation of Bose-Einstein condensates', Phys. Rev. A **74**, 033612 (2006).

[418]J. Lebreuilly, M. Wouters, and I. Carusotto, 'Towards strongly correlated photons in arrays of dissipative nonlinear cavities under a frequency-dependent incoherent pumping', Comptes Rendus Physique **17**, 836–860 (2016).

[419]F. Minganti, A. Biella, N. Bartolo, and C. Ciuti, 'Spectral theory of Liouvillians for dissipative phase transitions', Phys. Rev. A **98**, 042118 (2018).

[420]O. Scarlatella, R. Fazio, and M. Schirò, 'Emergent finite frequency criticality of driven-dissipative correlated lattice bosons', Phys. Rev. B **99**, 064511 (2019).

[421]J. Jin, A. Biella, O. Viyuela, L. Mazza, J. Keeling, R. Fazio, and D. Rossini, 'Cluster mean-field approach to the steady-state phase diagram of dissipative spin systems', Phys. Rev. X **6**, 031011 (2016).

[422]J. Jin, A. Biella, O. Viyuela, C. Ciuti, R. Fazio, and D. Rossini, 'Phase diagram of the dissipative quantum Ising model on a square lattice', Phys. Rev. B **98**, 241108 (2018).

[423]B. Grygiel and K. Patucha, 'Excitation spectra of strongly interacting bosons in the flat-band Lieb lattice', arXiv **2207**, 14614 (2022).

[424]T. Ackemann, W. Firth, and G.-L. Oppo, 'Chapter 6 – Fundamentals and applications of spatial dissipative solitons in photonic devices', in *Advances in atomic, molecular, and optical physics*, Vol. 57, Advances in atomic, molecular, and optical physics (Academic Press, 2009), pp. 323–421.

[425]A. Tikan, J. Riemensberger, K. Komagata, S. Hönl, M. Churaev, C. Skehan, H. Guo, R. N. Wang, J. Liu, P. Seidler, and T. J. Kippenberg, 'Emergent nonlinear phenomena in a driven dissipative photonic dimer', Nature Physics **17**, 604–610 (2021).

[426]K. Komagata, A. Tusnin, J. Riemensberger, M. Churaev, H. Guo, A. Tikan, and T. J. Kippenberg, 'Dissipative kerr solitons in a photonic dimer on both sides of exceptional point', Communications Physics **4**, 159 (2021).

[427]C. Jia, R. Wu, Y. Hu, W.-M. Liu, and Z. Liang, 'Dissipative magnetic soliton in a spinor polariton bose–einstein condensate', Frontiers in Physics **9**, 805841 (2021).

[428]N. Pernet, P. St-Jean, D. D. Solnyshkov, G. Malpuech, N. C. Zambon, Q. Fontaine, B. Real, O. Jamadi, A. Lemaître, M. Morassi, L. L. Gratiet, T. Baptiste, A. Harouri, I. Sagnes, A. Amo, S. Ravets, and J. Bloch, 'Gap solitons in a one-dimensional driven-dissipative topological lattice', Nature Physics **18**, 678–684 (2022).

[429]M. Wouters and I. Carusotto, 'Probing the excitation spectrum of polariton condensates', Phys. Rev. B **79**, 125311 (2009).

[430]L. M. Sieberer, M. Buchhold, and S. Diehl, 'Keldysh field theory for driven open quantum systems', Reports on Progress in Physics **79**, 096001 (2016).

[431]O. Scarlatella, A. A. Clerk, and M. Schirò, 'Spectral functions and negative density of states of a driven-dissipative nonlinear quantum resonator', New Journal of Physics **21**, 043040 (2019).

[432]G. C. and Z. P., *Quantum noise* (Springer Berlin, Heidelberg, 2004).

[433]D. Walls and M. G. J., *Quantum optics* (Springer Berlin, Heidelberg, 2008).

[434]C. Ciuti and I. Carusotto, 'Input-output theory of cavities in the ultrastrong coupling regime: The case of time-independent cavity parameters', Phys. Rev. A **74**, 033811 (2006).

[435]A. Chiocchetta, A. Gambassi, and I. Carusotto, 'Laser operation and Bose-Einstein condensation: Analogies and differences', in *Universal themes of bose-einstein condensation* (Cambridge University Press, 2017), pp. 409–423.

[436]E. Arrigoni and A. Dorda, 'Master equations versus Keldysh Green's functions for correlated quantum systems out of equilibrium', in *Out-of-equilibrium physics of correlated electron systems* (Springer International Publishing, 2018), pp. 121–188.

[437]M. Seclì, 'Topology and nonlinearity in driven-dissipative photonic lattices: Semiclassical and quantum approaches', PhD thesis (SISSA - International School for Advanced Studies, Trieste, Sept. 2021).

[438]A. Chiocchetta and I. Carusotto, 'Non-equilibrium quasi-condensates in reduced dimensions', EPL (Europhysics Letters) **102**, 67007 (2013).

[439]Y. Hidaka and Y. Minami, 'Spontaneous symmetry breaking and Nambu-Goldstone modes in open classical and quantum systems', Progress of Theoretical and Experimental Physics **2020**, 033A01 (2020).

[440]A. Loirette-Pelous, I. Amelio, M. Seclì, and I. Carusotto, 'Linearized theory of the fluctuation dynamics in two-dimensional topological lasers', Phys. Rev. A **104**, 053516 (2021).

[441]M. H. Szymańska, J. Keeling, and P. B. Littlewood, 'Nonequilibrium quantum condensation in an incoherently pumped dissipative system', Phys. Rev. Lett. **96**, 230602 (2006).

[442]F. Baboux, D. D. Bernardis, V. Goblot, V. N. Gladilin, C. Gomez, E. Galopin, L. L. Gratiet, A. Lemaître, I. Sagnes, I. Carusotto, M. Wouters, A. Amo, and J. Bloch, 'Unstable and stable regimes of polariton condensation', Optica **5**, 1163–1170 (2018).

[443]O. Scarlatella, A. A. Clerk, R. Fazio, and M. Schirò, 'Dynamical mean-field theory for Markovian open quantum many-body systems', Phys. Rev. X **11**, 031018 (2021).

[444]E. Boukobza and D. J. Tannor, 'Thermodynamic analysis of quantum light amplification', Phys. Rev. A **74**, 063822 (2006).

[445]E. Boukobza and D. J. Tannor, 'Three-level systems as amplifiers and attenuators: A thermodynamic analysis', Phys. Rev. Lett. **98**, 240601 (2007).

[446]J. Marino and S. Diehl, 'Driven Markovian quantum criticality', Phys. Rev. Lett. **116**, 070407 (2016).

[447]J.-B. You, W.-L. Yang, G. Chen, Z.-Y. Xu, L. Wu, C.-E. Png, and M. Feng, 'Optical signatures of Mott-superfluid transition in nitrogen-vacancy centers coupled to photonic crystal cavities', Opt. Lett. **44**, 2081–2084 (2019).

[448]K. Donatella, A. Biella, A. Le Boité, and C. Ciuti, 'Entanglement dynamics in dissipative photonic Mott insulators', Phys. Rev. Research **2**, 043232 (2020).

[449]J. T. Barreiro, M. Müller, P. Schindler, D. Nigg, T. Monz, M. Chwalla, M. Hennrich, C. F. Roos, P. Zoller, and R. Blatt, 'An open-system quantum simulator with trapped ions', Nature **470**, 486–491 (2011).

[450]K. Baumann, C. Guerlin, F. Brennecke, and T. Esslinger, 'Dicke quantum phase transition with a superfluid gas in an optical cavity', Nature **464**, 1301–1306 (2010).

451K. L. Hur, L. Henriet, A. Petrescu, K. Plekhanov, G. Roux, and M. Schiró, 'Many-body quantum electrodynamics networks: Non-equilibrium condensed matter physics with light', Comptes Rendus Physique **17**, 808–835 (2016).

452L. W. Clark, N. Schine, C. Baum, N. Jia, and J. Simon, 'Observation of Laughlin states made of light', Nature **582**, 41–45 (2020).

453D. Huybrechts and M. Wouters, 'Cluster methods for the description of a driven-dissipative spin model', Phys. Rev. A **99**, 043841 (2019).

454K. Mølmer, Y. Castin, and J. Dalibard, 'Monte Carlo wave-function method in quantum optics', J. Opt. Soc. Am. B **10**, 524–538 (1993).

455M. Seclì, M. Capone, and M. Schirò, 'Signatures of self-trapping in the driven-dissipative Bose-Hubbard dimer', New Journal of Physics **23**, 063056 (2021).

456R. Dragila, 'Laser physics and laser instabilities', Laser and Particle Beams **7**, 859–859 (1989).

457Y. Yamamoto, S. Machida, and G. Björk, 'Microcavity semiconductor laser with enhanced spontaneous emission', Phys. Rev. A **44**, 657–668 (1991).

458P. R. Rice and H. J. Carmichael, 'Photon statistics of a cavity-QED laser: A comment on the laser-phase-transition analogy', Phys. Rev. A **50**, 4318–4329 (1994).

459C. Gies, J. Wiersig, M. Lorke, and F. Jahnke, 'Semiconductor model for quantum-dot-based microcavity lasers', Phys. Rev. A **75**, 013803 (2007).

460M. A. Cazalilla, 'Differences between the Tonks regimes in the continuum and on the lattice', Phys. Rev. A **70**, 041604 (2004).

461P. Coleman, *Introduction to many-body physics* (Cambridge University Press, 2015).

462A. C. Olinto, 'Theory of condensates in superfluids', Phys. Rev. B **34**, 6159–6165 (1986).

463A. C. Olinto, 'Unified symmetry-breaking theory of Bose-Einstein condensation in superfluids', Phys. Rev. B **43**, 7737–7748 (1991).

464T. Kita, 'Quantum Field Theory of Correlated Bose–Einstein Condensates: II. Ward–Takahashi Identities and Correlation Functions', Journal of the Physical Society of Japan **90**, 024002 (2021).

465S. Wißmann, A. Karlsson, E.-M. Laine, J. Piilo, and H.-P. Breuer, 'Optimal state pairs for non-Markovian quantum dynamics', Phys. Rev. A **86**, 062108 (2012).

466R. Balakrishnan, I. I. Satija, and C. W. Clark, 'Particle-hole asymmetry and brightening of solitons in a strongly repulsive Bose-Einstein condensate', Phys. Rev. Lett. **103**, 230403 (2009).

Notation and Physical Constants

$\hat{b}_{\alpha,\mathbf{k}}$ Annihilation operator of the collective mode α with momentum $\mathbf{k}$

$\hbar$ Planck constant

c.c.   complex conjugate

H.c.   Hermitian conjugate

μ Chemical potential

$\omega_{\alpha,\mathbf{k}}$ Excitation energy of the collective mode α with momentum $\mathbf{k}$

$\omega_{\mathrm{Bog},\mathbf{k}}$ Excitation energy of the Bogoliubov-Goldstone mode with momentum $\mathbf{k}$

a Lattice spacing

c_i Speed of sound of the mode i

f_s Superfluid fraction

i Imaginary unit

m Bare particle mass on a lattice

n_s Superfluid density

U Bare value of the Hubbard interaction energy

V Lattice volume

z Lattice coordination number ($z = 2\,d$)

Greek Letters with Pronunciations

Character	Name	Character	Pronounciation
α, A	alpha *AL-fuh*	ν, N	nu *NEW*
β, B	beta *BAY-tuh*	ξ, Ξ	xi *KSIGH*
γ, Γ	gamma *GAM-muh*	o, O	omicron *OM-uh-CRON*
δ, Δ	delta *DEL-tuh*	π, Π	pi *PIE*
ϵ, E	epsilon *EP-suh-lon*	ρ, R	rho *ROW*
ζ, Z	zeta *ZAY-tuh*	σ, Σ	sigma *SIG-muh*
η, H	eta *AY-tuh*	τ, T	tau *TOW (as in "cow")*
θ, Θ	theta *THAY-tuh*	υ, Υ	upsilon *OOP-suh-LON*
ι, I	iota *eye-OH-tuh*	ϕ, Φ	phi *FEE, or FI (as in "hi")*
κ, K	kappa *KAP-uh*	χ, X	chi *KI (as in "hi")*
λ, Λ	lambda *LAM-duh*	ψ, Ψ	psi *SIGH, or PSIGH*
μ, M	mu *MEW*	ω, Ω	omega *oh-MAY-guh*

Acronyms and Special Terms

AB
    Andreev-Bashkin. 43

BdG
    Bogoliubov-de Gennes. 26

BEC
    Bose-Einstein Condensate. 3

BH
    Bose-Hubbard. 3

BLP
    Breuer-Laine-Piilo. 63

BR
    Brinkman-Rice. 106

BZ
    Brillouin Zone. 7

CFSF
    Counterflow Superfluid. 25

CI
    Commensurate-Incommensurate. 6

C-QED
    Circuit Quantum Electodynamics. 141

DMFT
    Dynamical Mean-Field Theory. 4

DoF
    Degrees of Freedom. 9

DoS
    Density of States. 20

FDT
    Fluctuation-Dissipation Theorem. 38

FGR
    Fermi Golden Rule. 20

FH
    Fermi-Hubbard. 102

FWM
    Four-Wave Mixing. 167

GA
    Gutzwiller Approximation. 100

GPE
    Gross-Pitaevskii Equation. 5

HCSF
    Hard-Core Superfluid. 66

List of Figures